Over the Top:

from $t\bar{t}$ measurements to the search for the associated production of the Higgs boson and a top quark pair with the ATLAS detector

Valerio Dao

Valerio Dao, 2014
Thesis, Radboud Universiteit Nijmegen
ISBN: 978-94-6259-429-6
Printed by Ipskamp Drukkers, Enschede www.ipskampdrukkers.nl
Cover design by Javier ("El Monty") Montejo Berlingen
Image credits to *Rdevany* at the English Wikipedia:
South-West side of Mt. Everest.

This work is part of the research programme of the Foundation for Fundamental Research on Matter (FOM), which is part of the Netherlands Organisation for Scientific Research (NWO).

Over the Top:

from $t\bar{t}$ measurements to the search for the associated production of the Higgs boson and a top quark pair with the ATLAS detector

Proefschrift

ter verkrijging van de graad van doctor
aan de Radboud Universiteit Nijmegen
op gezag van de rector magnificus prof. dr. Th.L.M. Engelen,
volgens besluit van het college van decanen
in het openbaar te verdedigen op dinsdag 25 november 2014
om 10:30 uur precies

door

Valerio Dao

geboren op 1 maart 1983
in Genua, Italië

Promotor:	Prof. dr. N. de Groot
Copromotor:	Dr. F. Filthaut
Manuscriptcommissie:	Prof. dr. A.N.J.J. Schellekens (voorzitter)
	Prof. dr. M. Merk - Vrije Universiteit Amsterdam
	Prof. dr. F.L. Linde - Universiteit van Amsterdam
	Dr. C.W.J.P. Timmermans
	Dr. P. Ferrari - Nikhef

Over the Top:

from $t\bar{t}$ measurements to the search for the associated production of the Higgs boson and a top quark pair with the ATLAS detector

Doctoral thesis

to obtain the degree of doctor
from Radboud University Nijmegen
on the authority of the Rector Magnificus prof. dr. Th.L.M. Engelen,
according to the decision of the Council of Deans
to be defended in public on Tuesday, November 25, 2014
at 10:30 hrs.

by

Valerio Dao

born on March 1, 1983
in Genova, Italy

Supervisor:	Prof. dr. N. de Groot
Co-supervisor:	Dr. F. Filthaut
Doctoral Thesis Committee:	Prof. dr. A.N.J.J. Schellekens (chair)
	Prof. dr. M. Merk - VU University
	Prof. dr. F.L. Linde - University of Amsterdam
	Dr. C.W.J.P. Timmermans
	Dr. P. Ferrari - Nikhef

Contents

Introduction

"Fatti non foste a viver come bruti, ma per seguir virtute e canoscienza"[1]; with these famous words in the early fourteenth century, Dante Alighieri described in a poem the wish of mankind to constantly seek a better understanding of the world in which we live. With time, this attitude has led to the formulation of the so-called *scientific method*; it is based on the formulation of an initial hypothesis aiming at explaining particular observations. From the hypothesis, a set of predictions is derived and new experiments are performed to test the validity of the predictions in order to accept or reject the initial hypothesis.

The formulation of the hypothesis often follows the path of attempting to reduce the complexity of the nature that surrounds us, to a set of simpler and more elementary principles. This is one of the primary tasks of particle physics; to identify the fundamental elementary constituents of matter, the rules that govern them and, ultimately, how they are organised to form the matter we see everyday.

In the last 150 years, a continuous application of the scientific method, coupled to increasingly refined experimental techniques and apparatus, have led to a significant breakthrough of our understanding of the fundamental laws of physics. This was accompanied by a change in what are considered the 'elementary' constituents of matter: from atoms to electrons and nuclei, and from protons and neutrons to quarks.

To date, the best knowledge of the fundamental particle physics landscape is represented by the Standard Model: a theoretical framework allowing to elegantly describe the properties of the fundamental particles and their interactions. While the Standard Model has been found to agree with experimental results to an impressive level of accuracy, additional theories, generally referred to as beyond the Standard Model (BSM) have been developed to extend the current framework. As happened in the past, only more precise tests of the predictions from the Standard Model could allow to rule out these newly proposed models or keep them still plausible. This is one of the purposes for which the Large Hadron Collider, the world's largest particle accelerator was built at CERN. It largely exceeds the reach of previous colliders both in energy and intensity, allowing to explore corners of parameter space previously inaccessible. It also makes possible a sensitivity to very rare physics phenomena. With the main goal of finding the Standard Model Higgs boson, the data provided by the LHC constitute an unprecedented test bench for the Standard Model predictions and its capability to describe data; any discrepancy could be the revealing indication for the effect of a more comprehensive theory.

The LHC is now in its technical stop phase after having provided collision data for three years. As more data were collected, the scope and the complexity of the physics analyses rapidly evolved. Very early collisions were used to assess the correct performance of the experiments and the reconstruction of the physics objects. An important milestone was the first measurement (or "rediscovery") of basic processes in the Standard Model at the new energy regime

[1]Dante Alighieri, *Inferno*, ch 26, vv. 119-120: "You were not made to live as brutes, but to follow virtue and knowledge." (personal translation by the thesis author).

of the LHC. After the first two years of data-taking, the amount of data collected was sufficient to perform precise measurements of Standard Model processes. Other than probing the theoretical predictions in uncovered regions of the phase space, these measurement represent a crucial ingredient in the search for BSM contributions where a good control over background is mandatory to establish the presence of an unexpected signal. Finally, the further increase of centre-of-mass energy and amount of raw data in the 2012 dataset represents the ideal ground for the search for new and rare phenomena.

A similar path has been followed in the content of this thesis work; for each of the three data taking years, a different analysis has been performed by the author using the data collected by the ATLAS detector, one of the two multipurpose detectors installed in the LHC ring. The common denominator among the analyses is the presence of a top quark pair in the final state.

Since its discovery in 1995, the top quark has played a central role in particle physics. It is the heaviest known fundamental particle, and in many BSM physics scenarios, it is supposed to have significant interplay with possible new, yet-undiscovered, particles. Given its mass, the LHC is the second collider where the top quark can be produced; the higher LHC centre-of-mass energy leads to a significant increase of the top quark pair production cross section. Also referred to as a "top-factory", the LHC has turned the top quark from an elusive particle into a powerful tool to perform precise measurements as well as to look for new physics scenarios,

With the first year of LHC data, the first milestone was represented by the measurement of the $t\bar{t}$ production at the new LHC energy scale. This proved to be a crucial step in the physics programme, to establish the performance of the detector as well as establish the ground for precise measurements. This thesis contains a description of the measurement of the inclusive $t\bar{t}$ cross section using a final state with exactly one lepton and multiple jets. The analysis was performed using the full 2010 dataset, adopting a robust template fitting technique for the signal extraction.

During 2011, steady operation of the accelerator allowed the LHC experiments to collect the world's largest sample of top anti-top pairs, which opened the era of precision physics in the top sector. Beyond the measurement of the inclusive cross section, probing the kinematic properties of $t\bar{t}$ events to fine accuracy is a way to challenge the theoretical predictions of the Standard Model to a scale not reached before and, at the same time, improve the understanding of backgrounds for future searches. A measurement of the jet multiplicity distribution in $t\bar{t}$ events has been performed using the full dataset collected by ATLAS during 2011. The choice of this topic is twofold; theoretical predictions of $t\bar{t}$+jets final states are particularly complex and sensitive to the contribution from multiple aspects of the event generation (properties of additional radiation, $t\bar{t}$ kinematics, fragmentation model). At the same time, many BSM physics scenarios or rare processes in the Standard Model contain events with a large number of particles in the final state, for which $t\bar{t}$+jets events represent the main background.

A precise measurement of the jet multiplicity distribution will provide important input to test our understanding of high energy QCD predictions, as well as to compare and ultimately to 'tune' the behaviour of the different Monte Carlo generators. An improved understanding of the systematics related to the modelling of the main background will also boost the sensitivity of most searches.

The analysis has been performed using the single lepton plus jets final state. The result has been corrected for all the detector effects with the aim of comparing with the prediction from Monte Carlo generators, which implement different approaches to the theoretical calculations of the $t\bar{t}$ process.

On the 4th of July 2012, the ATLAS and CMS collaboration announced the discovery of a new particle highly compatible with the Standard Model Higgs boson. The discovery completed a 48 year long search for the missing piece in the Standard model, which also motivated the very same construction of the LHC. At the same time, that date marked the beginning of a new range of analyses aiming at better characterising the newly discovered particle. Notably, its couplings to other known fundamental particles can be probed using a wealth of data. This allows for stringent comparisons with their Standard Model predictions and contributions from processes predicted by new theories. In this context, the measurement of the associated production of the Higgs boson in association with a top quark pair ($t\bar{t}H$), is of particular importance since it gives direct insight in the coupling between the Higgs boson and the top quark; a preferred place where new physics contributions can arise according to many models.

The measurement of this particular production mode is complicated by the extremely low cross section (200 times smaller than the inclusive Higgs boson production) and the large number of particles in the final state. The search for evidence for the $t\bar{t}H$ production mode constitutes the final main topic of this thesis; the final state where the Higgs boson decays into a $b\bar{b}$ pair and one of the top quarks produces an isolated lepton are considered. This choice maximises the number of expected signal events although it allows for a larger background contamination compared to other Higgs boson decay modes; the main background is indeed represented by the production of $t\bar{t}$ with additional jets. With its increase in the centre-of-mass energy and 4 times more data, the 2012 dataset allows to improve the sensitivity to rare processes substantially. At the same time, the analysis profits from the improved understanding of detector performance effects after three years of data-taking, and uses as a solid ground previous $t\bar{t}$ measurements performed at 7 TeV, which strengthens the confidence in a correct modelling of other background processes from the Standard Model.

Given the complexity and the topology of the final state, no single kinematic variable displays sufficient discrimination power between the signal and the background. Furthermore, a kinematic reconstruction of the $t\bar{t}H$ decay chain in the events has proven to be highly inefficient. For these reasons, a multivariate approach has been employed to better separate the signal from the backgrounds as it allows to take into account several kinematic quantities in the event and their correlations, as well as information from a partial reconstruction of the event topology. At the same time, multiple signal and control regions are exploited in order to increase the sensitivity to such a small signal and reduce the impact of the uncertainties from the estimation of the backgrounds.

The content of this thesis is organised as follows. The level of detail in the chapters describing each physics analysis reflects the specific contribution given by the author.

Chapter 1 gives an overview of the physics landscape at the LHC, with particular focus on the formalism used to describe high energy collision events as well as phenomenological aspects of $t\bar{t}$ and Higgs boson production. The 'raw' material for the presented analyses is described in Chapter 2: the world's largest particle accelerator, the Large hadron Collider, and the ATLAS detector. Chapter 3 outlines the reconstruction and identification of physics objects, such as charged leptons, jets and non interacting particles. A detailed description of the ATLAS trigger system is given in Chapter 4 with particular attention on the commissioning of the electron triggers.

Chapter 5 collects information on common aspects to all the presented analyses; the basic aspects of the event selection for $t\bar{t}$ events and the description of the estimation of the non-$t\bar{t}$ backgrounds. The description of the inclusive $t\bar{t}$ cross section using the 2010 dataset is presented in Chapter 6. Chapter 7 contains the description of the jet multiplicity distribution in $t\bar{t}$ events using the 2011 dataset.

Finally, the main topic of this thesis, the search for the Standard Model Higgs boson produced in association with a top quark pair and decaying into $b\bar{b}$ is outlined in Chapters 8, 9 and 10. They deal with the general description of the analysis ingredients and strategy, a detailed description of the multivariate technique used to extract the signal from data, and the statistical interpretation leading to the final result.

Chapter 1

Physics at the LHC

The role of particle physics is to investigate and describe the structure of the constituents of matter as wehll as the forces that act among them. The aim is to unveil the fundamental laws that allow to describe the observed phenomena in a coherent manner.

The Standard Model (SM) is, as of today, the theory that best summarises our current knowledge of the particle physics world, encompassing the three of the four fundamental interactions in a unique mathematical description. Thirty years of precision measurements performed at the LEP and Tevatron colliders have consolidated the capability of the SM to describe the observations and to 'accommodate' newly discovered particles. The Large Hadron Collider (LHC) at CERN represents the new testing ground for the Standard Model. With a collision energy and intensity significantly exceeding those of previous colliders, the data collected at the LHC allow to probe the predictions of the SM to an unprecedented level of accuracy as well as to explore an energy regime previously accessible only with cosmic rays. The main goal is to investigate the properties of the Higgs boson, the last 'piece' in the SM predicted by the mechanism which is responsible for the generation of the particle masses, At the same time, searches are performed for possible extension produced by new physics models than can manifest themselves with high energy signatures.
The scope of this chapter is to discuss the theoretical foundation of this thesis work. A brief outline of the Standard Model will be given. Particular emphasis will be put on the description of the Higgs mechanism and its implication in the phenomenology at the LHC. Finally an overview of the theory of $t\bar{t}$ production will also be presented.

1.1 The Standard Model of particle physics

The Standard Model is a theoretical framework that describes the interaction among the constituents of matter (*fermions*) through the exchange of 'force carrier' particles (*bosons*). The particles are treated as 'field quanta' and the mathematical description of the interactions 'naturally' arises from a given principle: the invariance of the Lagrangian under a local gauge transformation of given symmetry group [1]. A local gauge transformation implies that the considered fields vary differently at any point in space-time.

As for the case of classical mechanics where the invariance under displacements and time leads to the conservation of the momentum and energy, the requirement of gauge invariance leads to a conserved quantity (charge) [2] and to the introduction to a number of gauge bosons, which only interact with fields carrying some of the conserved charge. An example can be made considering the electromagnetic interactions described by Quantum Electrodynamics (QED) [3]; the requirement that the Lagrangian be invariant under a local phase transformation of the electron field leads to the introduction in the theory of a vector boson, the photon, as well as a conserved electrical charge. In general the number of vector bosons, the type of conserved charge and the nature of the interaction depend on the symmetry group the gauge transformation belongs to.

The model is completely specified once the symmetries are known and the particles have been assigned to a given representation of the symmetry groups. From the Lagrangian, the interactions among particles can be deduced (*Feynman's rules*) and from there, general observables (cross sections, branching ratios) can be computed using perturbation theory.
In the Standard Model the gauge symmetry group is: $SU(3)_C \otimes SU(2)_L \otimes U(1)_Y$ allowing to give a coherent description of the strong, weak and electromagnetic interactions.

- $SU(3)_C$ is the non-abelian group describing the strong interactions, also known as *Quantum Chromo Dynamics* (QCD) [3]. 'C' stands for the conserved charge of the interaction referred to as *colour*. The Lie algebra of the group [1] implies 8 massless generators known as *gluons*. The coupling constant relating the gluons to the quarks is referred to as g_s.

- $SU(2)_L$ represents the chiral symmetry describing the weak interactions. It is a non-abelian group with coupling g, which is mediated by three vector bosons: W^1, W^2 and W^3. The suffix 'L' indicates that the vector bosons only couple to the left handed component of the fermions[1]. The conserved quantity of the group is the weak isospin $\overrightarrow{I}$.

- $U(1)_Y$ is an abelian group with coupling g' mediated by a single vector boson B. The conserved charge is also known as *hypercharge* (Y).

$SU(2)_L \otimes U(1)_Y$ is the group proposed by Glashow, Salam and Weinberg [4] [5] in the 60s in order to achieve a unification of the electromagnetic and weak interactions. The electromagnetic interaction is described by the symmetry group $U(1)_Q$ whose mediator is the *photon* (γ). The photon does not distinguish between left-handed and right-handed fermions and interacts with all the particles with electric charge Q. Q is related to the quantum number of the other groups by the following relation:

$$Q = I_3 + \frac{Y}{2} \tag{1.1}$$

where I_3 represents the third component of the weak isospin. It is possible to re-define the vector boson of $SU(2)_L \otimes U(1)_Y$ as:

$$B = A \cos(\theta_W) - Z \sin(\theta_W), \tag{1.2}$$

$$W^3 = A \sin(\theta_W) + Z \cos(\theta_W) \tag{1.3}$$

where A represents a neutral boson with the specific interactions of the photon if the mixing angle and the coupling constants respect the following relations:

$$g \sin\theta_W = g' \cos\theta_W = e, \tag{1.4}$$

where e is the coupling constant of the electromagnetic force. The Z is another neutral boson with a different coupling to the left and right-handed fermion components. The remaining force carriers of the weak interaction can be rearranged as a linear combination of W^1 and W^2 in order to define two electrically charged bosons:

$$W^{\pm} = \frac{1}{\sqrt{2}}(W^1 \mp iW^2) \tag{1.5}$$

[1]Fermion fields are described by spinors containing four components. The right handed component is obtained by the action of the operator $(1 - \gamma_5)/2$; the left handed component is obtained from the $(1 + \gamma_5)/2$ operator.

Table 1.1 summarises the properties of the vector bosons for each interaction. As it has been experimentally observed, the neutral and charged weak bosons (Z, $W^{\pm}$) are massive and this accounts for the short distance nature of the weak interactions at low energies. For energies $\ll m_W$, the picture of the interaction between fermions mediated by a vector boson could be approximated by a direct fermions to fermions interaction, as originally postulated by Fermi. The effective coupling is suppressed by the mass of the boson in the propagator.

interaction	boson	charge Q	mass (GeV)
electromagnetic	γ	0	0
weak	$W^{\pm}$	± 1	80.385 ± 0.015
	Z	0	91.188 ± 0.002
strong	*gluons*	0	0

Table 1.1: Gauge bosons in the Standard Model. The masses for the weak bosons are taken from [6] .

Table 1.2 summarises the information on the fermions in the Standard Model. Fermions are elementary particles of spin 1/2; they can be arranged in three families with a striking mass hierarchy. Each family contains a charged lepton, a neutral lepton (neutrino) and two quarks with fractional electrical charges. With the exception of the first generation, within each family the particle masses increases from the neutral lepton to the positively charged quark. Stable matter in the universe is composed solely of particles from the first generation. The interactions that each particle is subject to are related to its quantum numbers which are specified by its representations in the symmetry group. Quarks are the only fermions subject to strong interactions; they carry an additional colour charge with three possible states ("red", "green", "blue") which allow the exchange of gluons. As already anticipated, only electrically charged particles interact with the photon. For what concerns the weak interactions, the left-handed fermions form weak isospin doublets of leptons (L) and quarks (Q):

$$L^i = \begin{pmatrix} \nu^i \\ l^i \end{pmatrix}_L \ , \quad Q^i = \begin{pmatrix} u^i \\ d^i \end{pmatrix}_L \ , \quad u^i_R \ , \quad d^i_R \ , \quad l^i_R \quad , \quad \text{with } i = 1, 2, 3 \tag{1.6}$$

The right-handed fermions belong to the trivial representation of $SU(2)_L$ (isospin singlet) and do not interact with the charged weak bosons. The Standard Model does not contain right-handed neutrinos since these particles are not involved in any interaction.

family	leptons			quarks		
	flavour	charge (e)	mass (GeV)	flavour	charge (e)	mass (GeV)
1st	ν_e	0	$< 3 \cdot 10^{-9}$	u (up)	2/3	$1.5 \div 4 \cdot 10^{-3}$
	e	-1	$511 \cdot 10^{-6}$	d (down)	-1/3	$4 \div 8 \cdot 10^{-3}$
2nd	ν_μ	0	$< 0.19 \cdot 10^{-3}$	c (charme)	2/3	$1.15 \div 1.35$
	μ	-1	$113.4 \cdot 10^{-3}$	s (strange)	-1/3	$0.08 \div 0.13$
3rd	ν_τ	0	< 0.018	t (top)	2/3	173.1
	τ	-1	1.777	b (bottom)	-1/3	$4.1 \div 4.7$

Table 1.2: Fermions in the Standard Model

Electroweak symmetry breaking

When basing the construction of the Standard Model on symmetries (gauge symmetry for bosons, chiral symmetry for fermions), one of the striking conclusions is that all the particles in the model should be massless; an explicit mass term in the Lagrangian both for bosons and fermions would in fact violate the local invariance. Nevertheless, experimental measurements have shown that both quarks and three of the electroweak gauge bosons are massive.

The simplest and most elegant way to solve this issue is through so-called *spontaneous symmetry breaking* in which the Lagrangian (and thus the interaction) remains invariant under the symmetry group, but the physical states, especially the ground state, are not. To this end a new field, the Higgs field, is introduced in the theory and this allows the other particles to acquire mass by interacting with it [7, 8].

In particular, for electroweak interactions, an isospin doublet of complex scalar fields (corresponding to four new degrees of freedom) is considered:

$$\Phi = \begin{pmatrix} \Phi_1 \\ \Phi_2 \end{pmatrix} \tag{1.7}$$

The most general[2] contribution of this term to the Lagrangian describing the dynamic and the interaction of this field can be expressed as:

$$\mathcal{L}_{\text{Higgs}} = (D_\mu \Phi)\,(D^\mu \Phi)^\dagger - V(\Phi) \quad \text{with} \quad V(\Phi) = \mu^2 \Phi^\dagger \Phi + \lambda (\Phi^\dagger \Phi)^2 \tag{1.8}$$

where D_μ represents the covariant derivative which implements the local electroweak gauge invariance. It is defined as:

$$D_\mu = \left(\partial_\mu - igW_\mu^i I_i - ig'\frac{Y}{2}B_\mu\right) \tag{1.9}$$

The spontaneous symmetry breaking is based on the non-invariance of the vacuum state with respect to the $SU(2)$ symmetry. When μ^2 and λ in Equation 1.8 are both positive, the minimum of the potential is found in the unique configuration $\Phi = 0$. For $\mu^2 < 0$, the minimum of the potential $V(\Phi)$ is described by an infinite number of solutions satisfying: $|\Phi_1|^2 + |\Phi_1|^2 = -\frac{\mu^2}{2\lambda}$. The value of the field in the minimum of the potential is also known as *vacuum expectation value*. It is the choice of any of this particular ground state configurations that produces the apparent 'symmetry breaking'. The theory can be then derived in a perturbative way around the new minimum configuration. Through a suitable rotation and re-parameterisation of the field[3], Φ can be re-defined as:

$$\Phi = \frac{1}{\sqrt{2}} \begin{pmatrix} 0 \\ v + H(x) \end{pmatrix} \tag{1.10}$$

where H is a scalar field with zero vacuum-expectation value, corresponding to the physical Higgs boson, and $v = \sqrt{-\mu^2/2\lambda}$. The ground state configuration $\Phi = 1/\sqrt{2}(0, v)^T$ has been chosen in order to respect the $U(1)_Q$ symmetry and thus does not generate a mass term for the photon. In this respect the hypercharge of the doublet is set to 1 so that, following relation 1.1, the scalar field H does not carry any electrical charge,

By substituting expression 1.10 in the covariant derivative of the Lagrangian (Equation 1.8), this gives rise to terms proportional to $W_\mu^+ W^{-\mu}$ and $Z_\mu Z^\mu$ which introduces explicit mass terms

[2] Terms containing odd powers of Φ can be discarded through symmetry considerations while terms containing Φ^6 or higher violate power counting, making the theory non renormalisable.

[3] Three of the four degrees of freedom of Φ can be re-absorbed by a suitable gauge transformation [9].

for the corresponding vector bosons. The three initial components of the additional scalar field have been absorbed by the bosons $W^{\pm}$ and Z creating longitudinal degrees of freedom. The masses for the vector bosons can be all expressed in terms of v and the $SU(2)_L \otimes U(1)_Y$ coupling constants:

$$m_W = \frac{1}{2} v g \quad , \quad m_Z = \frac{1}{2} \frac{vg}{\cos\theta_W} = \frac{1}{2} v \sqrt{g^2 + g'^2} \tag{1.11}$$

The mass of the Higgs boson particle derived from the expansion of the scalar potential is:

$$m_H = \sqrt{2\lambda} v \tag{1.12}$$

and represents one of the free parameters of the model given its dependence on λ.

The same scalar doublet used to generate the masses of the vector bosons is also sufficient to generate the masses for lepton and quarks. A generic interaction term between the scalar doublet and the fermion fields can be introduced:

$$\mathcal{L}_{\text{Yukawa}} = -\Gamma_u^{ij} \overline{Q_L^i} \epsilon \Phi^* u_R^j - \Gamma_d^{ij} \overline{Q_L^i} \Phi d_R^j - \Gamma_e^{ij} \overline{L_L^i} \Phi e_R^j + h.c. \tag{1.13}$$

where Γ_u^{ij}, Γ_d^{ij} and Γ_e^{ij} are generic 3×3 matrices that mix the contribution of the three fermion families; ϵ is the total antisymmetric tensor in two dimensions.

When applying Equation 1.10, the Yukawa term can be cast into:

$$\mathcal{L}_{\text{Yukawa}} = -\frac{1}{\sqrt{2}}(v+H) \cdot [h_l^i(\overline{e_L^i} e_R^i + \overline{e_R^i} e_L^i) + h_u^i(\overline{u_L^i} u_R^i + \overline{u_R^i} u_L^i) + h_d^i(\overline{d_L^i} d_R^i + \overline{d_R^i} d_L^i)] \tag{1.14}$$

giving rise to both a mass term for the fermions ($m_f = v h_f^i / \sqrt{2}$) and an interaction term between the fermions and the scalar Higgs boson. Both terms are controlled by the so-called Yukawa coupling h_f^i, demonstrating that the interaction of the Higgs boson with the fermions is proportional to the fermion masses. Equation 1.14 has been obtained by a suitable re-definition of the fermion fields that diagonalises the Γ matrices (fermions are then expressed in the mass eigenstate bases). The Yukawa couplings are thus the eigenvalue of these matrices.

In the leptonic channel this transformation has no effect given the absence of right-handed neutrinos, while in the quark sector, the rotation to the mass eigenstate basis introduces a mixing among fermion families which is manifest in the weak interactions. The mixing between the weak eigenstates of the down-type quarks[4] d', s' and b', and the corresponding mass eigenstates d, s and b, is described by the Cabibbo-Kobayashi-Maskawa (CKM) matrix [10][11]:

$$\begin{pmatrix} d' \\ s' \\ b' \end{pmatrix} = \begin{pmatrix} V_{ud} & V_{us} & V_{ub} \\ V_{cd} & V_{cs} & V_{cb} \\ V_{tb} & V_{tb} & V_{tb} \end{pmatrix} \begin{pmatrix} d \\ s \\ b \end{pmatrix} \tag{1.15}$$

Non-diagonal elements of the CKM matrix have the result that the W boson can couple to two quark belonging to two different families. The CKM matrix is fully specified by 4 parameters: 3 *mixing angles* controlling the mixing between each family pair and 1 *complex phase* responsible for CP-violating phenomena [9].

Quantum Chromo Dynamics

Although they can be described by similar mathematical formulations, electro-weak and strong interactions possess a quite different phenomenology which is ultimately driven by the different symmetry groups that govern them.

[4]By convention, the mixing takes place between down-type quarks only, while the up-type mass matrix is diagonal.

The suggestion of the $SU(3)_C$ symmetry group for QCD was mainly driven by the experimental evidence of an additional colour charge to explain the observation of particular hadrons (Δ^{++},Ω^{-}), together with the fact that only colourless bound states of quarks are found in nature: baryons which consist of the combination of three quarks and mesons composed of a quark and an anti-quark.

Contrary to the photon which is electrically neutral, gluons carry colour charge so they can interact among themselves. This has an effect on the way the strong coupling constant[5] $\alpha_S$evolves as a function of the energy (or distance). In quantum field theory the coupling constant is defined in an energy dependent way in order to account for divergencies arising when computing higher order loop corrections to the observables. In the case of QCD the full expression for α_S is given by [3]:

$$\alpha_S(Q^2) = \frac{12\pi}{(33 - 2n_f) \cdot \log(\frac{Q^2}{\Lambda^2_{QCD}})} \tag{1.16}$$

where n_f is the number of 'active flavour' quarks ($m_q < Q$) and the coefficient takes into account all possible interactions including the $g \to gg$ diagram.

As Eq. 1.16 suggests, the effective coupling is decreasing with increasing energy (or decreasing distance). In the high energy physics regime, α_S is sufficiently small that observables can be computed using perturbation theory, which gives very good mathematical properties and predictive power to the theory. This phenomenon is known to as *asymptotic freedom* [12], and it is particularly important in the definition and computability of cross sections at hadron colliders.

On the other hand, at lower energies or larger distances the α_S increases. This property is known as *confinement*: quarks and gluons, which always carry colour charge, cannot appear as free particles. Since the coupling increases with the distance, when trying to separate two quarks, the potential energy increases to a point when it becomes energetically preferable to create another pair of quarks with opposite colour charge from the vacuum; these quarks then create new bound states with the two initial quarks. This fact has the important experimental consequence that quarks produced in high energy particles interactions manifest themselves as collimated streams of hadrons called "jets". The process through which a quark evolves into a jet is usually referred to as *fragmentation* and will be addressed in more detail in Section 1.2.

At low energies the coupling increases to the point where the perturbation approximation is no longer valid and the quantum field theory approach cannot be used to compute observables. In general the value of $\Lambda_{QCD} \sim 200$ MeV is adopted as a cut-off scale for the perturbative definition of the running coupling constant. At energy scales lower than Λ_{QCD} numerical (*lattice QCD*) or phenomenological (hadronisation models) approaches have to be used in order to describe the processes.

In summary, the SM is a unitary, renormalisable theory, which can be used to perturbatively calculate processes at high energies. It incorporates 18 parameters that have to be provided through measurements:

- 3 coupling constants g_s, g, g' for $SU(3)_C$, $SU(2)_L$ and $U(1)_Y$;
- 2 parameters from EWSB: v and m_H;
- 9 Yukawa couplings for the fermion masses;
- 4 parameters for the CKM mixing matrix.

[5]α_S is related to the strong coupling constant g_s by the relation α_S=$g_s^2/4\pi$

1.1.1 Tests of the Standard Model and the discovery of the Higgs boson

The great success and popularity of the Standard Model not only derives from its description of three of the fundamental forces of nature based on similar mathematical principles, but mainly from its capability to describe accurately the experimental observations. Since a few years after its formulation in the 70s, the Standard Model distinguished itself by its high predictive power and a flexibility to accommodate new phenomena and particles that have been discovered afterwards.

The first case is represented by the observation at CERN of the neutral current processes with an intensity similar to that expected by the Z boson mediation[13]. Subsequently, the fundamental particles discovered in the 70s and 80s, the charm and bottom quarks [14], the τ [15] lepton and its respective neutrino, found a natural placement in the quark and lepton families. In particular, the discovery of a third quark family to which the b quark should belong, provided a natural mechanism for CP violation through the complex phase of the CKM matrix[6]. The vector gauge bosons W, Z were discovered at the CERN S$p\bar{p}$S collider in 1983[16].

In the theoretical framework of the Standard Model, physics observables can be computed using perturbation theory and higher order corrections arise from loop diagrams. Starting from the LEP experiments, many precision measurements of Standard Model quantities have been performed and together with accurate theoretical calculations of radiative corrections, they allow for a detailed test of the Standard Model performed through the so-called *electroweak fit*. The electroweak fit is used to test the consistency of the model with the measurements as well as for extracting indirect constraints on unknown parameters. For instance, massive particles can enter loop contributions as virtual states so they can manifest themselves even in energy regimes that do not allow a direct production. This is the case for the top quark, discovered in 1995 [17] at the Tevatron, whose mass was precisely predicted from radiative corrections to the W boson mass and the $Z \to b\bar{b}$ branching ratio.

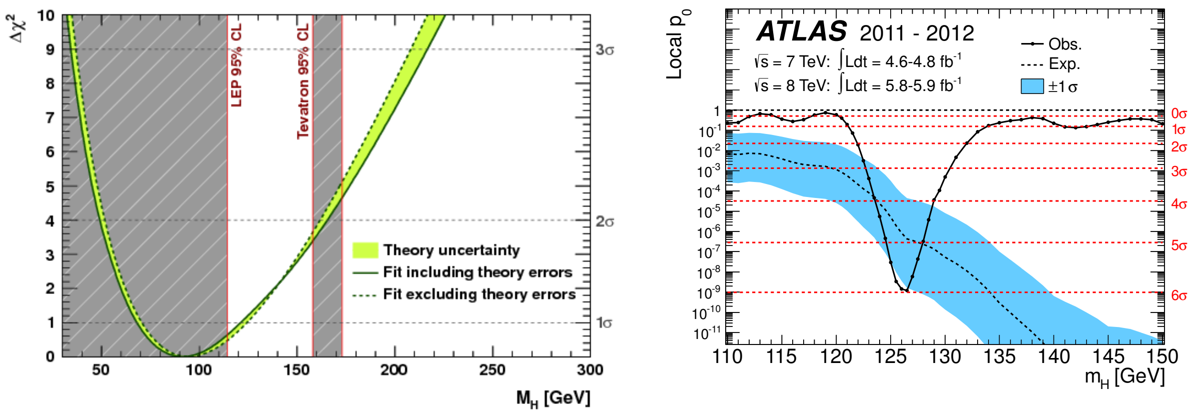

(a) (b)

Figure 1.1: (a) $\Delta\chi^2$ as a function of m_H for the electroweak fit. (b) The observed (solid) local significance of the Higgs signal measured by the ATLAS detector as a function of m_H.

In the case of the top quark, the loop-induced effects depend quadratically on the quark mass, while in the case of the Higgs boson the dependence is only logarithmic. A weaker indirect bound on the Higgs mass is then expected from precision measurements. Figure 1.1 (a) shows

[6] for a number of families smaller than three, no complex phase is present in the mixing matrix

the value of the variation of the χ^2 of the fit with respect to its minimal value as a function of the Higgs boson mass.

The curve was obtained considering only 'indirect' inputs from SM measurements up to the year 2011; the regions excluded by direct searches performed at the LEP and Tevatron colliders are also shown [18].

The last piece of the Standard Model was completed on the 4th of July 2012, when both the ATLAS and CMS collaboration at the LHC announced the observation of a new particle compatible with the Higgs boson hypothesis. Figure 1.1 (b) shows the significance of the excess in data with respect to the background-only hypothesis as a function of m_H from the ATLAS experiment [19]. The discovery was driven by the bosonic decay modes of the Higgs boson and the mass of the new particle was found to be $\sim$ 125 GeV, well within the mass interval allowed by the indirect constraint of the electroweak fit.

With additional data, further measurements of the newly discovered particle did not show any significant deviation from a SM Higgs boson-like behaviour. The particle has been confirmed to be a scalar and a positive CP eigenstate [20]. The mass of the particle has been measured to $m_H = 125.5 \pm 0.2(\text{stat.}) \pm 0.5(\text{sys.})$ GeV. As of today, the particle's couplings to the other SM particles have been found to be in agreement with those of the Standard Model Higgs boson. In particular high precision has been reached in the measurement of bosonic decay modes while evidence for its decay into fermions have also been found. With the discovery of the Higgs boson and the measurement of its mass, all the free parameters of the Standard Model are known and the electroweak fit is overconstrained. This allows a precise test of the internal consistency of its parameters. Figure 1.2 shows the differences between the predicted and the measurement quantities for several observables as obtained by the Gfitter collaboration [21]. Results are shown with and without the direct input from the measured Higgs boson mass. As can be observed, there is a good consistency between measured and expected quantities with no difference exceeding three standard deviations. The p-value for the fit is 8% when including the experimental value of the Higgs mass, and 9% when it is considered as a free parameter.

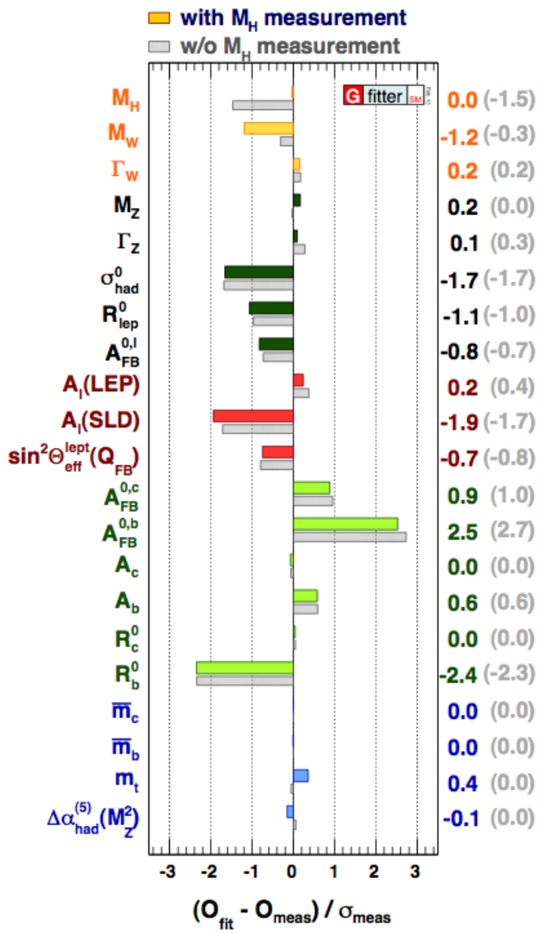

Figure 1.2: Differences between the SM prediction and the measured parameter, in units of the uncertainty for the fit including m_H (colour) and without (grey)

1.1.2 Limitations of the Standard Model

Despite the great experimental and theoretical success of the Standard Model, culminating in the discovery by the LHC detectors of the Higgs boson, several issues rest un-addressed by this theory:

- the observed mass hierarchy among fermions and the origin of the CP-violation.
- the observation of neutrino oscillations and hence the fact that neutrinos are not massless [6] [22]: mass terms for neutrinos could be easily incorporated in the SM Lagrangian by introducing right-handed neutrinos and then treating them as any other fermions (*Dirac* neutrinos). Since neutrinos do not carry any electrical or colour charge, neutrinos could also be described as *Majorana* fermions, meaning particles that represent their own anti-particle. The latter will receive confirmation in the measurement of neutrinoless double beta decay. At the same time, the hierarchy and the structure of the mixing in the neutrino sector seems different from the one in the quark sector.
- the lack of a candidate to explain the large amount of Dark Matter observed in the universe.
- the *naturalness* problem: the mass of a scalar receives large loop corrections in the Standard Model, which will inevitably lead to a > TeV Higgs boson mass. Only a precise arrangement of the parameters in the SM by several orders of magnitude (fine-tuning) allows m_H to remain below 200 GeV.
- the unification of the strong, weak and electromagnetic interactions: evolving the coupling constants of the these interactions to a scale of 10^{16} or 10^{19} GeV shows no convergence of the three to a common value.
- the impossibility to incorporate gravity for a more coherent description of all the interactions.

These considerations support the idea that the Standard Model represents the "low energy" expression of a more comprehensive theory. Among the various hypotheses, SuperSymmetry (SUSY) [23] is often considered one of the most elegant solutions. By postulating a symmetry between bosons and fermions, new 'supersymmetric' partners of existing particles in the Standard Model are introduced. This allows, for example, to 'solve' the naturalness problem since the loop-induced correction to the Higgs boson mass cancel between a particle and its super-particle.

So far no clear evidence has been seen to favour or accept any of the new proposed models. On top of direct searches for new physics, particular importance is given to indirect searches for effects produced by these new particles in loop corrections. Among the areas where precise tests of physics are very promising, investigation of observables in the top quark and Higgs sectors are extremely important since in most new physics models, these particles strongly couple to the new states predicted by the theories.

1.2 Physics at hadron colliders

Contrary to a e^+e^- collider like LEP, in a *p*-*p* machine the colliding particles are not fundamental objects. While the proton can be naively imagined to be formed from three "valence" quarks (*uud*), virtual pairs of quarks and gluons are continuously created and re-absorbed due to quantum fluctuations, resulting in a tight interaction among the constituents. As already outlined when discussing QCD, these phenomena are dominated by non-perturbative effects given the low energies involved.

As originally formulated for the case of deep inelastic e-p scattering, when the energy of the incoming particles is much higher than the binding forces within the proton, the interaction takes place between the electron and any of the proton constituents before non-perturbative effects can settle in[7]. This is granted by the "asymptotic freedom" properties of quarks and gluons. A p-p collision can thus be thought of as the incoherent superposition of the interactions between any two constituents of the two protons, each of them carrying a fraction $x_1$and x_2 of the proton incoming momentum.

The general formula for the cross section of a process is given by:

$$\sigma_X(s, \mu_R, \mu_f) = \sum_{a,b} \int_0^1 dx_1 dx_2 \cdot f_a(x_1, \mu_f) f_a(x_2, \mu_f) \cdot \hat{\sigma}_X(\hat{s}, \mu_R, \mu_f) \tag{1.17}$$

where a, b are the different parton types and s is the squared collider centre of mass energy. $f_a(x)$ represents the *parton density function*, namely the density of partons (quarks/gluons) in the proton to carry a fraction x of the proton momentum. The formalism of PDFs allows to decouple the non-perturbative effects from the hard scattering described by $\hat{\sigma}_X$.

Equation 1.17 is known as the *factorisation theorem.* The PDFs are generally independent of the specific parton level interaction. The dependence on a factorisation scale μ_f is introduced to renormalise singularities arising from collinear gluon splitting and emission of soft gluons. The removal of singularities is obtained by imposing the quantities to be finite at a given scale Q where the value could be extracted from data, and then introducing a dependency on a given energy scale (μ_f) that allows to evolve the calculation to other energies in expansion of μ_f/Q. The proton PDFs are extracted from the data of deep inelastic scattering experiments (HERA) and from specific measurements performed at hadron colliders (jet spectra or more recently vector boson production) [24]. Several sets of PDFs are available according to the approach that has been used to extract the information from the data, and the specific inputs from experiments. PDFs are determined at a given scale, the extrapolation to a different energy regime is obtained through the so-called DGLAP [25, 26, 27] equations which describe the evolution of the α_S coupling constant and the radiation branching properties with energy.

Figure 1.3 (a) shows an example of the parton distributions functions for the different type of proton constituents. Valence quarks carry most of the momentum of the proton so they represent the dominant contribution at high values of x. At lower values of x, gluons and sea quarks ($q\bar{q}$ pairs created by quantum fluctuations) become increasingly more abundant so that the LHC is often referred to as a "gluon collider".

$\hat{\sigma}_X$ represents the cross section for the parton-parton interaction occurring at a reduced squared energy $\hat{s} = x_1 x_2 s$. The advantage of a collider as a discovery machine is that, thanks to the momentum distribution of the proton constituents, a large interval of $\hat{s}$ can be implicitly scanned in searching for new physics. $\hat{\sigma}_X$ can be computed with the perturbation theory formalism up to a certain order in the coupling constants. This procedure introduces a dependence on a *renormalisation scale* μ_R. As for the factorisation scale, this parameter is introduced to deal with divergencies in the scattering amplitude computation; in this case, the 'ultraviolet divergencies' arising from loop contributions in higher order calculations. Physics observables are insensitive to these scales while theoretical estimations conserve a dependency on μ_R and μ_f due to the fact that they are only computed, due to practical limitations, up to a given order in perturbation theory. One of the main sources of theoretical uncertainty is obtained by varying these scales (usually by a factor 0.5 - 2 around the central value) and evaluating the

[7]Different energy ranges also imply different timescales for the phenomena so highly energetic events happen on much shorter timescales.

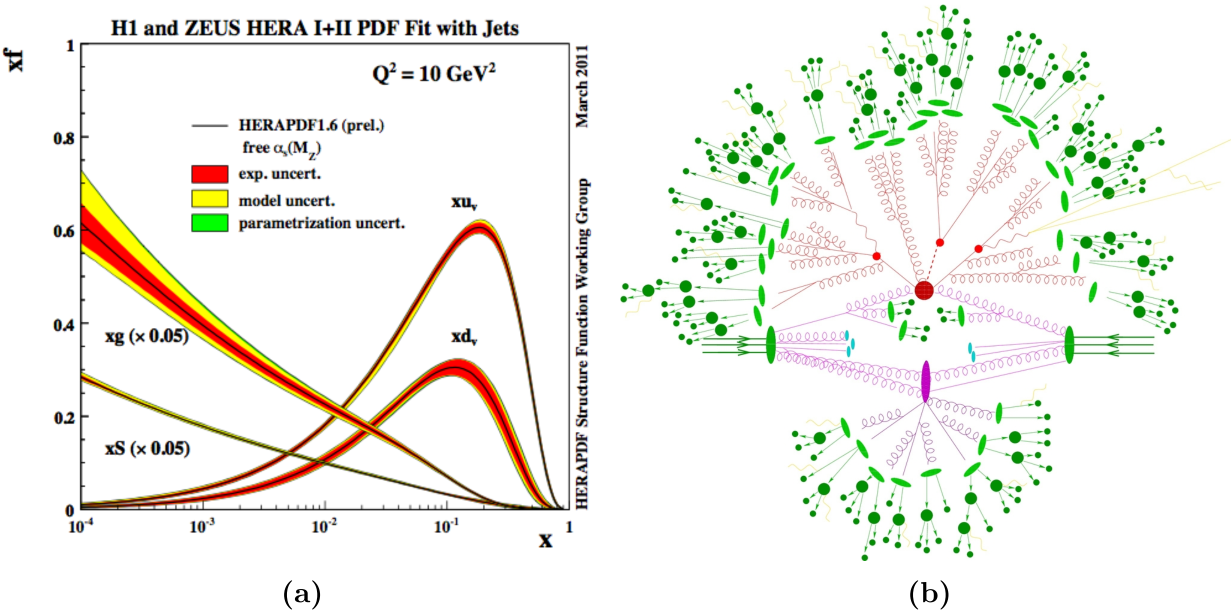

Figure 1.3: (a) Example of parton distribution function as extracted from a fit to HERA data [28]. (b) Schematic view of the interaction at a *p*-*p* collider.

impact on the result; this procedure is normally referred to as *scale variation* or *scale dependence*. The higher the order of the calculation, the smaller the impact of the scale uncertainty is expected to be. At present, *Next to Leading Order* (NLO) calculations are available for most of the processes. NLO takes into account virtual contributions to first order in α_S, meaning loop effects, and the emission of extra partons. The theoretical effort is progressively moving to a more complete set of *Next-to-Next to leading order* (NNLO) calculations also including two-loop effects.

Figure 1.3 (b) contains a schematic picture of the processes happening in typical *p*-*p* collisions. Each colour corresponds to a different energy (time) scale in the event and so they are considered in the calculation (or event generation by Monte Carlo) as subsequent steps.

One parton from each proton is involved in the main hard scattering collision (upper purple circle). The partons produced in the hard scattering as well as the incoming partons can undergo a series of radiation emission or splitting into other partons (red lines). The emission of soft partons exactly cancels the divergencies arising from loop contributions at all orders in perturbation theories[8]; the calculation of high order loop effects is limited by the computing power. A more effective approach in describing the various emissions is obtained with the *parton shower* approach. A series of branching is considered to construct a tree-like structure of partons. The branching is controlled by some 'time-dependent' variable ensuring that the subsequent emission happens with decreasing transfer of energy. Radiation from incoming colliding parton is normally referred to as *initial state radiation* (ISR) while emissions from final state partons are defined as *final state radiation* (FSR).

The evolution of the partons continues until the energy regime reaches the order of Λ_{QCD}. At that time, the quarks/gluons combine into colourless states (light green circles), which subsequently form hadrons that decay into stable particles (dark green circles). The latter process is know as *hadronisation* and it is the responsible for the evolution of the partons into collimated spray of hadrons called 'jets'. A jet reconstruction algorithm combines the hadrons together in an attempt to reproduce the properties of the original parton. Jet algorithms can be

[8]This is valid only in case of colourless initial states, like in e^+e^- colliders.

designed with the goal of being particularly insensitive to soft or collinear emissions which can happen during the parton shower evolution and to the specific hadronisation implementation. This property, known as *infrared and collinear safety*, allows a robust definition of physics observables in final states containing hadrons.

The interaction of the rest of the two proton remnants is normally referred to as *underlying events* or *multi-parton interactions* (bottom purple circle).

Different Monte Carlo techniques are used to describe the various steps of the collisions. The hard scattering process can be calculated in perturbation theory and the first emissions can also be included in the exact fixed order calculations of the scattering matrix element amplitude (ME) as implemented by several generators. Parton shower effects are modelled thought subsequent branching techniques and help in covering the kinematic range of soft and collinear radiation. The main Monte Carlo programs implementing the fragmentation process are Pythia [29] and Herwig [30]. In the parton shower implementation, they differ in the type of 'ordering' variable chosen to control the development of the shower. Hadronisation effects are non perturbative and they are described through phenomenological models with several parameters that can be tuned to match the observations in data.

1.3 Top physics at the LHC

The top quark is the heaviest quark in the Standard Model. Discovered at the Tevatron in 1995, the most precise measurement of the top mass yields $m_{\rm t} = 173.2 \pm 0.9$ GeV [31]. This value implies that the top quark is the only particle in the Standard Model to have a Yukawa coupling $y_{\rm t}$ very close to unity. While in the Standard Model $y_{\rm t}$ is one of the free parameters of the theory, such particular value could suggest that the top might have a special role in more comprehensive theories aiming at explaining the mass hierarchy pattern. At the same time, several proposed extensions of the Standard Model predict the presence of new particles strongly coupling to the top quark.

The unique features of the top quark extend also to its lifetime. Given that its width ($\Gamma_t = (2.0 \pm 0.4)$ GeV [6]) is much larger than Λ_{QCD}, the top quark decays before any hadronisation effect can occur. This means that the properties of the *free* quark like its spin can be directly assessed by studying its decay products without the dilution coming from non perturbative effects[9].

Top physics can be considered a privileged window for searches in high energy physics. Precise measurements of top quark production and decay can lead to a validation of QCD calculations at very high scales and simultaneously reveal indirect effects of new physics. At the same time, $t\bar{t}$ pairs (in particular $t\bar{t}$ plus additional jets) represent the main background in many direct searches for new physics and a good control on its modelling, in particular regions of phase space, is crucial for effective direct searches.

Due to its high mass, the top quark can be produced directly only at hadron colliders. Both the Tevatron and the LHC have enough energy in the centre of mass to produce a pair of top and anti-top quarks. This represents the dominant top quark production mode since it is mediated by the strong interaction. $t\bar{t}$ pair production will be described in detail in the following paragraph since it will be the main topic of this thesis work both for direct measurement and for being the major background for associated production of the Higgs boson with a $t\bar{t}$ pair. The production of single top is suppressed at the LHC by the fact that it proceeds through the electroweak interaction and it requires anti-quarks or b quarks in the initial state. Given

[9]non perturbative effects will still affect its decay products.

also the different final state topology (fewer jets produced), single top quark production is only considered as a background in the current thesis work.

1.3.1 $t\bar{t}$ production

Figure 1.4 shows the LO Feynman diagrams contributing to the $t\bar{t}$ pair production. Two production sub-processes can be identified: gg fusion and $q\bar{q}$ annihilation. The latter is the dominant process at the Tevatron where the colliding quarks are mainly the valence quarks from the p and the $\bar{p}$, accounting for $\sim$ 85% of the total production cross section. With increasing collider energy, gg fusion dominates for both p-p and p-$\bar{p}$ colliders. At the LHC, for a centre of mass energy of 7 TeV, $\sim$ 80% of the $t\bar{t}$ cross section is obtained from the gg initial state. The $t\bar{t}$ pair production cross section has been computed with increasing accuracy. The full NLO calculation [32] accounts for contributions from real parton emission as well as from particles in loops at first order in α_S. Some of the leading Feynman diagrams for NLO $t\bar{t}$ production are shown in Figure 1.5 (a).

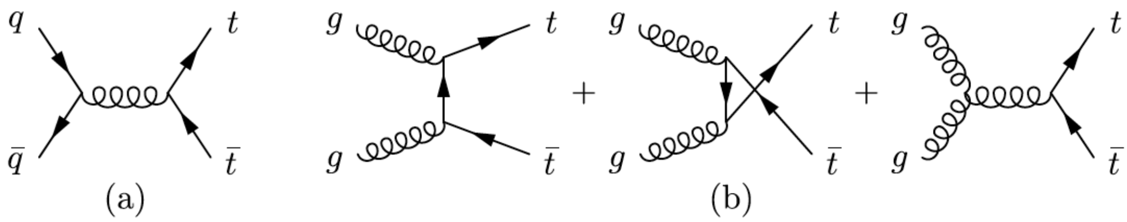

Figure 1.4: LO diagrams for the $t\bar{t}$ production: (a) quark-antiquark annihilation, (b) gluon-gluon fusion.

More refined calculations including the effect of additional soft gluon radiation were presented in [33] [34] and implemented in the Hathor [35] program for different values of the top quark mass. This is generally referred to *"approximate next-to-next-to-leading order"* (Approx. NNLO) or *"next-to-leading logarithm"* (NLL), and resulted in a few % increase with respect to the NLO calculation. This calculation was the prediction used by the analyses performed by ATLAS for the data sample collected during the years 2010 and 2011. Figure 1.5 (b) shows the trend of the approx. NNLO $t\bar{t}$ pair production cross section as a function the centre of mass energy both for p-p and p-$\bar{p}$ initial states. The total theoretical uncertainty of the approx. NNLO calculation is of the order of 6-8 %; the result varies by $\sim$ 3% for a change in the top quark mass of 1 GeV.

Currently the most precise prediction for the $t\bar{t}$ cross section includes the full *next-to-next-to* leading order (NNLO) calculation in α_S including resummation of next-to-next-to-leading logarithmic (NNLL) soft gluon terms [36, 37, 38, 39, 40] as implemented in the top++2.0 program [41].

For a mass of m_t = 172.5 GeV and using the MSTW 2008 NNLO parton distribution functions [42], the cross section for 7 TeV centre of mass energy collisions is equal to:

$$\sigma_{7\ \text{TeV}}(t\bar{t}) = 177.3\ ^{+10.2}_{-10.8}\ pb = 177.3\ ^{+4.56}_{-5.99}\ (\text{scale})\ ^{+9.02}_{-9.02}\ (\text{PDF}, \alpha_S)\ \text{ pb} \tag{1.18}$$

$$\sigma_{8\ \text{TeV}}(t\bar{t}) = 252.89\ ^{+13.30}_{-14.52}\ pb = 252.89\ ^{+6.39}_{-8.64}\ (\text{scale})\ ^{+11.67}_{-11.67}\ (\text{PDF}, \alpha_S)\ \text{ pb} \tag{1.19}$$

were the total uncertainty is reported as well as its breakdown in scale uncertainty and contribution due to α_S and PDF uncertainties. The latter is computed using the prescription from

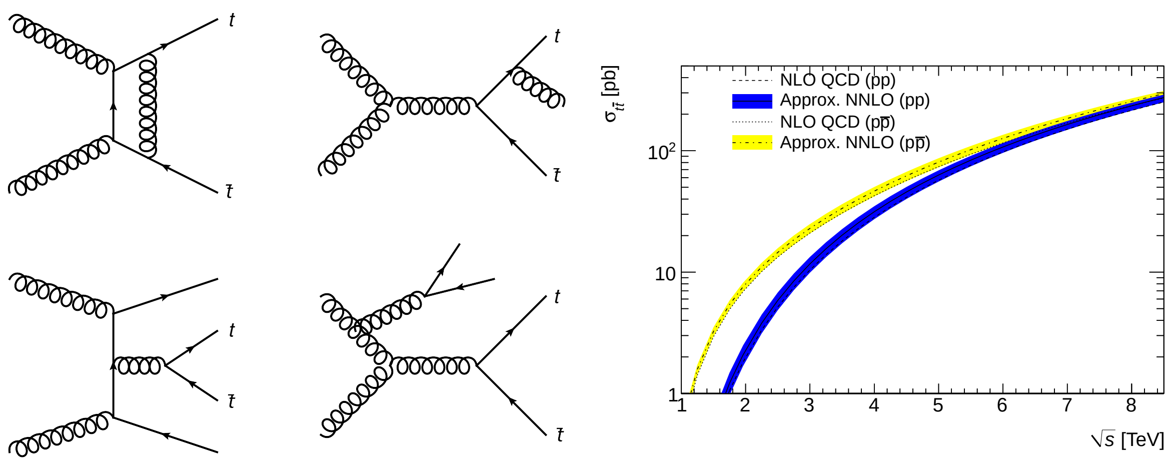

(a) **(b)**

Figure 1.5: (a) Examples of diagrams contributing to the $t\bar{t}$ production at higher order in α_S. Upper diagrams show examples of NLO 'virtual' and 'real' corrections. Bottom diagrams are the leading contributors to the production of $t\bar{t}$+2 partons. (b) $t\bar{t}$ production cross section for p-p and p-$\bar{p}$ colliders as a function of the centre of mass energy.

the PDF4LHC working group [43]. The calculation results to be $\sim 5\%$ higher than the approx. NLO result with a total theoretical uncertainty reduced to below the 6% level.

$t\bar{t}$+jets production

Higher order corrections to the $t\bar{t}$ cross section calculations already take into account additional parton emissions. The $t\bar{t}$+jets terms refer generally to events were the emission has a sufficiently high transverse momentum and is sufficiently separated from the rest of the event to be identified as a separated jet. The specific cross section depends on the kinematic cuts used to define the additional partons/jets; such selections are also necessary to stabilise the calculation and avoid soft and collinear divergencies. Since these processes arise only from higher order in the coupling constant[10], they display a large dependency on the choice and variation of the scale used in the calculation.

NLO calculations [44] predict that, at the LHC centre of mass energies, $\sim 50\%$ of inclusive $t\bar{t}$ events contain at least an additional jet in the typical kinematic range of physics analyses. The presence of additional jets in the event can alter the probability of selecting the event (high jet multiplicity events have higher probability to pass the event selection), as well as affect the possibility of correctly reconstructing the $t\bar{t}$ decay chain. Furthermore, $t\bar{t}$+jets often represents the main (irreducible) background for analyses searching for phenomena with a small cross section or new physics contributions.

One particular case is presented by the production of $t\bar{t}$ in association with a pair of b-quarks ($t\bar{t}+b\bar{b}$). This process is of primary interest since it represents the main irreducible background to the measurement of the $t\bar{t}H$ when the Higgs boson decays into b-quarks. One of the additional theoretical challenges in the $t\bar{t}+b\bar{b}$ resides in the mass of the b-quarks while gluon and light quarks are usually considered as massless in the calculations. This affects the balance between the two main production diagrams as shown in Figure 1.5 (a); contrary to the inclusive $t\bar{t}$+jets production, for $t\bar{t}+b\bar{b}$ the gluon splitting contribution dominates over the

[10]The inclusive $t\bar{t}$ cross section at lowest order depends on α_S^2, while $t\bar{t}$+jets cross section has a dependency at least of order α_S^3.

double initial state radiation[11]. At the same time, the description of the gluon splitting into massive quarks, in particular in the low angular separation regime, is a critical component in which fixed order calculations have similar precision as the analytical parton shower programs. Recently, NLO theoretical predictions for the $t\bar{t}$+$\bar{b}$ process have been computed [45, 46] with particular emphasis on the kinematics of the additional b-quarks. Nevertheless, these advances cannot be directly incorporated in physics analyses since no hadronisation effects are considered, in addition, the top quarks in the events are not decayed.

Finally, from an experimental point of view, the analyses related to the $t\bar{t}$+jets processes have the difficulty that the additional jets cannot be easily identified with respect to the $t\bar{t}$ decay products.

$t\bar{t}$ decay

Given its large mass and the fact that that the value of $|V_{tb}|$ is very close to 1 ($|V_{tb}| > 0.999$ at 90% confidence level [6]), the top quark in the Standard Model decays almost exclusively into an on-shell W boson and a b quark. This implies that, experimentally, the presence of two b-quark jets can be exploited to isolate and identify the events.

The final topology of a $t\bar{t}$ final state is thus determined by the decay of the two Ws present in the event. A W boson decays in about 1/3 of the cases into a charged lepton (e, μ, τ)and the corresponding neutrino, with all the three lepton flavours being produced with equal probability. In the remaining 2/3 of the cases, the W boson decays into a quark-antiquark pair and the relative amount of each combination is determined by the corresponding element in the CKM matrix. As $|V_{cb}|^2 \sim 1.7 \cdot 10^{-3}$ [6], production of b-quarks is highly suppressed and the W boson can be considered as a very pure source of light and c-quarks.

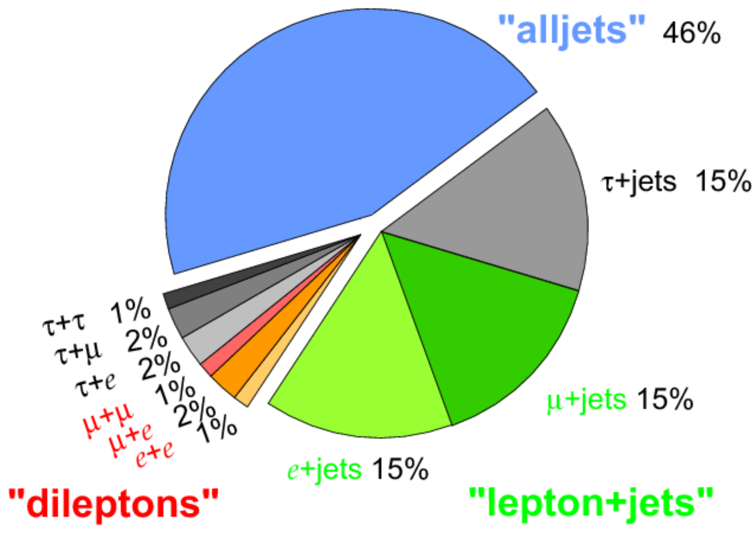

Figure 1.6: Top quark pair decay topologies.

Figure 1.6 illustrates the different decay modes of a $t\bar{t}$ event. Three different signatures are identified:

[11] This is because the $t\bar{t}$+jets production cross section receives a large contribution from the equivalent diagram in bottom left Figure 1.5 (a) where the quark line is replaced by a gluon.

- *fully hadronic* final state: both W bosons decay hadronically leading to a final state with at least six jets. This decay mode represents corresponds to the majority of the $t\bar{t}$ events, having a branching ratio of $\sim$ 46 %. Since no high-p_{T} lepton is present in the final state, the signal is difficult to isolate from the SM QCD multi-jet background which dominates by several orders of magnitude. Despite the lack of "invisible" particles, which allows a full reconstruction of the final state, this topology suffers from a large combinatorial background when attempting to obtain an estimate of the top mass.

- *fully leptonic* or *di-lepton* final state. This represents $\sim$ 10 % of the total $t\bar{t}$ decays or 4 % if only muons or electrons are considered. The event is characterised by the two oppositely charged leptons from the W decays, two neutrinos escaping detection and two jets from b-quarks. These characteristics made the identification of the events relatively easy and a high $t\bar{t}$ purity can be achieved. Nevertheless, this channel usually suffers from a low selection efficiency and difficulties in the event reconstruction due to the two escaping neutrinos.

- *lepton+jets* or *single lepton* final state: this corresponds to events where only one of the W bosons decays into leptons. The events are thus characterised by the presence of a high-p_{T} lepton, a neutrino and four jets. This channel represents the best compromise between high purity and collectable statistics. It accounts for 45 % of the total decays or 30% in case only the electron and the muon are considered as leptons. The high-p_{T} lepton is exploited to trigger and select the events while the presence of the neutrino allows to reduce the QCD multi-jet background. Since only one neutrino is produced, its p_{T} can be estimated from the missing transverse energy allowing for a reconstruction of the $t\bar{t}$ topology[12].

Topologies involving decays to τ leptons are considered separately given the specific experimental signature of the hadronically decaying τ. However, in the cases where the τ lepton decays into an electron or a muon those events are included in the corresponding single or di-lepton selection.

1.4 The Higgs at the LHC

The LHC machine was built with the primary goal of discovering the Higgs boson or definitively claiming its absence, as well as search for BSM effects. The large increase in centre of mass energy with respect to previous colliders was decided in order to have a Higgs boson production cross section above a few picobarns in a large mass interval.

Figure 1.7 (right) shows the cross section for the different Higgs boson production modes as a function of its mass for a centre of mass energy of 8 TeV [47]. Multiple production modes are exploited in order to increase the sensitivity for the discovery as well as to probe different coupling of the Higgs boson.

Due to the large density of low-x gluons inside the proton, the main process is the *gluon fusion* (ggH) illustrated in Figure 1.7 (a); the Higgs boson couples to the gluon only indirectly through a loop of top (or b) quarks. This process represents $\sim$90 % of the total Higgs cross section.

The sub-leading production mode is represented by the *Vector Boson Fusion* (VBF). As shown in Figure 1.7 (b), two W (or Z) bosons from colliding quarks interact to produce the

[12] An estimate for the longitudinal component of the neutrino momentum (p_z) can be extracted imposing that the invariant mass of the lepton and the neutrino should be equal to the mass of the W boson.

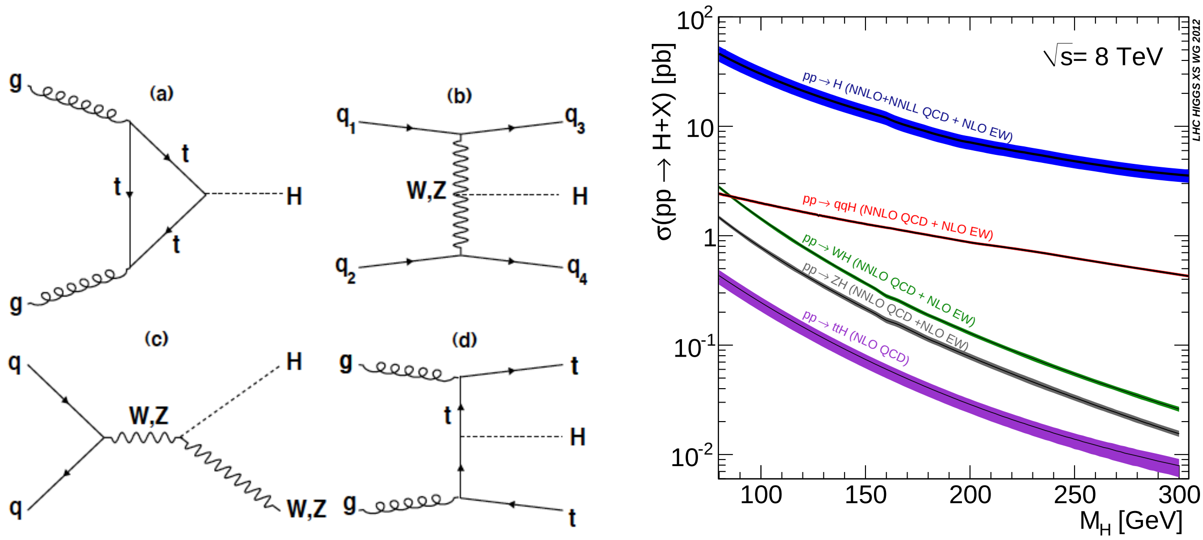

Figure 1.7: Leading diagram for the different Higgs production modes (left). Cross section of the different Higgs boson production modes (right).

Higgs boson. Given that the production is governed by the electroweak interactions, the process has the characteristic signature of forward jets and a central region where no hadronic activity is expected but for the decay of the scalar boson. Experimentally this is exploited to reduce background and allow to assess decays of the Higgs boson that in the gluon fusion channel are overwhelmed by QCD multi jet background.

Diagram 1.7 (c) illustrates the production of the Higgs boson in association with a vector boson (W or Z), generally referred to as VH. As for the VBF case, this channel is driven by quark-anti quark interaction and gives insight in the coupling to the electroweak bosons. The presence of the vector boson in the final state is used experimentally to better identify (trigger) the events as well as to reduce the contribution of the background.

The production mode with the smallest rate is the associated production with a pair of top quarks ($t\bar{t}H$). Despite the very low cross section the importance of this channels relies on the fact that it directly probes the top Yukawa coupling from a tree level diagram as described in Figure 1.7 (d). The coupling of the Higgs to top quark also enters the gluon fusion production mode but the latter could also be sensitive to any potential sign of beyond the Standard Model physics that can contribute to the loop connecting the Higgs boson to the two gluons.

From an experimental point of view, the associated production of a $t\bar{t}$ pair leads to an additional possibility for signal identification, but the large amount of particles in the final state makes the reconstruction of the Higgs boson candidate less straightforward. More information on the specific issues related to the experimental identification of $t\bar{t}H$ events will be given in Chapter 8. The inclusive cross section for the $t\bar{t}H$ production has been computed at the NLO accuracy [48, 49, 50, 51]. The calculation assumes a fixed top mass of $m_t = 172.5$ GeV (without experimental uncertainty) and a central scale set to $\mu_R = \mu_f = \mu_0 = m_t + m_H/2$. The MSTW 2008 NLO PDF set [42] was used for the central value, while for the PDF and α_S uncertainties the MSTW 2008, CTEQ6.6 [52] and NNPDF2.0 [53] sets have been considered. For a Higgs boson mass of 125 GeV, the inclusive crosse section at a centre of mass energy of 8 TeV yields:

$$\sigma_{pp \to t\bar{t}H} = 0.1293 \text{ pb } {}^{+3.8\%}_{-9.3\%} \text{ (scale)} \quad \pm 8.1\% \text{ (PDF} + \alpha_S). \tag{1.20}$$

where the first uncertainty corresponds to a scale variation by a factor of two around the central value and the second contribution takes into account PDF and α_S variations.

Due the presence of two additional heavy quarks in the final state, the cross section for this process is very sensitive to the centre of mass energy of the p-p interaction. While the other Higgs boson production modes increase by $\sim 20\%$ when the centre of mass energy is increased from 7 to 8 TeV, the $t\bar{t}H$ production cross section increases by 50%.

1.4.1 Higgs boson decay modes

As already outlined in the previous paragraph, the Higgs boson coupling to particles is proportional to their masses, so the Higgs boson will tend to decay to the pair of the most massive particles allowed by kinematics. The decay to massless particles like gluons or photons arises from loop corrections mainly involving top quarks and W bosons[13] and this is the case also for the decay to $Z\gamma$. Figure 1.8 shows the behaviour of the branching fractions as a function of the Higgs boson mass, while Table 1.3 summarises the values of the branching ratios for a mass of 125 GeV [47].

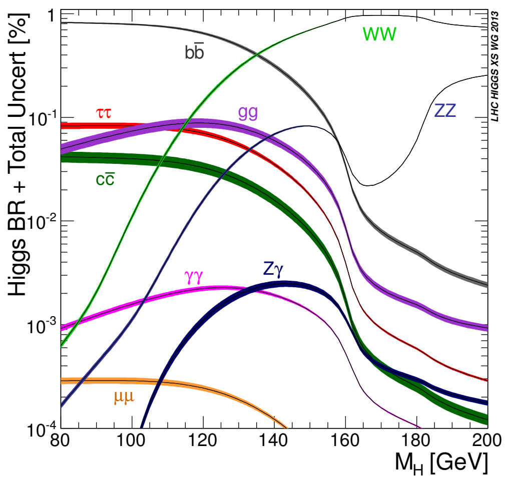

Figure 1.8: Branching ratios for a Standard Model Higgs boson as a function of its mass.

decay	Br
$b\bar{b}$	(57.7 ± 1.9) %
WW	(21.5 ± 0.9) %
gg	(8.57 ± 0.87)%
$\tau\tau$	(6.32 ± 0.36) %
$c\bar{c}$	(2.91 ± 0.36) %
ZZ	(2.64 ± 0.11) %
$\gamma\gamma$	(0.228 ± 0.014) %

Table 1.3: Values of the branching fractions and their uncertainties for a mass of 125 GeV.

For this specific mass value numerous decay channels open up or are in reach of the present or next generation of colliders, allowing a complete study of the nature of the Higgs boson and the exploration of deviation with respect to the Standard Model behaviour.

The largest contribution is the decay into a $b\bar{b}$ pair, which will be the focus of the last part of this thesis.

The second largest branching ratio is for the decay to WW; given the low mass of the Higgs boson, this decay is kinematically suppressed by the fact that one of the W bosons is off-shell. The highest sensitivity in this channel is obtained by considering both W's decaying to leptons for a signature containing two opposite sign leptons and missing transverse energy from the two neutrinos. Despite the impossibility of a full mass reconstruction, this channel was the third main contributor to the discovery of the Higgs boson particle.

The decay into a $\tau\tau$ pair has a branching fraction of 6%, it allows for a good mass resolution despite the neutrinos produced by the τ decays. It is particularly important for the sensitivity that it brings to the measurement of Higgs boson production modes other than gluon fusion.

[13]the loop diagram could also receive contributions from other massive particles predicted by new physics models

Channels with low branching ratios like a decay into a $\gamma\gamma$ or a ZZ pair where both Zs decay into leptons, have the advantages of the possibility of a complete reconstruction of the Higgs boson kinematics as well as an excellent mass resolution. This allows for better control and discrimination against the background, which leads to the highest sensitivity for the discovery of the Higgs particle.

Finally very rare decay channels $H \to \mu\mu$ or $H \to Z\gamma$ will be very important to test the contribution of possible new physics coupling to the Higgs particle.

Chapter 2

The Large Hadron Collider and the ATLAS Detector

This chapter is dedicated to the two key ingredients necessary for an analysis in high energy physics: the particle accelerator providing the collisions and the detector used to analyse them.

The first part describes to the world's largest and most powerful particle accelerator, the Large Hadron Collider, with a particular emphasis on the evolution of the running parameters over the first three years of operation, now denoted as *RunI*.

The second part focuses on the ATLAS detector, one of the four large experiments studying the collisions on the LHC. A brief summary of its sub-detector components and their performance will be given.

2.1 The Large Hadron Collider

The *Large Hadron Collider* (LHC) is a circular proton-proton collider built at the European Centre for Nuclear Research (CERN). It is hosted in a 27 km circumference tunnel built 100 m underneath the French-Swiss countryside outside Geneva. Not only is it the world's largest particle accelerator but, with the current operation at a beam energy of 4 TeV and the expected upgrade to 7 TeV, it is also the most powerful one.

Its construction[54] replied to the need of extending the reach of previous accelerators in the search for new phenomena and unmeasured aspects of the Standard Model. The centre of mass energy increased by an order of magnitude with respect to the Tevatron collider at Fermilab[[55], while the high instantaneous luminosity (up to 10^{34} cm^{-2}s^{-1}) allows access to very rare phenomena and precision measurements.

These considerations ultimately motivated the choice for a proton-proton collider. For protons the loss of energy in a curved trajectory due to synchrotron radiation is considerably smaller than for electrons[1] and this allows to accelerate protons more efficiently for a machine of fixed radius. At the same time a hadron collider permits to probe multiple energy ranges simultaneously due to the momentum distribution of partons inside the protons. A proton-antiproton collider alternative was rejected due to the difficulties of producing and operating high intensity anti-proton beams which would have resulted in a lower peak luminosity.

[1] The energy emission per turn is proportional to $(E/m)^4$[56]

Machine parameters and performance

One of the main constraints on the LHC construction was the need to re-use the tunnel previously hosting the LEP collider. The technological challenge of the LHC was the mass production of magnets necessary to maintain 7 TeV protons in a circular trajectory of a radius of 4.3 km. Approximately 1200 dipole magnets have been assembled in the LHC. Each magnet produces a bending field up to 8.7 T thanks to superconducting material kept at a temperature of 1.9 K by superfluid helium. This makes the LHC the largest cryogenic system in the world. Each dipole contains two cavities which, with a specific magnet field configuration, allow to accelerate two proton beams in opposite directions.
The other fundamental parameter for the machine is the luminosity, which is defined as the proportionality constant between the number of events produced in the unit of time for a given process and the cross section for this process. For a collider with beams composed of N bunches of particles, it can be expressed as:

$$L = N \cdot F \frac{n_1 n_2 f_{\mathrm{r}}}{4\pi \sigma_x \sigma_y} \tag{2.1}$$

The factor F takes into account the beam crossing angle at the interaction, f_{r} represents the revolution frequency of the machine, n_1 and n_2 are the number of protons in each bunch. σ_x and σ_y are the geometrical dimensions of the beam profile in the transverse plane. They are controlled by specific focusing elements placed on the beam trajectory. In order to achieve the peak luminosity of 10^{34} cm^{-2}s^{-1}, the LHC can accommodate beams of 2808 bunches with a 25 ns bunch spacing, resulting in a global collision frequency of 40 MHz. Each bunch can contain up to 10^{11} protons.

Table 2.1 summarises the rest of the key LHC design parameters. TheThe LHC is also able to accelerate and collide lead ions for which the nominal beam energy is 2.8TeV/nucleon.

beam energy	7 TeV
dipole magnetic field (7 TeV)	8.33 T
revolution frequency	11.1 kHz
peak luminosity	10^{34} cm^{-2}s^{-1}
number of bunches	2808
bunch spacing	24.95 ns
protons per bunch	$1.15 \cdot 10^{11}$
vertical beam size	18 μm
horizontal beam size	71 μm
beam crossing angle	285 μrad
beam lifetime	13.9 h
beam energy loss per turn	7 keV

Table 2.1: LHC design parameters.

The CERN accelerator complex

As for any other large particle collider, the energy of the colliding particles is gradually raised by subsequent acceleration steps before entering the final LHC ring; this solution increases the flexibility and allows for a more efficient production of the beams. In particular, the usage of multiple machines allows to reduce the dynamic range of the bending magnetic field in a single accelerator[2]. Since the transverse size of the beam decreases with increasing beam energy, different solutions to control the beam evolution can be adopted in each step.At the same time, intermediate accelerator machines provide beams that are used in other lower energy experiments.

Figure 2.1 shows the complex of accelerators used to inject particles in the LHC. The starting point is a simple tank with hydrogen gas which is then ionised and accelerated by two linear accelerator stages (RFQ and Linac). Circular accelerators are subsequently responsible for increasing the energy from few hundreds of MeV to the LHC injection energy of 450 GeV and at the same time give the beams the desired bunch structure. The final energy of each acceleration stage for protons and heavy ions is summarised in Table 2.2.

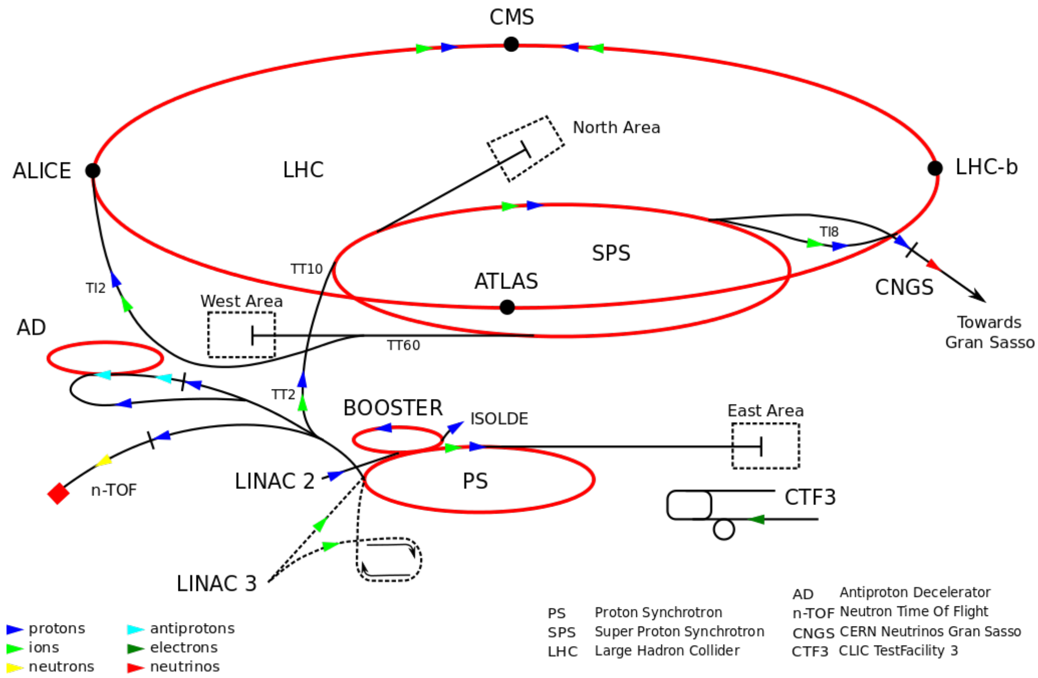

Figure 2.1: CERN accelerator complex.

protons		heavy ions	
accelerator	energy	accelerator	energy
RFQ	750 keV		
Linac 2	50 MeV	Linac 3	4.2 MeV/u
PS Booster	1.4 GeV	LEIR	14.8 MeV/u
PS	25 GeV	PS	4.25 GeV/u
SPS	450 GeV	SPS	177 GeV/u

Table 2.2: Injection chain for the LHC. For heavy ion beams, the energy refers to the energy per nucleon (u).

[2]The magnetic field needs to be increased as the particle energy increases.

LHC experiments

The LHC beams cross in 4 interaction points. In each of them a particle detector is installed to record the collisions.

ATLAS and CMS[57] (Compact Muon Solenoid) are multipurpose detectors designed to have broad sensitivity to many physics processes; they are located at opposite interaction points in the LHC ring. The independent design of the two experiments is of primary importance since it allows for cross-confirmation of measurements and possible new discoveries

The ALICE detector[58] was built to study heavy ion collisions in order to improve the knowledge of the dynamics of quarks and gluons at high energy density. LHCb[59] is a one-arm spectrometer designed to cover the forward region to perform detailed studies in the field of B-physics.

Two additional experiments, Totem and LHCf, focus on forward physics and are located along the beamline at $\sim$ 100 meters from the CMS and ATLAS interaction points respectively.

2.1.1 From first beam to word's record luminosity

In March 2010, LHC recorded the first collisions at a beam energy of 3.5 TeV. The centre of mass energy was kept at 7 TeV also during all of 2011. This choice was dictated by the need for a safety margin in the stability and operation of the magnets. For the 2012 data-taking the beam energy was increased to 4 TeV, for a collision center-of-mass energy of 8 TeV.

Figure 2.2 shows the trend of the delivered peak luminosity as a function of the day of data-taking. In early 2010 the machine was in a commissioning phase, with very few colliding bunches with a reduced number of protons. Towards the end of 2010 the peak luminosity reached $2 \cdot 10^{32}$ cm^{-2}s^{-1} obtained with 348 colliding bunches of approximately $0.9 \cdot 10^{11}$ protons each. The minimum distance between bunches was 150 ns.

In 2011, the number of bunches was raised to 1331 with a minimum separation of 50 ns. The number of protons per bunch increased to $1.15 \cdot 10^{11}$. In the second part of the year, a further increase in luminosity was achieved by reducing the transverse section of the beam at the interaction point in order to increase the probability of p-p collisions per crossing. The peak luminosity achieved in the year was $4 \cdot 10^{33}$ cm^{-2}s^{-1}.

For the 2012 datataking, a further reduction of the beam transverse profile and an increase to the bunch intensity to 1.3 times the designed value allowed to reach a peak luminosity of $6.8 \cdot 10^{33}$ cm^{-2}s^{-1}. This represents the current record for a hadron machine.

2.2 The ATLAS detector

ATLAS (*A Toroidal Lhc ApparatuS*), is a versatile multi purpose detector, designed to have the largest sensitivity for a broad range of physics processes that can be accessed through LHC collisions. The guidelines in the detector construction and specifications[60] were a focus on maximising the discovery potential for new phenomena while keeping the possibility of good precision measurements of known processes. One of the priorities of the experiment was the search for the Higgs boson (and measurement of its properties) as well as the search for supersymmetric particles that might be part of possible extensions of the Standard Model. Furthermore the luminosity delivered by the LHC allows to collect a very large sample of vector bosons (W,Z), B-mesons and top quarks which gives the possibility to perform detailed studies in the field of QCD, CP-violation and top quark properties. At the same time, the possibility to observe unexpected phenomena has demanded a very flexible design, not excessively tied to a specific physics model.

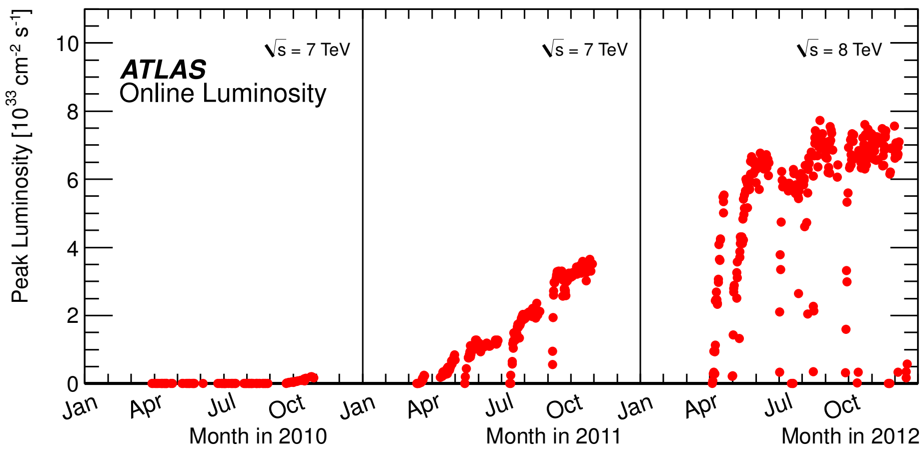

Figure 2.2: The peak instantaneous luminosity delivered by LHC per day versus time during the p-p runs of 2010, 2011 and 2012.

For this reason the detector is required to identify and measure the kinematic properties of a large spectrum of particles that are produced in proton-proton collisions over a wide energy range (from few GeV to TeV). This includes charged leptons (electrons, muons, taus), photons, jets produced by the hadronisation of quarks and gluons as well as particles that escape 'direct' detection like neutrinos and certain supersymmetric particles. These objects are identified through the measurement of un-balanced transverse energy in the event.

A schema of the detector is shown in Figure 2.3. It measures 45 m in length and 25 m in diameter for a total weight of 7000 tons.

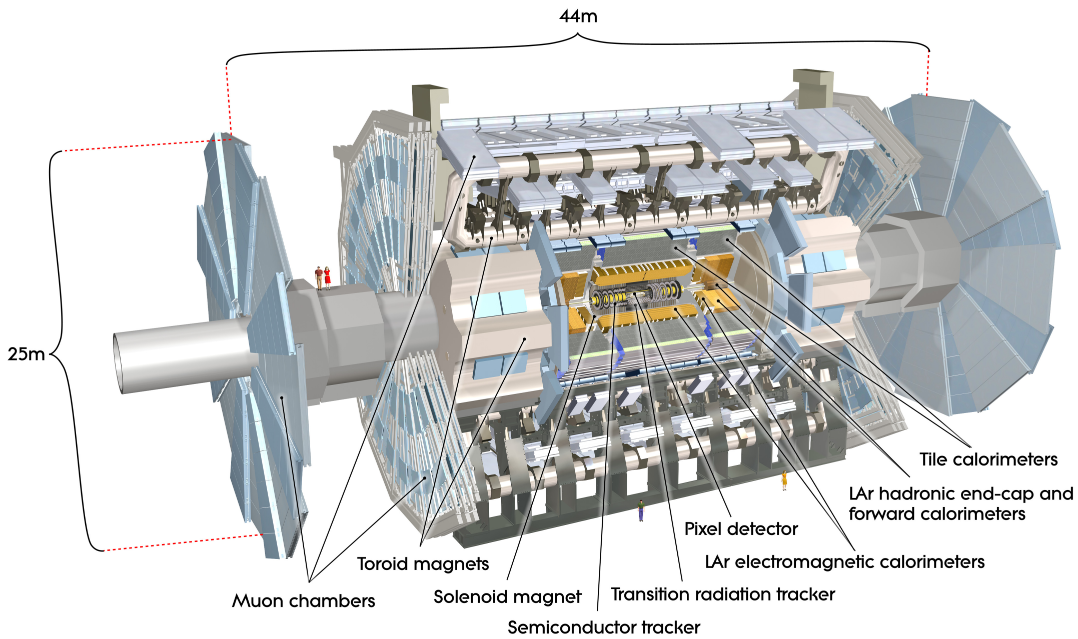

Figure 2.3: Cut-away view of the ATLAS detector.

Like most collider detectors, ATLAS has a cylindric structure with the various sub detectors arranged in concentric layers. Starting from the centre, the Inner Detector (ID) is designed to reconstruct the trajectories of charged particles (tracks) and measure their momenta thanks to the deflection in a solenoidal magnetic field. The ID is surrounded by an electromagnetic and a hadronic calorimeter which measure the energies of electrons/photons and hadrons by detecting the showers produced by the particles' interactions with their absorber materials. Muons are the only directly detectable particles that pass through the thick calorimeter. They are detected with a spectrometer which exploits the deflection in a toroidal magnetic field.

The following specifications have been taken into account in the construction of the detector [61]:

- a flexible trigger system capable of maintaining high selection efficiency and sufficient background rejection even for low/medium transverse momentum (p_{T}) objects;
- an electromagnetic calorimeter with excellent angular and energy resolution for the measurements of electrons and photons;
- a hermetic hadronic calorimeter with large angular coverage for the measurement of jets and missing transverse energy;
- efficient charged particles' track reconstruction and good track momentum resolution even in a high pile-up environment;
- precise measurement of track quantities and secondary vertices for the identification of jets produced by b/c-quarks and τ-leptons;
- good muon identification and momentum reconstruction up to highest luminosity with the possibility to determine unambiguously the charge of high p_{T} muons;
- large acceptance in pseudorapidity (η) with almost full azimuthal angle (ϕ) coverage[3].

In addition to these requirements, specific conditions from the LHC operation posed additional constraints on the detector design. Due to the high interaction rate of 40 MHz, fast electronics (order of 25 ns) was employed in the readout of all sub detectors, while the large number of interactions per crossing and the consequent large particle flux required sensors resistant to high radiation doses. At the same time, highly granular detectors are required to reduce the impact of overlapping interactions.

2.2.1 The magnet system

The measurement of charged particles' momenta is based on their deflection in a magnetic field. The magnet system [62] represents a particular characteristic of the ATLAS experiment which sets it apart in the panorama of high energy physics. It is composed of four large superconducting magnets designed to provide a field mostly orthogonal to the particle trajectory: a central solenoid and three open-air toroids as shown in Figure 2.4. This hybrid solution has the advantage of extending the pseudorapidity coverage of the muon spectrometer, and having no magnetic field inside the calorimeters in order not to degrade their performance.

[3]The coordinate system adopted by the experiment is defined as follows: the origin coincides with the interaction point, the z-axis is oriented in the counter clock direction of the beams, the x-axis is oriented from the interaction pointing to the centre of the accelerator while the y-axis is oriented upwards. The azimuthal angle ϕ is thus the angle around the beam axis while the pseudorapidity is defined as $\eta = -\ln(\tan\theta/2)$ with θ being the polar angle with respect to the z axis.

The *central solenoid* (CS) surrounds the Inner Detector and provides a magnetic field parallel to the beam axis bending particles in the ϕ direction. The CS' length is 5.3 m centred at the interaction point and it has a radius of 2.5 m. At the interaction point the value of the magnetic field is 2 T and it remains constant in the radial direction. As the distance from the interaction point increases in the z direction, the field strength decreases as a result of the finite size of the solenoid. In order to minimise the amount of material in front of the calorimeter, the solenoid and the liquid Argon calorimeter share the same cooling cryostat.

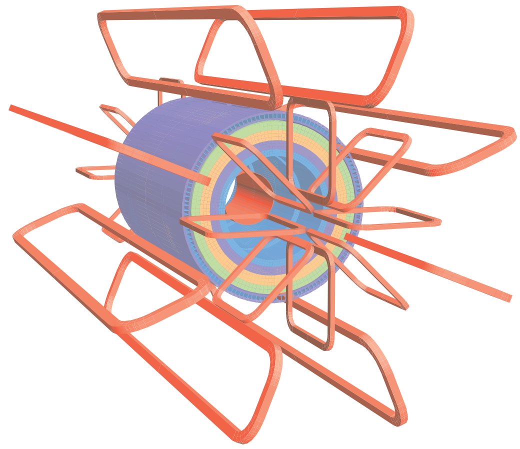

Figure 2.4: Schematic view of the ATLAS magnet system: three external toroids and the central solenoid enclosed by the calorimeters.

The toroid system produces the field needed by the muon spectrometer to deflect particles in the η direction: two *end-cap toroids* (ECT) at the two extremes of the detector and a *barrel toroid* (BT) centrally located around the calorimeters. Each toroid is composed of eight independent coils arranged in the radial direction from the beam axis. The choice of the "open air" toroid configuration was made to improve the muon reconstruction performance without relying on the Inner Detector. The toroids allow to efficiently generate the magnetic field over a large volume with a reduced amount of material. This minimises the amount of multiple scattering[4], which represents one of the factors limiting the momentum resolution.

The end-cap toroids are rotated by 22.5° with respect to the central barrel in order to improve the overlap of the respective magnetic fields and achieve a higher uniformity. Each coil of the BT has its own cryostat while for the end-cap toroids all the coils are arranged in the same cryostat that also contains the forward calorimeters. The barrel toroid generates a magnetic field of 3.9 T while the end-cap produces a field of 4.1 T. Both magnets are helium-cooled to a temperature of 4.5 K in order to reach the super-conducting state.

2.2.2 Inner Detector

The ATLAS Inner Detector (ID) is designed to provide efficient pattern recognition and good momentum resolution for charged particles in the range $|\eta| < 2.5$ from p_{T} as low as 0.5 GeV up to a few TeV. At the same time its capability of precisely reconstructing primary and secondary vertices and measuring the track parameters is of primary importance for identifying the decays of short-lived particles.

A precise measurement of the particle curvature in the magnetic field requires a good spatial resolution. In the presence of a large number of particles emerging from the interaction point, this can be achieved only with highly segmented detectors. The small size of the sensitive elements not only guarantees a better intrinsic resolution, but allows a reduced occupancy of the detector which is needed to maintain high efficiency for single events[5]. The chosen

[4]multiple scattering is defined as the (electromagnetic) interaction of a charged particle with the atomic structure of the medium. The result of the interaction with the very large number of nuclei and electrons results into a random smearing of the momentum of the incoming particle

[5]In general the time for which a detecting element remains inactive (dead time) after passage of a particle is

approach results from a compromise between high performance and other considerations like the amount of material used in the tracker. A large amount of material can in fact limit the intrinsic momentum resolution (multiple scattering) as well as degrade the performance of the calorimeter.

Three different technologies are employed in the ID reflecting the different track densities that can be found when increasing the distance to the centre of the detector. In the innermost region, a small number of detecting layers are located; they use semiconductor technology (pixels and strips) to provide high precision measurements. At larger distance to the interaction point, a transition radiation detector based on drift tubes allows to collect a larger number of measurements but with lower intrinsic resolution.

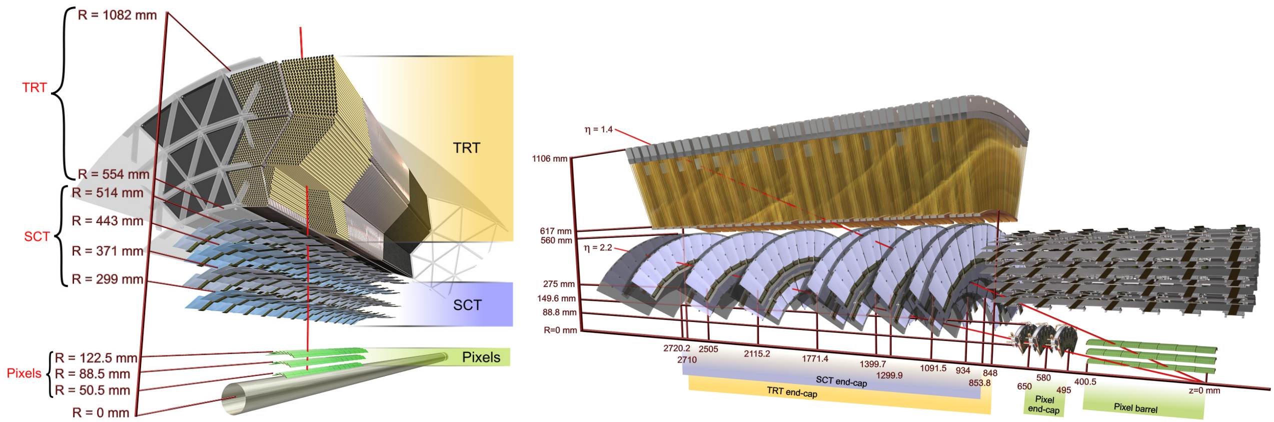

(a) **(b)**

Figure 2.5: Representation of the structure of the Inner Detector and its three sub components for the barrel (a) and end-cap (b).

The ID[63] is contained within a cylindrical envelope of length ± 3.5 m and of radius 1.15 m, fully immersed in the magnetic field produced by the solenoid. Figure 2.5 shows the structure of the ID in the barrel and end-cap region with the positions of the various sub-detectors indicated. Starting from the innermost components we find:

- Pixel Detector
- SemiConductor Tracker (SCT)
- Transition Radiation Tracker (TRT)

Each subdetector is organised in a central (*barrel*) part composed of concentric cylinders oriented in the direction of the beam axis, and two forward parts (*end-caps*) made of disks/wheels arranged orthogonally to the beam direction on each side of the barrel.

The relative precision of the three sub detectors is comparable so that no single measurement dominates the momentum resolution[6]; this redundancy also guarantees high efficiency even in case a part of one of the sub detector is malfunctioning. Combining the information from the three sub detectors the ID reaches a designed resolution of the track momentum [60] of:

$$\sigma_{p_{\mathrm{T}}}/p_{\mathrm{T}} = 0.05\% \cdot p_{\mathrm{T}}(\text{ GeV}) \oplus 0.1\% \tag{2.2}$$

longer than the time interval between consecutive collisions. Large granularity ensures a small probability for each element to be impacted by tracks in consecutive collisions.

[6]the lower intrinsic resolution of the TRT is compensated by the higher number of hits per track and by the possibility of analysing a longer track segment

The overall thickness of the Inner Detector is about 0.4 radiation lengths (X_0) and increases up to 1.5 X_0 in the forward region due to the presence of cables for electronic connections and the cooling system.

2.2.3 Pixel detector

The silicon pixel technology is the only solution that guarantees good pattern recognition performance in very dense track environments like the one close to the LHC interaction point.

The task of the sub-detector is to contribute to the track reconstruction by providing at least three precise hits in the proximity of the interaction point; these hits are crucial also for the precise reconstruction of the primary vertex. Due to its design and location, the pixel detector is particularly important for the measurement of the track impact parameter defined as the minimum distance of the track to the primary vertex. This quantity is one of the main ingredients for the identification of jets coming from b/c quarks and τ leptons. The resolution on the track impact parameter is completely dominated by the performance of the pixel detector.

The sub detector is organised in a barrel and two end-caps. The barrel is composed of three 80 cm length cylinders with radii 5.05 cm (B-layer), 8.85 cm (layer 1) and 12.25 cm (layer 2). Each end-cap contains three disks with radii of 34 cm placed at distances of $|z| = 49.5$, 58.0 and 65.0 cm from the centre of the detector.

The required high granularity is obtained using silicon chips segmented in a matrix of pixels allowing a simultaneous measurement of the two spatial coordinates. The dimension of the single "pixel" is 50×400 μm^2 and it has a thickness of 250 μm. The shortest dimension of the sensor is aligned in the direction of the bending plane of the particle in order to achieve the best performance. The average position resolution is equal to 10 μm in the direction of the short pixel pitch, and 115 μm in the long one.

The basic unit of the detector is the module, which contains the silicon sensor of size 6.28×2.2 cm^2 together with all the required electronics. Each module is segmented in a matrix of 144×328 pixels; in total $\sim$ 1800 modules are assembled in the barrel and endcap for a total of 80 million channels.

2.2.4 SemiConductor Tracker

The SCT has been designed to provide at least four precise points per track over the full η range covered by the Inner Detector. Thanks to its high granularity, it contributes to the track reconstruction and momentum measurement.

The SCT barrel is composed of four cylinder (layers) of radii 30.0, 37.3, 44.7 and 52.0 cm. Each layer is an assembly of several longitudinal staves on which the modules are mounted. Each SCT end-cap is composed of nine disks with modules arranged in the radial direction. The module is the basic unit of the sub-detector and contains two single sided silicon microstrip sensors mounted back to back; it has an active area of 6.36×6.40 cm^2, a thickness of 350 μm and contains 768 microstrips with a 80 μm width.

In the barrel the R–ϕ coordinate of the hit is determined by the strip position while a precise measurement of the z-position is obtained exploiting the stereoscopic effect: the back-to-back sensors are mounted with a 40 mrad 'tilt' angle so the crossing point of the strips on both sensors on each module is used to determine the space point position. In the endcap, the ϕ position of the track is determined using the strip position and the R-position with the 'stereo' effect.

The achieved spatial resolution is of 17 μm in the direction of the strip pitch, and of 580 μm in the direction determined by the strip crossing.

Transition Radiation Tracker

The TRT is based on the drift (straw) tube technology, particularly suited to LHC conditions due to good resistance to radiation. It is designed to provide on average 36 hits per track in the region $|\eta| < 2$; at the same time, it provides information for electron identification due to the measurement of the so-called transition radiation.

The TRT barrel extends from a radius of 56 cm to the edge of the cryostat ($R = 107$ cm). It contains about $5 \cdot 10^4$ straw tubes with a length of 114 cm arranged in the direction of the beams. Each TRT end-cap contains $3.2 \cdot 10^5$ 37 cm long tubes oriented in the radial direction and arranged on 192 “wheels”.

Each straw tube has a diameter of 4 mm[7], it contains a 30 μm tungsten anode wire and it is filled with a gas mixture of 70% Xe, 20% CO_2 and 10% CF_4. The space between the tubes is filled with plastic material (polyethylene) in order to produce the transition radiation; the emission of photons largely depends on the Lorentz boost γ (E/m) of the particles and, in the energy range of interest, is present only for electrons.

Through the tube drift time measurement, each channel is able to infer one of the track hit coordinates (R-ϕ in the barrel, z in the end-cap) with a spatial resolution of ~ 130 μm. Two independent thresholds are applied during signal processing. The high threshold signals are used to identify photons from the TR process and are thus exploited to discriminate electrons from other charged particles (muons, pions and kaons).

2.2.5 Calorimeters

Figure 2.6 (a) shows an overview of the ATLAS calorimeter system: an inner electromagnetic calorimeter surrounded by a hadronic calorimeter. Both detectors are designed to be fully ϕ-symmetric for a complete coverage around the beam axis. They are divided into a central barrel part and two symmetric end-caps for a pseudorapidity coverage up to $|\eta| <5$. In the acceptance region covered by the Inner Detector the electromagnetic calorimeter has very fine segmentation for precise measurement of photons and electrons. The hadronic and forward calorimeters have coarser segmentation but still allow a precise measurement of jet kinematics as well as containment for missing energy calculation.

Electromagnetic calorimeter

The electromagnetic calorimeter (ECAL)[64] uses liquid argon (LAr) as active material and 1.8 mm thick lead plates as absorber. The liquid argon solution was adopted for its intrinsic linear behaviour, high ionisation yield, stability and resistance to radiation. The lead plates have a characteristic ‘accordion’ shape and are oriented in the radial direction. This allows a complete symmetric coverage without cracks in the azimuthal direction. High voltage is applied between absorber plates to collect the ionisation electrons from the interaction in the liquid argon as well as to produce the signal amplification. The electric signal is read from shaped cathodes in the plates through capacitive coupling.

The ECAL barrel ($|\eta| <1.475$) is composed of two identical half-barrels separated by a 4 mm gap at z=0. Each end-cap is mechanically divided into two co-axial cylinders covering the region $1.375< |\eta| < 3.2$. In the central region a *pre-sampler* layer is located in close contact to the cryostat wall. The information from this layer is exploited in the calibration to estimate the energy lost by the electron or photon in the passive material of the solenoid.

[7] the radius of the tube is the main characteristic affecting the speed of the detector

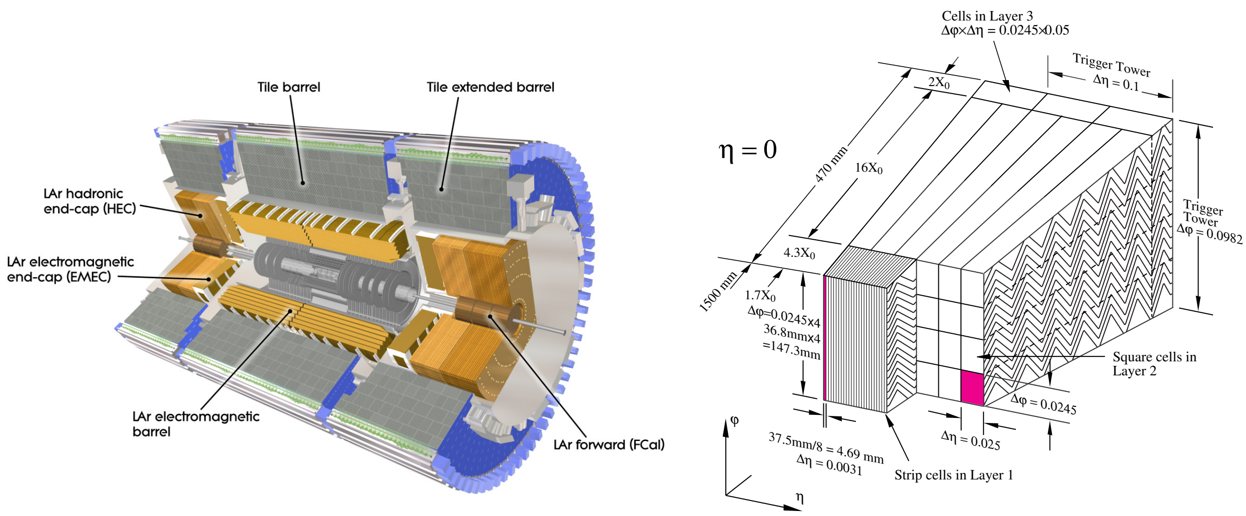

(a) **(b)**

Figure 2.6: Layout of the ATLAS calorimetry system (a). Schematic view of the the segmentation of the EM calorimeter (b).

The total thickness of the ECAL is at least 22 radiation lengths (X_0), increasing with η from 22 X_0 to 33 X_0 in the barrel and from 24 X_0 to 38 X_0 in the endcap. This guarantees a full containment of electrons and photons up to transverse momenta of a few TeV.

The designed energy resolution [60] is equal to:

$$\frac{\sigma_E}{E} = \frac{9\%}{\sqrt{E}} \oplus 0.3\% \quad \text{with } E \text{ expressed in GeV} \tag{2.3}$$

Another important characteristic of the electromagnetic calorimeter is its granularity. Figure 2.6 (b) shows the geometry of a slice of the calorimeter. The readout on the absorber plates is segmented in order to create three longitudinal sections with very different depth and a cell structure in the η-ϕ plane. The second layer, containing most of the thickness of the calorimeter, is divided into squared cells of size $\Delta\eta \times \Delta\phi = 0.025 \times 0.025$ and it will contain the largest part of the shower. The back third compartment has a coarser granularity and it is used to estimate the amount of energy lost beyond the ECAL. In the first layer ($\sim 4\ X_0$), the readout is finely segmented in the η direction with 'strips' of $\Delta\eta = 0.003$, for a precise determination of the shower properties. The strip layer is of particular importance for photon and electron identification (electron,photon/π_0 separation) and, combined with the information from the second layer, can be used to obtain precise information on the photon's production vertex (photon pointing).

Hadronic calorimeters

The ATLAS hadronic calorimeter is composed of different independent sampling calorimeters, each with its own particular technology and choice of material. The choice was dictated by the different conditions in term of radiation flux and performance requirements encountered as a function of the pseudorapidity of the particles.

In the central region the *Tile Calorimeter* [65] covers the range $0 < |\eta| < 1.7$ (11.4 m long cylinder with an inner radius 2.28 m and an outer radius of 4.25 m). It consists of a sampling calorimeter employing iron (tiles) as passive material (absorber) and plastic scintillators read by wavelength shifting fibres as sensitive material. The structure is organised in periodic towers in the z and ϕ direction while the grouping of fibres for the readout provides a coarse three-layer longitudinal segmentation.

The region 1.5< $|\eta|$ < 3.2 is covered by the *Hadronic End-cap Calorimeter* (HEC), which uses copper plates as absorbers and liquid argon as active material for its superior radiation resistance. As for the electromagnetic calorimeter the electric signal produced in the LAr is collected by cathodes on the plates.

Finally, in the most forward part (3.1< $|\eta|$ <4.9) a *Forward Calorimeter* (FCAL) is present. It is assembled with tungsten rod absorbers embedded in a copper matrix. Between the two, a thin gap filled with liquid argon provides the active material.

The radial depth of the hadronic calorimeter is approximately 7.4 interaction lengths (λ) with minimal variation across the η range. This allows a very good hermeticity for the measurement of missing transverse energy as well as "shielding" the muon spectrometer ensuring that only muons having momenta exceeding a few GeV can reach the outer detector.

The resolution achieved in this configuration [60] is:

$$\frac{\sigma_E}{E} = \frac{50\%}{\sqrt{E}} \oplus 3\% \qquad \text{for } Tile \text{ and } HEC \tag{2.4}$$

$$\frac{\sigma_E}{E} = \frac{100\%}{\sqrt{E}} \oplus 10\% \qquad \text{for the } FCAL \tag{2.5}$$

2.2.6 Muon Spectrometer

The goal of the ATLAS muon spectrometer is to provide a precise measurement of the muon momentum up to very high energy ($\sim$ 3 TeV) in the pseudorapidity range $|\eta| < 2.7$. The capability of reconstructing the muon track without requiring information from the inner detector is particularly important for fast event triggering as well as for the redundancy of the pattern recognition.

The size of the apparatus (which ultimately defines the colossal size of the entire detector) was determined from a compromise between the highest toroidal magnetic field value and the required precision for high energy muons, since the momentum measurement is based primarily on the muon deflection[8].

It is composed of planar elements (stations or *chambers*) located in the volume covered by the toroids. Several different detector solutions are employed in the muon spectrometer given the multiple tasks that it has to perform [66]. Precision chambers usually provide only the track coordinate in the bending plane. Precision tracking chambers are supported by detectors with a coarser spatial resolution but with very fast response time (< 25 ns) used to provide a trigger signal and timing calibration for the event. At the same time, given the large size of the spectrometer, the particle flux from the interaction point has a large variation according to the position of the muon chambers, for instance it increases substantially at high pseudorapidities. Different technologies have been adopted in order to keep similar performance in terms of radiation hardness, low occupancy and detector efficiency.

The conceptual layout of the muon spectrometer is shown in Figure 2.7: four different types of muons chambers are present for a total of $\sim$ 1 M readout channels.

tracking chambers :

[8] the magnetic deflection is governed by the formula $p(\text{ GeV}/c) = 0.3 \cdot B(T) \cdot R(m)$ were R represents the radius of curvature of the particle. For a fixed field, with increasing muon momentum the radius of the trajectory increases implying that a large path of the muon in the detector is needed in order to provide a measurable deflection of the trajectory.

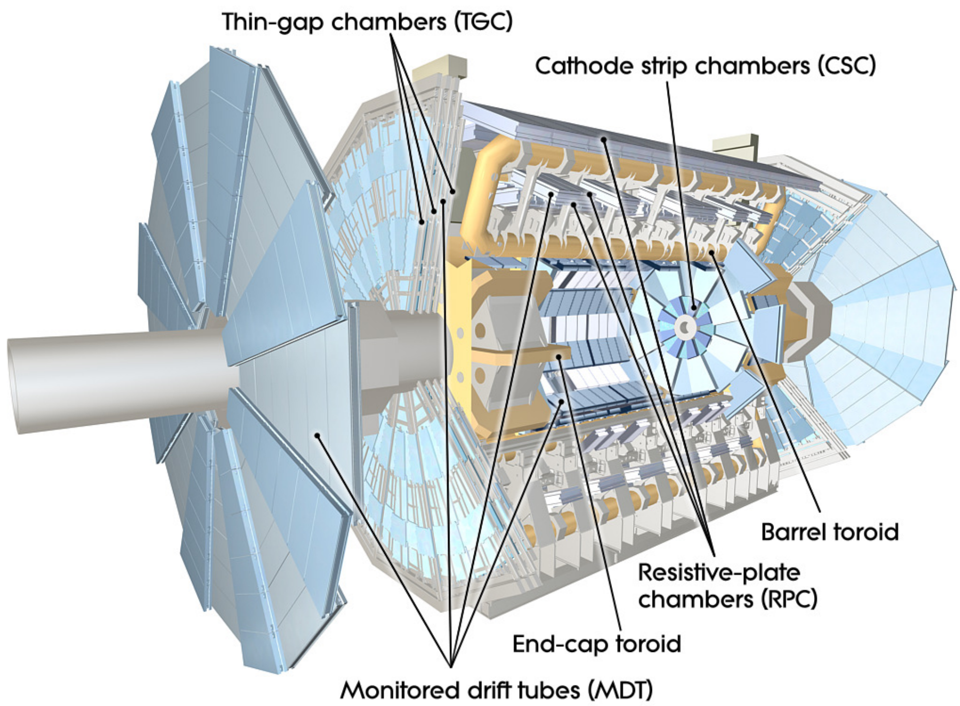

Figure 2.7: Cut view of the muon spectrometer with the location of the different type of muon chambers.

MDT (*Monitored Drift Tube* chambers): chambers based on the drift tube technology positioned in the ϕ direction. All regular MDT chambers consist of two groups of tube layers separated by a mechanical spacer. Due to their reliability, mechanical robustness and simpler operation, MDT chambers are employed to cover the larger area of the spectrometer ($|\eta|$ <2.7, 2.0 for the innermost layer). MDTs are used to measure the coordinate only in the bending plane achieving a precision of 35 μm.

CSC (*Cathode Strip Chambers*): multi-wire proportional chambers with the wires oriented in the radial direction and with the two cathodes segmented in strips with orthogonal directions. The maximum drift time for signal collection is 40 ns compared to the 700 ns of the MDTs; this gives the possibility to achieve higher acquisition rates. Due to this capability, together with the high radiation resistance, CSCs are used in the range 2.0< $|\eta|$ <2.7. The spatial resolution is $\sim$ 40 μm in the bending plane and $\sim$ 5 mm in the non-bending one.

triggering chambers :

RPC (*Resistive Plate Chambers*): detectors with parallel electrode plates and a gas-filled gap are mounted in the barrel to cover the region $|\eta| < 1.05$. A spatial resolution of $\sim$ 10 mm is achieved both in the bending and in the non-bending direction, while the time resolution is of a few ns.

TGC (*Thin Gap Chamber*): multi-wire proportional chambers with the characteristic that the wire-to-cathode distance is smaller than the wire-to-wire distance for a fast collecting time. They are assembled in the end-cap wheels, covering the region 1.05 < $|\eta|$ < 2.7 (2.4 for triggering). The timing resolution is comparable to the RPC one while the spatial resolution is in the range of 2-7 mm for both coordinates.

In the barrel region, muon tracks are measured with MDT chambers and RPCs assembled on three cylindrical layers: the coordinate in the bending plane is provided by the MDT chambers, while the coordinate in the non-bending plane is provided by the RPCs (together with timing information). In the endcap region, MDT and CSC provide the coordinate in the bending plane while the non-bending coordinate is provided by the TGCs.

The muon spectrometer is designed to measure in standalone mode muons with transverse momenta down to 3 GeV (softer muons are stopped) up to a few TeV. The achieved momentum resolution is $\sim$ 10% at p_{T}= 1 TeV. At lower energies the resolution is improved substantially by combining the track reconstructed in the muon spectrometer with a track reconstructed in the Inner Detector.

2.2.7 Luminosity detectors and luminosity measurements

A good determination of the integrated luminosity is of particular importance to reach the ultimate precision in measurement of SM process of interest. The luminosity L in a p-p collider can be expressed as:

$$L = \frac{\mu_{\mathrm{vis}} n_{\mathrm{b}} f_{\mathrm{r}}}{\sigma_{\mathrm{vis}}} \tag{2.6}$$

where f_{r} is the collider revolution frequency, n_{b} the number of colliding bunches and σ_{vis} the visible inelastic cross section (total inelastic cross section times the detector acceptance and efficiency).

μ_{vis} (or simply μ in the following) represents the visible interaction rate per bunch crossing. It is extracted mainly from the signals coming from specific luminosity detectors. The simplest algorithm consists in 'simple counting' of bunch crossings where detectors reported a signal, but more refined algorithms[67] are used in particular when the probability that two or more pp interactions occur in the same bunch crossing is no longer negligible (a condition referred to as pile-up).

The main detectors for luminosity measurement are listed below:

- *Minimum Bias Trigger Scintillators* (MBTS): located at $z = \pm 365$ cm from the interaction point, they cover the pseudorapidity region 2.09$< |\eta| <$ 3.84. The MBTS were employed during 2010 to trigger on events with minimal requirement on collision activity. During 2011 and 2012, they were not considered as a luminosity detectors given the saturation effect produced by the high interaction rate.

- *Beam Conditions Monitor* (BCM): 1 cm^2 diamond detectors located at $z = \pm 184$ cm around the beam pipe. Their fast readout and good time resolution (0.7 ps) allow them to provide luminosity information for each bunch crossing. At the same time they are also employed to trigger on beam losses and induce the dump of the beam, thus protecting the silicon detectors from damage that might result from an uncontrolled beam.

- *LUCID*: a Cherenkov detector specifically designed for luminosity measurement. It consists of 16 aluminium tubes surrounding the beam pipe at 17 m from the interaction point. Each tube is filled with C_4F_{10} and is coupled to a photomultiplier in the backend.

In addition, cross-checks of the luminosity measurement have been performed using information from other standard sub detectors: counting of primary vertices reconstructed by the Inner Detector and integrated signals from the Tile and forward calorimeter.

In order to use the measured μ_{vis} for luminosity determination, each detector and algorithm must be calibrated by determining its visible cross section σ_{vis}. The calibration technique exploits the so-called van der Meer scans[68]; they are special low-intensity LHC runs where the beam separation in the transverse planes is varied ('scanned') in order to determine the beams' overlap profile. Through the determination of the beam lateral profile the luminosity of the particular run can be inferred using formula 2.1.

The achieved precision is of a few % depending on the data taking year.

2.2.8 Trigger and data acquisition

Due to technical and practical limitations, not every LHC collision can be recorded by the ATLAS detector; the goal of the ATLAS trigger and data acquisition (DAQ) system is to select in real time and to record efficiently events with interesting characteristics for physics analyses. The implementation results in a multi-level system optimised to cope with the very high interaction rate and short bunch spacing of the LHC. Three decision levels are implemented corresponding to different strategies and technologies for the buffering of the information coming from the subdetectors, as shown in Figure 2.8. The aim is to achieve an "as early as possible" rejection of events to reduce the throughput in the down stream acquisition chain. The input rate to L1 is given by the beam crossing rate and is 40 MHz when all the LHC bunches are used. L1 reduces this to 75-100KHz. L2 subsequently reduces this to a few kHz. The output rate of the EF is 300-400 Hz of data events which are written to disk for offline analysis[9].

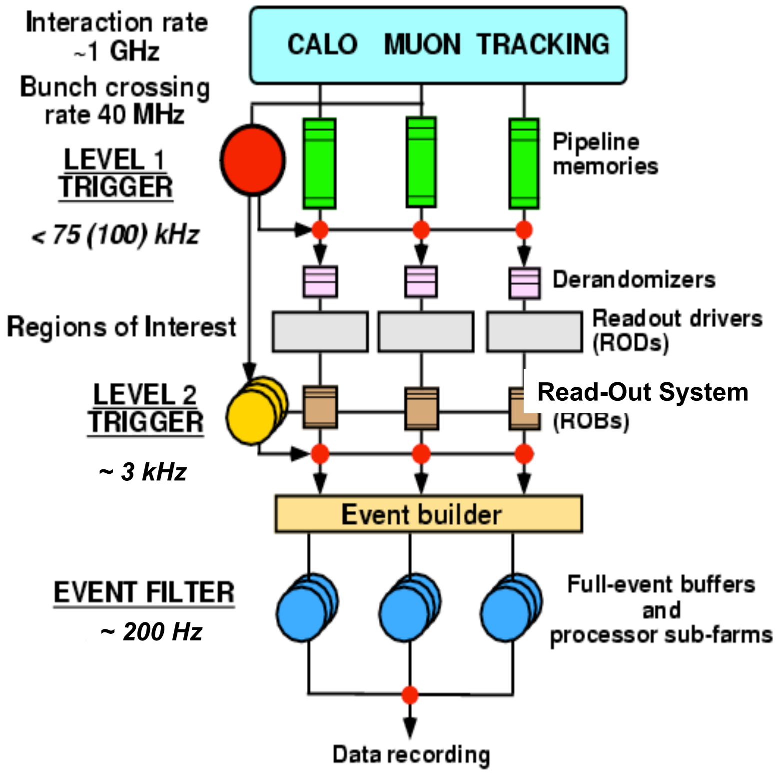

Figure 2.8: The ATLAS trigger and data acquisition system including the design value for the output rate after each trigger level.

Before the decision of the first level trigger (L1), information is stored in the on-detector front-end memory buffers. The accepted events are transferred to the ReadOut Drivers (ROD)

[9]Thanks to a more efficient re-distribution of computing and storage resources, the final recording rate has been increased to up to 400 Hz with respect to its design value of 200 Hz.

located outside the detector. From the ROD, partial detector information can be extracted by the second trigger level (L2) to improve the event decision. If the event is not rejected by the L2, full information from the RODs is passed to the event building farm. Speed-optimised full event reconstruction can be performed and used by the third trigger level (Event Filter) to decide on the event final storage.

Additional details on the ATLAS trigger architecture, implementation and performance will be given in Chapter 4.

Once recorded, the events are processed offline and prepared for the analysis. Analog and digital signals from each detector component are converted into basic physics quantities through proper calibrations. Signals from the silicon detectors are converted into 3D space coordinates and the associated energy deposited by the particle. Analogue signals from the calorimeter are sampled and compared to reference pulse shapes to obtain the energy release in the particular calorimeter elements. These quantities will serve as an input to the reconstruction of physics objects (electrons, muons, jets), as will be described in the next chapter.

2.2.9 Monte Carlo simulation

The simulation of events follows several steps in the ATLAS computing chain[69]. For a specific process, Monte Carlo programs are used to generate events containing the hard scattering part as well as the evolution of the parton shower and the hadronisation. Several programs are available for these purposes and they will be discussed with additional details in the analysis chapters.

The outcome of the event generation is a list of stable[10] particles originating from the interaction point (including subsequent decay product of long-lived particles). The subsequent step consists in the precise simulation of the interactions of such particles with the detector; this simulation is performed with the GEANT4[70] program. A less refined simulation [71] (know as Atlfast-II or AF2) is also available. This considerable reduces the CPU time necessary to process the events by applying a parameterised description of the particle showers in the calorimeters.

At this stage, all Monte Carlo events are overlaid with additional inelastic events generated to simulate the effect of pile-up. A reweighting procedure is then applied to the Monte Carlo samples so that the distribution of the average number of interactions per bunch crossing (or the number of primary vertices for what concerns the 2010 analyses) matches the corresponding distribution of the data sample that is being analysed. The reweighting approach is also adopted to adapt the simulation of the LHC beam parameters like the spatial dimensions beams interaction region.

After the detector simulation the events are reconstructed and analysed by the same software chain also used for data in terms of converting the signal measured in each sensitive element of the detector to a physical quantity. Particular attention is put into simulating also temporary defects from ATLAS data taking or localised detector malfunctioning in order to improve the description of data.

Finally, as will be described in more detail in the next chapter, the Monte Carlo simulation is corrected for any disagreement with data in the description of the performance of the object reconstruction and identification algorithms.

[10]in this context 'stable' particle indicates all the particles with lifetime long enough to travel macroscopic distances before decaying.

2.3 ATLAS operation

Table 2.3 summarises the number of readout channels for each subdetector together with the fraction of operational channels at the end of the 2012 data-taking. More than 95% of each subdetector was fully operational for a total of 90M channels.

Subdetector	Number of Channels	Operational Fraction
Pixels	80 M	95.0%
SCT Silicon Strips	6.3 M	99.3%
Transition Radiation Tracker	350 k	97.5%
LAr EM calorimeter	170 k	99.9%
Tile calorimeter	9800	98.3%
Hadronic endcap LAr calorimeter	5600	99.6%
Forward LAr calorimeter	3500	99.8%
Muon Drift Tubes	350 k	99.7%
Cathode Strip Chambers	31 k	96.0%
Barrel Muon Chambers	370 k	97.1%
Endcap Muon Chambers	320 k	98.2%

Table 2.3: number of channels and operating fraction of each ATLAS subdetectors.

The integrated luminosity for each of the three years of data taking is reported in Figure 2.9. The luminosity delivered by the LHC machine is shown in green while the amount of luminosity collected by the ATLAS detector is reported in yellow. The inefficiency in the data-taking arises partly from the so-called 'warm start' procedure which consists in ramping up the voltages for the silicon detector only after the LHC has declared stable beam, or transient problems in the trigger and detector data acquisition. The ATLAS data taking efficiency was above 90% in each year.

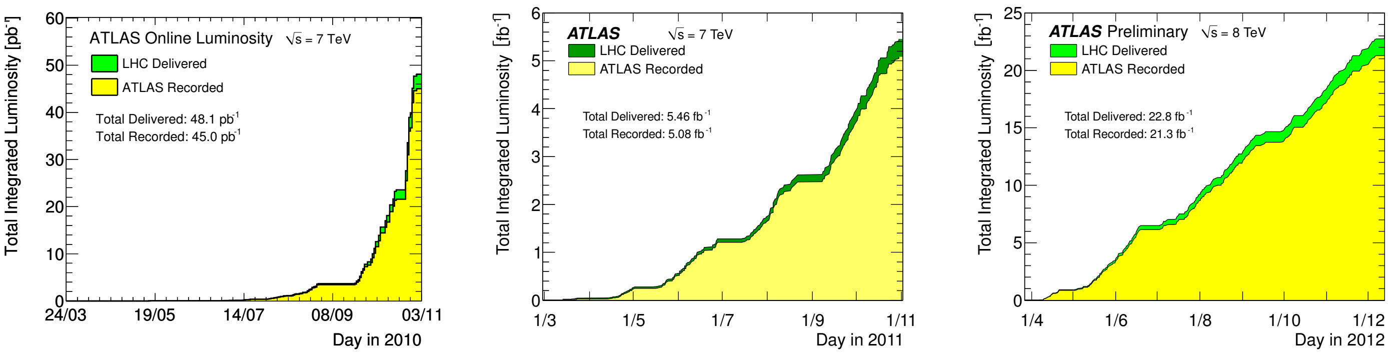

(a) (b) (c)

Figure 2.9: Integrated luminosity delivered by LHC in the year 2010 (a), 2011 (b), 2012 (c) as a function of data taking days.

The fraction of good data delivered by each subdetector is shown in Figure 2.10 for each of the three years of data-taking. The fraction is above 90% for each subdetector and it is increasing in each year; a sign of a constant improvement in the operation of the detector.

Table 2.4 summarises the integrated luminosity collected by ATLAS and flagged as 'good quality data' from all the subdetectors for each of the three years of data-taking.

Inner Tracking Detectors			Calorimeters				Muon Detectors			
Pixel	SCT	TRT	LAr EM	LAr HAD	LAr FWD	Tile	MDT	RPC	CSC	TGC
99.1	99.9	100	90.7	96.6	97.8	100	99.9	99.8	96.2	99.8

Luminosity weighted relative detector uptime and good quality data delivery during 2010 stable beams in pp collisions at √s=7 TeV between March 30th and October 31st (in %). The inefficiencies in the LAr calorimeter will partially be recovered in the future.

ATLAS p-p run: March-October 2011

Inner Tracker			Calorimeters		Muon Spectrometer				Magnets	
Pixel	SCT	TRT	LAr	Tile	MDT	RPC	CSC	TGC	Solenoid	Toroid
99.8	99.6	99.2	96.9	99.2	99.4	98.8	99.4	99.1	99.8	99.3
All good for physics: 89.9%										

Luminosity weighted relative detector uptime and good quality data delivery during 2011 stable beams in pp collisions at √s=7 TeV between March 13th and October 30th (in %) - corresponding to 5.2 fb-1 of recorded data. This data quality status refers to the data after the summer reprocessing campaign.

ATLAS p-p run: April-December 2012

Inner Tracker			Calorimeters		Muon Spectrometer				Magnets	
Pixel	SCT	TRT	LAr	Tile	MDT	RPC	CSC	TGC	Solenoid	Toroid
99.9	99.1	99.8	99.1	99.6	99.6	99.8	100.	99.6	99.8	99.5
All good for physics: 95.5%										

Luminosity weighted relative detector uptime and good quality data delivery during 2012 stable beams in pp collisions at √s=8 TeV between April 4th and December 6th (in %) – corresponding to 21.3 fb-1 of recorded data.

Figure 2.10: The fraction of good data delivered by each subdetector during the year 2010 (top), 2011 (middle) and 2012 (bottom).

year	LHC delivered	ATLAS recorded	ATLAS 'good' quality'
2010	48.1 pb^{-1}	45.0 pb^{-1}	35.2 pb^{-1}
2011	5.46 fb^{-1}	5.06 fb^{-1}	4.7 fb^{-1}
2012	22.8 fb^{-1}	21.3 fb^{-1}	20.3 fb^{-1}

Table 2.4: Integrated luminosity for each year of data-taking. Columns correspond to LHC delivered luminosity, luminosity recorded by ATLAS and luminosity with good data quality flag from all the subdetectors.

The impressive instantaneous luminosity delivered by the LHC came at the cost of high pile-up. Due to the large amount of protons in each bunch and the reduced transverse profile of the beam, multiple *pp* collisions can happen at every bunch crossing. Figure 2.11 shows the distribution of the average[11] number of interactions per crossing in 2011 and 2012. While in 2010 the maximum number of simultaneous interactions per crossing was alway smaller than 5, in 2011 the average was around 9-10 with maximum values up to 25. In 2012 the maximum number of interactions per crossing reached up to 40. The multiple interactions per crossing produce two types of effects: 'in-time' and 'out-of-time' pileup. The former refers to the presence of an additional number of particles in the event produced by the multiple interactions and it is usually estimated by the number of reconstructed primary vertices in an event. The latter is the effect of multiple interactions from events prior or posterior to the analysed one; they can leave signal traces in the detector due to the readout electronics dead time and the integration time required to collect the signal, especially in the LAr calorimeter.

The object reconstruction and identification algorithms have evolved with time particularly to adapt to and compensate for the degradation of the optimal detector performance due to pileup (tracking efficiency, resolution of the calorimeter and missing transverse energy).

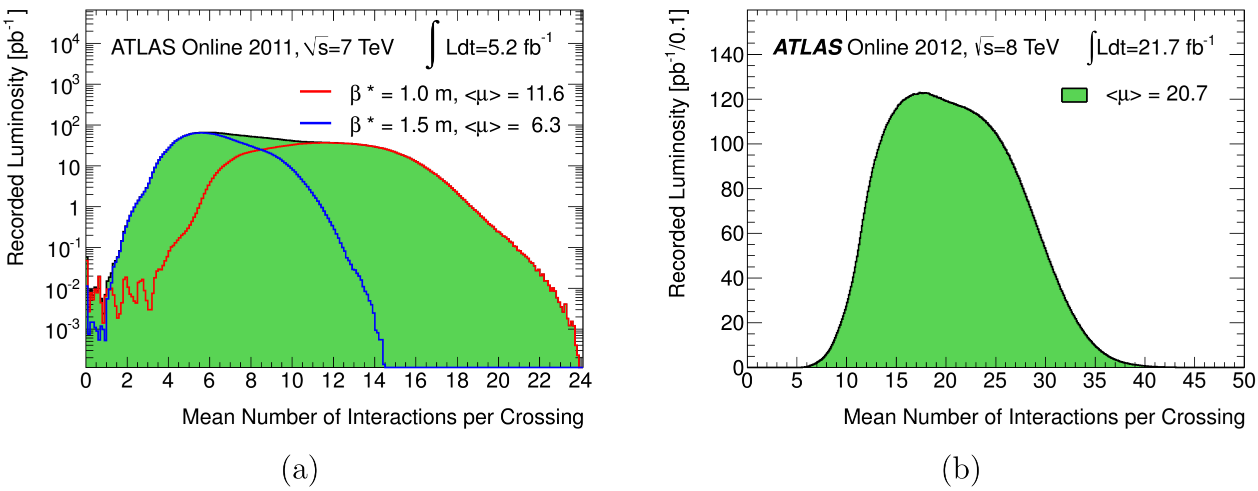

Figure 2.11: Distribution of the average number of interactions per bunch crossing over the year 2011 (a) and 2012 (b). For 2011 the two periods are shown corresponding to different values of β^* a quantity describing the transverse beam size at the interaction point.

[11]the average is performed over a single luminosity block (*lumiblock*). A luminosity block is the smallest unit of time in the ATLAS data-taking defined as the minimal period where all the data-taking configurations are constant. In general the duration of a luminosity block is of the order of 1 minute.

Chapter 3

Object definition and selection

Each recorded event undergoes offline event reconstruction. The output information from all sub-detectors is combined to form basic quantities such as tracks and calorimetric clusters. These quantities are then used to reconstruct final physics objects.

The reconstruction and identification of $t\bar{t}$ and $t\bar{t}H$ decays requires the usage of different types of physics objects (leptons, jets, missing transverse energy) for which a good performance of all the detector components is necessary.

This chapter describes the definition of the various physics objects used in the presented analyses. A brief description of the systematic uncertainties associated with the usage of the object is also included. In general, the criteria for the object definition vary over the three years of LHC RunI to adapt to different pile-up conditions and to reflect an improved detector understanding. More emphasis will be put on the description of the conditions/parameters for the 2012 run period.

3.1 Tracks and primary vertices

Reconstructed tracks from charged particles enter at multiple levels in the definition of the physics objects used for physics analyses; from the reconstruction of electrons and muons to the calculation of lepton isolation and the pile-up suppression in jets. Several different pattern recognition algorithms are used to find tracks in the Inner Detector [72]. The tracks typically used in physics analyses are found using an *inside-out* pattern recognition algorithm, which starts building track “seeds” considering space points in the silicon detectors and then extending the track candidate outwards to the TRT. An *outside-in* (also referred to as back-tracking) sequence takes into account all the hits not considered by the previous algorithm; it is seeded in the TRT and the track candidate is then extrapolated inwards in the silicon detectors. A second inside-out sequence with less stringent pattern recognition requirement is executed after the back-tracking. It aims to recuperate tracks with $p_{\mathrm{T}} > 150$ MeV and is therefore referred to as *low p_{T} tracking.* A reconstructed track is fully specified by the following parameters:

$$(d_0, z_0, \phi, \theta, q/p) \tag{3.1}$$

where d_0 and z_0 represent the minimum distance to the centre of the detector in the transverse plane and in the longitudinal direction respectively. ϕ and θ describe the direction and q/p the charge over momentum. Impact parameters and direction are often expressed with respect to the main primary vertex in the event.

Quality cuts are applied to the track parameters and to the number of hits in the silicon subdetectors, at several stages during the track reconstruction. This allows to improve the performance of the algorithms (reducing combinatorics), improve the resolution and reduce the fake rates especially in the critical pile-up condition of 2012.

Due to the large number of protons per bunch crossing, multiple interaction vertices can be reconstructed in the event. Primary vertices are reconstructed from the combination of well measured tracks with an *adaptive vertex fitting* algorithm [73] and they are constrained to lie within the estimated position of the beam spot[1].

In order to improve the resolution on the vertex spatial position, only vertices that have at least 4 tracks with $p_{\rm T} > 500$ MeV associated with them are considered. The number of reconstructed primary vertices is used as a measure of the in-time pile-up and several calibration parameters depend on it. During 2012, up to 20 primary vertices have been reconstructed in a single event; it is thus of primary importance to ensure that all the physics objects of interest in the events originate from the same vertex.

The vertex with the highest sum of track $p_{\rm T}^2$ is typically assumed to be the main vertex of the event corresponding to the hardest p-p interaction. The kinematics of the physics objects are then recomputed considering this vertex as a new reference point. Monte Carlo studies have shown that this choice allows to select the correct production vertex of process containing high-$p_{\rm T}$ charged leptons or jets in the final state in almost 100 % of the cases.

3.2 Leptons

The reconstruction and identification of electrons and muons will be discussed. Tau-lepton reconstruction is not considered since they will not explicitly be used in any of the analyses described in this thesis. According to the particular tau decay topology, they would be identified either as isolated electrons or muons, or as (narrow) jets.

3.2.1 Electrons

The reconstruction of electron candidates combines energy deposits (clusters) in the electromagnetic calorimeter and matches them to tracks in the inner detector. In the $\eta - \phi$ plane, calorimetric towers[2] of size $\Delta\eta \times \Delta\phi = 0.025 \times 0.025$ are used as inputs to a *sliding-window* algorithm [74]. The size of the window is 3×5 towers and a cluster seed is produced if the combined transverse energy of the towers inside the window exceeds 5 GeV.

Tracks from the inner detector are extrapolated to the middle layer of the electromagnetic calorimeter and a loose matching is performed to the cluster seed. The absolute value of $\Delta\eta$ between the cluster and the track has to be smaller than 0.05 while the $\Delta\phi$ must satisfy the relationship $-0.05 < q \cdot \Delta\phi < 0.10$. The sign corrected $\Delta\phi$ selection takes into account the bending direction of the electron in the solenoidal magnetic field. Matched clusters are then rebuilt with a 3×7 or 5×5 cells window around the centre depending on wether they are located in the barrel or in the end-cap. The choice for different windows aims to maximise the reconstruction quality by taking into account the changes in the granularity and shower development profile.

The final cluster energy is obtained by correcting for the energy losses in the material in front of the calorimeter, the lateral leakage due to the fixed cluster size and the longitudinal leakage in the hadronic calorimeter. All the corrections are obtained by detailed studies in Monte Carlo

[1]The beam spot is defined as the spatial region around the interaction point where the profiles of the two beams overlap.

[2]A tower contains the energy measured in all the layers of the calorimeter.

simulation and test beams and parameterised as a function of the energy deposited in each of the layers of the calorimeter [75].

For usage in physics analyses, the four-momentum of the electrons is computed using the energy given by the electromagnetic cluster while the direction is taken from the track $\eta - \phi$ coordinates which are computed with respect to the primary vertex in the event. This choice ensures the best resolution on the electron kinematic parameters. Electrons used in the analyses presented in this thesis are required to have $|\eta_{\text{cluster}}| < 2.47$ and to be outside the transition region between the barrel and end-cap EM calorimeter ($1.37 < |\eta_{\text{cluster}}| < 1.52$) since this region shows worse reconstruction and energy resolution performance. Given that the selection criteria described above are related to the geometrical acceptance of the calorimeter, the coordinates of the cluster are used to implement them.

In order to improve the quality of the electron reconstruction, electrons coming from regions of the detector where the EM calorimeter did not show optimal operating performance are excluded. This includes regions with read-out problems, with high-voltage failures and particularly noisy cells in the core of the cluster. These requirements are also applied when analysing Monte Carlo samples ensuring that even temporary conditions are correctly simulated.

The electron identification relies on a cut-based selection using calorimeter, tracking and combined variables. The aim is to provide good separation between isolated signal electrons and non-isolated electrons, electrons from photon conversions and jets faking electrons. Three reference selections have been produced with increasing background rejection power: *loose*, *medium* and *tight*. The increase in discrimination against background is obtained by both the addition of more variables and a change of cut values. The list of variables used for all of the selections [76] is summarised in Table 3.1 for each of the three years of data-taking. The variations with time are justified by an improved knowledge of the detector effects, the need to improve the robustness of the selection against pile-up effects and the increase of instantaneous luminosity which required a tighter selection to reduce the trigger rate. The selected variables are related to the shower evolution and profile in the different layers of the calorimeter (including the highly granular first strip layer) and the quality of the inner detector track and of the track-cluster matching. For selections aiming at larger rejection, particle identification using the TRT as well as vertex reconstruction to veto conversions are also used. The specific cut values for each variable have been optimised as a function of electron p_{T} and η in each year of data-taking.

Figure 3.1 shows the comparison of the efficiency for each benchmark selection in 2012. The analyses presented in this document all use the *tight* electron definition since they require the largest possible rejection of non-isolated electrons. The *tight* selection has an efficiency of $\sim$ 80% for electrons coming from Z decay with a rejection against jets faking electron of 10^5 as estimated from Monte Carlo samples [74]. In addition, for analyses using 2011 and 2012 data, each electron is required to have a longitudinal impact parameter relative to the primary vertex smaller than 2 mm.

In order to further reject background electrons originating from hadron fakes or semileptonic b-hadron decays, isolation requirements are applied to the electron. The selection exploits both track-based and calorimetry-based isolation. The track isolation variable p_{T}^{xx} is the sum of the transverse momenta of all the tracks in a cone of $\Delta R < xx$ around the electron direction. Only tracks with $p_{\text{T}} > 1$ GeV and compatible with the primary vertex are considered with the exception of the track used to build the electron object. The calorimetric isolation variable called E_{T}^{xx} represents the sum of the transverse energy of the calorimetric cells in the cone of $\Delta R < xx$ around the electron with the deposit associated with the electron itself subtracted.

Type	Name	Description	Loose		Medium		Tight	
			10	11/12	10	11/12	10	11/12
Hadronic leakage	R_{had1}	Ratio of E_T in the first layer of the hadronic calorimeter to E_T of the EM cluster	$\surd$	$\surd$	$\surd$	$\surd$	$\surd$	$\surd$
Middle layer of EM calorimeter	R_η	Ratio of the energy in 3×7 cells over the energy in 7×7 cells centred at the electron cluster position	$\surd$	$\surd$	$\surd$	$\surd$	$\surd$	$\surd$
	$w_{\eta 2}$	Lateral shower width: RMS of the energy weighted η position of all the cells in the second calorimeter layer of the cluster	$\surd$	$\surd$	$\surd$	$\surd$	$\surd$	$\surd$
Strip layer of EM calorimeter	w_{stot}	Lateral shower width, $\sqrt{(\sum E_i(i-i_{\max})^2)\,(\sum E_i)}$, where i runs over all strips in a window of $\Delta\eta \times \Delta\phi \approx 0.0625 \times 0.2$, corresponding typically to 20 strips in η, and i_{max} is the index of the highest-energy strip		$\surd$	$\surd$	$\surd$	$\surd$	$\surd$
	E_{ratio}	Ratio of the energy difference between the largest and second largest energy deposits in the cluster over the sum of these energies		$\surd$	$\surd$	$\surd$	$\surd$	$\surd$
3^{rd} layer of EM calorimeter	f_3	fraction of energy in the 3^{rd} layer of the EM calorimeter (2012 only)				$\surd$	$\surd$	$\surd$
Track quality	n_{pixel}	Number of hits in the pixel detector		$\surd$	$\surd$	$\surd$	$\surd$	$\surd$
	n_{Si}	Number of total hits in the pixel and SCT detectors		$\surd$	$\surd$	$\surd$	$\surd$	$\surd$
	d_0	Transverse impact parameter			$\surd$	$\surd$	$\surd$	$\surd$
TRT	n_{TRT}	Total number of hits in the TRT				$\surd$	$\surd$	$\surd$
	f_{HT}	Ratio of the number of high-threshold hits to the total number of hits in the TRT				$\surd$	$\surd$	$\surd$
Conversions	n_{BL}	Number of hits in the b-layer				$\surd$	$\surd$	$\surd$
		Veto electron candidates matched to reconstructed photon conversions					$\surd$	$\surd$
Track–cluster matching	$\Delta\eta$	$\Delta\eta$ between the cluster position in the strip layer and the extrapolated track			$\surd$	$\surd$	$\surd$	$\surd$
	$\Delta\phi$	$\Delta\phi$ between the cluster position in the middle layer and the extrapolated track					$\surd$	$\surd$
	E/p	Ratio of the cluster energy to the track momentum					$\surd$	$\surd$

Table 3.1: Definition of variables used for *loose*, *medium* and *tight* electron identification cuts for the central region of the detector with $|\eta| < 2.47$.

Additional corrections are applied to improve the performance of the calorimetric isolation [77]. Due to the fixed size of the electron cluster, higher-energy clusters tend not to be fully contained and, as a net effect, the isolation energy increases as a function of the electron p_{T} even for well isolated electrons. A so-called p_{T}-leakage correction is derived from Monte Carlo to compensate for this effect. In order to compensate for the pile-up effect, an ambient energy density (ED-correction) subtraction is applied. This technique is very similar to the one used for the jet calibration and will be further discussed in the jet section. For analyses using the 2011 and 2012 datasets, the variables $E_{\mathrm{T}}^{0.2}$ and $p_{\mathrm{T}}^{0.3}$ have been chosen. This stems from the fact that, even after the pile-up suppression, smaller cone sizes are preferable due to the topology of $t\bar{t}$ events where jets are likely to be found closer to the selected electrons. The cut values were chosen in order to obtain a constant efficiency of 90% as a function of p_{T} and η for real electrons already fulfilling the *tight* identification criteria. For the 2010 data sample, the isolation was only corrected for the effect of pile-up through a dependence on N_{PV} and a fixed cut of $E_{\mathrm{T}}^{0.2} < 4$ GeV was applied.

Reconstruction/identification/isolation cut efficiency

The efficiency of the reconstruction, identification and isolation selection have been determined in data using the *tag&probe* techniques. The method will be discussed in more detail in Chapter 4. For the reconstruction efficiency measurement, $Z \to ee$ events have been used since they allow for the purest selection of probes. To assess the identification efficiency, a combined analysis using $J/\psi \to ee$, $Z \to ee$ and $W \to e\nu_e$ events has been performed to cover as wide a p_{T} range as possible and collect sufficient statistics for a 2D p_{T}-η efficiency determination. The isolation efficiency for the electrons satisfying the tight identification criteria has been then assessed using $Z \to ee$ events.

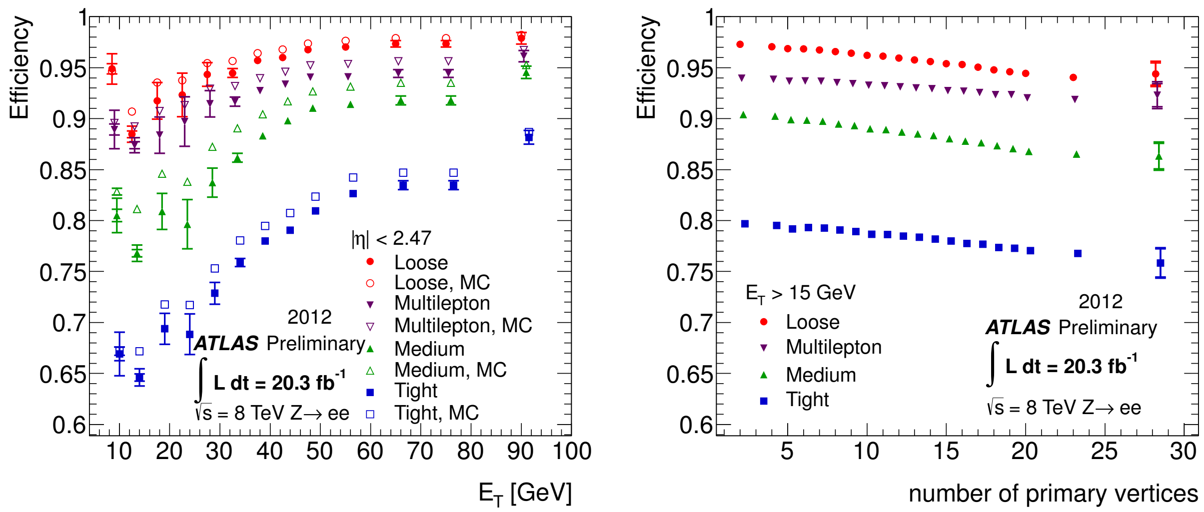

(a) (b)

Figure 3.1: (a) Electron identification efficiency as a function on electron E_{T} for the 2012 benchmark selections in data and Monte Carlo [78]. (b) Measured electron identification efficiency in data for the different benchmark selection as a function of the number of reconstructed primary vertices in the event. The *MultiLepton* selection is a specific benchmark optimised for analyses with more than two leptons in the final state in particular $H \to ZZ \to 4l$.

Figure 3.1 illustrates the electron identification efficiency as a function of the electron E_{T} (a) and the number of reconstructed primary vertices in the event (b). All the benchmark selection criteria result in efficiencies that are reasonably stable versus pile-up, as a result of a careful optimisation process. Scale factors (SF) as a function of electron η (and electron E_{T} for what concerns the identification efficiency) have been derived to account for the discrepancies in the efficiencies between data and Monte Carlo simulation. Scale factors typically deviate from unity by only a few %. The combined uncertainties on the reconstruction/identification and isolation requirement scale factors are also at the level of a few %. For $t\bar{t}$ related analyses, an additional uncertainty of 2% is assumed for the isolation efficiency, due to the extrapolation from the $Z \to ee$ environment to the $t\bar{t}$ environment implying smaller angular distances between the electron and surrounding jets [79].

Electron energy scale/resolution

The electron energy scale has been measured in data using $Z \to ee$ and $J/\psi \to ee$ events. Correction factors as a function of electron η have been obtained by fitting the mass line shape of the two resonances. The total uncertainty on the electron in-situ calibration is $< 1\%$ in the central region and increases up to a few % in the most forward region of the calorimeter. An additional procedure exploiting the combined measurement of the track momentum in the inner detector and the energy in the calorimeter (E/p) has also been adopted. This method profits from the very large sample of collected $W \to e\nu_e$ events. The two analyses have been widely used to monitor the azimuthal uniformity of the calorimeter response, the p_{T}-linearity and the stability over time and pile-up conditions. Figure 3.2 (a) illustrates the result of a fit to the Z mass shape using the 2011 dataset . The data/mc ratio for the peak position as a function of the number of primary vertices displays an excellent stability versus the pile-up (Figure 3.2 (b)).

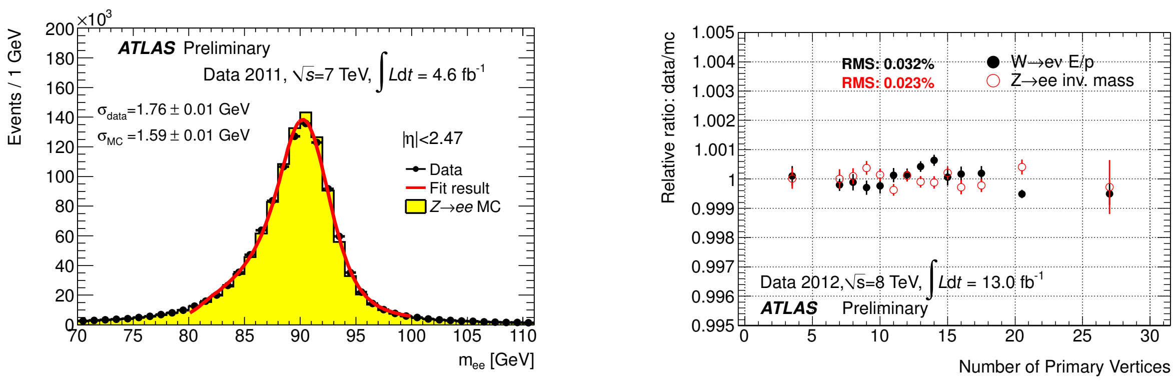

(a) **(b)**

Figure 3.2: (a) Z mass peak line-shape as extracted from the 2011 dataset. (a) Stability of the data/mc mass scale as a function of the number of primary vertices in the event in the 2012 dataset.

A fit to the Z and J/ψ mass peaks has also been used to determine the data/MC agreement for the electron energy resolution. Electrons from J/ψ decays are used to measure the calorimeter sampling term which dominates the resolution at low p_{T}. The resolution from MC has been found to agree with data within 10%. The experimental width of the Z mass peak has been used to assess the resolution in the high p_{T} regime where the calorimeter constant term dominates. A value of $\sim 1\%$ has been found for the 'effective' constant term which takes into account also all the possible sources of non uniformity. The value is in good agreement with the ATLAS construction specifications [61].

3.2.2 Muons

Several types of algorithms for reconstructing muons are available in ATLAS as described in Ref. [75]. The analyses presented in this document make use only of *combined* muons from the *MuId* collection [80]. The algorithm relies on the independent reconstruction of a track in the Inner Detector and a track segment in the muon spectrometer. All track pairs with a small ΔR distance are considered and combined muons are then identified by a common track re-fit to the hits of both tracks[3]. In the fitting procedure, the muon energy loss in the calorimeter is taken into account. This fit has high rejection power against mismatches between inner detector and stand-alone muon tracks.

Additional selection criteria are applied to further improve the quality of the muon and reduce the misidentification rate:

- combined muons are required to have $|\eta| < 2.5$ in order to be confined in the region where the ID has the best track reconstruction;
- the longitudinal impact parameter relative to the primary vertex is required to be less than 2 mm (this cut was not applied in analyses considering 2010 data);
- a series of requirements are set in order to make sure that the track is properly reconstructed in the Inner Detector. A minimal number of hits in the Pixel, SCT and TRT sub-detectors is required together with a hit in the innermost pixel layer when the track crosses an active module. The track is also required not to cross too many Si detector layers without leaving an associated hit. The value of the cut on each quantity was changed in every data-taking year to adapt to the evolving pile-up conditions [81][82][79].

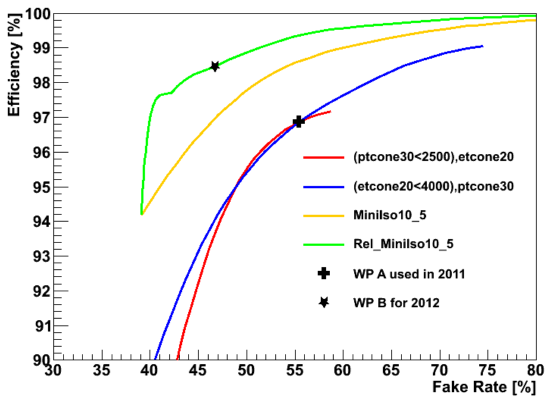

Figure 3.3: Efficiency vs fake rate for different choices of muon isolation. From Ref. [83].

As for the electrons, a further separation between real muons arising from physics processes in the primary interaction from muons mainly originating from decay chains of b/c-hadrons or kaons, is achieved through an isolation requirement.

The chosen variables and the specific cuts applied have evolved as a function of time in order to cope with different levels of pile-up and analysis optimisation requests. The implementation consists of a combination of calorimetric and track isolation. The calorimetric isolation variable called E_{T}^{xx} represents the sum of the transverse energy of the calorimetric cells in the cone of $\Delta R < xx$ around the muon direction excluding the expected muon energy deposition by a minimum ionising particle. The track isolation variable p_{T}^{xx} is the sum of the transverse momenta of all the tracks in a cone of $\Delta R < xx$ around the muon direction. Only tracks with $p_{\mathrm{T}} > 1$ GeV and compatible with the primary vertex are considered.

- 2010: $E_{\mathrm{T}}^{0.3} < 4$ GeV and $p_{\mathrm{T}}^{0.3} < 4$ GeV;
- 2011: $E_{\mathrm{T}}^{0.2} < 4$ GeV and $p_{\mathrm{T}}^{0.3} < 2.5$ GeV;

[3] the algorithm allows also for other hits to be included in the fitting procedure

- 2012: the mini-isolation (I^l_{mini}) [83] variable was introduced to achieve better performance in case of boosted topologies. It is defined as the sums of the transverse momentum of all the tracks satisfying the relation $\Delta R_{(l,track)} < k_T/p^l_{\mathrm{T}}$ where p^l_{T} is the transverse momentum of the muon and k_T is a scale parameter set at 10 GeV. The selection applied corresponds to:

$$I^l_{mini}/p^l_{\mathrm{T}} < 0.05 \tag{3.2}$$

  With increasing lepton p_{T}, the cut on the mini-isolation is loosened by the denominator, while at the same time the size of the considered cone shrinks making the isolation cut less susceptible to pile-up effects and more efficient when the real lepton gets closer to a jet. Figure 3.3 shows the signal efficiency extracted from $Z \rightarrow \mu\mu$ events versus background rejection curves for different isolation definition illustrating the superior performance of the relative mini isolation with respect to the solutions adopted in 2010 and 2011.

Reconstruction/identification/isolation efficiency

The reconstruction/identification and isolation efficiencies have been measured in data with the *tag* & *probe* method using $Z \rightarrow \mu\mu$ events. Figure 3.4 shows the data/mc comparison for the reconstruction plus identification efficiency and the isolation efficiency as extracted from the 2012 data sample. The level of agreement is $\sim$ 1% and found to be very stable versus other kinematic quantities as well as versus the number of primary vertices in the event. Muon

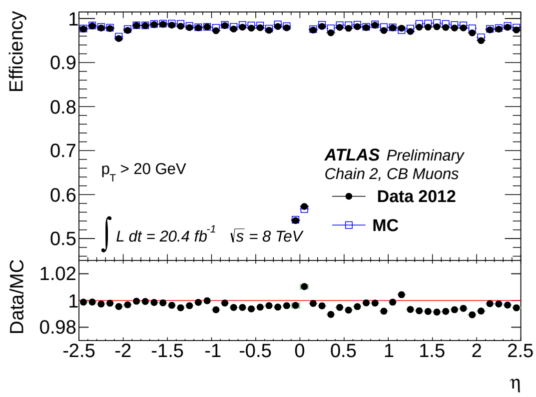

(a)

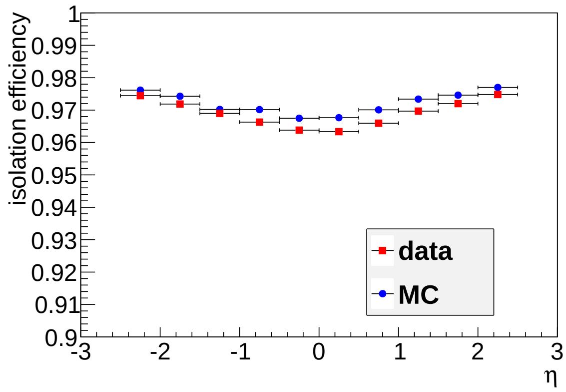

(b)

Figure 3.4: (a) 2012 muon reconstruction+identification efficiency and SF as a function of muon η. (b) Mini Isolation efficiency as a function of muon η for data and Monte Carlo.

triggers and the scale factor corresponding to trigger efficiency will be discussed in Chapter 4.

Muon momentum scale/resolution

The large amount of clean $Z \rightarrow \mu\mu$ events collected in 2011 and 2012 allow a very precise determination of the muon momentum scale from the Z peak position [84]; separate scales are considered for the Inner Detector and the Muon Spectrometer part. Figure 3.5 (a) illustrates the central value and the uncertainty of the correction to the scale in the Muon Spectrometer as extracted from the 2012 data. The amount of the correction, as well as the uncertainty, are at few per mille level. The momentum scale has been tested with other resonances (J/ψ and Υ) and their extracted mass values are found to be in good agreement with the PDG value

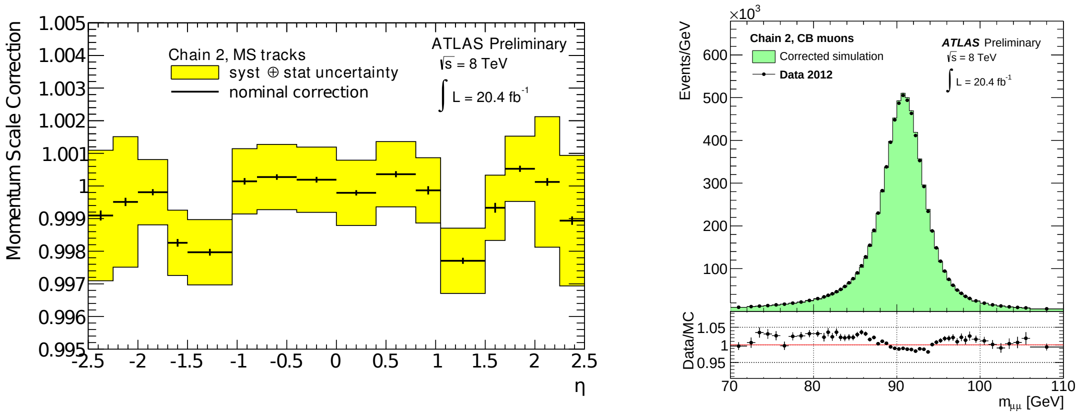

(a)

(b)

Figure 3.5: Scale correction for the muon momentum in the muon spectrometer as a function of muon η (a). (b) Comparison of di-muon invariant mass in 2012 data. Monte Carlo has muon smearing and scale corrections applied.

within the uncertainties [84]. This demonstrates the stability of the estimate as well as the good alignment achieved in the detector.

The muon momentum resolution depends on multiple factors like the amount of material that the muon traverses, the spatial resolution of the individual track points and the quality of the relative alignment of the sub-detectors. For this reason, a separate parameterisation has been used for the Inner Detector and the Muon Spectrometer part. The muon resolution has been measured in data analysing the Z boson mass line shape as well as the relative difference in momentum measurement between the ID and the muon spectrometer. By combining both analyses, correction factors are extracted to modify the Monte Carlo resolution both for the intrinsic term and the multiple scattering one in the ID and MS[4]. These factors (and their relative uncertainties) are used to introduce additional smearing in Monte Carlo to match the data. Figure 3.5 (b) shows the di-muon invariant mass for data and Monte Carlo after such corrections have been applied.

3.3 Jets

Jets are collimated sprays of hadrons produced by the hadronisation process of quarks and gluons. The jet definition aims at re-combining this set of particles in order to obtain a physics object whose characteristics are as close as possible to those of the initial parton.

What defines a jet are the type of inputs and the algorithm used to aggregate them together and build a jet. Jets reconstructed from truth stable particles in Monte Carlo samples are denoted as *particle jets*. Jets built from reconstructed tracks in the detector are called *track jets* and they are normally used as an additional tool to extract jet quantities. Finally, the jets used in ATLAS analyses are built from energy deposits in the calorimeter called *topo-clusters* [85]. The topo-clusters are groups of calorimeter cells topologically connected, all presenting a significant signal above the noise. The noise threshold is varied according to the position of the cell in the topo-cluster in order to control the effect of pile-up. Topo-clusters are calibrated at the electromagnetic (EM) scale which correctly measures the energy deposition

[4] the muon p_{T} resolution can be expressed as: $\sigma(p_{\mathrm{T}})/p_{\mathrm{T}} = a \oplus b \cdot p_{\mathrm{T}}$ where a represents the contribution from multiple scattering and b describes the intrinsic resolution caused by the spatial resolution of the detector components, and any residual misalignment.

by particles produced in electromagnetic showers in the calorimeter. Subsequently the Local Cluster Weighting[86] (LC or LCW in the following) calibration is performed. A correction factor is applied to each topo-cluster according to its energy density profile and longitudinal shower depth. The factors are derived from single particle Monte Carlo simulation and they aim at taking into account the non-compensating nature of the ATLAS calorimeter as well as signal losses due to noise thresholds and energy loss in non-instrumented regions.

The algorithm used to combine topo-clusters into jets is the anti-k_T algorithm[87] with distance parameter R=0.4. It is a sequential recombination algorithm, meaning that particles are clustered into jets one at the time, using as a two-particle distance parameter the formula

$$d_{ij} = \min\left(1/p_{\mathrm{T}i}^2, 1/p_{\mathrm{T}j}^2\right) \cdot \Delta R_{ij}^2/R^2$$

with ΔR_{ij} the angular distance between particles i and j.. The algorithm has been chosen for its theoretical properties of infrared and collinear safety, and for the fact that is produces rather circular jets in the $\eta-\phi$ plane since the hardest particles are clustered at an early stage.

3.3.1 Jet calibration

The aim of the jet calibration is to restore the energy scale of the reconstructed jets in the detector to the one of the truth particle jets. A critical point for the running conditions in 2012 is to correct for the large effect of pile-up where the additional *p-p* interactions produce a large number of particles that enter the jet reconstruction. For jets constructed from LCW clusters the calibration for the 2012 data and Monte Carlo sample proceeds in the following steps:

- *pile-up correction*: the corrected jet p_{T} is given by the formula:

$$p_{\mathrm{T}}^{\mathrm{corr}} = p_{\mathrm{T}} - \rho \cdot A - \alpha \cdot (N_{PV} - 1) - \beta \cdot <\mu> \tag{3.3}$$

  The first term represents the so called *jet-area correction* which allows an event-by-event, jet-by-jet estimation and subtraction of the energy added to the jet by the pile-up [88]. ρ is the pile-up energy density of the event defined by the median of the per-event distribution of p_{T}/A for each jet reconstructed in the central region of the detector. The jet area A is calculated from the ghost association method [89]. By targeting the correction specifically to each jet, this method helps in improving the jet resolution, as can be seen in Figure 3.6 (a). It compares the jet energy resolution as a function of pile-up quantities in the case of jet-area subtraction to the previous approach using a global correction function depending on the event pile-up quantities and to the original un-corrected value. The additional terms in the formula represent residual offset corrections that remove the remaining effects for both in-time (α) and out-of-time (β) pile-up. Figure 3.6 (b) shows the dependence of jet p_{T} on the number of primary vertices in the event as a function of jet η at each step of the correction processes, demonstrating the correctness of the procedure.

- *jet origin correction*: each jet direction is modified so that the jet points back to the selected primary vertex instead of the origin of the ATLAS detector.

- *jet energy scale correction*: factors are applied to restore the reconstructed jet energy to the truth jet energy, also called jet response. The correction is derived for isolated jets in an inclusive Monte Carlo sample and is applied as a function of the p_{T} and η of the jet [90].

- *in-situ calibration.* This is finally applied to data in order to compensate for residual effects not present in the Monte Carlo. The calibration consists in comparing the jet energy scale to a better known reference both in data and Monte Carlo. First the η-intercalibration is performed. It exploits the p_{T}-balance between jets in different η regions where forward jets are calibrated against central jets whose energy scale can be assessed in a more precise way. For central jets in-situ techniques combine Z+jets, γ+jets and multi-jet balance calibration. Figure 3.7 (a) shows the ratio of the jet response, defined as $p_{\mathrm{T}}^{\mathrm{measured}}/p_{\mathrm{T}}^{\mathrm{reference}}$, between data and Monte Carlo. A good agreement is observed with small deviation at high p_{T}. The plot well illustrates the complementarity of the various analyses each of them covering a specific p_{T} range; Z+jets at low/medium p_{T} γ+jets for medium/high p_{T} range and multi-jet balance in the very high p_{T} range.

For analyses using the 2010 and the 2011 dataset both the LCW and jet-area correction method were not applied. Pile-up correction was performed with simple factors dependent on N_{PV} and μ [90] while the use of EM calibrated topo-clusters required larger corrections to restore the truth jet energy. In-situ calibration was not available for 2010 analyses.

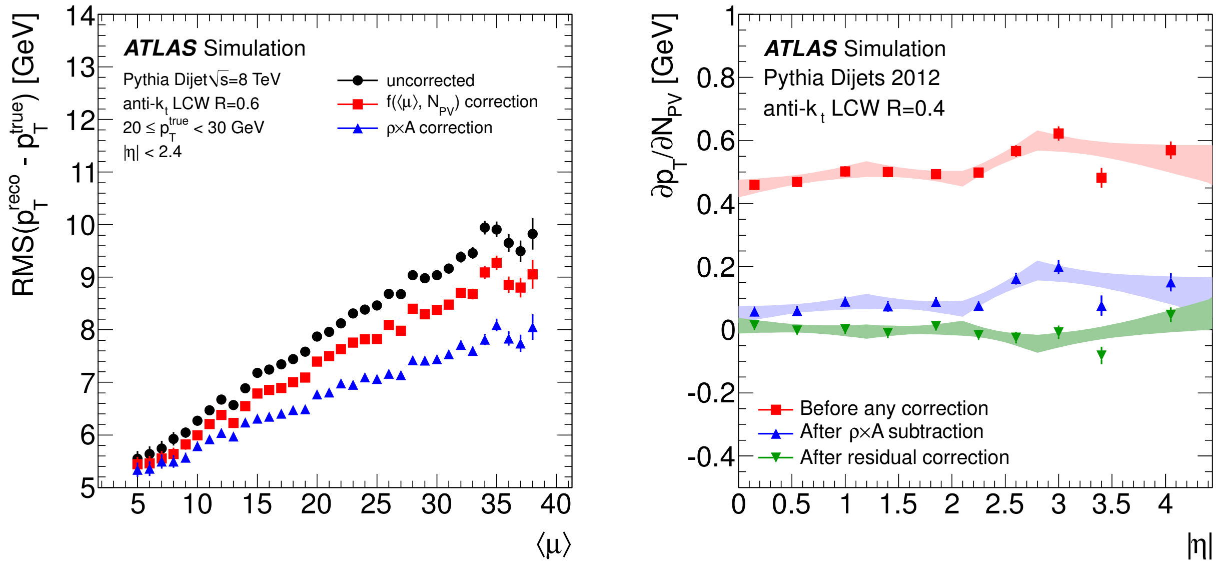

(a) (b)

Figure 3.6: (a) Jet p_{T} resolution as a function of the average number of interactions per bunch crossing. (b) Dependence of the corrected jet p_{T} on the number of reconstructed primary vertices in the event. Plots are described in Ref. [91]

"Semi-leptonic" b-jet corrections

In cases when a b-hadron decays semileptonically[5], the energy of the jet containing that hadron is underestimated by the fact that both the muon and the neutrino could carry a substantial part of the hadron energy and they are not considered in the jet clustering process. Since b-hadron decays produce muons in $\sim 20\%$ of the cases (including direct decays and cascade decays via charm-hadrons and τ leptons), the effect could be particularly important for analyses requiring a large number of tagged jets like the $t\bar{t}H(H \to b\bar{b})$ final state. A conservative approach is taken

[5] semi-leptonic b-hadron decays are in this case only considering decays chain of type: $B \to X + \mu + \nu_{\mu}$

where only the energy losses due to muons are corrected for. The final jet p_{T} four-momentum is given by:

$$p_{\mathrm{jet}}^{\mathrm{corr}} = p_{\mathrm{jet}} + \sum_{i}^{\mathrm{muons}} (p_{\mu_i} - E_{\mathrm{loss}}(\mu_i)) \tag{3.4}$$

where p_{μ_i} is the combined muon and $E_{\mathrm{loss}}(\mu_i)$ is the estimated energy loss of the muon in the calorimeter which is subtracted to avoid double-counting. All muons passing the standard MuId selection cut with p_{T}> 4 GeV and within a distance $\Delta R < 0.4$ to the jet axis are considered in the correction term.

The correction is applied to all jets overlapping with muons, independently of whether they are tagged as b-jets. The energy losses due to the escaping neutrino are not considered since a correction term would heavily rely on Monte Carlo assumptions. It has been shown in [79] that the application of the semi-leptonic correction helps in improving the jet response and p_{T} resolution in case of b-quark jets. The correction above is applied only to the 2012 dataset. Figure 3.7 (b) shows the effect of each correction on a sample of b-jets in simulated $t\bar{t}$ events.

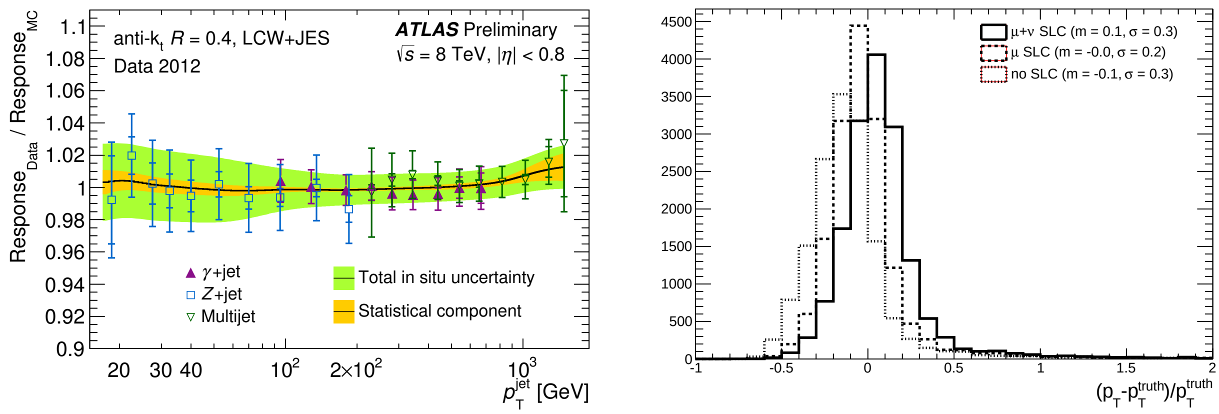

(a) (b)

Figure 3.7: (a) Jet response from *in-situ* jet calibration methods. The response is shown for very central jets, as a function of jet p_{T}. (b) Jet p_{T} resolution for an inclusive jet sample in MonteCarlo $t\bar{t}$ events. The dotted line describes calibrated jets, the dashed line jets after the muon correction and the solid line jets after both the muon and the neutrino corrections.

Jet energy scale uncertainty

The determination of the jet energy scale uncertainty takes into account multiple sources of systematic uncertainties:

- uncertainties due to pile-up are assigned to the correction term in expression 3.3, to cover the residual mis-modelling of multiple interaction in Monte Carlo. The impact of the uncertainty rapidly reduces with increasing jet p_{T}.
- for very high p_{T} jets (p_{T} > 2 TeV) in-situ techniques are limited in statistics so knowledge of detector response from Monte Carlo based studies and extrapolated test-beam results are used to assess the systematic uncertainty. In the following they will be referred to as *single particle response.*
- η-intercalibration uncertainties are divided into a statistical component and a Monte Carlo modelling one. They are the dominant source of JES systematics at large η ($|\eta| > 3$).

- uncertainties coming from in-situ techniques are divided in different categories (statistical, detector, modelling, mixed) according to their origin. Particular attention has been paid to preserving the correlation information among the various sources of uncertainty across the different p_{T} bins. The so-called "diagonalisation and reduction" method has been applied [86]. The method identifies the most relevant sources of uncertainty and organises them into un-correlated variations which can thus been applied independently. The remaining (small) sources of uncertainty are grouped together in a residual component.

- flavour-related uncertainties: the response of the calorimeter differs for jets initiated by quarks and jets initiated by gluons. In-situ techniques mainly measure quark-initiated jets by the nature of the process involved; the baseline uncertainty is then increased using the MC estimates of the response difference between quarks and gluons. To correctly assess the uncertainty a knowledge of the jets quark/gluon fraction is needed which makes the contribution dependent on the topology under consideration [92]. In the 2012 analyses, the uncertainty is evaluated by conservatively assuming a 50%/50% mix of quarks and gluons; for the 2011 analysis described in this thesis, a detailed study of the flavour composition was performed to reduce the impact of the jet energy scale uncertainty.

- an additional source of uncertainty in the range of 1.5 % to 3 % is considered for jets originating from b-quarks. The uncertainty has been obtained comparing the jet calibration to an estimate of jet p_{T} performed with track jets and evaluating the difference between an inclusive jet sample and a sample enriched in jets from b-quarks [93].

Figure 3.8 (a) shows the relative JES uncertainty as a function of jet p_{T} for the 2012 calibration. The contribution from the different sub categories are also highlighted while the b-jet scale uncertainty is not shown. The relative JES uncertainty is below 4% in the whole jet p_{T} range, reaching a precision below 2% in the range [100:1000] GeV. This represents a considerable improvement with respect to the calibration used during 2010 where the jet energy scale uncertainty was ranging between 4 and 8 % [94].

The level of sophistication in the treatment of JES uncertainty depends on the general complexity of the analysis and sensitivity to the jet properties. Using the total variation of the JES uncertainties produces a general overestimate of the uncertainties when considering the normalisation and an underestimate of the shape systematics. This is related to the fact that the energies of all the jets in the event are simultaneously shifted in the same direction. For analyses with a refined statistical treatment (profiled likelihood) and dependence on jet kinematics, the usage of multiple uncertainty components is recommended since it allows to take into account the correlation effects correctly, leading to a better estimation of the effect of systematic uncertainties.

Jet energy resolution uncertainties

The jet energy resolution has been measured in data with the bisector technique [95]. The method relies on the decomposition of the two leading jet vectorial sum p_{T} in orthogonal directions, one of them being the bi-section of the $\Delta\phi$ angles between the two jets in diet events. The sensitivity to jet energy resolution is different for the two since in the bisector direction the p_{T} is the sum of two small components while in the orthogonal direction a subtraction of much larger projection is performed.

The measured values are in reasonable agreement with the Monte Carlo prediction with some differences in particular regions of the phase space (high-η, high-p_{T}) where the resolution in data has been found to be larger than the expectations as shown in Figure 3.8. The effect

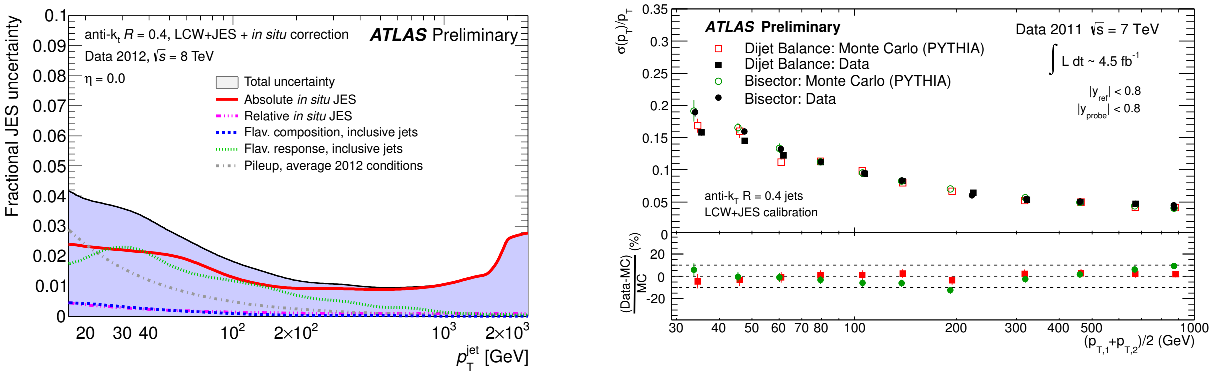

(a) **(b)**

Figure 3.8: (a) Relative jet energy scale uncertainty as a function of p_{T} for central jets in the detector. (b) Comparison of jet energy resolution as a function of jet p_{T} for data and Monte Carlo in the 2011 dataset.

has been considered as a source of systematic uncertainty where additional smearing of the p_{T} of the simulated jets is applied to cover the difference with data.

3.3.2 Jet reconstruction efficiency

The jet reconstruction efficiency for calorimeter jets was derived relative to jets built from charged tracks reconstructed in the inner detector system, using a tag and probe technique. The reconstruction efficiency was defined as the fraction of probe track-jets matched to a calorimeter jet. Small differences are observed between Data and MC in the range $p_{\mathrm{T}} < 30$ GeV. As a source of systematic uncertainties the difference is applied to Monte Carlo events by discarding a fraction of jets taken at random within the inefficiency range.

3.3.3 Jet cleaning and JVF cut

Jets are reconstructed in the detector not only from energy deposits from the in-time event but they could also be generated by various transient problems in the calorimeter hardware, LHC beam gas interaction and showers induced by cosmic ray. Those are the so-called *fake* (or bad) jets. Quality criteria are applied to reject such jets:

- The shape of the electrical signal collected in every calorimeter cell is compared to the reference (quality factor) and jets with significant deviation are rejected.
- The energy of the jet deposited in the electromagnetic calorimeter must be between 5% and 95%. This helps reducing noise effects from the EM calorimeter and from non-collision backgrounds.
- Due to the larger noise in the hadronic endcap calorimeter, the energy fraction of jet in this component has to be smaller than 50%.
- The energy fraction of a jet from charged particles (tracks) should be smaller than 99%.

This selection is also particularly important for the missing transverse energy calculation since the presence of fake jets could give rise to a large p_{T} imbalance.

In order to further reduce the impact of in-time pile-up a cut on the Jet Vertex Fraction (JVF) is applied [91]. The JVF is defined as the sum p_{T} of all tracks from the primary

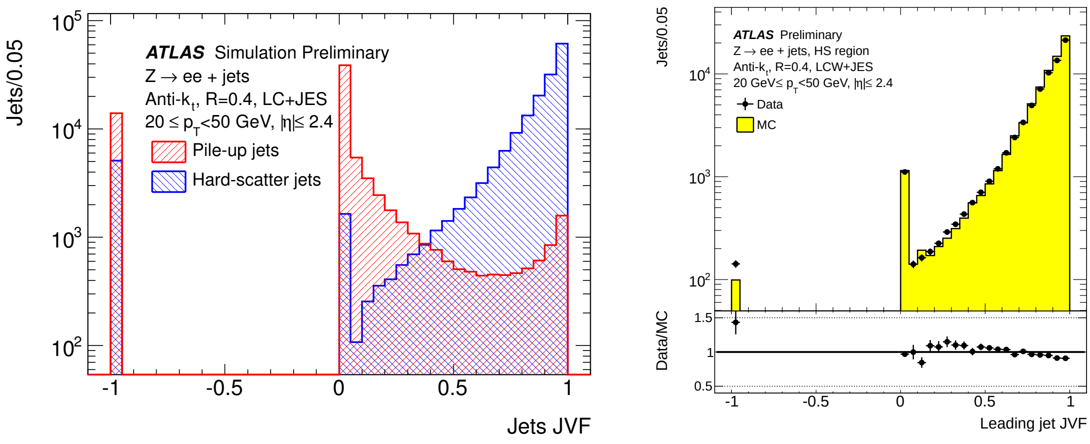

(a) (b)

Figure 3.9: (a) JVF distribution for hard-scatter (blue) and pile-up (red) jets with $20 \leq p_{\mathrm{T}} \leq 50$ GeV and $|\eta| < 2.5$ in simulated Z+jets events. (b) JVF distribution for jets well balanced against $Z \rightarrow ee$ candidates in 2012 data and Monte Carlo simulation. Plots are taken from Ref. [91].

vertex matched to a jet divided by the total jet-matched track p_{T} from all vertices. A track is considered matched to a jet if the angular distance to the jet direction (ΔR) is smaller than 0.4. The distribution of the JVF for jets originating from the primary (hard scatter) interaction and for pile-up originated jets is illustrated in Figure 3.9 (a). JVF has a good separation power between hard-scatter jets (peaking at 1) and pile-up jets (having substantially lower fraction of tracks from the primary vertex). A value of -1 is attributed to jets with no associated tracks (mainly at large rapidities).

In the 2012 dataset the adopted selection requires $|\mathrm{JVF}| > 0.50$; the cut gives a 95% selection efficiency for jets from primary interaction and a 75 % rejection for pile-up induced jets. The cut is applied only to jets with $p_{\mathrm{T}} < 50$ GeV since the pile-up contribution at high p_{T} is negligible and with $|\eta| < 2.4$ since tracking information is required. For analyses performed on the 2011 data, a requirement of $|\mathrm{JVF}| > 0.75$ is applied over the full p_{T} range[6] , while no cut was applied on the 2010 dataset. This cut allows the average jet multiplicity to stay constant as a function of the number of primary vertices in the event.

The effect of the cut has been tested on data and MC using $Z \rightarrow \mu\mu$ and $Z \rightarrow ee$ events where a specific selection allows to to obtain a sample of hard-scatter jets and of pile-up jets. Figure 3.9 (b) displays the comparison between data and Monte Carlo for a sample enriched in jets from hard scattering. The procedure to compute the uncertainty associated to the JVF selection require to vary the cut values in MC in a way that the changes of selection efficiency in Monte Carlo covers the discrepancies with data. For analyses using the 2011 dataset, scale factors were instead computed to correct for the data/Monte Carlo differences [82].

3.4 *b*-tagging

The identification of jets resulting from *b*-quarks fragmentation (*b*-tagging) is of primary importance for an analysis looking at $H \rightarrow b\bar{b}$ as well as other interesting physics signals at the LHC. In the energy regime above 10 GeV, the long lived ($\tau \sim 1.5$ ps) *b*-hadrons produced in

[6] The cut has an average efficiency for jets from primary interaction ranging from 94%(light jets) to 98% (*b*-jets). The efficiency increases as a function of jet p_{T}, reaching the plateau at ~ 80 GeV.

the hadronisation of b-quarks decay at a sufficiently large distance from the production vertex that a secondary vertex could be resolved in the detector, as shown in Figure 3.10.

A number of quantities can be exploited to identify this signature. If the secondary vertex can be identified within a jet, its distance to the primary vertex[7] (*decay length*) as well as the the mass of all the particles associated to the vertex represent the quantities used for the identification. Secondary vertices from b-hadron decays are expected to be significantly displaced from the primary vertex and to have a vertex mass up to ~ 5 GeV (due to neutral decay products not being included). Without the need to correctly reconstruct the secondary vertex, the impact parameter of each track in the jet can be inspected. The longitudinal and transverse impact parameter are defined as the minimum distance of the track to the primary vertex respectively in the z direction and in the x-y plane. The quantities are divided by their error in order to reduce the influence of poorly reconstructed tracks. The sign of the impact parameter is determined by whether the point of minimum approach to the vertex in the same hemisphere as the one defined by the jet direction. For a jet originating from a b-quark, typically one or more tracks are expected to show a large and positive impact parameter significance.

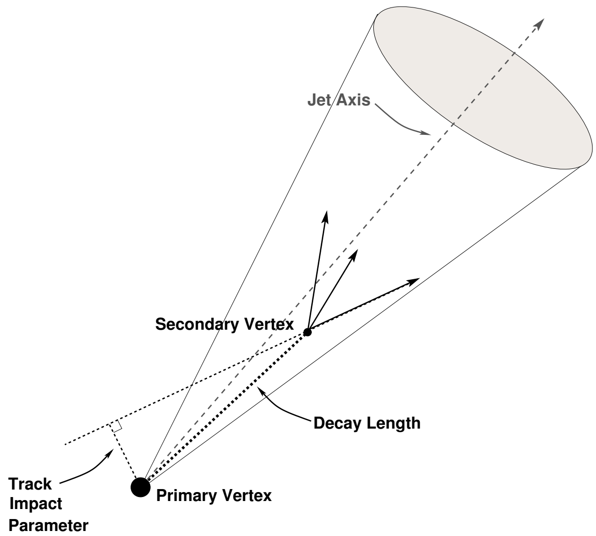

Figure 3.10: Most relevant variables for the identification of jet originating from b-quark.

Several algorithms have been developed in ATLAS to perform the b-tagging of jets exploiting the properties described above. They have been developed at different stages during the data-taking and their increase in complexity reflects the increase in knowledge of the tracking quantities that has been obtained with larger amounts of data.

- The *SV0* algorithm[96] is one of the first algorithms used since early data. It relies on the reconstruction of a secondary vertex in the jet using tracks fulfilling specific quality criteria, and a simple cut is applied to the decay length significance to determine if the jet is tagged.

- The *JetProb* algorithm[97] uses the transverse impact parameter significances of tracks in jets to compute the compatibility of the tracks within the jet with the primary event vertex. The probability of the jet to be tagged is derived from the combination of the single probability of each track with positive impact parameter.

- The *IP3D* algorithm[98] uses both the longitudinal and the transverse impact parameter of tracks taking advantage of the correlation between the two with a 2D likelihood ratio technique. Input variables are compared to pre-defined smoothed and normalised distributions for both the b and light jet hypotheses, obtained from Monte Carlo simulation.

- The *SV1* algorithm[98] is an extension of the SV0 algorithm. Other than the L/σ_L additional variables like the invariant mass of all tracks associated with the vertex, the

[7] the decay length is divided by its error to obtain the *decay length significance* L/σ_L in order to reduce the effect of poorly measured vertices

ratio of the sum of the energies of the tracks in the vertex to the sum of the energies of all tracks in the jet, and the number of two-track vertices. These variables are combined using a likelihood ratio technique.

- The *JetFitter* algorithm[99] attempts to reconstruct the decay chain inside the jet. A Kalman-fitter approach is used to identify secondary and tertiary vertices with the assumption that they lie on the flight direction of the b-hadron.
- The *JetFitterCombNN* algorithm is a neural network algorithm that combines the output of IP3D and JetFitter. *JetFitterCombNNc* is a particular version of the algorithm where the neural network is explicitly trained to separate c-jets from b-jets.
- The *MV1* algorithm has neural network-based implementation that uses as inputs the output weights of IP3D, SV1 and JetFitterCombNN. The *MV1c* algorithm is a particular version of the MV1 algorithm trained to achieve a better separation between jets originating from b-quarks and jets originating from c-quarks.

The figure of merit for the performance of the algorithms is their capability to correctly identify jets coming from a real b-quark compared to the probability of mistakenly tagging a jet originating from a c-quark or a light-flavour parton (u, d, s-quark or gluon) as a b-jet; the latter quantity are commonly referred to as the c-jet tagging efficiency[8] and mistag rate respectively. The b-tagging efficiency versus the light-jet and c-jet rejection, for some of the algorithms discussed above, is summarised in Figure 3.11. The MV1 algorithm shows the best performance in rejecting light quark jets and is therefore used as the b-tagging algorithm of choice for the analyses presented in this thesis.

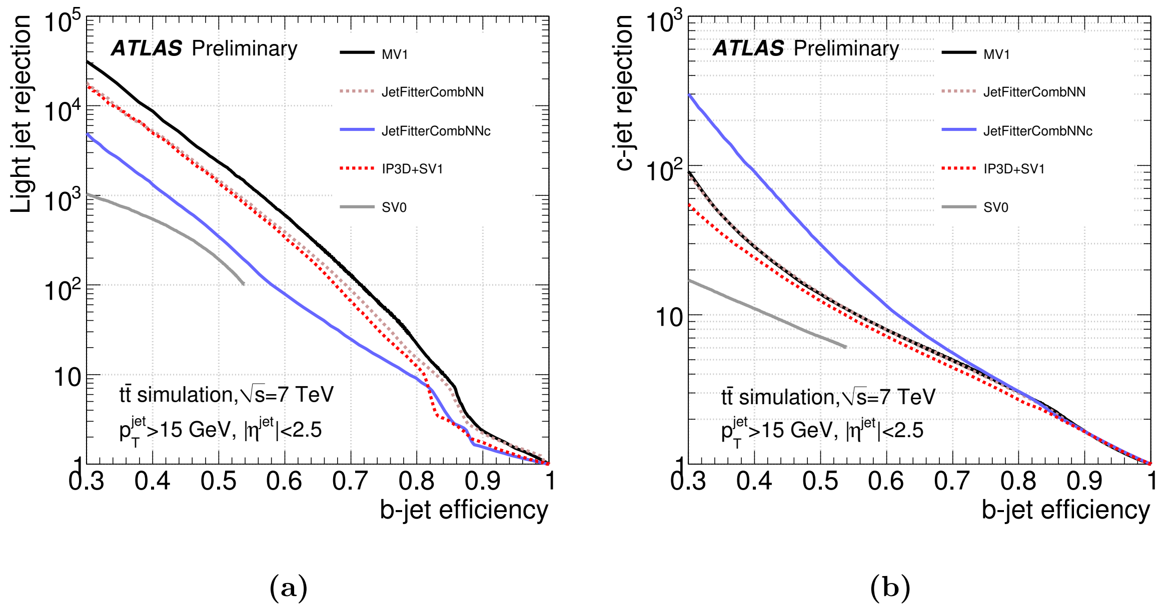

Figure 3.11: Light-jet rejection (a) and c-jet rejection (b) as a function of the b-tag efficiency for the b-tagging algorithms calibrated in this note, based on simulated $t\bar{t}$ events [100].

Several operating points have been considered based on the average efficiency of the algorithm on simulated $t\bar{t}$ events. Some of them are listed in Table 3.2.

The 70% operating point has been chosen for most of the $t\bar{t}$ based analyses given the good compromise between efficiency and rejection. Figure 3.12 contains the efficiency, obtained from

[8] Often this is improperly referred to as *c-tagging* efficiency.

b-jet efficiency	c-jet rejection	light jet rejection
60 %	7.9	590
70 %	5.0	140
80 %	3.1	25

Table 3.2: The MV1 algorithm operating points and their performance. The b-jet efficiency is the average obtained for b-jets from a $t\bar{t}$ sample.

the simulation, of the 70% MV1 operating point for b,c and light jets as a function of the jet p_{T} and $|\eta|$. Efficiencies increase at high p_{T} where the jets get more collimated; the mistag rate is more important for large $|\eta|$ values due to the worse track resolution.

The efficiency of each operating point has been calibrated in data using samples enriched in b-jets/c-jets and light jets respectively. The result is presented in terms of scale factors, SF= $\epsilon_{\mathrm{data}}/\epsilon_{\mathrm{MC}}$. This allows to correct for mis-modelling in the input variables used in the b-tagging algorithms.

For the mis-tag rate the so-called 'negative tag' method is used [101]. Light jets are expected to have a rather symmetric track impact parameter or vertex decay length significance distribution[9] where large absolute values could arise due to the finite resolution of the tracker. The negative side of this distribution is then used as an estimate for the positive side distribution since in the former the shape of the distribution is rather similar between light, b and c-jets thus reducing the effect of contaminations. The performance of the tagger is evaluated by using tracks/vertices with negative impact parameter/decay length significance and reverse their sign within the algorithm. For the MV1 70% operating point, the uncertainties range between 25% and 35% as a function of p_{T} and $|\eta|$ of the jet.

An enriched sample of jets originating from c-quarks has been derived by reconstructing D-mesons within a jet from the decay from the decay chain $D^{*+} \rightarrow D^0(\rightarrow K^-\pi^+)\pi^+$. The fraction of D^{*+} originating from hadronic b decays has been extracted by a fit to the pseudo-proper time of the selected candidates [102]. The b-tagging efficiency for c-quark initiated jets has thus been measured by comparing the corrected yields of D^* mesons before and after the application of the MV1 cut. In 2012, a correction factor covering the extrapolation from semileptonic D-mesons decay to the inclusive sample is also applied [103]. Uncertainties on the data/MC scale factors for the 70% MV1 operating point span in the range of 10 % to 20 % .

Several methods were used to calibrate the efficiency on a b-jet enriched samples; they can be divided into two different families according to the sample they use.

Di-jet based calibrations rely on semileptonic b-hadron decays identified through the presence of a 'soft' muon inside the jet. The $p_{\mathrm{T}}^{\mathrm{rel}}$ method exploits the fact that the relative momentum of the muon with respect to the jet axis is larger for a jet originating from a b-quark. A template fit procedure is performed to extract the fraction of b-hadrons before and after the application of the tag requirement to the jet. The system8 method combines three uncorrelated selection criteria to construct a system of eight equations based on the number of events surviving any given subset of these criteria. The first criterion is the selection of the b-tagging algorithm under consideration, the second requires that the 'soft' muon has a $p_{\mathrm{T}}^{\mathrm{rel}} > 700$ MeV and the third criterion demands the presence of another jet opposite the selected one that contains a well identified secondary vertex. Di-jet based calibrations were the first methods used in the 2010 and 2011 data taking. They cover the low/medium p_{T} range for jets since at high jet p_{T} (> 200 GeV) other than reduction of the data statistics, the method becomes less performing due to the similarity of the $p_{\mathrm{T}}^{\mathrm{rel}}$ distributions.

[9]sources of asymmetries like long lived meson decays are taken into account with a correction factor

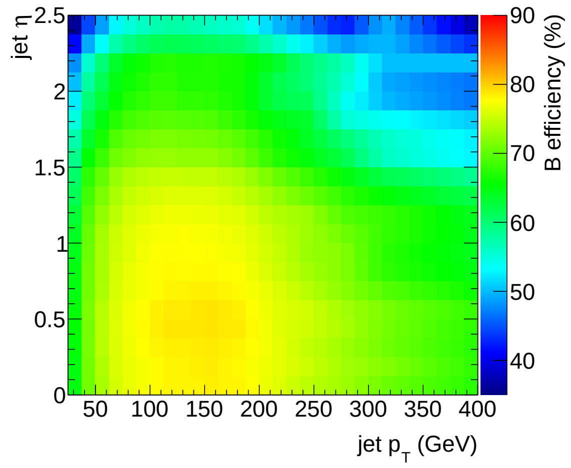

(a)

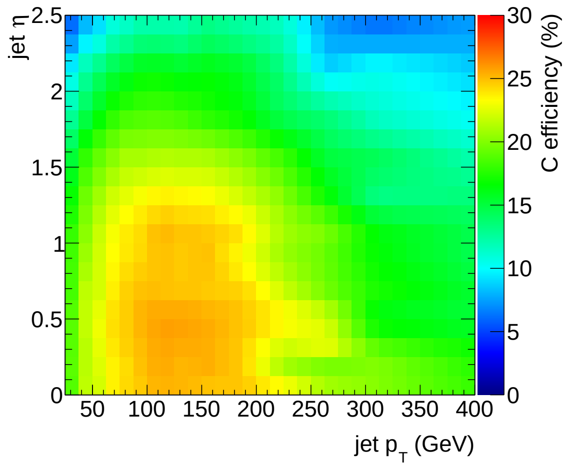

(b)

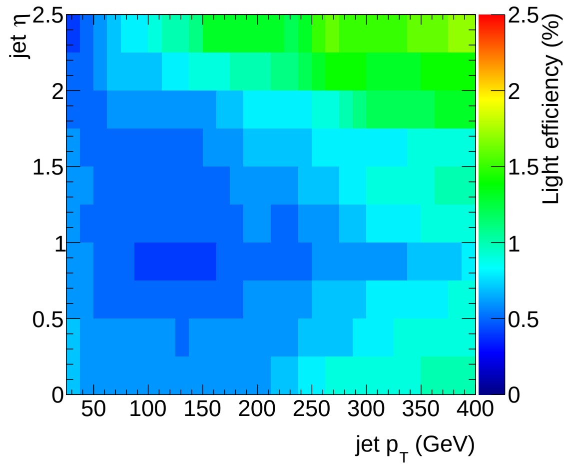

(c)

Figure 3.12: b-tagging efficiency for the MV1 70% operating point as a function jet p_{T} and $|\eta|$. Efficiencies are shown separately for b-jets (a), c-jets (b) and light jets (c) from simulated $t\bar{t}$ events.

$t\bar{t}$-based calibrations exploit the presence of b-jets produced in a $t\bar{t}$ decay. As will be discussed later in this document, a $t\bar{t}$ enriched sample can be easily obtained with a l+jets or di-lepton selection and a specific kinematic selection allows to identify a b-jet sample with a purity ranging from 50% to 90%. $t\bar{t}$-based calibrations have become a very precise tool especially for the 2012 dataset given the large amount of collected $t\bar{t}$ events. Currently, the most precise method is based on a likelihood approach which uses correlated information from multiple jets in dileptonic $t\bar{t}$ events [104]; it achieves a precision of a few % for jet p_{T} ranging between 30 and 200 GeV. Nevertheless a correct use in a $t\bar{t}$ analysis requires some additional care in order to avoid a re-use of the same data sample as well as double counting of systematic uncertainties. In this respect di-jet based calibrations are easier to use in a $t\bar{t}$ analysis since the analysis sample and the sample used for calibration are independent and the two analyses have very different sources of systematic uncertainties.

For the 2011 analysis, scale factors measured with the di-jet calibration method are used. The 2012 $t\bar{t}H$ analysis relies on scale factors obtained with the more precise $t\bar{t}$-based calibration method. Since the chosen $t\bar{t}$-based calibration has been derived using a dileptonic $t\bar{t}$ sample, no overlap of data events exists with analyses looking only at single lepton final state.

Scale factors as a function of jet p_{T} for b-, c- and light jets as extracted from the 2012

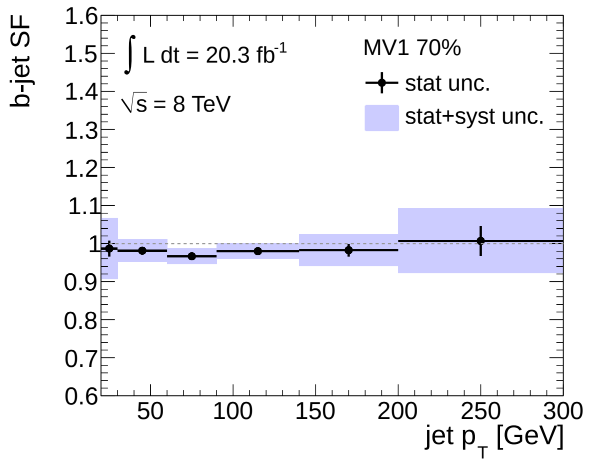

(a)

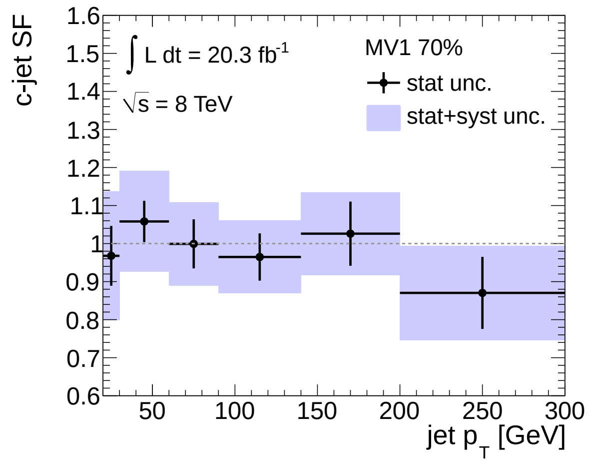

(b)

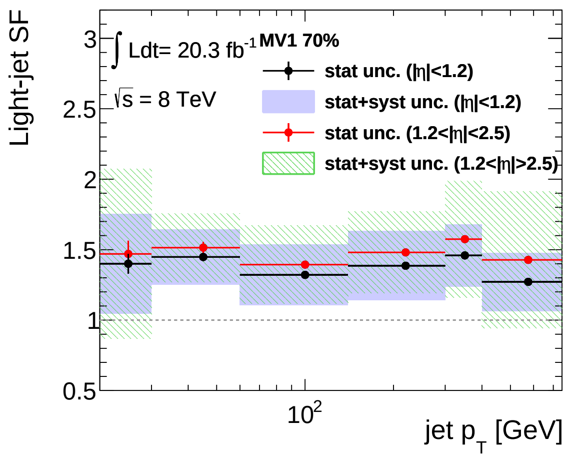

(c)

Figure 3.13: Data/MC scale factor for the tagging efficiency of b (a), c (b) and light jets with the 70% MV1 operating point. Total uncertainty are shown as well as the statistics components. Scale factors are measured as a function of jet p_{T} and, in case of mistag rate, the result for the two $|\eta|$ bins are shown.

dataset are reported in Figure 3.13. The scale factors are applied to Monte Carlo samples as event weight corrections. For each jet tagged by the b-tagging algorithm, a weight equal to the b-tagging scale factor of the corresponding jet flavour is considered. If a jet fails the b-tagging criterion, a weight corresponding to $(1 - SF * \epsilon_{\mathrm{MC}})/(1 - \epsilon_{\mathrm{MC}})$ is assumed. The individual jet weights for all the selected jets are multiplied in order to obtain an event level weight.

3.5 Missing transverse energy

Particles like neutrinos and other neutral weakly-interacting particles predicted in exotic and super-symmetric scenarios escape ATLAS undetected, thus creating an apparent imbalance of the momentum in the transverse plane. This effect is identified by considering the vector sum of all the detected particles and is referred to as missing transverse energy $\boldsymbol{E}_{\mathrm{T}}^{\mathrm{miss}}$ whose absolute value will be denoted as $E_{\mathrm{T}}^{\mathrm{miss}}$.

The reconstruction of $E_{\mathrm{T}}^{\mathrm{miss}}$ [105] takes into account information from the calorimetric system as well as from the muon spectrometer. In order to ensure an optimal calibration, calorimetric deposits (cells) are associated with identified high-p_{T} physics objects and are considered in the calculation with the calibration of these associated objects. Double counting is avoided by considering physics objects in a specific order. For the $t\bar{t}$ and $t\bar{t}$H analyses [79] the following order was adopted: electrons, muons and jets. The $E_{\mathrm{T}}^{\mathrm{miss}}$ in the two transverse directions is then computed as:

$$E_{\mathrm{x(y)}}^{\mathrm{miss}} = E_{\mathrm{x(y)}}^{\mathrm{miss,e}} + E_{\mathrm{x(y)}}^{\mathrm{miss,jet}} + E_{\mathrm{x(y)}}^{\mathrm{miss,soft-jet}} + E_{\mathrm{x(y)}}^{\mathrm{miss,muon}} + E_{\mathrm{x(y)}}^{\mathrm{miss,cell-out}} \tag{3.5}$$

where each term is obtained from the negative sum of the calibrated reconstructed objects, projected onto the x and y directions, and the magnitude is given by

$$E_{\mathrm{T}}^{\mathrm{miss}} = \sqrt{(E_{\mathrm{x}}^{\mathrm{miss}})^2 + \left(E_{\mathrm{y}}^{\mathrm{miss}}\right)^2} \tag{3.6}$$

Electron and jet calibrations have been discussed previously in this chapter. The $E_{\mathrm{x(y)}}^{\mathrm{miss,softjet}}$ term is constructed considering jets with 10 GeV $< p_{\mathrm{T}} <$ 20 GeV; they enter the calibration at the LCW scale without jet area correction. Both jet terms do not take into account a jet if its JVF is equal to 0. The muon term ($E_{\mathrm{x(y)}}^{\mathrm{miss,muon}}$) contains the combined muon momenta; calorimetric cells associated to the muon energy loss are then excluded. The $E_{\mathrm{x(y)}}^{\mathrm{miss,cell-out}}$ term collects all the deposits that are not associated with any physics object.

The real challenge in the missing transverse energy reconstruction is the robustness to the effects of pile-up, particularly important in 2012 data. This is primarily achieved by using the specific jet calibration described previously. For the analysis presented in this document the $E_{\mathrm{T}}^{\mathrm{miss}}$ uses pile-up suppressed jets only if their p_{T} is greater than 20 GeV; as a result the soft-jet term is more sensitive to pile-up effects. Additional pile-up suppression techniques are available for the soft-jet and the cell-out terms but they are not applied since they have been shown to produce little effect given that the $t\bar{t}$ topology with leptons in the final state has a real source of missing energy (the neutrino from the W decay) [106].

The effects of systematic uncertainties in the $E_{\mathrm{T}}^{\mathrm{miss}}$ computation are divided into two main sources: uncertainties affecting high-p_{T} objects and uncertainties affecting the soft-jet and the cell-out terms. For the former, systematic uncertainties on the physics object calibrations are directly translated into the missing transverse energy computation through Eq. 3.5. The latter have been evaluated in events with no real source of $E_{\mathrm{T}}^{\mathrm{miss}}$ such as $Z \to \mu\mu$ events with no jets with $p_{\mathrm{T}} >$ 20 GeV. An uncertainty of 2.5% and 8% has been assigned respectively to the resolution and scale of the soft-jet term.

Chapter 4

The ATLAS electron trigger

The trigger system is one of the key components of the ATLAS detector due to its capability of selecting in real time specific events out of the very frequent interactions. This is achieved by rapidly identifying specific signatures of physics objects. Among these, electrons are present in the final state of relevant physics processes that are being investigated at the LHC.

This chapter gives an overview of the implementation and performance of the electron triggers in ATLAS. Initially a description of the structure of the ATLAS trigger will be given. The central part of the chapter will be dedicated to the description of the electron trigger in ATLAS together with the steps performed during its commissioning during the 2010 data-taking. Finally the measurement of the electron trigger efficiency for the single electron triggers will be documented.

The emphasis on single electron triggers is motivated by the fact that, due to their large acceptance, they are among the most common triggers used in physics analyses. The chapter mainly discusses results obtained with data collected during 2010 data-taking since it corresponds to the period were the author made the most significant contribution to the development of the trigger in the detector. The evolution of the performance in 2011 and 2012 will be briefly summarised at the end of the chapter, together with the description and performance of the muon triggers.

4.1 The ATLAS trigger system

When operating at the designed number of colliding bunches, the LHC provides a 40 MHz bunch crossing rate. Due to limitations in the computing resources available for data processing and storage the recording event rate in the ATLAS detector is limited to 200/300 Hz[1]. The goal of the ATLAS trigger system is thus to reduce in real time the input rate by a factor of $2 \cdot 10^5$ while retaining interesting events for physics analyses. This is achieved by basing the trigger selections on the identification of final state objects like electrons, photons, muons, taus, jets and missing transverse energy. These objects are clear signatures of key processes in the Standard Model as well as in new physics scenarios.

In order to achieve the necessary performance, flexibility and, in particular, the earliest possible rejection of the events, it is organised in three consecutive "decision levels". Each level has an increased rejection power and complexity with respect to the previous one. This is due to the increased granularity of the detector information and a larger processing time available.

- Level 1 (L1): this is a hardware-based system which has the task to reduce the output rate to less than 100 kHz. The rejection of the events needs to happen while the information is

[1]For short periods of time the output rate can reach up to 600 Hz.

still in the detector front-end pipeline memories: for this reason, the event processing time is limited to 2.5 μs. The L1 uses reduced granularity information from the calorimeter and muon sub-detectors. The goal is to rapidly identify events with high-p_{T} muons (from standalone muon spectrometer reconstruction) and electrons/photons, jets, τ-leptons as well as events with large missing or total transverse energy (from the energy deposits in the calorimeter). Both the transverse energy threshold and the object multiplicity is configurable in each specific trigger. In addition to performing the first selection step, the L1 triggers identify *Regions of Interest (RoIs)* to be passed to the next levels. Each RoI represents a portion of the detector where the relevant physics object has been identified by the L1 system. The size of the RoI depends on the trigger signature (e/γ, τ, jets) and typically contains 2%-4% of the data in one event.

- Level 2 (L2): this is the first level with a software implementation. The full granularity detector information is available but only within the RoIs selected by the L1; this allows to reduce the data transfer time and speed up the processing. In particular tracking information can be exploited to differentiate electrons from photons and hadronically-decaying taus from jets. Fast customised object reconstruction algorithms are employed in order to obtain an average event processing time of $\sim$ 40 ms. The output rate reaches 3 kHz.

- Event filter (EF): for events accepted by the L2 trigger, the full event information is available and an increase in the rejection can be achieved by (for instance) looking at other physics objects not present in the RoI. This is the so-called *full-scan* mode. Due to an available processing time up to a few seconds per events, the event filter adopts the same reconstruction and identification algorithms employed by the offline event processing but with specific 'settings' to reduce the execution time. This allows to apply more sophisticated techniques for object/event selection.

Level 2 and Event filter are collectively referred to as *High Level Trigger* (HLT) given that both have a software implementation in a common computing farm.

The full configuration of the trigger system consists of a collection (*trigger menu*) of so-called chains which, starting from the L1, specify a sequence of reconstruction and selection steps for the specific trigger signatures required in the trigger chain. A trigger chain is often referred to simply as a trigger. Several hundreds of triggers are present in the trigger menu. They can be divided into:

- *single object triggers*: requiring the presence of at least one characteristic object;

- *multiple object triggers*: requiring the presence of two or more characteristic object of the same type. Different kinematic and identification selections can be requested for the two objects;

- *combined triggers*: requiring the presence of two or more characteristic objects of different type;

- *topological triggers*: combining information from objects belonging to different RoIs in order to apply further rejection.

Each trigger is characterised by the transverse energy threshold of the object as well as by the specific object reconstruction and set of identification criteria. These parameters are usually varied to control the output rate and in particular to reduce it with the increasing LHC luminosity. Prescale factors which allow to randomly accept one over N events fulfilling the selection, can be applied to further control the output trigger rate of each trigger.

The specific composition of the trigger menu results from a delicate balance between the maximum output bandwidth, the instantaneous luminosity of the LHC and the physics programme of the experiment. Un-prescaled triggers are the ones that benefit from the full recorded luminosity and are normally used for physics analyses, especially the ones looking for new or rare events. The transverse energy threshold of such triggers was progressively increased over the years to respond to the increase of the instantaneous luminosity of the LHC. Triggers with lower thresholds or looser identification criteria are still present in the menu but are prescaled. These triggers are typically used for analyses that do not require the full luminosity, to collect specific data for detector calibration as well as for *supporting* triggers used to measure the performance of the primary triggers.

The specific design of the ATLAS trigger system allows to change the trigger composition (enabling new triggers or changing their prescale factors) within a single LHC fill to make optimal use of the available bandwidth. This is illustrated in Figure 4.1 (a) where the output rate for each data *stream* is shown as a function of the instantaneous luminosity. A data stream is the ensemble of events collected by the triggers selecting a given physics object (electron/photon, muons, jets); physics streams are not exclusive and events fulfilling multiple trigger requirements might end up in more than one stream. The sudden changes in output rate are due to the increase in prescale factors of specific triggers. Figure 4.1 (b) shows how the output bandwidth was shared among the various streams during 2011 data-taking.

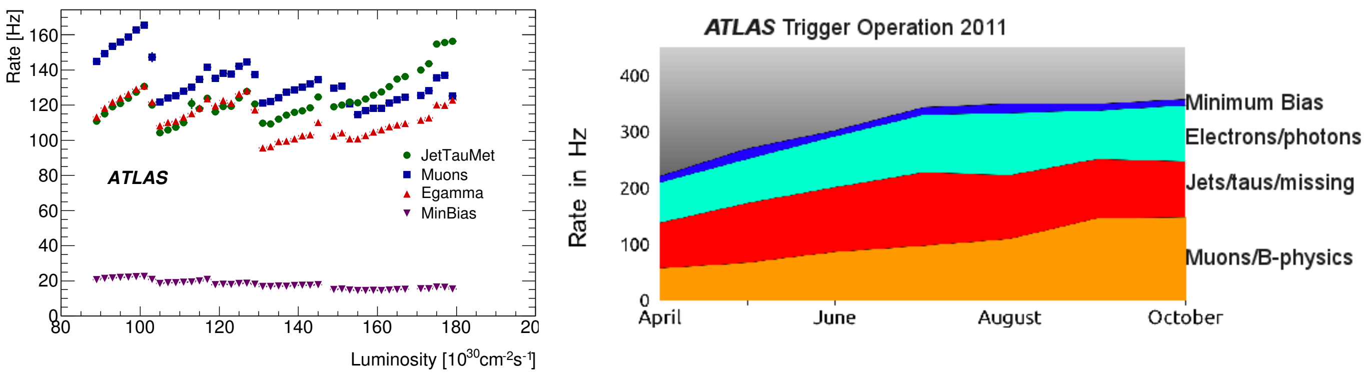

(a) **(b)**

Figure 4.1: (a) Total output trigger rates as a function of instantaneous luminosity in a sample run from the end of 2010 data-taking for each stream. (b) Event Filter stream recording rates during 2011 LHC operation for the periods in which the LHC declared stable beams.

4.2 The electron trigger implementation

Electrons are clear signatures of many SM processes of interest at the LHC (W/Z and top-quark production) as well as of many scenarios expected in theories beyond the Standard Model. The excellent capability of the ATLAS detector to identify electrons and measure precisely their properties is exploited by the trigger system to reject uninteresting p-p collisions. This is achieved by using a combination of both tracking and calorimetric information.

At L1, the trigger decision is built considering dedicated analogue signals provided by the calorimeter independently from the information used in the HLT and offline reconstruction. The reduced-granularity information is organised in *Trigger Towers* (TT), covering approximately a region $\Delta\eta \times \Delta\phi \approx 0.1 \times 0.1$ in the central part of the detector ($|\eta| < 2.5$), and a larger area in the forward region. For each TT, the calorimeter signals for the cells of the EM or hadronic calorimeter are summed. EM-clusters are formed by identifying local maxima using a sliding window algorithm based on a 4×4 group of TTs, as shown in Figure 4.2 (a). A given cluster satisfies the trigger selection if the core-region of the window, which is the central 2×2 TT, contains one pair of neighbouring TT with a combined energy greater than the transverse energy threshold. Additional requirements are made on the energy deposit in the 4×4 TT 'ring' around the cluster core as well as the amount of energy deposited in the hadronic calorimeter layer.

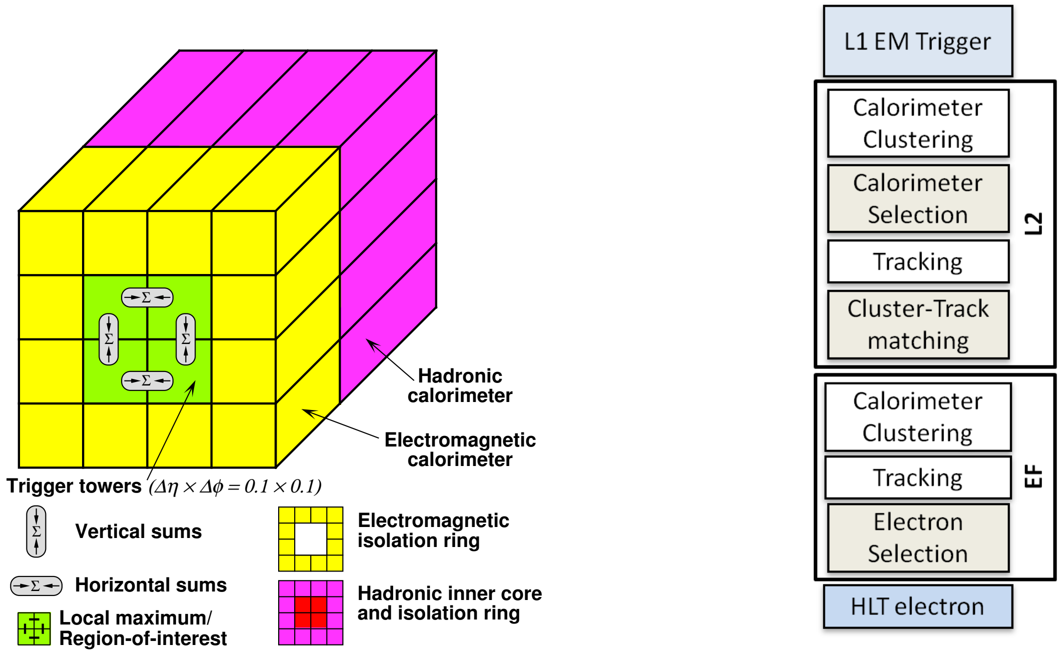

(a) (b)

Figure 4.2: (a) Schematic representation of the information used by the L1 calorimetric trigger. (b) Building blocks and information flow for an electron trigger implementation.

At the HLT, the trigger decision incorporates also tracking information from the Inner Detector. The logical steps for the computation of the trigger decision are summarised in Figure 4.2 (b).

At L2, a fast calorimeter reconstruction is performed, followed by a fast inner detector track reconstruction[107]. Identification criteria on the shape of the distribution of energy deposits in the calorimeter are applied before attempting to reconstruct the track in order to achieve a faster rejection of events not containing real electrons (as well as to share this step with the photon triggers). The calorimeter reconstruction works in a similar way as the offline algorithms, although only a region of $\Delta\eta \times \Delta\phi = 0.4 \times 0.4$ around the L1 seed position is used. Systematic differences are present between the L2-trigger and offline algorithms; they are due to time limitations on the decision latency. Contrary to the offline strategy which implies a sliding window approach, the L2 cluster reconstruction algorithm begins by considering the most energetic cell of the second EM-layer within the central region of of the RoI (only the energy deposits in the $\Delta\eta \times \Delta\phi = 0.2 \times 0.2$ RoI core are considered). The size of the electron cluster is 3×7 cells in the $\eta - \phi$ plane for the whole η range[2]. The calibration of the objects is

[2] For the 2011 and 2012 data-taking the size of the cluster was made the same as in the offline reconstruction.

also different between trigger and offline since the offline reconstruction can apply a more precise energy reconstruction to take into account transient hardware issues like power supply failures. These corrections cannot be applied during online processing. For the track reconstruction at L2, a fast pattern recognition algorithm is used by first determining the z-position of the interaction point along the beam axis and then performing the tracking by pairing/combining the available space points only is the resulted track segment points back to the determined interaction position[108].

As in the offline reconstruction, the cluster reconstruction at the EF is performed using a sliding window algorithm acting on towers containing the energy summed in depth by regions. After the seed-finding step, fixed window clusters are built starting from the second EM layer using the same cluster size used offline. Energy-weighted η and ϕ positions are calculated in the second calorimeter layer and cluster building is then extended to include the remaining layers. The track reconstruction adopts the same techniques as the offline reconstruction but only tracks seeded by hits in the silicon detector and then extrapolated to the TRT are considered (*inside-out* tracking). Contrary to L2, an EF electron candidate is built from a match between an electromagnetic cluster and a reconstructed track. Only at a later stage, the selection based both on calorimeter and tracking quantities is applied to reduce the output rate.

The selection algorithms used to identify good electron candidates at the HLT are configured in close connection with the offline reconstruction. The variables considered have already been described in Chapter 3 and include shower shape, tracking information and cluster-track matching. The identification at L2 does not rely on variables related to the lateral width of the calorimetric shower ($w_{\eta 2}$,w_{stot}) and on the number of silicon hits in the track.

The same benchmark set of selections as the offline reconstruction (*loose*, *medium* and *tight*) are implemented at the trigger level. The selection cuts applied at EF are equivalent to those used in the offline, but they are not p_{T}-dependent[3]. A subset of these variables is used at L2 with looser selection cuts. The motivation for this choice is to have each trigger to be as efficient as possible with respect to the corresponding offline benchmark selection. Inefficiency are caused by the different reconstruction algorithms at trigger level as well as the resolution effects between trigger and offline in the determination of the same variable. As a net result, this approach consists in a close connection between offline and online selection. With increasing LHC instantaneous luminosity, the latter was progressively tightened, in order to allow the trigger to fulfil the allocated bandwidth requirements (as will be described in more detail in the next sections).

The naming convention for each trigger tends to provide as much information as possible on the trigger selection. As an example *e20_medium* indicates a single electron (the"*e*" refers to the object type) with a transverse energy threshold of 20 GeV requiring *medium* identification selection. A prefix (L2_ , EF_) could be used to indicate the specific trigger level. While the threshold in the name is the same for L2 and EF trigger, the L2 threshold is usually 1 to 2 GeV lower than the corresponding EF one. In order to indicate the L1 trigger, the notation L1_EMXX is used where XX indicates the transverse energy threshold in units of 'bit counts'. The transverse energy at L1 is the results of signal ADC conversion where one bit corresponds to a deposited energy of $\sim$ 1GeV. The notation L1_EM2 indicates that the bit count is required to be $\geq$ 2, corresponding approximately to a 3 GeV threshold.

[3]The offline selection gets tighter with increasing electron p_{T}, while at the trigger lever it is fixed for a given trigger but changes for trigger with different threshold

4.3 Commissioning of electron triggers in 2010

Prior to the first 7 TeV collisions, the ATLAS trigger system was exercised on cosmic ray data-taking and on the first LHC collisions during 2009 at a centre of mass energy of 900 GeV [109]. During 2010 the instantaneous luminosity of LHC increased by several orders of magnitude, from 10^{27} to 10^{32} cm^{-2}s^{-1}. These conditions posed a real challenge to the trigger system since triggers with increasing selection and complexity needed to be deployed to control the output rate. The performance of each trigger component was carefully evaluated before actively using it for online rejection. At the same time the commissioning process had to be as careful as possible in order to allow the collection of good data for physics analyses.

During the first period of data-taking, events were collected using the Minimum Bias Trigger Scintillators (MBTS) producing an unbiased sample of inelastic collisions[4] used for the validation of other triggers. The performance of the L1 calorimeter system was evaluated especially with respect to the more refined offline reconstruction. Given the little available integrated luminosity, in order to increase the statistics all offline electromagnetic clusters were considered for the comparison without any additional identification. The sample was dominated by photons from π^0 decays and electrons from photon conversions and hadron fakes.

Figure 4.3 shows the efficiency of the L1 triggers with thresholds of 3, 4, 6, 11 and 15 GeV. Only electromagnetic clusters in the range $|\eta| < 2.47$ were considered, excluding the transition between the barrel and end-cap of the calorimeter . An offline cluster was considered selected by the trigger if it was within an angular distance $\Delta R < 0.15$ from the L1 cluster passing the trigger decision. The uncalibrated offline cluster energy has been used in this study since the L1 did not perform a refined calibration taking into account, for instance, the dead material in front of the calorimeter. As shown in the plots, the turn-on from L1 is reasonably sharp with a plateau efficiency of $\sim$ 100 % reached a few GeVs above the threshold. The plots attest to the correct configuration and good performance of the L1 calorimetry system. In particular a precise time alignment of its components influences the uniformity of the applied threshold. The comparison with Monte Carlo predictions was performed using a large sample of 7 TeV, non-diffractive, minimum bias events generated with Pythia 6 using the underlying events tune described in Ref. [110]. Overall a good description of the shape of the turn on was obtained by the simulation.

For a luminosity greater than $5 \cdot 10^{27}$ cm^{-2}s^{-1}, the L1 calorimeter trigger system was activated in rejection mode allowing to collect more efficiently a sample of events to probe the performance of the HLT triggers.

In order to perform a validation of the HLT triggers, the distributions of kinematic and signal/background discriminating variables were compared at the different trigger levels with the offline distributions as well as with the expectations from Monte Carlo simulations. Electron objects reconstructed at the trigger levels (both L2 and EF) were matched to offline electron candidates by requiring an angular distance of $\Delta R < 0.15$. As in the case of the L1 performance studies, no identification requirement was applied to the offline electron candidates so the distributions were dominated by fakes. Nevertheless the comparison helped investigating the correct description of the trigger rejection of background.

Figure 4.4 shows a comparison between data and Monte Carlo simulation for the calorimetric shower shape variables used to build the trigger decision. On the left column L2 variables are shown; on the right, the corresponding variables computed at EF. Two representative variables for the electron identification are displayed:

[4]The MBTS was found to be 100% efficient with respect to the majority of events of interest at LHC containing high p_{T} physics objects.

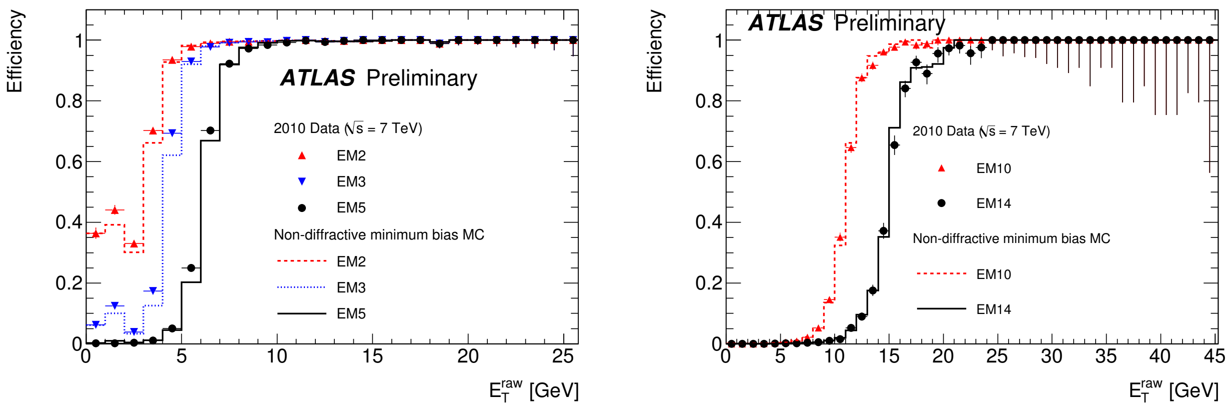

(a) **(b)**

Figure 4.3: L1 trigger efficiency for electron candidates as a function of the raw (uncalibrated) offline cluster E_{T}. The turn-on is shown for data (markers) and MC simulation (lines). The trigger efficiencies for the three lowest energy thresholds EM2, EM3 and EM5 are shown in (a) while for EM10 and EM14 in (b). The bump in EM2 and EM3 below the turn-on is a result of false matches between trigger and offline clusters.

- $R_\eta = E_{3\times7}/E_{7\times7}$, where $E_{3\times7}$ is the energy deposited in the central 3×7 cells of a calorimeter cluster and $E_{7\times7}$ is the energy deposited in the surrounding 7×7 cells. This variable peaks near unity for electrons and photons, which leave calorimeter deposits well contained in 3×7 cells. Fake electrons have broader tails expanding to lower values. Typical identification cuts are placed in the range [0.8-0.9].

- E_{ratio} defined as the ratio of the energy difference between the largest and second largest energy deposits in the strips belonging to the cluster over the sum of these energies. The distribution of the variable peaks at 1 for signal since no substructure is present in the shower while lower values are expected for fake electrons/photons where the cluster can originate from the deposit of multiple particles (for instance $\pi^0 \to \gamma\gamma$). The identification cuts are generally applied in the region [0.3-0.7].

A reasonable agreement was observed between data and simulations. The discrepancies were traced to a mis-modelling in the Monte Carlo of the cross-talk effects in the second layer of the calorimeter and missing material in the detector material description by the simulation. The differences were already visible at the offline level[76]. The cut values were carefully chosen to avoid the region with the largest data/MC disagreement.

Another crucial component in the commissioning was the check on the agreement between the offline reconstruction and the trigger levels in the description of the variables. The resolution effects between the different levels can affect the bias introduced by the trigger on the offline reconstruction/selection for the analyses. Resolution plots are shown in Figure 4.5 for both L2 and EF. No bias was observed in the distributions and for the majority of candidates the resolution on the variables is below a few %. The broader resolution at L2 is due to the faster, and thus less refined, clustering algorithm and calibration.

The performance of the tracking was assessed using specific monitoring triggers that did not require a track to be present for the event to be accepted, and thus unbiased for track efficiency measurements. Offline *medium* electrons were considered since the *medium* identification criterion required a minimum number of total hits in the pixel detector (at least 1) and a minimum number of hits in the silicon detector (at least 7) to ensure a good measurement of the track properties. The matching requirement between the offline electron and the HLT

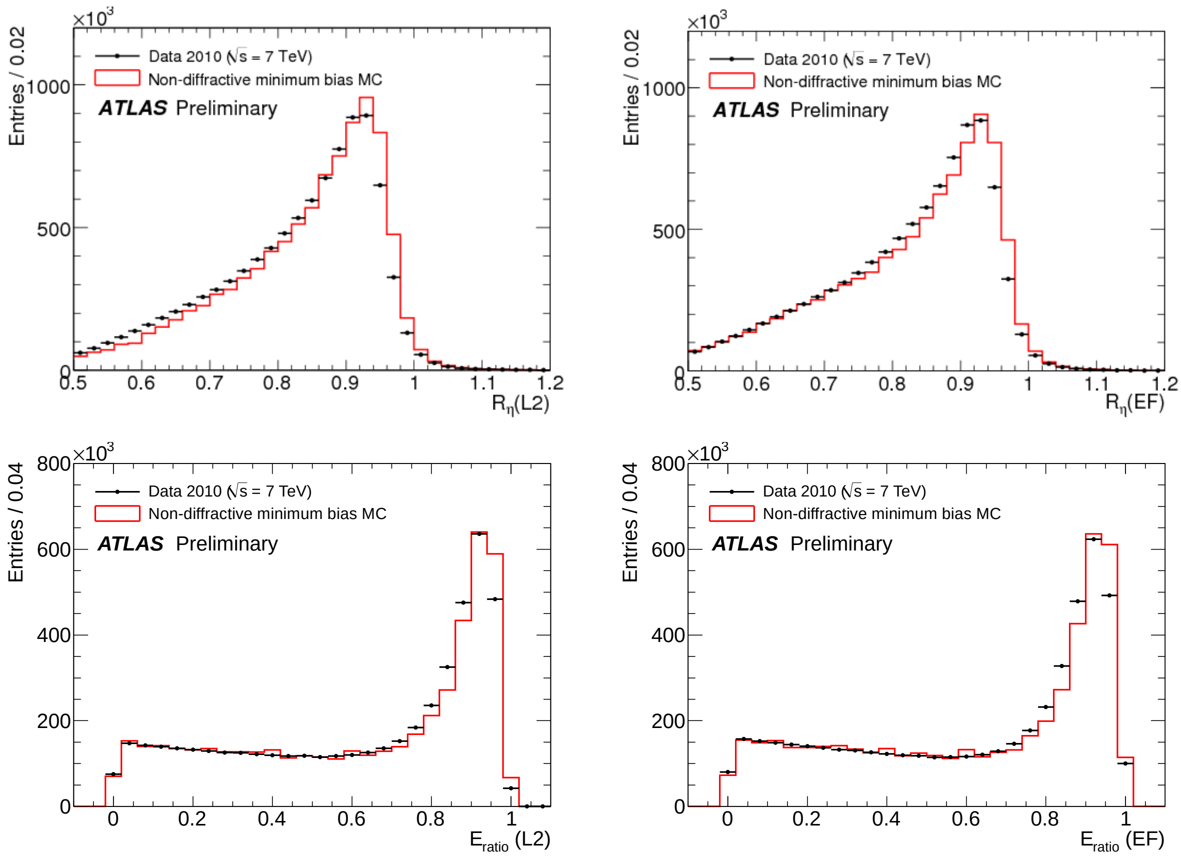

Figure 4.4: Data/Monte Carlo comparison for the R_η (top) and E_{ratio} (bottom) identification variables computed at L2 (left), EF (right). Distribution from Monte Carlo have been normalised to the same number of events in data.

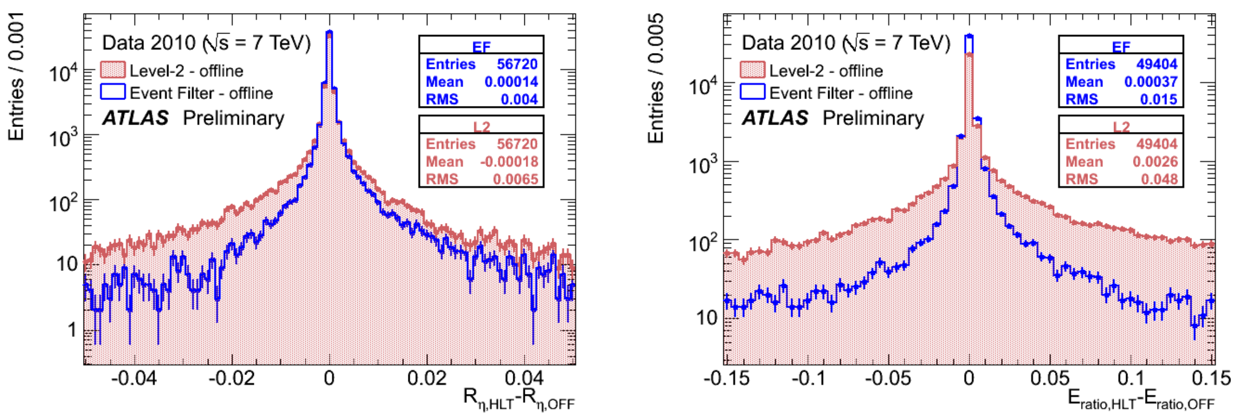

(a) **(b)**

Figure 4.5: HLT trigger level resolution with respect to offline reconstruction for the R_η (a) and E_{ratio} (b) variables. L2 (EF) distributions are shown in red (blue).

track was set at $\Delta R < 0.1$. Figure 4.6 (a) shows the HLT tracking efficiency (L2 and EF separately) as a function of the offline electron p_T; the efficiency is close to 100% over all the p_T range. Figure 4.6 (b) illustrates, as a function of η, the inverse-p_T resolution defined as the RMS of the core 95% (RMS_{95}) of the residual $((\frac{1}{p_T})^{\text{trigger}} - (\frac{1}{p_T})^{\text{offline}})$. All candidates with track $p_{\mathrm{T}} > 5$ GeV were considered. The high value of the efficiency demonstrated the good agreement between the HLT and offline reconstruction. The p_{T} resolution is worse at L2 than at the EF particularly at high $|\eta|$ as a consequence of the speed optimisations made at L2.

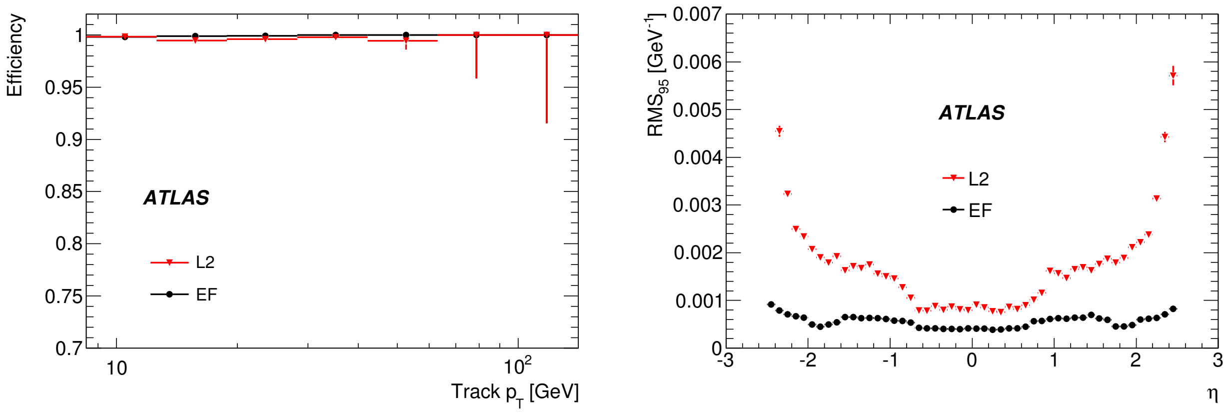

(a) **(b)**

Figure 4.6: (a) L2 and EF tracking reconstruction efficiency with respect to selected offline electron candidates as a function of the electron p_{T}. (b) The RMS of the core 95% (RMS_{95}) of the inverse-p_{T} residual as a function of offline track η. Plots taken from [111].

Figure 4.7 shows the distribution of $\Delta\eta$ between the cluster and the track directions. Comparisons between data and MC are shown for the L2 and EF reconstruction as well as the resolution of the two trigger levels with respect to the offline reference. As described in Chapter 3, this variable is not only used to build the electron candidate but a tighter cut (< 0.01) is used in the medium selection to further reduce fakes and photon conversions where the track and the cluster are less aligned. A good description of the data by the Monte Carlo is observed in particularly in the tail of the distributions. The $\Delta\eta_{\text{cluster}-\text{track}}$ spectrum is broader at L2 compared to the EF because the track reconstruction is less sophisticated at L2, due to time constraints. Cuts used in the L2 electron selections were therefore looser than in the offline reconstruction.

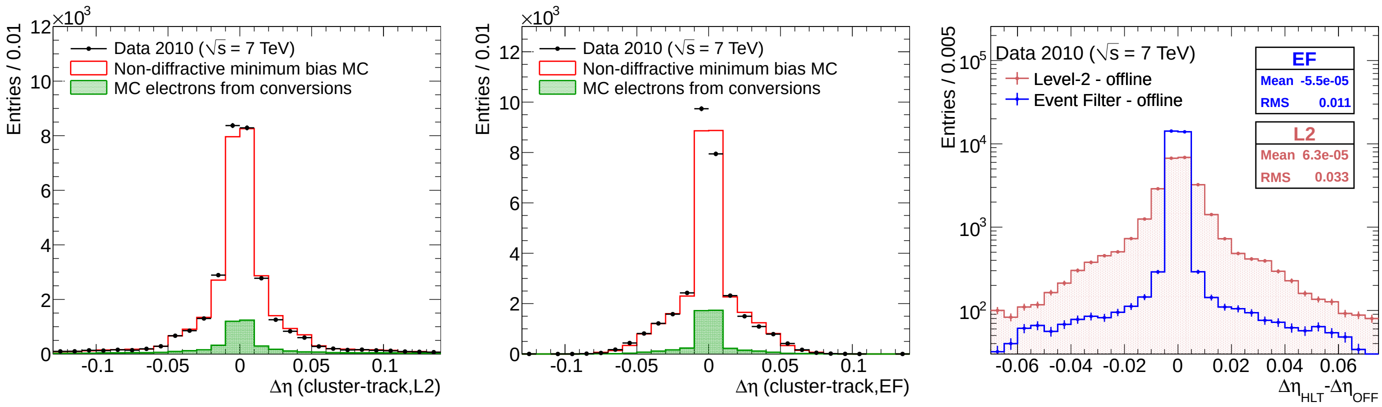

(a) (b) (c)

Figure 4.7: Data/MC comparison for the track-cluster $\Delta\eta$ at the L2 (a) and EF (b). (c) shows the resolution between each trigger level and offline reconstruction.

The presented results provided the evidence that the implementation of the initial trigger selection criteria developed using MC simulations was safe and robust for the HLT to be activated in rejection mode for an instantaneous luminosity greater than 10^{29} cm^{-2}s^{-1}. At a luminosity of 10^{30} cm^{-2}s^{-1}, the so-called 'physics menu' was deployed, containing all the trigger items used for the rest of 2010 datataking. Each trigger was carefully checked for its correct implementation by measuring its efficiency in early data (where the trigger decision was recorded but not applied to actively reject events), using the *bootstrap* method. The method consisted in measuring the trigger efficiency with respect to another (looser) trigger selection with known efficiency. Towards the end of the year, the amount of recorded luminosity was sufficient to allow the use of real sources of electrons from $J/\psi \to ee$, $W \to e\nu$ and especially $Z \to ee$ to assess the trigger performance.

4.4 Evolution of the electron triggers during data-taking

As described in the previous section, the rejection power ensured by the HLT is a key component to limit the output rate of recorded events within specification, while maintaining high efficiency for interesting physics channels. The trigger selecting at least one electron is the most widely used for physics analyses involving electrons given its large acceptance on many physics processes in the SM and BSM and the minimal bias introduced on the event selection (only one object is selected). In addition, it allows to collect a very large sample of electron candidates from the $Z \to ee$ process to be used for calibration and identification studies.

In order to control the output rate of the unprescaled single electron trigger with the increase of the LHC luminosity, the strategies adopted consisted in a progressive increase of the transverse energy threshold and in tightening the electron selection criteria. In general only one unprescaled single electron trigger is maintained in the menu corresponding to the lowest affordable E_{T} threshold and electron selection.

The variety of thresholds and electron selections results from a compromise between the acceptance of a given physics process defined by the electron p_{T} threshold, and the *tightness* of the electron identification. On one side, a too high threshold reduces the statistics for the targeted signals. The distribution of electron E_{T} from Z, W and $t\bar{t}$ events peaks between 24 and 40 GeV. On the other hand, a too stringent electron identification already in the online stage will not guarantee enough flexibility to the offline analyses and could prevent the possibility to correct for some detector effects. Between 2010 and 2011, an increase of the transverse energy threshold was applied to counteract the rise in the instantaneous luminosity. During 2011, a progressive tightening of the electron selection was also performed to reduce the rate, up to the point of introducing an isolation requirement initially at L1 and then in the HLT. Since such isolation requirements produce an inefficiency at very high p_{T}, a second lepton trigger with much higher E_{T} threshold and no isolation requirement was then introduced to recover these losses.

Table 4.1 summarises the list of the lowest threshold single electron triggers recommended for physics analyses for each year of data-taking.

In the year 2010, the largest part of the dataset was collected after the deployment of the physics menu (only 0.7 pb^{-1} of data out of total 35 pb^{-1} corresponds to the period were the HLT was in commissioning state and they are not included in physics analyses). In this configuration the two available unprescaled triggers were e15_medium and e20_loose, with a maximum rate of $\sim$ 20/22 Hz[111] at the peak luminosity of $2 \cdot 10^{32}$ cm^{-2}s^{-1}. The choice of a two trigger approach allowed analyses for a choice between a lower electron threshold (e15_medium is fully efficient for electrons above 18 GeV), or a reduced assumption on the electron identification (the e20_loose trigger has been particularly adopted by analyses looking at high p_{T} electrons). The e15_medium trigger is the trigger used for the $t\bar{t}$ analysis presented in Chapter 6.

year	trigger	avail. fraction	L1 threshold	HLT threshold
2010	e15_medium	$\sim$ 100%	10 GeV	15 GeV
	e20_loose	$\sim$ 100%	14 GeV	20 GeV
2011	e20_medium	37%	12 GeV	20 GeV
	e22_medium	12%	18 GeV	22 GeV
	e22vh_medium1	52%	18 GeV(vh)	22 GeV
	e45_medium1	52%	30 GeV	45 GeV
2012	e24vhi_medium1	100%	18 GeV(vh)	24 GeV
	e60_medium1	100%	30 GeV	60 GeV

Table 4.1: Unprescaled single electron triggers used for physics analysis in each year of data-taking. The p_{T} threshold at L1 and HLT are also indicated together with the fraction of the recorded luminosity for which these triggers were available un-prescaled in that particular year. The symbol (vh) indicates a variable E_{T} threshold ('v') and an isolation requirement ('h') applied at L1 stage.

For the year 2011, the deployed triggers were modified to face an increase in luminosity up to a factor 20 with respect to the peak in luminosity in 2010, with a variation from 0.5 to 4 10^{32} $\mathrm{cm}^{-2}\mathrm{s}^{-1}$. The transverse energy threshold was first raised to 20 GeV and subsequently to 22 GeV and only the medium selection was supported. After the September technical stop and the increase in luminosity of the LHC due to a smaller beam profile, the output trigger rate was controlled with a double trigger approach. The low threshold trigger e24vh_medium1 was introduced[5]. The "v" label indicates that a variable E_{T} threshold was introduced at L1, to compensate for the different amount of dead material in front of the calorimeter as a function of η. The label "h" represents a requirement that the energy deposition in the hadronic calorimeter for the core part of the L1 cluster is smaller than 1 GeV. Both selections were necessary to reduce the output rate of the L1 system and consequently the network traffic for L2. Given that the requirement of the hadronic core veto at L1 produces an inefficiency for very high p_{T} electrons ($p_{\mathrm{T}} \gg 100$ GeV), a second trigger (e45_medium1) with higher E_{T} threshold but without such requirement was introduced to recover these losses. For these reasons, physics analyses were using events collected by the logical OR of these two triggers.

During the year 2012 the instantaneous luminosity delivered by LHC maintained a reasonably constant profile in the range of 6-7$\cdot$ 10^{33} $\mathrm{cm}^{-2}\mathrm{s}^{-1}$. This allowed to deploy a basically stable trigger configuration throughout the year. The trigger rejection benefited from the re-optimisation of the offline identification criteria; nevertheless, to reduce the output rate further, an increase in transverse energy threshold of 2 GeV was necessary together with the introduction of an isolation requirement at the EF. The choice of track isolation $p_{\mathrm{T}}^{\mathrm{cone20}}/E_{\mathrm{T}} < 0.1$ was adopted where $p_{\mathrm{T}}^{\mathrm{cone20}}$ represents the sum of the p_{T} of the tracks with $p_{\mathrm{T}} > 1$ GeV in a cone of $\Delta R < 0.2$ around the electron direction. As for 2011, a second trigger with a higher E_{T} threshold of 60 GeV but no L1 hadronic leakage and EF isolation requirement was introduced to recover the losses at high energy introduced by these two criteria.

[5]During 2011 the offline electron selection was re-optimised for better rejection and smaller dependence on pileup conditions. The selection was then retroactively applied to the full year in offline analyses. The term "_medium" refers to triggers whose identification is derived from the being-of-year initial year selection while the term "_medium1" refers to triggers whose identification is tailored to the re-optimised selection.

4.5 Electron trigger efficiency measurement in 2010

This section describes the measurement of the trigger efficiency for the most commonly used single electron triggers during 2010 data-taking (e15_medium and e20_loose) using $Z \rightarrow ee$ events. The efficiency was measured with respect to offline electron identification criteria for which the trigger was designed to be almost 100% efficient; for this reason only *medium* and *tight* offline electrons are considered. Since the trigger selection criteria are designed to be slightly looser than the corresponding offline ones, the trigger efficiency is not expected to be very different between signal and background after the offline identification cuts have been applied. The main sources of inefficiency are:

- readout problems of the L1 system;
- reconstruction efficiency at trigger level;
- limited resolution of HLT levels with respect to offline reconstruction for electron identification variables.

A good knowledge of the electron trigger efficiency for real isolated electrons is crucial for precision analyses. Differences between the efficiency in data with respect to the value obtained from MC are accounted for with scale factors defined as the ratio of the efficiencies measured in the two samples.

4.5.1 Methodology

$Z \rightarrow ee$ events represent an ideal sample for providing a sample of real electrons through the so-called *tag & probe* method[76]. One of the electrons from the Z is used to select ('tag') the event; this electron is required to be well identified and matched to a valid trigger object. The other electron in the decay is then not biased by any selection and can be used to measure ('probe') the efficiency of a specific set of cuts, defined as the fraction of probe candidates satisfying the considered selection.

A requirement of opposite charge (OS) and on the invariant mass of the two electrons is used to reduce the background contamination in the probe sample.

4.5.2 Event selection and dataset

For the measurement, the tag were offline *tight* electrons with $E_{\mathrm{T}}>$ 20 GeV and $|\eta| < 2.47$ matched to EF trigger objects fulfilling the e15_medium selection[6]. Probe electrons were selected by requiring *medium* or *tight* electrons with opposite sign with respect to the tag and an invariant mass in the range 80 GeV $< m_{ee} <$ 100 GeV. Only electrons with $|\eta| < 2.47$ and outside the transition region between the barrel and endcap calorimeter ($1.37 < |\eta| < 1.52$) were considered. In case both electrons from the Z boson passed the 'tag' selection, both electrons were considered in the 'probe' sample. No background subtraction technique was applied on the probe samples since the background contamination when requiring a *medium* probe was at the order of 1% (the impact of background subtraction was considered as a source of systematic uncertainties).

The measurement was restricted to the dataset in which the triggers were active and this corresponds to a luminosity of 38.2 pb^{-1}. Figure 4.8 shows the distribution of *medium* probes'

[6] Events tagged by the e15_medium trigger have been used for probing both the e15_medium and e20_loose trigger efficiency since they provide more statistics due to the lower E_{T} cut. No difference has been observed when using events collected with the e20_loose trigger.

E_T and η for the data and the Monte Carlo simulation, while Figure 4.9 (a) illustrates the tag-probe invariant mass distribution. $Z \to ee$ events were generated with PYTHIA and processed through the full ATLAS simulation. Monte Carlo events were scaled to match the same integral as data. The Monte Carlo simulation was re-weighted to have a similar distribution of the number of primary vertices as the data, although this procedure did not introduce an appreciable effect on the measured efficiencies. A sample of $\sim$ 14k (12k) probes passing the *medium* (*tight*) selection were collected for the measurement. As the plot shows, a good description of the probe kinematics was provided by the simulation (the differences in the di-electron invariant mass resolution have been considered as uncertainties in the electron energy resolution but they do not affect the presented result).

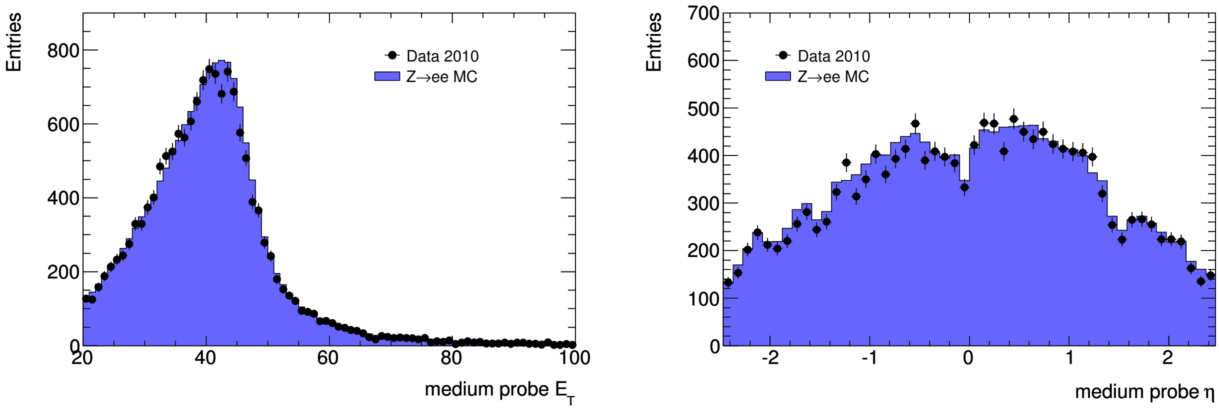

(a) **(b)**

Figure 4.8: E_T (a) and η (b) distributions of selected electron probes passing the *medium* identification cuts for data and Monte Carlo. Monte Carlo distributions are normalised to the data integral.

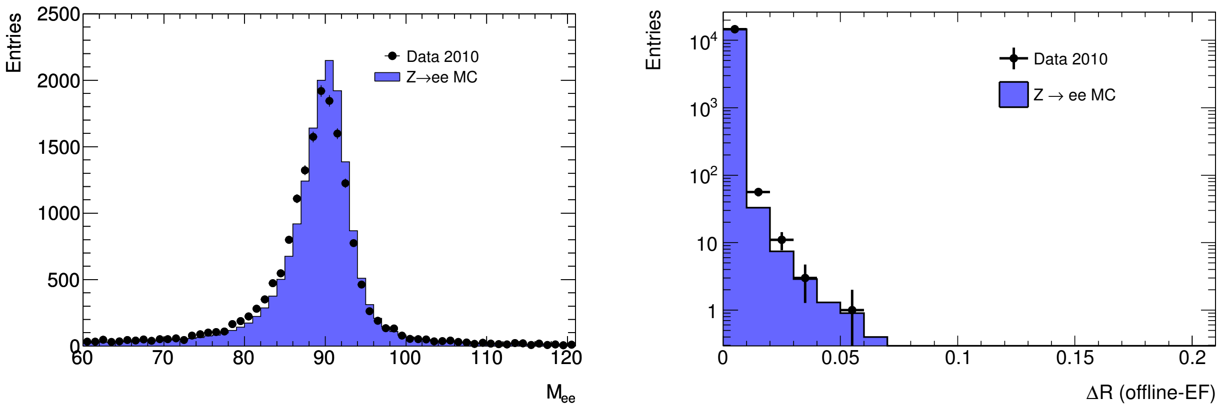

(a) **(b)**

Figure 4.9: M_{ee} distributions of tag-probe pairs for data and Monte Carlo simulation. (b) Angular distance (ΔR) distance between *medium* probes and the closest EF trigger object fulfilling the e15_medium trigger identification. Monte Carlo distributions are normalised to the data integral.

The trigger efficiency was defined as the fraction of probe events matched to an EF trigger object fulfilling the trigger selection for the considered trigger. Figure 4.9 (b) shows the distribution of the closest $\Delta R = \sqrt{\Delta\eta^2 + \Delta\phi^2}$ between the trigger and offline electrons calculated using the track coordinates of each object. The matching is defined by requiring $\Delta R < 0.15$ and as can be seen this criterion did not introduce any inefficiency. For usage in physics analyses, only the match to a valid EF object is required without any explicit requirement on L1 and L2. Given the architecture of the ATLAS trigger, a valid EF object is created only if L1 and L2 objects fulfilling the trigger selection are found in the same RoI. Nevertheless, a direct match to objects at all trigger levels is required for debugging the trigger performance and showing the efficiency for each trigger level.

4.5.3 Results

Figure 4.10 illustrates the efficiency of the e15_medium and e20_loose triggers as a function of the electron E_T for offline *medium* probes as measured from data. The efficiencies are shown for each trigger level in a cumulative way (L1, L1+L2, L1+L2+EF)[7]. Only statistical uncertainties are shown. The numerator of the efficiency is a subset of the denominator so binomial statistics was used for the computation of the statistical error. For values of efficiency close to zero or unity, the frequentist formula is replaced with the Bayesian evaluation of the uncertainty as described in [112].

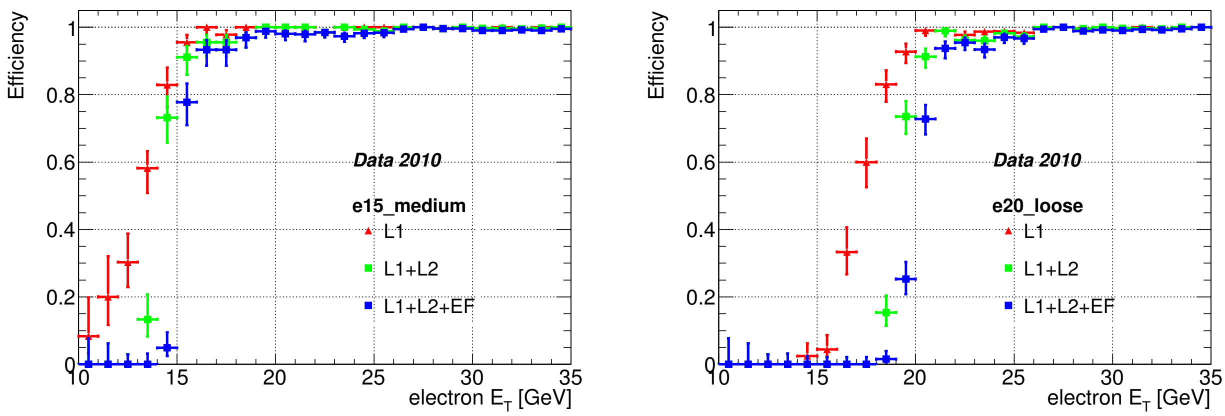

(a) **(b)**

Figure 4.10: Efficiencies for the e15_medium (a) and e20_loose (b) triggers at L1, L2, and EF measured in $Z \to ee$ events in data. The efficiencies are measured with respect to the offline *medium* electrons E_T. Only statistical uncertainties are shown.

As can be seen from the plots, each level progressively increases the E_T threshold to increase the rejection. In particular the L1 threshold is significantly lower than the EF one since the energy resolution is worse at L1, while the L2 threshold is only 1 GeV lower than the EF one. For physics analyses, a cut on the offline transverse energy was applied to consider only electrons in the plateau region of the efficiency. For analyses using the e15_medium trigger, a 20 GeV offline E_T cut was considered. Analyses relying on the e20_loose trigger had a 25 GeV offline E_T cut.

The comparison of the efficiency between data and simulation is shown in Figure 4.11. For both triggers and the two offline benchmark selections, the trigger efficiency is above 98% in the plateau region. The trigger efficiency is slightly higher when using *tight* offline electrons due to the cut on E/p; it rejects electrons with a large amount of bremsstrahlung radiation which are less efficiently reconstructed by the fast L2 tracking algorithm. For the η dependence plots, only electrons in the plateau region were considered.

[7] in order to compute the efficiency of each level a trigger matching to all levels is required.

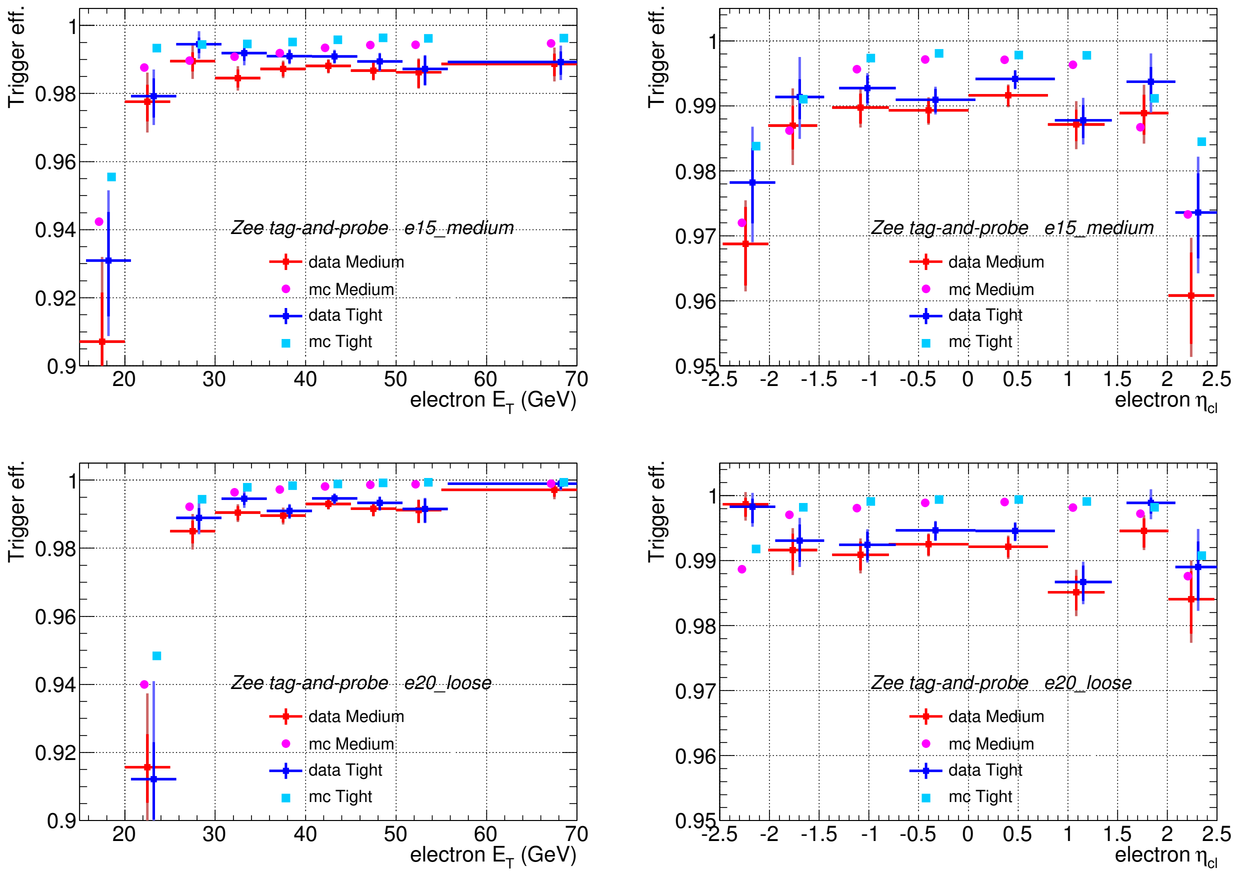

Figure 4.11: Trigger efficiency for e15_medium (top) and e20_loose (bottom) triggers as a function of offline electron E_{T} (left) and η (right) from $Z \to ee$ events; each plot shows efficiency for offline *medium* and *tight* candidates in both data and Monte Carlo. η plots consider only candidates with $E_{\mathrm{T}} > 20(25)$ GeV. For each data point the inner error bars correspond to the statistical error while full error bars are the total uncertainty.

The values of the integrated efficiency for electrons with $E_{\mathrm{T}}> 20$ (25) GeV in the case of e15_medium (e20_loose) triggers are summarised in Table 4.2 together with the data/MC scale factors. Values are reported with only statistical uncertainties.

Scale factors are also shown in Figure 4.12 as a function of the probe kinematic variables. For both triggers the SF values are again fully compatible for the two different offline selections and they do not show any significant trend as a function of the electron E_{T} and η.

Systematic uncertainties were estimated by considering the following variations for the event selection:

- *identification requirement on the tag*: offline tags fulfilling the medium identification criteria have been used to check the effect of an increased level of background;
- *tag E_{T} cut*: raised to 25 and 30 GeV;
- *signal region definition*: invariant mass regions of ($70 \leq M_{ee} \leq 110$ GeV) and ($83 \leq M_{ee} \leq 96$ GeV) have been tested;
- *background subtraction*: the effect of the background subtraction using the standard OS-SS sideband technique has been tested. It assumes that the shape of the M_{ee} distribution

trigger	data efficiency	MC efficiency	Scale Factor
Offline medium Electrons			
e15_medium	98.67 ± 0.10	99.235 ± 0.006	0.9943 ± 0.0010
e20_loose	99.11 ± 0.08	99.728 ± 0.004	0.9938 ± 0.0008
Offline tight Electrons			
e15_medium	99.02 ± 0.09	99.540 ± 0.005	0.9948 ± 0.0009
e20_loose	99.33 ± 0.08	99.834 ± 0.003	0.9949 ± 0.0008

Table 4.2: The integrated efficiency above for E_T> 20 (25) GeV for the e15_medium (e20_loose) trigger thresholds from $Z \to ee$ events; the data/MC SF is also reported. Only statistical uncertainties have been considered.

for background is similar for opposite sign (OS) and same sign (SS) electron pairs. Side-bands in M_{ee} SS distribution ($60 < M_{ee} < 80$ GeV and $100 < M_{ee} < 120$ GeV) are used to predict the amount of background inside the signal window with a linear extrapolation.

- *trigger-offline matching cut*: the ΔR cut has been varied by ± 0.05 .

Table 4.3 summarises the systematic uncertainties on the integrated data/MC scale factors for the two triggers and each of the offline selection criteria. Each uncertainty has been symmetrised before being included in the plots.

sys	e15_medium		e20_loose	
	offline medium	offline tight	offline medium	offline tight
tag sel.	0.0001	<0.0001	<0.0001	<0.0001
tag E_T	0.0004	0.0008	0.0003	0.0003
signal region	0.0004	0.0004	0.0001	0.0001
bkgd subtraction	0.0002	<0.0001	<0.0001	<0.0001
ΔR cut	<0.0001	<0.0001	<0.0001	<0.0001
total	0.0006	0.0009	0.0004	0.0004

Table 4.3: Systematic uncertainties on the integrated data/MC scale factors for electron trigger efficiency.

Table 4.4 summarises the values of the data-MC scale-factors extracted from the analysis of the $Z \to ee$ decays.

trigger	offline selection	SF from $Z \to ee$
e15_medium	medium	0.9943 ± 0.0012
e15_medium	tight	0.9948 ± 0.0013
e20_loose	medium	0.9938 ± 0.0009
e20_loose	tight	0.9949 ± 0.0009

Table 4.4: Scale factors for e15_medium and e20_loose trigger efficiency from $Z \to ee$ events (errors contains both statistical and systematic uncertainties).

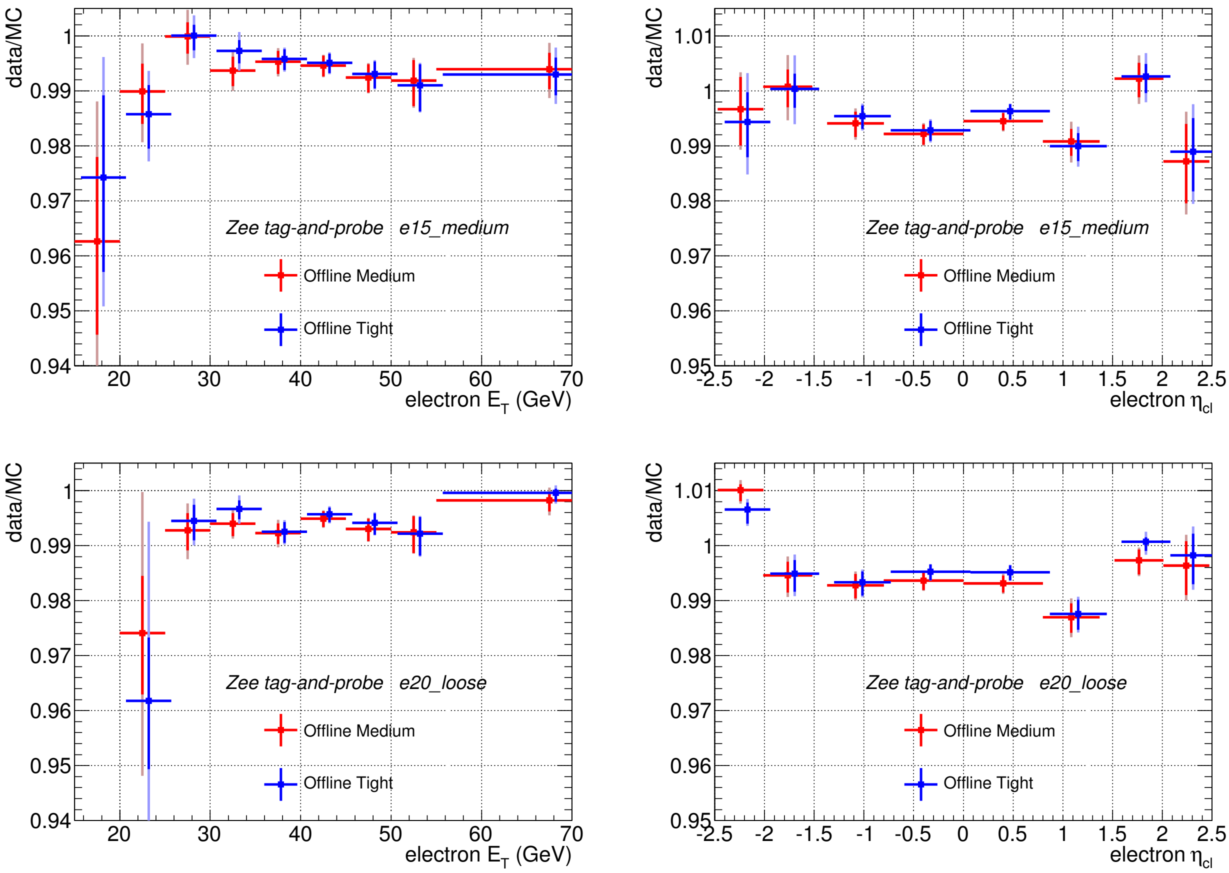

Figure 4.12: Data/MC scale factors for e15_medium (top) and e20_loose (bottom) triggers as a function of offline electron E_{T} (left) and η (right) from $Z \to ee$ events. For each data point both statistical and statistical plus total systematic errors are reported.

Data/MC scale factors had also been computed with a complementary method exploiting $W \to e\nu$ events[113]. Missing transverse energy triggers were used to collect an unbiased sample of electrons. Additional cuts on the transverse mass built from the electron and the $E_{\mathrm{T}}^{\mathrm{miss}}$ and the $\Delta\phi$ between the two was used to enhance the fraction of W events. Results of the two methods are in excellent agreement.

Given the lack of evidence for a trend in the SF as a function of electron η and even more of electron E_{T}. The official prescription for all the physics analyses in 2010 using single electron triggers was to use a single value for the trigger efficiency SF.

$$SF = 0.995 \pm 0.005 \tag{4.1}$$

The enlarged uncertainty with respect to the results previously shown is derived by taking into account the uniformity of the SF versus η. The systematic has been chosen as the r.m.s. obtained considering the value in each η bin and the integrated value.

4.6 Electron trigger performance for the full 2011 and 2012 dataset

The same procedure outlined previously in this chapter has also been used to assess the performance of the triggers used in 2011 and 2012. The large amount of collected statistics allowed for a more precise determination of the trigger efficiency in finer binning of E_{T} and η. Figure 4.13 (a) shows a comparison of the trigger efficiency as a function of electron η for the three main single electron triggers in use in 2011[114]. Efficiencies were extracted from data for electron fulfilling the *medium* selection and with E_{T}> 25 GeV. The efficiency of the triggers used for the 2012[79] data-taking is displayed in Figure 4.13 (b). It was measured for the logical OR of the e24vhi_medium and the e60_medium chain as a function of the E_{T} of offline electrons fulfilling the *medium* selection criteria. The variation observed at around ∼ 60 GeV is due to the onset of the e60_medium trigger. This trigger, other than not having a requirement on isolation both at L1 and EF, also implements a selection with looser cuts on the discrimination variables than e24vhi_medium.

Scale factors were computed with respect to the final selection used in the analysis and outlined in Chapter 3 as a function of the offline electron E_{T} and η. SF values differ from unity by a few percent only, with a maximal uncertainty of 1.5 % at high E_{T}.

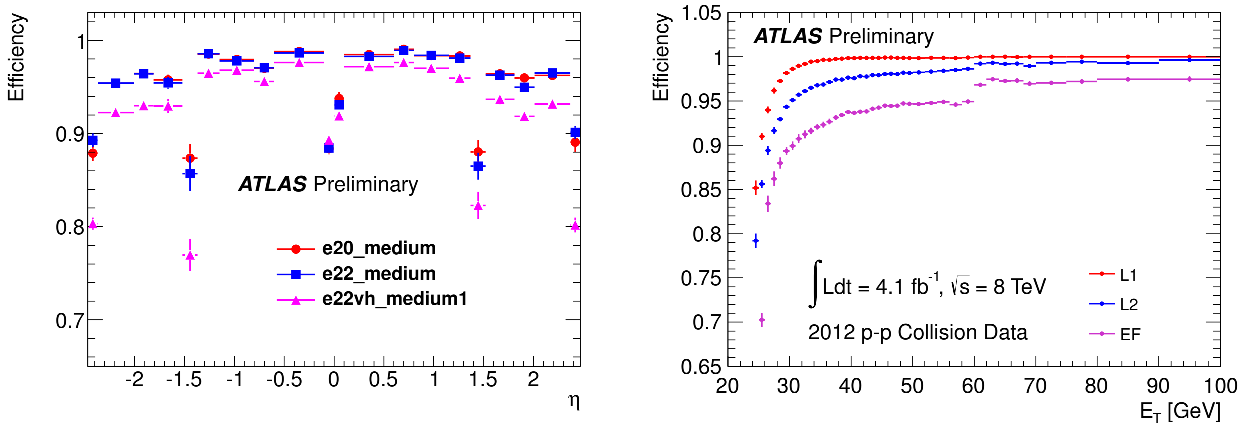

(a) **(b)**

Figure 4.13: (a) Trigger efficiency measured from data for the 3 main unprescaled single electron triggers used during 2011 data-taking as a function of electron η. Efficiency is shown for offline *medium* electron candidates with E_{T}> 25 GeV. (b) Trigger efficiency measured from data for the logical OR of the two single electron triggers used in the 2012, as a function of the E_{T} of the medium electron candidates. Cumulative efficiencies for each trigger level are shown.

4.7 Single muon trigger for physics analyses

The analyses presented in this thesis all exploit the lepton (electron or muon) plus jets $t\bar{t}$ decay topology hence the necessity to rely on single lepton triggers. The evolution and the performance of the single electron trigger have been extensively discussed in the previous sections of this chapter.

This section gives a brief overview of the single muon triggers commonly used in physics analyses during the three years of data-taking. The muon trigger at L1 relies only on the information provided by the 'fast' muon chambers (RPC and TGC). Timing coincidence of hits in different layers of the muon chambers is required to build a muon candidate. In order to form a coincidence, hits are required to lay within parameterised geometrical muon roads. A road represents an envelope containing the trajectories, from the nominal interaction point, of muons of either charge with a p_{T} above a given threshold. The geometrical coverage of the L1 trigger system is ∼ 99% in the end-cap region and ∼ 80% in the barrel region, due to a

year	trigger	avail. fraction	L1 threshold	HLT threshold
2010	mu10_MSonly	6%	1 GeV	10 GeV
	mu13	13%	1 GeV	13 GeV
	mu13_tight	81%	10 GeV	13 GeV
2011	mu18	31%	10 GeV	18 GeV
	mu18_medium	69%	15 GeV	18 GeV
2012	mu24i_tight	100%	15 GeV	24 GeV
	mu36_tight	100%	15 GeV	36 GeV

Table 4.5: Unprescaled single muon triggers used for physics analysis in each year of data-taking. The p_{T} threshold at L1 and HLT are also indicated with the fraction of the recorded luminosity for which these triggers were available un-prescaled in that particular year.

crack around $\eta = 0$ and the support structure of the whole ATLAS detector. At the HLT, information from the precision muon chambers (MDT, CSC) are included for the standalone muon spectrometer reconstruction. In addition, a combination of the muon track with a track in the inner detector is required to improve the precision and further reduce the rate[107].

Table 4.5 shows the list of lowest-threshold primary (unprescaled) single muon triggers available for each data-taking year. As already shown in the electron case, the p_{T} threshold increases in each year to compensate for the increase of luminosity of the LHC but the values are generally lower than for the electron due to the smaller fake rate of muons from multi-jet events.

For the years 2010 and 2011 the listed triggers are used in an "exclusive" mode meaning that each trigger was used in a specific period of the data-taking. As can be noted from the table, the suffix *_tight* refers to a tighter cut on the muon p_{T} applied at L1. The same applies to the *_medium* suffix.

For the year 2012, in order to limit the output rate without an excessive increase of the p_{T} threshold, an isolation requirement was added to the lowest unprescaled trigger. The isolation, from which the indication "i", is applied at EF and requires $p_{\mathrm{T}}^{0.2}/p_{\mathrm{T}} < 0.12$ where $p_{\mathrm{T}}^{0.2}$ is the sum of the p_{T} of the tracks in a cone of $\Delta R < 0.2$ around the muon direction. A second trigger without such requirement but with a higher p_{T} threshold (36 GeV) was deployed to support the analyses requiring very high p_{T} muons. The analyses thus require a logical OR of the two trigger chains. It has been verified that below the onset of the mu36_tight trigger, the mini-isolation requirement applied in the offline event selection for the muon is more stringent than the trigger track isolation so the latter does not introduce any bias.

The trigger efficiency with respect to the offline muon selection presented in Chapter 3 has been measured in data using $Z \to \mu\mu$ events with the tag&probe technique in 2010[115], 2011[116] and 2012[117]. Figures 4.14 and 4.15 show a selection of the performance of the muon trigger in 2011 and 2012, comparing data and Monte Carlo simulations. For the 2011 data, the efficiency of mu_18 is displayed as a function of the muon p_{T} for the first part of the data sample where the trigger was unprescaled. Finally, the combined efficiency of the two main trigger used during 2012 is presented still as a function of the muon p_{T}.

Data/Monte Carlo scale factors are normally computed as a function of muon p_{T}, η and ϕ since the coverage of the spectrometer does not have azimuthal symmetry. Uncertainties on the scale factors are at the few % level.

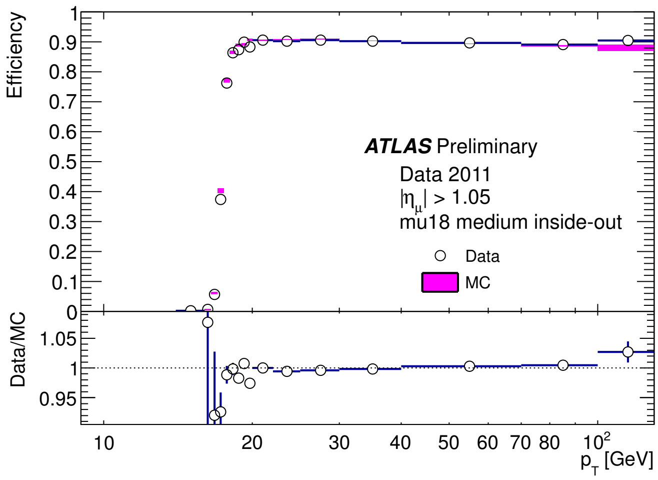

Figure 4.14: mu_13_tight trigger efficiency measured in 2011 data and in $Z \to \mu\mu$ Monte Carlo events. The efficiency is shown as a function of muon p_{T} for muons in the endcap region of the muon spectrometer.

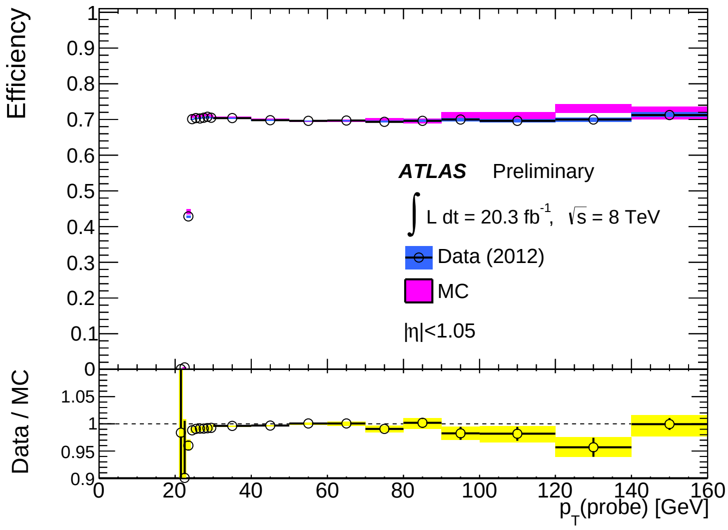

Figure 4.15: Trigger efficiency measured in 2012 data and $Z \to \mu\mu$ Monte Carlo events for the logical OR of mu24i_tight and mu36_tight. The efficiency is shown as a function of muon p_{T} for candidates in the central part of the muon spectrometer.

Chapter 5

$t\bar{t}$ measurements: definitions

This chapter summarises the general aspects for analyses aiming at measuring $t\bar{t}$ events in the lepton plus jets final state at the LHC. The event selection will be outlined together with the properties of the sample and the Monte Carlo samples used to model it. The last part of the chapter is dedicated to the description the backgrounds and the method used to obtain a data-driven estimation for the most important ones.

5.1 Event selection for the lepton+jets channel

As already outlined at the end of Chapter 1, among the possible $t\bar{t}$ decay modes, the *lepton+jets* decay topology represents the best compromise between low background contamination and a high branching ratio necessary to collect large statistics. This consideration also applies in the search for the $t\bar{t}H$ process, since the event identification mainly exploits the properties of the top anti-top quark pair.

The event selection closely follows from the characteristics of the final state: one isolated lepton, large $E_{\mathrm{T}}^{\mathrm{miss}}$ due to the escaping neutrino, and a large number of jets. The lepton and the $E_{\mathrm{T}}^{\mathrm{miss}}$ should be compatible with the leptonic decay of a W boson.

The specific values for the selection cuts resulted from an optimisation taking into account the efficiency for $t\bar{t}$ events and the need to reduce the background contribution. Additional requirements from the detector operation like the availability of the trigger have also been considered. Minor adjustments to the baseline $t\bar{t}$ event selection were made during the three years of data-taking in order to adapt to the different conditions and to reflect the improved degree of detector understanding. This reflects also the specific needs of each analysis which will be outlined in the relevant chapters.

Among the possible leptonic decays of the W boson, those involving electrons and muons, either from direct decays of from τ-lepton decay offer the best performance since those leptons can be efficiently identified and used as a source of triggering; hadronically decaying τ-leptons have not been considered since they generally have a much lower selection efficiency and higher fake rate. The selected events are separated into two categories according to the flavour of the selected lepton: *electron channel* and *muon channel*. The event selection in the two channels can differ as a result of a separate optimisation particularly targeted at reducing the much larger multijet background in the electron channel.

The requirements on the identification of the single physics objects have been described in detail in Chapter 3. The full event selection steps are summarised in the following:

- *trigger selection*: the event is required to satisfy the lowest unprescaled single lepton triggers listed in Sections 4.4 and 4.7.

- *lepton selection*: the specific p_{T} cut on the lepton was driven by the threshold of the lowest unprescaled single lepton trigger available in each year. For the analyses performed on the 2010 dataset a cut of 20 GeV was applied; the cut was raised to 25 GeV during 2011 and 2012. The selection requires exactly one selected lepton for each channel and vetoes the presence of any additional electron or muon fulfilling similar identification and kinematic requirements. The selected lepton is also required to match a lepton reconstructed at the trigger level and fulfilling the trigger selection. This condition allows to reduce the contamination from backgrounds with two isolated leptons like Z+jets as well as ensuring the orthogonality with analyses using the dilepton $t\bar{t}$ final state.

- *missing transverse energy*: $t\bar{t}$ events have a genuine source of missing transverse energy in the neutrino originating from the leptonic W boson decay. A requirement on $E_{\mathrm{T}}^{\mathrm{miss}}$ allows to reduce the contribution from backgrounds with no neutrinos in the final state where the $E_{\mathrm{T}}^{\mathrm{miss}}$ is due only to instrumental effects. Table 5.1 summarises the cut values for the electron and muon channel in the three analyses described in this thesis work.

channel	2010	2011	2012
$e+$jets	35 GeV	35 GeV	–
$\mu+$jets	20 GeV	30 GeV	–

Table 5.1: $E_{\mathrm{T}}^{\mathrm{miss}}$ selection cut for the electron and muon channel for the analyses performed in each year of data-taking. No cut is applied in 2012 to increase the $t\bar{t}H$ signal acceptance.

- *transverse mass*: in lepton+jets events both the lepton and the neutrino responsible for the $E_{\mathrm{T}}^{\mathrm{miss}}$ originate from a W boson decay. Since the information on the neutrino longitudinal momentum cannot be directly measured, the invariant mass in the transverse plane $m_{\mathrm{T}}(W)$ defined as:

$$m_{\mathrm{T}}(W) = \sqrt{E_{\mathrm{T}}^{l} \cdot E_{\mathrm{T}}^{\mathrm{miss}} \cdot \cos(\phi^{l} - \phi^{\mathrm{miss}})} \tag{5.1}$$

  is used. E_{T}^{l} and ϕ^{l} represent the coordinates of the lepton, $E_{\mathrm{T}}^{\mathrm{miss}}$ is the scalar value of the missing transverse energy and $\phi^{miss} = \arctan(E_{y}^{\mathrm{miss}}/E_{x}^{\mathrm{miss}})$ the direction of the missing momentum vector in the transverse plane[1]. The expected peak in the lepton-neutrino invariant mass translates into a broader peak just below ~ 80 GeV in $m_{\mathrm{T}}(W)$. The peak is broadened by $E_{\mathrm{T}}^{\mathrm{miss}}$ resolution effects as well as by the projection in the transverse plane.

  The particular shape of the $m_{\mathrm{T}}(W)$ distribution can be exploited to further reduce the contribution from background events with a mis-identified lepton and in general from events where the lepton and the $E_{\mathrm{T}}^{\mathrm{miss}}$ do not originate from the W. This can be achieved by a direct cut on the $m_{\mathrm{T}}(W)$ or a requirement on the sum of the $m_{\mathrm{T}}(W)$ and $E_{\mathrm{T}}^{\mathrm{miss}}$ (also referred to as 'triangular cut'). The latter was found to be more effective to reduce the contribution of mis-identified leptons in the muon channel. The specific selections for the two channels in each year of data-taking are summarised in Table 5.2.

[1] More precisely the function *atan2* is used; it is an extension of the arctan function allowing to map the vector projections into the four quadrants resolving the ambiguity between opposite angles. A compact definition is: $atan2(x, y) = 2\arctan\frac{y}{\sqrt{x^2+y^2}+x}$ where x and y are the projections of the initial vector along orthogonal axis.

channel	2010	2011	2012
e+jets	$m_{\mathrm{T}}(W) > 25$ GeV	$m_{\mathrm{T}}(W) > 35$ GeV	–
μ+jets	$E_{\mathrm{T}}^{\mathrm{miss}} + m_{\mathrm{T}}(W) > 60$ GeV	$m_{\mathrm{T}}(W) > 35$ GeV	–

Table 5.2: $m_{\mathrm{T}}(W)$ selection cut for the electron and muon channel for the analyses performed in each year of data-taking. No cut is applied in 2012 to increase the $t\bar{t}H$ signal acceptance.

- *jet multiplicity*: only jets with $|\eta|$ <2.5 are considered since $t\bar{t}$ events are expected to produce more central topologies. Jets are required to pass the JVF selection and have a p_{T} greater than 25 GeV. The requirement on the jet multiplicity varies according to the analysis needs. The lepton+jets $t\bar{t}$ topology will on average produce four jets in the final state. In order to increase the statistics a requirement of at least three jets is made to recover events where the 4th jet falls outside the geometrical acceptance or is too soft.

- *b-tagged jets requirement*: among the selected jets, a number of them can be required to be 'tagged' as originating from a b quark using the MV1 algorithm with the 70% working point. Since $t\bar{t}$ decays normally produce two b quarks, imposing a minimum number of b-tagged jets can be used to substantially improve the purity of $t\bar{t}$ in the selected events at the expense of a smaller number of events due to the inefficiency of the algorithm. The exact requirement on the number of b-tagged jets varies for the different analyses presented in this thesis since it stems from a compromise between the desired purity and the statistics available as well as the impact of systematic uncertainties associated with the use of b-tagging algorithms.

Prior to the requirement on the number of b-tagged jets the selection is generally referred to as the *pretag* selection.

Additional requirements are related to the overlap removal among selected objects and the so-called "event-level quality cuts". Event-level selection ensures that the collected data do not suffer from problems in the acquisition chain of the sub detectors or from conditions affecting the object reconstruction.

Before applying the event level selection previously described, an overlap removal procedure is also applied. Only the physics objects surviving the overlap removal procedure are used in the event selection. This serves multiple purposes. It prevents double-counting of objects in the final state (calorimetric deposits from electrons and muons also reconstructed as jets), it guarantees that selected objects are sufficiently separated in the detector so that they do not affect each other's properties and finally, in the case of muons, it also contributes to suppressing the background originating from semileptonic b-jets decays.

Event cleaning

- *data quality*: since the measurement of $t\bar{t}$ events requires information from all the ATLAS components, only events where all the subdetectors were fully functional are retained. The fraction of 'good quality' data is shown in Section 2.3 and it is used to compute the effective luminosity of the data sample and to normalise the Monte Carlo prediction accordingly. This requirement is most commonly known as the application of the *good runs list* selection.

- *corrupted data removal*: the granularity of the good runs list selection is represented by the luminosity block which covers about two minutes of data-taking time. Problems and malfunctions happening for shorter periods are rejected with event-level flags without losing the entire luminosity block. This is the case for data integrity problems or noise 'bursts' in the calorimeters.

- *non-collision collision background removal*: the reconstructed primary vertex of the event is required to have at least four tracks associated with it. This ensures a good position resolution for the vertex and, at the same time, rejects events produced by the interaction of cosmic muons and other non-collision sources.

- *'bad jets'* removal: events are rejected if a "bad" jet (defined in Section 3.3.3) with $p_{\mathrm{T}} > 20$ GeV and $|\eta| < 4.5$ is found with no requirement on the JVF. This condition is particularly important to protect the $E_{\mathrm{T}}^{\mathrm{miss}}$ computation from mis-measured jets.

Overlap Removal

- *electron-jet* overlap removal: given that the jet finding algorithm uses as input all the energy deposits in the calorimeter, isolated electrons will also be reconstructed as jets. The overlap removal procedure requires the removal of the jet closest in ΔR to each selected electron. In addition, the electron is removed if any other of the selected jets is within $\Delta R < 0.4$ to it. This requirement was introduced in analyses of the 2011 and 2012 data, in order to remove any perturbation produced by the close-by jet activity to the calculation of the electron shower shape and isolation variables.

- *muon-jet* overlap removal: muons are required to have an angular distance $\Delta R > 0.4$ to any selected jets. The jet p_{T} cut is lowered to 20 GeV for the 2010 analysis to match the lower lepton p_{T} cut. This selection allows for a further reduction of muons arising from heavy flavour decays inside jets.

- *electron-muon* overlap removal: electrons sharing the ID track with a selected muon (before the muon-jet overlap removal procedure) are neglected.

The described event selection is targeted to $t\bar{t}$ events with only one W boson decaying into an electron or muon or a leptonically decaying τ. While all-hadronic $t\bar{t}$ events are rejected by the lepton identification and isolation criteria, $t\bar{t}$ events where both W bosons decay into leptons can satisfy the event selection. ee, $e\mu$ and $\mu\mu$ events can have one of the two leptons failing the identification requirement of the geometrical and kinematic acceptance. Dilepton events with one τ lepton decaying into hadrons show a topology similar to lepton+jets decays since the τ is reconstructed as a jet.

Dilepton events usually display larger values for $E_{\mathrm{T}}^{\mathrm{miss}}$ and $m_{\mathrm{T}}(W)$ due to the presence of two energetic neutrinos in the final state; at the same time, these events tend to have a lower number of jets since no hadronic W boson decay is present. For a selection requiring at least three jets, the dilepton contamination varies between 15% and 20% of the total selected $t\bar{t}$ events; the number reduced to below 10% when at least four jets are present in the final state.

Combining lepton plus jets and dilepton $t\bar{t}$ events, the overall efficiency of the above selection including acceptance effects is of the order of 3-5 % when no specific requirement on the number of b-tagged jets is applied. The event selection has higher acceptance (20% to 40% higher) for the muon channel, partly because of the looser lepton identification requirements and secondly due to the looser selection on $E_{\mathrm{T}}^{\mathrm{miss}}$ and $m_{\mathrm{T}}(W)$ in certain analyses.

5.2 $t\bar{t}$ Monte Carlo samples

Other than theoretical calculations for the inclusive $t\bar{t}$ cross sections, the physics analyses rely also on kinematic properties of the process. To this end, Monte Carlo simulation programs are exploited since they are capable of generating events where the full correlation between the various kinematic quantities in the final state is retained. At the same time, the generated events can be evaluated through the full detector simulation.

The critical aspect is to achieve a good description of the $t\bar{t}$ final state over the largest possible portion of the phase space; in particular inclusive quantities are exploited for extracting the $t\bar{t}$ signal over the background and study the top quark properties, while extreme corners in phase space (very high p_{T} or large object multiplicity) are generally used in searches for new physics where the $t\bar{t}$ pair production represents the main background.

Event generators for $t\bar{t}$ events reach an accuracy beyond the leading order approximation. As already outlined in the first chapter, when discussing the factorisation theorem, the event generation process is divided into two steps: computation of the exact matrix element amplitude to a fixed order in perturbation theory and the subsequent interface of the results to a parton shower Monte Carlo for the shower evolution and the final hadronisation. In the case of ISR/FSR radiation, the matrix element calculations are generally well suited to describe high energy emissions or situations where the emission happens at very large angle with respect to the initial parton. The contribution from soft and collinear parton radiation or gluon splitting is better modelled with the parton shower approach, which approximates the effect of corrections to all orders in perturbation theory[2]. Normally the two steps are performed by different generators and attention must be paid to ensure that the full phase space is covered without overlaps (double counting).

Two main generator concepts are available. They differ in the approach they adopt for the hard scattering computation as well as in the interface with the parton shower.

- *NLO generators*: they contain the full matrix element scattering amplitude computed at NLO. This implies that virtual corrections and the first real parton emission are treated within the perturbation approach. The matching with the parton shower is performed by specifically including in the matrix element calculation a counter term for the part of the phase space covered by the parton shower program.

  NLO generators are designed to give the best possible description of inclusive quantities while they are expected to be less performing in case of multiple parton emission (high number of jets in the final state) since the radiation beyond the leading additional parton is handled by the parton shower program. Examples of NLO generators using such approach are MC@NLO [118] and POWHEG [119].

- *multi-leg LO generators*: they implement the LO matrix element of $t\bar{t}$ plus additional partons. The current computational limit reaches up to 5 extra partons in the final state. The advantage of this choice is a more accurate description of hard emissions, since additional partons (jets) are generated using the exact LO amplitude rather than the approximation performed by the parton shower. Apart from higher processing time, the downside of this approach is the missing of virtual correction for inclusive quantities and the fact that the LO matrix element emission has a larger dependence on the renormalisation and factorisation scales. The additional partons are generated with given kinematic cuts in

[2] This is generally referred to as 'resummation'

order to avoid divergencies in the calculation ($p_{\mathrm{T}} > p_{\mathrm{T}}^{\mathrm{min}}$, $\Delta R_{jj} > \Delta R_{\mathrm{min}}$[3]). The merging with the subsequent parton shower Monte Carlo corrections is performed through MLM or CKKW approaches [120, 121]. Both approaches ensure that in an event with n-partons produced by the matrix element calculation, the parton shower is forbidden to produce emissions resulting in one additional partons in the kinematic region already covered by the matrix element. Examples of such generators are ALPGEN [122], MADGRAPH [123] and ACERMC [124].

Several generators for production of $t\bar{t}$ events have been incorporated in the ATLAS framework. Table 5.3 contains the list of the generators for which events have been produced after full detector simulation. Additional information like the specific program used for parton showering as well as the PDF are also provided. For generators interfaced to HERWIG for the parton shower, underlying events were simulated with JIMMY [125][4]. The configuration of Herwig parameter is described in Ref. [126]. For generators interfaced with PYTHIA, specific parameters in the generator can be varied to modify the simulation of underlying events. 'Tunes' of these parameters are determined considering ATLAS measurements of global underlying event properties as well as jet shapes variables. The AMBT1 and AUET2B tunes are described in Ref. [127] and [128], while the PERUGIA tune is detailed in Ref. [129]. Only Monte Carlo generators used as nominal generator in at least one of the analyses described in this thesis work are included in the tables. Additional events produced with the MADGRAPH and ACERMC generators interfaced to PYTHIA are used for assessing the systematic uncertainties, as will be specified in the dedicated chapters.

generator	MC@NLO	POWHEG	ALPGEN
parton shower	HERWIG	HERWIG / PYTHIA 6	HERWIG / PYTHIA 6
PDF	CTEQ6.6 (2010) CT10 (2011/2012)	CTEQ6.6 (2010/2011) CT10 (2012)	CTEQ6.1 (HERWIG) CTEQ5L (PYTHIA)
PYTHIA UE TUNE		AMBT1 (2010) AUET2B (2011) PERUGIA2011C (2012)	PERUGIA2011C (2011)
used in analysis	2010/2011	2010/2011/2012	2011
nominal Monte Carlo	2010	2012 (POWHEG+PYTHIA)	2011 (ALPGEN+HERWIG)

Table 5.3: Main generators available in ATLAS for the generation of $t\bar{t}$ events and some of their parameters. For parameters that evolved in the different analyses, the specific year, corresponding to the ATLAS data sample, is indicated. The 'used in analysis' entry indicates for which of the analyses in this thesis the particular Monte Carlo sample was available and the last line indicates which sample was used for the 'nominal' description of $t\bar{t}$ events.

The choice of the 'nominal' generator stems from physics considerations related to the phase space under study, the capabilities of describing the data and the availability[5]. It will be motivated in each chapter describing the considered analyses. Comparison among various generators as well as specific variations of the generator parameters are usually considered as a source of systematic uncertainty. Events from these samples are processed through the detector simulation or are available only as 'truth samples' with no detector simulation.

[3]The expression represents a simplification since depending on the generator different variables/cutoff are used.

[4]This procedure is applied also to the background samples described in the following

[5]Not all the listed generator combinations were available in each year of the ATLAS data-taking with sufficient statistics.

For the purpose of the analyses considered in this thesis, only events where the $t\bar{t}$ pair decays in lepton+jets or dilepton final states have been considered. The events are normalised to the most precise calculation of the inclusive $t\bar{t}$ production cross section available at the time when the analysis was carried out. For analyses based on the 2010 and 2011 dataset, the approximate NNLO results are used. The analysis performed over the 2012 dataset rely on the full NNLO+NNLL prediction made available in the summer of 2013.

5.3 Backgrounds

The background processes to $t\bar{t}$ events in the lepton+jets final state can be divided in two categories: irreducible backgrounds and reducible backgrounds. While the former possess final state topologies similar to the signal one, the latter only pass the event selection due to instrumental effects like large $E_{\mathrm{T}}^{\mathrm{miss}}$ arising from mis-measured jets and jets faking leptons. Figure 5.1 summarises the cross sections of important physics processes at hadron colliders as a function of the collider centre of mass energy. QCD processes like jet and multijet production dominate all the other processes by several orders of magnitude. The cross section for W and Z boson production is of the order of 1-10 nb. The $t\bar{t}$ cross section is highlighted in red with the label σ_t. In the following an overview of the main sources of background to $t\bar{t}$ events will be given in order of their importance.

5.3.1 W boson plus additional jets

The production of a W boson in association with jets has a cross section which is two orders of magnitude higher than the $t\bar{t}$ one. The leptonic decay of the W boson produces an isolated lepton as well as a large $E_{\mathrm{T}}^{\mathrm{miss}}$ from the neutrino making this process the largest background for a $t\bar{t}$ measurement in the lepton+jets final state. The additional jets can either originate from light partons (u,d,s, gluon) or heavy flavour (HF) ones ($W + b\bar{b}$, $W + c\bar{c}$, $W + c$). In the case of $W + b\bar{b}$ especially, the final state topology is identical to the $t\bar{t}$ one making W+jets an irreducible background. Given that the production of heavy flavour partons represents only a few percent of the total cross section, the contribution of W+jets to the final background can be largely suppressed by explicitly requiring b-tagged jets in the final state. The W+jets represents the dominant contribution to the event selection when fewer than four jets in the final state are required.

MC description

Given that a large number of jets are required in the event selection, 'multi-leg' Monte Carlo generators have been employed to produce W+jets events. The Alpgen program with the CTEQ6L1 PDF set [130] was used to generate events with a W boson and up to five partons in the final state with exact leading order matrix element calculations. The 'MLM' approach was applied to remove the double-counting among the different parton[6] multiplicities when applying the parton shower. For the development of the parton shower and hadronisation, Alpgen was interfaced to Herwig for the 2010 and 2011 analyses, and to Pythia for the 2012 results[7]. For analyses explicitly relying on the presence of b-tagged jets in the final state,

[6] in this context 'parton' includes gluons, light and c quarks all considered massless. b-quarks are not included and their contribution arises from the parton shower

[7] The motivation for the change resides in the decision to uniform the hadronisation and fragmentation model among the nominal processes. At the same time, Pythia was found to have a more accurate description of the properties of hadron decays (branching ratios, lifetimes).

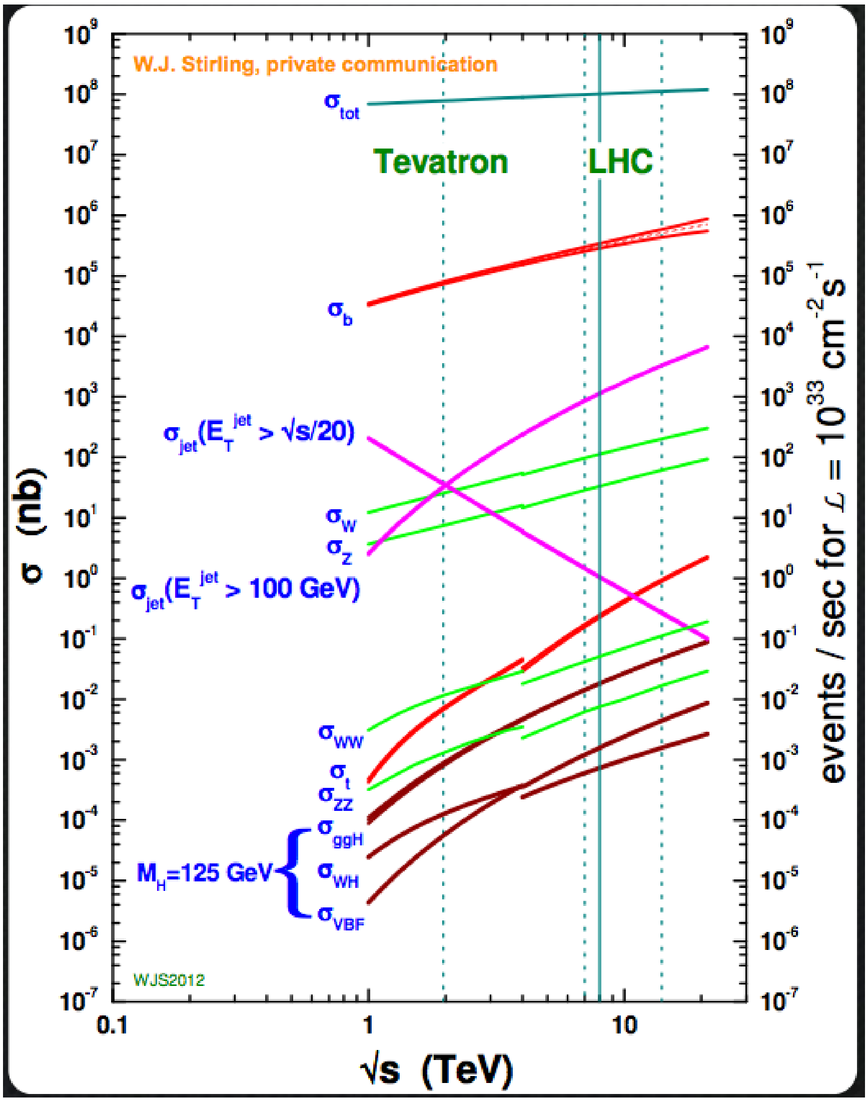

Figure 5.1: Cross sections of important physics processes at centre-of-mass energies reached at the Tevatron and the LHC. The vertical line on the left indicates the centre-of-mass energy at the Tevatron, while the dotted lines and the solid lines represent the LHC centre-of-mass energies of 7, 8 and 14 TeV.

specific samples with $W + c$, $W + c\bar{c}$ and $W + b\bar{b}$ events plus up to three additional partons were generated. These samples allow for a better description of the HF production due to the direct presence of the heavy flavour quark in the matrix element computation as well as the inclusion of the quark mass effects. In this configuration, additional heavy flavour partons can arise both from the direct hard scattering as well as from parton shower evolution of W+light partons events. In order to avoid double counting, a *heavy flavour overlap removal* procedure was put in place exploiting angular variable information. Events with a small ΔR (ΔR <0.4) between the additional heavy flavour partons are taken from the parton shower description while events with large ΔR value are taken from direct HF production in the hard scattering. The procedure takes advantage of the better description given by the parton shower in the limit of collinear radiation.

Generated events were normalised to the NNLO inclusive W boson production cross section calculated using FEWZ [131]. The normalisation is corrected with data-driven scale factors which also adjust the relative fraction of HF, as will be described in Section 5.5.

5.3.2 QCD multijet background

The main reducible background is represented by QCD multijet events where one of the jets is mis-identified as an isolated lepton. The origin of these so-called "fake" leptons is different according to the lepton flavour. In the case of muons, "fake" muons are primarily produced by semi-leptonic decays of b-hadrons within a jet and long lived weakly decaying states such as $\pi^{\pm}$ or K mesons. Electrons can be faked by semi-leptonic decays of b-hadrons as in the case of muons, but also by photon conversions and jets with high electromagnetic content (fragmenting into π^0).

Despite the high rejection power of the identification and isolation criteria, the QCD multijet cross section is several orders of magnitude above the $t\bar{t}$ production cross section. As a net result, events with mis-identified leptons still constitute a sizeable background and specific cuts are introduced in the event selection to keep it at a reasonable level. Other than the lepton selection, the main handle to reduce multijet background is the requirement on the $E_{\mathrm{T}}^{\mathrm{miss}}$ and $m_T(W)$: given that such events do not have a real source of sizeable $E_{\mathrm{T}}^{\mathrm{miss}}$ like events containing neutrinos from leptonic W decays, $E_{\mathrm{T}}^{\mathrm{miss}}$ can only arise from mis-measurement in jet momenta that creates transverse energy imbalance. The contribution of QCD multijet production is typically below 10%, decreasing with increasing requirement on the number of b-tagged jets since the QCD b-jet production represents only a few % of the total cross section.

The estimation of the QCD multijet background is obtained with data-driven techniques and it will be described in more detail in the following section.

5.3.3 Z boson plus additional jets

Events with a Z boson produced in association with additional jets can constitute another source of isolated leptons due to the $Z \to l^+l^-$ decay[8]. The process is normally referred to as Z/γ^*+jets (Z+jets will be used as abbreviation) since the contribution from the mediation by the two bosons leads to the identical final states. When the dilepton invariant mass is not far from the m_Z peak, the Z diagram prevails, while well below the Z boson resonance peak, the contribution from the virtual photon dominates and the process is known as Drell-Yan.

In order to enter the event selection one of the two lepton has to fall outside acceptance or fail the identification/isolation criteria. In the latter case, if the the lepton is an electron, it can be accounted for as an additional jet. Another important aspect of Z+jets production is that, as for QCD multijet production, no real sources of missing transverse energy are present in the event hence the requirement of large $E_{\mathrm{T}}^{\mathrm{miss}}$ largely reduces its contribution. As for the W+jets production, requiring a number of jets in the event to be b-tagged further contributes to reducing this background since only in a few % of the cases the additional partons produced with the bosons are b-quarks.

This process represents the third largest source of background when no requirement on the number of b-tagged jets is imposed. Its importance is higher in the electron channel due to the lower efficiency of the electron identification selection which increases the possibility of rejecting one of the two electrons from the Z decay. The lack of physics origin for $E_{\mathrm{T}}^{\mathrm{miss}}$ makes it also more sensitive to pile-up effects which generally worsens the energy resolution creating E_{T} imbalance. For this reason the contribution of Z+jets significantly increases in the 2012 analyses.

[8] l here can represent e,μ or leptonically-decaying τ

MC description

The generation of Z+jets events follows very closely the approach used for the W+jets events. The ALPGEN generator was employed interfaced to HERWIG for 2010 and 2011 and to PYTHIA for 2012. The main difference consists in the separation of the samples in two categories according to the invariant mass of the two leptons. For 10 GeV $< m_{ll} <$ 40 GeV, only samples with Z+additional partons were produced with no special treatment for the heavy flavour. In the range 40 GeV $< m_{ll} <$ 2000 GeV, separate samples for the production of $Z + \bar{b}$ and $Z + c\bar{c}$ were generated and an overlap removal procedure similar to the one described for the W+jets events was implemented.

As for the W+jets processes, events generated with ALPGEN are normalised to the inclusive cross section calculated at NNLO accuracy with FEWZ [131]. For the 2012 analysis a data-driven correction is applied as a function of the Z boson truth p_{T}. The correction has been derived from a dilepton control region where the two leptons are required to have an invariant mass within 10 GeV of m_{Z} and the dilepton system p_{T} is used as an estimate of the vector boson p_{T} [132].

5.3.4 Single top quark production

Single top quark production at hadron colliders is governed by electro-weak interactions. Three main production modes are possible. The t-channel presents the largest contribution and generally results in a top quark plus one additional jet in the final state. The production of a top quark in association with a W boson (Wt) is the second largest contribution and might lead to the final state closest to the $t\bar{t}$ one. The s-channel produces a top quark and an additional b-quark and has the smallest cross section of the three.

At the LHC, the single top quark production cross section is a factor of two smaller than that for $t\bar{t}$ production. The requirement of the large number of jets further reduces the single top quark contamination, given that single top topologies produce on average a lower number of jets. Its relative contribution to the full background increases when an explicit requirement on the number of b-tagged jets is imposed, given that at least one b-quark is present in the final state.

The importance of the single top quark process also resides in the fact that it affects the data-driven estimation of the W+jets background since its contribution is more important in lower jet multiplicities and that, together with the W+jets process, it exhibits a lepton charge asymmetry due to the production mechanism.

MC description

For the 2010 and 2011 analyses, events for the s and Wt channel were generated with the MC@NLO generator using the CTEQ6.6 PDF set. The 8 TeV sample was generated with POWHEG using the CT10 PDF set [133]. The generators used the 'diagram removal scheme' to avoid double counting between single top Wt and $t\bar{t}$ events [134].

The t-channel was simulated with the MC@NLO generator with the CTEQ6.6 PDF set in 2010 and with the ACERMC using the MRST LO** PDF set [135] for the years 2011 and 2012.

For the implementation of the parton shower MC@NLO was interfaced to HERWIG while POWHEG and ACERMC were interfaced to the PYTHIA 6 generator. The cross sections from the generators have been normalised to an approximate NNLO prediction as found in [136, 137].

5.3.5 Diboson production

Diboson production (WW, WZ, ZZ) represents a minor contribution to the total background to $t\bar{t}$ measurement, due to its small total cross section. Channels with at least one of the two bosons decaying leptonically are the significant ones. In particular, events with the leptonic decay of one W boson and hadronic decay of the other boson possess a topology similar to $t\bar{t}$ in terms of lepton and $E_{\mathrm{T}}^{\mathrm{miss}}$, but with a smaller number of jets. Additional jets in the event can be obtained through ISR and FSR effects.

MC description

For the 2010 and 2011 analyses, the diboson events are generated with the Herwig Monte Carlo generator using CTEQ6.1 PDF. For the 2012 $t\bar{t}H$ analysis, in order to achieve a better description of events with large jet multiplicity, diboson events with up to two additional partons from the matrix element are produced with the Alpgen generator interfaced with Herwig for the parton shower/hadronisation. Events were produced by requiring at least one charged lepton with $p_{\mathrm{T}} > 10$ GeV and $|\eta| < 2.8$, and their rate normalised to the NLO prediction obtained from MCFM [138] .

5.4 QCD multijet background estimation

Two main considerations required a data-driven estimation of the QCD multijet background; primarily the simulation of instrumental effects like large $E_{\mathrm{T}}^{\mathrm{miss}}$ from mis-measured jets and the mis-identification of jets as leptons are very difficult quantities to be modelled correctly by the Monte Carlo. In addition, given the large rejection factor obtained with the selected electron identification, it is very impractical to generate a large number of Monte Carlo events in order to have acceptable statistics after the final selection.

The data-driven techniques not only have to provide the correct normalisation for the multijet background but also an as precise as possible description of the kinematics of the events to be used in advanced shape analyses. Two methods were adopted for the measurement: the Matrix Method approach and the 'anti-electron' selection. The former is used in both the electron and the muon channel while the latter is only used in the electron channel, as its name suggests. Both methods rely on an alternative lepton selection in addition to the one used for the main event selection.

The uncertainties on the QCD multijet estimation are related to both the shape of the distribution as well as the total event normalisation. For the former, the comparison of different methods is employed to assess the shape systematics. The uncertainty on the normalisation is also estimated comparing different methods since the differences between two estimates are generally larger than the intrinsic precision of the individual methods. Given that the multijet background does not represent the main source of uncertainty for most of the analysis a conservative approach in the uncertainties on the normalisation can be applied, leading to uncertainties of the order of 40% to 100% depending on the specific selection.

5.4.1 Matrix method

The Matrix Method (MM) technique relies on the difference in the lepton identification efficiency between prompt isolated leptons from W boson decays and 'fake' leptons originating from semi-leptonic decays of b-hadrons within jets, photon conversions or simply mis-identified jets. Two lepton identification requirements are used: the 'tight' requirement corresponds to the full lepton identification criteria as used for the final analysis. The 'loose' lepton selection is obtained from the tight one by relaxing some of the identification requirements. Every lepton fulfilling the 'tight' selection is automatically a 'loose' lepton[9].

Two data samples are defined according to whether the lepton fulfils the 'loose' or 'tight' requirement. All the other kinematic requirements from the event selection previously described are applied to both data samples[10]. Due to the relaxation of the selection criteria, the 'loose' sample contains a higher fraction of fake leptons. The number of selected events in each sample (N_{loose} and N_{tight}) is the sum of events containing real and fake leptons:

$$N_{loose} = N_{loose}^{\text{real}} + N_{loose}^{\text{fake}} \tag{5.2}$$

$$N_{tight} = N_{tight}^{\text{real}} + N_{tight}^{\text{fake}} \tag{5.3}$$

The number of events passing the tight requirement can be expressed as a function of the events in the loose sample through the related 'efficiencies'.

$$N_{tight}^{\text{real}} = \epsilon^{\text{real}} \cdot N_{loose}^{\text{real}} \tag{5.4}$$

$$N_{tight}^{\text{fake}} = \epsilon^{\text{fake}} \cdot N_{loose}^{\text{fake}} \tag{5.5}$$

By replacing Eq. 5.5 in Eq. 5.3, an estimate for the number of events with fake leptons in the 'tight' selection:

$$N_{tight}^{\text{fake}} = \frac{\epsilon^{\text{fake}}}{\epsilon^{\text{real}} - \epsilon^{\text{fake}}} \cdot \left(\epsilon^{\text{real}} \cdot N_{loose} - N_{tight}\right) \tag{5.6}$$

is defined as a function of the number of events in the 'loose' and 'tight' data sample as well as the efficiency of the 'tight' selection with respect to the 'loose' one for real and fake leptons.

The last equation clearly demonstrates that the power of the method resides in the different efficiencies for the real and fake leptons. The 'loose' selection criteria are chosen to maximise the difference in efficiency taking into account the limit imposed by the selection applied at the trigger level[11] in order to be able to use the unprescaled single electron trigger.

The method not only allows to estimate the number of events from QCD multijet background but can be used to estimate the shape of the relevant kinematic distributions. The formula 5.6 can be generalised to produce a per-event weight w_i:

$$w_i = \frac{\epsilon^{\text{fake}}}{\epsilon^{\text{real}} - \epsilon^{\text{fake}}} \cdot \left(\epsilon^{\text{real}} \cdot isLoose(i) - isTight(i)\right) \tag{5.7}$$

to be applied to data events in the loose data sample. In the formula $isLoose(i)$ is 1 by definition while $isTight(i)$ indicates whether the selected lepton in the event also fulfils the 'tight' selection; events where the lepton fulfils the 'tight' lepton selection are given a negative weight. The sum of the weights automatically produces the normalisation expressed in Eq. 5.6.

The efficiencies ϵ^{real} and ϵ^{fake} are extracted from data in specific control regions designed to increase the fraction of real and fake leptons. For ϵ^{real} the tag & probe method is employed to extract a very pure sample of prompt isolated leptons from $Z \to ll$ decay. The obtained

[9] The usage of tight and loose in this context should not be confused with the different working point for the electron identification described in Chapter 3. For this purpose the notation 'loose' and 'tight' will indicate in the following the two selections used for the matrix method (also applicable to the muon channel), while *loose*, *medium* and *tight* will refer to the electron identification criteria.

[10] In the case of the 'loose' data sample, the overlap removal is performed using 'loose' leptons. This implies that events with 2 'loose' leptons but only 1 'tight' lepton are discarded while such events appear in the 'tight' datasample. The effect of neglecting such events has been found to be negligible.

[11] In order to control the bias introduced by the trigger selection, the offline selection is generally required to be tighter than the selection applied online.

efficiencies are then corrected taking into account the differences between Z and $t\bar{t}$ events. For the 2012 dataset, real efficiencies are also extracted from a high $E_{\mathrm{T}}^{\mathrm{miss}}$ region ($E_{\mathrm{T}}^{\mathrm{miss}} > 150$ GeV) dominated by W+jets and $t\bar{t}$ events; low jet multiplicity regions are used to keep orthogonality with final states used in $t\bar{t}$ analyses.

The ϵ^{fake} efficiencies are determined in control regions obtained by inverting the selection on the $E_{\mathrm{T}}^{\mathrm{miss}}$ and $m_{\mathrm{T}}(W)$. In the case of the muon channel, a control region is also defined by requiring a large impact parameter significance in order to increase the contribution from fake muons from semi-leptonic b-hadron decays. The contamination from events containing real electrons (W, Z and $t\bar{t}$) in the fakes control regions is subtracted using MC predictions.

ϵ^{real} and ϵ^{fake} depend on the lepton η and are parameterised as a function of this variable. With the increased amount of data, a more precise determination of the efficiencies has demonstrated their dependence on other kinematic variables. Instead of considering a full multi-dimensional efficiency parameterisation, the dependence on each variable has been factorised into 1-D corrections. For the *pretag* selection estimate, efficiencies are extracted from *pretag* control regions, while for the b-tagged sample, the efficiencies are obtained after the b-tag requirement or measured as a function of the number of jets in the event.

The uncertainties on the determination of the QCD multijet background with the Matrix Method technique are connected to the determination of the efficiencies and are obtained comparing different control regions and parameterisations. In the case of the electron channel, the contamination from real isolated electrons in the control region is more substantial than in the muon channel, reaching up to 50% in the 'tight' sample. A related uncertainty is assigned by varying the amount of Z, W and $t\bar{t}$ events.

electron channel

In the electron channel, the fake leptons from QCD multijet background have multiple origins; electrons from semileptonic decays of b-hadrons within jets, asymmetric photon conversions where one of the electrons takes away most of the photon energy, and jets mis-identified as electrons due to high electromagnetic components for instance due to fragmentation into π_0s. For this reason the choice of the 'loose' selection is particularly important in order not to alter the fake composition between 'loose' and 'tight' sample.

The 'loose' selection for the electrons consists in requiring the *medium* electron identification criteria and the conversion veto bit from the 'tight' electron identification. The isolation criteria are also relaxed with respect to the final selection used in $t\bar{t}$ analyses; in the 2011 analysis the cuts on the calorimeter and track isolation were relaxed to 6 GeV. For the 2012 analysis no isolation was required to define the 'loose' sample.

For the 2011 analyses, ϵ^{real} and ϵ^{fake} are parameterised as a function of electron η with an additional correction depending on the electron p_{T}. Fake efficiencies are determined in events containing at least one jet and $E_{\mathrm{T}}^{\mathrm{miss}} < 20$ GeV . Additional requirements on the lepton and on the number of b-tagged jets are used to explore the dependence of the efficiency on the QCD multijet composition[12].

For the 2012 analyses, ϵ^{real} is parameterised as a function of electron η with additional corrections depending on electron E_{T} and the minimum ΔR between the electron and the jets. Fake efficiencies were determined in a sample containing at least 2 jets and satisfying the condition $E_{\mathrm{T}}^{\mathrm{miss}} < 20$ GeV and $E_{\mathrm{T}}^{\mathrm{miss}} + m_{\mathrm{T}}(W) < 60$ GeV . This region was chosen as the best compromise between the available statistics and real electron contamination. ϵ^{fake} is parameterised as a function of electron η with additional corrections as a function of electron

[12]Since b-quarks are often produced in pairs in QCD multijet events, the requirement of at least one tagged jet in the event increases considerably the fraction of electrons originating from b-hadron decays.

E_{T} and ratio between the p_{T} and the ΔR to the lepton for the jet closest to the selected electron[13]. A separate efficiency determination was performed for events with 0 b-tagged jets and at least 1 b-tagged jet and in ranges of lepton p_{T} corresponding to the coverage of the two single electron triggers employed during the data-taking ($p_{\mathrm{T}} < 62$ GeV and $p_{\mathrm{T}} > 62$ GeV). The method was not used for analyses on 2010 data where the 'anti-electron' method was preferred.

Figure 5.2 shows the ϵ^{real} and ϵ^{fake} extracted from the 2011 dataset as a function of the electron η. Full descriptions of the efficiencies determination and related uncertainties can be found in Refs. [82] (2011) and [139] (2012).

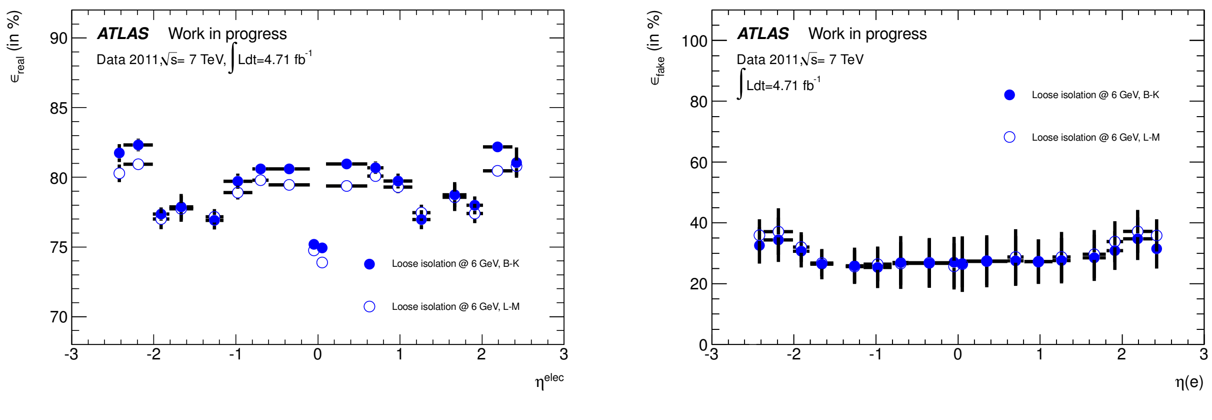

(a) **(b)**

Figure 5.2: ϵ^{real} (a) and ϵ^{fake} (b) for the electron channel matrix method measured in the 2011 datasample. Efficiencies are shown as a function of electron η. The error band includes both statistical and systematic uncertainties.

muon channel

In the muon channel the main origin of fake muons is represented by the semi-leptonic decay of b-hadrons inside jets. The definition of the 'loose' selection consists in dropping the isolation requirement from the standard 'tight' muon selection criteria. The parameterisation of the efficiency reflects the increase in the understanding of the background through the data-taking period:

- 2010: ϵ^{real} and ϵ^{fake} parameterised as a function of muon $|\eta|$
- 2011: ϵ^{real} and ϵ^{fake} parameterised as a function of muon $|\eta|$ with additional corrections depending on the leading jet p_{T} to account for the level of hadronic activity in the event.
- 2012: ϵ^{real} and ϵ^{fake} parameterised as a function of muon $|\eta|$ with additional corrections depending on the ratio of the p_{T} of the closest jet to the muon to its ΔR distance and the p_{T} of the muon (leading jet) in the case of real (fake) efficiencies. The efficiencies are computed separately for two different ranges of the lepton p_{T} corresponding to different ranges where the two different single lepton triggers are expected to provide the bulk of the events ($p_{\mathrm{T}} < 37$ GeV and $p_{\mathrm{T}} > 37$ GeV).

Two control regions have been used to extract ϵ^{fake} in order to get a handle on the systematic effect on the efficiency determination. The first one is defined by $E_{\mathrm{T}}^{\mathrm{miss}} < 20$ GeV and $E_{\mathrm{T}}^{\mathrm{miss}}$ +

[13] An alternative parameterisation considering electron η, leading jet p_{T} and the minimum ΔR between lepton and jets was considered as a systematic uncertainty.

$m_{\mathrm{T}}(W) < 60$ GeV while a second control region has no requirement on the $E_{\mathrm{T}}^{\mathrm{miss}}$ but selects muons with large impact parameter significance ($\sigma_{d_0}/d_0 > 5$) to increase the fraction of muons from semi-leptonic b-hadron decays. The latter region displays a much smaller contamination from real isolated muons from W or Z boson decays.

As an example, ϵ^{real} and ϵ^{fake} measured for the first half of 2011 dataset[14] as a function of the muon $|\eta|$ are reported in Figure 5.3. Full description of the efficiencies determination and related uncertainties can be found in Refs. [140] (2010), [82] (2011) and [139] (2012).

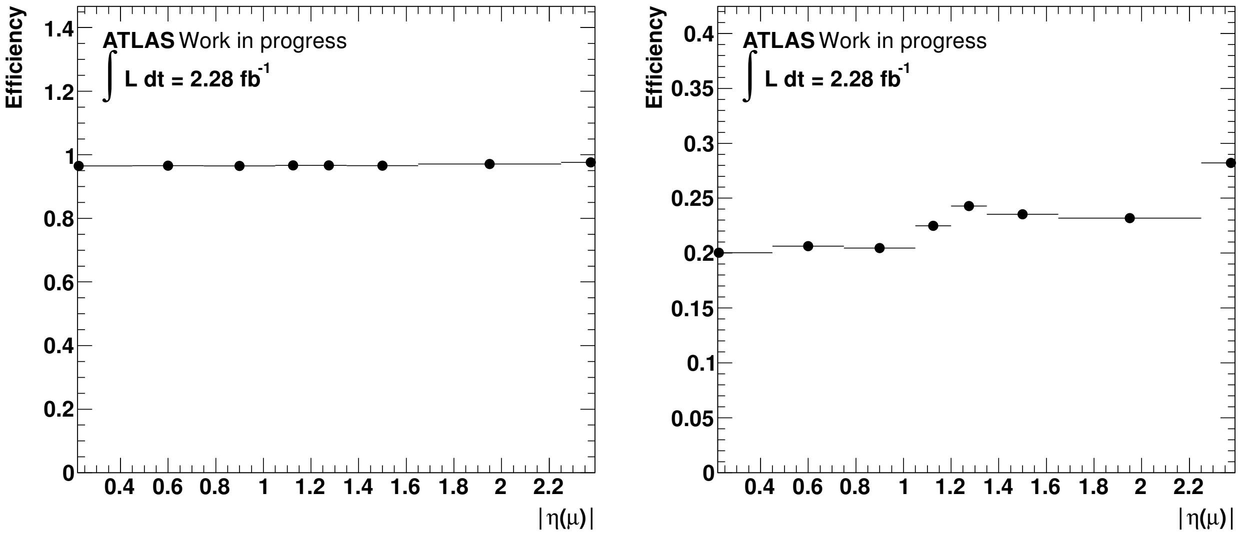

(a) (b)

Figure 5.3: ϵ^{real} (a) and ϵ^{fake} (b) for the muon channel matrix method measured on the first half of the 2011 datasample. Efficiencies are shown as a function of muon $|\eta|$.

5.4.2 'Anti' electron method

The 'anti' electron method relies on the assumption that the kinematic properties of QCD multijet events with fake electrons are reasonably independent of the electron identification variables. Some of the cuts used for the electron selection are then inverted ('anti-electron') to select a sample orthogonal to the signal region selection and dominated by fake electrons. Events are required to contain exactly one such 'anti-electron' and no other electron fulfilling the default selection criteria. The 'anti-electron' is considered as the selected electron in the event and all the other kinematic selections of the default signal region are applied. The collected events can be used to model any relevant kinematic distribution.

The critical aspect of the method is the choice of the criteria to be inverted in the electron selection. This results from a compromise between the amount of real electron contamination in the 'anti-electron' selection, the bias introduced by the specific selection on the fake lepton composition and the available statistics of the template. The latter in particular is also strongly influenced by the trigger used to collect events. If the inverted selection is still tighter than the selection in the single electron trigger, the full collected data statistics can be used to extract the 'anti-electron' events. During 2010, the presence of a trigger compatible with the *loose*

[14] Separate measurements have been performed corresponding to the different pileup conditions of the 2011 data-taking.

electron ID allowed to consider several variables for candidates in the cut reversal procedure. The selection for the 'anti-electron' required the electron to pass the *loose* electron identification and the isolation criteria but fail the *tight* identification requirement. An alternative definition used to assess the systematic uncertainties on the shape of the distribution required the electron to pass the *loose* identification criteria and the track-based requirement of the *tight* selection but fail the full *tight* identification criteria as well as the calorimeter or the track isolation requirements.

As discussed in Chapter 4, the selection at the trigger level was progressively made more restrictive during the various years of data-taking. This implied a reduced difference between the trigger and analysis selection which limits the choice of variables for the anti-electron selection to achieve the necessary reduction of real electrons. In 2011, dedicated pre-scaled triggers with looser selections were used to collect events for the 'anti-electron' method which required a looser selection than the *medium* electron ID. Given that the effective[15] prescale of the triggers was ~ 70, the collected 'anti-electron' sample was found to have generally low statistics in most of the phase space used by $t\bar{t}$ analyses. For this reason the Matrix Method approach was preferred.

The normalisation of events obtained with the 'anti-electron' method is performed with a sideband technique. The $E_{\mathrm{T}}^{\mathrm{miss}}$ distribution was found to be the most sensitive variable to discriminate QCD multijet background from events containing a real source of $E_{\mathrm{T}}^{\mathrm{miss}}$ like neutrinos from W boson decays. A template fit is performed in the low $E_{\mathrm{T}}^{\mathrm{miss}}$ region orthogonal to the signal region. The templates for the W/Z+jets, $t\bar{t}$ and single top events are obtained from Monte Carlo simulation. The fit returns a normalisation factor for the QCD multijet template which is then extrapolated into the high-$E_{\mathrm{T}}^{\mathrm{miss}}$ signal region.

The dependence on Monte Carlo predictions in the 'anti-electron' method is related to the template fit procedure used to normalise the multijet template in the sideband region; no real electron contamination is subtracted from the template and no parameterisation of the electron selection is performed. For this reason, the method offers fewer tuneable handles to correct for the any data/Monte Carlo mis-modelling than the Matrix Method approach. Additional information on the implementation of the 'anti-electron' method can be found in Ref. [140].

5.4.3 Results / Validation

Since the contribution of the QCD multijet background to the total yields after event selection is not dominant, the correctness of the background estimation has been validated in specific 'multijet enriched' regions. The fraction of multijet background is increased by relaxing/inverting the selection on the $E_{\mathrm{T}}^{\mathrm{miss}}$ and $m_{\mathrm{T}}(W)$ variables while keeping the same topology (number of jets) of the signal region. The precise definition of the validation region stems from a compromise between high multijet fraction and available data statistics; given the good rejection performance of the lepton identification and isolation requirements, it is difficult to enhance the multijet fraction above 40% in events with at least 4 jets, in particular after the b-tag selection. For this reason some of the presented multijet-enriched selections partly overlap with the signal regions or the regions used for the matrix methods efficiency determinations.

Figures 5.4 and 5.5 show examples of data/Monte Carlo comparisons in 'multijet enriched' validation regions. The uncertainty band contains the Monte Carlo statistical error and the multijet background normalisation uncertainty. A conservative normalisation uncertainty of 50% has been adopted for analyses in all the years; such a large value covers both the differences in the comparison between different methods and the variation observed within each method (for

[15] averaged over triggers and period

instance dependence on the control region used to extract the efficiencies). Shape uncertainties will be discussed on an analysis-by-analysis basis.

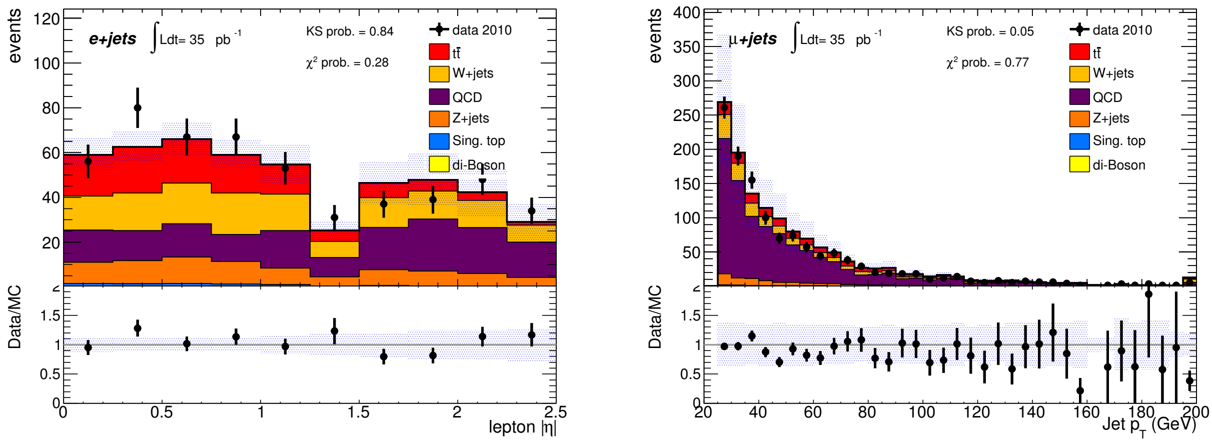

(a) **(b)**

Figure 5.4: Data/Monte Carlo comparison for 'multijet enriched' regions with at least four jets in the electron (a) and muon (b) channel for the 2010 dataset. The electron $|\eta|$ is shown in the electron channel after requiring $E_{\mathrm{T}}^{\mathrm{miss}} < 60$GeV and $m_{\mathrm{T}}(W) > 20$ GeV (a); the p_{T} of all the jets is shown in the muon channel after inverting the triangular cut (b). The uncertainty band contains the Monte Carlo statistical uncertainty as well as the multijet normalisation.

For the 2010 analysis, the $|\eta|$ distribution is shown in the electron channel after requiring $E_{\mathrm{T}}^{\mathrm{miss}} < 60$GeV and $m_{\mathrm{T}}(W) > 20$ GeV; the p_{T} distribution of all the jets is shown in the muon channel after inverting the triangular cut. Only events with at least 4 jets are considered.

For the 2012 dataset, Figure 5.5 (top) displays the $m_{\mathrm{T}}(W)$ distribution for the electron and muon channel in events with at least 4 jets. The multijet contribution has been increased up to 15-25 % by requiring 0 b-tagged jets and $E_{\mathrm{T}}^{\mathrm{miss}} < 50$ GeV, but a larger fraction is visible in low $m_{\mathrm{T}}(W)$ regions. The jet multiplicity distribution for events with at least 1 b-tagged jet is shown in Figure 5.5 (bottom) for events satisfying $E_{\mathrm{T}}^{\mathrm{miss}} < 50$ GeV and $m_{\mathrm{T}}(W) < 30$ GeV; this tight selection allows for a multijet fraction of 10-20% despite the b-tag requirement

A good agreement between data and predictions is observed in the 'multijet-enriched' regions within the assumed normalisation uncertainties on the multijet estimation. The contribution of the multijet background to each analysis after the final selection will be detailed in the relevant chapters.

5.5 W+jets background estimation

In the analyses presented in this thesis, the shape of the W+jets background is obtained from Monte Carlo simulation. At the same time the normalisation is extracted from a data-driven technique, since the theoretical prediction of the production of a W boson in association with a large number of jets suffers from large theoretical uncertainties. After requiring at least one b-tagged jet, the contribution of the W+jets process is intimately linked to the relative fraction of W+heavy flavours. The data-driven estimate also aims at correcting the fractions of $W+b\bar{b}$, $W+c\bar{c}$, $W+c$ with respect to the values predicted by the Monte Carlo simulation, which are also affected by large theoretical uncertainties.

At a p-p collider, there is an overall charge asymmetry in the production of W bosons due to relative differences in the quark and anti-quark parton density functions. Positively charged

W-bosons can be produced from processes involving a $u\bar{d}$ pair while negatively charged W bosons arise from processes involving a $\bar{u}d$ pair. While PDF distributions for $\bar{u}$ and $\bar{d}$ in a proton are rather similar, there is a difference in the u and d PDF distribution due to the impact of valence quarks; this generates the charge asymmetry.

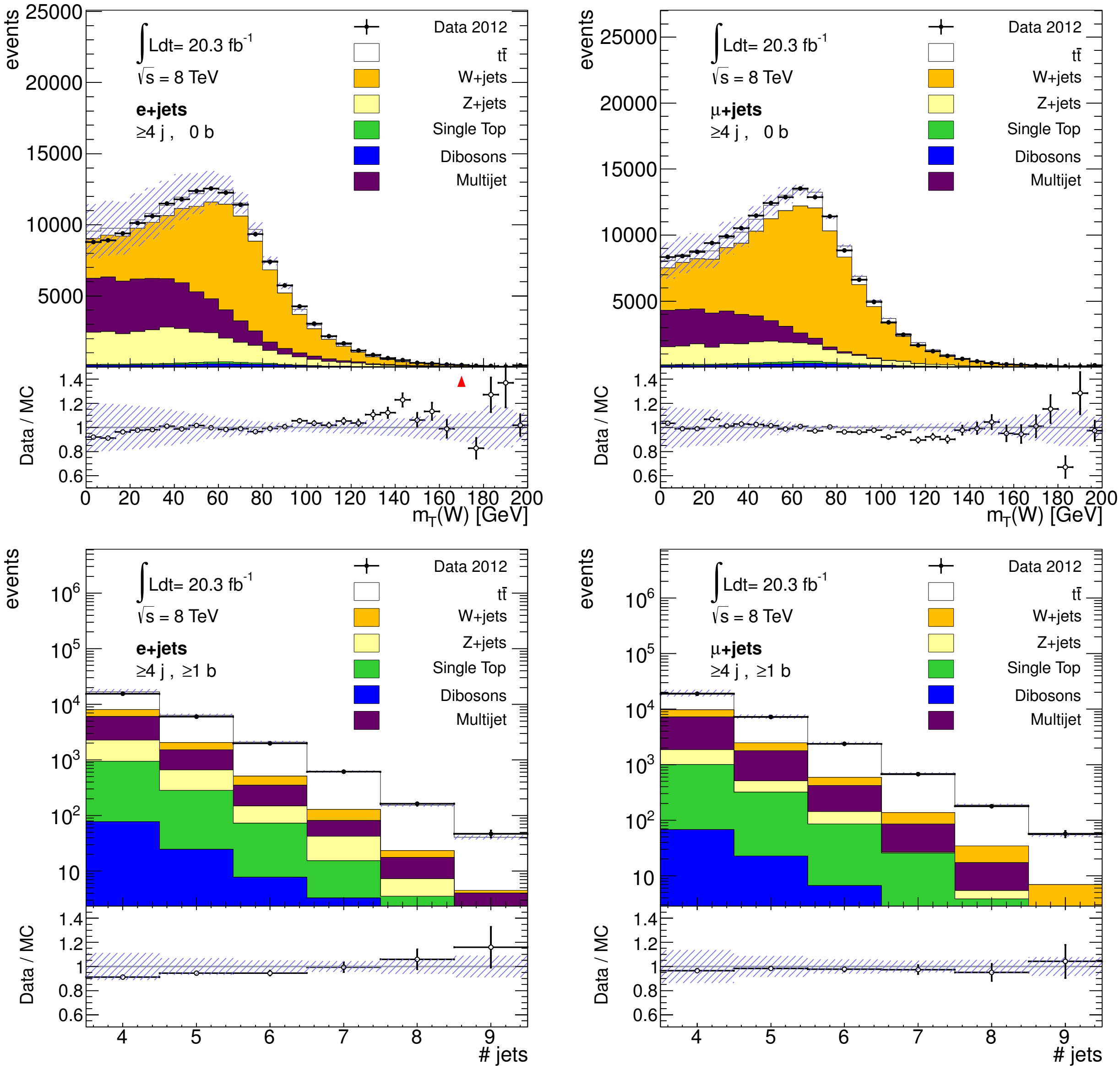

Figure 5.5: Data/Monte Carlo comparison for a 'multijet enriched' selection for events with in the at least four jets in the 2012 dataset. (top) m_{T} distribution for events with no b-tagged jets and $E_{\mathrm{T}}^{\mathrm{miss}} < 50$ GeV. (bottom) jet multiplicity distribution in events with at least 1 b-tagged jet and satisfying $E_{\mathrm{T}}^{\mathrm{miss}} < 50$ GeV and $m_{\mathrm{T}}(W) < 30$ GeV. Electron (left) and muon (right) channels are shown separately. The uncertainty band contains the Monte Carlo statistical uncertainty as well as the multijet normalisation uncertainty.

The ratio of the cross sections $r = \sigma(pp \to W^+)/\sigma(pp \to W^-)$ depends mainly on the ratio of PDFs and is theoretically relatively well understood [141] to a few % accuracy in the LHC energy regime.

This information can thus be used to estimate the amount of W+jets events after the final selection by comparing events with a positive or a negative selected lepton. A relatively clean sample of W+jets can be isolated given that the other major contributors to the final yield ($t\bar{t}$

pair production, Z+jets, QCD multijet background) do not display a lepton charge asymmetry. This approach is well suited for the *pretag* selection for all jet multiplicities. However, when estimating the W+jets contribution after a b-tagged selection (≥ 1 b-tagged jet), the selected approach is to estimate from data the heavy flavour fractions as well as the W+jets yields in the 2-jets bin and then extrapolate to higher jet multiplicities using Monte Carlo simulation and assign related uncertainties. The reason for this choice is the requirement to reduce the large dominance of $t\bar{t}$ events in b-tagged selections starting from 3 jets.

The rest of the section illustrates the two step approach adopted for the W+jets estimation. The procedure was mainly used for the analyses performed over 2011 data; for the 2012 data, a less refined method is adopted since the analysis is less sensitive to the W+jets contribution. For the analysis using the 2010 dataset, a simultaneous determination of the $t\bar{t}$ and W+jets normalisation was performed.

5.5.1 W+jets normalisation

The W+jets background after the *pretag* selection can be extracted through the formula:

$$N_{W^+} + N_{W^-} = \frac{(N^{\rm MC}_{W^+} + N^{\rm MC}_{W^-})}{(N^{\rm MC}_{W^+} - N^{\rm MC}_{W^-})}(D^+ - D^-) = \left(\frac{r_{\rm MC}+1}{r_{\rm MC}-1}\right)(D^+ - D^-) \tag{5.8}$$

where $D^{+(-)}$ represents then number of data events with a positively (negatively) charged lepton. The formula simply consists in applying the ratio $(W^+{+}W^-)/(W^+{-}W^-)$ to the charge-subtracted estimation from data. The assumption $(N^{\rm data}_{W^+} - N^{\rm data}_{W^-}) \sim D^+ - D^-$ is well motivated since most of the other processes are charge symmetric and their contributions thus cancel in the difference. The only exception is represented by single top quark t-channel production whose contribution is of the order of a few %; it is subtracted based on expectations from the Monte Carlo.

Scale factors are computed as the ratio of the outcome of Eq. 5.8 to the prediction from Monte Carlo. The SFs are computed for different values of the jet multiplicity and separately for the electron and muon channel in order to account for the dependence of r_{MC} on the number of jets and the difference in the event selection between the electron and muon channel which introduces kinematic effects. For the 2011 analyses, the obtained SFs are compatible with 1 with an uncertainty ranging from 10% to 15% for the 3-jets, 4-jets and $\geq$5-jets selection [82].

A mixed data-driven/Monte Carlo approach was then used to estimate the fraction of W+jets events having at least one b-tagged jet. The amount of W+jets in the *n-th* jet bin is given by the formula:

$$W^n_{\geq 1\rm tag} = W^n_{\rm pretag} \cdot f^{2j}_{\rm tag} \cdot f^{2\to n}_{\rm tag} \tag{5.9}$$

where $f^{2j}_{\rm tag}$ represents the 'tagging' probability for W+jets events in the 2-jet bin, while $f^{2\to n}_{\rm tag}$ represents an extrapolation factor from the 2-jet selection to the n-th jet selection. $f^{2j}_{\rm tag}$ is extracted from data by comparing the number of events in the *pretag* and b-tagged selection after subtracting the contribution from the other non-W+jets processes, the largest of them being represented by the QCD multijet background. The advantage of using the 2-jet region is to minimise the contribution of $t\bar{t}$ events. $f^{2\to n}_{\rm tag}$ is the ratio of the W+jets tagging probabilities in two regions having different requirements on the numbers of jets and it is obtained from Monte Carlo predictions. Its definition as a ratio helps in strongly reducing the impact of experimental uncertainties like the ones related to b-tagging and the theoretical ones related to the flavour composition.

Due to the additional uncertainties from the extrapolation as well as the dependency on the b-tagging, the uncertainties on the W+jets normalisation SFs in the b-tagged selections are larger than the *pretag* ones and range between 15% and 20%. Additionally, the W+jets normalisation SF depends on the knowledge of the heavy flavour composition since the different heavy flavour production modes ($W+b\bar{b}$, $W+c\bar{c}$, W+c) display different levels of lepton charge asymmetry (in particular W+c); the interplay between these two components will be better outlined in the next subsection.

For selections requiring two or more b-tagged jets, the same data/Monte Carlo normalisation factors obtained for the ≥ 1 b-tagged jet selection are used. In this case, the contribution from W+jets represents only a few percent of the total $t\bar{t}$ yields and the uncertainties on the W+jets normalisation generally have a negligible impact on the analysis.

5.5.2 W+jets flavour composition

The data-driven procedure for the normalisation of the W+jets background also includes the determination of the heavy flavour fractions. The relative amounts of W+$b\bar{b}$, W+$c\bar{c}$, W+c and W+light jets (F_{bb}, F_{cc}, F_c, F_{light} in the following), not only influence the probability of a W+jets event to fulfil the b-tagged jet requirement of the event selection but they might also affect the shapes of relevant distributions. The amount of W+jets after requiring at least 1 b-tagged jet for events with i selected jets can be expressed as:

$$N_i^{\mathrm{W,tag}} = N_i^{\mathrm{W,pretag}} \left(F_{bb,i}P_{bb,i} + F_{cc,i}P_{cc,i} + F_{c,i}P_{c,i} + F_{\mathrm{light,i}}P_{\mathrm{light,i}}\right) \tag{5.10}$$

where the $P_{xx,i}$ represent the b-tagging probability of each subprocess depending on the b-tagging performances and on the event kinematics. Their values are taken from the Monte Carlo simulation. For each jet bin separately, the flavour fractions $F_{xx,i}$ add up to unity:

$$F_{bb,i} + F_{cc,i} + F_{c,i} + F_{\mathrm{light,i}} = 1 \tag{5.11}$$

The flavour fractions obtained from data are expressed in terms of the Monte Carlo fractions and data-driven scale factors (K_{xx}) such that: $F_{xx}^{data} = K_{xx} \cdot F_{xx}^{MC}$.

Given that the Feynman diagrams for the production of W+$b\bar{b}$ and W+$c\bar{c}$ are similar, the same scale factor is adopted for the two processes. The three scale factors ($K_{bb,i}$,$K_{c,i}$,$K_{light,i}$) are extracted from a system of three equations: Eq. 5.10 considered separately for positively and negatively lepton charge and Eq. 5.11. This procedure is known as the 'tag counting' method [82]. The number of W+jets events is extracted from data by subtracting the other non-W+jets backgrounds. QCD multijet events are estimated with the data-driven methods described in the previous section, while for Z+jets, single top and $t\bar{t}$, Monte Carlo predictions are used. The measurement is performed in the 2-jet bin to increase the purity of W+jets events.

An interplay is present between the W+jets normalisation described in the previous paragraph and the determination of the HF fractions since the different W+jets processes display different degrees of charge asymmetry and the normalisation SF is expressed as a correction factor on the Monte Carlo prediction that already takes into account the best estimate for the F_{xx}. Therefore an iterative procedure is adopted: the number of events in the *pretag* selection of Eq. 5.10 is already normalised to data using the charge asymmetry method explained above. The fractions F_{bb}, F_c and F_{light} are determined and correction factors are computed with respect to the Monte Carlo values. With these fractions, the overall normalisation is re-determined and this procedure is iterated until no significant change is observed.

The results obtained with the 2-jet selection are extrapolated to the other jet multiplicity bins by re-evaluating Eq. 5.11 in each jet multiplicity using K_{xx} extracted from the 2-jets region and the F_{xx}^{MC} for that specific jet multiplicity bin from the Monte Carlo predictions. The heavy flavour scale factors (K_{xx}) are renormalised to ensure that the left terms in Eq. 5.11 still sum up to unity.

As for the W+jets normalisation scale factors, the heavy flavour correction factors are extracted separately for the electron and muon channel. Given that the method relies on the Monte Carlo predictions for both the *pretag* and the b-tagged selection, the largest uncertainties are due to the tagging efficiency differences between data and Monte Carlo and the jet energy scale. For selections requiring a number of jets different from 2, additional uncertainties concerning the extrapolation of the heavy flavour fractions are considered. They are extracted considering several variations of the parameters governing the hard scale and the matching algorithm in W+jets events simulated with ALPGEN.

The normalisation condition correlates the uncertainties on the various K_{xx}. For each systematic variation on the heavy flavour scale factors, the variations are corrected in a way to preserve the total W+jets *pretag* normalisation. The uncertainties are grouped in 4 variations:

- *'light'* versus *'HF'* variations: the fractions of $W+b\bar{b}$, $W+c\bar{c}$, $W+c$ are varied in a correlated way and uncorrelated to W+light fraction.
- *'bb/cc* versus *'c'* variations: the fractions of $W+b\bar{b}$, $W+c\bar{c}$ are varied in a correlated way and anti-correlated to the $W+c$ fraction. The W+light fraction stays unchanged.
- extrapolation uncertainties on K_{bb}.
- extrapolation uncertainties on K_c.

5.5.3 W+jets estimation for the 2012 analysis

As will be highlighted in Chapter 8, the analysis searching for the $t\bar{t}H$ process requires at least 4 jets, two of which being b-tagged jets in the final state. After this selection, the W+jets yields are dominated by W+HF, and, at the same time, its contribution to the final events selection is of the order of a few percent. The knowledge of the W+jets background is not a critical aspect for the sensitivity of the analysis and large conservative uncertainties can be applied.

For this reason a less refined approach has been applied to the W+jets normalisation. No specific data-driven normalisation or determination of the heavy flavour fraction is performed. The $W + HF$ component has been increased by 30% following the data/MC comparison in Z+HF enriched events described in Ref. [132].

It has been verified that the 'modified' Monte Carlo estimates are consistent with data in W+jets-enriched regions obtained with the 'charge' asymmetry approach. Additional data-driven corrections to the shape of the W boson p_{T} distribution have been applied. Dilepton events have been used to obtain a high purity sample of Z+jets events. The Z boson p_{T} has been estimated from the transverse momentum of the lepton pair in events containing at least 2 jets; it has been found [132] that ALPGEN has a harder spectrum for the Z boson p_{T} with respect to data. The correction, applied to the W+jets events[16], is found to improve significantly the description of the lepton p_{T}, jets p_{T} and $E_{\mathrm{T}}^{\mathrm{miss}}$ in the events.

Figure 5.6 shows the comparison between data and Monte Carlo predictions for events with at least 4 jets and no b-tagged jets in the electron or the muon channel.

The last requirement allows to suppress the $t\bar{t}$ contamination and make the W+jets the dominant process; the p_{T} of the selected lepton is shown together with the p_{T} of the third leading jet in the events. The charge asymmetry approach can be used to further increase the

[16] Truth information is used to define the p_{T} of the W boson and no detector level information due to $E_{\mathrm{T}}^{\mathrm{miss}}$ resolution.

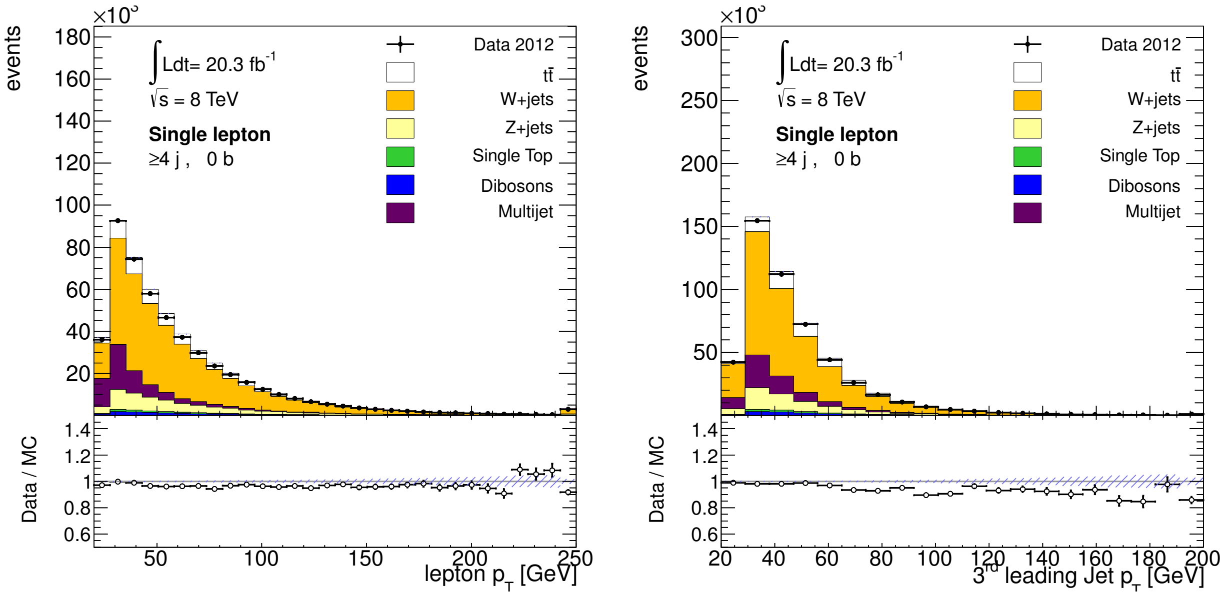

(a) (b)

Figure 5.6: Data/Monte Carlo comparison for events containing at least 4 jets and no b-tagged jets in the electron or muon channel combined. The lepton p_{T} (a) and the p_{T} of the third leading jet (b) are shown. The uncertainty band contains only the Monte Carlo statistical uncertainty contribution.

purity of W+jets. Figure 5.7 (top) shows the data/MC comparison for the distributions of events with a positively charged lepton minus the corresponding distribution for events with a negatively charged one. $m_{\mathrm{T}}(W)$ and the jet multiplicity are shown for events with at least 4 jets in the electron or muon channel. In the charge subtraction technique, the contributions from $t\bar{t}$, Z+jets and multijets backgrounds cancel since they are charge symmetric. The same distributions are shown after requiring at least 2 b-tagged jets in Figure 5.7 (bottom).

The plots confirm that the estimate of the W+jets contribution from Monte Carlo is in agreement with data within the available statistics for the charge asymmetry method. Additional information on the considered systematic uncertainties will be given in Chapter 10.

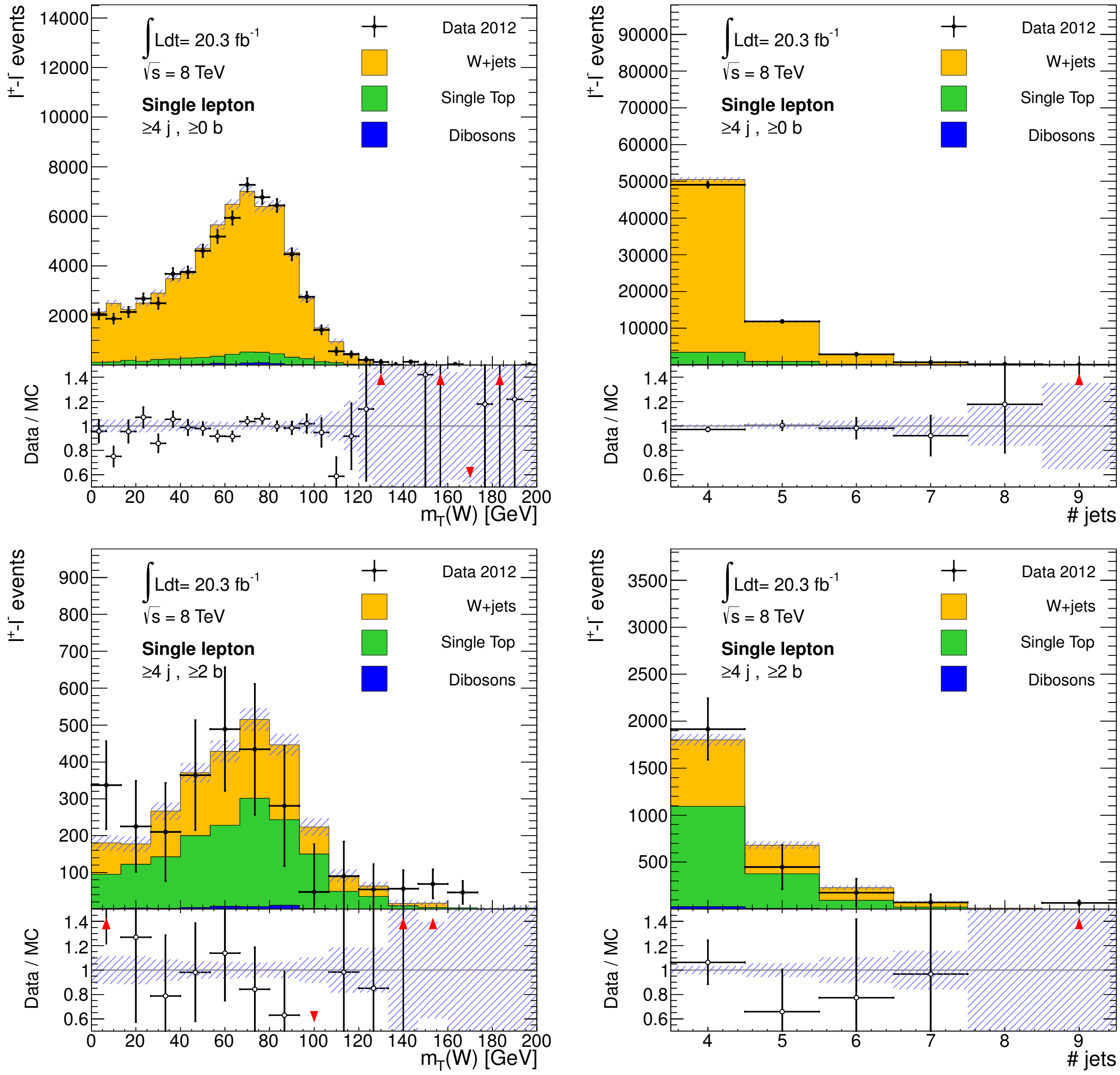

Figure 5.7: Data/Monte Carlo comparison for positively charged minus negatively charged lepton events. (left) $m_{\mathrm{T}}(W)$ and (right) jet multiplicity are shown for events with at least four jets (top) and events with at least 4 jets, at least two of which are b-tagged (bottom). Electron and muon channels are combined and the uncertainty band contains only the Monte Carlo statistical uncertainty. Other samples are not shown since their expectation is compatible with 0.

Chapter 6

Inclusive $t\bar{t}$ cross section measurement with early ATLAS data

One of the important milestones in the initial ATLAS physics programme was the measurement of the top pair production cross section. Other than serving as a benchmark for detector performance, the analysis represented a first step in the direction of an improved understanding of QCD in the new energy regime accessible at the LHC.

This chapter describes the measurement of the inclusive $t\bar{t}$ cross section in the lepton+jets final state, based on 35 pb^{-1} collected by the ATLAS detector in 2010. The initial part of the chapter outlines the choice of the particular analysis method. The central part contains the performance of the method from Monte Carlo studies. Finally, the result of the measurement will be presented together with a brief overview of the ATLAS measurements of the $t\bar{t}$ cross section using different techniques and larger data samples.

6.1 Analysis strategy

The 2010 run represented the first possibility to study the top quark in an energy regime much higher than the previous measurement at the Tevatron. Based on a sub-set of the 2010 data sample (2.9 pb^{-1}), an initial analysis aiming at first evidence for $t\bar{t}$ production was performed at ATLAS using simple, but robust cut & count techniques [142].

The full 2010 dataset contained ten times more data than the very first analysis. This allowed to use more refined approaches like *template fitting*; the data distribution of a discriminating variable was fitted with templates obtained from Monte Carlo simulation for the signal and each of the backgrounds. The number of signal events and the number of events from one or more of the dominant background processes can be determined simultaneously. The advantages of this technique originate partly from the fact that the separation between signal and background is achieved by using the variable shape information. Secondarily, no absolute predictions for the number of events for the main background is required thus reducing the systematic uncertainty on the measurement compared to a cut & count one.

Several approaches to the *template fitting* technique have been followed for the 2010 dataset. The particular solutions adopted for the analysis described in this chapter were dictated by the need to keep the analysis simple and robust, given the early stage of the detector understanding and the available data statistics. A single kinematic variable was used in the template fits in order to reduce the complexity of the analysis. Despite the potential gain in separation obtained with a multivariate approach, the relatively small amount of data did not allow a complete validation of the input variables and their correlations.

The general selection adopted for the identification of $t\bar{t}$ events has been outlined in the previous chapter. The analysis was carried out selecting events with ≥ 4 jets since this reflects the corresponding lepton plus jets $t\bar{t}$ decay topology.

The electron and muon channels were considered separately to check the consistency and then combined to increase the sensitivity. No additional b-tagging information for the jets was used. Identifying one or more jets as coming from a b-quark allowed to increase the signal purity but came at the expense of a lower signal efficiency and additional sources of systematic uncertainties.

Table 6.1 shows the expected numbers of events for $t\bar{t}$ and the background components after the final selection for a luminosity of 35 pb^{-1}. The MC@NLO generator was used to produce the nominal $t\bar{t}$ template. For samples derived from Monte Carlo simulation, the uncertainty in the table contains the detector related uncertainties as well as the uncertainties from the theoretical cross section calculations. The QCD multijet background was obtained with data-driven estimates as detailed in the previous chapter and the uncertainty in the table reflects the precision of the method.

	$e+\geq$ 4jets	$\mu+\geq$ 4jets
$t\bar{t}$	194 $\pm$ 27	270 $\pm$ 40
W+jets	170 $\pm$ 110	300 $\pm$ 190
QCD Multijet	22 $\pm$ 11	51 $\pm$ 25
Z+jets	18 $\pm$ 11	25 $\pm$ 16
Single-top	11 $\pm$ 3	15 $\pm$ 4
Di-bosons	3 $\pm$ 1	4 $\pm$ 1
Total background	230 $\pm$ 110	390 $\pm$ 190
Total expected	420 $\pm$ 110	660 $\pm$ 200
Observed	400	653

Table 6.1: Number of events for data, signal and background processes in the electron, muon channels. Monte Carlo predictions are scaled to an integrated luminosity of 35pb^{-1}. All the statistical and systematic uncertainties have been considered in the error calculation. The W+jets normalisation uncertainties follow the prescription used for the first ATLAS $t\bar{t}$ cross section publication [142].

The table displays a good agreement between data and the sum of expected Monte Carlo events. Figures 6.1 and 6.2 show the basic kinematic variables after the final selection with the same Monte Carlo normalisation used for the table. The agreement between data and the prediction was quantified by a Kolmogorov-Smirnov (KS) and a χ^2 test [143] [144]. The former took into account only the shape compatibility while the latter also tested the normalisation. In both cases only data and Monte Carlo statistics of the template were considered in the calculation; this choice represented a conservative approach that avoids to make any assumption on the bin-by-bin correlation of systematic uncertainties. A good agreement is achieved in the description of the event kinematics.

As can be seen from the table, a $\sim$ 50% purity for the $t\bar{t}$ process was obtained after the final events selection with the W+jets representing by far the largest background contribution. For this reason, the fitting procedure was particularly designed to simultaneously determine the number of W+jets and $t\bar{t}$ events in order to avoid to rely on the large Monte Carlo uncertainties for the normalisation.

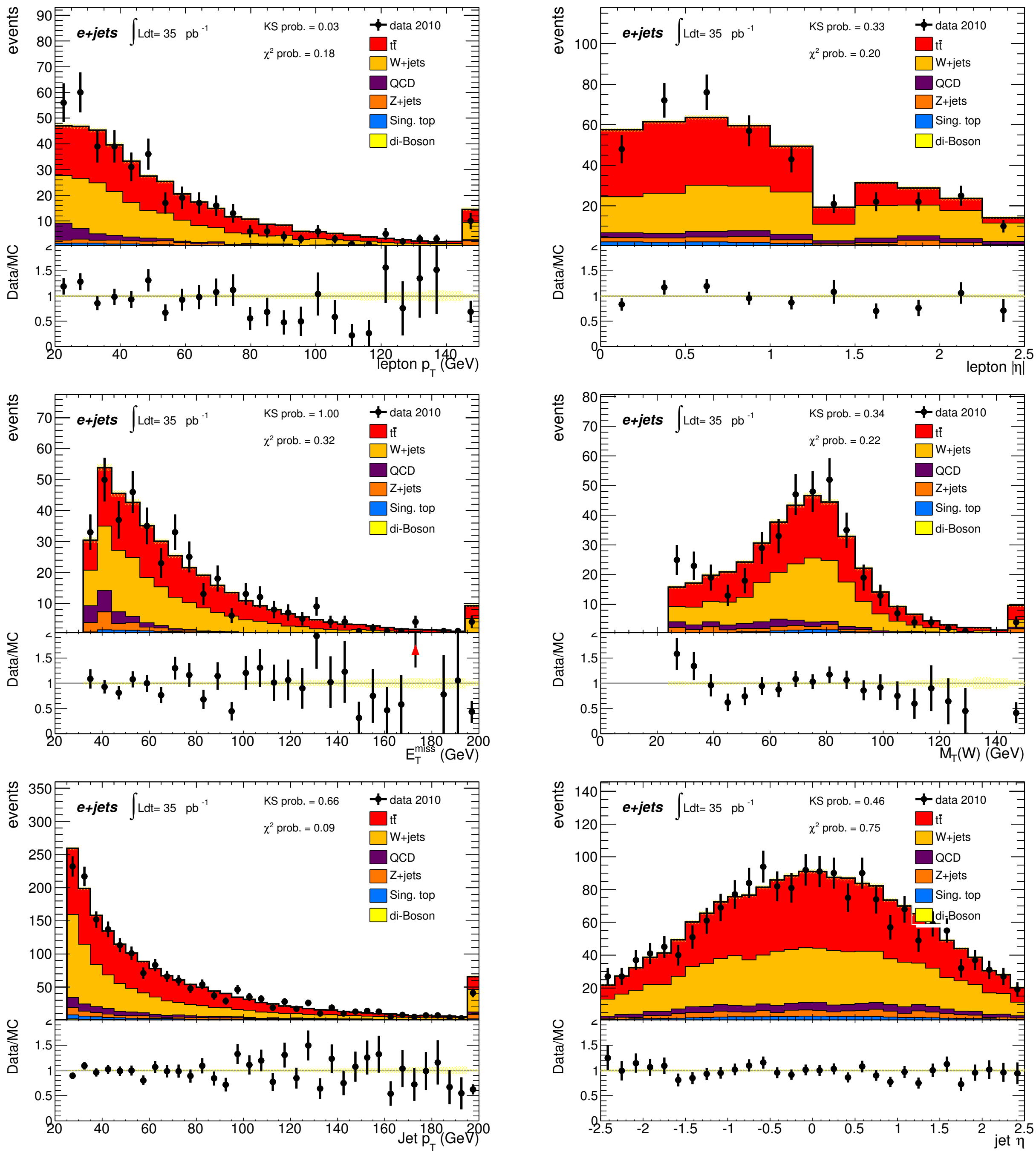

Figure 6.1: Data/ Monte Carlo comparison for basic kinematic variables after the full selection in the electron channel. The uncertainty band takes into account the finite statistics of the Monte Carlo samples. Variables shown are: lepton p_{T}, lepton $|\eta|$, $E_{\mathrm{T}}^{\mathrm{miss}}$, $m_T(W)$, jet p_{T}, jet η. For the last two variables, the plot contain one entry for each jet in the event.

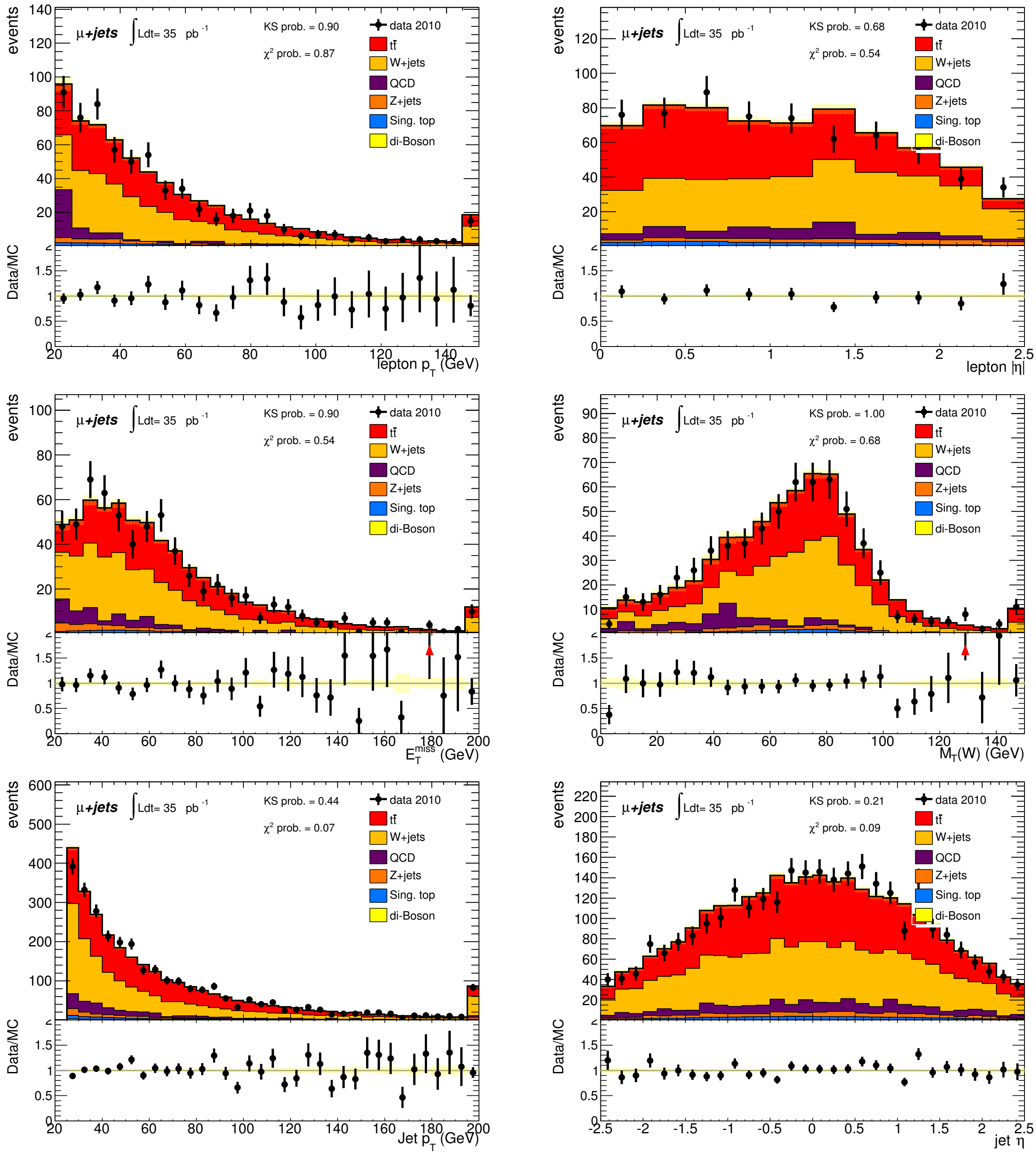

Figure 6.2: Data/ Monte Carlo comparison for basic kinematic variables after the full selection in the muon channel. The uncertainty band only takes into account the finite statistics of the Monte Carlo samples. Variables shown are: lepton p_{T}, lepton $|\eta|$, $E_{\mathrm{T}}^{\mathrm{miss}}$, $m_T(W)$, jet p_{T}, jet η. For the last two variables, the plot contain one entry for each jet in the event.

6.1.1 Choice of variable

Several variables were investigated for their power to separate $t\bar{t}$ from the main W+jets background. Other than a good separation power between signal and background, the potential dependence on systematics was also taken into account. With the jet energy scale being the largest source of experimental systematic uncertainties, variables relying on jet p_{T} were discarded in favour of angular variables. The latter were found to have a shape that is less sensitive to detector systematic effects.

The variable of choice was "$\max \Delta\eta(\mathrm{l}, \mathrm{j})\, 3\mathrm{j}$": the maximum pseudorapidity difference between the lepton and one of the three highest p_{T} jets. Due to the higher $\sqrt{\hat{s}}$ necessary to produce a $t\bar{t}$ pair in the final state and the specific production mechanism, $t\bar{t}$ events tend to be more central in the detector. A $\Delta\eta$ variable between two objects is smaller the more the objects are central. Furthermore the variable exploits the fact that in case of W+jets the origin of the jets in the event is QCD radiation while for $t\bar{t}$ events they are the result of the top decay.

This variable was found to fulfil the requirements above and to be the variable with the largest signal-background separation. As an example, the separation obtained from the the lepton $|\eta|$ variable was 20% lower than the one obtained with the chosen variable. The choice of limiting the number of jets to the three leading ones was made in order to reduce the dependence of the variable to soft radiation, which is difficult to model in the Monte Carlo simulation. At the same time the shape of the variable was similar in the 3-jets region and this was used to validate the shape of the template for the W+jets background in a data-driven way.

The templates for $t\bar{t}$ and W+jets background are illustrated in Figure 6.3 for the e+jets and μ+jets channels. Twenty bins were used for the discriminating variable in the fit. It was found that, within reason, the expected performance from Monte Carlo studies was stable under the variation of the number of bins for the template.

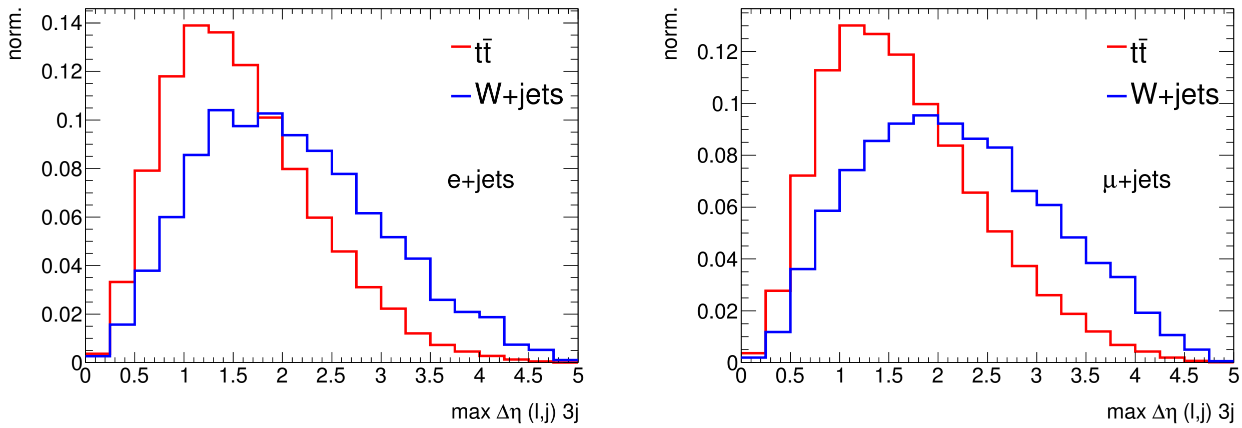

Figure 6.3: Templates for the chosen discriminating variable in the e+jets (left) and μ+jets (right) channel. Templates for $t\bar{t}$ and W+jets Monte Carlo are shown, normalised to unit area.

6.1.2 Fit definition

The templates for W+jets, Z+jets, single-top, and di-boson production were taken from Monte Carlo samples. The template for the multijet background was extracted from the data using the *anti-electron* method for the electron channel, and the *matrix method* for the muon channel, as outlined in the previous chapter.

The extraction of the number of $t\bar{t}$ events was performed through the minimisation of a modified binned χ^2 function as implemented by the MCLIMIT package [145]. The expression is as follows for a template with I bins:

$$\chi^2 = 2 \cdot \sum_{i=1}^{I} \left[(t_i(\theta) - n_i) - n_i \cdot \ln \left(\frac{t_i(\theta)}{n_i} \right) \right] + \sum_{k=1}^{K} S(\theta_k) \tag{6.1}$$

where n_i is the number of data events in the i^{th} bin. $t_i(\theta)$ represents the estimated number of events in bin i from the sum of all the templates defined as:

$$t(\theta) = n^{t\bar{t}} + n^{W+\text{jets}} + n^{\text{multijet}}_{\text{exp.}} + \sum_{k=1}^{\text{background}} \theta_k \cdot n^k_{\text{exp.}} \tag{6.2}$$

The 'exp.' suffix indicates the expected number of events from Monte Carlo normalised to their theoretical cross section, or to the data-driven prediction in the case of the QCD multijet background. The $t\bar{t}$ and W+jets templates are thus allowed to float freely in the fit. The rest of the Monte Carlo templates are constrained within some range of their standard model prediction though a series of nuisance parameters θ_k. The terms $S(\theta_k)$ in the χ^2 implement a gaussian constraint for each template normalisation. The width of the gaussian (also known as "prior uncertainty") were driven by the theoretical uncertainty on the sample normalisation:

- 48 % for Z+jets
- 10 % for single-top
- 5 % for diboson

The values for single top and diboson production directly originated from the uncertainties on the inclusive cross section as reported in Chapter 5. For Z boson production, the uncertainty on the inclusive normalisation is 4% but additional uncertainties had to be considered given that the process enters the event selection only due to the presence of a large number of additional jets. The uncertainties were calculated exploiting the so-called Berends scaling [146], namely the fact that the ratio of the boson plus jets prediction in two consecutive jet multiplicity bins is relatively constant as a function of the number of jets. The uncertainty on the ratio between consecutive jet multiplicity bins was found to be 24% from the variations of Alpgen generator parameters. This uncertainty was added in quadrature for any additional jet required in the analysis leading to a 48% uncertainty in the 4-jet signal region.

The QCD multijet background template normalisation is kept fixed in the fit. The reason is due to the very low statistics of the multijet templates since they are obtained from data-driven techniques. It has been verified that this choice did not impact the final uncertainty on the measurement in a negative way.

In total 5 normalisation parameters were considered in the fitting procedure; two free floating normalisation parameters for $t\bar{t}$ and W+jets templates, and three nuisance parameters for the gaussian-constrained normalisation of the rest of the backgrounds. Due to the early stage in the knowledge of detector effects, the systematic uncertainties were not considered in the fit through nuisance parameters but their effect on the final result was estimated with ensemble testing as explained later in this chapter.

The statistical uncertainty of the Monte Carlo templates is taken into account in the χ^2 formula though a series of nuisance parameters that are minimised separately in each bin following the prescription from [147]. The impact on the result due to finite Monte Carlo statistics was found to be negligible since the statistical precision of the templates for the leading samples ($t\bar{t}$, W+jets, single top) was much larger than the available data statistics for a luminosity of 35 pb^{-1}.

The number of $t\bar{t}$ events extracted from the fit was converted into a cross section measurement using the luminosity of the data sample and the efficiency/acceptance factor according to the formula:

$$\sigma_{t\bar{t}} = \frac{n^{t\bar{t}}}{A \cdot \mathscr{L}} \tag{6.3}$$

The A term contains three effects: the branching ratio of $t\bar{t}$ into non fully hadronic decay (54%)[1], the acceptance of the kinematic selection on the physics objects and the efficiency of the various identification and cleaning cuts. The product of the last two terms is equal to 5.8% in the electron channel and 8.6% in the muon channel for the nominal Monte Carlo simulation corrected for all the relevant data/Monte Carlo mis-modelling.

6.2 Fit performance study

The expected performance of the analysis as well as the effect of systematic uncertainties were obtained through ensemble testing, which required the evaluation of the fit result on a series of pseudo-experiments (PEs). For the estimation of the statistical uncertainty, each pseudo experiment consisted of a distribution obtained from the nominal templates; the expected number of events from each bin of each Monte Carlo sample template was smeared according to its finite statistical uncertainty. Random numbers were successively drawn in each bin assuming that the expected total number of events is Poisson-distributed. The PEs were then fitted as if they were the real data. For the estimation of the systematic uncertainties the pseudo experiments were generated in a similar way but using as initial inputs, the shifted template as a result of the application of the given systematic effect,

In case of pseudo-experiments generated from the nominal templates, the width of the distribution of the fit result is used as an estimator of the statistical uncertainty of the method, while the shift of the mean with respect to the nominal value is a measure of the bias introduced by the procedure. Figure 6.4 (top) shows the distribution of the pulls for the number of $t\bar{t}$ events from the fit to pseudo-experiments. The pull is defined as $\frac{(\text{fitted value}-\text{expected})}{\text{fit error}}$. As it can be seen, pull distributions have an average of zero and unit width, demonstrating that the fit is unbiased for what concerns the determination of the number of $t\bar{t}$ events as well as its error.

The statistical uncertainty and the uncertainty due to finite Monte Carlo statistics as extracted from the width of the fit results distribution from PEs as illustrated in Figure 6.4 (bottom), is reported in Table 6.2. Values are shown separately for the two lepton channels and for the combined fit. The combined fit has been performed by simultaneously considering the electron and muon channel distributions (doubling of bins in the definition of the χ^2), rather than performing the fit on the sum of the distributions.

The higher uncertainty in the electron channel was due to the lower efficiency of the topological selection and the electron identification criteria. The gain of the combination is very clear.

As an additional check, the linearity of the fit result has been tested generating pseudo-experiments with the number of $t\bar{t}$ events ranging from a quarter to three times the expected values. 5000 pseudo-experiments have been produced in each configuration. The results are shown in Figure 6.5, where no appreciable bias could be observed.

[1]Since the final state aims at identifying real leptons, $t\bar{t}$ events passing the event selection due to a jet faking a lepton were taken into account in the QCD multijet background.

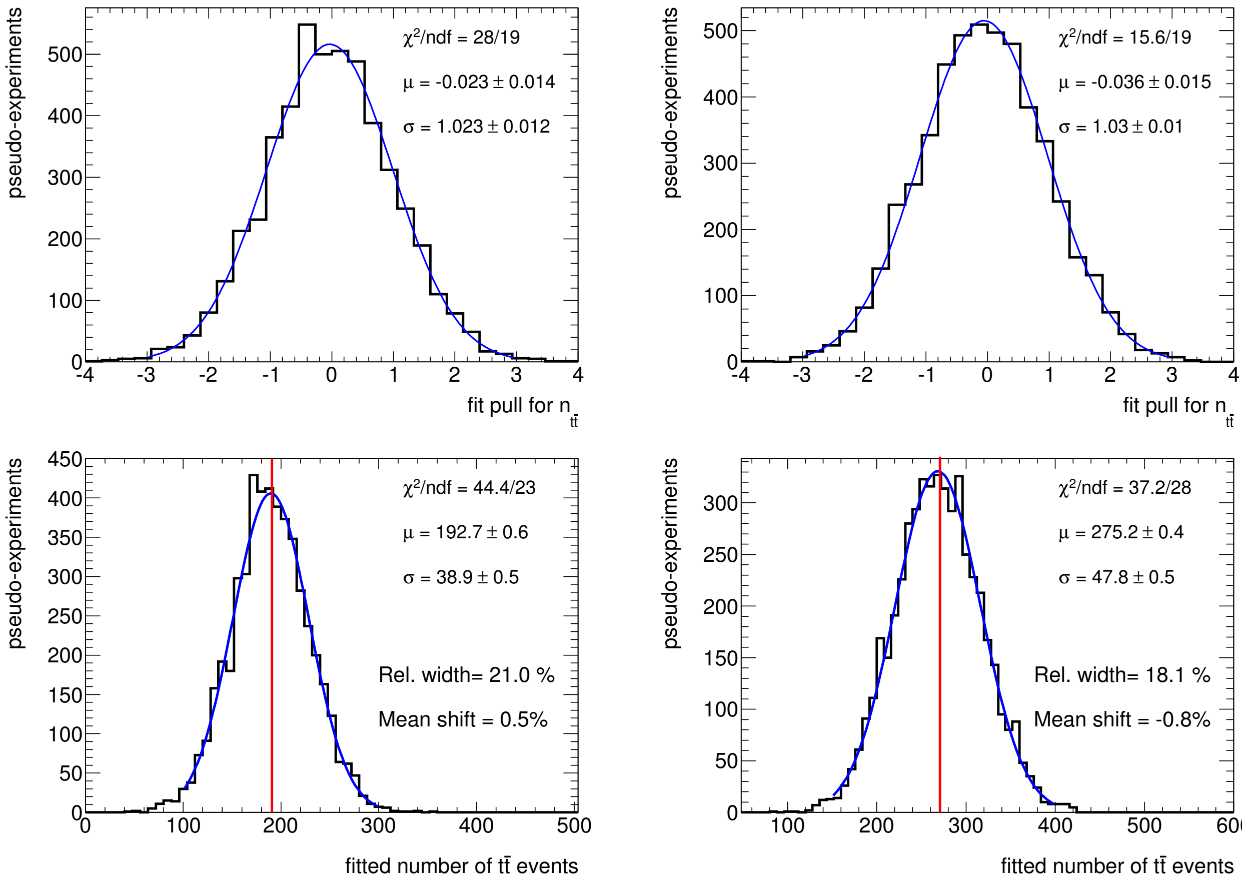

Figure 6.4: (top) Pull distributions for 5000 pseudo-experiments generated from the nominal templates. (Left) electron channel, (Right) muon channel. (Bottom) Distribution of the fitted number of $t\bar{t}$ events from each pseudo experiment.

channel	stat. uncertainty
e+jets	21.0 %
μ+jets	18.1 %
l+jets	13.3 %

Table 6.2: Statistical uncertainty on the number of $t\bar{t}$ events from the fit procedure in each channel and combination.

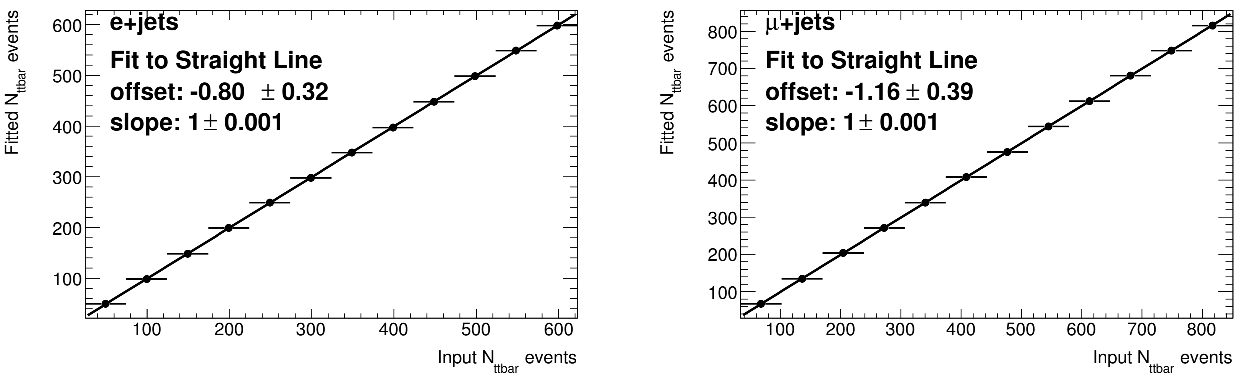

Figure 6.5: The fitted number of $t\bar{t}$ events as a function of the number of input $t\bar{t}$ events. Each point is the average result of 5000 pseudo-experiments. (Left) electron channel, (Right) muon channel.

6.2.1 Systematic uncertainties

The ensemble testing approach has also been employed for estimating the impact of systematic uncertainties. For each source of uncertainty, the corresponding templates are re-derived and 1000 pseudo-experiments are generated using the 'modified' templates in the same way described for the sensitivity studies. Each set of pseudo-experiments is then fitted using the nominal templates and the deviation of the mean of fit results with respect to the nominal prediction is used as an estimate for the impact of the systematic. The $t\bar{t}$ cross section is obtained from the number of $t\bar{t}$ events extracted from the fit, the efficiency/acceptance factor taking into account the effect of the objects and event selection, and the luminosity of the collected data.

The effect of systematic uncertainties can be to vary the number of $t\bar{t}$ events extracted from the fit by altering the shape of the signal template as well as the shape/normalisation of the background templates; they can also impact the signal efficiency/acceptance factor and thus affect the derivation of the cross section from the fitted number of events. For the evaluation of the detector-related uncertainties and the $t\bar{t}$ modelling uncertainties, the two effects are treated in a correlated way: the effect of the systematic modifies both the shape and the normalisation of the signal templates. The $t\bar{t}$ cross section from each pseudo-experiment is then always obtained by considering the nominal value for the efficiency/acceptance factor.

The uncertainty on the luminosity determination for the full 2010 dataset was 3.2 % [148]. Uncertainties related to the calibration and identification of physics objects (electron, muon, jets) have been outlined in Chapter 3. They are applied consistently to all the Monte Carlo samples and new templates are produced after applying proper smearing/scaling of the objects momentum or modifying the scale factor associated to the object identification. The adopted procedure consists in symmetrising the effect of the $+1\sigma$ and -1σ systematic variations on the fit output by averaging their absolute values.

Uncertainties on the background are assigned to cover both shape and normalisation effects.

- QCD multijet: given that the template is not allowed to vary in the fit, a dedicated uncertainty has been considered where the template normalisation is varied up and down by 50 % of the nominal value. The uncertainty on the shape of the template has been assessed by comparing different methods for the estimation of the QCD multijet background. In the muon channel, a different control region has been used to extract the fake efficiencies; in the electron channel, an alternative definition of the electron for the anti-electron method has been applied.

- Z+jets: the normalisation is varied up and down by an amount equivalent to the prior normalisation uncertainty. The shape uncertainty is obtained by comparing the nominal template obtained from the ALPGEN+HERWIG Monte Carlo to a Z+jets template generated with SHERPA.

- single top: the normalisation is varied up and down by an amount equivalent to the prior normalisation uncertainty.

- di-bosons: the normalisation is varied up and down by an amount equivalent to the prior normalisation uncertainty.

- W+jets: since the template normalisation is floated in the fit no uncertainty on the normalisation applies. For the shape uncertainty, several settings of the ALPGEN configuration parameters have been considered. The variation of the minimal parton p_{T} produced at the Matrix Element stage (10 GeV and 20 GeV with 15 GeV being the default) and a different functional form of the factorisation scale have been considered. The configuration that produced the largest variation on the fitted number of $t\bar{t}$ events has been taken as systematic variation.

Since the fit relies on the Monte Carlo distributions to extract the number of events, particular attention has been paid to considering the sources of systematic uncertainty that could also affect the shape of the signal template. Those systematic uncertainties affecting the $t\bar{t}$ predictions are:

- *Monte Carlo generator*: the effect of uncertainties on the parton level modelling of $t\bar{t}$ is evaluated by comparing the distributions from the nominal template obtained with MCNLO and with POWHEG generators both interfaced to HERWIG for the parton shower part. The variation affects both the normalisation (through acceptance effects) and the shape of the templates.

- *Parton Shower and fragmentation model*: this uncertainty is obtained by comparing two different hadronisation models applied to the same parton level generator (POWHEG): HERWIG and PYTHIA. The relative effect of the variation with PYTHIA/HERWIG is then applied to the nominal template which is showered with HERWIG.

- *ISR/FSR*: the uncertainty coming from the initial and final state radiation (ISR/FSR) parameterisation has been evaluated using the ACERMC LO generator interfaced to PYTHIA, by changing specific PYTHIA parameters in order to vary the amount of initial and final state radiation. Six variations have been considered: respectively varying ISR[2] and FSR[3] independently or in a correlated way. For each variation, the relative difference with respect to the nominal PYTHIA settings have been computed and applied to the nominal template. The largest positive and negative variation of the fit result distributions are considered as estimation of the uncertainty and then further symmetrised. In both electron and muon channels, the samples with the modified ISR configuration are responsible for the largest effect on the final result.

- *PDF*: the effect of using different parton density functions has been evaluated with the 'envelope prescription' previously described. The following NLO PDFs have been considered: NNPDF20, MSTW2008nlo90cl and CTEQ66 with their corresponding error sets.

[2]Corresponding PYTHIA parameters are PARP(67) and PARP(62)
[3]Corresponding PYTHIA parameters are PARP(72) and PARP(82)

Only the effect of each variation on the template normalisation has been taken into account since the shape effects were found to be negligible.

Table 6.3 summarises the relative uncertainties on the estimated inclusive $t\bar{t}$ cross section due to each source of systematics. Results are shown separately for each lepton channel as well as the combination

	e+jets	μ+jets	l+jets
luminosity	3.2 %	3.2 %	3.2 %
object related			
jet energy scale	9.8 %	5.2 %	7.2 %
jet energy resolution	0.7 %	0.2 %	1.0 %
jet efficiency	3.3 %	2.9 %	3.1 %
electron trigger SF	0.5 %	-	0.4 %
electron reco SF	1.4 %	-	1.1 %
electron ID SF	3.2 %	-	2.4 %
electron energy scale	0.2 %	-	0.1 %
electron energy resolution	1.4 %	-	0.7 %
muon trigger SF	-	1.4 %	0.9 %
muon ID+reco SF	-	1.0 %	0.6 %
muon momentum scale	-	0.7 %	0.6 %
muon momentum resolution	-	1.2 %	0.9 %
background-related			
multijet normalisation electron	0.8 %	-	1.4 %
multijet normalisation muon	-	2.5 %	1.1 %
multijet shape electron	5.5 %	-	3.3 %
multijet shape muon	-	2.4 %	1.0 %
Z+jets shape	0.1%	0.5 %	0.6 %
Z+jets normalisation	0.1%	$\leq$ 0.1 %	$\leq$ 0.1 %
single top normalisation	0.3%	0.2 %	0.3 %
di-boson normalisation	$\leq$ 0.1 %	$\leq$ 0.1 %	$\leq$ 0.1 %
W+jets shape	0.7%	0.5 %	0.8 %
signal-related			
MC generator	6.3%	6.8%	6.0%
Parton Shower	5.3%	5.4%	5.4%
ISR/FSR	7.0%	3.2 %	4.7 %
PDF	1.7%	1.7 %	1.7%
total sys.	17.8 %	13.7 %	14.9 %
statistics	21.0 %	18.1 %	13.3 %
total	27.5 %	22.7 %	19.9 %

Table 6.3: Relative uncertainties on the inclusive $t\bar{t}$ cross section estimated from a separate fit in each channel as well as in the combined fit.

The largest contribution to the systematic uncertainty in the final measurement comes from the knowledge of the jet energy scale and resolution and from the modelling of the signal. For the single channel measurements the statistical uncertainty dominates the final error while for the combined fit the effect of statistical and systematic uncertainties are at a similar level.

A global uncertainty of approximately 20 % is expected on the determination of the $t\bar{t}$ cross section with this analysis method.

Figure 6.6 shows the relative effect of the systematic uncertainty on the shape and normalisation for the jet energy scale uncertainty as well as for the MC generator and parton shower signal modelling uncertainties.

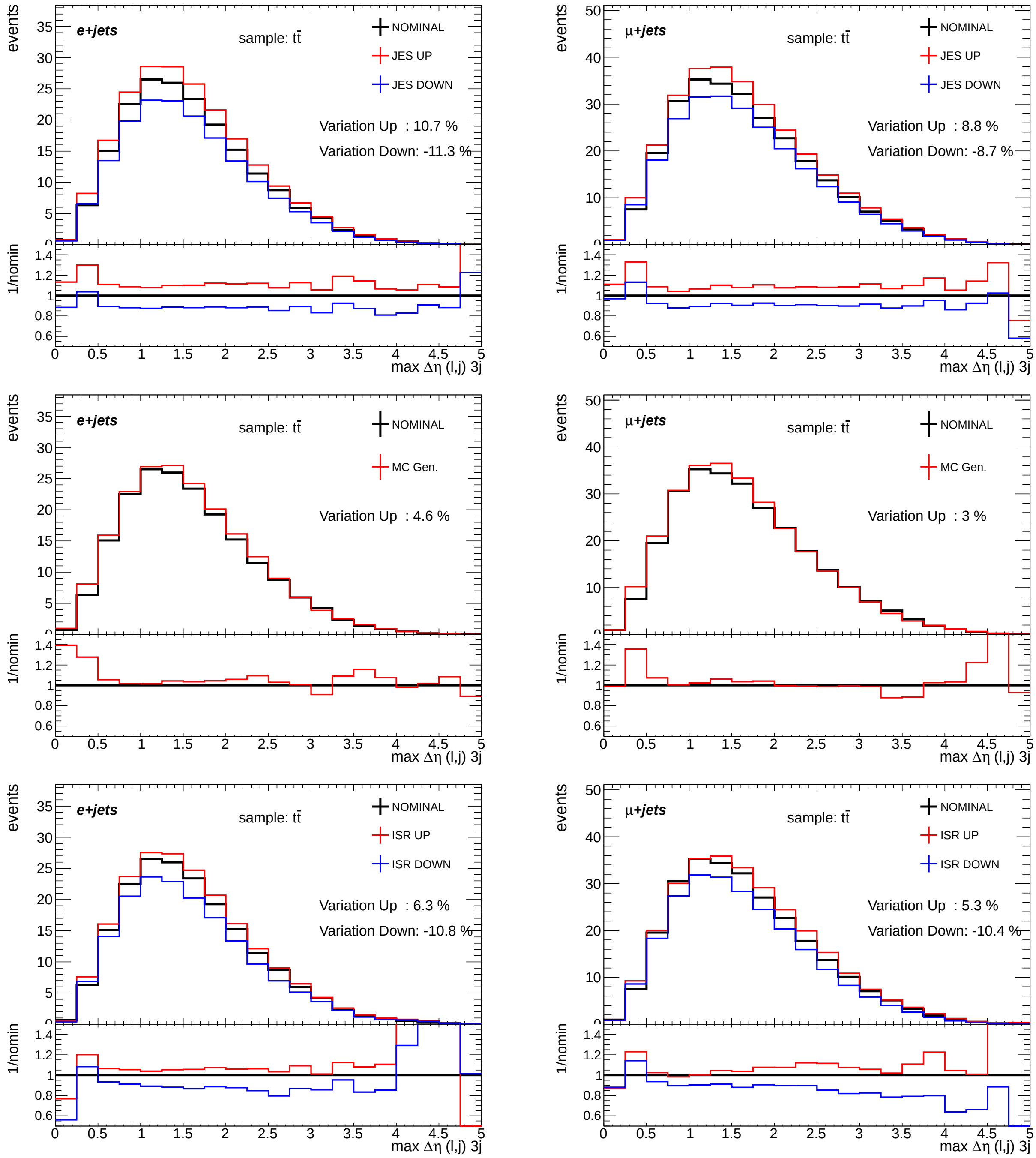

Figure 6.6: Relative effect of the main systematic uncertainties on the $t\bar{t}$ template of the discriminating variables. Distributions for the electron (muon) channel are shown on the left (right) column. Systematics are jet energy scale (top), MC generator (middle), ISR/FSR (bottom). Indicated is also the effect of the systematic on the template normalisation.

As it can be seen, the jet energy scale uncertainties do not significantly alter the shape of the variable.

6.3 Fit to data

The comparison between data and Monte Carlo expectations for the chosen discriminating variable is presented in Figure 6.7. Templates from Monte Carlo samples are normalised according to the theoretical cross section. The prediction describes reasonably the distribution of the discriminant in data.

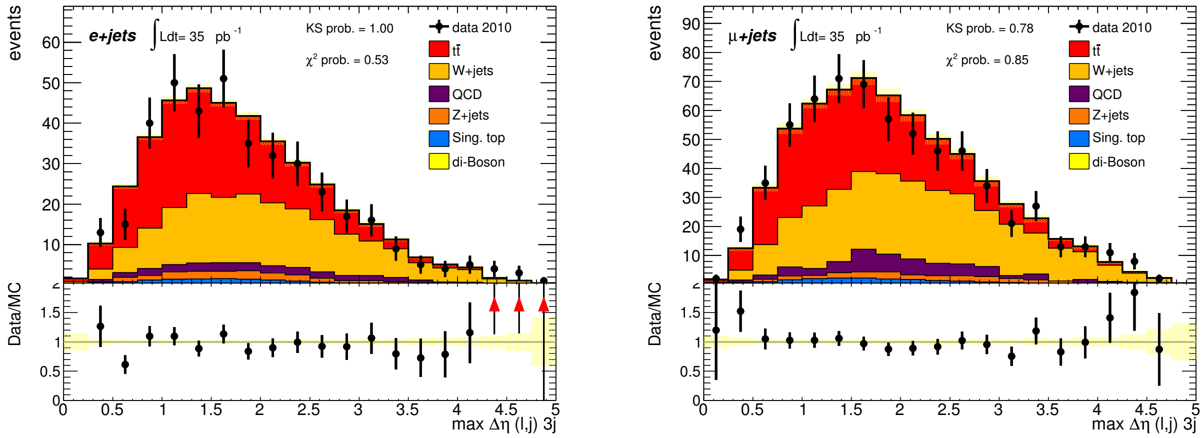

(a) **(b)**

Figure 6.7: Comparison between data and Monte Carlo prediction for the discriminating variable ($\max \Delta\eta(\mathrm{l,j})\,3\mathrm{j}$) in the signal region for the electron channel (a) and muon channel (b).

In order to validate the shape of the template for the W+jets background, events fulfilling the same lepton selection but with exactly 3 selected jets have been used. This region contains much higher statistics than the $\geq$ 4-jets region and the expected contamination from $t\bar{t}$ is smaller than 10%. The comparison is presented in Figure 6.8 confirming the good agreement in the description of the kinematics in the W+jets events.

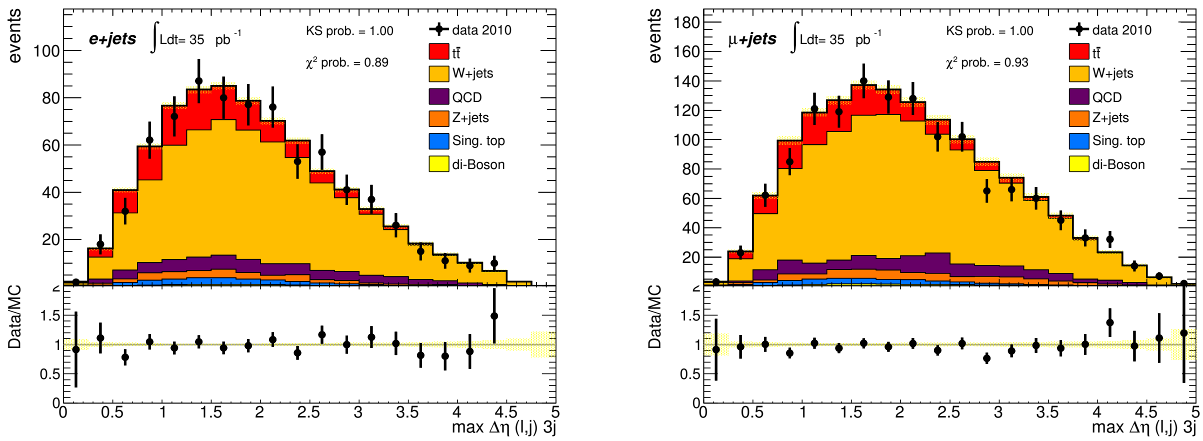

(a) **(b)**

Figure 6.8: Comparison between data and Monte Carlo prediction for the discriminating variable ($\max \Delta\eta(\mathrm{l,j})\,3\mathrm{j}$) in the 3-jets validation region in the electron channel (a) and muon channel (b).

The result of the fit to data in each region and for the combined case is summarised in Table 6.4. It contains the values of the normalisation parameters returned by the fit for the $t\bar{t}$ and W+jets templates. They are expressed in term of scale factors defined as the ratio between the number of events for each template returned by the fit, and the corresponding value from Monte Carlo prediction. The uncertainty on the SF represents the uncertainty on the normalisation which can be achieved not considering the effect of systematic uncertainties. In both channels as well as in the combination, $t\bar{t}$ and W+jets scale factors are well compatible with the nominal value within one standard deviation. The uncertainty on the $t\bar{t}$ normalisation is in agreement with that expected from pseudo experiments.

In has been verified that the other normalisation nuisance parameters for the small background components are not modified by the fitting procedure with respect to their initial values. This confirms that the information contained in the data does not allow to improve over the a priori knowledge of the normalisation given the small contribution from such backgrounds to the total yields in the signal region.

Sample	Scale Factor		
	e+jets	μ+jets	l+jets
$t\bar{t}$	0.95 ± 0.19	1.08 ± 0.17	1.02 ± 0.13
W+jets	0.98 ± 0.23	0.91 ± 0.16	0.95 ± 0.13

Table 6.4: A summary of the fit output to data. Scale factor for $t\bar{t}$ and W+jets templates are reported for each channel and for the combination.

As outlined in the previous paragraph, the SF for the $t\bar{t}$ template is then converted to a measurement of the inclusive $t\bar{t}$ cross section. The fitted values for the cross section in each separate channel and in the combination are reported in Figure 6.9.

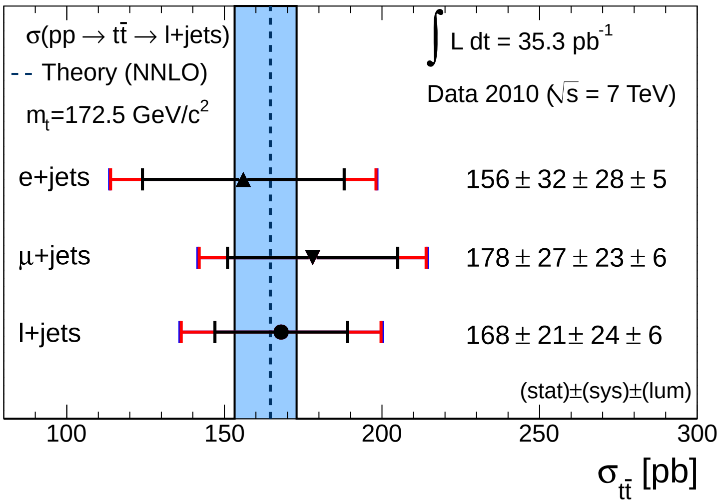

Figure 6.9: Summary of the fitted values of the $t\bar{t}$ cross section in each channel and the combination. The blue band represents the approx. NNLO theory prediction.

The blue band in the plot represents the predicted theoretical cross section calculated at approx. NNLO accuracy for a top mass of 172.5 GeV:

$$\sigma_{t\bar{t}}^{\text{theory}} = 164.6 \ {}^{+4.3}_{-9.3}\,(\text{scale}) \ {}^{+7.2}_{-6.5}\,(\text{PDF}) \ \text{pb}$$

The independent measurements in the two lepton channels yield consistent results and the combined fit returns a total inclusive $t\bar{t}$ cross section of:

$$\sigma_{t\bar{t}} = 168 \pm 21\,(\text{stat.}) \ \pm 24\,(\text{sys.}) \ \pm 5\,(\text{lumi.}) \ \text{pb}$$

The final measurement has a total uncertainty of 19 % and is in good agreement with the perturbative QCD calculation.

The comparison between data and Monte Carlo prediction scaled to the combined fit result is shown in Figure 6.10, confirming that the result of the fit does not spoil the initially good agreement between data and Monte Carlo.

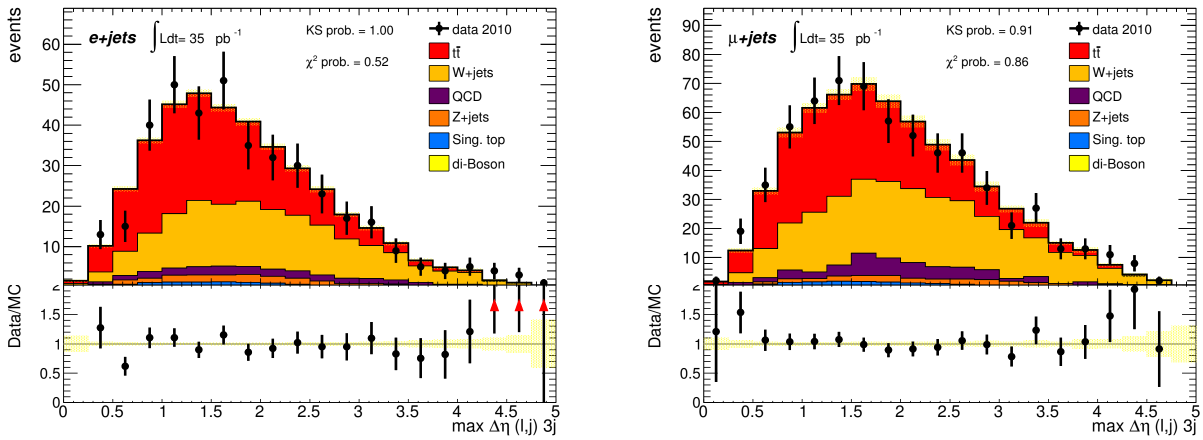

(a) **(b)**

Figure 6.10: Comparison between data and Monte Carlo prediction scaled to the combined fit results, for the discriminating variable used in the analysis in the electron channel (a) and muon channel (b). Uncertainty band only contains Monte Carlo statistics.

6.4 Overview of ATLAS results on $t\bar{t}$ cross section measurements

Figure 6.11 (a) summarises the status of the $t\bar{t}$ cross section measurements in the l+jets channel without use of b-tagging information as presented at the Moriond 2011 conference [149]. Different complementary techniques were used to strengthen the robustness of the result. The single results are all consistent with the Standard Model expectation and compatible with each other. As can be seen, the analysis presented in this chapter (third from the top) has a smaller uncertainty than the cut & count approach and the analysis using lepton η as a discriminating variable. The analysis implementing the multivariate approach used a likelihood-based discriminant based on three variables: lepton charge, lepton η and the *aplanarity*[4]. The usage of multivariate techniques improved the presented single variable result by ~ 20 %.

The dataset collected over 2011 allowed a measurement of the inclusive $t\bar{t}$ cross section in several final state channels. At the same time, the larger statistics and a more precise knowledge of detector uncertainties led to considerably more precise measurements in the main channels. The ATLAS results on the inclusive $t\bar{t}$ cross section at $\sqrt{s} = 7$ TeV, using part of the 2011 dataset, are summarised in Figure 6.11 (b). The measurement in the l+jets final state in particular [150] achieved a remarkable precision of 6.9 % thanks to the usage of multivariate techniques and the combination of signal regions containing 3 jets, 4 jets and $\geq$ 5 jets in a profiled likelihood technique approach. The combination of the main orthogonal channels (l+jets, di-lepton and all-hadronic) [151] yields a value of:

$$\sigma_{t\bar{t}} = \; 177 \pm \; 3\,(\text{stat.})\,^{+8}_{-7}\,(\text{sys.}) \;\; \text{pb}$$

[4] *Aplanarity* will be better defined in Chapter 8.

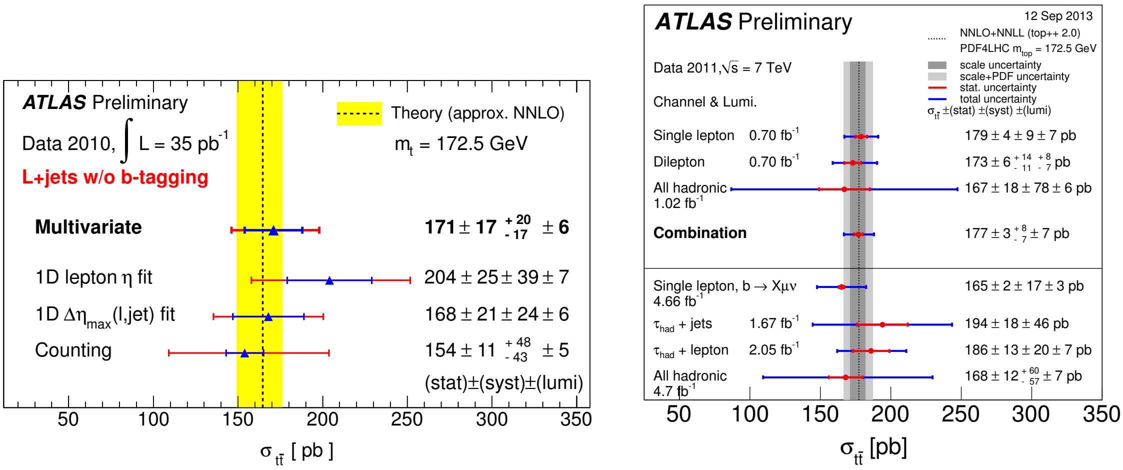

(a) **(b)**

Figure 6.11: (a) Inclusive $t\bar{t}$ cross section measurements in the l+jets channel without using b-tag information at the time of the Moriond 2011 conference. (b) Summary of ATLAS results on inclusive $t\bar{t}$ cross section measurements at a centre of mass energy of 7 TeV.

in excellent agreement with the most precise theoretical predictions.

Finally, Figure 6.12 contains a summary of the measurements of the inclusive top-pair production cross section at the centre of mass energy of 8 TeV, using the data collected during 2012. The most precise determination of the cross section [152] exploits events with a pair of electron and muon with opposite charge and one or two b-tagged jets in the final state. The analysis reaches a precision of 4.8%; a value comparable with the uncertainties on the theoretical calculation.

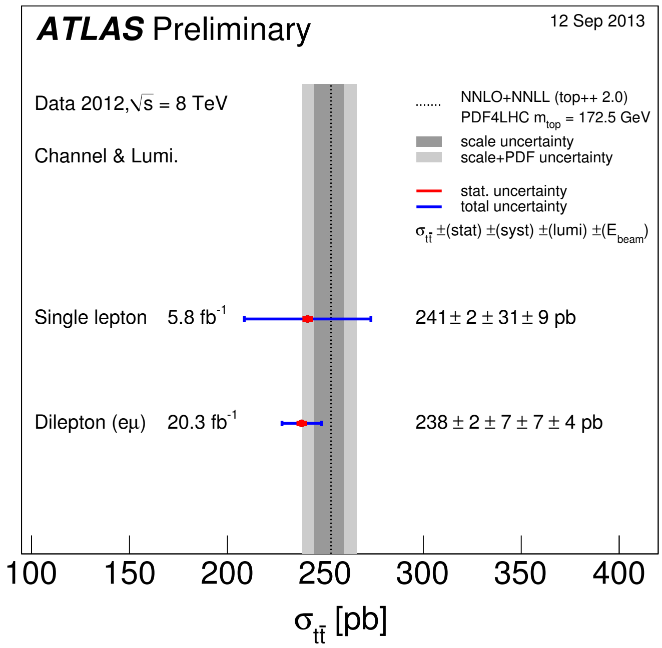

Figure 6.12: Summary of measurements of the top-pair production cross section at 8 TeV. The grey band represents the NNLO QCD calculation complemented with NNLL resummation.

Chapter 7

Measuring jet multiplicity in $t\bar{t}$ events

With the dataset collected during the year 2011 the LHC experiments surpassed the Tevatron in terms of the recorded number of $t\bar{t}$ events. The large data-sample allows analyses to go beyond the measurement of the inclusive $t\bar{t}$ cross section. One possibility consists of probing the kinematic properties of events containing a $t\bar{t}$ pair through differential measurements (the determination of the cross section as a function of a given observable). This type of measurement can be used to extract information on the validity of the QCD calculations for $t\bar{t}$ production and can help in constraining/tuning the behaviour of the different generators. At the same time, an improved knowledge of the properties of $t\bar{t}$ events is a key ingredient in most of the searches for beyond the Standard Model physics since the new potential signal could manifest itself in particular corners of the space space of top production.

This chapter describes the measurement of the jet multiplicity spectrum (differential cross section as a function of jet multiplicity) in l+jets $t\bar{t}$ events using the full 2011 dataset. The result is corrected for all detector effects and reported for a kinematic range corresponding to the acceptance of the reconstruction level event selection.

7.1 Motivation

As already outlined in Chapter 1, the use of jet algorithms allows to infer the properties of the partons produced in the hard scattering in a robust way. As an example, Figure 7.1 (a) shows the distribution of the number of reconstructed jets with $p_{\mathrm{T}} > 25$GeV and $|\eta| < 2.5$ for $t\bar{t}$ events in different Monte Carlo generators fulfilling the event selection described in Chapter 5. A typical $t\bar{t}$ decay in the lepton+jets channel is expected to give rise to four quarks and hence naively four jets in the final state. Events with a higher number of jets are primarily due to the production of a $t\bar{t}$ pair with additional jets. In the Monte Carlo implementation, such jets originate either directly from the hard scatter interaction or are described as initial state radiation and represent the system the $t\bar{t}$ pair recoils against. The jet multiplicity is also a variable sensitive to various theoretical aspects of the $t\bar{t}$ production:

- *the kinematics of the $t\bar{t}$ pair*: the direction and energy of the $t\bar{t}$ pair are transferred to the decay products and might affect their probability to fall within the kinematical acceptance;
- *final state radiation (FSR)*: $t\bar{t}$ decay products and ISR partons can produce additional radiation leading to *jet splitting*;
- *hadronisation*: this controls the conversion from partons to hadrons and ultimately it affects the way the jets are constructed;

- *underlying event*: the results from the interaction of proton remnants can typically produce soft particles that are clustered together with the contribution from hard partons in the event.

At the same time the effect of pileup and other detector effects like jet energy reconstruction and jet energy scale can also affect the final distribution.

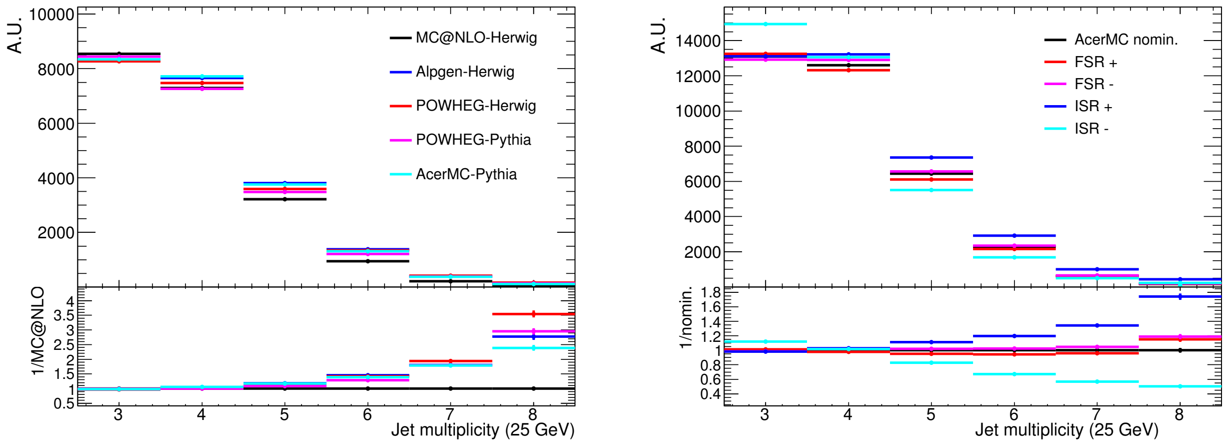

(a) **(b)**

Figure 7.1: (a) Number of reconstructed jets with $p_{\mathrm{T}} > 25$GeV and $|\eta| < 2.5$ for different $t\bar{t}$ Monte Carlo generators after the final event selection. (b) Reconstructed jet multiplicity for the default AcerMC sample and for the samples used to evaluate the ISR and FSR systematic uncertainties in the 2010 analysis.

These aspects are the ones in which the approaches of different Monte Carlo generators generally differ, and as a result, each generator shows a characteristic distribution as can be noted in the same Figure 7.1 (a). A precise measurement could help in reducing the uncertainties due to the modelling of the $t\bar{t}$ events; as demonstrated in the previous chapter, those uncertainties represented the largest contribution to the systematic error on the inclusive $t\bar{t}$ cross section measurement. Figure 7.1 (b) shows in particular the effect of the uncertainties related to the ISR and FSR on the jet multiplicity distribution. The nominal AcerMC is compared to the samples with modified Pythia parameters to increase and decrease the amount of radiation as used in the 2010 analysis. The variation of initial state radiation produces a large effect while the uncertainties due to final state radiation are only at the level of a few %. As can be seen, the jet multiplicity spectrum has the potential to give information on the QCD radiation properties at the high energy scale of the $t\bar{t}$ production.

At the same time, $t\bar{t}$ plus additional jets represents the main background in searches for specific Higgs boson production modes as well as for physics beyond the Standard Model that involves a large number of particles in the final state. A good understanding of $t\bar{t}$+jets production is a key ingredient to increase the sensitivity of the analyses. The new potential signal could manifest itself in particular corners of the space of the $t\bar{t}$ production.

Contrary to the differential measurement of the $t\bar{t}$ kinematics [153], in this analysis no attempt is made to determine the origin of each specific jet. This choice was made in order to reduce the number of assumptions and the dependence on the Monte Carlo information that are necessarily introduced when requiring a direct match between a parton and a reconstructed jet.

Additional information could be extracted by considering the jet multiplicity distributions for different values of the jet p_{T} cut, since ISR jets exhibit a harder p_{T} spectrum than FSR jets and jets from underlying events. The analysis presented in this chapter uses a jet p_{T} cut of 25 GeV which represents the 'default' value for many $t\bar{t}$ analyses. Results for different higher jet p_{T} cuts (not derived by the author) will be briefly mentioned at the end of the chapter.

The jet multiplicity spectrum in lepton+jets $t\bar{t}$ events was previously measured by ATLAS using the first 0.7 fb^{-1} of data collected during 2011 [154]. This measurement was not corrected for detector effects and was dominated by systematic uncertainties, which made it impossible to further constrain the impact of the ISR systematic uncertainty. The analysis described in the following extends the previous results to larger jet multiplicities, taking advantage of the reduced detector and background related systematic uncertainties obtained with the full 2011 dataset. Furthermore the distribution will be corrected for all detector effects in order to make an easier comparison with current and future Monte Carlo models.

7.2 Analysis strategy

The event selection for the analysis closely follows the 'standard' selection for $t\bar{t}$ events described in Chapter 5. The key differences are outlined:

- at least 3 selected jets: lowering the requirement on the number of jets allows to inspect the effect of the kinematic selection on the $t\bar{t}$ decays;
- at least 1 b-tagged jet: this choice allows to reduce substantially the contribution from the other Standard Model backgrounds like W+jets;
- veto second lepton with $p_{\mathrm{T}} > 15$ GeV. The lowering of the p_{T} for the lepton veto requirement from 25 GeV to 15 GeV has a two-fold effect, namely to decrease the contribution from di-lepton $t\bar{t}$ events inside the event selection and to significantly reduce the number of electrons reconstructed as jets;
- identical $E_{\mathrm{T}}^{\mathrm{miss}}$ and $m_{\mathrm{T}}(W)$ kinematic selection criteria are applied to the electron and muon channels in order to reduce the differences between the two channels due to kinematic effects. The selection $E_{\mathrm{T}}^{\mathrm{miss}}$>30 GeV and $m_{\mathrm{T}}(W)$ >35 GeV were optimised to reduce substantially the QCD multijet background in the electron channel.

The number of $t\bar{t}$ events in each jet multiplicity bin is extracted from data using a cut&count approach, subtracting from data the expectation from each source of background. For the small backgrounds like diboson, Z+jets and single top, the Monte Carlo expectations are used, while the main backgrounds (W+jets and QCD multijet) have been estimated using the data-driven techniques described in Chapter 5. Tables 7.1 and 7.2 summarise the event yields for signal and each background in each jet multiplicity bin for the electron and muon channel scaled to a luminosity of 4.7 fb^{-1}. As a result of requiring at least 1 b-tagged jet, the contribution of backgrounds is substantially suppressed; it ranges from 50% of the selected events in the 3-jet bin to $\sim$ 10% in events containing 8 or more jets.

7.2.1 Reconstruction-level distributions

To model the $t\bar{t}$ signal events, the ALPGEN generator interfaced to HERWIG is used as a 'nominal' Monte Carlo generator for this analysis. This multi-leg generator gives a fair description of data also for high jet multiplicities, as demonstrated by Figures 7.2.

Electron channel						
sample	$n_{\text{jets}}^{\text{reco}}$=3	$n_{\text{jets}}^{\text{reco}}$=4	$n_{\text{jets}}^{\text{reco}}$=5	$n_{\text{jets}}^{\text{reco}}$=6	$n_{\text{jets}}^{\text{reco}}$=7	$n_{\text{jets}}^{\text{reco}}\geq$8
$t\bar{t}$	9900 ± 1000	9600 ± 1200	4900 ± 1100	1900 ± 600	590 ± 250	220 ± 120
W+jets	5300 ± 1300	1650 ± 400	440 ± 130	99 ± 32	21 ± 9	6.7 ± 3.3
QCD multijet	1900 ± 1000	890 ± 400	380 ± 190	160 ± 80	36 ± 19	18 ± 10
single top	1980 ± 250	820 ± 120	240 ± 50	58 ± 16	13 ± 5	2.3 ± 2.1
Z+jets	610 ± 270	260 ± 120	100 ± 60	25 ± 18	7 ± 5	0.9 ± 1.8
Diboson	150 ± 50	35 ± 10	7.3 ± 2.5	1.2 ± 0.6	0.2 ± 0.2	0.1 ± 0.1
Expectation	19900 ± 1900	13200 ± 1400	6100 ± 1100	2300 ± 600	670 ± 250	250 ± 120
Data	20320	12704	5632	1856	566	188

Table 7.1: Observed yields in the electron channel together with the predicted events for the signal and background processes for an integrated luminosity of 4.7 fb^{-1}. The numbers of events passing all selection requirements are shown as a function of the number of reconstructed jets ($n_{\text{jets}}^{\text{reco}}$). The uncertainties on the expected values include all systematic uncertainties including data-driven normalisation of W+jets and QCD multijet backgrounds.

Muon channel						
sample	$n_{\text{jets}}^{\text{reco}}$=3	$n_{\text{jets}}^{\text{reco}}$=4	$n_{\text{jets}}^{\text{reco}}$=5	$n_{\text{jets}}^{\text{reco}}$=6	$n_{\text{jets}}^{\text{reco}}$=7	$n_{\text{jets}}^{\text{reco}}\geq$8
$t\bar{t}$	11500 ± 1100	11100 ± 1100	5900 ± 1100	2300 ± 600	710 ± 280	250 ± 140
W+jets	7300 ± 1500	2300 ± 500	560 ± 140	122 ± 31	29 ± 10	11 ± 5
QCD multijet	2200 ± 600	800 ± 240	280 ± 50	85 ± 26	23 ± 7	11 ± 4
single top	2360 ± 290	970 ± 140	290 ± 50	70 ± 19	14 ± 5	4.0 ± 1.4
Z+jets	380 ± 180	140 ± 80	49 ± 29	14 ± 10	1.3 ± 2.8	0.5 ± 0.8
Diboson	170 ± 40	41 ± 13	7.2 ± 2.1	1.2 ± 0.5	0.0 ± 0.3	0.1 ± 0.2
Expectation	24000 ± 2000	15400 ± 1200	7100 ± 1100	2600 ± 600	780 ± 280	280 ± 140
Data	24422	15162	6578	2348	722	252

Table 7.2: Observed yields in the muon channel together with the predicted events for the signal and background processes for an integrated luminosity of 4.7 fb^{-1}. The numbers of events passing all selection requirements are shown as a function of the number of reconstructed jets ($n_{\text{jets}}^{\text{reco}}$). The uncertainties on the expected values include all systematic uncertainties including data-driven normalisation of W+jets and QCD multijet backgrounds.

Both the tables and the plots contain the full systematic uncertainties on the backgrounds and the signal predictions. For what concerns the backgrounds, the uncertainties are a key ingredient in the cut&count techniques, while for the signal, the uncertainty values are only for visualisation purposes since their impact will be re-assessed after the unfolding procedure described in the next section.

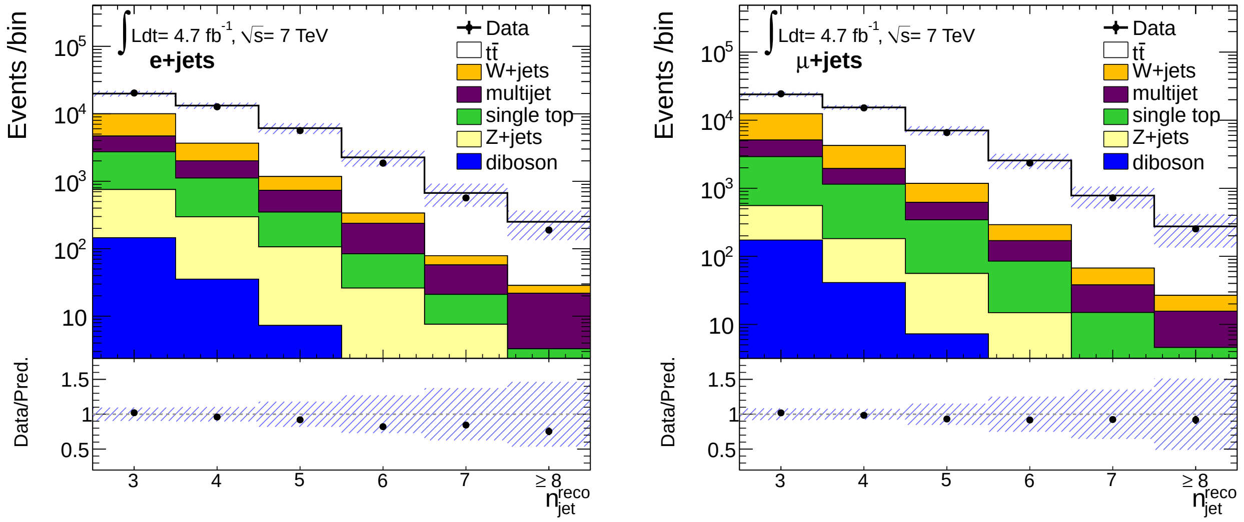

(a) (b)

Figure 7.2: Comparison between the observed and predicted jet multiplicity distributions in the electron (a) and muon (b) channels. The shaded band shows the total systematic and statistical uncertainties on the signal plus background estimates.

Sources of systematic uncertainty related to the physics objects are similar to those in the 2010 inclusive $t\bar{t}$ cross section analysis with the addition of the uncertainties related to the jet vertex fraction cut and the b-tagging requirements. The change in the nominal sample used to model the $t\bar{t}$ signal prompted a modification of the procedure to compute the systematic uncertainties related to the signal modelling with respect to the 2010 analysis.

- *Monte Carlo generator*: the uncertainties on the $t\bar{t}$ kinematics and hard scattering are assessed by comparing the nominal distributions from ALPGEN+HERWIG with events generated with POWHEG+HERWIG. The MC@NLO generator is not considered since it was found to give a poor description of data.

- *Parton Shower and fragmentation model*: this uncertainty is obtained by comparing two different hadronisation models applied to the same parton level generator (POWHEG): HERWIG and PYTHIA. The relative effect of the variation with PYTHIA/HERWIG is then applied to the nominal distribution which is showered with HERWIG.

- *ISR/FSR*: the uncertainty coming from the initial and final state radiation (ISR/FSR) parameterisation has been evaluated using the ALPGEN generator interfaced to PYTHIA. ISR/FSR variation samples are obtained by modifying the scale at which the value of α_S is computed for emission vertices in the matrix element calculation[1]; on the contrary, the α_S used for the PDF and parton shower is kept constant. Those samples are generally referred to as α_S-up and α_S-down. These settings have been shown to produce variations that enclose the uncertainty band of the $t\bar{t}$ jet veto measurement[2] [155]. The largest relative variation with respect to the default ALPGEN+PYTHIA sample is taken as a systematic uncertainty and applied to the nominal ALPGEN+HERWIG sample.

- *PDF*: the systematic is obtained by comparing the nominal ALPGEN+HERWIG sample generated with CTEQ6.1L PDF to the one obtained with the MSTW2008lo68cl PDF

[1]The KTFAC parameter in ALPGEN

[2]This analysis assessed the properties of radiation in $t\bar{t}$ events by looking at the 'survival' probability of a third jet in di-lepton events with two b-tagged jets.

set[3]. Furthermore, the variation related to the different eigenvectors of MSTW2008lo68cl is also added in quadrature.

Tables 7.3 and 7.4 show the relative effect of the systematic uncertainties on the signal predictions. Except for the jet energy scale uncertainties, detector related systematic uncertainties do not significantly vary as a function of the number of selected jets. For high jet multiplicities, similar contributions are observed from signal MC modelling and jet energy scale uncertainties, of the order of $\sim$ 30-35 %.

Electron channel						
uncertainty	$n_{\text{jets}}^{\text{reco}}$=3	$n_{\text{jets}}^{\text{reco}}$=4	$n_{\text{jets}}^{\text{reco}}$=5	$n_{\text{jets}}^{\text{reco}}$=6	$n_{\text{jets}}^{\text{reco}}$=7	$n_{\text{jets}}^{\text{reco}}\geq$8
MC statistics	0.4	0.4	0.5	0.6	1.1	1.9
Luminosity	3.9	3.9	3.9	3.9	3.9	3.9
electron reconstruction	0.9	0.9	0.9	0.9	0.9	0.9
electron identification	2.2	2.2	2.2	2.2	2.2	2.2
electron trigger	0.6	0.6	0.6	0.6	0.6	0.6
electron energy scale	0.4	0.4	0.4	0.4	0.3	0.3
electron energy resolution	$\leq$ 0.1	$\leq$ 0.1	0.1	0.1	$\leq$ 0.1	0.1
b-jet tagging	4.9	4.6	4.6	4.4	4.5	3.8
c-jet tagging	0.4	0.4	0.4	0.4	0.4	0.5
light-jet tagging	0.4	0.3	0.3	0.4	0.5	0.5
jet reconstruction	0.1	$\leq$ 0.1	0.2	0.2	0.2	0.3
JVF selection	1.2	1.4	1.7	2.0	2.3	2.7
jet energy scale	3.8	3.2	8.5	16	22	28
jet energy resolution	0.6	0.4	1.4	2.5	6.1	4.2
$E_{\text{T}}^{\text{miss}}$cell-out	$\leq$ 0.1	0.1	0.1	0.1	0.3	0.5
$E_{\text{T}}^{\text{miss}}$pileup	$\leq$ 0.1	0.1	0.1	$\leq$ 0.1	0.2	0.3
MG generator	1.9	11	17	18	19	20.
Parton Shower	2.6	2.2	2.3	2.2	5.0	20
ISR	6.5	0.9	9.2	20	29	33
PDF	2.7	4.3	5.9	7.2	8.7	9.4
Total	10	13	22	32	42	52

Table 7.3: Relative effects (expressed in %) of the sources of systematic uncertainties on the signal predictions in each jet multiplicity bin for the electron channel.

The background-subtracted data distributions are reported in Figure 7.3; the uncertainty band contains the data statistical uncertainty as well as the contribution from the background uncertainty. The former dominates the high jet multiplicity region while the latter is more important for low jet multiplicities where the background contribution is larger. The individual contributions to the background subtracted uncertainties are summarised in Tables 7.5 and 7.6. The normalisation uncertainties on the small backgrounds are the same used in the 2010 inclusive cross section analysis. Uncertainties on the data-driven estimation of the W+jets and multijet backgrounds have been extensively discussed in Chapter 5. In particular, since the W+jets data-driven estimation is performed separately in events with 3 jets, 4 jets and $\geq$ 5 jets, additional 'shape' uncertainties are considered for higher jet multiplicities[4].

[3]The results for other PDF sets are obtained through an event re-weighting method.

[4]A 24% normalisation uncertainty is assigned for each additional jet above 6; subsequently the effect of the

Muon channel						
uncertainty	$n_{\text{jets}}^{\text{reco}}$=3	$n_{\text{jets}}^{\text{reco}}$=4	$n_{\text{jets}}^{\text{reco}}$=5	$n_{\text{jets}}^{\text{reco}}$=6	$n_{\text{jets}}^{\text{reco}}$=7	$n_{\text{jets}}^{\text{reco}}\geq$8
MC statistics	0.4	0.4	0.4	0.6	1.0	1.7
Luminosity	3.9	3.9	3.9	3.9	3.9	3.9
muon reconstruction	0.3	0.3	0.3	0.3	0.3	0.3
muon identification	0.7	0.7	0.7	0.7	0.7	0.7
muon trigger	1.3	1.3	1.3	1.3	1.3	1.3
muon momentum scale	0.3	0.3	0.3	0.2	0.2	0.1
muon momentum resolution (ID)	$\leq$ 0.1	$\leq$ 0.1	$\leq$ 0.1	$\leq$ 0.1	$\leq$ 0.1	$\leq$ 0.1
muon momentum resolution (MS)	$\leq$ 0.1	$\leq$ 0.1	$\leq$ 0.1	$\leq$ 0.1	$\leq$ 0.1	$\leq$ 0.1
b-jet tagging	5.0	4.7	4.5	4.4	4.6	4.0
c-jet tagging	0.4	0.4	0.4	0.5	0.4	0.6
light-jet tagging	0.4	0.3	0.3	0.4	0.5	0.3
jet reconstruction	$\leq$ 0.1	$\leq$ 0.1	0.2	0.1	0.2	0.4
JVF selection	1.2	1.4	1.7	2.0	2.3	2.7
jet energy scale	4.2	2.4	7.6	14	21	32
jet energy resolution	0.9	0.4	0.5	1.9	5.3	7.8
$E_{\text{T}}^{\text{miss}}$cell-out	0.2	0.2	0.1	0.1	0.1	0.1
$E_{\text{T}}^{\text{miss}}$pileup	0.1	0.2	0.1	0.1	0.1	0.2
MG generator	2.2	7.3	12	9.9	12	17
Parton Shower	0.8	1.8	2.4	2.1	4.7	24
ISR	6.7	0.7	10	22	29	37
PDF	2.7	4.3	5.9	7.2	8.7	9.4
Total	9.9	9.4	18	28	39	57

Table 7.4: Relative effects (expressed in %) of the sources of systematic uncertainties on the signal predictions in each jet multiplicity bin for the muon channel.

Finally it should be noted that detector-related uncertainties on the background generally play a minor role in the total uncertainty.

The predictions for the different Monte Carlo generators after full detector reconstruction are also shown; their uncertainty bands only contain the statistical components. A more detailed comparison is performed after the unfolding procedure described in the next section.

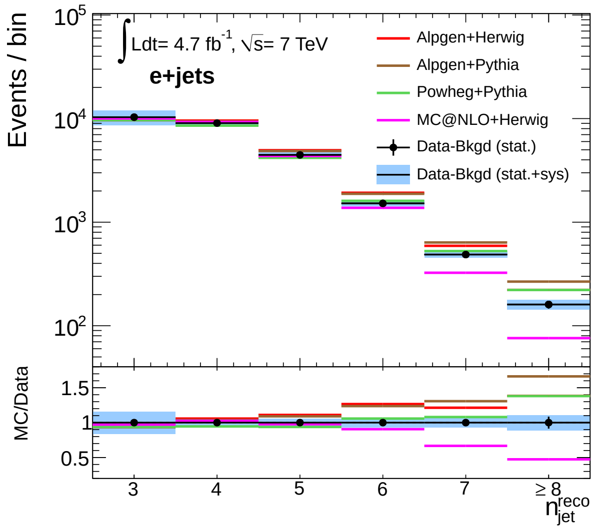

(a)

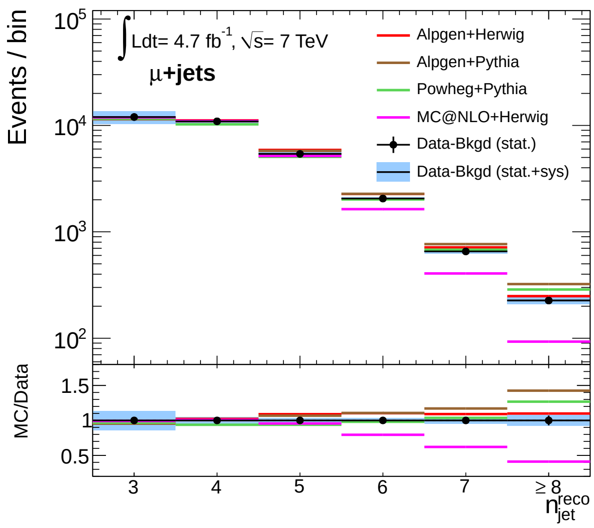

(b)

Figure 7.3: The reconstructed jet multiplicities after background subtraction for the electron (a) channel and the muon (b) channel. The data are shown in comparison to the ALPGEN+HERWIG, ALPGEN+PYTHIA, POWHEG+PYTHIA and MC@NLO+HERWIG predictions for the $t\bar{t}$ signal. The data points and their corresponding statistical uncertainty are shown in black, whereas the statistical and systematic uncertainties due to the background are included in the blue band. The signal curves are shown with their statistical uncertainty only.

uncertainty is corrected by imposing no change in the total W+jets normalisation in events with ≥ 5 jets. At the same time, the effect of the detector uncertainties was also considered for events with ≥ 5 jets with the condition of not affecting the overall normalisation.

Electron channel						
uncertainty	$n_{\text{jets}}^{\text{reco}}$=3	$n_{\text{jets}}^{\text{reco}}$=4	$n_{\text{jets}}^{\text{reco}}$=5	$n_{\text{jets}}^{\text{reco}}$=6	$n_{\text{jets}}^{\text{reco}}$=7	$n_{\text{jets}}^{\text{reco}}\geq$8
bkgd. MC stat.	0.8	0.5	0.6	0.9	1.5	2.7
W+jets: charge asymm. norm.	5.1	2.0	1.8	1.2	0.8	0.8
W+jets: light VS HF	8.6	3.0	1.6	1.1	0.8	0.6
W+jets: bb+cc VS c	2.0	1.0	0.5	0.7	0.6	0.4
W+jets: bb+cc extrapolation	5.6	2.2	1.1	0.9	0.7	0.5
W+jets: c extrapolation	4.1	1.1	0.5	0.3	0.1	0.2
W+jets: shape	$\leq$ 0.1	$\leq$ 0.1	0.3	0.4	0.7	1.0
Multijet: normalisation	9.4	4.9	4.3	5.1	3.7	5.8
Multijet: shape	0.3	0.2	0.1	0.2	0.3	0.6
single top: normalisation	1.9	0.9	0.5	0.4	0.3	0.1
Z+jets: normalisation	2.5	1.4	1.2	1.0	1.0	0.4
diboson: normalisation	0.1	$\leq$ 0.1	$\leq$ 0.1	$\leq$ 0.1	$\leq$ 0.1	$\leq$ 0.1
detector related	1.4	1.2	1.2	1.6	1.0	2.0
data stat.	1.4	1.2	1.7	2.8	4.9	8.6
data+background	16	7.1	5.7	6.5	6.7	11

Table 7.5: Relative effect (expressed in %) of the sources of systematic uncertainties on the background subtracted data distribution in the electron channel. The contribution of the data statistics as well as the uncertainties on each of the backgrounds are considered.

Muon channel						
uncertainty	$n_{\text{jets}}^{\text{reco}}$=3	$n_{\text{jets}}^{\text{reco}}$=4	$n_{\text{jets}}^{\text{reco}}$=5	$n_{\text{jets}}^{\text{reco}}$=6	$n_{\text{jets}}^{\text{reco}}$=7	$n_{\text{jets}}^{\text{reco}}\geq$8
bkgd. MC stat.	0.7	0.4	0.4	0.5	0.8	1.6
W+jets: charge asymm. norm.	5.1	1.8	1.5	0.9	0.7	0.7
W+jets: light VS HF	7.7	2.8	1.4	0.7	0.5	0.5
W+jets: bb+cc VS c	2.0	1.0	0.5	0.7	0.6	0.4
W+jets: bb+cc extrapolation	5.2	2.2	1.1	0.6	0.5	0.6
W+jets: c extrapolation	6.1	1.7	0.7	0.4	0.2	0.2
W+jets: shape	$\leq$ 0.1	$\leq$ 0.1	0.3	0.4	0.7	1.1
Multijet: normalisation	5.5	2.2	1.5	1.2	1.1	1.5
Multijet: shape	0.3	0.2	0.2	0.1	0.1	0.2
single top: normalisation	2.0	0.9	0.5	0.3	0.2	0.2
Z+jets: normalisation	1.3	0.6	0.5	0.4	0.1	0.1
diboson: normalisation	0.1	$\leq$ 0.1	$\leq$ 0.1	$\leq$ 0.1	$\leq$ 0.1	$\leq$ 0.1
detector-related	1.2	1.1	0.8	0.9	1.1	0.7
data stat.	1.3	1.1	1.5	2.4	4.1	7.0
data+background	14	5.3	3.5	3.2	4.6	7.6

Table 7.6: Relative effect (expressed in %) of the sources of systematic uncertainties on the background subtracted data distribution in the muon channel. The contribution of the data statistics as well as the uncertainties on each of the backgrounds are considered.

7.3 Unfolding

The background-subtracted jet multiplicity distribution, while allowing a comparison with different Monte Carlo predictions, still carries the effect of the particular event reconstruction based on the measurements using the ATLAS detector. This implies that measurements from different experiments cannot be easily combined and a comparison with any new Monte Carlo generator model still requires processing of the events through the full ATLAS simulation and reconstruction chain.

Multiple detector-level effects can affect the reconstructed jet multiplicity distribution: the jet energy scale and resolution introduce a smearing in the jet kinematic quantities that impact their acceptance. The jet reconstruction efficiency and in particular the efficiency due to the JVF cut can also alter the number of reconstructed jets in the events. Furthermore, the multiple interactions per crossing happening at the LHC can not only create soft particles that enter in the jet reconstruction and spoil the resolution; they also contribute to additional jets in the final state.

The procedure to correct for detector effects is generally referred to as *unfolding*; it originates from the fact that the distribution that is observed with the detector is the initial 'true' spectrum convoluted ('folded') with a generic detector response. In the context of this analysis the 'true' spectrum will be denoted as *'particle level'* distribution (*part* in the following) as opposed to the distribution after detector reconstruction ('reconstruction' or *reco* level in the following). In the Monte Carlo generators, the particle level is the stage that precedes the simulation of the particles with the detector. After the hadronisation, only 'stable' particles with a lifetime greater than $0.3{\cdot}10^{-10}$ s are considered in the event and used to build *particle jets* [5]. Particle level jets allow a very robust and generator independent definition of the hadronic activity in the event, in contrast (for instance) to the parton level which considers the partons directly coming from the matrix element interaction in the generator or the $t\bar{t}$ decay.

7.3.1 Particle level selection

The background-subtracted reconstructed jet multiplicity is corrected to the particle level one in a kinematic region as similar as possible to the selection used to collect the events. The motivation for this stems from the need to reduce the extrapolation of the measurement to a phase space not covered by the detector. At the same time, the jet multiplicity distribution is very dependent on the event selection, which might affect, in particular, the relative composition of single lepton and dilepton $t\bar{t}$ events in the final state. Dilepton $t\bar{t}$ events fulfilling the single lepton final selection, typically display a smaller number of jets.

A particle level event selection is obtained by building physics objects out of stable particles. Electrons and muons are required to be decay products of generated W bosons, either directly or via a leptonic τ decay. The electrons are further 'dressed' with all the prompt photons found within a cone of radius ΔR=0.1[6]. The vector sum of the generated neutrino four momenta is used to compute $E_{\mathrm{T}}^{\mathrm{miss}}$ and the corresponding azimuthal angle. 'Particle level' jets are computed clustering stable particles, with the exclusion of muons and neutrinos, with the same anti-k$_T$ algorithm with a 0.4 radius parameter. Particle jets matched to a b-hadron with $p_{\mathrm{T}}>$ 5 GeV within a radius ΔR=0.3 are defined as b-jets. Once the objects are defined, the particle level selection strictly mimics the event selection concerning the kinematic selection of the objects, the overlap removal procedure and the event level cut on $E_{\mathrm{T}}^{\mathrm{miss}}$ and $m_{\mathrm{T}}(W)$. The only exception is related to the JVF cut which has no counterpart in the particle level selection since no jets

[5]This definition thus includes the effect of underlying events but not the effect of pile-up

[6]This mimics the behaviour of the electromagnetic calorimeter with respect to QED radiation.

from pile-up are present at that stage. Figure 7.4 shows the comparison of the lepton p_{T} (in the case of electrons) and the $E_{\mathrm{T}}^{\mathrm{miss}}$ between the reconstructed level and the particle level definition. A good correlation is obtained for the lepton p_{T} (and lepton-related quantities in general), while for the $E_{\mathrm{T}}^{\mathrm{miss}}$ a much broader resolution is observed due to the fact that the $E_{\mathrm{T}}^{\mathrm{miss}}$ is indirectly reconstructed from all the other physics objects in the event.

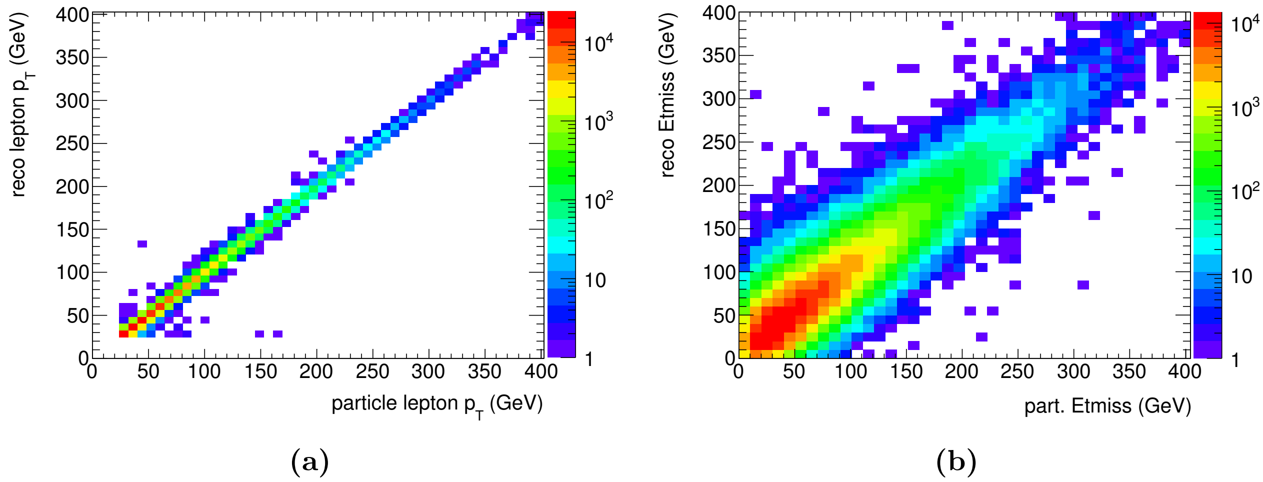

Figure 7.4: Comparison between the reconstructed and particle level definition for the electron p_{T} (a) and $E_{\mathrm{T}}^{\mathrm{miss}}$ (b).

7.3.2 Unfolding definitions

The unfolding procedure not only has to be corrected for the 'smearing' of the relevant distribution by detector effects, but also for the differences between the event selection at reconstruction and particle level and the possible biases on the considered distributions. These originate from detector effects on the lepton and the $E_{\mathrm{T}}^{\mathrm{miss}}$ reconstruction used in the event selection. Furthermore, the event selection explicitly cuts on the distribution under consideration for unfolding. A typical situation consists in three classes of events considered in the unfolding procedure:

- **reco!part events**: events failing the particle level selection but fulfilling the reconstruction level selection and thus being present in the data sample. These events are referred to as 'fake' events since they do not correspond to the particle level phase space under consideration. This class of events arises from the resolution effects in the variables defining the event selection (lepton p_{T}, $E_{\mathrm{T}}^{\mathrm{miss}}$) and migration from events with fewer than three selected particle jets where three or more jets are reconstructed in the detector.

- **part!reco events**: events fulfilling the particle level selection but failing the reconstruction level one. These events are due, as above, to the resolution on the event selection quantities as well as to the inefficiencies in the detector reconstruction and object identification (in particular lepton identification). This class also contains events that fulfil the particle level event selection but have fewer than three selected jets at the reconstruction level.

- **matched events**: events fulfilling both particle and reconstruction level selections. In this class of events the migration matrix connecting particle level and reconstructed level variable is calculated.

The full unfolding procedure which corrects from the reconstructed to the particle-level jet multiplicity distribution, as implemented in the ROOT TUnfold class, is given by:

$$N^j_{\mathrm{part}} = \sum_i \frac{1}{f^j_{\mathrm{acc}}} \cdot \mathbf{M}^{\mathrm{reco}}_{\mathrm{part}}(i,j) \cdot f^i_{\mathrm{purity}} \cdot (1 - f^i_{\mathrm{bgnd}}) \cdot N^i_{\mathrm{reco}} \tag{7.1}$$

where the index j refers to bins in the particle level jet multiplicity distribution and the index i to bins in the reconstructed distribution. All the terms f_{purity}, $\mathbf{M}^{\mathrm{reco}}_{\mathrm{part}}$ and f_{acc}, are extracted from the nominal $t\bar{t}$ Monte Carlo sample generated with Alpgen+Herwig.

- f_{bgnd} is the fraction of background events in the data sample fulfilling the reconstructed level selection. The term $(1 - f_{\mathrm{bgnd}})$ simply implements the background subtraction procedure of the cut&count analysis as previously discussed.

- f_{purity} is the purity of the signal sample at reconstruction level with respect to the particle level selection ($N_{\mathrm{reco\&part}}/N_{\mathrm{reco}}$). It implements the subtraction of 'fake' events performed through a 1-dimensional histogram. Figure 7.5 shows the purity of the reconstructed event sample as a function of the reconstructed jet multiplicity. An overall value of $\sim 70\%$ is found for both the electron and the muon channel, with the 10% decrease in the 3-jet bin due to reconstruction effects generating one extra jets in events with fewer than three particle jets.

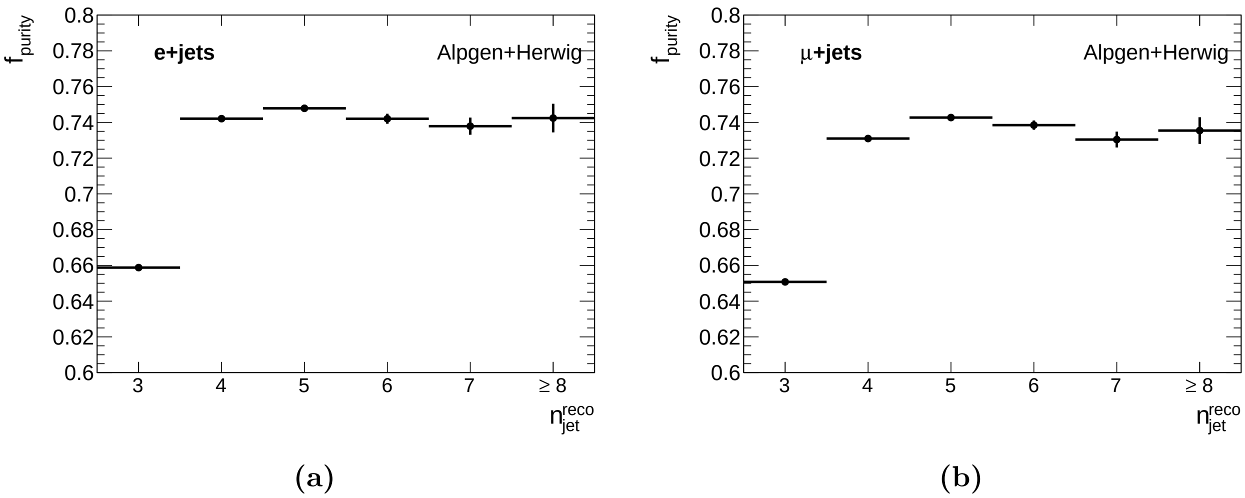

Figure 7.5: Fraction of events fulfilling the reconstruction level selection also fulfilling the particle level selection (f_{purity}) as a function of the reconstructed jet multiplicity for the electron (a) and muon channel (b).

- $\mathbf{M}^{\mathrm{reco}}_{\mathrm{part}}$ is a matrix that corrects from the reconstructed to the particle level distribution within the overlapping phase space. In general the detector effects can be described using a migration matrix that represents the probability for a given value of the particle level variable to be reconstructed with a different value. In the case of the jet multiplicity, the matrix contains the jet resolution contribution as well as the effect of the JVF cut. The migration matrix is shown in Figure 7.6 where each row is normalised to unity. As can be seen, large off-diagonal elements are present in the matrix leading to large bin-to-bin migration. The aim of the unfolding procedure is to invert this matrix. The Bayesian iterative unfolding [156] is used in the current analysis as discussed in the following; it is preferred to direct matrix inversion, which might suffer from instabilities due to limited statistics. It has to be underlined that no attempt is made in the analysis to match particle and reconstructed level in the same event and only the multiplicity distributions are compared in order to maximise the robustness of the analysis.

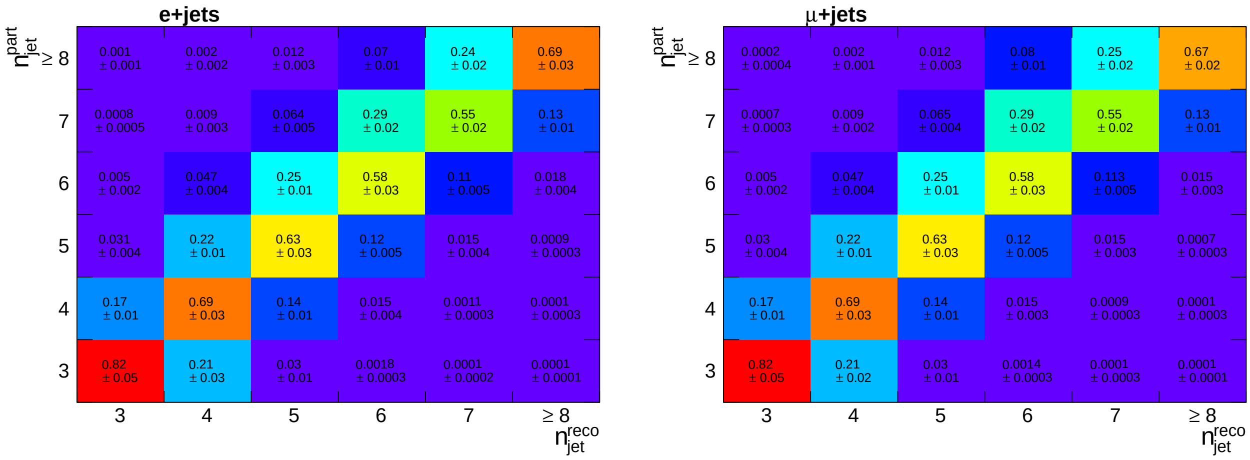

(a) **(b)**

Figure 7.6: Migration matrix describing the smearing from particle to reconstruction level distribution. Matrices are shown for the electron (a) and muon (b) channel. Each row is normalised to unity giving the probability for each particle jet multiplicity to be converted into a given reconstructed jet multiplicity.

- f_{acc} represents the correction for the inefficiencies at the reconstruction level ($N_{reco\&part}/N_{part}$). It is implemented as a 1-dimensional histogram correction as a function of the particle jet multiplicity as shown in Figure 7.7. A reasonably constant behaviour of the corrections is observed apart from the initial bin where an additional inefficiency is caused by events with fewer than 3 reconstructed jets which fall out of the reconstruction level selection. The differences in the average efficiency between the electron and the muon channel are due to the different efficiency of the lepton ID selection in the two cases.

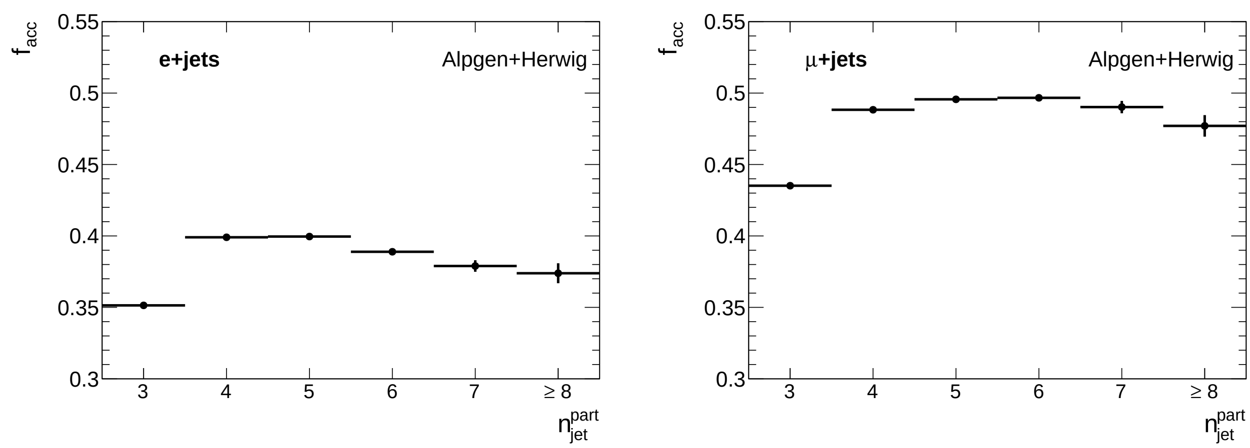

(a) **(b)**

Figure 7.7: Fraction of events fulfilling the particle level selection also fulfilling the reconstruction level selection (f_{acc}) as a function of the particle jet multiplicity for the electron (a) and muon channel (b).

Bayesian unfolding stems directly from the principles of Bayes' theorem:

$$P(C_i|E_j) = \frac{P(E_j|C_j) \cdot P(C_i)}{\sum_k P(E_j|C_k) \cdot P(C_k)} \tag{7.2}$$

allowing to link, on a probabilistic basis, a list of 'causes' to their 'effects'. In the considered case, C_i represents the number of particle jets in the event, and E_j the number of reconstructed jets; $P(E_j|C_j)$ represents the migration matrix that describes the detector effects discussed previously. With the knowledge of the migration matrix, the particle level distribution can be estimated from the reconstructed level distribution with the formula:

$$\hat{n}(C_i) = \sum_j n(E_j) \cdot P(C_i|E_j) \tag{7.3}$$

As any Bayesian approach, the method relies on a prior knowledge (or *belief*) of the probability distribution of the causes ($P(C_i)$ or, in this case, of the particle level distribution), which is further modified by the information contained in the analysed data.

In order to reduce the dependence on the prior assumption, the equation 7.2 is applied iteratively each time using as $P(C_i)$ the outcome of the previous iteration[7]. The number of iteration results from a compromise between the need to reduce the dependence on the prior which, in this context, is represented by the specific choice of the Monte Carlo sample used to derive the unfolding 'ingredients', and the increase of the statistical uncertainty due to multiple usage of the same input information. An example is collected in Figure 7.8; the input distribution and the particle level distribution are taken from the nominal signal sample but the prior distribution in the unfolding procedure is distorted mimicking the largest difference between the generators considered[8]. In the considered case 4 iterations are found to be sufficient re-obtain a good agreement of the unfolded distribution with the reference particle level spectrum thus eliminating any effect of the prior. Concerning the statistical precision, pseudo experiments have been generated smearing the input distribution and considering as final error the RMS of the distribution of the unfolded values in each jet multiplicity bin; the uncertainty on the final distribution doubles when increasing the number of iterations from 4 to 20. Therefore, 4 iterations are used for the Bayesian unfolding in the presented analysis.

Finally, Figure 7.9 shows the full closure of the unfolding procedure. Contrary to Figure 7.8 the efficiency and purity correction factors have also been taken into account. The particle level distribution (black band) can be precisely re-obtained after unfolding (red dashed line) the respective input distribution of the reconstructed number of jets.

7.3.3 Systematic uncertainties

The list of uncertainties in the analysis can be divided into two categories:

- uncertainties originating from the data statistics and the background estimation
- uncertainties related to the unfolding procedure; in particular the dependence of the nominal unfolding corrections on the uncertainties related to physics objects and on the modelling of the signal events

[7]It should be noted that, while Bayesian iterative unfolding reduces the dependence on the prior in the connection between reconstructed and particle-level distribution, in the use case of this analysis, the dependence on the specific Monte Carlo used in the nominal unfolding is also present in the purity and acceptance correction factor.

[8]This was obtained by comparing ALPGEN with MC@NLO predictions at particle level.

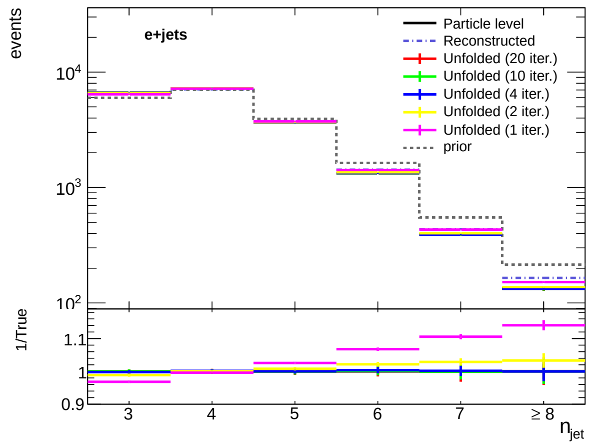

(a)

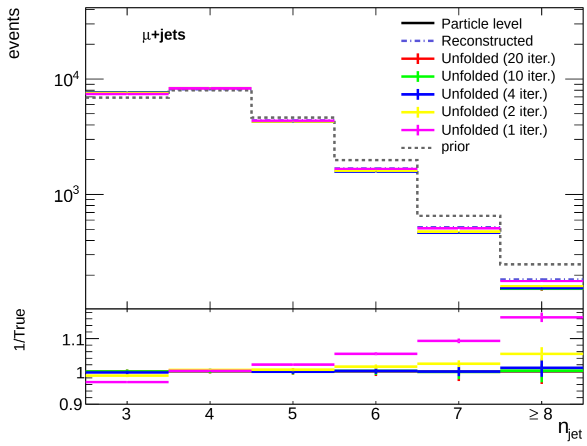

(b)

Figure 7.8: Dependence of the unfolded n^{jet} distribution on the number of iterations used in the Bayesian unfolding. The input n^{jet} distribution is shown as a dashed blue line, the reference particle level distribution is shown in black. The grey dashed line represents the prior distribution used in this particular test. No purity and acceptance correction factors have been considered. Results are shown for the electron (a) and the muon (b) channel.

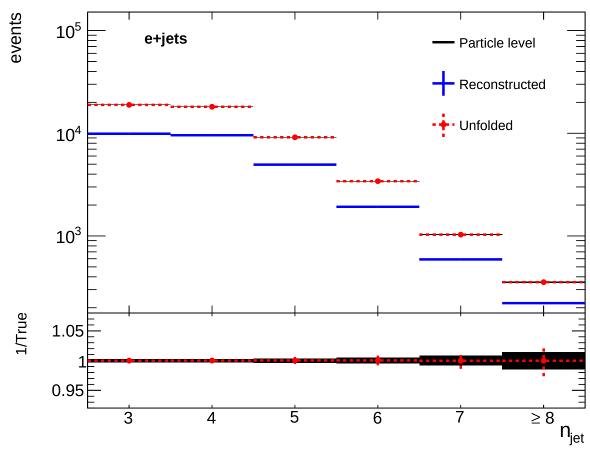

(a)

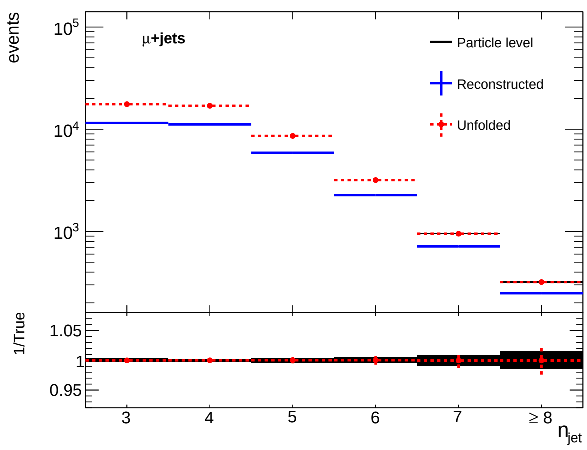

(b)

Figure 7.9: Closure test for the unfolding procedure for the electron (a) and muon (b) channel. The plots display the reconstructed jet multiplicity distribution from the nominal $t\bar{t}$ MC (blue), the reference particle jet multiplicity distribution (black) and the result of the unfolded pseudo experiments. Only MC statistical uncertainties are shown.

The effect of the systematics is evaluated with pseudo experiments; if not otherwise specified, 2000 pseudo experiments are generated ensuring a precision on the estimated uncertainties better than one percent.

For the first category, pseudo experiments are generated by smearing each bin of the background-subtracted data distribution assuming gaussian distributions of the errors reported in Tables 7.5 and 7.6. In the case of the data statistical uncertainties, the smearing is applied independently to each jet multiplicity bin. For the uncertainties related to the background estimation, each individual component is considered correlated across the various bins; therefore, each bin in the jet multiplicity spectrum is shifted coherently. The final uncertainty on the unfolded distribution is obtained by unfolding the set of pseudo experiments with the nominal corrections and computing the square root of the variance of the results in each bin.

The uncertainties related to the unfolding method originate from the closure test and the finite Monte Carlo statistics used to compute the correction factors $\vec{f}_{\rm purity}$, $\mathbf{M}^{\rm reco}_{\rm part}$and $\vec{f}_{\rm acc}$. The latter uncertainties have been estimated by generating pseudo experiments where all the bins of the 1-dimensional purity and acceptance factors and the response matrix are smeared according to their statistical uncertainties. The new correction factors from each pseudo experiment are used to unfold the nominal input distribution and compared with the nominal particle level jet multiplicity reference. The uncertainty is again obtained from the r.m.s. of the unfolded distribution. As shown in Figure 7.9, no appreciable non-closure of the methods is observed within the available Monte Carlo statistics.

Detector related uncertainties do not affect directly the particle level distribution but they alter the evaluation of the unfolding correction factors; as an example, uncertainties on b-tagging efficiency and lepton identification/reconstruction mainly impact the $\vec{f}_{\rm acc}$ term. The effect of the uncertainties after the unfolding procedure is evaluated using the nominal Monte Carlo signal sample. Pseudo experiments are generated using the $t\bar{t}$ jet multiplicity spectrum at reconstructed level obtained by applying the 1-sigma variation of a given systematic uncertainty; each bin content is smeared according to the statistical uncertainty of the Monte Carlo. Unfolded pseudo experiments are compared with the nominal particle level template and the shift of the mean is interpreted as a systematic uncertainty.

Finally, different Monte Carlo generators predict different jet multiplicity distributions at the particle level. At the same time, further differences can appear in the correction factors that link the particle level distribution to the one at the reconstructed level. In the context of the unfolding, only the latter effects have to be considered as modelling uncertainties. They allow to assess the level of bias obtained by using a specific nominal sample for the computation of the correction ingredients or equivalently, how much they depend on the modelling of the various aspects of the $t\bar{t}$ production (parton radiation, fragmentation).

Initially the bias introduced by the unfolding procedure on each $t\bar{t}$ sample has been evaluated; the reconstruction level $n_{\rm jet}$ distribution has been unfolded[9] with the nominal unfolding correction factors and the results have been compared to the corresponding particle level distribution.

The uncertainty related to the modelling systematics has been obtained by comparing the relative bias, the difference of the bias observed for the 'systematic' sample and the bias observed for the baseline sample for that particular uncertainty[10]. As an example, for the *Parton Shower* systematic, the bias on the ALPGEN+PYTHIA sample was compared to the bias for the nominal ALPGEN+HERWIG generator; the latter being zero as previously shown. In the case of the *Monte Carlo* generator and *ISR* systematics, the nominal bias was obtained

[9]Pseudo experiments have been considered by smearing each input following the statistical uncertainty.

[10]The described approach is found to give results compatible with those obtained by unfolding data with correction factors obtained from the different generators.

from the ALPGEN+PYTHIA sample and compared respectively to the ones measured with POWHEG+PYTHIA and the ALPGEN+PYTHIA samples with modified α_S values. A similar procedure has been applied for the propagation of the PDF uncertainties.

Given that the unfolding corrections are evaluated requiring an event selection at particle and reconstruction level that closely matches, the differences between the various generators or the dependence on the generator parameters are generally reduced.

7.4 Results

Figure 7.10 shows the final unfolded distribution in the electron and muon channel. The number of events shown in each of the distributions corresponds to an integrated luminosity of 4.7 fb^{-1}. The particle level jet multiplicity distribution is compared to various $t\bar{t}$ Monte Carlo predictions.

The plots show a reasonable consistency between the electron and muon channel. The results are not combined in the current analysis due to the residual kinematic differences between the two channels, namely the different η acceptance and the different overlap removal procedure. At the same time, a combination will not improve dramatically the result since the main sources of uncertainties are correlated between the two channels.

In the low jet multiplicity bins (3 and 4 jets) all MC predictions agree well with the data. At higher multiplicities, larger differences emerge due to the different approaches in describing the additional parton emission. ALPGEN+HERWIG, due to its multi-leg approach, is in reasonable agreement with data even at high multiplicity.

MC@NLO+HERWIG displays a consistent underestimation of the fraction of events with larger numbers of jets (≥ 6 jets). This is not surprising since MC@NLO is a NLO Monte Carlo which therefore has a description of additional jets beyond the leading one only at logarithmic order in α_S (parton shower).

At the same time, POWHEG+PYTHIA, which is another NLO generator, shows a reasonable agreement with data also at high multiplicity. The agreement has been found to be independent of the parton shower generator POWHEG is interfaced with.

The breakdown of systematic uncertainties after the unfolding procedure is summarised in Tables 7.7 and 7.8. Common sources of systematics have been grouped (added in quadrature) for an easier visualisation; this is the case for the uncertainties related to lepton reconstruction/identification and energy momentum scale, as well as uncertainties related to the background subtraction. Even in the high multiplicity region, the measurement is systematically limited. Uncertainties due to background subtraction dominate at low jet multiplicity values while high jet multiplicity bins are dominated by the jet energy scale uncertainty. With respect to the reconstructed level values of Tables 7.3 and 7.4, the impact of $t\bar{t}$ modelling uncertainties is reduced substantially after the unfolding procedure.

The data also provide information on the effect of the scale uncertainties in multi-leg generators. Figure 7.11 shows a comparison of the unfolded data with the ALPGEN+PYTHIA predictions and the corresponding α_S variations. The magnitude of the effect of the variation of α_S is comparable to the total uncertainty of the analysis demonstrating that the prescription adopted for the computation of the ISR uncertainty for the 2011 analyses is consistent with the data and not over-conservative. At the same time, an improvement in the data/Monte Carlo agreement is obtained with a lower value of α_S for the parton emission in ALPGEN+PYTHIA.

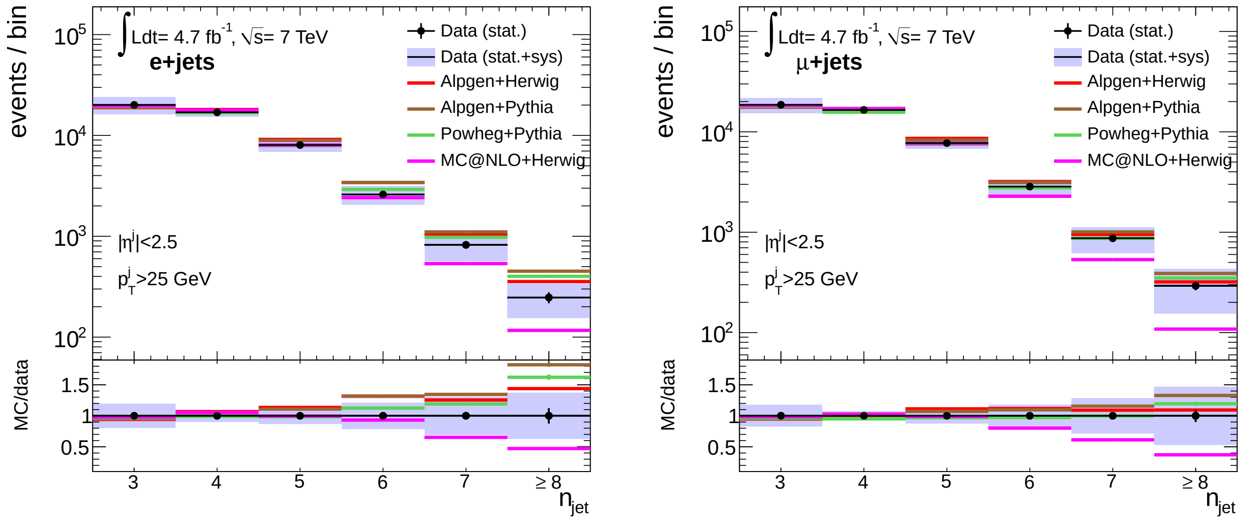

(a) (b)

Figure 7.10: Particle jet multiplicity distribution extracted from data for the electron (a) and muon (b) channel. The uncertainty band contains the total uncertainty, while the black line indicates the uncertainty stemming from the data statistics. The Monte Carlo predictions are shown with their respective statistical uncertainties.

	$n_j = 3$	$n_j = 4$	$n_j = 5$	$n_j = 6$	$n_j = 7$	$n_j \geq 8$
Background subtraction	17	5.6	4.3	5.4	4.3	6.6
jet energy scale	5.3	3.7	10	19	26	32
jet reconstruction	0.1	≤ 0.1	0.2	0.2	0.2	0.4
jet energy resolution	0.7	0.5	1.7	3.3	7.3	4.5
JVF selection	1.2	1.4	1.7	2.1	2.5	2.9
$E_{\mathrm{T}}^{\mathrm{miss}}$ cell-out	≤ 0.1	0.1	0.1	0.1	0.3	0.7
$E_{\mathrm{T}}^{\mathrm{miss}}$ pileup	≤ 0.1	0.1	0.1	≤ 0.1	0.3	0.5
Lepton systematics	2.5	2.5	2.5	2.5	2.5	2.5
b-tagging	5.0	4.5	4.5	4.4	4.4	3.6
PDF	1.3	0.7	1.2	3.1	2.2	1.2
MC generator	0.5	4.4	4.6	0.4	7.7	8.4
Parton shower	3.7	0.1	0.43	2.6	3.8	2.8
ISR/FSR	2.3	1.1	2.1	3.4	5.1	4.8
Unfolding (stat.)	0.4	0.3	0.4	0.6	1.0	1.8
Luminosity	3.9	3.9	3.9	3.9	3.9	3.9
All systematics	20	10	14	21	30	36
Data stat.	1.6	1.5	2.1	3.6	6.1	12
Total	20	11	14	22	31	37

Table 7.7: Effect of the systematic uncertainties on the unfolded distribution in the electron channel. The uncertainties are shown as a relative percentage of the unfolded data yields in each jet multiplicity bin.

	$n_j = 3$	$n_j = 4$	$n_j = 5$	$n_j = 6$	$n_j = 7$	$n_j \geq 8$
Background subtraction	15	3.8	1.9	1.5	1.7	2.6
jet energy scale	5.6	2.7	9.1	16	25	38
jet reconstruction	0.1	≤ 0.1	0.2	0.1	0.3	0.5
jet energy resolution	1.0	0.5	0.7	2.5	6.7	9.8
JVF selection	1.2	1.4	1.7	2.1	2.5	3.0
$E_{\mathrm{T}}^{\mathrm{miss}}$ cell out	0.1	0.3	0.1	0.1	0.1	0.1
$E_{\mathrm{T}}^{\mathrm{miss}}$ pileup	0.1	0.2	0.1	0.1	0.1	0.3
Lepton systematics	1.5	1.5	1.6	1.6	1.6	1.6
b-tagging	5.0	4.7	4.5	4.5	4.7	4.0
PDF	1.6	0.3	1.6	3.5	6.8	5.5
MC Generator	1.5	2.5	4.7	1.2	2.2	2.8
Parton shower	0.7	0.6	1.2	2.3	5.1	19
ISR/FSR	2.6	0.6	2.4	2.8	6.4	8.0
Unfolding (stat.)	0.3	0.3	0.4	0.5	0.9	1.7
Luminosity	3.9	3.9	3.9	3.9	3.9	3.9
All systematics	18	8.5	13	19	29	46
Data stat.	1.5	1.4	1.8	3.0	5.0	9.7
Total	18	8.5	13	19	29	47

Table 7.8: Effect of the systematic uncertainties on the unfolded distribution in the muon channel. The uncertainties are shown as a relative percentage of the unfolded data yields in each jet multiplicity bin.

This type of information will play an important role in improving the description of data provided by the Monte Carlo generators and in better defining the modelling uncertainties.

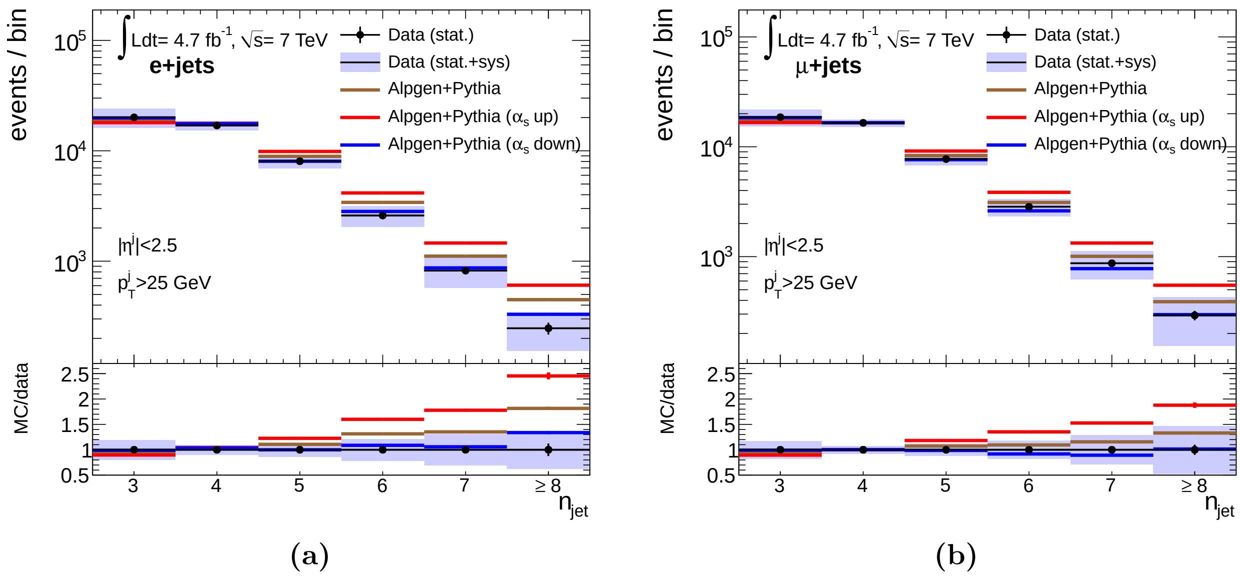

Figure 7.11: Particle jet multiplicity distribution extracted from data for the electron (a) and muon (b) channel. The measurement is compared to the ALPGEN+PYTHIA $t\bar{t}$ sample and the corresponding samples with different α_S scale for the radiation used to estimate the ISR systematics. The Monte Carlo predictions are shown with their respective statistical uncertainties.

Similar conclusions can be obtained by inspecting the jet multiplicity distributions with a higher jet p_{T} cut as documented in Ref. [157]. As an example, Figure 7.12 shows the unfolded jet multiplicity distributions computed for a jet p_{T} cut of 40 GeV. The results presented here use the same input and systematic prescription as the ones described by the quoted official ATLAS document but implement a simpler and more intuitive unfolding procedure which nevertheless leads to very consistent results in terms both of the central values and of the impact.

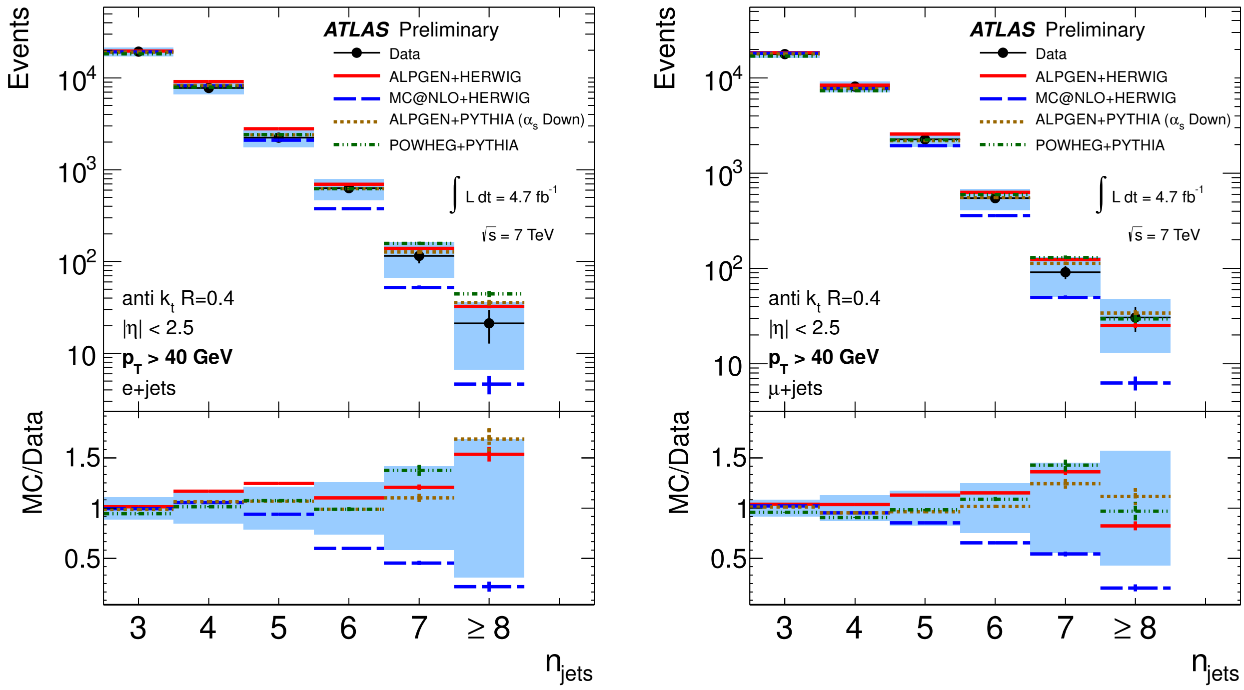

(a) (b)

Figure 7.12: Particle jet multiplicity distribution for jet $p_{\mathrm{T}} > 40$ GeV. Unfolded data are shown in the electron (a) and in the muon (b) channel. The uncertainty band contains the total uncertainty, while the black line indicates the uncertainty stemming from the data statistics. The Monte Carlo predictions are shown with their respective statistical uncertainties.

Chapter 8

Search for $t\bar{t}H(b\bar{b})$: definitions

The $\sqrt{s}$=8 TeV 2012 data sample collected by ATLAS represents a perfect opportunity to search for rare phenomena that could improve our current understanding of the Standard Model or be the footprints of new physics scenarios.

The present chapter contains the description of the analysis aiming at the measurement of the associated production of the Higgs boson and a top quark pair using the 2012 ATLAS data sample. The initial part will summarise the properties of the signal as well as the analysis strategy and the event selection. The second part will be devoted to the description of the modelling of of $t\bar{t}$ events which represent the main background for the analysis.

8.1 Motivation

After the discovery of a particle highly compatible with the Standard Model Higgs boson at a mass of approximately 125 GeV, the attention has turned to a precise characterisation of this particle, in particular through a measurement of its couplings. Identifying the new state in as many production and decay modes as possible is a key ingredient to probing the consistency of the Standard Model Higgs boson hypothesis or looking for unexpected deviations.

The decays of the particle into vector bosons (WW, ZZ, $\gamma\gamma$) have driven the discovery and the measurement of its mass, spin and parity. Direct evidence for its production through vector boson fusion and its coupling to fermions (mainly $H \to \tau\tau$) has also been obtained [158].

The associated production with a $t\bar{t}$ pair is the Higgs boson production mode with the smallest cross section. Its measurement represents a key ingredient in the measurement of the Yukawa coupling of the top quark. The $t\bar{t}H$ vertex also yields the dominant contribution to the main Higgs boson production mode (gluon fusion) and it also intervenes in Higgs boson decay to a photon pair[1]. However, its contribution to these processes only enters through loop effects which cannot be disentangled from the possible presence of 'new physics' interactions. The measurement of the $t\bar{t}H$ production mode will allow to probe directly the top Yukawa coupling from a tree-level diagram. Several final states can be considered according to the Higgs boson decay mode. This can be exploited in the search for $t\bar{t}H$.

Given the small production cross section and the available integrated luminosity, decay modes with the largest branching ratio are the most promising ones. For a Higgs boson mass of 125 GeV, the decay into a b quark pair has the largest branching fraction. A measurement of $t\bar{t}H$ with the Higgs boson decaying into $b\bar{b}$ will also contribute to probing the Higgs boson coupling to bottom quarks. This decay mode is not accessible for the dominant gluon fusion production

[1]The decay into a photon pair is mainly driven by the W boson loop; the W and fermion loops interfere destructively.

mode due to the overwhelming QCD multijet background. The associated production with a top quark pair (or a vector boson) allows the reduction of the background to a manageable level.

The interest in this topology extends beyond Higgs boson physics as several other 'new physics' scenarios predict final states with top quark pairs and additional heavy flavour quarks; this is the case of heavy top quark partners [159] or two Higgs doublets models (2HDM) [160].

Analyses searching for $t\bar{t}H$ with the Higgs boson decaying into a bottom quark pair have been performed both at ATLAS [161] and CMS [162] with no significant excess observed on top of the background-only predictions. Using the 7 TeV 2011 dataset and the lepton+jets final state, a 95% CL upper limit of 13.1 times the Standard Model value was set by ATLAS on the $t\bar{t}H$ cross section for a Higgs boson with a mass of 125 GeV. Combining the 2011 7 TeV and the 2012 8 TeV datasets, exploiting both single lepton and dilepton final states, the CMS collaboration set an upper limit of 4.5 times the Standard Model $t\bar{t}H$ cross section for the same mass.

Given the new boson discovery, the attention and optimisation of the analysis are focused on probing the $t\bar{t}H$ production mode in particular for a Higgs boson mass of 125 GeV. Results are also interpreted for other mass values.

8.2 Event Selection

Signal events feature a $t\bar{t}$ pair and a Higgs boson in the final state. The decay products of $t\bar{t}$ are exploited to collect the events (trigger) and to reduce the non-$t\bar{t}$ background. As for the other analyses presented in this thesis, the single lepton $t\bar{t}$ decay topology is used in the search for the $t\bar{t}H$ process since it ensures a good compromise between signal efficiency and background rejection. The typical final state contains one isolated lepton and six jets, four of which originating from b-quarks: two from the Higgs boson decay and two from the decay of the top quarks. While the best sensitivity to the channel is obtained for events with at least 6 jets and at least 4 b-tagged jets, a looser preselection has been applied. As will be outlined later in the chapter, this helps in increasing the signal acceptance as well as improve the knowledge of the background.

The detailed selection of $t\bar{t}$ events has been outlined in Chapter 5. The following modifications are applied for the $t\bar{t}H$ analysis:

- *jets requirement*: events are required to have at least 4 selected jets.
- *b-tagged jets requirement*: events are required to have at least two b-tagged jets. This requirement has little effect on $t\bar{t}H$ with $H \to b\bar{b}$ events, which are expected to contain four b-quarks in the final state; at the same time it brings a considerable reduction of the non-$t\bar{t}$ background.
- *kinematic selection*: no selection is applied on the $E_{\mathrm{T}}^{\mathrm{miss}}$ and the hadronic W transverse mass in the events. These cuts are usually introduced to reduce the non-$t\bar{t}$ background, which in the current analysis is already significantly reduced by the requirement of two or more b-tagged jets. The signal over background ratio of the analysis is not altered by the relaxation of the selection since $t\bar{t}H$ and the main background ($t\bar{t}$) are affected in the same way. Nevertheless, it brings an increase in acceptance of ~ 15 % which helps to improve the statistical precision of the analysis.
- *second lepton veto*: a lower p_{T} cut and looser selection is considered when vetoing on additional leptons. Events are rejected if an additional muon or electron with p_{T}>15 GeV

is selected. Additional muons are required to pass the same identification and isolation criteria used in the main analysis while additional electrons are required to pass the *medium likelihood* identification criteria[2] and fulfil the isolation requirement $p_T^{0.3}/p_{\mathrm{T}} < 0.12$. The tighter veto was motivated by the need to keep orthogonality in the event selection with $t\bar{t}H$ analyses using the dileptonic $t\bar{t}$ final states or non-$b\bar{b}$ Higgs decay modes. The application of this veto brings a yield reduction of a few percent in events with at least 6 jets and up to 10% in events with 4 jets.

After this preselection, events are further categorised into independent analysis "regions" defined by the number of jets with $p_{\mathrm{T}} > 25$ GeV and by the number of b-tagged jets; three 'bins' in jet multiplicity (4, 5, ≥6) and three 'bins' in b-tagged jet multiplicity (2, 3, ≥4) are considered. In the following, a given region with m jets and n b-tagged jets will be referred to as "(mj, nb)".

The analysis uses the full $\sqrt{s} = 8$ TeV collision data sample collected by ATLAS during 2012, corresponding to a luminosity of 20.3 fb^{-1}, after data quality requirements. All the results presented in the rest of this thesis will contain the combination of the electron and muon channels. Similar performance and similar background composition is obtained in the two channels with a yield ratio between electron and muon channel of ~ 0.8. This ratio does not display any significant deviation in any of the considered analysis regions. The main differences, apart from the small effect of η acceptance, are related to the identification and trigger efficiencies. The identification efficiency is higher in the muon channel due to lower requirement on background rejection, while a higher trigger efficiency is observed in the electron channel due to the configuration of the muon spectrometer.

The event display for a data event in the muon channel matching the signal topology (6 jets and 4 b-tagged jets) is described in Appendix G.

8.2.1 Tag rate function method

With an average efficiency of 70% for tagging jets originating from b-quarks and a <1% mistag rate, the requirement of a large number of b-tagged jets can lead to a severe impact on the available Monte Carlo statistics. Large fluctuations in the predicted Monte Carlo distributions negatively impact the sensitivity of the analysis and lead to unreliable estimates of the effect of systematic uncertainties.

In order to mitigate this problem, the so-called *tag rate functions* (TRF) method is applied. Instead of 'direct' tagging the Monte Carlo jets with the output of the b-tagging algorithm, parameterised efficiencies are used to extract the probability of the jet to be tagged. Efficiencies are extracted from $t\bar{t}$ events as a function of the jet p_{T}, $|\eta|$ and the Monte Carlo flavour of the jet[3].

For a given requirement on the number of b-tagged jets in the events (n_b), all the possible permutations of labelling n_b jets as "tagged" are considered. For each permutation, a weight is applied to each jet; jets considered "tagged" are assigned a weight equal to the tagging

[2] A likelihood-based electron identification has been introduced to combine the discriminating variables used in the standard electron identification in one multivariate discriminant. It is used mainly in analyses selecting two or more leptons, their use in a single electron analysis is limited by the cut-based selection applied at the trigger level. The *medium likelihood* operating point has similar efficiency as the *medium* operating point but a smaller fake rate.

[3] the Monte Carlo jet flavour is defined by looking at partons with p_{T}>5 GeV within a $\Delta R < 0.3$ cone around the jet direction. If a b-quark is found, the jet is labelled with b origin. If no b-quarks are found, c-quarks are considered. If no c-quarks are also found either, a jet is labelled as a 'light' jet.

probability, jets considered as "un-tagged" are assigned a weight equal to one minus the tagging efficiency. Multiplying all jet weights gives the probability for that event to contain the selected number of tags, independently of the number of jets selected by the b-tagging algorithm. This allows the use of all events in the pre-b-tagged sample to predict the normalisation and shape after any b-tagging selection. The shape of the distributions built using b-tagged jet information is reproduced by randomly choosing one of the possible permutations based on their relative probability.

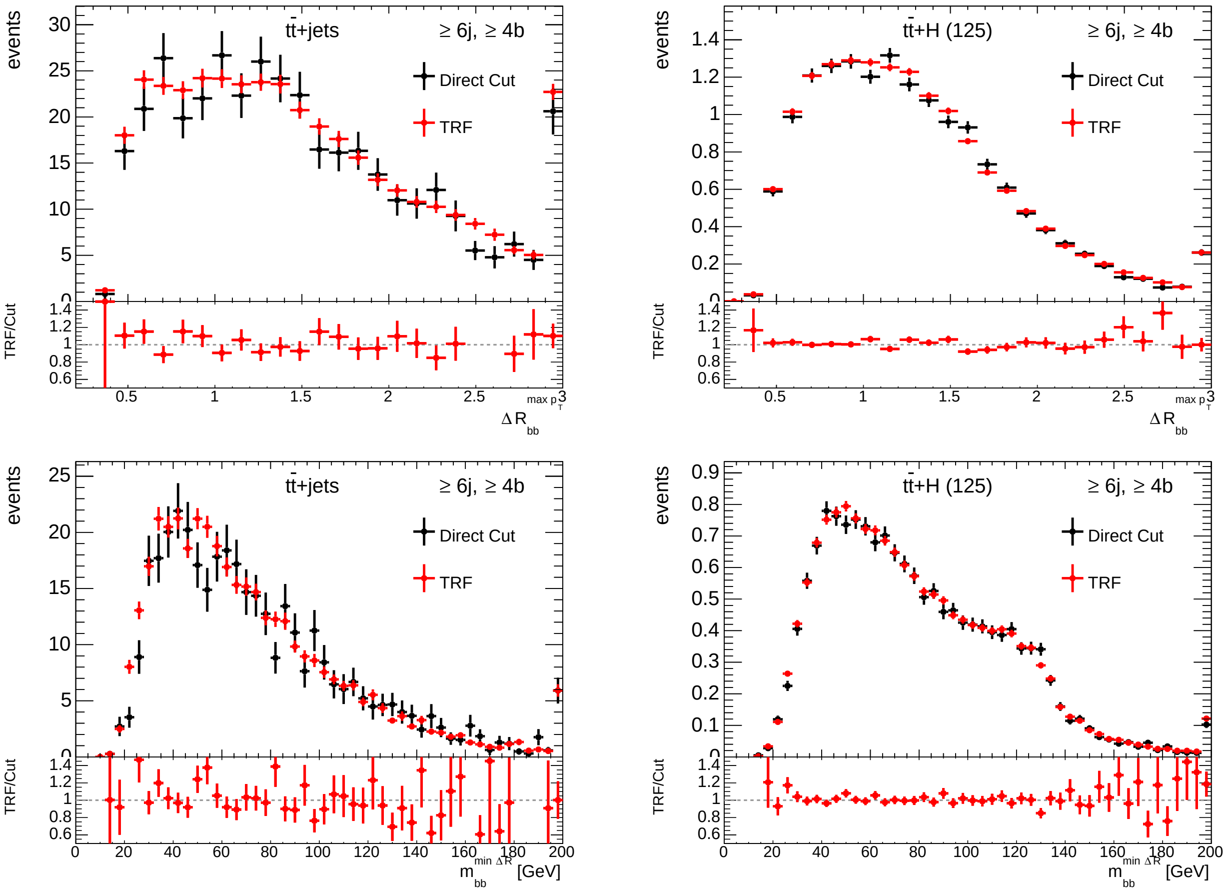

Figure 8.1: Comparison between the predictions obtained with a direct cut on b-tagging algorithm and with the TRF method for variables in the ($\geq$ 6j, $\geq$ 4b) region. The ΔR between the pair of b-tagged jets with the highest vectorial sum p_{T} (top) and the invariant mass of the pair of b-tagged jets closest in ΔR (bottom) are shown for the $t\bar{t}$+jets (left) and the $t\bar{t} + H$ (right) samples.

The TRF method relies on two main assumptions: the tagging efficiencies of individual jets in a given event can be considered independent of each other and the variables used to parameterise the efficiency are sufficient to describe the detector effects. It should be noted that the former assumption is also at the basis of the data-driven correction of the tagging efficiencies with scale factors. Careful validation and closure tests on Monte Carlo have been performed; within the available statistics, the TRF method provides a good description of yields and shapes with respect to the direct application of the b-tagging algorithm in the analysis regions and for all processes.

The good results from the closure tests also indirectly demonstrate that no additional parameterisation of the tagging efficiency is needed other than jet flavour type and kinematics, and that the efficiencies obtained from an inclusive $t\bar{t}$ sample are applicable to events with a larger number of b-tagged jets. In particular, within the phase space and for the variables considered in the analysis, no significant need for an efficiency correction as a function of the ΔR distance between two jets is observed.

Figure 8.1 shows the comparison between the prediction obtained with the TRF method and the direct application of the cut on the b tagging algorithm output for the $t\bar{t}$+jets background and the $t\bar{t}H$ signal samples; the comparison is shown for the ($\geq$ 6j, $\geq$ 4b) region which contains the largest number of jets and b-tagged jets. Two of the variables used to build multivariate discriminants to separate signal and background that will described in detail in Chapter 9, are displayed: the ΔR between the pair of b-tagged jets with the highest vectorially summed p_{T} and the invariant mass of the pair of b-tagged jets closest in ΔR. No significant deviations between the 2 methods are found and, at the same time, the figures give an idea of the gain in statistical uncertainty that is obtained when using the TRF approach especially for $t\bar{t}$+jets. Additional technical information on the tag rate function method can be found in AppendixA.

8.3 Signal properties

$t\bar{t}H$ events are generated using NLO matrix elements obtained from the HELAC-Oneloop package [163]. Powheg Box [119] is employed as an interface to shower Monte Carlo programs; this joint approach is usually referred to as PowHel generation. The samples are produced using the CT10NLO PDF sets and with factorisation and renormalisation scales set to $\mu_0 = \mu_{\mathrm{F}} = \mu_{\mathrm{R}} = m_t + m_H/2$. A value of 172.5 GeV is used for the top quark mass. Samples with Higgs boson masses of 115 GeV, 120 GeV, 125 GeV, 130 GeV and 135 GeV were produced with fully inclusive $t\bar{t}$ and Higgs boson decays. Powhel was interfaced with Pythia 8.1 [164] with the AU2 underlying event tune [127]. Events were normalised to the NLO cross section from Ref. [47] and NNLO Higgs boson decay branching fractions [165] are used.

While signal events are expected to be mainly concentrated in the region with six jets and four b-tagged jets, significant migration to other jet and b-tag multiplicity regions can occur. Acceptance effects and jet merging can reduce the number of reconstructed jets in the detector. Dileptonic $t\bar{t}$ decay modes (ll or $l + \tau$) can still fulfil the event selection criteria in cases where one of the leptons does not fulfil the requirement for the veto or is a tau lepton that decays hadronically. These types of events mainly arise at low jet multiplicity. Furthermore, additional jets can be produced by ISR or FSR effects.

Given that the chosen operating point for the b-tagging algorithm has an average 70% efficiency for tagging jets originating from b-quarks, it is expected that roughly only one quarter of events where the four b-quarks in the final state are within the detector acceptance will present four b-tagged jets. A significant migration of signal events in regions with a b-tag multiplicity smaller than four is observed. In addition, other Higgs boson decay modes do not involve b-quarks[4] and they become more important in analysis regions where the requirement on the number of b-tagged jets is reduced.

Table 8.1 summarises the described effects showing the expected yields for the $t\bar{t}H$ process after the event selection, in different jet and b-tag multiplicities. A mass of 125 GeV for the Higgs boson has been considered. As discussed, $t\bar{t}H$ events clearly concentrate in $\geq$ 6 jets topologies with only 14% of the selected events in these regions having at least 4 b-tagged jets.

The fraction of the selected $t\bar{t}H$ events containing a Higgs boson decaying into $b\bar{b}$ is shown in Table 8.2. This decay mode largely dominates in events with at least 4 b-tagged jets, contributing for at least 93 % of the total $t\bar{t}H$ yields. With a decreasing number of b-tagged jets, the $H \to b\bar{b}$ fraction decreases to as low as 50%. The main additional contributors are

[4]The exception. $H \to ZZ \to b\bar{b} + X$, has a very small branching ratio

	2 b-tags	3 b-tags	$\geq$4 b-tags
4 jets	31.3	12.1	1.8
5 jets	40.9	22.3	5.8
$\geq$6 jets	63.8	39.1	16.4

Table 8.1: Expected numbers of $t\bar{t}H$ events for a Higgs boson mass of 125 GeV. Events are normalised to an integrated luminosity of 20.3 fb^{-1}. Each row corresponds to a specific jet multiplicity (4,5,$\geq$6) and each column corresponds to a specific b-tagged jet multiplicity (2,3,$\geq$4).

the Higgs boson decay into τ lepton pairs and into W boson pairs; the latter represents $\sim$ 30 % of the total $t\bar{t}H$ yields in the region with 2 b-tagged jets and $\geq$ 6 jets. Finally, it has been verified that other Higgs boson production modes bring a negligible contribution after the event selection.

	2 b-tags	3 b-tags	$\geq$4 b-tags
4 jets	62 %	90 %	98 %
5 jets	57 %	87 %	97 %
$\geq$6 jets	48 %	80 %	93 %

Table 8.2: Fraction of selected $t\bar{t}H$ events where the Higgs boson decays into $b\bar{b}$ with respect to the total selected $t\bar{t}H$ events. Numbers are extracted for a sample with m_H=125 GeV after the full event selection. Each row corresponds to a specific jet multiplicity (4,5,$\geq$6) and each column corresponds to a specific b-tagged jet multiplicity (2,3,$\geq$4).

8.4 $t\bar{t}$ as a background to $t\bar{t}H$

Given that in signal events the Higgs boson is produced in association with a top quark pair, $t\bar{t}$+jets production (in particular $t\bar{t}$+b-jets) clearly constitutes the main background to the analysis. $t\bar{t}$+light jets and $t\bar{t}$+c jets events can also appear in the high b-tagged jets multiplicity signal regions due to tagging of light jets and jets from c-quarks.

Since a good control over the background predictions is of primary importance in the search for small signals, the modelling of $t\bar{t}$+jets events over a large variety of topologies characterised by different jet and b-tagged jet multiplicities is one of the critical aspects of the analysis. This refers to the normalisation in each topology as well as the description of kinematic quantities within each region.

The $t\bar{t}$+jets sample is generated inclusively using the Powheg generator with the CT10 PDF set. Hadronisation and fragmentation effects are implemented with Pythia 6 using the Perugia2011C underlying event tune. Events are normalised to the inclusive $t\bar{t}$ cross section computed at NNLO accuracy. Being an NLO generator, Powheg implements only the first additional parton emission (at LO accuracy); additional parton emissions are treated by the parton shower implementation. While in principle this approach is not the ideal one for describing high multiplicity events, analyses based on the 2011 dataset, like the one presented in Chapter 7, have shown that Powheg is capable of giving an equally good description as the LO multi-leg generators of the jet multiplicity distribution in $t\bar{t}$-enriched events.

At the same time, the NLO gives good modelling of inclusive quantities related to the kinematics of the $t\bar{t}$ decay products; these will represent an important ingredient in the search for the $t\bar{t}H$ signal. For what concerns the $t\bar{t}$+HF production, only diagrams of the type $gb \rightarrow t\bar{t}b$ are directly included in POWHEG while the production of the additional HF partons is obtained with the parton shower though gluon splitting or evolution of the incoming b-quark. Nevertheless, POWHEG is capable of providing a good description of the event kinematics in $t\bar{t}$+HF enriched data with three or more b-tagged jets as will be outlined in the next chapter. The description of $t\bar{t}$+HF events with POWHEG has been compared with the results from the MADGRAPH generator; a sample with $t\bar{t}$ plus up to three additional partons (including b and c quarks) at LO has been generated and interfaced with PYTHIA for the parton shower. The comparisons have been performed using truth particle information since the MADGRAPH sample was not available with full detector simulation. Figure 8.2 shows the comparison of the kinematics of additional b-jets in $t\bar{t}$+HF events. The precise definition used will be outlined later in this section. Large angular separation or high invariant mass of the b-jet pair are the region of the phase space were the approximation used by the parton shower are supposed to become less valid. Although no perfect agreement between generators is found, differences are within 20% demonstrating a general capability of POWHEG to describe with the parton shower formalism, a region of phase space generally covered by matrix element calculations. Ultimately the observed differences will be treated as a source of systematic uncertainty. Additional technical details on the production of $t\bar{t}$+jets events with MADGRAPH are reported in Appendix B.

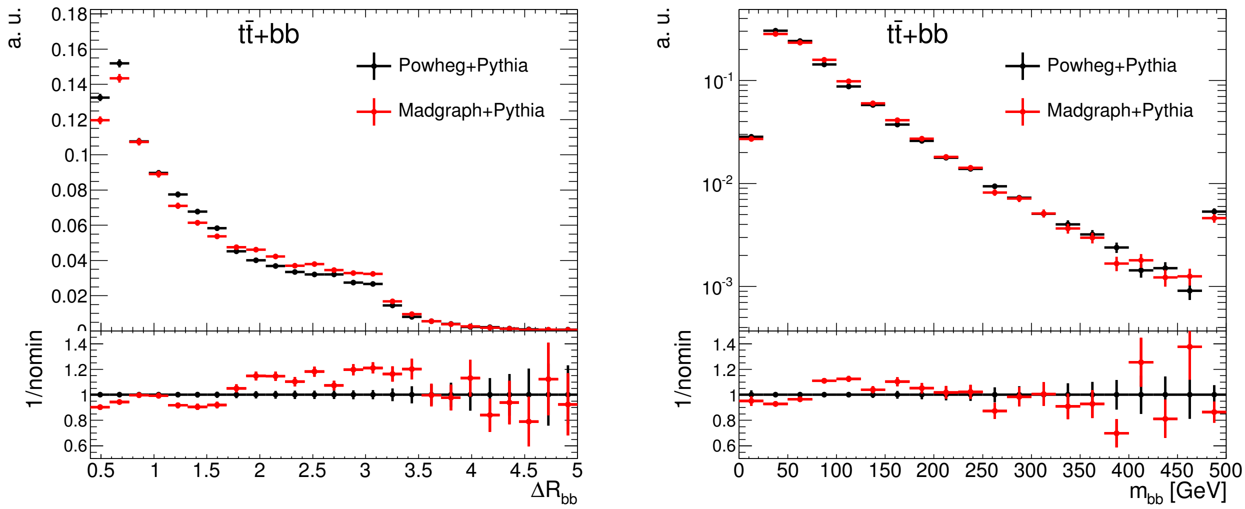

(a) (b)

Figure 8.2: Comparison between POWHEG and MADGRAPH of the kinematics of additional HF jets in $t\bar{t}$+HF events. The ΔR (a) and invariant mass (b) of the pair of b-jets in events not originating from $t\bar{t}$ decay products is shown.

It has also been found that the ALPGEN generator is not able to provide a detailed description of the heavy flavour content. In the available version of ALPGEN, no merging between the parton shower and matrix element calculation is available for massive b and c quarks. Without the possibility to use LO diagrams[5], the production of heavy flavour (even single heavy flavour) relies almost entirely on the parton shower. At the same time ALPGEN does not provide an NLO description of inclusive quantities. Therefore, it has been decided not to rely on the ALPGEN generator in the analysis.

[5]The default $t\bar{t}$ event generation with ALPGEN does take into account b-partons as proton constituents, therefore diagrams like $gb \rightarrow t\bar{t}b$ are not included.

The ability of the POWHEG generator to describe the characteristics of $t\bar{t}$ events has been intensively investigated using the data sample collected at 7 TeV. Detailed studies of the differential cross-sections for kinematic distributions of the top partons in $t\bar{t}$ events using the full 2011 dataset collected by the ATLAS detector can be found in Ref. [166]. Differences have been observed between the unfolded data distributions and the predictions from POWHEG+PYTHIA for the transverse momentum of the top quark[6] and of the $t\bar{t}$ system. Monte Carlo distributions were found to be harder than data, and in the high p_{T} regime, the differences are larger than the combined statistical and systematic uncertainties.

Corrections derived from the data/Monte Carlo ratio measured in the 7 TeV analysis are applied to the 8 TeV $t\bar{t}$ samples used in the current analysis; they have been implemented as two multiplicative reweighting factors computed event-by-event as a function of the top quark p_{T} and the $t\bar{t}$ system p_{T}. Table 8.3 summarises the correction factors with the corresponding binning and the total uncertainties.

$t\bar{t}$ p_{T}				
Bins[GeV]	[0, 40]	[40, 170]	[170, 340]	[340, 1000)
Rew. factor	1.04 ± 0.12	0.99 ± 0.14	0.81 ± 0.18	0.68 ± 0.22

top p_{T}							
Bins[GeV]	[0, 50]	[50, 100]	[100, 150]	[150, 200]	[200, 250]	[250, 350]	[350, 800)
Rew. factor	1.01±0.01	1.01±0.02	1.01±0.01	1.00±0.01	0.96±0.04	0.91±0.09	0.88±0.17

Table 8.3: Reweighting factors for the POWHEG+PYTHIA sample as a function of the $t\bar{t}$ system p_{T} (top) and the top quark p_{T} (bottom). The two factors are multiplied to obtain the event weight correction.

The derivation of the correction takes into account the non-negligible correlation ($\sim 30\%$) between the top quark p_{T} and the p_{T} of the $t\bar{t}$ system. In the case of the $t\bar{t}$ p_{T}, the factors are directly obtained from the corresponding data/MC distribution ratio in the 7 TeV analysis. Corrections as a function of top quark p_{T} have been re-derived from the unfolded differential data distribution after applying the $t\bar{t}$ p_{T} correction to the Monte Carlo.

Figures 8.3 and 8.4 show the effect of the reweighting procedure for $t\bar{t}$ events on the data/Monte Carlo agreement in regions with at least two b-tagged jets. An improvement in the data description is clearly visible in the jet multiplicity distribution and the p_{T} of the leading jet. The former is driven by the $p_{\mathrm{T}}^{t\bar{t}}$ component of the correction while the latter is mainly due to the residual correction as a function of the top quark p_{T}; similar improvements are observed also in other variables like $H_{\mathrm{T}}^{\mathrm{had}}$.

The $t\bar{t}$+jets events have been categorised according to the flavour of the additional jets. Initially the procedure considers b/c hadrons with $p_{\mathrm{T}}>$ 5 GeV[7] not originating from $t\bar{t}$ decay products; this excludes jets originating from b quarks from top decay as well as jets produced by c quarks from hadronic W boson decays.These hadrons are then matched to particle jets that satisfy the acceptance selection of the analysis (p_{T} >25 GeV and $|\eta|$ <2.5); a match is confirmed if the angular distance (ΔR) is smaller than 0.3. Events where at least one such particle jet is matched to a b-hadron defined above (or a c-hadron originating from a b-hadron cascade) are labelled in the following as $t\bar{t}+b\bar{b}$ events. Events failing this selection and with at least one particle jet matching to a selected c-hadron are labelled as $t\bar{t}+c\bar{c}$. Events labelled as

[6] In this context, one of the two top quarks in the event is randomly considered.

[7] The usage of hadrons helps in reducing the dependence on the Monte Carlo evolution of particles during fragmentation and improves the matching with particle level jets. The p_{T} cut mimics the selection used to classify jets in the application of the flavour tagging scale factors.

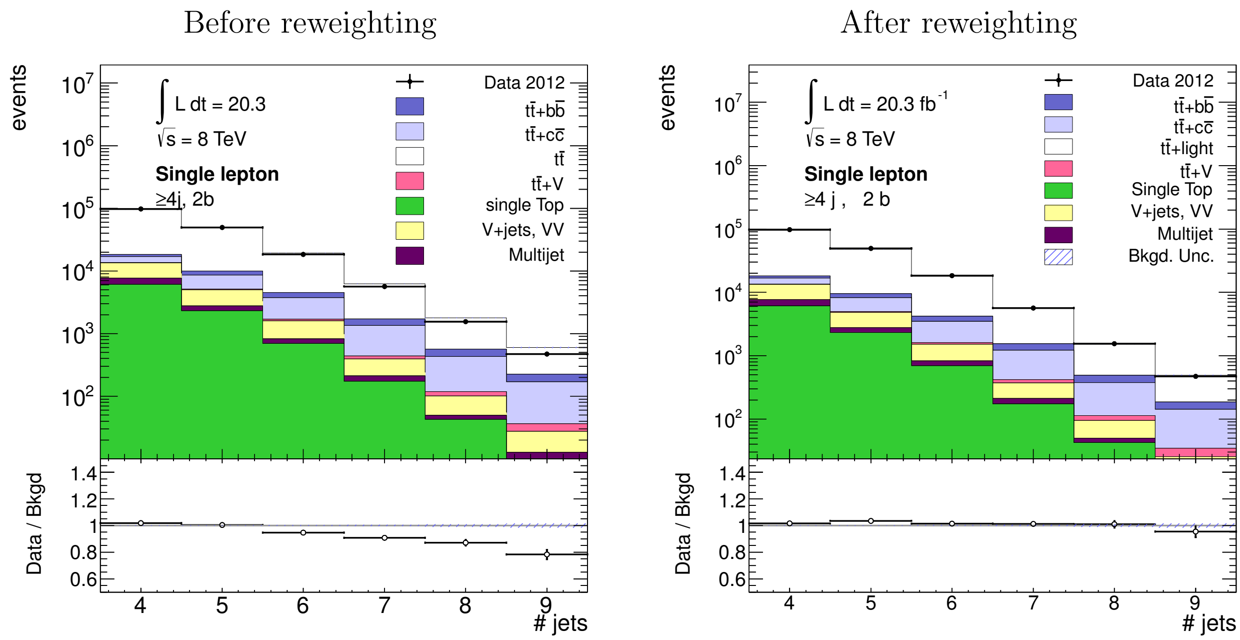

Figure 8.3: Jet multiplicity distribution before and after the reweighting procedure based on the top quark and $t\bar{t}$ system p_{T}. Events with exactly 2 b-tagged jets are considered. The uncertainty band only contains the Monte Carlo statistical error.

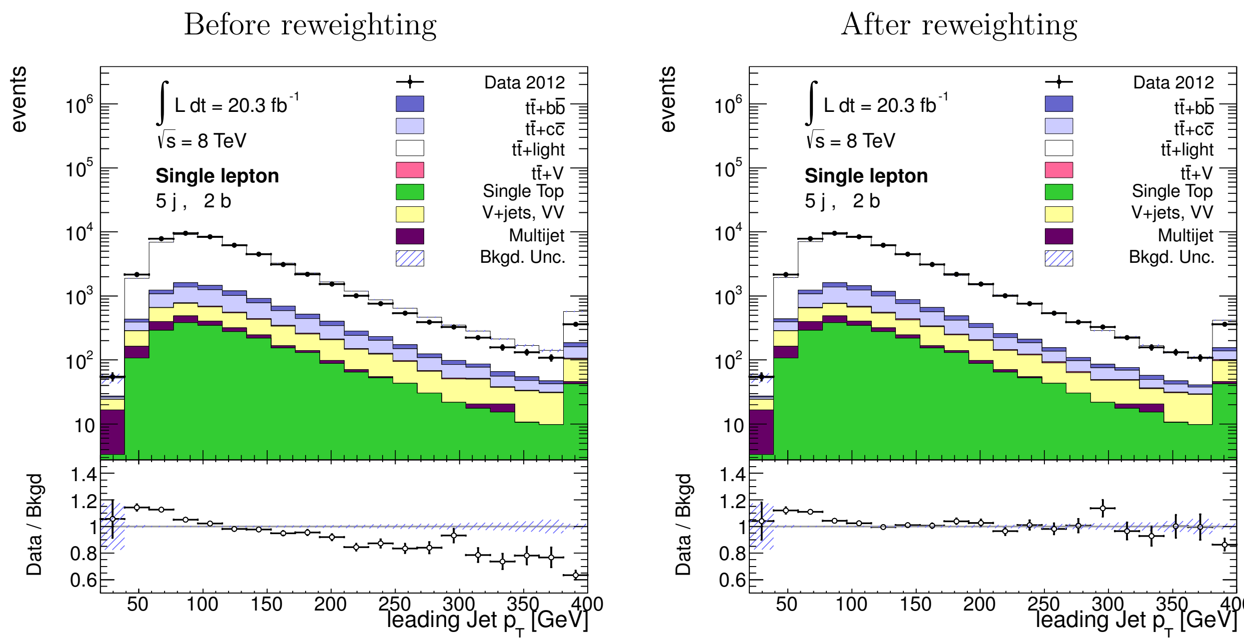

Figure 8.4: Leading jet p_{T} distribution before and after the reweighting procedure based on the top quark and $t\bar{t}$ system p_{T}. Events in the (5j, 2b) region are considered. The uncertainty band only contains the Monte Carlo statistical error.

either $t\bar{t}$+$b\bar{b}$ or $t\bar{t}$+$c\bar{c}$ will generically be referred to as $t\bar{t}$+HF events. The remaining events are labelled as $t\bar{t}$+light jet events, including those with no additional jets on top of the $t\bar{t}$ decay products.

The advantage of this classification procedure is that the additional heavy flavour jets are only considered if they fall within the detector acceptance where they can produce a visible effect. It also helps to better define and decouple the effect of tagging systematic uncertainties[8]. Two b-tagged jets in the final state can appear in each $t\bar{t}$+jets category due to the b-quarks produced in the $t\bar{t}$ decay.

$t\bar{t}$+light jets events do not have any additional source of heavy flavour partons. A third b-tagged jet in the event has to originate from the tagging of one of the $t\bar{t}$ decay products or an additional radiated jet originating from light quarks or gluons. The hadronically decaying W boson produces a c-quark in $\sim 30\%$ of the cases [6]. Since the tagging probability of c-quark jets is approximately 20 to 25 times larger than the tagging probability of light-flavour jets, the former is the main process responsible for the development of a third b-tagged jet in $t\bar{t}$+light events. At most one c-quark can be produced by the hadronic decay of a W boson; a fourth b-tagged jet necessarily has to come from the mistagging of a light-flavour jet. For $t\bar{t}+c\bar{c}$ events, at least one additional c-quark is present in the detector acceptance. Additional b-tagged jets are then mainly generated by the tagging of jets from c-quarks. Finally, in the $t\bar{t}+b\bar{b}$ process, at least one additional b-quarks is present in the event. The possible of tagging jets not originating from b-quarks is important only to obtain a fourth b-tagged jet in the event.

Detailed studies using a finer classification of the heavy flavour content have been performed in the context of the comparison between Powheg and Madgraph and the determination of systematic uncertainties. $t\bar{t}$+HF events are categorised based on the number of jets matched to additional b- or c-hadrons; furthermore, the number of b- or c-hadrons matched to a single jet is considered. Jets containing only one hadron are labeled with 'b' and 'c', while the label 'B' and 'C' indicate jets matched to more than one hadron as a result of a collinear unresolved gluon splitting into $b\bar{b}$ or $c\bar{c}$. Figure 8.5 shows the decomposition of $t\bar{t}$+HF events into sub categories for different jet and b-tagged jet multiplicities.

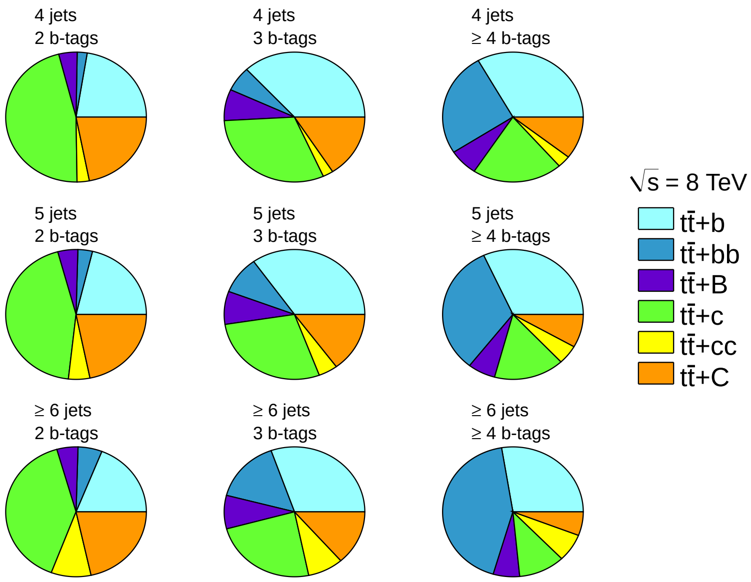

Figure 8.5: Relative contributions of the various $t\bar{t}$+HF categories in different jet and b-tagged jet multiplicity bins. The categorisation is based on the number of particle jets matched to additional heavy flavour hadrons not originating from the $t\bar{t}$ decay chain; jets matched to more than one hadron indicating a collinear gluon splitting are labelled with 'B' and 'C'.

[8]This procedure was not adopted in the analysis performed using 2011 data where events were flagged as $t\bar{t}$+HF simply based on the information of the particular diagrams used to generate them, without any acceptance cut on the additional heavy flavour partons.

The relative contribution from $t\bar{t}$ plus additional b-quarks increases with the number of b-tagged jets. Even after requiring at least four b-tagged jets in the event, a non-negligible contribution from events with only one additional b-quark remains. On the contrary, events with low ΔR gluon splitting give a sub leading contribution in high b-tagged jet multiplicity regions.

Finally $t\bar{t}$ production in association with a a vector boson ($t\bar{t}$+V with V=W,Z) also needs to be considered. $t\bar{t}$+V events with up to two additional partons in the final state are generated with MADGRAPH using the CTEQ6L1 PDF set and showered with PYTHIA. The estimates from the Monte Carlo samples are normalised to the NLO cross section predictions [167, 168]. $t\bar{t}+Z$ production with Z decaying into b-quarks represents the most irreducible background for this analysis with the two additional b-quarks having similar properties as the Higgs decay products but a lower invariant mass. Nevertheless, the contribution from $t\bar{t}+V$ in the regions with at least four b-tagged jets is at most one half of the expected signal. The relative contribution with respect to the signal increases with a decreasing number of b-tagged jets due to the different branching ratios between the Higgs and the Z boson, as well as the larger contribution from $t\bar{t}+W$.

8.5 Analysis strategy

The purpose of the classification of events in various jet and b-tagged jet multiplicity regions is to improve the sensitivity to the $t\bar{t}H$ signal. A simultaneous template fit approach to all the considered regions is adopted, incorporating the effect of systematic uncertainties directly in the fit model. Multiple advantages are obtained with this approach:

- different signal fractions in the various regions are exploited for a more effective statistical combination;
- signal depleted regions are used to improve the knowledge on background normalisation and to reduce the effect of systematic uncertainties.

Figure 8.6 shows the $S/\sqrt{B}$ and S/B in the regions considered in the analysis. Highlighted in red are the three regions with the highest sensitivity to signal. The ($\geq$ 6j, $\geq$ 4b) region represents by far the most sensitive category; due to the stringent requirement on the number of jets and b-tagged jets, the expected S/B reaches a value of $\sim 1/20$ with an $S/\sqrt{B}$ of 0.7. Given the fact that the $H \rightarrow b\bar{b}$ decay accounts for more than 93% of the total signal yield in this region, the analysis is almost exclusively sensitive to the decay of the Higgs boson into b-quarks.

As previously anticipated, due to kinematic cuts and a limited b-tagging efficiency, the signal can migrate to regions with lower jet or b-tagged jet multiplicity; additional information on the signal can be obtained from the ($\geq$ 6j, 3b) and (5j, $\geq$ 4b) regions which have an expected signal fraction of the order of 1-2 %. It is worth mentioning that the sensitivity to the signal in a given region does not solely depend on $S/\sqrt{B}$; this number is a good approximation of the signal only to the extent that statistical uncertainties dominate over the systematic uncertainties. This condition does not hold for instance in the ($\geq$ 6j, 2b) region where the large amount of data causes a few percent error on the luminosity to exceed already the statistical uncertainty. For this reason, ($\geq$ 6j, 2b) is far less sensitive than (5j, $\geq$ 4b) which has similar $S/\sqrt{B}$, but ten times better S/B.

Finally, in other categories in the analysis, the expected signal contribution is smaller than 0.5 %; these 'signal-depleted' regions are in fact used to control the background contributions.

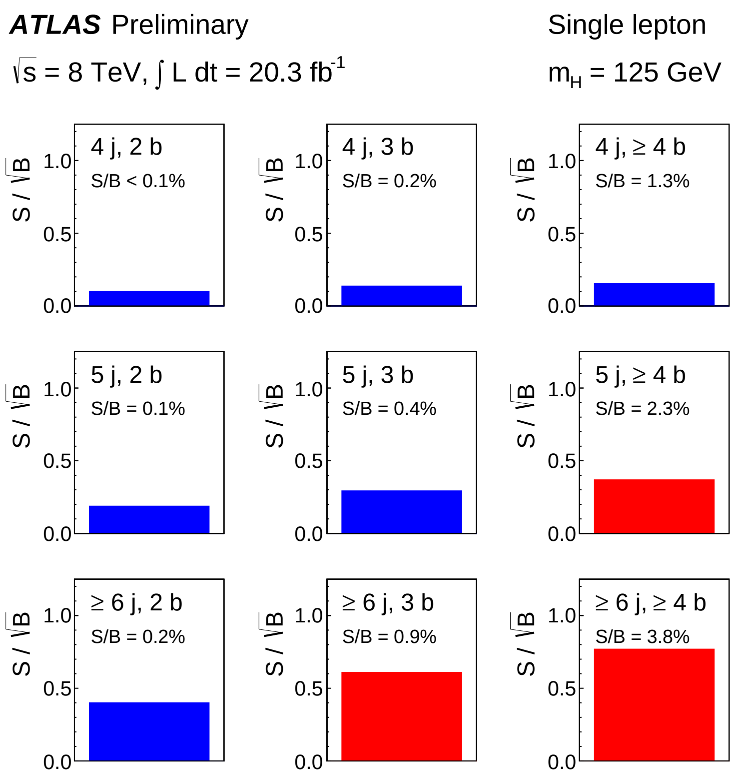

Figure 8.6: $S/\sqrt{B}$ ratio for each of the considered analysis regions. The S/B ratio in each region is also noted. The Standard Model cross section and m_H=125 GeV are assumed for the signal.

Nevertheless, signal-depleted and signal-enriched regions are treated in the same way by the fitting procedure.

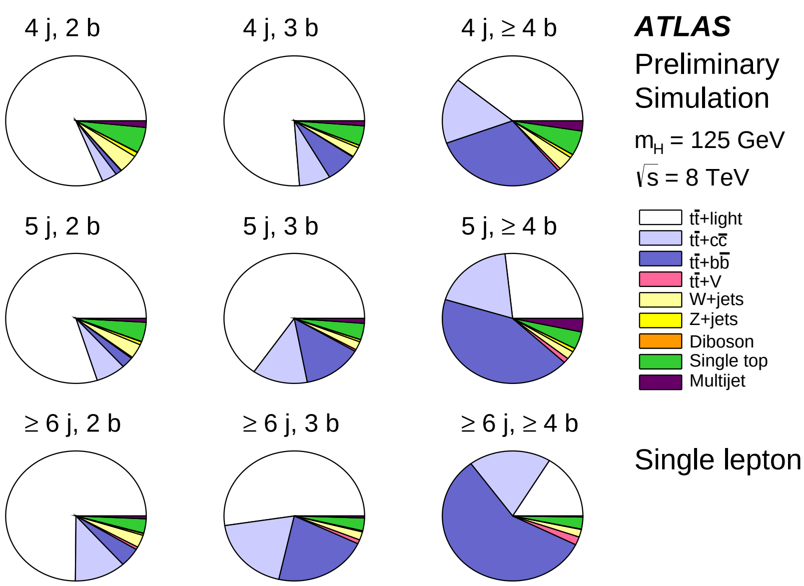

Figure 8.7: The fractional contributions of the various backgrounds to the total background prediction in the single lepton selection. Each row shows the plots for a specific jet multiplicity (4, 5, ≥6), and the columns show the b-jet multiplicity (2, 3, ≥4).

Figure 8.7 shows the background composition in the various analysis regions. In all the topologies, $t\bar{t}$+jets represents at least 90% of the total background. The contribution from $t\bar{t}$+HF increases from 10% in 2 b-tagged jets regions to become the dominant source of background when at least 4 b-tagged jets are selected.

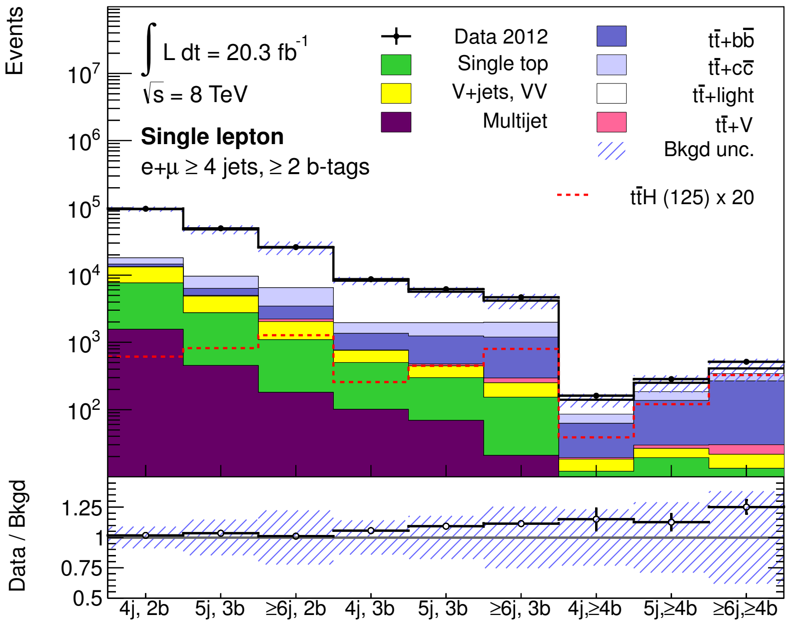

Figure 8.8: Comparison between observed and predicted event counts in all analysis regions before the fit to data. The dashed red line represents the signal contribution normalised to 20 times the SM predictions. The dashed area corresponds to the total uncertainty on the background yields.

The comparison between data and Monte Carlo predictions prior to the fit procedure ('prefit' in the following) is shown in Figure 8.8 for all the 9 analysis regions. Reasonable agreement is found between the data and Monte Carlo; some excess in the data is present in regions with increasing $t\bar{t}$+HF contributions.

More detailed numbers are reported in Tables 8.4 and 8.5. Yields for each background as well as the signal are compared to the number of events observed in data. The total uncertainty is reported including both the statistical and systematic component before the fitting procedure. A detailed explanation of the sources of systematic uncertainties will be given in Chapter 10.

It can be observed that even in the signal-enriched regions, the 'initial' uncertainties on the background are at least one order of magnitude larger than the expected signal contribution. The main cause is the uncertainty on the normalisation of $t\bar{t}$+HF events set to 50% of the expected yields. This reason ultimately motivates the usage of the fitting technique that allows the data under study to constrain the normalisation of the backgrounds and in general to mitigate the impact of the systematic uncertainties on the signal extraction. The background-enriched regions are specifically added to achieve this purpose particularly for the case of the $t\bar{t}+X$ backgrounds.

	4 jets, 2 b-tags	4 jets, 3 b-tags	4 jets, 4 b-tags	5 jets, 2 b-tags	5 jets, 3 b-tags	$\geq$ 6 jets, 2 b-tags
$t\bar{t}$+light	78000 ± 8000	6300 ± 800	55 ± 12	38000 ± 6000	3700 ± 700	19000 ± 5000
$t\bar{t}+c\bar{c}$	3300 ± 1700	590 ± 310	23 ± 12	3300 ± 1700	700 ± 400	3000 ± 1600
$t\bar{t}+b\bar{b}$	1350 ± 700	600 ± 310	43 ± 23	1300 ± 800	800 ± 400	1200 ± 700
$t\bar{t}$+V	110 ± 40	15 ± 5	0.9 ± 0.3	140 ± 40	26 ± 8	170 ± 50
W+jets	4300 ± 2100	200 ± 100	5.0 ± 2.7	1700 ± 900	120 ± 70	800 ± 500
Z+jets	1100 ± 300	50 ± 20	1.2 ± 0.7	370 ± 100	31 ± 11	129 ± 40
Single top	6100 ± 1900	400 ± 130	8.6 ± 3.2	2300 ± 800	230 ± 80	920 ± 340
Diboson	210 ± 60	11.6 ± 3.4	0.2 ± 0.1	98 ± 27	8.2 ± 2.4	51 ± 15
Multijet	1600 ± 600	100 ± 40	3.5 ± 2.1	450 ± 160	69 ± 26	180 ± 70
Total Bkgd.	96000 ± 8000	8200 ± 900	142 ± 30	48000 ± 7000	5700 ± 900	26000 ± 5000
$t\bar{t}H$ (125)	30.6±2.5±2.9	12.8±1.3±1.5	1.8±0.3±0.2	41.0±1.8±4.2	22.4±1.6±2.0	64.2±4.7±7.4
Data	97450	8692	161	49402	6168	26033

Table 8.4: Pre-fit event yields for signal, backgrounds, and data in each of the signal-depleted regions. The quoted uncertainties on the backgrounds are the sum in quadrature of the total systematic uncertainties on the yields. For the signal, the first component of the uncertainty is the contribution from acceptance and efficiency effects and the second is the contribution from the inclusive NLO cross section uncertainty.

	5 jets, $\geq$ 4 b-tags	$\geq$ 6 jets, 3 b-tags	$\geq$ 6 jets, $\geq$ 4 b-tags
$t\bar{t}$+light	67 ± 16	2200 ± 600	67 ± 20
$t\bar{t}+c\bar{c}$	47 ± 25	800 ± 400	80 ± 40
$t\bar{t}+b\bar{b}$	110 ± 60	900 ± 500	240 ± 130
$t\bar{t}+V$	3.1 ± 1.0	43 ± 13	8.4 ± 2.8
W+jets	5.1 ± 3.2	90 ± 50	8 ± 5
Z+jets	2.3 ± 1.3	10 ± 7	0.3 ± 0.2
Single top	11 ± 4	130 ± 50	12 ± 4
Diboson	0.4 ± 0.2	6.0 ± 1.9	0.6 ± 0.2
Multijet	8 ± 4	21 ± 11	1.1 ± 2.5
Total Background	250 ± 70	4200 ± 900	410 ± 140
$t\bar{t}H$ (125)	$5.8 \pm 0.7 \pm 0.6$	$39.4 \pm 3.2 \pm 4.1$	$15.6 \pm 1.9 \pm 2.0$
Data	283	4671	516

Table 8.5: Pre-fit event yields for signal, backgrounds, and data in each of the signal-enriched regions. Similar conventions as in Table 8.4 have been adopted.

Since categories with two b-tagged jets are dominated by $t\bar{t}$+light flavour production, the use of multiple jet multiplicity 'bins' is particularly sensitive to the effect of jet energy scale uncertainty and Monte Carlo modelling systematics. The contribution from $t\bar{t}$+HF increases with the number of selected jets and in particular with a higher requirement on the number of b-tagged jets, reaching up to 75%. Contrary to $t\bar{t}$+light jets, analysis regions dominated by $t\bar{t}$+HF are characterised by either low data statistics or a significant expected signal contribution. Information on the normalisation of the $t\bar{t}$+HF is then to be extracted from the relative fraction in the analysis regions; it has been previously shown that $t\bar{t}+b\bar{b}$ and $t\bar{t}+c\bar{c}$ events are distributed in a characteristic way over regions with different numbers of jets and b-tagged jets. This is also the reason for the inclusion of the $(4\text{j}, 3\text{b})$ and $(4\text{j}, 4\text{b})$ regions, which bring additional information on the $t\bar{t}$+HF fraction and the relative inter-normalisation of its sub-categories.

The categorisation of events enhances the signal fraction up to an S/B of 4% in $(\geq 6\text{j}, \geq 4\text{b})$. In order to further improve the sensitivity of the analysis, multivariate discriminants trained to separate the signal from the backgrounds are adopted in the signal-enriched regions: $(\geq 6\text{j}, 3\text{b})$, $(5\text{j}, \geq 4\text{b})$ and $(\geq 6\text{j}, \geq 4\text{b})$. In the $(5\text{j}, 3\text{b})$ region, a multivariate discriminant is used to separate the two main sources of background. Detailed information on the multivariate methods used will be found in the next chapter.

In all the other regions, the variable used in the template fit is the scalar sum of the jet p_{T}s ($H_{\text{T}}^{\text{had}}$). The reason for the choice of $H_{\text{T}}^{\text{had}}$ is its sensitivity to detector effects like jet energy scale and modelling of $t\bar{t}$ events. These characteristics will be exploited in a profile likelihood fit to reduce the impact of systematic uncertainties. Figure 8.9 shows the distribution of $H_{\text{T}}^{\text{had}}$ for data and the Monte Carlo prediction in all the categories used in the fit. The comparison is shown before the fitting procedure and the full uncertainty band is displayed.

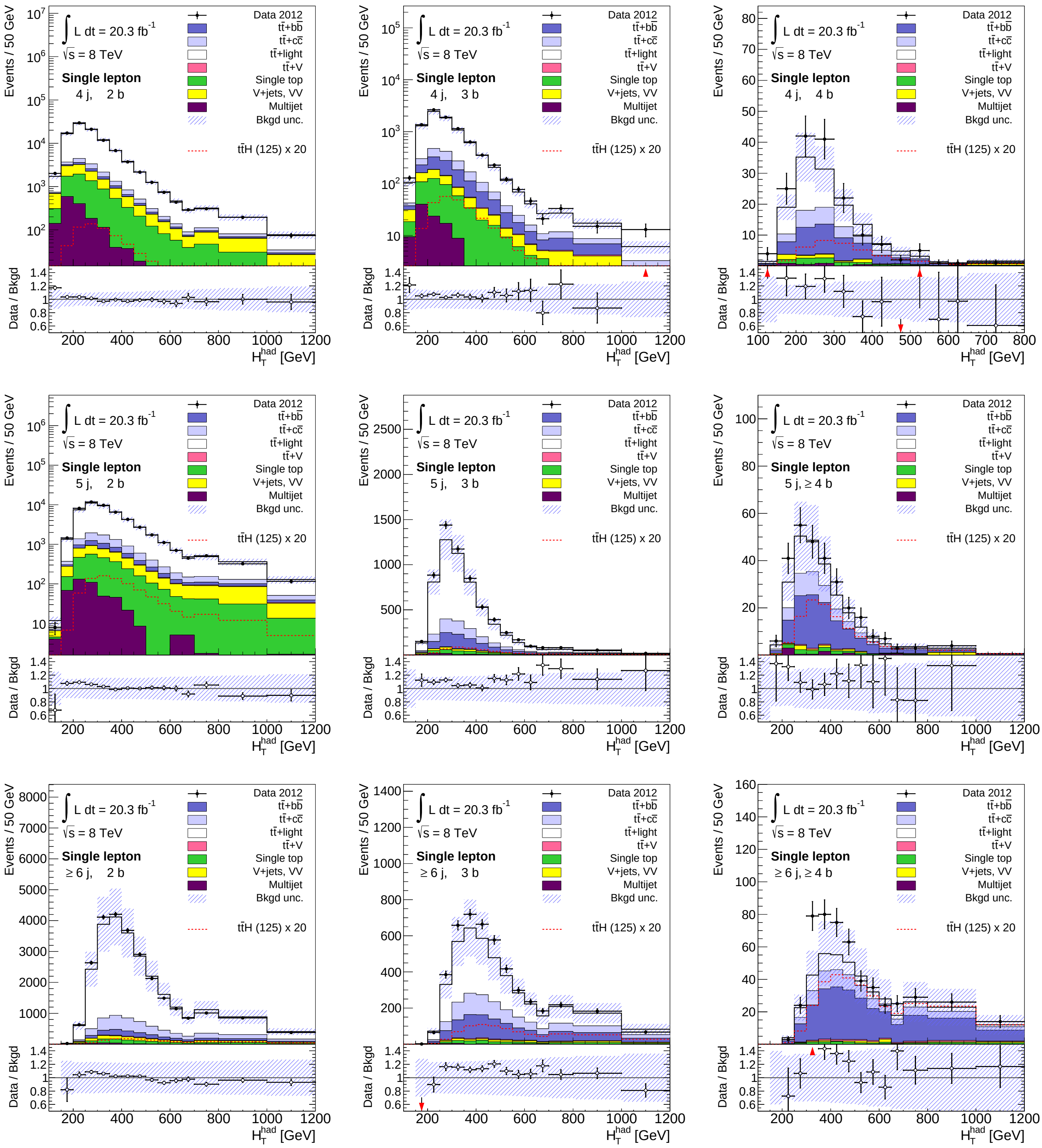

Figure 8.9: $H_{\mathrm{T}}^{\mathrm{had}}$ distributions in data and Monte Carlo for the nine regions considered in the analysis. The uncertainty band contains both Monte Carlo statistical uncertainty and systematic uncertainties. Distributions are shown prior to the fit procedure.

Chapter 9

Search for $t\bar{t}H(b\bar{b})$: Multivariate Analysis

After having defined the signal regions in order to maximise the $S/\sqrt(B)$, an event shape analysis can be exploited to further improve the sensitivity to the signal. This chapter describes the implementation of a multivariate discriminant trained to achieve the best separation between signal and background. The first part is dedicated to the motivation for the choice of a Neural Network (NN) approach. Subsequently, the procedure for selecting the discriminating variables and the 'training' of the neural network is outlined. Finally, the last part contains the steps performed to validate the usage of the multivariate discriminants.

9.1 Neural Networks

Neural network output distributions are adopted as final analysis discriminants in four analysis regions. In the topologies with the highest S/B as $(\geq 6\text{j}, 3\text{b})$, $(5\text{j}, \geq 4\text{b})$, $(\geq 6\text{j}, \geq 4\text{b})$[1], dedicated neural network discriminants are used to increase the shape separation between the signal and the backgrounds.

In the $(5\text{j}, 3\text{b})$ region, a neural network is used place to separate the two main sources of backgrounds: $t\bar{t}$+light jets and $t\bar{t}$+HF. This region presents a small expected signal contamination; at the same time, the $t\bar{t}$+HF fraction is of the order of 25% and a sizeable amount of data statistics is available. The reasons for such a choice are twofold. On one hand, an additional shape separation between backgrounds[2] helps in disentangling degenerate effects of systematic uncertainties and background normalisation. On the other, the neural network output also is used to select a sub-region further enriched in $t\bar{t}$+HF which allows a validation of NN input variables and description of the HF content of $t\bar{t}$ events in a high-statistics, very depleted signal region with lower jet multiplicity.

9.1.1 Motivation for a multivariate approach

Multivariate approaches are obtaining increasing visibility in high energy physics. They are particularly useful in cases where no single variable exhibits a clear separation power between signal and background. They are chosen for their ability to maximise the amount of information that can be extracted from a given set of events. A typical multivariate algorithm allows to

[1]The $(4\text{j}, 4\text{b})$ region was not considered due to its low statistics.

[2]The main discriminating power between the different backgrounds arises from the relative normalisation in the analysis regions.

combine the information from several input variables into one output discriminant that can exploit the correlation among the variables and can reproduce a non-trivial selection in the variables' phase space.

The $t\bar{t}H$ analysis is an ideal ground for the application of a multivariate approach given the large number of physics objects in the final state and the complexity of the topology. The analysis performed with the 2011 dataset exploited a full kinematic reconstruction of the events [161]; jets were assigned to particular partons in the list of $t\bar{t}$ decay products and the remaining jets not assigned to the $t\bar{t}$ hypothesis were considered as the decay product of the Higgs boson and their invariant mass was used as the final discriminant in the analysis. The method yielded a relatively low 'matching' efficiency for $t\bar{t}H$ events: only 4 % of the events can be fully reconstructed in the correct way and in 20% of the events, the two jets coming from the Higgs particle could be correctly identified. This is the result of large combinatorics as well as the fact that, because of acceptance, all the products from the $t\bar{t}H$ decay might not be present in the event. In contrast, a multivariate approach can combine several quantities/properties in a given event and hence reduce the need for a full event reconstruction.

The Neural Network multivariate method, as implemented by the NeuroBayes package [169, 170], has been used in the context of this analysis. It has been preferred over other methods like Boosted Decision Trees for its greater robustness against overtraining and the particular features of the NeuroBayes package that will be subsequently outlined.

9.1.2 Implementation and strategy

A neural network is a man-made attempt to reproduce the functionalities of the human brain, where neurons are interconnected among themselves. Although a neural network can have an arbitrary architecture, for most applications, a simpler structure like the one shown in Figure 9.1 is sufficient. Nodes ('neurons') are arranged into layers. The input layer contains a node for each input variable. In the hidden layer, the information from previous nodes are multiplied by a given set of weights and then summed together; the output of each node is a specific function of this sum, called the neuron response function. The output of the final node thus maps the values of the n input variables into one single variable. In the figure, each node can only be connected to nodes in the successive layer so the information can only be propagated forward, hence the name"feed forward" neural network. In general, the use of only one hidden layer is sufficient and the complexity could be increased by adding more nodes to this layer rather than adding further hidden layers. The behaviour of an artificial neural network is uniquely determined by its layout, the weights of the inter-neuron connections, and by the type of the response of the neurons to the input.

9.2 The NeuroBayes package

NeuroBayes is a commercial package that implements a three layer feed forward neural network. The program has three distinctive features: a very effective variable pre-processing step, a ranking of the input variables according to their effectiveness in separating the signal from the backgrounds, and a Bayesian regularisation for the training procedure. The steps performed by the program are outlined in the following sections.

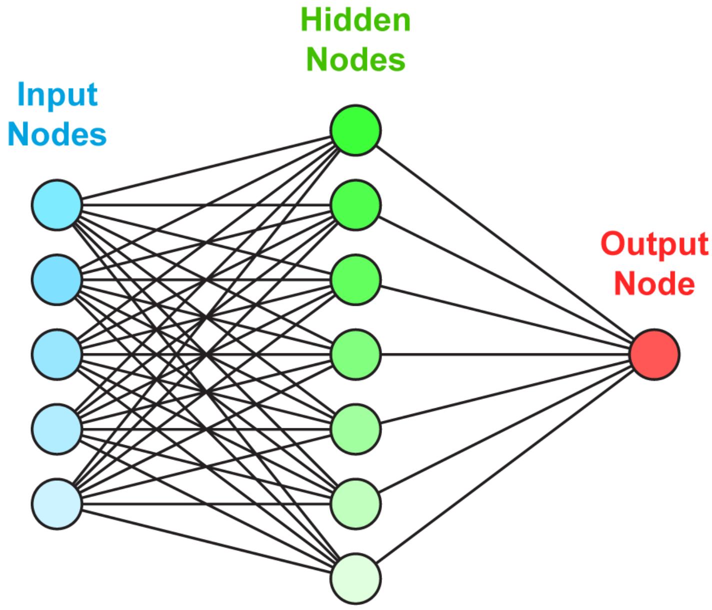

Figure 9.1: Example of a three layer neural network.

9.2.1 Pre-processing of input variables

The input variables pre-processing stage is a fully automated procedure aiming at improving the stability and robustness of the next steps, as well as at significantly reducing the execution time of the training. All input variables are initially equalised and re-mapped within the interval [-1,1][3]; this allows to reduce the influence of extreme values in the training procedure as well as helping the output of each node to be confined between -1 and 1 avoiding saturation effects. Subsequently, each variable distribution is converted into a gaussian with zero mean and unit width. The pre-processing can be modified for variables assuming only discrete values, like the number of jets in the event. Finally, variables are (linearly) de-correlated by diagonalising the covariance matrix with the Jacobi rotation procedure [171].

9.2.2 Ranking of input variable

The ranking of input variables is one of the reasons for the choice of NeuroBayes in the present analysis. The procedure takes into account the individual discrimination power of each variable as well as its correlation to the rest of the inputs. This is particularly desirable when many possible discriminating variables are being tested and no precise ranking based on first principles (like direct interpretation of the variables) can be performed.

NeuroBayes follows an iterative approach to rank the variables. After the variables have been pre-processed, the total correlation of the input set of variables to the target is computed. The 'target' is defined as 1 for signal events and 0 for background events. The correlation to target is obtained as the quadratic sum of each Pearson's correlation coefficient: To first order, the correlation between two variables can be described by the linear correlation coefficient between each variable and the target. The general form of the linear correlation coefficient is

[3]This is achieved by obtaining the cumulative density distribution and computing intervals corresponding to the same area.

given by:

$$r_{xy} = \frac{\sum_i^{\text{events}}(x_i - \bar{x}) \cdot (y_i - \bar{y})}{\sqrt{\sum_i^{\text{events}}(x_i - \bar{x})^2}\sqrt{\sum_i^{\text{events}}(y_i - \bar{y})^2}} \tag{9.1}$$

where x_i and y_i represent the values of two of the variables in a given event, and $\bar{x}$, $\bar{y}$ their respective 1-dimensional averages.

Each variable is removed, one at the time, from the list of inputs and the correlation to target re-computed; the variable with the smallest loss of correlation to target is then discarded as the least discriminating one, leaving a $n-1$ set of input variables. The procedure is iterated until one variable is left and this is considered the most relevant variable. Quantitatively, each variable is assigned a significance which is defined as the loss of correlation at the specific point in the iteration process divided by $\sqrt{n_{ev}}$, with n_{ev} being the number of events considered. The definition implies that the significance of a variable depends on the training statistics and on the other variables present in the initial list; it is thus particularly difficult to compare the value of the significance for two variables in two separate training processes. Only the first n variables from the sorted list provided by the package are used in the training. The number n can be either controlled by the user or set automatically by keeping all the variables with a significance larger than a given cut. The latter option was not used in the current analysis since a more direct control over the choice of the number of variables has been preferred, as described later.

9.2.3 Training

The total output of a neural network with n input variables and L nodes in the hidden layer can be expressed as:

$$o = f\left(\sum_{j=0}^{L} w_j \cdot f\left(\sum_{i=0}^{n} w_{ij} \cdot x_i + \mu_i\right) + \mu_0\right) \tag{9.2}$$

where x_i is the i-th input variable, w_{ij} is the weight in the nodes j from the variable i, and w_j is the weight in the output node from the j-th node in the hidden layer. μ_0 and μ_j are the weights associated with the so-called *bias nodes*; they provide additional input information that can be used to shift the central value of the output of each node they enter. This helps in stabilising the training procedure by avoiding the saturation[4] of the nodes and ensuring that the output values are always in the central range of the neuron activation function where the largest response variation is possible.

The neuron activation function $f(x)$ relates the weighted sum of the inputs to a given node to its output. A modified sigmoid function of type:

$$f(x) = \frac{2}{1 + e^{-x}} - 1 \tag{9.3}$$

is chosen in order to ensure the output of the node to be limited to the range [-1,1].

The training of the neural network consists in finding the optimal values for the weights w_{ij}, w_j as well as μ_0 and μ_j. This is achieved by minimising, in the multidimensional space represented by the weights, the difference between the output value of the network and the true target value. This is called the error or loss function and is defined as:

$$E = \sum_i^{\text{events}} \log\left(\frac{1}{2} \cdot (1 + T_i) \cdot o_i\right) \tag{9.4}$$

[4]Here saturation refers to the situation in which the output of the node has a minimal variation with respect to a change in the inputs.

where for each event i, the target (0 or 1) is represented by T_i and o_i is the final output of Eq. 9.2. The minimisation is performed with the BFGS algorithm [172]; it is based on the usage of the approximate second derivatives of the error function to determine the 'direction' in which to adjust the node weight. The BFGS algorithm is in general more robust and has faster convergence than the standard *back-propagation* minimisation algorithm [173]. Instead of considering all the events at once for the minimisation, the sample is sub-divided into smaller subsamples and the weights are updated after each subsample is considered.

An important step in the training process is to ensure that the determination of the optimal set of weights is based on real features of the signal and background and not on the particular realisation of the background and signal sample used in the training due to finite statistics. The latter is usually referred to as *overtraining*. Bayesian regularisation techniques are used to reduce or prevent the overtraining effects [170]; during the training process, the node weights are systematically reduced with a weight decay factor in addition to the variation calculated BFGS procedure. In this way, only recurring structures in the node weights' values are intensified while the influence of random statistical fluctuations are progressively 'pruned' away leaving only significant connections in the network architecture. At the same time, in order to further minimise the risk of overtraining, the evaluation of the performance of the neural network as well as the usage of the neural network are performed using samples that are statistically independent of the ones used in the training phase.

9.3 Discriminating variables

Given the variety of regions considered and the rich topology of the events, many variables have been inspected for their discriminating power. They can be classified in four 'categories':

- *object kinematics*: p_{T} and η of the lepton, of each jet and of the b-tagged jets;
- *global event variables*: the scalar sum of the jet p_{T}s ($H_{\mathrm{T}}^{\mathrm{had}}$), the mass of the vector combination of all the objects in the event (M_{eff}), the number of jets above a given p_{T} threshold (40, 60 and 80 GeV), and the missing transverse energy;
- *event shape variables*: well defined combinations of the eigenvalues of the linear momentum tensor (sphericity, aplanarity), the centrality and the Fox-Wolfram moments. The latter are used to describe the geometrical correlation among objects in the event in terms of spherical harmonics [174]. Global and event shape variables have the advantage that they can be examined in all topologies and are less sensitive to the loss of jets. For each variable three possible definitions have been tested: one that makes use of the lepton and all the jets in the event to build the variables, another one using only the jets, and the last one considering only the b-tagged jets.
- *object pair properties*: scalar sum p_{T}, invariant mass and ΔR of many possible di-jet pair definitions have been considered: largest vectorial sum p_{T}, largest invariant mass or smallest ΔR. Possible combinations contained pairs formed from any type of jets, a b-tagged jet and any jet, or two b-tagged jets. One additional di-jet combination is built out of the pair of jets failing the b-tagging requirement with smallest angular distance; it is designed to identify the hadronically decaying W boson candidate.

All variables are defined by considering at most seven jets in the events. In case more than seven jets are present, first the b-tagged jets are considered, then the remaining ones ordered in p_{T} until seven are kept. This conservative approach is related to the fact that the signal simulation is only known at NLO accuracy and limiting the number of jets ensures that the discrimination power does not come from the presence of soft jets that are difficult to model correctly. Less than 15% of the signal events (and less than 10% of the background events) in the ($\geq$ 6j, $\geq$ 4b) region are affected by this procedure. No further use of the b-tagging algorithm output (weight) information is exploited in the analysis, other than a straight cut to define the different regions. Despite the fact that the shape of the weight distribution could bring additional discrimination particularly against $t\bar{t}$+$c\bar{c}$ and $t\bar{t}$+light jets background where some of the b-tagged jets do not originate from b-quarks, only single cut values were fully calibrated and ready to be used in physics analyses. In addition variables displaying very poor data/MC agreement in the signal-depleted regions or exhibiting a large shape dependence for different generators were discarded.

The separation between signal and background originates from the nature of the additional b-quarks produced in the events (ISR/FSR versus Higgs boson decay) as well as the different mechanism (diagram) for the production of the $t\bar{t}$ pair which is ultimately reflected in the kinematics of its decay products. On average, events are expected to be more energetic in the case of signal and being more central in the detector; this as a result of the higher $\hat{s}$ needed to produce a $t\bar{t}$ pair in association with a Higgs boson in the event. As already described previously, no attempt is made to reconstruct the full kinematics of the events due to the large inefficiency and the computation penalty. Nevertheless, in particular conditions, some of the di-jet pair combinations could be interpreted as originating from the candidate Higgs boson. As an example, the mass of the b-tagged jets combination with the highest vectorial sum p_{T} exhibits a peak at the Higgs mass for the signal. The advantage of the neural network approach is specifically in the possibility to consider and combine all these variables exploiting 'partial' event reconstruction and their correlations, without requiring a complete event reconstruction.

The neural network in (5j, 3b) separates $t\bar{t}$+light jets and $t\bar{t}$+HF mainly by exploiting the different origin of the third b-tagged jet in the event given that two real b-quarks are produced in the $t\bar{t}$ decay. As already outlined in Chapter 8, for $t\bar{t}$+HF processes the additional heavy flavour partons produced in the hard scattering or from ISR are likely to become b-tagged jets. In the case of $t\bar{t}$+light jets, ISR or additional partons are likely to be gluon enriched, therefore the best candidates to produce additional b-tagged jets in the event are the jets from the hadronically decaying W boson. Differences between $t\bar{t}$+light and $t\bar{t}$+HF are then expected in the kinematics of the b-tagged jets pair as well as in the ability to reconstruct the hadronic W boson candidate from jets failing the b-tagging requirement. Such differences are exploited through the NN discriminant to better constrain the normalisation of the $t\bar{t}$+HF component in the low b-tagged jet multiplicity region.

The choice of the variables that enter the neural network discriminant is made by NeuroBayes using the ranking procedure previously described. In the ($\geq$ 6j, 3b), (5j, $\geq$ 4b) and ($\geq$ 6j, $\geq$ 4b) regions, the sample with a Higgs boson mass of 125 GeV has been used as a signal sample and all the background processes have been considered in the procedure apart from the QCD multijet background, given that it is extracted from data events. All Higgs boson decay modes are considered, weighted by their respective branching fractions. In the (5j, 3b) region, $t\bar{t}$+HF has been considered as the 'signal' process and $t\bar{t}$+light jets as the background one.

The choice of the discriminating variables is made independently in each considered region given the differences in jet and b-tagged jet multiplicities. As a result, different variables can be exploited to increase the separation. The number of used input variables in each region stems from a compromise between the performance of the neural network and the practical aspect of the validation of a large number of variables. The evolution of the correlation to target

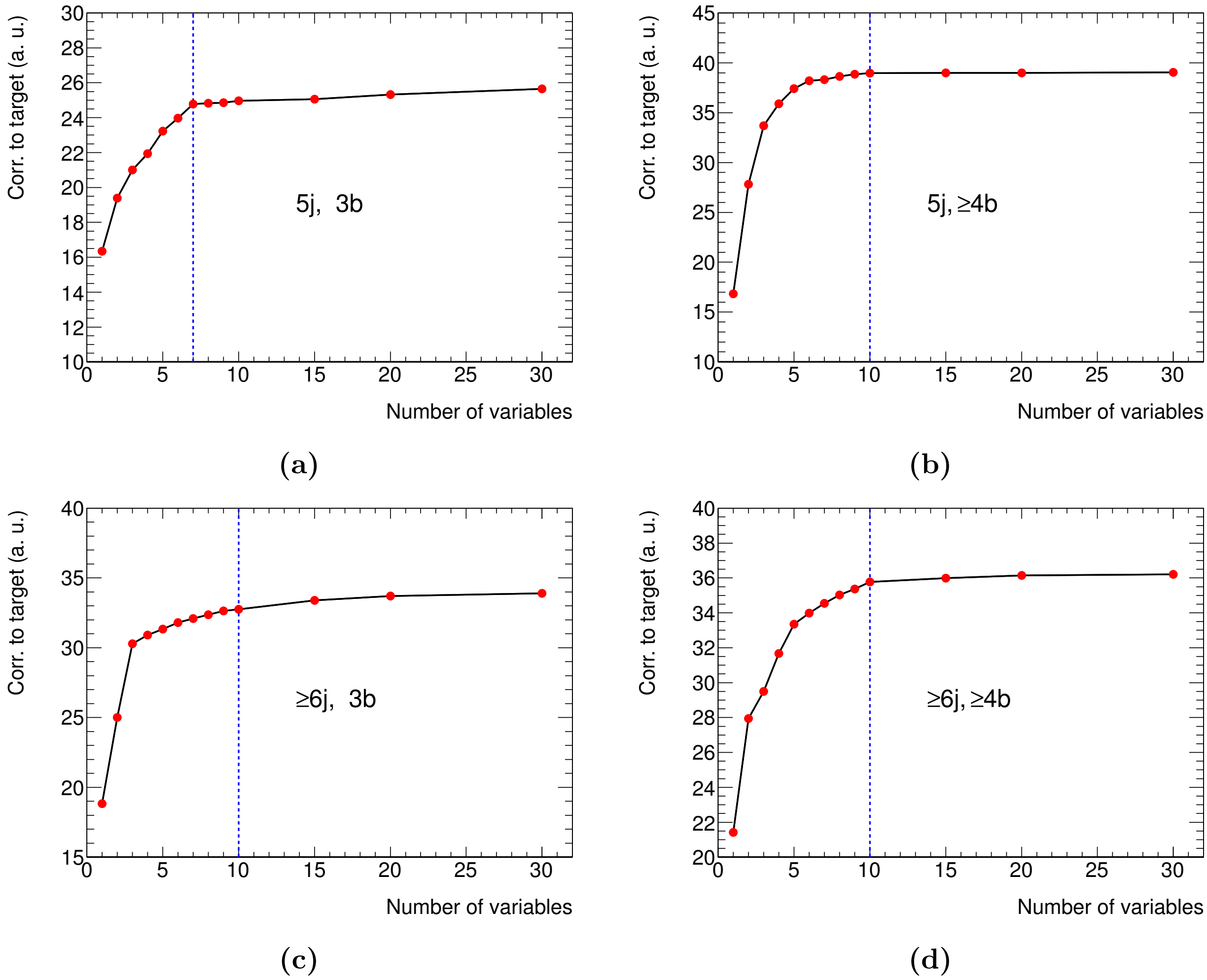

Figure 9.2: Evolution of the correlation to target as a function of the number of variables considered in the training of the neural networks in the (5j, 3b) (a) and (5j, ≥ 4b) (b), (≥ 6j, 3b) (c) and (≥ 6j, ≥ 4b) (d) regions. The last point represents a training performed with 45 variables (the point is set at 30 for better visualisation).

in each region as a function of the number of considered inputs is presented in Figure 9.2; variables are added in the order suggested by the NeuroBayes ranking. As can be seen, the increase in the separation rapidly flattens out with the increase of the number of inputs. For the NN discriminating signal from background, 10 variables are considered while for the NN in the (5j, 3b) region, only 7 input variables are considered. This is due to the fact that fewer variables show an appreciable difference between $t\bar{t}$+light and $t\bar{t}$+HF processes.

Table 9.1 contains a detailed description of each of the 20 inputs variables used in at least one of the four considered neural network discriminants. The variables ranking in each region is summarised in Table 9.2.

Figures 9.3, 9.4, 9.5 and 9.6 show the shapes of the chosen discriminating variables in each region. In each plot, the value of the separation between signal and background is also reported. This is a measure of the discriminating power of that variable related to the non-overlapping area of the normalised distributions. it is defined as:

$$\text{separation} = \frac{1}{2} \cdot \sum_{i}^{bin} \frac{(N_i^{\text{signal}} - N_i^{\text{background}})^2}{(N_i^{\text{signal}} + N_i^{\text{background}})}. \quad (9.5)$$

Variable	Definition
Centrality	Sum of the p_{T} divided by sum of the E for all jets and the lepton
H1	Second Fox-Wolfram moment computed using all jets and the lepton
$m_{\mathrm{bb}}^{\mathrm{min}\ \Delta\mathrm{R}}$	Mass of the combination of two b-tagged jets with the smallest ΔR
N_{40}^{jet}	Number of jets with $p_{\mathrm{T}} \geq 40$ GeV
$\Delta R_{\mathrm{bb}}^{\mathrm{avg}}$	Average ΔR for all b-tagged jet pairs
$m_{\mathrm{jj}}^{\mathrm{max}\ \mathrm{p_T}}$	Mass of the combination of any two jets with the largest vector sum p_{T}
$\mathrm{Aplanarity}_{\mathrm{b-jet}}$	$1.5\lambda_2$, where λ_2 is the second eigenvalue of the momentum tensor built with b-tagged jets
$H_{\mathrm{T}}^{\mathrm{had}}$	Scalar sum of jet p_{T}
$m_{\mathrm{jj}}^{\mathrm{min}\ \Delta\mathrm{R}}$	Mass of the combination of any two jets with the smallest ΔR
$\Delta R_{\mathrm{lep-bb}}^{\mathrm{min}\ \Delta\mathrm{R}}$	ΔR between the lepton and the combination of two b-tagged jets with the smallest ΔR
$m_{\mathrm{bj}}^{\mathrm{min}\ \Delta\mathrm{R}}$	Mass of the combination of a b-tagged jet and any jet with the smallest ΔR
$m_{\mathrm{bj}}^{\mathrm{max}\ \mathrm{p_T}}$	Mass of the combination of a b-tagged jet and any jet with the largest vector sum p_{T}
$m_{\mathrm{uu}}^{\mathrm{min}\ \Delta\mathrm{R}}$	Mass of the combination of two untagged jets with the smallest ΔR
$p_{\mathrm{T}}^{\mathrm{jet5}}$	Fifth leading jet p_{T}
$\Delta R_{\mathrm{bb}}^{\mathrm{max}\ \mathrm{p_T}}$	ΔR between two b-tagged jets with the largest vector sum p_{T}
$m_{\mathrm{bb}}^{\mathrm{max}\ \mathrm{m}}$	Mass of the combination of two b-tagged jets with the largest invariant mass
$p_{T,\mathrm{uu}}^{\mathrm{min}\ \Delta\mathrm{R}}$	Scalar sum of the p_{T}'s of the pair of untagged jets with the smallest ΔR
m_{jjj}	Mass of the jet triplet with the largest vector sum p_{T}
$\Delta R_{\mathrm{uu}}^{\mathrm{min}\ \Delta\mathrm{R}}$	Minimum ΔR between two untagged jets
$m_{\mathrm{bb}}^{\mathrm{max}\ \mathrm{p_T}}$	Mass of the combination of two b-tagged jets with the largest vector sum p_{T}

Table 9.1: List of variables used in the building of NN discriminants in at least one analysis region.

where N_i^{signal} and $N_i^{\mathrm{background}}$ are the entries in each bin after histograms have been normalised to unity.

9.3.1 Neural network training

The training of all the four neural networks is performed using fast-simulation samples for both signal and background. Signal and background samples processed though full ATLAS simulation are used for the evaluation of the NN performance and the creation of the template distributions for the fitting procedure and they represent statistically independent samples with respect to the ones used for training.

A detailed list of all the options used in the NeuroBayes configuration is provided in Table 9.3. It has been verified that the obtained performance is reasonably stable with respect to changes in the neural network architecture (number of hidden nodes), type of loss function, and 'learning' options.

Variable	$(\geq 6\text{j}, \geq 4\text{b})$	$(\geq 6\text{j}, 3\text{b})$	$(5\text{j}, \geq 4\text{b})$	$(5\text{j}, 3\text{b})$
$\Delta R^{\text{avg}}_{\text{bb}}$	1	5	5	-
$m^{\text{min }\Delta\text{R}}_{\text{bb}}$	2	9	3	1
Centrality	3	2	1	-
H1	4	3	2	-
$p^{\text{jet5}}_{\text{T}}$	5	8	-	-
$\text{Aplanarity}_{\text{b-jet}}$	6	-	7	-
$m^{\text{min }\Delta\text{R}}_{\text{uu}}$	7	7	-	2
$\Delta R^{\text{max p}_\text{T}}_{\text{bb}}$	8	-	-	-
$\Delta R^{\text{min }\Delta\text{R}}_{\text{lep-bb}}$	9	10	10	-
$m^{\text{max p}_\text{T}}_{\text{bj}}$	10	6	-	-
N^{jet}_{40}	-	1	4	-
$m^{\text{min }\Delta\text{R}}_{\text{bj}}$	-	4	-	-
$m^{\text{max p}_\text{T}}_{\text{jj}}$	-	-	6	-
$H^{\text{had}}_{\text{T}}$	-	-	8	-
$m^{\text{min }\Delta\text{R}}_{\text{jj}}$	-	-	9	-
$m^{\text{max m}}_{\text{bb}}$	-	-	-	3
$p^{\text{min }\Delta\text{R}}_{T,\text{uu}}$	-	-	-	4
m_{jjj}	-	-	-	5
$\Delta R^{\text{min }\Delta\text{R}}_{\text{uu}}$	-	-	-	6
$m^{\text{max p}_\text{T}}_{\text{bb}}$	-	-	-	7

Table 9.2: The lists and rankings of the variables considered in each of the analysis regions where a NN is used.

nodes in hidden layer	$\text{n}_{\text{variables}}+2$
update weights interval	100 events
learning speed factor	1
max learning speed	0.01
number of iterations	100
training algorithm	BFGS

Table 9.3: Details of the NeuroBayes settings. The parameters *learning speed factor* and *max learning speed* control the rate at which the node weights evolve during the training procedure. The number of iterations represents the number of times the training set of events is evaluated for the minimisation of the loss function. In general fewer than 20 iterations are sufficient to reach the convergence condition where the variation of the loss function becomes negligible after each iteration.

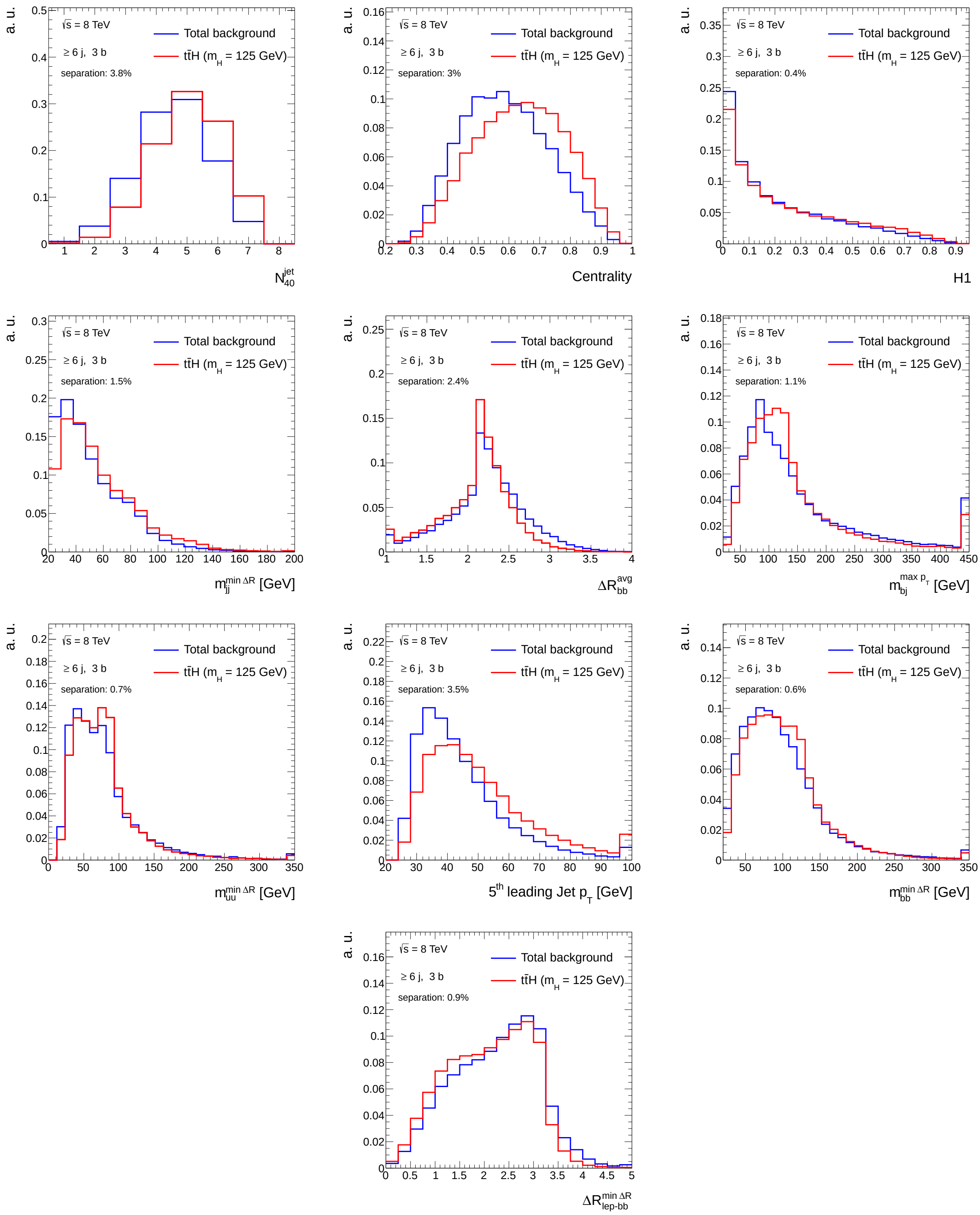

Figure 9.3: Disciminating variables used for the NN in the ($\geq 6j, 3b$) region. Each plot shows the normalised distribution for signal with a mass of 125 GeV (red) and the summed background (blue).

The plots of the neural network discriminant distributions in the four considered regions are shown in Figure 9.7. In the following, these neural network outputs are labelled according to the region in which they were trained[5]. The distributions for the signal and background

[5]For validation purposes NN outputs can be displayed in different regions from those they were trained in.

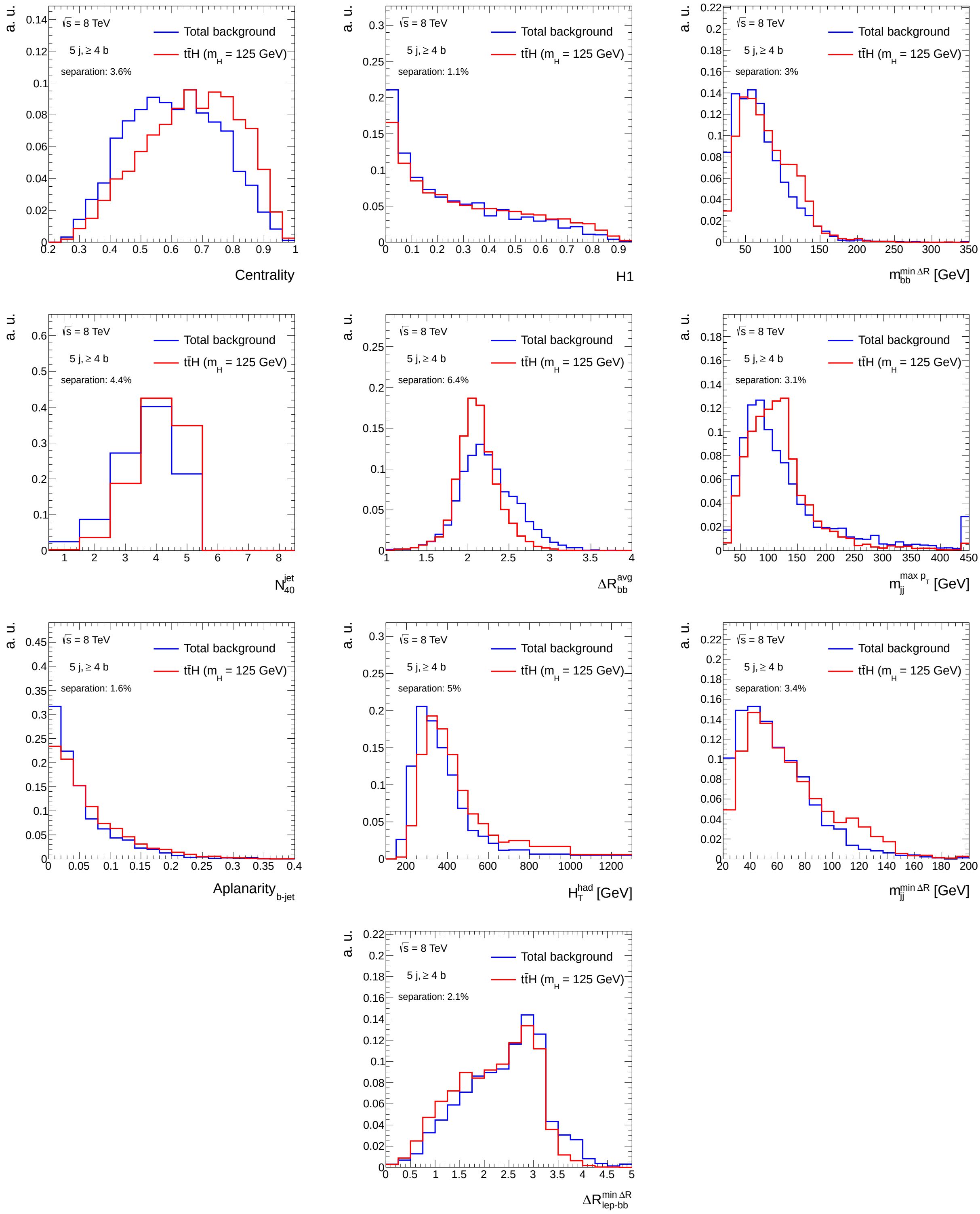

Figure 9.4: Discriminating variables used for the NN in the $(5j, \geq 4b)$ region. Each plot shows the normalised distribution for signal with a mass of 125 GeV (red) and the summed background (blue).

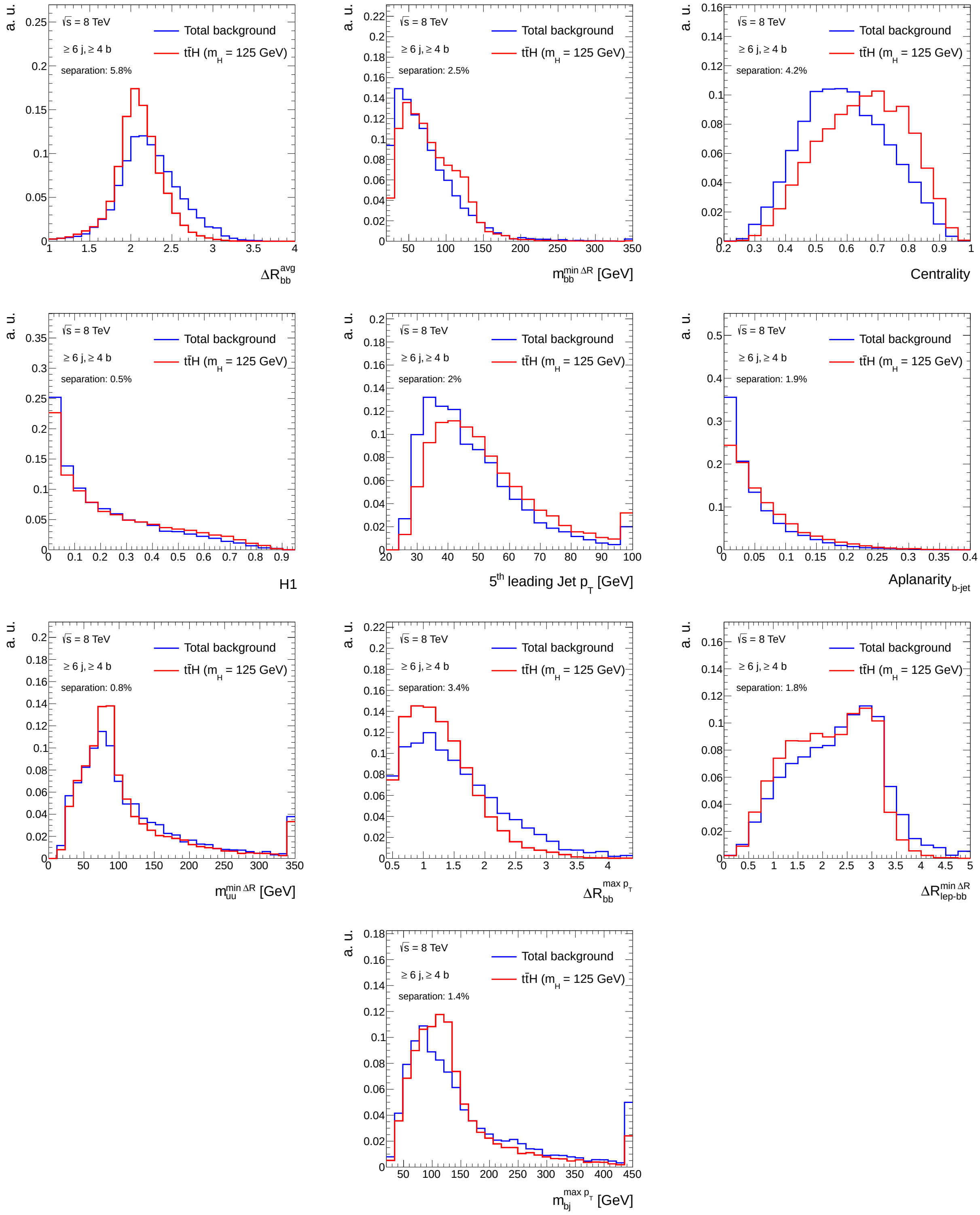

Figure 9.5: Discriminating variables used for the NN in the ($\geq$ 6j, $\geq$ 4b) region. Each plot shows the normalised distribution for signal with a mass of 125 GeV (red) and the summed background (blue).

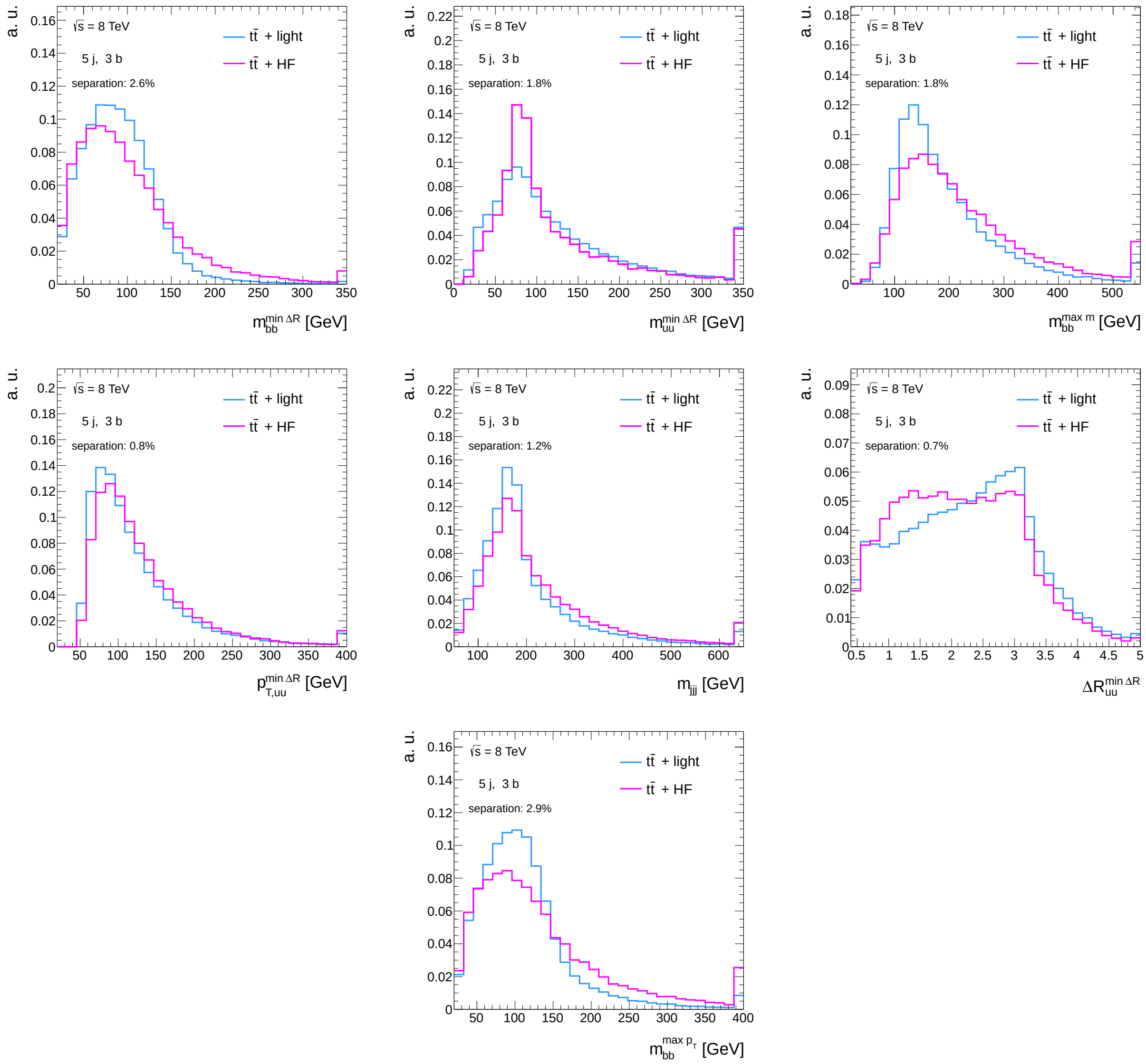

Figure 9.6: Discriminating variables used for the NN in the (5j, 3b) region. Each plot shows the normalizaed distribution for $t\bar{t}$+HF (red) and $t\bar{t}$+light jets(blue).

are reported together with the shape of the three $t\bar{t}$+jets categories separately. As expected, the separation obtained from the neural network is significantly higher than the one from each single variable. In regions where the neural network is trained to separate the $t\bar{t}H$ signal from the backgrounds, very similar NN output distributions are obtained for all the $t\bar{t}$ categories. Only with the explicit training in the (5j, 3b) region can the $t\bar{t}$+light and $t\bar{t}$+HF shapes can be separated. This observation suggests that an additional gain in the analysis could be achieved by combining multiple neural networks in the same analysis region as applied in other analyses searching for the Higgs boson's decay to b quarks [175]. Nevertheless, this approach is not exploited in the current analysis.

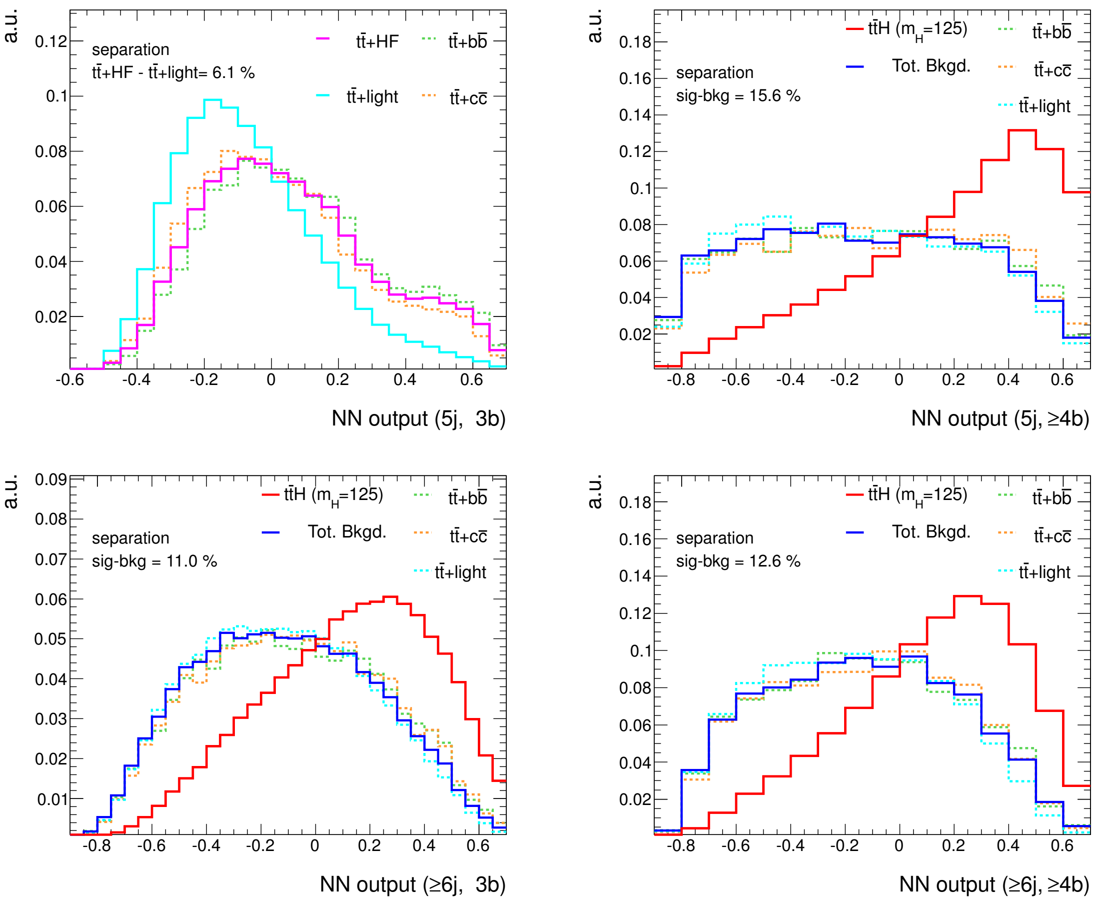

Figure 9.7: Neural network output distributions for signal and the background in the (5j, 3b), (5j, $\geq$ 4b), ($\geq$ 6j, 3b) and ($\geq$ 6j, $\geq$ 4b) analysis regions together with the value of the separation obtained from the evaluation samples. The shapes for the different categories of the different categories for $t\bar{t}$+jets events are also shown.

Figure 9.8 illustrates the characterisation of the neural network performance. The signal efficiency and the background rejection are reported for various cuts on the NN output (also known as ROC curves). For each NN, curves are shown for the training samples and for the evaluation samples. Very similar performance is observed in the training and evaluation samples; a sign that the overtraining effects are minimal, as is to be expected for a robust neural network.

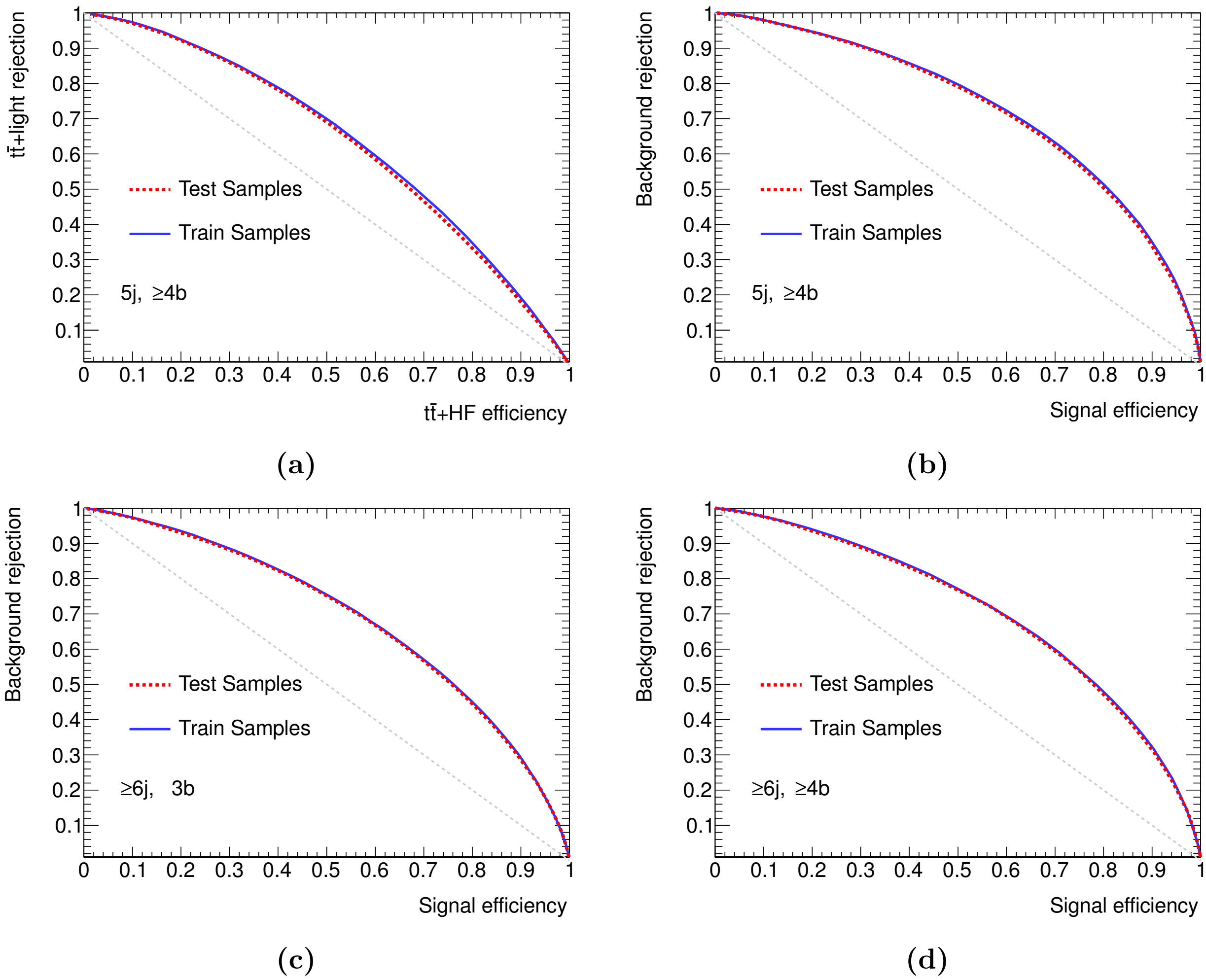

Figure 9.8: signal efficiency versus background rejection curves for the neutral network discriminants in the four analysis regions. Results are shown for the training and the evaluation samples. For the (5j, 3b) region (a), efficiency for $t\bar{t}$+HF process versus rejection of $t\bar{t}$+light process is shown.

Dependence on the Higgs boson mass

The primary goal of the analysis is to explore the coupling of the newly discovered boson. For this reason, the training of the NN is performed with a $t\bar{t}H$ sample corresponding to a mass of 125 GeV. Other mass points are considered in the analysis in order to probe a potential excess over the background prediction. Nevertheless, the limited statistics of these samples does not allow an optimal NN training for these mass points.

Figure 9.9 shows the NN output distributions for the $t\bar{t}H$ process for different masses of the Higgs boson; mass values of 115, 120, 125, 130 and 135 GeV are considered. The change in mass is also responsible for a change in the contributions from the various Higgs boson decay modes through the modification of the branching fractions. No particular dependence is observed with a maximum shape effect reaching 10% in the ($\geq$ 6j, 3b) region. This is partly explained by the di-jet mass resolution which is at the level of 15-20%, and by the large combinatorics which make it difficult to identify the di-jet combination corresponding to the Higgs boson decay products.

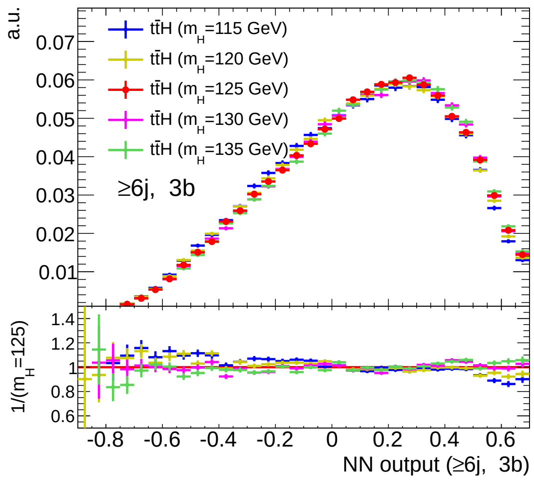

(a)

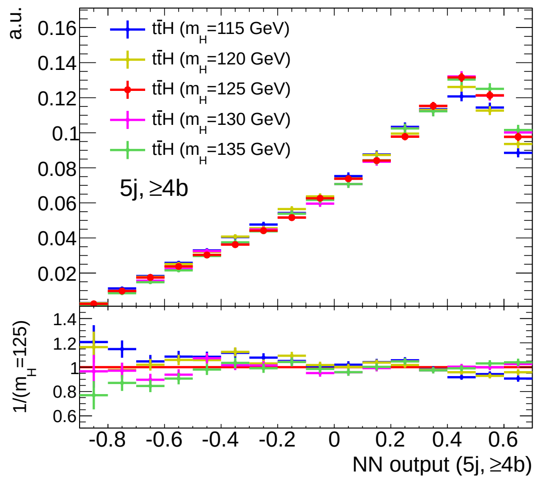

(b)

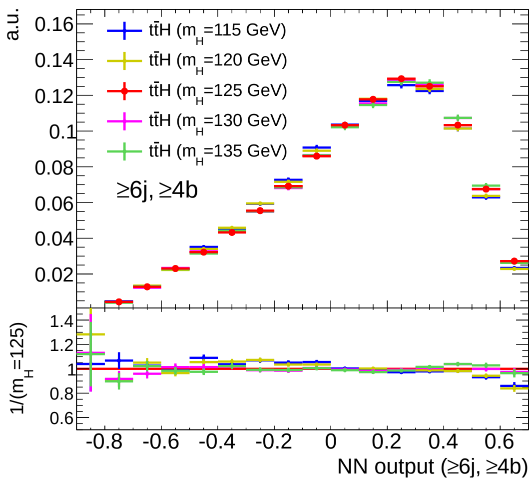

(c)

Figure 9.9: Neural network output distributions for different values of m_H in the $t\bar{t}H$ sample. NNs for region ($\geq$ 6j, 3b) (a), (5j, $\geq$ 4b) (b) and ($\geq$ 6j, $\geq$ 4b) (c) are shown. The bottom pad of each plot shows the ratio with respect to the distribution obtained for the reference Higgs boson mass of 125 GeV.

9.4 Validation of input variables

The usage of multivariate techniques requires particular care in the validation of the variables used. In particular, not only does the Monte Carlo have to provide a good description of the discriminating variables, but also the correlation among them needs to be verified since this is one of the ingredients that are exploited by the NN. The description of the variables by the Monte Carlo simulation has been checked in multiple analysis regions. This allows to increase the robustness of the validation by probing different final state topologies in terms of number of jets and b-tagged jets as well as varying $t\bar{t}$+HF fraction.

Initially, background regions have been used to verify the modelling of the input variables. Regions like $(\geq 6\text{j}, 2\text{b})$ and $(5\text{j}, 3\text{b})$ have the advantage of very high statistics and the drawback of a low $t\bar{t}$+HF fraction and lower b-tagged jet multiplicity with respect to the main signal regions. The $(4\text{j}, 4\text{b})$ region has a much higher $t\bar{t}$+HF fraction, but suffers from low statistics. As a result, limited information on the modelling of $t\bar{t}$+HF events can be extracted. Figures 9.10, 9.11 and 9.12 show the data/MC comparison in these three regions for the 12 most sensitive variables combining all the regions[6].

As an intermediate step, the validation of the input variables has been performed on the three signal regions after applying a 'signal-depleting' selection. A cut on the output NN distribution was chosen in order to remove bins where the expected S/B was greater than 2%. After the selection, the expected signal contamination in each region dropped below 1% while retaining 30% to 70% of the background events in those regions. Such configuration is referred to as 'partially blinded' and also represented an important step in the validation of the analysis since it allowed to exercise the fitting procedure without suffering from bias of a potential signal excess in data.

At the same time, additional checks have been performed for variables depending on the number of b-tagged jets in the final state ($\Delta R^{\text{avg}}_{\text{bb}}$, $m^{\text{min}\ \Delta\text{R}}_{\text{bb}}$, etc). In regions with 3 b-tagged jets, one additional jet was 'promoted' to be a b-tagged jet and the relevant variables were recalculated with the new set of jets. This allowed to check, with higher statistics, in particular the description of variables computed with 4 b-tagged jets for the $t\bar{t}$+light process. No significant degradations of the data/Monte Carlo agreement with respect to the 'standard' definition of the variables have been observed .

Finally, the modelling of the input variables has been verified in the totality of the signal regions allowing to profit from the full available statistics in $t\bar{t}$+HF dominated regions with at least 4 b-tagged jets. Plots are collected in Figures 9.13, 9.14 and 9.15. No significant shape disagreement is visible, confirming the results obtained in the 'partially blinded' regions. The observed normalisation differences are within the total uncertainty band; no significant shape differences are present with the available statistics. The level of agreement was established using a Kolmogorov-Smirnov test performed after normalising the distributions for the data and the sum of the background to the same area. Similar plots for the variables only used in the NN trained to separate $t\bar{t}$+light from $t\bar{t}$+HF in the $(5\text{j}, 3\text{b})$ region are collected in Figure 9.16.

All the distributions are presented prior to any fit procedure (referred to in the following as *pre-fit*); the profile likelihood fit (which will be described in 10.1.1) is designed to improve the knowledge of the background normalisation and, at the same time, a reduction of the systematic uncertainties is observed. It has been verified that the level of agreement does not degrade after extrapolating the result of the fit performed on the final discriminants to each of the considered variables[7].

[6] Variables with a high rank in at least one of the NN.

[7] As an intermediate step in the analysis, the modelling of the variables was verified after performing a fit using the $H_{\text{T}}^{\text{had}}$ distribution in all regions and the blinding NN cut in the signal regions.

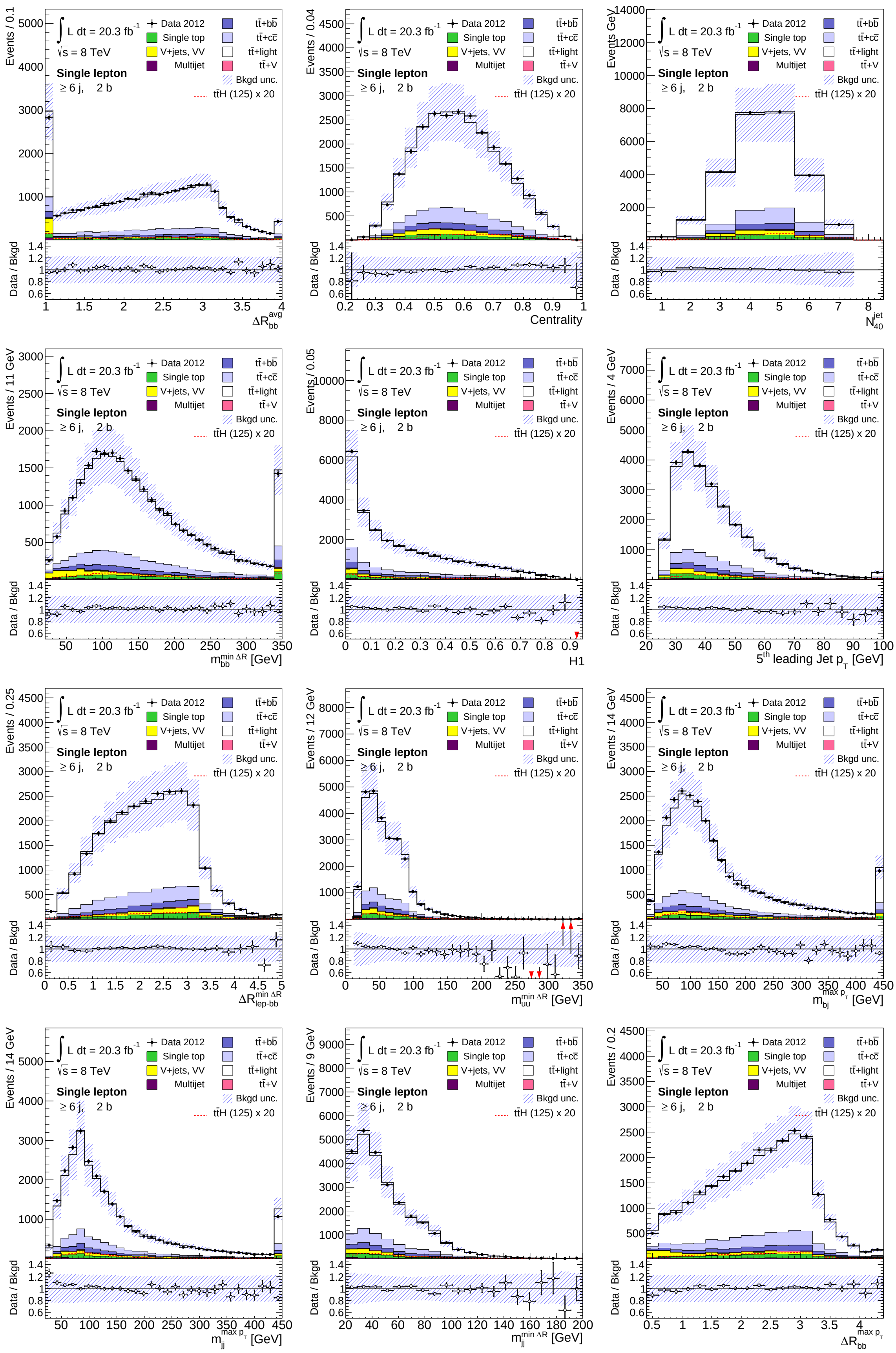

Figure 9.10: Data/MC comparison for a set of the most discriminating variables used in the NN. Distributions are shown in the ($\geq$ 6j, 2b) analysis region before the fitting procedure. The uncertainty band contains the statistical and systematic contribution.

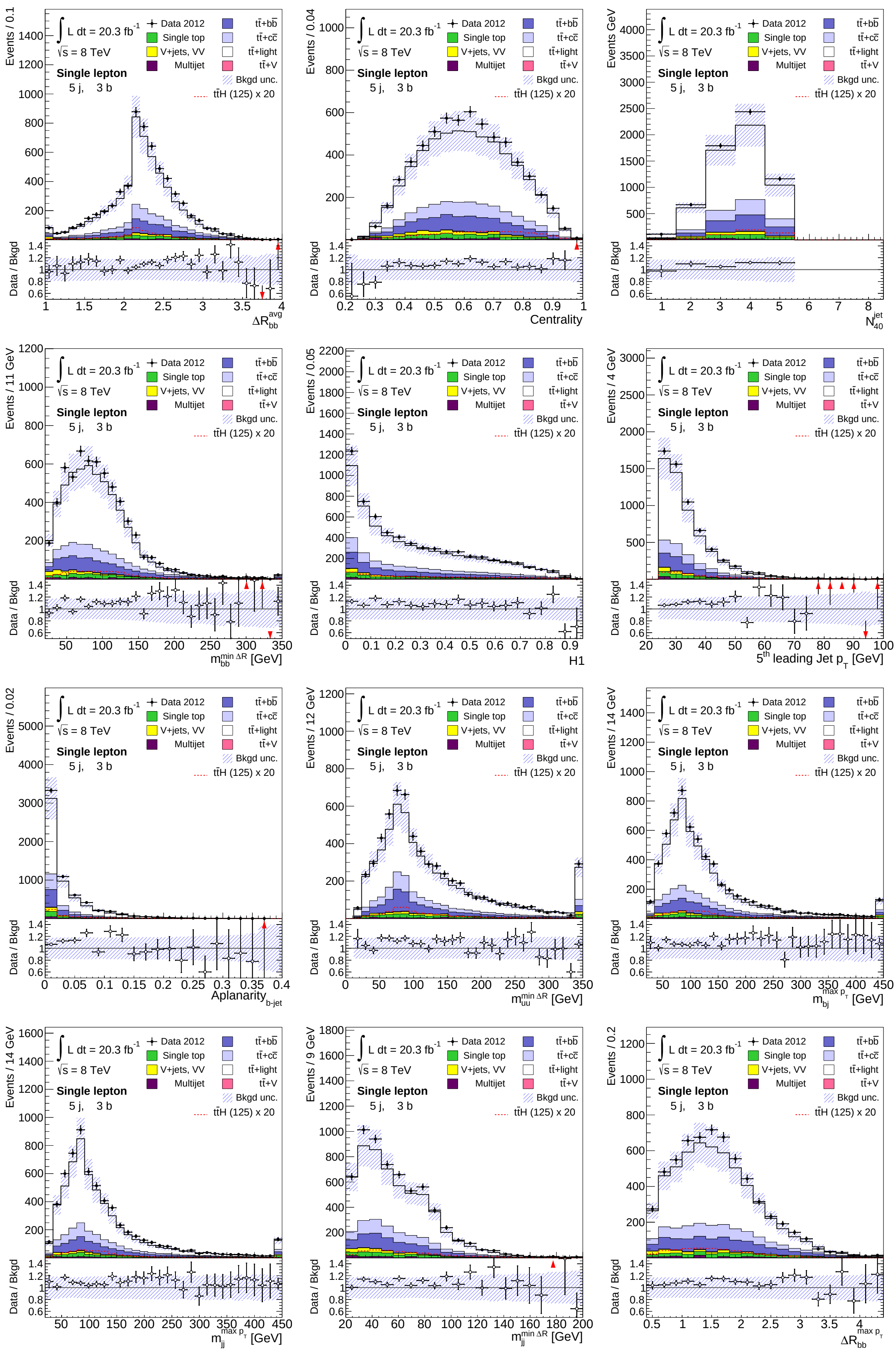

Figure 9.11: Data/MC comparison for a set of the most discriminating variables used in the NN. Distributions are shown in the (5j, 3b) analysis region before the fitting procedure. The uncertainty band contains the statistical and systematic contribution.

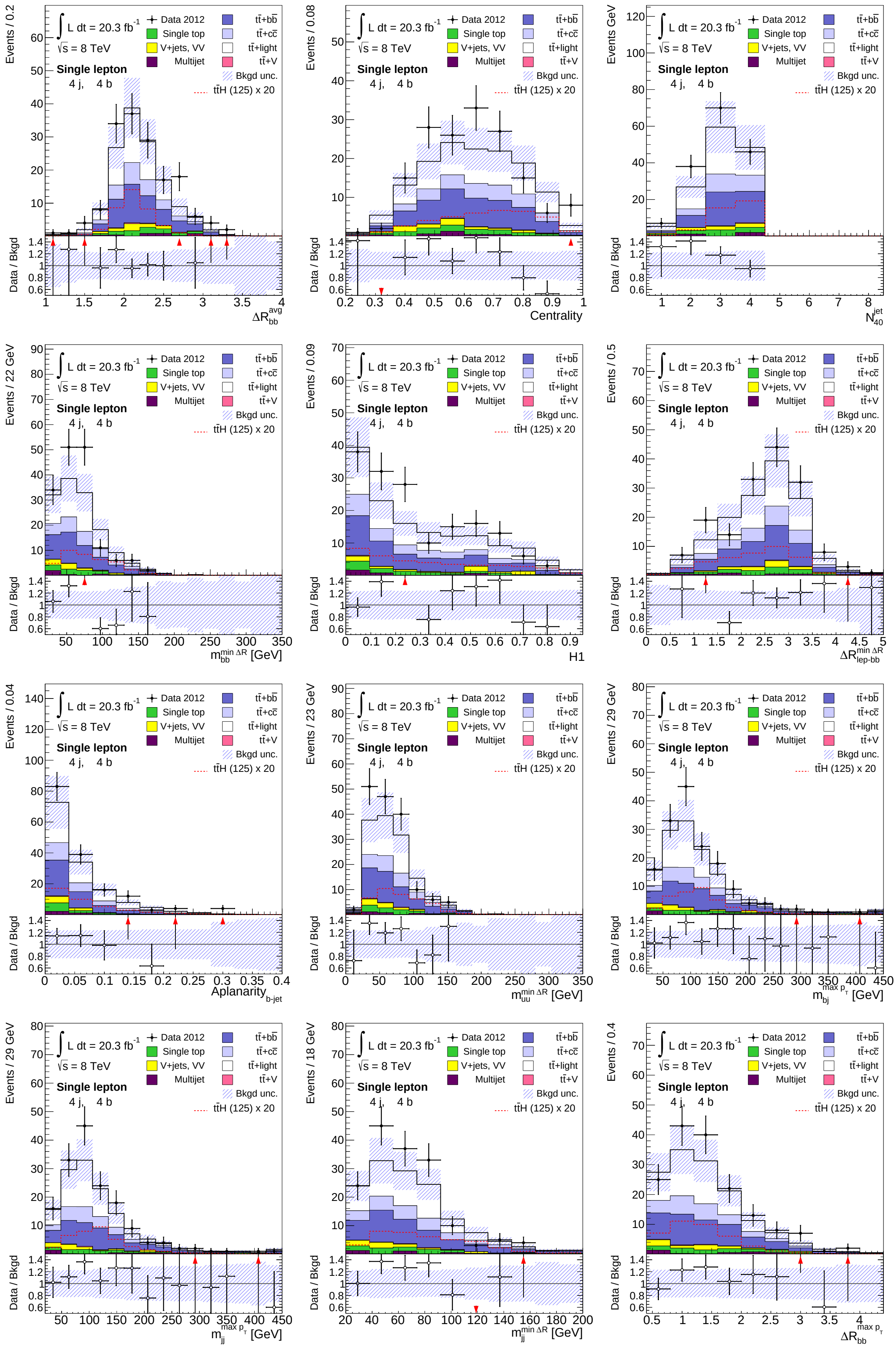

Figure 9.12: Data/MC comparison for a set of the most discriminating variables used in the NN. Distributions are shown in the (4j, 4b) analysis region before the fitting procedure. The uncertainty band contains the statistical and systematic contribution.

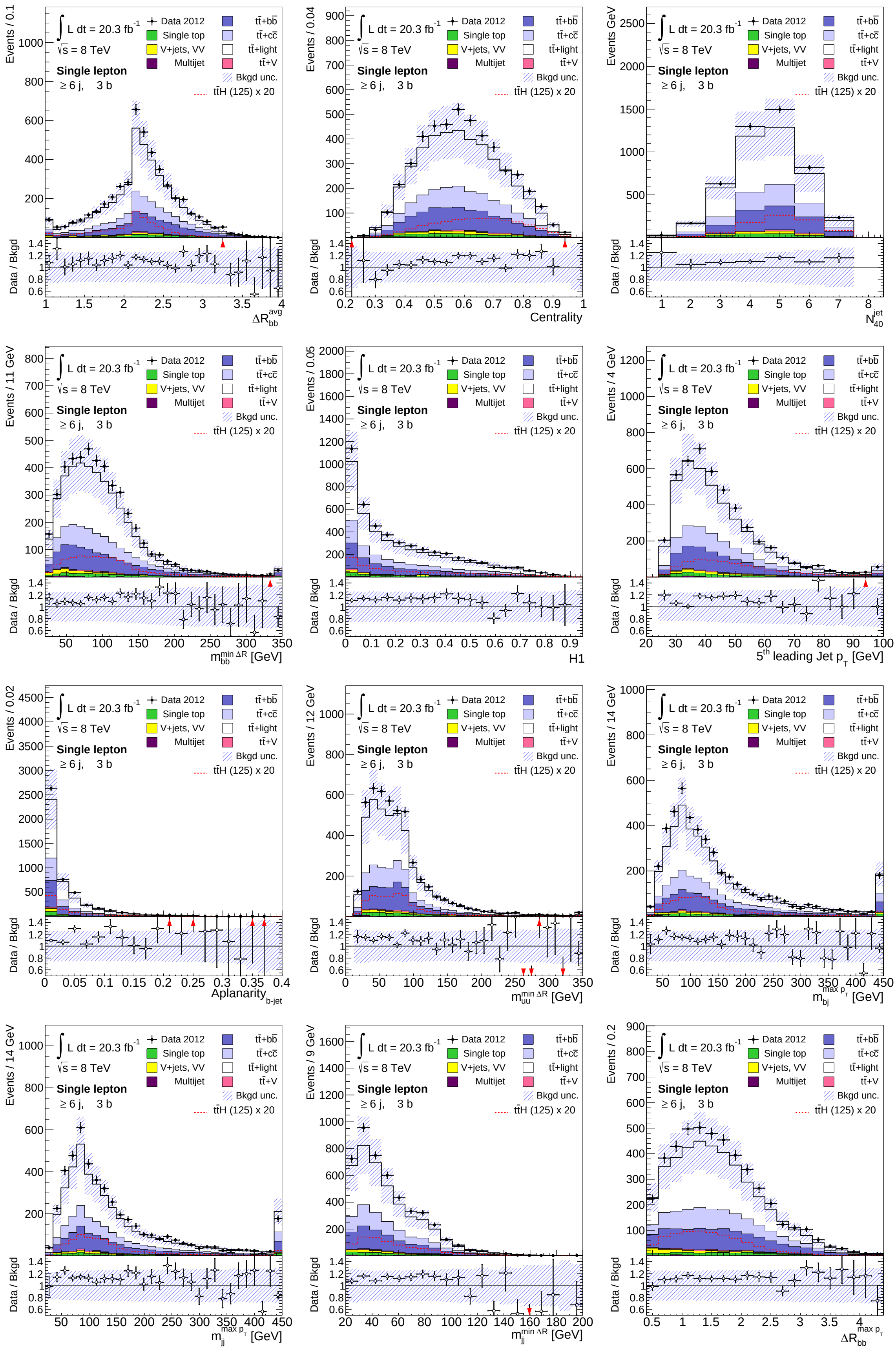

Figure 9.13: Data/mc comparison for a set of the most discriminating variables used in the NN. Distributions are shown in the ($\geq 6j, 3b$) analysis region before the fitting procedure. The uncertainty band contains the statistical and systematic contribution.

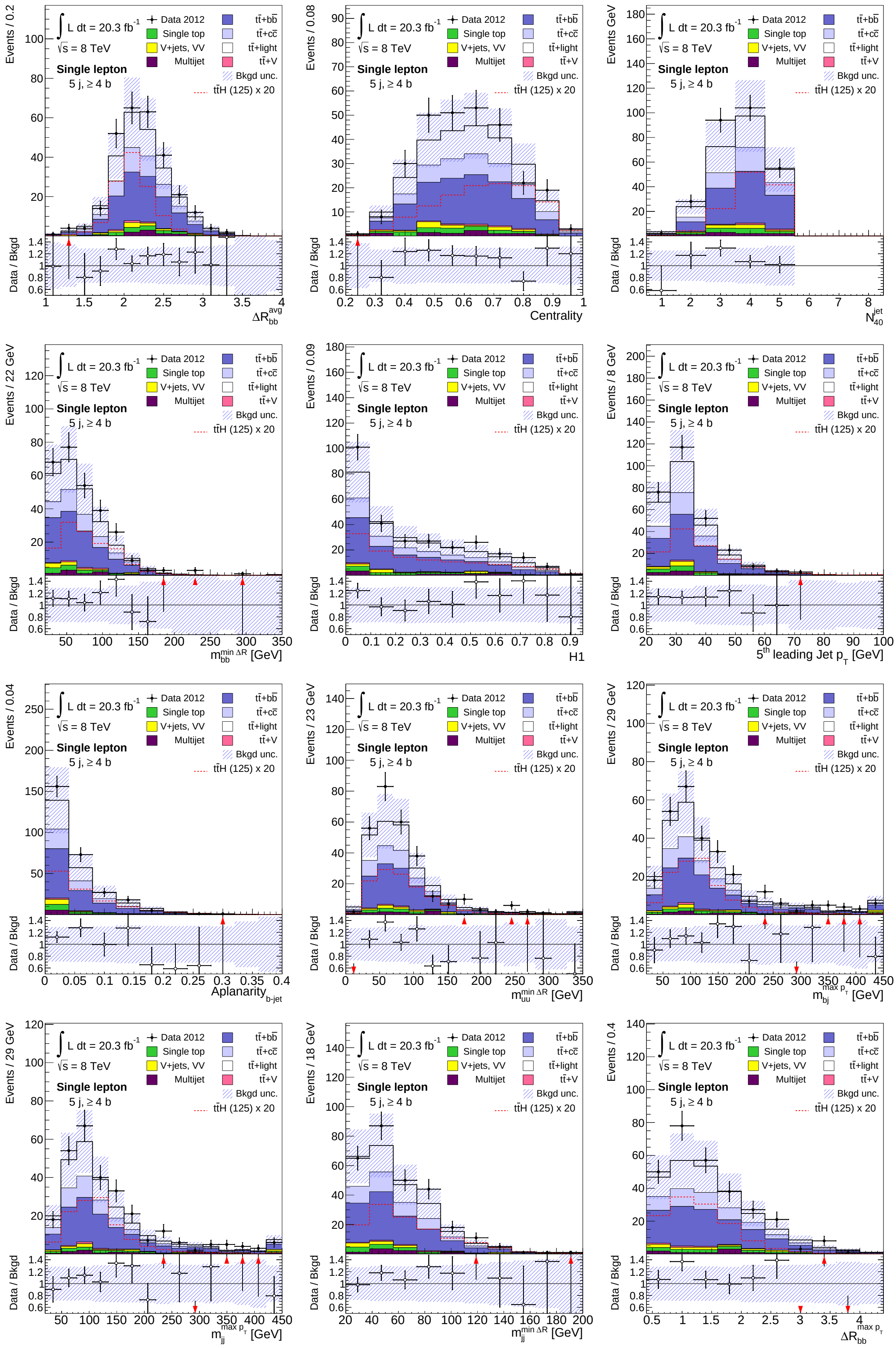

Figure 9.14: Data/mc comparison for a set of the most discriminating variables used in the NN. Distributions are shown in the (5j, $\geq$ 4b) analysis region before the fitting procedure. The uncertainty band contains the statistical and systematic contribution.

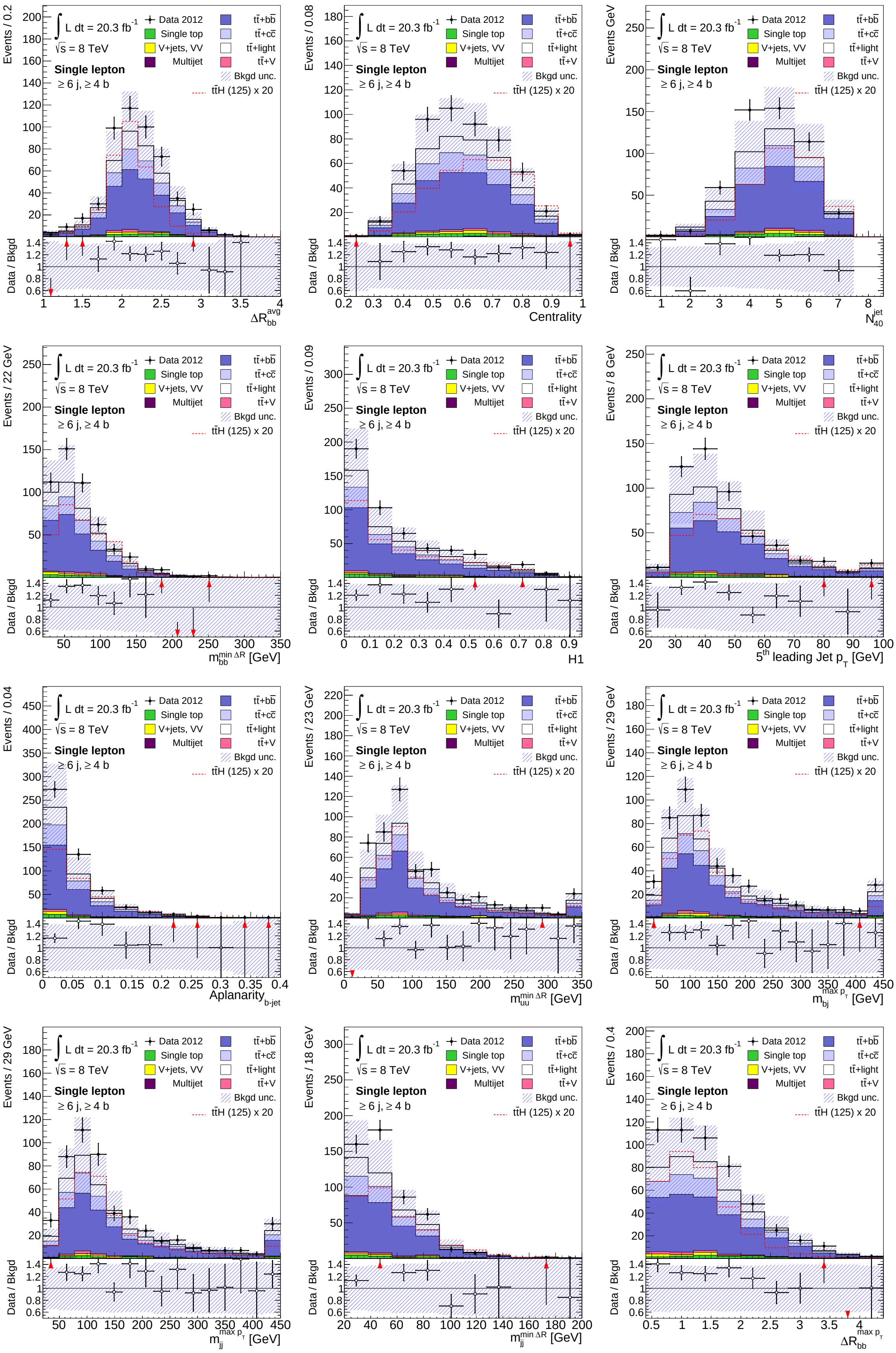

Figure 9.15: Data/mc comparison for a set of the most discriminating variables used in the NN. Distributions are shown in the (4j, 4b) analysis region before the fitting procedure. The uncertainty band contains the statistical and systematic contribution.

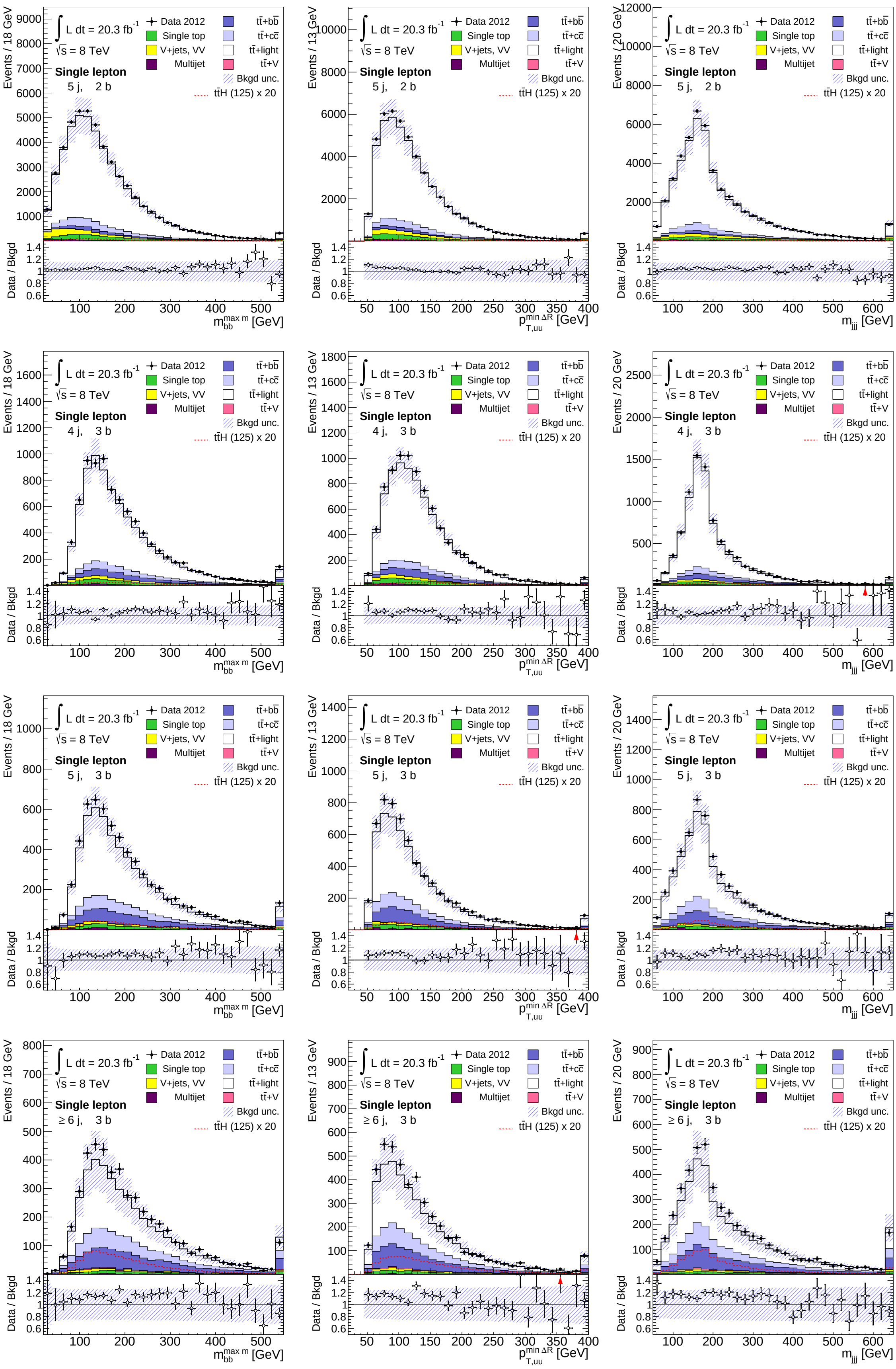

Figure 9.16: Data/MC comparison for a set of the most discriminating variables used in the NN to separate $t\bar{t}$+light from $t\bar{t}$+HF. Each row corresponds to a different analysis region: (5j, 2b), (4j, 3b), (5j, 3b), ($\geq$ 6j, 3b).

Distributions after the final fitting procedure (*post-fit*) can be found in Appendix E.

9.4.1 Variables correlation

The correlation among input variables is an important ingredient in the building of the neural network discriminant and it is also exploited in the ranking procedure performed by NeuroBayes.

To first order, the correlation between two variables can be described by the linear correlation coefficient already introduced in Eq. 9.1.

Figures 9.17 and 9.18 show the correlation coefficients for each pair of variables in the data sample and in the background sample. Large correlations between variables are present but this is dealt with by the NeuroBayes program; the important aspect is the modelling of these correlations in the data by the Monte Carlo simulation.

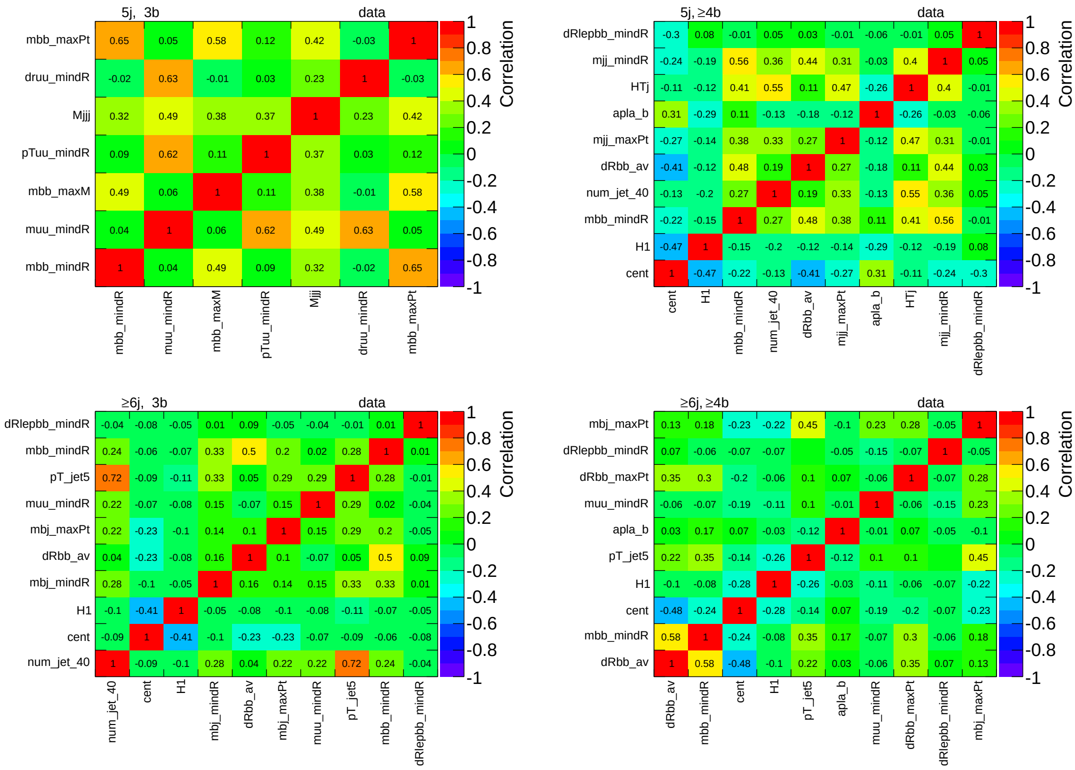

Figure 9.17: Linear correlation coefficients among NN input variables in each region. The values are extracted from the data sample.

The differences between the correlation coefficient between data and Monte Carlo are reported in Figure 9.19. Generally a good agreement is observed between data and MC with deviations up to 20% in regions with four b-tagged jets. In those regions, the limited data statistics (300-500 events) can lead to larger statistical fluctuations. When evaluating the difference in the correlation among the same set of variables but in the respective higher statistics regions with 3 b-tagged jets, a better consistency is found.

In order to understand the modelling of the correlation effects, the mean of each input variable as a function of the NN output was considered. Examples of comparisons between data and Monte Carlo are shown in Figure 9.20 for the three most discriminating variables

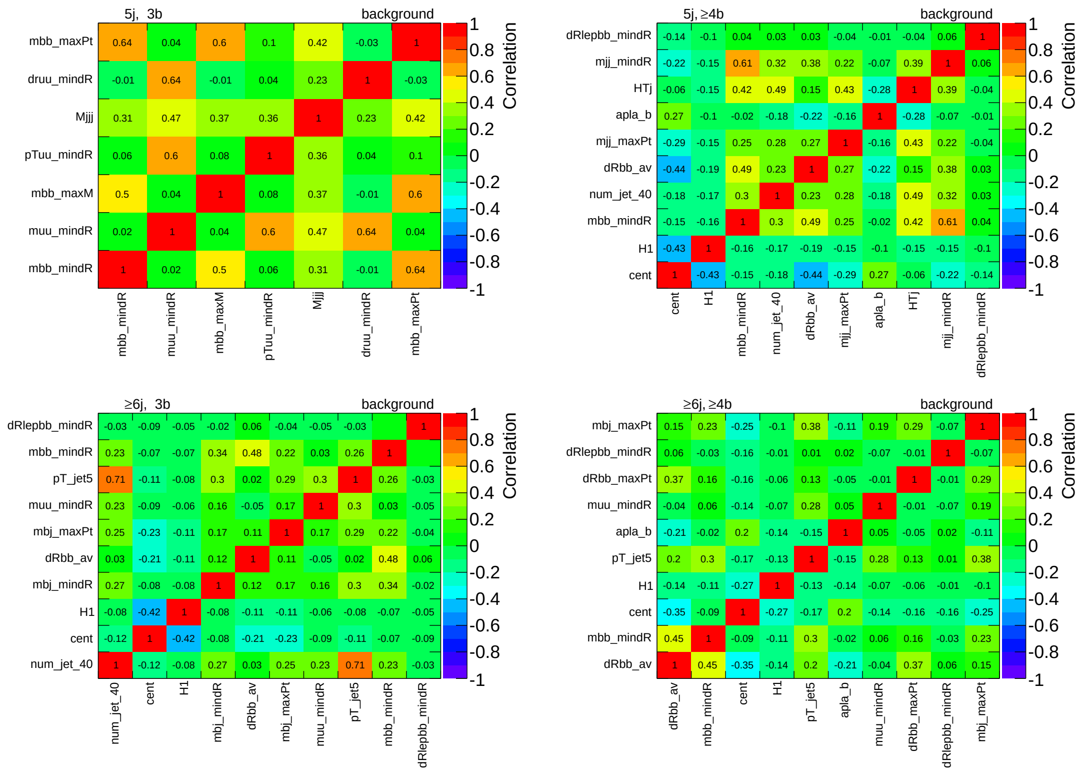

Figure 9.18: Linear correlation coefficients among NN input variables in each region. The values are extracted from the Monte Carlo sample containing the sum of all the backgrounds.

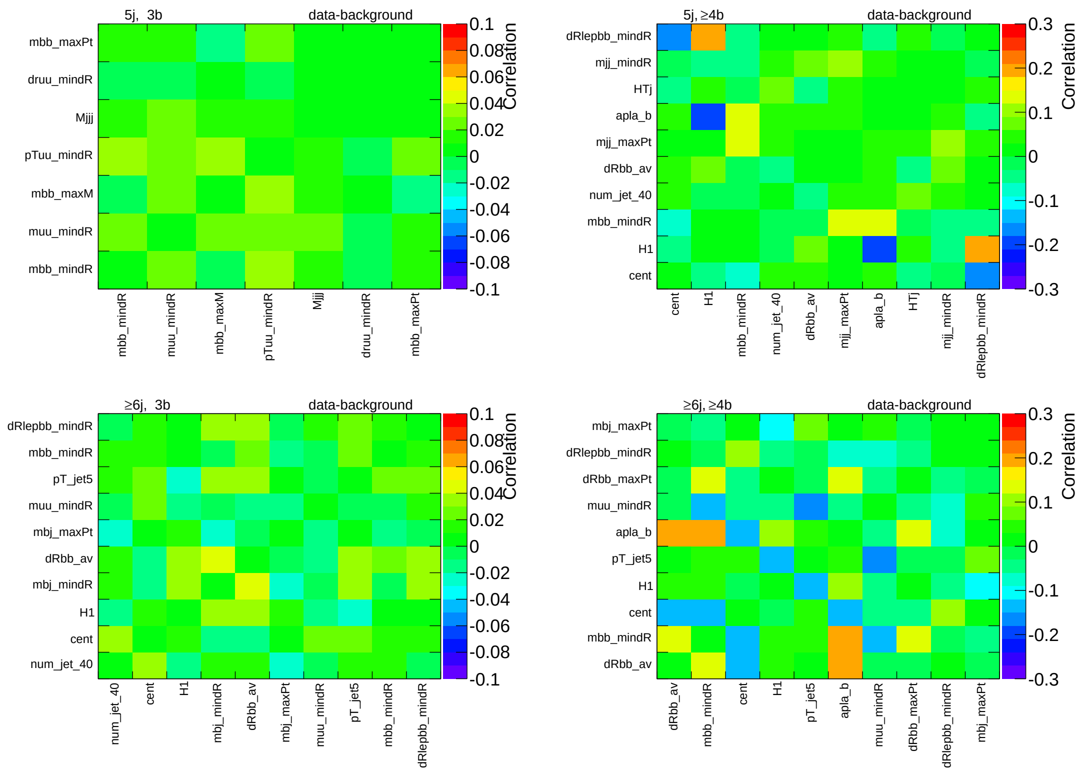

Figure 9.19: Difference between the linear correlation coefficients among NN input variables in each region estimated in the data and the background sample.

in each region. The behaviour of data and Monte Carlo is found to be consistent within the uncertainties.

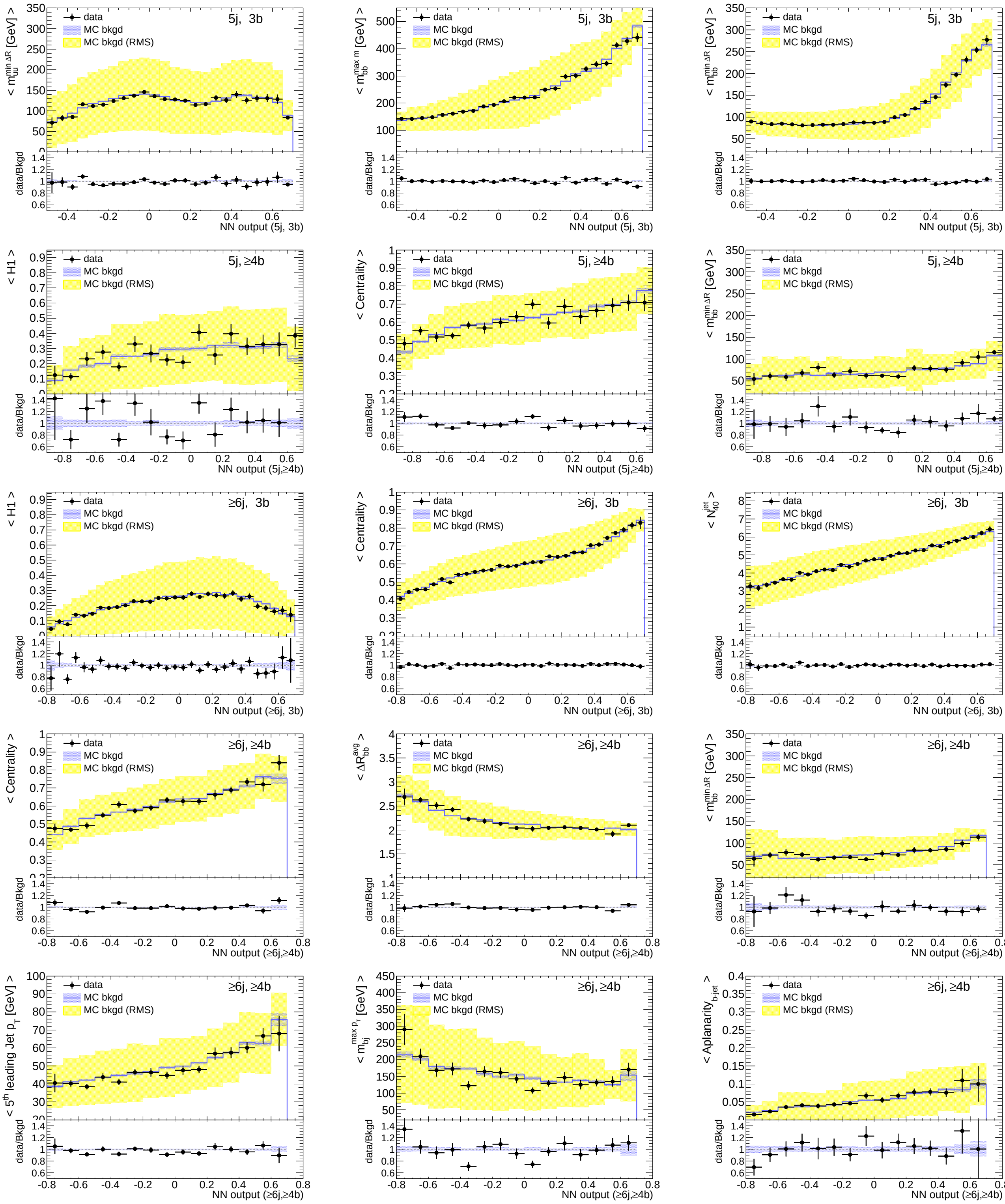

Figure 9.20: Profile distribution for input variables as a function of the NN output. The mean value of each variable in bins of the NN output is shown for data and background Monte Carlo. The yellow band displays the RMS of the variable distribution in the specific NN output bin. For each of the four analysis regions, the most sensitive discriminating variables are shown.

9.5 Final discriminants

Figure 9.21 shows the distribution of the NN outputs in the (5j, 3b), (5j, ≥ 4b), (≥ 6j, 3b) and (≥ 6j, ≥ 4b) regions. They represent the final discriminants used in these regions with the same binning used in the fitting procedure. The choice of the binning stems from a compromise between exploiting the shape separation of the NN and the available statistics both in data and in the Monte Carlo samples.

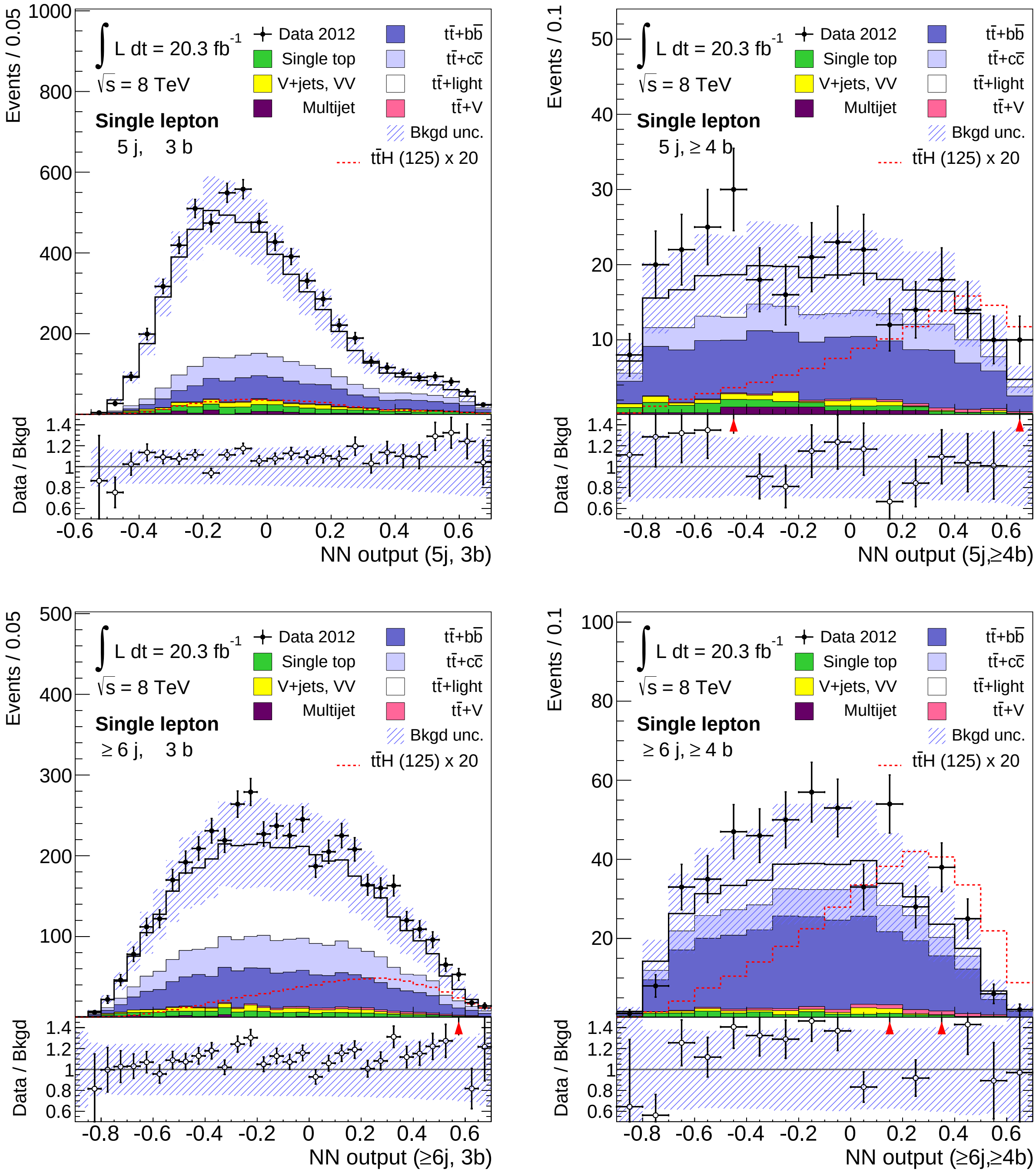

Figure 9.21: NN output distributions in data and Monte Carlo for both the four regions where multivariate discriminants are used in the analysis. The uncertainty band contains both Monte Carlo statistical uncertainty and systematic uncertainties. Distributions are shown prior to the fit procedure.

An excessively large number of bins can lead to situations where some bins in the signal-enriched part of the NN contain signal events but no background events, resulting in a bias in the signal extraction. Furthermore, Monte Carlo statistics is of primarily importance also for the reliable determination of the effect of systematic uncertainties affecting the shape of the discriminants. It has been verified that the expected performance is hardly affected if the current number of bins is varied within a factor of 2.

As a final validation step, also the NN output distributions have been evaluated in analysis regions other than the ones used for the training. This allows to verify the behaviour of the specific NN in final states with different topologies and varying $t\bar{t}$+HF fraction. As in the case of the variables validation, the ($\geq$ 6j, 2b), (4j, 4b) and (5j, 3b) regions have been considered. Furthermore, other signal-enriched regions have been taken into account; as an example, the NN trained in the (5j, $\geq$ 4b) topology is evaluated in the ($\geq$ 6j, $\geq$ 4b) region. Data/MC comparisons are summarised in Figure 9.22. A similar level of agreement is observed for the NN output distributions for a large variety of topologies considered, all featuring a different value for the fraction of $t\bar{t}$+HF.

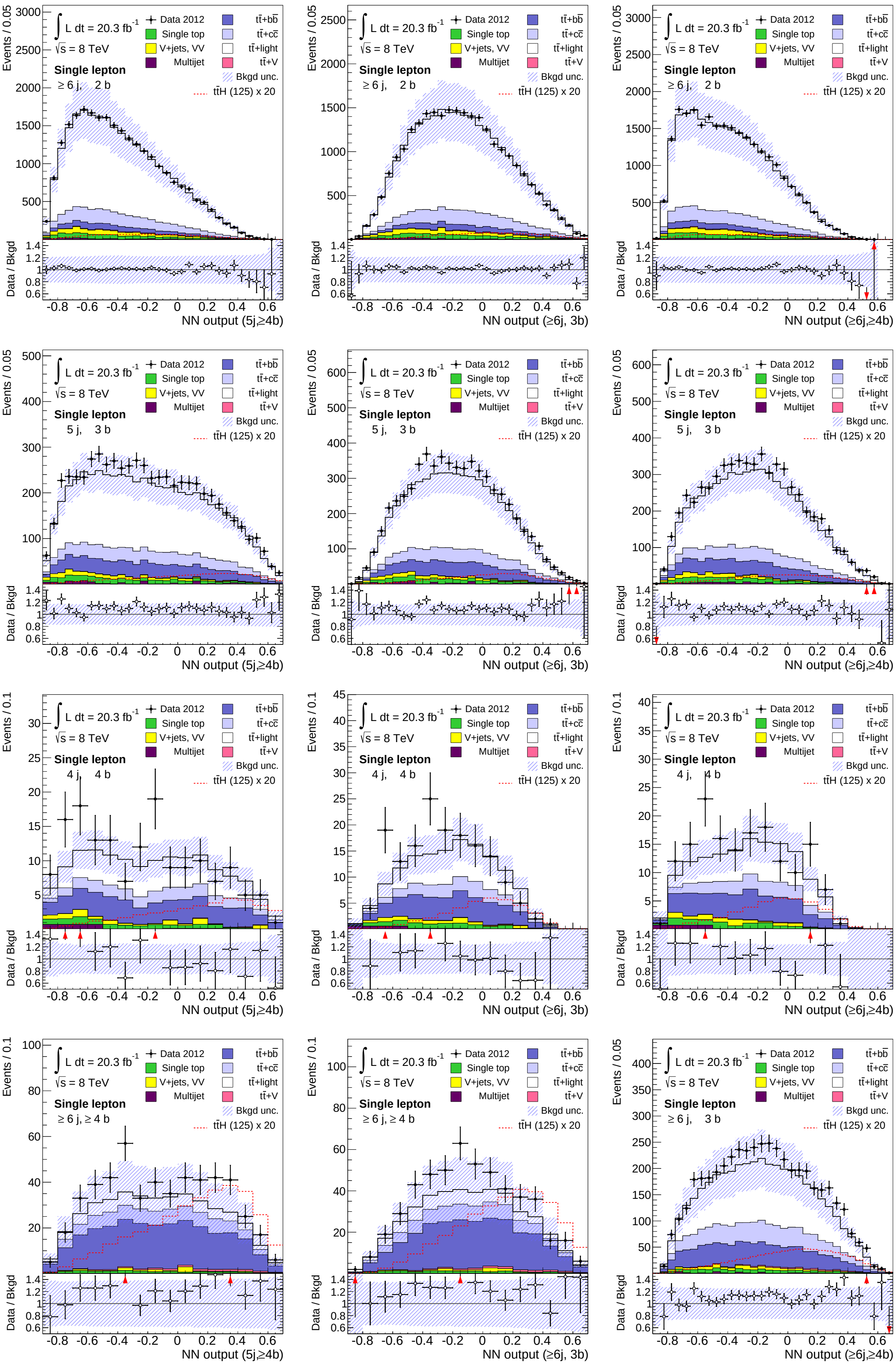

Figure 9.22: NN output distributions evaluated in regions other from the one used for their training, prior to the fit procedure. Each row corresponds to a different analysis regions: $(\geq 6j, 2b)$, $(5j, 3b)$, $(4j, 4b)$. The last row corresponds to a different signal region according to the variable.The uncertainty band contains both Monte Carlo statistical uncertainty and systematic uncertainties.

Chapter 10

Search for $t\bar{t}H(b\bar{b})$: Statistical analysis and results

This chapter contains the description of the statistical methods used in the $t\bar{t}H$ analysis. A fit is performed to the data in order to extract the amount of signal and each background. Subsequently, the significance of the obtained signal is evaluated.

The first part of the chapter will illustrate the template fitting procedure; the *profiled likelihood* approach is employed in order to reduce the impact of systematic uncertainties on the final result. Detailed descriptions of the sources of systematic uncertainties and their implementation in the fitting procedure will be given.

The second part describes the procedure leading to the determination of the signal significance and the upper limit on the $t\bar{t}H$ production cross section. The combination of the result described in this thesis with the analysis exploiting a dilepton final state topology will also be described.

10.1 Fitting procedure

The template fitting procedure was already employed for the inclusive $t\bar{t}$ cross section analysis described in Chapter 6; for the given discriminant variable in the analysis, template distributions for the signal and each of the backgrounds are compared to the data distribution with the aim to extract the normalisation factor for the signal process.

In the context of the search for the $t\bar{t}H$ process, the fitting procedure is based on the maximisation of a likelihood function. The effect of systematic uncertainties is incorporated in the likelihood definition through so-called *nuisance parameters*; these are unknown parameters that also need to be estimated from data or external measurements but are not directly of interest. The next sections will describe the general idea of the 'nuisance parameter approach' and the specific implementation in the $t\bar{t}H$ analysis.

10.1.1 'Profile' likelihood fit

A likelihood function is obtained from the probability of data given a certain hypothesis. In the context of this analysis, the hypothesis is represented by a single *signal strength* parameter:

$$\mu = \frac{\sigma_{t\bar{t}H}}{\sigma^{\mathrm{SM}}_{t\bar{t}H}} \tag{10.1}$$

Here, $\mu = 0$ represents the background-only hypothesis where no $t\bar{t}H$ is present, while $\mu = 1$ coincides with the SM Higgs boson production.

The data in each bin of each distribution are expected to follow a Poisson probability distribution around its expected number of events. For an analysis fitting template distributions in multiple signal and control regions, the likelihood L(μ)[1] can be expressed as:

$$L_{\text{main}}(\mu) = \prod_{j}^{\text{reg}} \prod_{i}^{\text{bins}_\text{j}} \frac{(\mu s_{ij} + b_{ij})^{n_{ij}}}{n_{ij}!} e^{-(\mu s_{ij} + b_{ij})} \tag{10.2}$$

where n_{ij}, s_{ij} and b_{ij} represent respectively the number of data events, the expected number of signal and background events in the i^{th} bin of the fitted distribution in the region j. The best estimate for μ is obtained by maximising the likelihood or, equivalently, minimising the negative logarithm of the likelihood[2]. The error on the signal strength parameter is determined through a scan of the likelihood values as a function of μ. The 1-σ band is defined by determining the points in which the logarithm of the likelihood decreases by 0.5 with respect to the maximum value.

In the cross section analysis described in Chapter 6, the effect of systematic uncertainties was taken into account with ensemble testing: pseudo experiments are generated from the modified template for each systematic variation and the effect on the fitted value of μ is taken as the impact of the systematic itself.

A more effective approach consists in including the systematic uncertainties directly in the definition of the likelihood through a suitable set of continuous parameters $\boldsymbol{\theta}$ that parameterise the effect of each systematic on the template distributions. As a net effect, the various terms in the likelihood (n_{ij}, s_{ij}, b_{ij}) acquire a dependence on $\boldsymbol{\theta}$; varying the values of the nuisance parameters allows to modify both the shape and normalisation of the templates. The aim is to increase the flexibility of the model we use to fit the data and its capability to better agree with the data for certain values of the nuisance parameters. The maximisation of the likelihood thus produces a joint measurement of the parameter of interest μ and the nuisance parameters $\boldsymbol{\theta}$. These 'best fit' values will be indicated in the following as $\hat{\mu}$ and $\hat{\boldsymbol{\theta}}$. Such a framework also directly allows to estimate the effect of the systematic uncertainties on the determination of μ through the scanning of the likelihood profile.

Systematic uncertainties usually derive from auxiliary measurements[3] which provide the central value and uncertainty of a given set of parameters, for instance the scale factors associated to the electron efficiency. By convention, the value θ=0 corresponds to the nominal central value of the prediction, while values of $\pm$1 represent the "$\pm$1-σ" variations of that particular systematic uncertainty. This is obtained by including in the likelihood formulation of Equation 10.2 additional terms:

$$L(\mu, \boldsymbol{\theta}) = L_{\text{main}}(\mu, \boldsymbol{\theta}) \cdot \prod_{k} Gaus(\theta_k | 0, 1) \tag{10.3}$$

where $Gauss(\theta_k|0,1)$ represents the distribution of the nuisance parameter, following the 'prior' knowledge of it. Although a gaussian distribution is most commonly assumed as prior distribution, other functional forms (log-normal, gamma) could be more suited in other specific cases. Equation 10.3 is valid under the assumption that all systematic uncertainties can be considered uncorrelated so that independent multiplicative terms can be included in the likelihood definition.

[1]The likelihood is also always a function of the observed data. This is omitted in the notation for simplicity.

[2]The negative logarithm of the likelihood (often referred to as *LogLikelihood*) is often used for numerical purposes and historical reasons.

[3]A similar approach is applied also to theoretical uncertainties although strictly speaking they cannot be associated with a measurement.

The nuisance parameters are unknown parameters that need to be determined by the fit. This profiled likelihood approach allows the data under study to potentially improve the initial knowledge of systematic uncertainties obtained from external inputs to the analysis. In case the data are not particularly sensitive to a given source of systematics, the constraint term in the likelihood ensures that the nuisance parameter stays at 0 and its error is dominated by the input uncertainties. On the other hand, the fit procedure could shift (pull) a nuisance parameter to achieve a better data/MC description or, at the same time, produce a reduction (constraint) of the error of the nuisance parameter with respect to its initial value. This usually happens when the large effects of a particular systematic uncertainties are not supported by the available data statistics. Furthermore, during the likelihood maximisation process, correlations can be established among nuisance parameters that have similar effects in the regions considered by the fit and this further aids in the reduction of the final effect of the total systematic uncertainties.

The implementation of the profiled likelihood relies on a continuous parameterisation of the effect of the systematics on the templates. Usually only the 'nominal' templates (θ=0) and the ones corresponding to one sigma variations of the uncertainty are given in forms of histograms; an interpolation/extrapolation procedure is applied to compute the template corresponding to an arbitrary value of the nuisance parameter. Different approaches are adopted for the component of the uncertainty acting on the normalisation of the template and the part affecting only the shape of the template, although they are controlled by the same nuisance parameter [176]. For the shape uncertainty, the *vertical morphing* of histograms is applied; each content of each bin is adjusted with a linear function, interpolating between the nominal bin content and the bin content in case of ± 1 σ variation. Each bin of the template is treated independently.

For what concerns the normalisation effect of the uncertainty, for values of θ between -1 and 1, the interpolation approach uses a 6^{th} order polynomial function; the extrapolation of the effect of the uncertainty outside the 1-σ boundaries is implemented with an exponential function. This approach allows a 'smooth' parameterisation as a function of θ with no discontinuity[4], while the use of the exponential function prevents the normalisation of each template from becoming negative even for a value of the nuisance parameters far from the nominal one.

In case only the up or down 1-sigma variation is available (as in the case of the jet energy resolution uncertainty), the effect of the 'one sided' variation is symmetrised.

Finally the finite statistics of the templates used for the fit, usually determined from Monte Carlo simulation, is also incorporated in the likelihood definition. Following a simplified version of the approach used by Barlow and Beeston [147], a single nuisance parameter is introduced for each bin of the fitted distributions allowing the total template prediction in that bin to vary within its statistical uncertainties. The full implementation in the likelihood expression is described in Ref. [176]; in regimes where the per-bin Monte Carlo statistical uncertainty is not large, the prior term for this nuisance parameter can be approximated by a gaussian distribution with mean of 1 and a standard deviation equal to the relative statistical uncertainty of the sum of all templates in that bin.

10.1.2 The fit model

The *fit model* is completely specified by the variable used to build template distributions in each fitted region, the list of systematic uncertainties and the way they are correlated across regions and for the various templates.

Table 10.1 summarises the regions used in the fit as well as the corresponding variable:

[4]The continuity is also imposed for the for the first and second derivative function at the values $\sigma = 1$.

$H_{\mathrm{T}}^{\mathrm{had}}$ distribution in 'signal-depleted' regions, multivariate discriminants in 'signal-enriched' ones. The fit is performed directly combining events from the electron and muon channel when building the templates, rather than considering them as a two separate channels in the fit. The main reason for this choice is not to dilute the Monte Carlo template statistics in the building of the templates as well as not to double the number of regions used in the fit.

	4 jets	5 jets	≥6 jets
2 b-tagged jets	$H_{\mathrm{T}}^{\mathrm{had}}$	$H_{\mathrm{T}}^{\mathrm{had}}$	$H_{\mathrm{T}}^{\mathrm{had}}$
3 b-tagged jets	$H_{\mathrm{T}}^{\mathrm{had}}$	NN_{5j3b}	NN_{5j4b}
≥4 b-tagged jets	$H_{\mathrm{T}}^{\mathrm{had}}$	NN_{6j3b}	NN_{6j4b}

Table 10.1: Summary of regions included in the fit and variable used in each region. The sub-script in the neural network output variables indicates that a specific neural network is trained in each region.

Considering the nine regions, a total of 160 bins are included in the likelihood construction. The additional nuisance parameter taking care of the template statistics is considered only for bins for which the relative uncertainty is larger than 1%.

The signal strength is considered as a free-floating parameter in the fit. None of the background templates has a free-floating normalisation; their normalisation is controlled through specific nuisance parameters that implement the theoretical knowledge of the respective cross section or the uncertainty on the data-driven estimates. Additional nuisance parameters related to the other systematic uncertainties can impact the acceptance factor for each sample, the distribution of events among the analysis regions and finally the shape of the discriminant distributions.

Individual sources of systematic uncertainty are considered uncorrelated. Table 10.2 presents a summary of the systematic uncertainties considered in the analysis indicating if they affect the normalisation ('N') and shape ('S') of the templates. The table also indicates the number of specific sub-components for each category. The breakdown into sub components is particularly desirable in the implementation of the profile likelihood fit since it results in a more flexible model, it allows to decouple the effect of each uncertainty better and to treat them as initially uncorrelated. It also helps preventing false overconstraints of the source of systematics[5].

The aim of the profiled likelihood procedure is to use the background dominated regions to improve the knowledge of the background (through constraints of nuisance parameters or creation of correlations) and extrapolate this knowledge into signal-enriched regions where a smaller uncertainty on the background predictions can lead to an improvement in sensitivity.

In the following sections, a brief description of the sources of systematic uncertainties will be provided with particular emphasis on the modelling of $t\bar{t}$ events.

Detector-related systematics

The uncertainty on the determination of the amount of collected integrated luminosity is 2.8%, derived following the same methodology as that detailed in [67]. The systematic uncertainty is applied to all the processes determined from the MC simulation.

Uncertainties originating from the usage of the physics objects have been already outlined in Chapter 3. Systematic uncertainties related to the lepton selection efficiencies are separated into

[5] As an example, using just a single envelope for the jet energy scale uncertainty will result in a larger normalisation effect (that could be easily constrained by the fit), but also to neglect shape uncertainties that a finer breakdown in components can induce.

Systematic uncertainty	Type	Components
Luminosity	N	1
Physics Objects		
Electron	SN	5
Muon	SN	6
Jet energy scale	SN	22
Jet energy resolution	SN	1
Jet vertex fraction	SN	1
Jet reconstruction	SN	1
b-jet tagging efficiency	SN	6
c-jet tagging efficiency	SN	6
Light jet-tagging efficiency	SN	12
Background Model		
$t\bar{t}$ cross section	N	1
$t\bar{t}$ modelling: p_{T} reweighting	SN	9
$t\bar{t}$ modelling: parton shower	SN	2
$t\bar{t}$+heavy-flavour: normalisation	N	2
$t\bar{t}$+heavy-flavour: HF reweighting	SN	2
$t\bar{t}$+heavy-flavour: generator	SN	5
W+jets cross section	N	3
W p_{T} reweighting	SN	1
Z+jets cross section	N	1
Z p_{T} reweighting	SN	1
Multijet normalisation	N	2
Single top cross section	N	1
Diboson cross section	N	1
$t\bar{t}V$ cross section	N	1
$t\bar{t}V$ modelling	SN	1
Signal		
$t\bar{t}H$ modelling	SN	3

Table 10.2: List of systematic uncertainties considered. A "N" means that the uncertainty is taken as normalisation-only for all processes and channels affected, whereas a "S" denotes systematics that are considered shape-only in all processes and channels. A "SN" means that the uncertainty is taken as both shape and normalisation. Some of the systematic uncertainties are split into several different components for a more accurate treatment (number indicated under the column labeled as "Components").

components corresponding to the reconstruction efficiency, identification and isolation efficiency and trigger efficiency. Their effects on the analysis are sub-leading: uncertainties have similar values in all the analysis regions and they do not introduce any distortion in the shape of the discriminants. The effects of uncertainties on the lepton energy/momentum scale and resolution are minimal.

Separate nuisance parameters are considered for the jet energy resolution, jet reconstruction efficiency and the uncertainty on the application of the JVF cut; they mainly affect low p_{T} jets and hence the lower side of $H_{\mathrm{T}}^{\mathrm{had}}$ distribution. The breakdown of the uncertainties on the jet energy scale has been described extensively in section 3.3.1; in total 22 components are considered. The components related to the *in-situ* calibration are grouped into categories: statistical uncertainties (*Stat*), detector-related (*Det*), modelling of physics processes (*Model*) and residual uncertainties (*Mixed*). In each category, components are numbered according to their effect; low indices correspond to larger effects. In general the effect of jet energy scale uncertainties increases with the number of selected jets; a wide range of shape differences is possible since the various components can selectively affect specific kinematic regions (low or high p_{T} jets, more forward regions).

In the same way as the jet energy scale, the uncertainty related to the b-tagging efficiency of jets originating from b, c, light quarks or gluons, is also split into sub-components. These are obtained from a diagonalisation procedure which allows to maintain the correlation among jet p_{T} bins from the measured scale factors and, at the same time, produce variations that can be considered as uncorrelated. Each component corresponds to a characteristic variation of the efficiency as a function of the jet p_{T}; the number of components is equal to the number of p_{T} bins used to measure the efficiency in data[6]. They are numbered according to the magnitude of the variation, more precisely, according to the absolute value of the eigenvalue obtained from the diagonalisation procedure: low indices correspond to components that produce the smaller effects.

Since the analysis does not make direct use of the missing transverse energy information, no uncertainties related to the determination of the 'soft' component of the $E_{\mathrm{T}}^{\mathrm{miss}}$ are considered.

Small backgrounds uncertainties

Non-$t\bar{t}$ processes (W/Z+jets, single top, diboson, multijet) represent a minor fraction of the total background; in regions with exactly 2 b-tagged jets they account for $\sim 10\%$ of the background, while with increasing tag multiplicity, their contribution becomes increasingly smaller. In the most sensitive signal regions, their yields are comparable to or smaller than the ones expected for the SM Higgs boson signal. For this reason a less refined treatment of the uncertainties related to these small backgrounds has been adopted. Normalisation uncertainties are treated as fully correlated across all the regions used in the fit; in case of W+jets, single top and multijet backgrounds, conservatively large values have been adopted to cover also for possible extrapolation uncertainties across regions. It has been verified that the implemented uncertainties have a subleading effect on the sensitivity of the analysis.

- *Multijet*: a conservative 50% normalisation uncertainty has been adopted for the normalisation of the multijet template. The effects on the muon and electron channel are treated as uncorrelated. The chosen uncertainty is sufficient to cover systematic effects in the multijet estimation described in Chapter 5 (real lepton subtraction, fake efficiency extrapolation). No specific shape uncertainties have been considered since, in the regions

[6] b-jet and c-jet efficiency scale factors are parameterised only as a function of the jet p_{T}, while mis-tag rate scale factors are parameterised as a function of jet p_{T} in two separate $|\eta|$ bins.

used in the fit (and in particular in the signal regions), the large statistical uncertainty of the template exceeds the shape variations resulting from the background estimation methodology.

- *W+jets*: contrary to the 2011 analysis, no data-driven normalisation is applied to the W+jets sample in the 2012 analysis. A conservative normalisation uncertainty of 48% has been adopted. This value covers both W+jets normalisation as well as the W+HF composition since the regions used in the analysis are largely dominated by $W+b\bar{b}$. An additional uncertainty of 24% is applied for the regions with 5 and and for the regions with $\geq$ 6 jets following the predictions from the Berends scaling discussed previously; these two uncertainties are considered as uncorrelated to the normalisation one. In order to assess shape systematics, the full effect of the data-driven reweighting on the W boson p_{T} is considered.

- *Z+jets*: the normalisation uncertainty for the Z+jets process is 24%. This originates from the uncertainty on the extrapolation of the cross section to high jet multiplicity. Since the Monte Carlo predictions are corrected with a data-driven reweighting of the Z boson p_{T}, the full size of the correction is considered as a systematic uncertainty. This affects both the inter-normalisation across jet multiplicities as well as the shape of the discriminants (the effect is uncorrelated to the W boson p_{T} reweighting uncertainty).

- *single top*: the uncertainty on the inclusive single top cross section at NNLO is 5%. This number is obtained combining the uncertainties for the t-, s- and Wt channels weighted by their respective cross sections, adopted for the normalisation of the single top process. In the most sensitive signal region 2/3 of the single top contribution originates from the Wt channel while the remaining 1/3 from the t-channel. An additional normalisation uncertainty of 30% has been adopted. The number represents the largest difference obtained in the analysis regions by comparing the nominal single top Monte Carlo sample with alternative estimates from other Monte Carlo generators. For the t-channel, predictions from POWHEG+PYTHIA and aMC@NLO have been compared to the nominal ACER+PYTHIA predictions. For the Wt channel, the nominal implementation with the 'diagram removal' is compared with the 'diagram subtraction' approach for the overlap removal with respect to $t\bar{t}$ events.

- *diboson*: the normalisation uncertainty on diboson processes includes an uncertainty of 5% from the NNLO theoretical calculation of the inclusive cross section [138], and an uncertainty of 24% due to the extrapolation to high jet multiplicity. The two contributions are added in quadrature.

$t\bar{t}$-related uncertainties

Since it represents by far the largest source of background, great attention has been paid to in the description of the modelling of $t\bar{t}$ events. A large spectrum of uncertainties have been considered; they can affect the absolute normalisation, the acceptance and the redistribution across analysis regions as well as the shape of the discriminants.

- A global normalisation uncertainty ($t\bar{t}\_XS$) of 6% is considered following the theoretical uncertainties on the inclusive $t\bar{t}$ cross section described in section 1.3.1. This uncertainty applies to $t\bar{t}$+light, $t\bar{t}+b\bar{b}$ and $t\bar{t}+c\bar{c}$ processes in a correlated way.

- A 50% uncertainty has been assumed on the normalisation of $t\bar{t}$+HF events. Uncorrelated uncertainties are considered for $t\bar{t}+b\bar{b}$ and $t\bar{t}+c\bar{c}$ events ($t\bar{t}+b\bar{b}\_norm$, $t\bar{t}+c\bar{c}\_norm$). The chosen value represents a conservative assumption with respect to the 30% normalisation uncertainty of NLO cross section calculations [45] and was obtained varying factorisation and renormalisation scales in LO generators [161]. These uncertainties are considered correlated across all analysis regions.

- Uncertainties on the data-driven reweighting procedure applied to correct $t\bar{t}$ and top p_{T} are obtained from the corresponding 7 TeV measurement [166]; a detailed breakdown of the uncertainty on the unfolded data distributions is provided. The nine largest sources of uncertainties cover approximately 95% of the total experimental uncertainty on the measurement; they include the radiation modelling (using scale variations in the Alpgen+Pythia generator), the choice of the generator(comparing Alpgen with Powheg), fragmentation model and uncertainties on particular components of the jet energy calibration and jet resolution and jet flavour tagging. The detector-related components of the uncertainty on the reweighting can safely be considered as uncorrelated to the detector-related uncertainties used in the analysis since the differential measurement is performed on the 7 TeV data sample.

  For each uncertainty component, correction factors to the $t\bar{t}$ and top p_{T} distributions are recomputed and applied to the 8 TeV Monte Carlo in the same way as the nominal correction described in section 8.4; this produces characteristic variations on the $t\bar{t}$ top p_{T} that affects the shape of the distributions and the acceptance of events within the analysis regions. As already shown in Chapter 8, the $t\bar{t}$ p_{T} is very correlated to the jet multiplicity distribution. As an example, Figure 10.1 (a) shows the effect of the uncertainty component due to the difference between generators on the $H_{\mathrm{T}}^{\mathrm{had}}$ distribution for the $t\bar{t}$+light sample in the $(\geq 6\mathrm{j}, 2\mathrm{b})$ region.

  All the nine uncertainties are considered uncorrelated in the analysis, and will be denoted in the following with the *DataRw* prefix.

  Each component is applied to the $t\bar{t}$+light, $t\bar{t}+b\bar{b}$ and $t\bar{t}+c\bar{c}$ processes, since the data measurement was done on the inclusive $t\bar{t}$ sample.

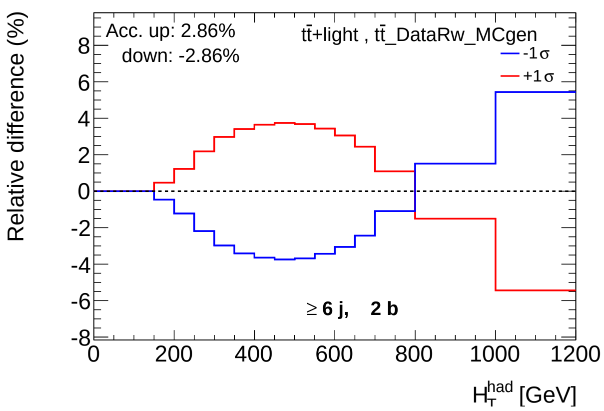

(a)

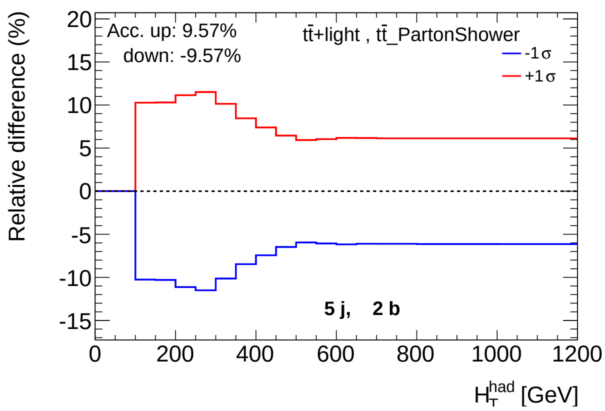

(b)

Figure 10.1: Relative effects of systematic uncertainties on the $t\bar{t}$+light templates used in the fit. (a) component of the top and $t\bar{t}$ reweighting uncertainties due to the difference between MC generators in the $(\geq 6\mathrm{j}, 2\mathrm{b})$ region. (b) Uncertainties due to parton shower modelling in the $(5\mathrm{j}, 2\mathrm{b})$ region (the variation has been symmetrised). Acceptance effects are also indicated in the plots.

- Since no specific measurement exists for the top kinematics in $t\bar{t}$+HF, additional uncertainties on the modelling of the top p_{T} and $t\bar{t}$ p_{T} are considered. The full size of the correction to the $t\bar{t}$ p_{T} and the top p_{T} distributions are independently taken as two sources of systematic uncertainties on $t\bar{t}$+HF; they are considered correlated between $t\bar{t}+b\bar{b}$ and $t\bar{t}+c\bar{c}$. Other than the shape of the discriminants, these conservative uncertainties allow to introduce flexibility in the relative normalisation of $t\bar{t}$+HF across jet multiplicities. As an example, the variation of the $t\bar{t}$ p_{T} distribution can alter the acceptance factor of regions with ≥ 6 jets up to 15% as shown in Figure 10.2 (a).

- An uncertainty due to the choice of the parton shower and hadronisation model is derived by comparing the nominal events produced with Powheg interfaced with Pythia with events produced with Powheg interfaced with Herwig. In order to avoid double counting of uncertainties, the $t\bar{t}$ p_{T} and top p_{T} are reweighted to the same distribution. The effect of the uncertainty is considered as uncorrelated between $t\bar{t}$+light and $t\bar{t}$+HF. In the first case, the different fragmentation model mainly affects the jet p_{T} distribution with an effect on the jet multiplicity reaching up to 10% in the regions with at least 6 jets. In the second case, since Powheg relies on the parton shower for the generation of part of the additional HF component, the fragmentation also affects the event distribution across tag multiplicities through for example the modelling of collinear gluon splitting. The effect of the parton shower uncertainty on the $t\bar{t}$+light sample in the $(5\mathrm{j}, 2\mathrm{b})$ region is reported in Figure 10.1 (b).

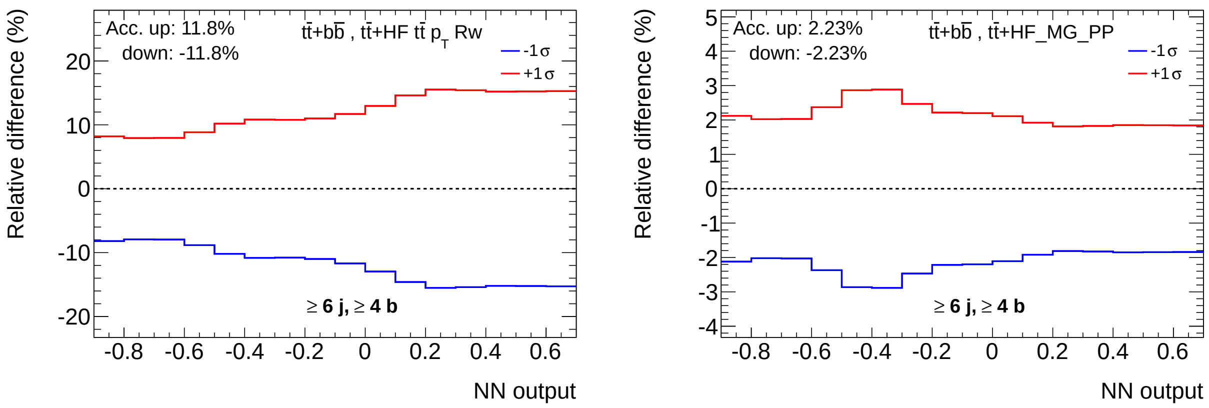

(a) (b)

Figure 10.2: Relative effects of systematic uncertainties on the $t\bar{t}+b\bar{b}$ templates used in the fit. (a) Full effect of the $t\bar{t}$ p_{T} reweighing on NN distribution in the $(\geq 6\mathrm{j}, \geq 4\mathrm{b})$ region. (b) Difference between Powheg and Madgraph prediction in the $(\geq 6\mathrm{j}, \geq 4\mathrm{b})$ region (the variation has been symmetrised). Acceptance effects are also indicated in the plots.

- Dedicated systematic uncertainties are considered for $t\bar{t}$+HF production: the dependence of the process on some of the generator parameters has been obtained using the LO multi-leg generator Madgraph interfaced with Pythia. The choice of Madgraph as a generator is motivated by its capability to cover part of the phase space of $t\bar{t}$+HF with matrix element predictions, as outlined in Chapter 8. As for Powheg, it still relies on the parton shower generator for the production of $b\bar{b}$ and $c\bar{c}$ from collinear gluon splitting. Four variations are considered: factorisation and renormalisation scale, the matching scale which controls the sharing of the phase space between matrix element and parton shower, the variation of the mass of the b and c quarks. The mass of the quark affects the probability and the kinematics of gluon splitting to $q\bar{q}$. The dynamic factorisation and renormalisation scales in MADGRAPH have been varied by a factor 2 around their nominal values and the variation has also been propagated to the parton shower program. The nominal matching scale of 20 GeV in MADGRAPH was doubled as a systematic variation[7]. The mass of the b (c) quarks was varied by 250 (100) MeV as suggested by a private communication with theorists [177].

The relative effect of each variation with respect to the nominal MADGRAPH sample is applied to the POWHEG sample. Ultimately, the residual differences between MADGRAPH and POWHEG predictions have been considered as an additional uncertainty. As for the case of the parton shower, the effects of systematic uncertainties are considered correlated between $t\bar{t}$+$b\bar{b}$ and $t\bar{t}$+$c\bar{c}$ given the common production mechanism.

All the variations are normalised to the same common phase space used to define $t\bar{t}$+HF events in Chapter 8; at least one particle jet from additional HF partons is present within the detector acceptance and in the kinematic range covered by the analysis. The effect of each uncertainty is parameterised as a function of the additional jet p_{T} and $|\eta|$ in case of single heavy flavour production and as a function of di-jet p_{T} and ΔR in case of events with two additional heavy flavour jets. This allows to compute how the uncertainty propagates in the specific analysis region after full detector reconstruction. In particular, MADGRAPH-related systematics allow the flexibility to vary the relative fraction of single to double heavy flavour production although they are combined in the same template for the fitting procedure.

All variations will be indicated in the following with the *'MG'* prefix followed by the specific component name; *'MB'* and *'MC'* for quark mass variations, *'Q2'* for the scale variations, *'MATCH'* for the variation of the matching scale and *'PP'* for the direct comparison with POWHEG.

Finally, a 30% normalisation uncertainty is assumed for the $t\bar{t}+V$ process, following the theoretical predictions for the inclusive NLO cross section [167, 168]. Additional acceptance and shape effects are considered by varying the factorisation scale; this will be referred to as *$t\bar{t}V$_ISR* in the following. Among all the possible variations of the generator parameters, ISR uncertainties have been found to produce the largest effect on the $t\bar{t}+V$ acceptance as well as on the shape of the discriminants; nevertheless its absolute effect remains small.

Signal modelling

The extraction of the number of signal events in data mainly relies on the shape information from the discriminants in the signal regions. The uncertainty on the modelling of $t\bar{t}H$ events has been obtained by varying the factorisation and renormalisation scales in the POWHEL generator. The two considered uncertainty components are related to the variation of the nominal static scale as well as the change in its functional form; both scales are varied simultaneously. The nominal static scale of the process ($\mu_r = \mu_f = m_{\mathrm{t}} + m_{\mathrm{H}}/2$) is varied by a factor of two. An additional sample where μ_r and μ_f are set to the dynamic function[8] $(m_{\mathrm{t}}^T m_{\mathrm{t}}^T m_{\mathrm{H}}^T)^{1/3}$ has also been considered since this functional form is the one used in the $t\bar{t}H$ process implementation in PYTHIA. While the static scale is theoretically more robust against divergences, a dynamic scale in principle allows a better description of the process for energies higher than the production threshold.

[7]The variation was symmetrised since the corresponding samples with halved scale were not available on time.

[8]The transverse mass of a particle is defined as: $\sqrt{p_{\mathrm{T}}^2 + m^2}$.

The effect of each variation is parameterised as a function of the $t\bar{t}H$ p_{T} of the event as well as the p_{T} of the top quark and is computed requiring the normalisation of the inclusive sample to be unchanged. This results in a typical uncertainty of a few percent on the normalisation in each of the analysis regions induced by acceptance effects and migration across regions, as well as variations of the shapes of the discriminants reaching up to 10%. Examples of these effects are shown in Figure 10.3.

PDF uncertainties have also been taken into account following the prescriptions outlined in Ref. [43], computing the envelope of the differences among three PDF sets (MSTW2008, CTEQ6.6 and NNPDF2.0) and their internal uncertainties. The change in the PDF can affect the total inclusive $t\bar{t}H$ cross section as well as the acceptance factor in each region (due to a redistribution of events across regions) and the shape of the discriminant distributions. Only the last two effects have been considered since the goal of the analysis is to measure the $t\bar{t}H$ cross section.

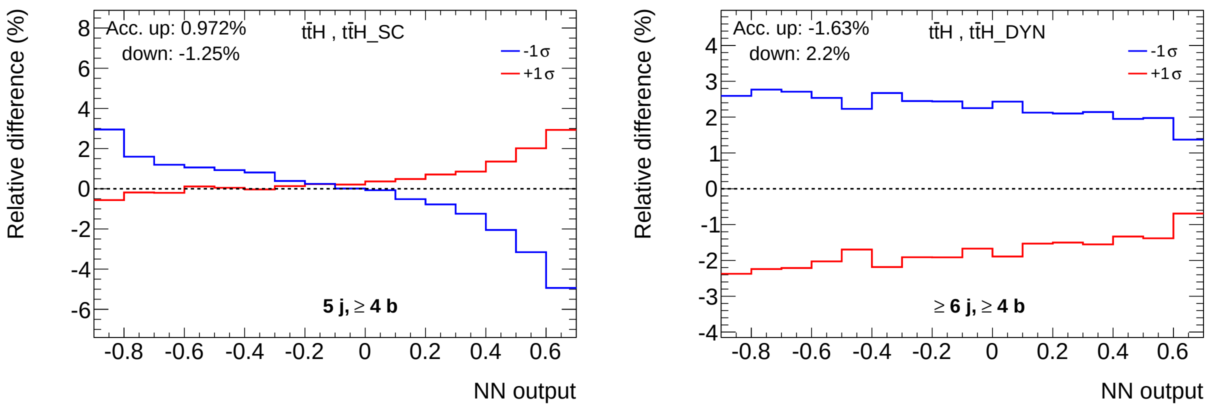

(a) **(b)**

Figure 10.3: Relative effect on the signal NN discriminant distribution from the change in factorisation and renormalisation scales: (a) effect due to the variation of the static scale in the $(5\mathrm{j}, \geq 4\mathrm{b})$ region. (b) difference between discriminant distributions using static and dynamic scales in the $(\geq 6\mathrm{j}, \geq 4\mathrm{b})$ region (the variation has been symmetrised). Acceptance effects are also indicated in the plots.

Table 10.3 summarises the relative effect of systematic uncertainties on the yields prediction for the signal, the three components of the $t\bar{t}$+jets backgrounds and the total background in the two most sensitive signal regions: $(5\mathrm{j}, \geq 4\mathrm{b})$ and $(\geq 6\mathrm{j}, \geq 4\mathrm{b})$. Uncertainties have been grouped for an easier visualisation. As can be seen, the leading sources of systematic uncertainties before the fitting procedure are represented by the normalisation of the $t\bar{t}$+HF process, the modelling of $t\bar{t}$ events and the uncertainties related to b-tagging.

An important requirement for the implementation of the uncertainties in the profile likelihood fit is to ensure that the shape effects from the systematic uncertainties are not distorted by the finite statistics used to build the nominal and the systematic templates. This is particularly crucial in cases where the evaluation of the effect of the systematics leads to a change in the value of the discriminating variables for a given event or to the usage of statistically independent sets of events; an example of this is given by the jet energy scale components and modelling systematics like the comparison of Powheg+Pythia and Powheg+Herwig. Systematic uncertainties whose effects are evaluated by reweighting events are less affected.

	(5j, ≥ 4b)					(≥ 6j, ≥ 4b)				
	$t\bar{t}H$	$t\bar{t}$+light	$t\bar{t}+c\bar{c}$	$t\bar{t}+b\bar{b}$	Bkgd	$t\bar{t}H$	$t\bar{t}$+light	$t\bar{t}+c\bar{c}$	$t\bar{t}+b\bar{b}$	Bkgd
Luminosity	2.8	2.8	2.8	2.8	2.7	2.8	2.8	2.8	2.8	2.8
Lepton efficiencies	1.6	1.6	1.5	1.6	1.4	1.5	1.5	1.5	1.6	1.5
Jet energy scale	3.9	8.7	4.2	4.5	4.6	6.5	14	10	8.2	9.5
Jet efficiencies	1.5	2.5	–	0.9	0.3	1.6	5.4	2.5	2.4	3.0
Jet energy resolution	3.2	3.7	2.8	5.1	2.7	–	8.5	4.1	4.3	3.8
b-jet tagging	10	5.8	5.2	9.3	7.4	9.0	5.8	5.1	9.2	7.9
c-jet tagging	1.9	7.9	15	3.5	6.8	1.9	7.3	14	2.8	5.7
Light jet-tagging	0.7	16	3.2	1.6	6.0	1.0	17	4.4	1.5	4.6
$t\bar{t}$ cross section	–	6.2	6.3	6.3	5.5	–	6.2	6.3	6.3	5.7
$t\bar{t}+c\bar{c}$ normalisation	–	–	50	–	9.2	–	–	50	–	9.3
$t\bar{t}+b\bar{b}$ normalisation	–	–	–	50	21	–	–	–	50	28
$t\bar{t}$ model: parton shower	–	7.1	0.9	3.1	2.4	–	7.5	1.8	10	6.0
$t\bar{t}$ model: reweighting	–	5.7	8.9	11	7.9	–	11	13	13	12
$t\bar{t}$+HF: reweighting	–	–	4.0	6.0	3.3	–	–	11	12	8.9
$t\bar{t}$+HF: generator	–	–	0.9	2.3	1.0	–	–	2.2	2.9	1.9
small backgrounds	–	–	–	–	1.9	–	–	–	–	1.4
$t\bar{t}H$ modelling	4.0	–	–	–	–	2.2	–	–	–	–
Total	12	24	54	54	29	12	30	57	56	38

Table 10.3: Prefit normalisation uncertainties (expressed in %) on signal, main background processes and total background for the systematic uncertainties considered. The "–" value indicates that the systematic does not act on the sample or the effect is negligible. The (≥ 6j, ≥ 4b) and (5j, ≥ 4b) regions are shown. The uncertainties have been grouped into categories for a better visualisation; "$t\bar{t}$ model: reweighting" includes all the 9 components of the data-driven reweighting. "$t\bar{t}$+HF: generator" contains all the uncertainties computed with MADGRAPH. "$t\bar{t}$+HF: reweighting" contains the uncertainties on the $t\bar{t}$ and top p_{T} reweighting in $t\bar{t}$+HF events.

Statistical fluctuations can lead to artificially large and irregular shape variations that could easily produce overconstraints in the fit. To prevent this, a *smoothing* procedure has been adopted. The relative effect of the systematic uncertainty is iteratively 're-binned' until it is significant with respect to the statistical uncertainty of the considered nominal template for a given fraction of the bins[9]; according to the re-binning configuration, direct smoothing of the systematic shape is also applied.

As the same time, a *pruning* procedure is applied: systematic uncertainties inducing a normalisation effect smaller than 0.5% are neglected as well as uncertainties where the shape component does not induce a variation greater than 0.5% in at least one bin in each distribution. The pruning is applied independently for each systematic uncertainty, for each template process and in each analysis region. The result of the pruning is to 'ease' the convergence of the minimisation procedure as well as considerably reducing the fit execution time. It has been verified that the introduction of the pruning procedure does not affect the final result. Additional plots of the effect of the systematic uncertainties can be found in Appendix D.

Expected performance

The performance of the fit has been evaluated using 'pseudo data' built from the sum of background templates and the nominal signal. The error in each bin of the 'pseudo data' distributions in each region has been modified to mimic the expected data statistics in 20.3 fb^{-1}.

[9] The procedure could also lead to completely neglecting the shape effect of the systematic in a given analysis region for a given sample.

When performing the fit over the 'pseudo-data', the error on the signal strength is found to be 1.44; this gives an initial measure of the sensitivity of the analysis.

Figure 10.4 illustrates the constraints on the nuisance parameters which are expected with the described fit model. All the nuisance parameters are fitted to a value of 0 since no shift is needed to improve the agreement[10]. The error on the nuisance parameters obtained from the fit is reported in unit of the 'pre-fit' (prior) uncertainty so that they are expected to be close to unity if these data do not provide any further improvement on that uncertainty.

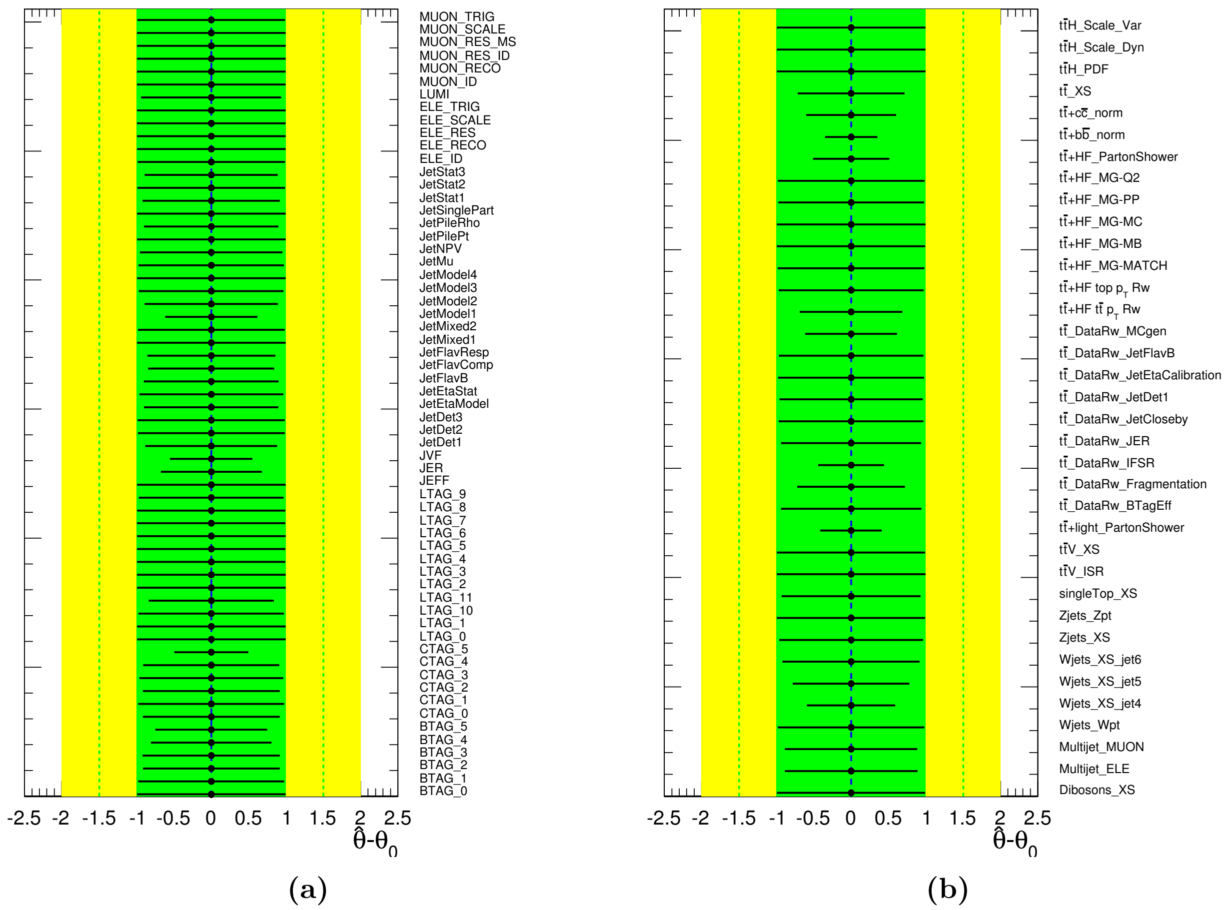

Figure 10.4: Expected constrains on systematic uncertainties nuisance parameters extracted from a fit to pseudo data. (a) Shows detector-related uncertainties while (b) displays uncertainties related to background modelling and normalisation.

For what concerns the detector-related systematics no major constraints are observed with the exception of *JVF*, the jet energy resolution, one component of the jet energy scale uncertainty and the largest component of the c-jet tagging efficiency systematics. The first three uncertainties give a larger contribution at low jet p_{T} (and hence low $H_{\mathrm{T}}^{\mathrm{had}}$) where large data statistics is available, especially in the 2 b-tagged jets regions. For the latter, additional constraints on the c-jet tagging efficiency arise from considering the $t\bar{t}$+light jets contribution to regions with 3 b-tagged jets and regions with 2 b-tagged jets, especially when only 4 jets are selected. As previously described in Chapter 8, the 2-to-3 b-tagged jets ratio in $t\bar{t}$+light events

[10] The figure shows the result of the fit to a single pseudo-experiment that represents the exact sum of the input templates. For some of the nuisance parameters and the statistical uncertainties, the correctness of the results has been cross checked with a more refined approach that includes generation of pseudo-data where the effect of the systematic was randomised according to the prior distribution. Both methods gave consistent results but the latter was extremely computationally expensive.

is mainly controlled by the tagging of a c-jet from hadronic W boson decay. This feature brings a lot of potential for a better derivation of the c-jets scale factor but has not been exploited so far.

Different is the case for the background-related nuisance parameters where the analysis is specifically designed to improve over uncertainties that often originate from conservative theoretical considerations rather than previous direct measurements. It should be noted that, up to date, no specific measurements of properties and kinematics of $t\bar{t}$ events have been performed by the ATLAS collaboration using the 2012 dataset.

As a notable example, an improvement by a factor of ~ 2 on the normalisation uncertainty for $t\bar{t}$+$b\bar{b}$ and $t\bar{t}$+$c\bar{c}$ is expected corresponding to a final uncertainty of the order of 15-20%. This is due to the large amount of data collected at 8 TeV combined with the event categorisation in multiple jet and b-tagged jet multiplicity regions. The other important aspect is related to the modelling of $t\bar{t}$+jets events; nuisance parameters that are constrained are the ones which correspond to large variations not compatible with the available data precision. This is the case for the *parton-shower* systematics which produces effects up to 10% as a function of the number of jets while the statistical uncertainty of data in the 2 b-tagged jets regions is of the order of few %. In case of the uncertainty related to the 7 TeV measurement of the top quark and $t\bar{t}$ system p_{T}, additional constraints arise from the fact that the 8 TeV sample allows to explore the available phase space in more detail than the binning used to apply the p_{T} correction. In particular this is the case for the components of the uncertainty due to the different Monte Carlo generator which mainly affect the high p_{T} regime. These constraints suggest that the data collected during 2012 offer a lot of possibilities to improve the understanding of the kinematics of $t\bar{t}$+jets and of $t\bar{t}$+HF production in particular.

10.2 Fit to data

The result of the log likelihood minimisation in data yields a best-fit value for the signal strength:

$$\hat{\mu} = (1.3 \pm 1.6)$$

The error on the signal strength has been derived by scanning the log likelihood profile obtained by minimising the function for each value of μ. The profile is shown in Figure 10.5.

The best-fit value for the set of nuisance parameters is summarised in Figure 10.6; shifts from the initial values of 0 and errors are reported in unit of the pre-fit uncertainty of the given parameter.

The observed constraints on the systematics are compatible with the expected values from Figure 10.4. The plot also contains the result of the fit performed in the 'background-only' configuration with μ fixed at 0. No significant differences are observed in the values or errors of the nuisance parameters demonstrating that their determination is dominated by background-enriched regions.

A number of shifts are observed, the most noticeable being the one of the $t\bar{t}$+$b\bar{b}$ normalisation uncertainty. The value of $\hat{\theta} = 0.65$ corresponds to an increase of the $t\bar{t}$ yields by 33% contributing to improve the normalisation difference between data and Monte Carlo predictions observed in regions with at least 4 b-tagged jets as already shown in Figure 8.8. In total only one parameter is shifted by more than one standard deviation with respect to the central value. Part of the observed 'pulls' are produced by the fit to improve the data/Monte Carlo agreement in the high statistics background dominated regions. It has been verified with 'pseudo-data' that the shift in nuisance parameters driven by these regions does not bias the possibility to

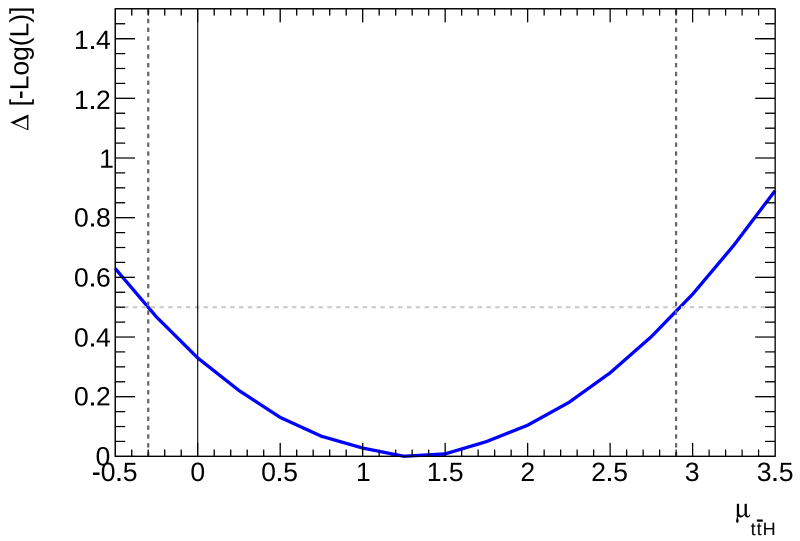

Figure 10.5: Profile of the $\Delta LL = -(\log(L(\mu)) - \log(L(\hat{\mu})))$ value as a function of the signal strength. The minimum value corresponds to the best-fit signal strength, the error on $\hat{\mu}$ is computed from the points at which the function reaches 0.5.

correctly extract the signal in the signal-enriched regions[11].

The actual dependence of the best fit $\hat{\mu}$ on the different nuisance parameters will be discussed later in the chapter. Additional tests of the assumptions used in the fit model and the stability of the results are collected in Appendix F.

The other key aspect of the profile likelihood fit is that it creates correlations between the nuisance parameters; Figure 10.7 displays the correlation coefficients obtained by the full fit to data. While initially all the sources of systematic uncertainties are treated as uncorrelated, correlations are built by the fitting procedure depending on the effect of the parameters in the phase space considered by the analysis and the amount of data. As an example, the anti-correlation between the $t\bar{t}+b\bar{b}$ normalisation uncertainty and the mis-tag rate uncertainties originates from the inclusion in the fit of regions with 4 b-tagged jets. Both uncertainties contribute to the expected yield uncertainty in these regions in complementary ways; one directly affecting the normalisation of the main source of background, the other acting on the amount of $t\bar{t}$+light jets background.

For a better visualisation, only nuisance parameters with at least one correlation greater than 30% are shown. The correlation of nuisance parameters with the signal strength (μ) is one of the important factors affecting the sensitivity of the analysis[12]. A 39% anti-correlation is present between the uncertainty on the signal strength and the uncertainty on the $t\bar{t}+b\bar{b}$ normalisation. Given that $t\bar{t}+b\bar{b}$ becomes the largest background only in the most sensitive analysis regions, this correlation is related to the ability to separate the signal from the back-

[11]A fit performed setting μ=0 in the 'blinded' configuration described in Chapter 9.4 was extrapolated into the signal region and pseudo experiments were generated from the modified background distribution adding a given amount of signal. A nominal fit was performed combining real data in the 'blinded' region with pseudo pseudo data in the signal region. The extracted signal strength was found to be in agreement with the injected one.

[12]Given the particular definition of the nuisance parameters (in particular the ones deriving from the break-down of systematic uncertainties), it is not guaranteed that a positive shift in the parameters corresponds to a increase of yields in the template. For this reason, the sign of the correlation can be difficult to interpret in a direct way.

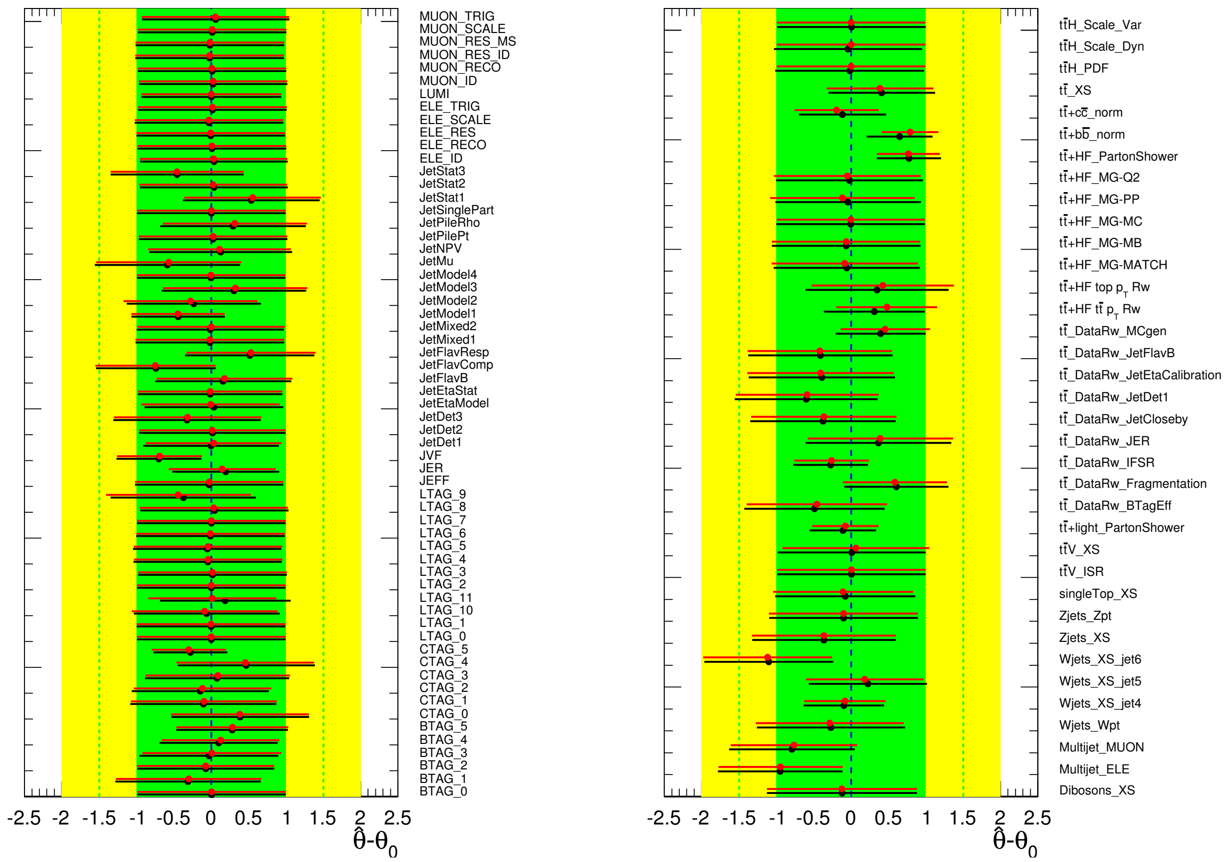

(a) **(b)**

Figure 10.6: Nuisance parameters obtained from the fit to data. Red points represent the result of the fit considering μ as a floating parameter; black points are the result of a fit to data performed with μ fixed at 0. (a) shows detector-related uncertainties while (b) displays uncertainties related to background modelling and normalisation.

ground based on the shape of the template. Larger values are obtained when considering a variable with lower discrimination power in signal regions like $H_{\mathrm{T}}^{\mathrm{had}}$. At the same time, the uncertainty on the signal strength is found to be anti-correlated with the uncertainty related to the shape of the $t\bar{t}$ p_{T} distribution in $t\bar{t}$+HF events.

Some correlations arise from the normalisation constraints in high-statistics regions with 2 b-tagged jets. In these regions $t\bar{t}$+jets represents more than 90% of the total background and on average each $t\bar{t}$ event contains at least 2 b-jets in the final state. Therefore, the effect of the uncertainty on the $t\bar{t}$ cross section, the uncertainties on b-tagging and on the collected luminosity all have almost degenerate effects.

Both the constraints on the nuisance parameters and their correlations need to be taken into account when displaying the fit result. The yields for each process after the fitting procedure are shown in Tables 10.4 and 10.5. They have been computed starting from the nominal yield and modifying them by the amount produced by the shift of the nuisance parameters; uncertainties per sample and total uncertainties are computed taking into account the normalisation effect of any nuisance parameters and the effect of correlations[13]. Compared to the equivalent 'prefit'

[13]Postfit uncertainties on yields are computed with the approximated formula $err = \sqrt{\sum_{\mathrm{sys}}^{i} \sum_{\mathrm{sys}}^{j} c_{ij} \cdot \Delta y_i \Delta y_j}$

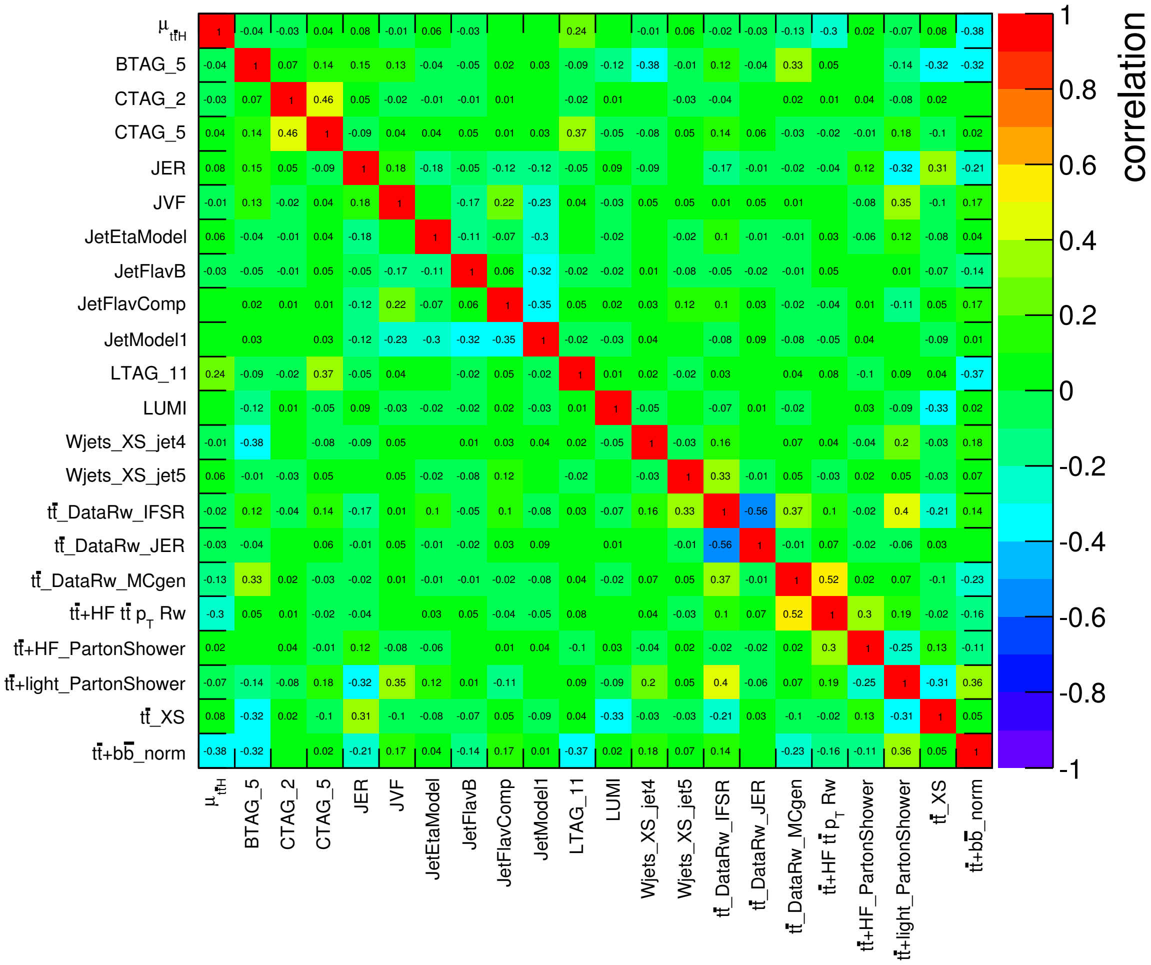

Figure 10.7: Correlation coefficients for the signal strength and the nuisance parameters in the fit. Only nuisance parameters with at least one absolute correlation coefficient greater than 30% are shown.

Tables 8.4 and 8.5, a noticeable reduction of systematics can be observed. A more detailed breakdown of the effect of systematic uncertainties after the fit for the two most sensitive signal regions is shown in Table 10.6 which has to be compared to the prefit equivalent Table 10.3.

where c_{ij} is the correlation coefficient and Δy_i is the effect of the effect of the yields due to the variation of the i^{th} nuisance parameters within its error.

	4 jets, 2 b-tags	4 jets, 3 b-tags	4 jets, 4 b-tags	5 jets, 2 b-tags	5 jets, 3 b-tags	$\geq$ 6 jets, 2 b-tags
$t\bar{t}$+light	79900 ± 1500	6460 ± 170	59 ± 8	39400 ± 1000	3870 ± 170	19600 ± 700
$t\bar{t}$+$c\bar{c}$	3000 ± 900	560 ± 170	22 ± 7	3100 ± 900	710 ± 200	2900 ± 800
$t\bar{t}$+$b\bar{b}$	1950 ± 330	890 ± 140	63 ± 9	1810 ± 300	1100 ± 180	1620 ± 290
$t\bar{t}$+V	115 ± 35	15 ± 5	0.9 ± 0.3	140 ± 40	26 ± 8	170 ± 50
W+jets	4200 ± 1200	190 ± 50	4.9 ± 1.7	1700 ± 600	120 ± 40	600 ± 220
Z+jets	1030 ± 260	49 ± 13	1.0 ± 0.5	350 ± 90	29 ± 8	111 ± 30
Single top	6100 ± 1500	410 ± 90	8.8 ± 2.1	2300 ± 500	230 ± 60	910 ± 240
Diboson	210 ± 60	11.5 ± 3.4	0.3 ± 0.1	96 ± 26	8.1 ± 2.3	50 ± 14
Multijet	960 ± 300	62 ± 23	2.2 ± 1.8	280 ± 90	41 ± 17	110 ± 40
Total Bkgd.	97520 ± 320	860 ± 90	163 ± 6	49110 ± 240	6150 ± 70	26110 ± 190
$t\bar{t}H$ (125)	39.8 ± 2.2	16.3 ± 1.2	2.4 ± 0.3	52.9 ± 2.0	28.7 ± 1.5	82.9 ± 4.1
Data	97450	8692	161	49402	6168	26033

Table 10.4: Post-fit event yields for signal, backgrounds and data in each of the background-dominated regions. The quoted uncertainties on the backgrounds are the sum in quadrature of statistical and total systematic uncertainties on the yields, computed taking into account correlations among nuisance parameters and among processes. For signal, the uncertainty only takes into account the normalisation effect of the nuisance parameters but not the error on the extracted signal strength.

	5 jets, $\geq$ 4 b-tags	$\geq$ 6 jets, 3 b-tags	$\geq$ 6 jets, $\geq$ 4 b-tags
$t\bar{t}$+light	73 ± 10	2290 ± 140	73 ± 11
$t\bar{t}$+$c\bar{c}$	47 ± 13	790 ± 220	78 ± 21
$t\bar{t}$+$b\bar{b}$	155 ± 23	1220 ± 200	310 ± 50
$t\bar{t}$+V	3.2 ± 1.0	44 ± 13	8.8 ± 2.7
W+jets	5.3 ± 2.0	65 ± 23	5.7 ± 2.7
Z+jets	2.1 ± 1.0	10 ± 5	0.4 ± 0.2
Single top	11 ± 4	130 ± 40	13 ± 4
Diboson	0.5 ± 0.3	6.0 ± 1.9	0.6 ± 0.2
Multijet	3.2 ± 3.0	13 ± 8	0.6 ± 2.5
Total Background	302 ± 13	4640 ± 90	493 ± 32
$t\bar{t}H$ (125)	7.7 ± 0.7	51.6 ± 2.6	20.8 ± 1.6
Data	283	4671	516

Table 10.5: Post-fit event yields for signal, backgrounds and data in each of the signal-enriched regions. The quoted uncertainties on the backgrounds are the sum in quadrature of statistical and total systematic uncertainties on the yields, computed taking into account correlations among nuisance parameters and among processes. For signal, the uncertainty only takes into account the normalisation effect of the nuisance parameters but not the error on the extracted signal strength.

	(5j, ≥ 4b)					(≥ 6j, ≥ 4b)				
	$t\bar{t}H$	$t\bar{t}$+light	$t\bar{t}+c\bar{c}$	$t\bar{t}+b\bar{b}$	Bkgd	$t\bar{t}H$	$t\bar{t}$+light	$t\bar{t}+c\bar{c}$	$t\bar{t}+b\bar{b}$	Bkgd
Luminosity	2.6	2.6	2.6	2.6	2.5	2.6	2.6	2.6	2.6	2.7
Lepton efficiencies	1.5	1.5	1.5	1.5	1.4	1.5	1.5	1.5	1.5	1.5
Jet energy scale	3.2	3.6	1.8	2.7	2.6	2.8	6.5	4.7	3.8	4.2
Jet efficiencies	0.8	1.4	–	0.5	0.1	0.9	3.0	1.4	1.4	1.6
Jet energy resolution	2.3	2.9	2.7	4.3	2.7	–	6.3	4.0	4.2	3.7
b-jet tagging	7.6	4.5	4.1	7.3	6.0	7.1	4.6	4.1	7.2	6.4
c-jet tagging	1.2	4.6	8.8	2.1	3.7	0.9	4.2	8.2	1.7	3.1
Light jet tagging	0.6	14	2.9	1.4	4.9	0.9	15	4.0	1.3	3.7
$t\bar{t}$ cross section	–	4.5	4.5	4.5	4.0	–	4.5	4.5	4.5	4.1
$t\bar{t}+c\bar{c}$ normalisation	–	–	32	–	5.0	–	–	32	–	5.0
$t\bar{t}+b\bar{b}$ normalisation	–	–	–	17	8.7	–	–	–	17	11
$t\bar{t}$ model: parton shower	–	3.2	0.4	1.3	0.9	–	3.3	0.8	4.5	2.9
$t\bar{t}$ model: reweighting	–	3.3	5.2	6.5	4.8	–	6.5	7.5	7.9	6.9
$t\bar{t}$+HF: reweighting	–	–	2.6	4.0	2.4	–	–	7.1	7.6	5.9
$t\bar{t}$+HF: generator	–	–	0.9	2.2	1.2	–	–	2.2	2.9	1.9
small background	–	–	–	–	1.0	–	–	–	–	0.8
$t\bar{t}H$ modelling	4.0	–	–	–	–	2.2	–	–	–	–
Total	8.6	13	28	15	4.3	7.9	15	27	15	6.4

Table 10.6: Postfit normalisation uncertainties (expressed in %) on signal, main background processes and total background for the systematic uncertainties considered. The uncertainties have been grouped into categories for a better visualisation. The "–" value indicates that the systematic does not act on the sample or the effect is negligible. The ($\geq$ 6j, $\geq$ 4b) and (5j, $\geq$ 4b) regions are shown. The total uncertainty can be different from the sum in quadrature of individual sources due to the correlations induced by the fitting procedure. The same convention on the grouping of systematics as in Table 10.3 has been adopted.

Final discriminants plots

As for the final yields, also the shapes of the distributions are modified by the fit. Figure 10.8 shows the effect of the fit on the total background template. Prefit distributions are shown with the uncertainty band reflecting the uncertainties used as input to the fit. Post-fit distributions are obtained by modifying the pre-fit templates by the effects of the shifts in the nuisance parameters; no large shape modifications are produced by the fit in the main signal regions.

The figures also report the post-fit uncertainties when the correlations are not taken into account and the systematic uncertainties are still considered as fully uncorrelated. A considerable part of the reduction of the final background uncertainties is due to correlations among nuisance parameters; in particular, as a result of the profiled likelihood approach, in the high statistics regions the total uncertainty is of the same order as the data statistical uncertainty.

Finally, the agreement between the data and the expected distribution from the signal and background processes after the fitting procedure is shown in Figure 10.9 for the distribution used in each region. As expected, compared to the pre-fit plots in Figures 8.9 and 9.21, the fit improves the description of the data in the model, since part of the discrepancies have been absorbed by the nuisance parameters.

The convention adopted in this chapter regarding yields tables, tables of systematic uncertainties and plots, consists in comparing the total background, with the full uncertainty band, to the signal contribution obtained from the fit. The total uncertainty on the background takes into account the correlations among all the nuisance parameters affecting each background prediction, while the error on the signal considers all the sources of uncertainties but the error on

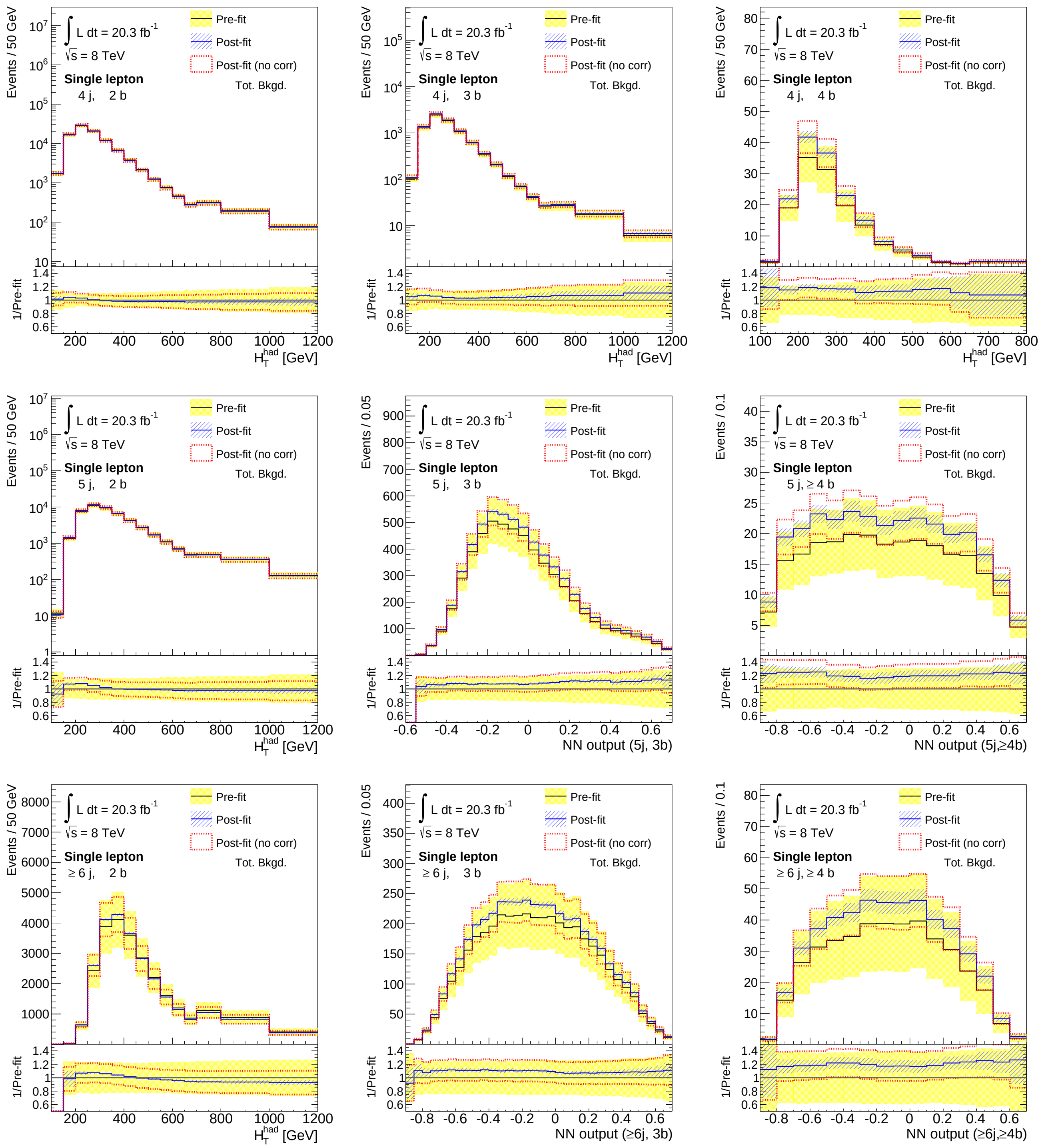

Figure 10.8: Distribution of the total background in each analysis region before and after the fit procedure. Pre-fit distributions have yellow uncertainty bands, Post-fit distributions are shown with final uncertainty bands (blue) and with the uncertainty band computed neglecting the post-fit correlation among nuisance parameters (red lines).

the signal strength[14]. This approach does not allow to directly appreciate the non-negligible correlation between the error on the signal strength and the error on the total background (notably the $t\bar{t}$+$b\bar{b}$ normalisation component). In the most sensitive signal regions their absolute contribution is comparable; hence taking into account the correlation would lead to a further reduction of the uncertainty on the total signal plus background prediction. This also implies that the uncertainty on the total background predictions will be smaller if a background-only fit is performed; this is due to the reduction of one of the fit degrees of freedom. In the ($\geq$ 6j, $\geq$ 4b) and (5j, $\geq$ 4b) regions, the uncertainty reduction can be as large as 20%.

μ uncertainty breakdown

As previously defined, the uncertainty on the signal strength is obtained by minimising the negative log likelihood function for different values of μ. The breakdown of the final uncertainty into components is obtained by keeping particular nuisance parameters fixed during the minimisation process.

The statistical component of the uncertainty on the signal strength is computed by scanning the likelihood profile around the minimum position not allowing any variation of the nuisance parameters; a value of 0.8 is found. The best fit signal strength can then be re-written as:

$$\hat{\mu} = 1.3 \ \pm 0.8\,(\text{stat.}) \ \pm 1.5\,(\text{sys.})$$

The result is then largely dominated by systematic uncertainties. At the same time, the amount of data statistics is also responsible for the constrains of the nuisance parameters and the correlation among then. The impact of the finite Monte Carlo statistics has been found to be 0.17, hence one order of magnitude smaller than the total error.

The dependence of the final result on each source of systematic uncertainty has been assessed by repeating the fit while keeping the corresponding nuisance parameter fixed at different values. Explicit tests have shown that the approach is equivalent to evaluating the contribution to the error by subtracting in quadrature the total error and the error obtained by fixing the nuisance parameter at its best fit value. All the other nuisance parameters are allowed to vary to reach another configuration that maximises the likelihood. Table 10.7 shows the variation of the fitted signal strength when the considered nuisance parameter is kept fixed at the two values $\hat{\theta} \pm \sigma_\theta$ where σ_θ is the postfit error on the parameter itself. This will be denoted in the following as 'impact on μ'. Only the 10 nuisance parameters with the largest impact on the signal strength have been reported.

The systematic uncertainties with the largest impact on the signal strength are those related to the $t\bar{t}$+$b\bar{b}$ process; its normalisation and the shape of the $t\bar{t}$ system p_{T}. These two nuisance parameters are also the ones with the largest (anti)correlation with μ. Additional uncertainties related to the modelling of $t\bar{t}$+HF events also appear with high rank.

The third largest contribution is given by one of the components of the light-jet tagging efficiency. The mistag uncertainties affect primarily the $t\bar{t}$+light process (the third largest background) in the regions with at least 4 b-tagged jets; they cannot be constrained by information in the lower b-tagged jet multiplicity regions.

Subleading contributions originate from the normalisation of the $t\bar{t}$+$c\bar{c}$ templates and the additional $t\bar{t}$+jets modelling uncertainties. All remaining uncertainties give a much smaller individual contribution to the final error.

Additional information is reported in Table 10.8; the contribution from systematics uncertainties to the error on the signal strength is shown. The sources of systematics have been

[14] the uncertainties have been omitted in the plots since their percent-level contribution would have not been visible

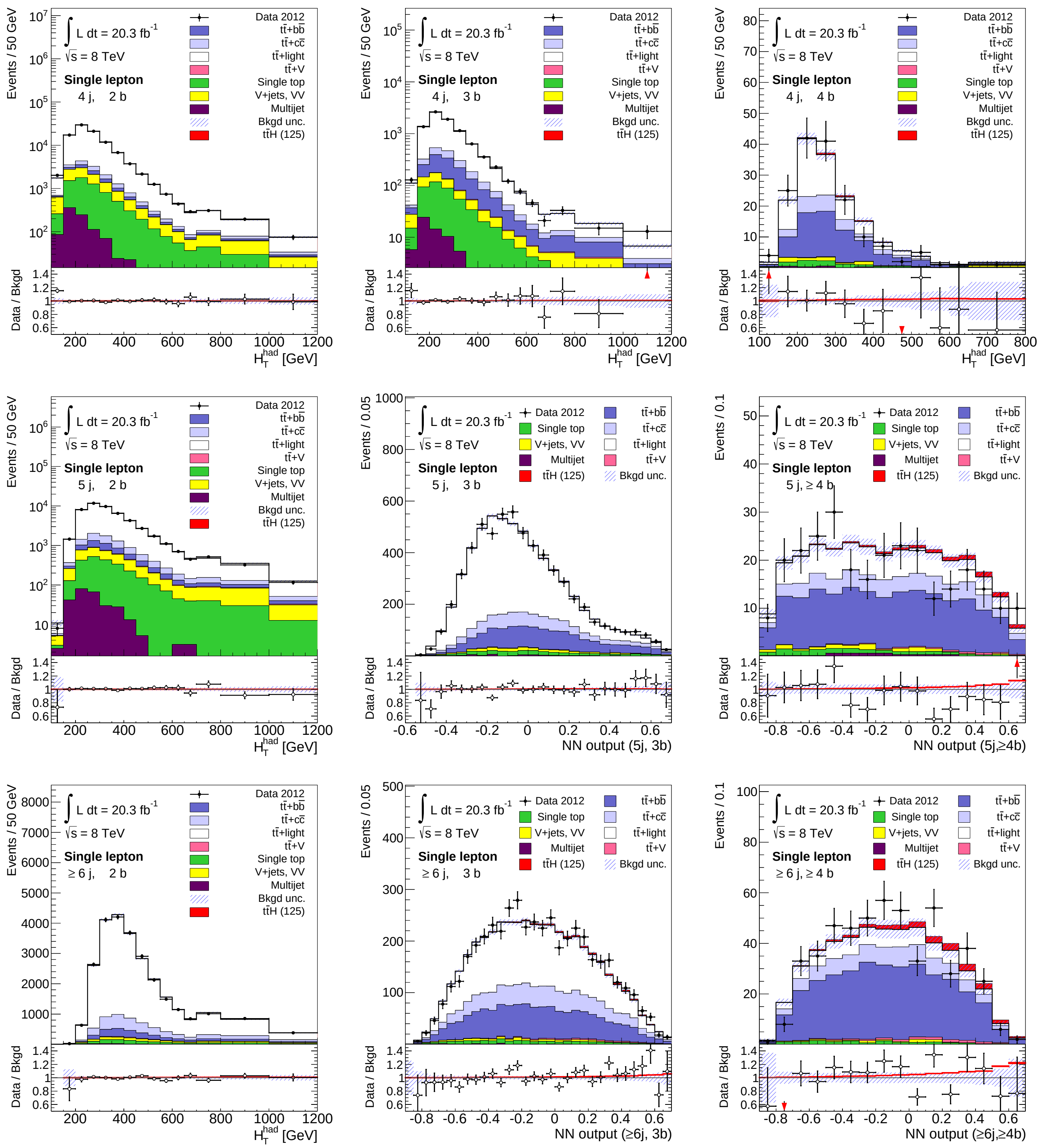

Figure 10.9: Comparison between data and predictions for the variables used in each of the nine analysis regions. Signal and background predictions have been corrected with the result of the fit to data. The uncertainty band contains statistical and systematical uncertainties and takes into account the correlations among the nuisance parameters induced by the fit. In the ratio part of each plot the red line represents the signal contribution with respect to the total background.

uncertainty	postfit impact on μ
$t\bar{t}$+$b\bar{b}$: normalisation	0.66
$t\bar{t}$+HF: $t\bar{t}$ p_T Rw	0.49
LTAG_11	0.44
$t\bar{t}$: DataRw (MCgen)	0.25
$t\bar{t}$+$c\bar{c}$: normalisation	0.25
$t\bar{t}$+HF: MG_PP	0.17
LTAG_9	0.16
$t\bar{t}$+HF: top p_T Rw	0.15
$t\bar{t}$+light: PartonShower	0.13
JER	0.13

Table 10.7: Ranking of the nuisance parameters according to their effect on the extraction of the signal strength. For each source of systematic uncertainty, the fit has been repeated by keeping its corresponding nuisance parameter fixed at the postfit value ± the postfit error. The quoted number represents the variation of the signal strength with respect of its best fit value. Absolute variations of μ from up and down shifts of the nuisance parameters are averaged. Only the 10 nuisance parameters with the highest impact are shown; naming conventions are the same as adopted in Figure 10.6.

uncertainty category	error on μ
b-jet tagging	0.17
c-jet tagging	0.16
Light jet tagging	0.43
jet-related uncertainties (jes,jer,jvf)	0.26
$t\bar{t}$+X normalisation	0.67
$t\bar{t}$ model: parton shower	0.13
$t\bar{t}$ model: reweighting	0.26
$t\bar{t}$+HF: reweighting	0.55
$t\bar{t}$+HF: generator	0.18
small backgrounds	0.19
other detector uncertainties	0.05
signal modelling	0.11

Table 10.8: Contributions from different sets of nuisance parameters to the final error on μ. Sources of systematic uncertainties have been grouped following the same conventions as in Table 10.6. The '$t\bar{t}$ normalisation' category contains the contribution from the $t\bar{t}$+$b\bar{b}$, $t\bar{t}$+$c\bar{c}$ and top cross section uncertainties.

grouped into categories[15]; within each category the correlations among the nuisance parameters induced by the fit have been taken into account. The numbers substantially confirm the trend extracted from the ten nuisance parameters with the largest impact on μ: $t\bar{t}$+X normalisation, the effect of the reweighting on $t\bar{t}$+HF events and the uncertainty on the tagging of light jets, have the largest impact on the uncertainty on the signal strength. When combining all the various components, detector uncertainties related to the use of jets (jet energy scale, jet energy resolution and JVF efficiency) represent the fourth largest contribution to the error on the signal strength together with the uncertainties on the top p_T and $t\bar{t}$ system p_T for $t\bar{t}+X$ events. The uncertainty on the tagging of b- and c-jets bring similar contributions.

Finally, it should be kept in mind that since correlations exist between nuisance parameters belonging to different categories, the values from the table cannot be simply combined in quadrature to obtain the total systematic error.

10.3 Limit setting

Once a given $t\bar{t}H$ signal strength is measured the question to address is how significant the observed excess is with respect to the background only prediction. In case no significant excess is found, an upper limit can be set on the production cross section for the $t\bar{t}H$ process. Since the obtained value of μ is intuitively compatible with 0, this section will mainly concentrate on the description of the upper limit determination procedure; a modified frequentist confidence level (CL$_s$) approach described in [178, 179] is used, implemented in the RooStat framework [180].

The CL$_s$ 95% upper limit is designed to be greater than the true value of the parameter with a probability of at least 95%. It is based on a test statistic q_μ which is constructed to separate the *null* hypothesis from the *test* hypothesis (the presence of signal with a strength μ). The ingredients of the CL$_s$ method are summarised in Figure 10.10. It shows a hypothetical example of the distributions of the test statistic for the two hypothesis; the right distribution under the background only hypotheses $f(q_\mu|b)$ and on the left the signal plus background hypothesis $f(q_\mu|s+b)$.

Given the value of the test statistic on data q_{obs}, the compatibility of the result with the signal+background hypothesis is given by the p-value:

$$p_{s+b} = P(q \geq q_{\text{obs}}|s+b) = \int_{q_{\text{obs}}}^{\infty} f(q_\mu|s+b)dq_\mu. \tag{10.4}$$

representing the probability to find a result less compatible with the signal plus background hypothesis than the observed data.

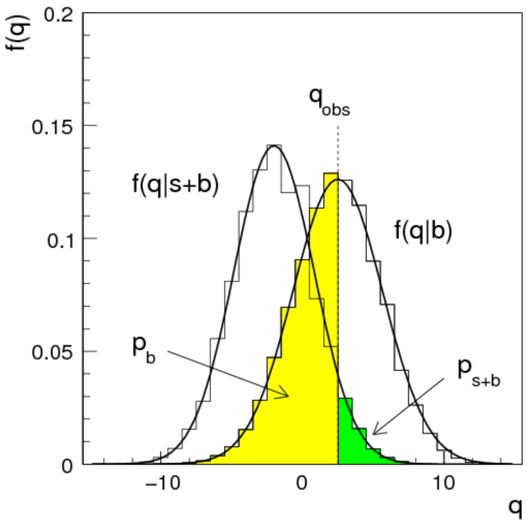

Figure 10.10: Example distribution of the test statistics for b-only and $s+b$ hypothesis.

The usage of p_{s+b} to extract the upper limit (also often referred to as "CL$_{s+b}$" approach) has the disadvantage that it ignores the compatibility of the observation with the background-only

[15] All the nuisance parameters corresponding to a given categories have been fixed simultaneously in order to determine the contribution to the total uncertainties

hypothesis. This can be defined as:

$$p_b = P(q \geq q_{\text{obs}}|b) = \int_{-\infty}^{q_{\text{obs}}} f(q_\mu|s+b)dq_\mu. \tag{10.5}$$

This value is also used to define the significance of the signal, as will be shown later. By setting upper limits using the condition $p_{s+b} < \alpha^{16}$, a signal could be excluded simply as a result of a background under-fluctuation, even if the analysis is not a-priori sufficiently sensitive to the signal itself. This can be the case in a regime where $s \ll b$.

To avoid this possibilities the CL_s variable defined as:

$$\text{CL}_s = \frac{p_{s+b}}{1-p_b} \tag{10.6}$$

is used. When the sensitivity to the signal model is low, the two distributions in Figure 10.10 have a large overlap and $(1 - p_b)$ could be significantly different from one. By dividing the p-value by $(1 - p_b)$, a 'penalty' term is introduced thus preventing to exclude models for which low sensitivity is expected. Therefore CL_s is used instead of CL_{s+b} in the definition of the upper limit.

For the limit setting procedure used in the analysis described in this thesis, the test statistic is based on the *likelihood ratio* defined as[17]:

$$q_\mu = \begin{cases} -2\ln\frac{L(\mu,\hat{\hat{\boldsymbol{\theta}}}(\mu))}{L(\hat{\mu},\hat{\boldsymbol{\theta}})} & \mu > \hat{\mu} \\ 0 & \mu < \hat{\mu} \end{cases} \tag{10.7}$$

L is the likelihood function previously defined and dependent on the signal strength μ and the set of nuisance parameters $\boldsymbol{\theta}$. The denominator represents the maximum value of the likelihood which produces the best estimate of the signal strength ($\hat{\mu}$) and the nuisance parameters ($\hat{\boldsymbol{\theta}}$). The numerator is the 'conditional' maximum likelihood value for a given value of μ with $\hat{\hat{\boldsymbol{\theta}}}$ the new best estimate for the set of nuisance parameters. For the purpose of computing exclusion upper limits, the test statistic is 0 for $\mu < \hat{\mu}$ since values of the signal strength smaller than the one preferred by data cannot be excluded

In other to compute the expected and observed upper limit as well as the signal significance, the probability distribution of the test statistic $f(q_\mu|\mu')$ needs to be evaluated. In the used notation, the subscript of q represents the hypothesis being tested while the second argument refers to the signal strength assumed in the (pseudo) data. These distributions are obtained with the 'asymptotic approximation' formulae described in Ref. [181]: as an example, the distribution of the test statistic for a value of the signal strength equal to the hypothesis under testing is well represented by a χ^2 distribution with one degree of freedom. The use of this approximation is made possible by the sufficiently large background yields ($b > 10$) in the most sensitive signal regions.

The computation of the expected upper limit requires the knowledge of the median value of the test statistic distribution assuming no signal in data $f(q_\mu|\mu' = 0)$. This is obtained through the so-called "Asimov dataset" approach [181]; this procedure replaces the ensemble testing performed with Monte Carlo pseudo-experiments with a single 'representative' dataset which returns the true value for each estimated parameter. This dataset can also be used to obtain the error bands on the median value resulting from the expected uncertainty in the

[16] A value of α of 5 % corresponds to a 95% CL exclusion.

[17] A more comprehensive set of formulae separating the case where $\hat{\mu} < 0$ is reported in Ref. [181]

determination of μ. The expected exclusion limit is defined as the value of μ for which the median of $f(q_\mu|\mu' = 0)$ has a p-value of 5%. The observed upper limit is obtained in a similar way by considering the value of the test statistic extracted from data; values of μ for which the CL_s is smaller than 0.05 are excluded at 95% confidence level. The 95% CL upper limit on the signal cross section over Standard Model expectation is thus the value for which CL_s is equal to 0.05.

Finally the significance of the signal is computed from the probability of having a fluctuation in the background-only hypothesis that produces an effect as signal like as the observed data[18]. This will be referred in the following as p_0 and it is computed from the distribution of the test statistic $q_0 = -2\ln\frac{L(0,\hat{\hat{\boldsymbol{\theta}}}(0))}{L(\hat{\mu},\hat{\boldsymbol{\theta}})}$ which is set to 0 if $\hat{\mu} < 0$. Since in the considered model the presence of the signal can given a positive contribution to the final yields, only value of $\hat{\mu} > 0$ can actually lead to the exclusion of the background-only hypothesis. Signal significance and p_0 are related by the formula:

$$Z = \Phi^{-1}(1 - p_0)$$

where Z is the significance in unit of standard deviations and Φ^{-1} is the inverse cumulative distribution of the standard Gaussian. A p-value of 5% corresponds to a significance of 1.64 standard deviations.

10.3.1 Results

Tables 10.9 and 10.10 summarise all the relevant parameters obtained from the analysis of the test statistic distributions. Only the combined result from the 9 regions in the analysis is considered.

signal strength	1.3 ± 1.6	
	observed	expected ($\mu = 1$)
b-only p-value (p_0)	21%	26 %
signal significance	0.80 s.d.	0.65 s.d.

Table 10.9: Signal strength measured in the analysis. p_0 and significance for the measured signal. The 'expected' value correspond to the case there the SM signal ($\mu = 1$) is injected on top of the background predictions.

The p-value for the background only hypothesis is 21%, corresponding to a (local) significance of 0.8 standard deviations, where the expected significance for a Standard Model signal is 0.65 standard deviations.

For a Higgs boson mass of 125 GeV the expected upper limit on the $t\bar{t}H$ production is 3.1 times the Standard Model value. This represents a significant improvement over the analysis performed by ATLAS with the 2011 dataset (exp. limit=10.4) and the analysis performed by CMS in the same final state using 2012 data (exp. limit=4.7). When neglecting the systematic uncertainties in the formulation of the likelihood, the expected 95% upper limit lowers to 1.38 times the Standard Model production; this confirms that the sensitivity is dominated by the impact of systematic uncertainties.

[18]It is worth mentioning that in the context of signal discovery the null hypothesis is represented by the background only case and the alternate hypothesis is represented by the signal+background case. In the context of setting upper limits, the role of the two hypotheses is reversed.

95% CL upper limit on $\mu_{t\bar{t}H}$						
observed	-2 s.d.	-1 s.d.	median (exp.)	+1 s.d.	+2 s.d.	injected ($\mu = 1$)
4.2	1.7	2.2	3.1	4.4	6.0	3.9

Table 10.10: Observed 95% CL upper limit on the production cross section for $t\bar{t}H$ in units of the Standard Model value for a Higgs boson mass of 125 GeV. The expected upper limit and its 1 and 2 standard deviation bands are also shown together with the expected upper limit in case the SM signal ($\mu = 1$) is injected on top of the background predictions.

As reported in the previous sections, the best fit value for the signal strength for a mass of 125 GeV is larger than unity and this results in an observed upper limit of 4.2 times the Standard Model production.

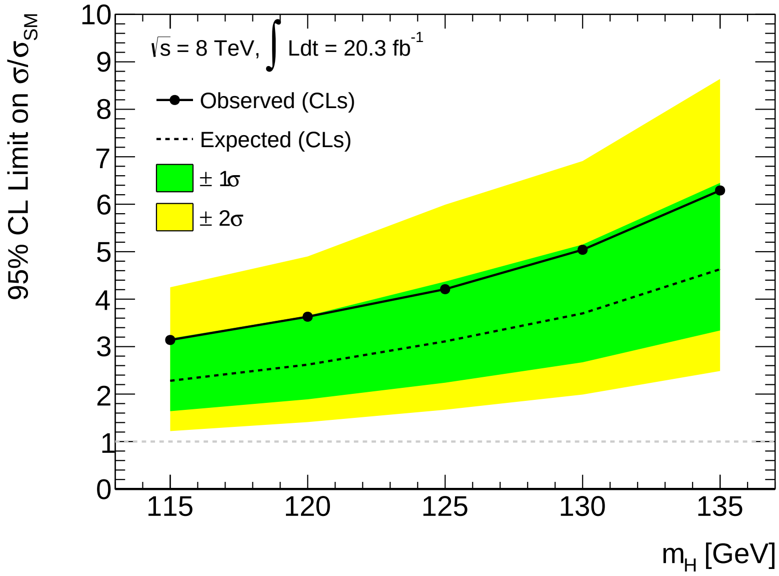

Figure 10.11: Observed 95% upper limit on the production cross section for $t\bar{t}H$ in unit of the Standard Model value as a function of the Higgs boson mass. The expected upper limit together with its ± 1 and ± 2 standard deviation ranges are also shown.

Finally, Figure 10.11 shows the expected and observed 95% upper limit on the signal strength as a function of the Higgs boson mass in the interval 115 - 135 GeV. A similar excess is found for any of the considered Higgs boson mass hypothesis. As discussed in the previous chapter, the shape of the discriminant does not have a strong dependence on the Higgs boson mass in the considered mass range. The degradation of the limit as a function of mass is due to reduction of the branching fraction into $b\bar{b}$ pairs which leads to a signal yields reduction in the most sensitive signal region. Contrary to the analysis performed on the 7 TeV dataset, this result cannot be easily interpreted as a model independent upper limit of a production of a generic particle produced in association with $t\bar{t}$ and decaying into b-quarks. One one side, the signal templates also receive (small) contributions from Higgs boson decays other than $b\bar{b}$; on the other, knowledge of the structure of the $t\bar{t}H$ production as well as angular distributions of the Higgs boson decay products, are included although with some dilution, in the variables used for the multivariate approach.

10.3.2 Combination with the dilepton final state analysis

The analysis described in this thesis exploits the single lepton plus jets final state. A search for the $t\bar{t}H$ process with $H \to b\bar{b}$, the dilepton final state has also been performed [182]; it requires exactly two opposite sign leptons (electrons or muons) and applies a similar classification of events according to the number of jets and number of b-tagged jets. The event selection in the two analyses is made orthogonal by the veto on the second lepton in the lepton plus jets analysis. Furthermore the same fit model has been implemented so that the two analyses could be combined by fully correlating the majority of the systematic uncertainties[19]. For the combination with the dilepton analysis three of the systematics previously described in the chapter were not considered: the signal PDF uncertainty, the ISR uncertainty on $t\bar{t}+V$ background and the additional normalisation uncertainty on single top sample. The impact of ignoring such systematics has found to be minimal.

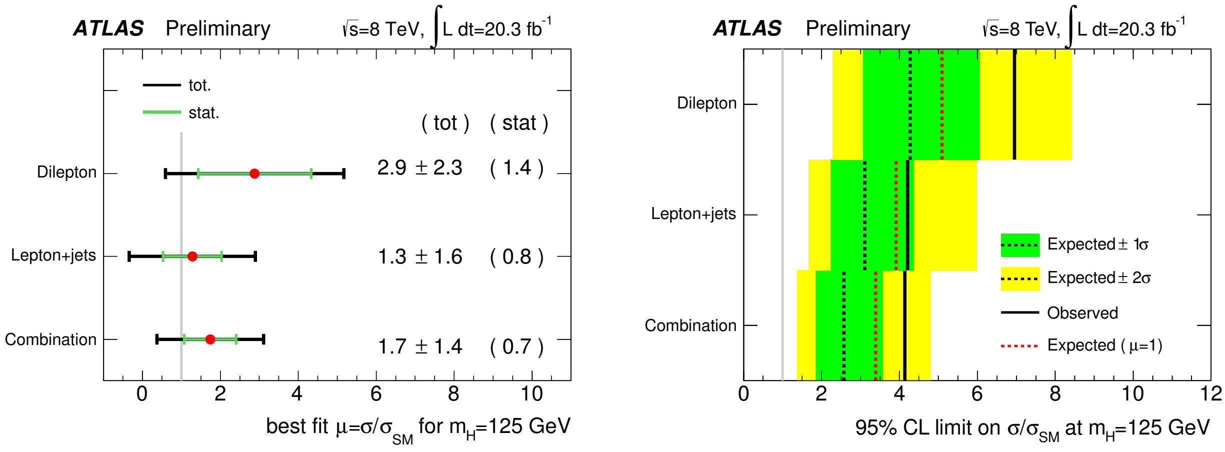

(a) (b)

Figure 10.12: (a) The fitted value of signal strength and its uncertainty for the individual channels and their combination, assuming m$_H$=125 GeV. The green line shows the statistical error on the signal strength. (b) Observed and expected limits for the background only hypothesis (dashed black line) and the corresponding ±1 s.d. and ±2 s.d. bands, and for the assumed SM Higgs Boson signal at m$_H$=125 GeVare shown for each of the channels and the combination.

Figure 10.12 (a) displays the best fit value for the signal strength in each channel independently as well as in the combination. Very consistent results are found for the two channels and the best value for the signal strength in the combination yields:

$$\mu_{\text{comb}} = 1.7 \pm 1.4$$

corresponding to a 1.3 standard deviation excess over the background only-prediction. An excess of 0.8 standard deviations was expected in case of the Standard Model Higgs boson.

The observed and expected 95% CL upper limit on μ are summarised in Figure 10.12 (b). The combination with the dilepton analysis improves the expected limit in the current lepton plus jets analysis by 17 %. The observed upper limit is only minimally affected by the combination since the dilepton channel presents a larger excess with respect to the background-only prediction. The combination yields an observed 95% CL upper limit on the $t\bar{t}H$ cross section of 4.1 times the Standard Model value.

[19]The exception is represented by the Z+jets normalisation, multijet background normalisation and systematics from the scale factor on the electron identification/isolation since different definitions are used in the two analyses.

Summary and Conclusions

To date, the Standard Model is the theory that best encompasses our knowledge of particle physics; it elegantly describes matter in terms of elementary constituents and their interactions and gives a coherent description of three out of four fundamental forces of nature.

In the last decades, increasingly precise measurements have probed the predictions of the Standard Model looking for discrepancies that could lead the way to the formulation of a more comprehensive theory. For this purpose the world's largest particle accelerator, the LHC, was built; it greatly exceeds the reach of previous colliders both in energy and intensity, allowing to explore corners of parameter space previously inaccessible. After 3 years of LHC data-taking (Run1), the validity of the predictions from the Standard Model framework has not been contradicted. Its greatest success is the discovery of the first fundamental scalar particle whose properties are compatible with those of the so-called Higgs boson; the particle that in the Standard Model is directly related to the mechanism by which other particles can have mass. The observation concluded a 40 years long search for the 'last piece' of the Standard Model description and opened a new direction of precise measurements.

In this thesis three different analyses have been presented. They have been performed at different stages during the LHC Run1 period, each of them exploiting data collected in one of the three years of data-taking. The common factor of each analysis is the presence of a top quark pair in the final state of signal events. The increasing amount of data and the constantly improving detector understanding naturally is naturally reflected in the precision and the scope of each analysis.

The 2010 data at $\sqrt{s}$ = 7 TeV have been used to measure the inclusive $t\bar{t}$ cross section, re-assessing the well know processes in the new energy regime. With the higher statistics of 2011 dataset, the measurement of the jet multiplicity spectrum in $t\bar{t}$ events has been performed; understanding this [spectrum] is of key importance in searches for new or rare phenomena where also top quark pairs are produced.

Finally, the search for the Standard Model Higgs boson produced in association with a top quark pair has been performed using the $\sqrt{s}$ = 8 TeV 2012 dataset; the increased centre of mass energy and data statistics allowed for the search of the Higgs boson in its rarest production mode.

$t\bar{t}$ measurements

The top quark is the heaviest known fundamental particle; its importance in high energy physics stems directly from its particular properties. A Yukawa coupling close to unity might indicate that the particle plays special role in extensions of the electroweak symmetry breaking mechanism that is an essential ingredient of the Higgs mechanism. Furthermore, due to its short lifetime, it decays before hadronising, giving a unique chance to study the properties of a 'bare' quark. In the recent years a huge effort from the theoretical community has led to significant improvements in the precision of the theoretical predictions for the production cross section and its properties.

For a proton-proton collider with 7 TeV centre of mass energy, , the production cross section for $t\bar{t}$ pairs is greater than 150 pb, making the collider a so-called 'top quark factory'. $t\bar{t}$ events can be efficiently collected and identified especially when decay modes involving leptons are considered.

The very large collected sample of top quarks is used for a variety of purposes. The specific characteristics of $t\bar{t}$ events allow to use them as 'standard candles' for detector calibration, in particular for the data-driven measurements of the b-tagging efficiency. Precise measurements of the event kinematics allow to gain knowledge of the evolution of QCD predictions at very high energy scales; its properties, like branching ratios and production modes, can be altered by BSM contributions. Last but not least, $t\bar{t}$ events often represent the main background in the search for new or rare phenomena.

The inclusive measurement of the $t\bar{t}$ production cross section using the 2010 dataset has been presented. The measurement with early data represented an important milestone for the ATLAS physics programme in order to, firstly, assess the $t\bar{t}$ production in the new LHC energy regime and secondly, test the detector performance. Various measurements have been performed, each of them using a different technique for signal extraction, event selection and categorisation. The analysis presented in the thesis uses a simple and robust approach; a template fitting procedure was applied using a single discriminating variable to separate the $t\bar{t}$ signal from the W+jets background; final states with a single electron or muon and at least 4 jets have been considered. Without the usage of any b-tagging information nor any sophisticated treatment of the systematic uncertainties, the analysis reached a total uncertainty of 20% with similar contributions from statistical and systematic uncertainties. The result was found to be in agreement with the NNLO theoretical calculations. The early cross section measurement demonstrated the good performance of the LHC and ATLAS allowing the achievement, after one year of data-taking, of results that required several years at the previous collider.

A more precise determination of the inclusive $t\bar{t}$ cross section in the lepton plus jets final state has been achieved using 0.7 fb^{-1} of data collected in 2011; the usage of multiple signal regions together with profile likelihood techniques allowed to reach a precision of $\sim$ 7%. The most precise single measurement of the cross section to date has been performed using the dilepton final states and events with at least one b-tagged jet. Considering the full 2012 dataset, a final precision of 4% has been achieved; this represents a smaller value than the theoretical uncertainty on the cross section calculation.

While precise inclusive cross section measurements can give important insight in specific aspects of the theoretical calculations and can be used to constrain the PDF, differential cross section measurements can be valuable to further improve the understanding of the production process and test the approach of different Monte Carlo generators. At the same time, specific regions of the phase space can be probed in order to increase the sensitivity to a specific generator parameter or to cover the phase space used in BSM searches. With the 2011 dataset, the LHC experiments greatly surpassed the number of $t\bar{t}$ events collected at the Tevatron. The analysis presented in this thesis concentrated on the measurement of the jet multiplicity spectrum in $t\bar{t}$ events with a single lepton in the final state.

The jet acceptance and kinematic selection followed the ones used in the standard event selection used by many analyses in the ATLAS collaboration. The jet multiplicity is particularly sensitive to the production of additional partons in $t\bar{t}$ events. Though initial state radiation effects, modelled either as parton shower effects or directly through matrix element calculations, have the dominant effect on the distribution, the distribution of the number of jets in the final state is also sensitive to the kinematics of the $t\bar{t}$ decay products as well as final state radiation and fragmentation effects. Furthermore, the evaluation of the jet multiplicity distribution does not require the reconstruction of the $t\bar{t}$ system in the event; this allows to minimise the model dependence of the measurement.

The analysis has been performed separately in the single electron or single muon channel with at least three jets in the final state. The measurement has been corrected for detector effects (unfolding) and the result has been reported for a phase space closely matching the detector acceptance (fiducial measurement). This choice has been made to minimise the uncertainties originating from the extrapolation of the result to the full phase space.

Consistent results have been obtained in the electron and muon channels; at low jet multiplicities the final uncertainty is dominated by the uncertainty on the background estimation and detector acceptance effects (b-tagging), while for high jet multiplicity the jet energy scale uncertainty gives the largest contribution, ranging between 25% and 50%.

The high jet multiplicity region is the one showing the largest differences in the predictions of the various Monte Carlo generators used to describe $t\bar{t}$ events. This is not surprising since the main differences are precisely related to the way additional parton radiation is modelled. All the tested generators have been found to provide a reasonable description of the jet multiplicity distribution up to events with 8 jets, with the exception of MC@NLO; the latter was found to underestimate the fraction of events with high jet multiplicity. The result is consistent with the fact that MC@NLO is an NLO generator where parton emissions beyond the leading one are described by the parton shower approach. At the same time POWHEG, another NLO generator, was found capable of giving a description of the jet multiplicity similar to the one obtained with more suited LO multi leg generators. Also due to the presented result, POWHEG (interfaced to PYTHIA) was adopted as the default generator to model $t\bar{t}$ events.

Finally, it has also been shown that data can also be used to tune generators parameters in order to improve their capability of describing the data. The example of ALPGEN interfaced to PYTHIA was provided; better agreement with the observed data is obtained by reducing the value of α_S used in the emission vertices.

The presented analysis was performed using the detector calibration available in summer 2012. The final publication using the best knowledge of the detector uncertainties for the 2011 dataset is in preparation. The improvements of the systematic uncertainties are particularly related to the b-tagging and the implementation of the more refined breakdown of the uncertainties related to the jet energy scale (as applied in the 2012 analysis). Other than the already presented jet multiplicity distribution, it will also include the jet multiplicity distribution for a higher jet p_T cuts and the p_T distributions of the jets in the events.

Fiducial differential measurements of $t\bar{t}$ event kinematics represent a great legacy of the LHC Run1; they allow to perform precise tests of the current theoretical predictions from Monte Carlo generators. At the same time, they will be used for the tuning of the generator parameters with the goal to improve the description of data for the LHC Run2 phase. One example is related to the validation of the recently available generators capable of describing the emission of extra partons at NLO accuracy.

Search for associated production of the Standard Model Higgs boson with a top quark pair.

The associated production of the Higgs boson with a top quark pair ($t\bar{t}H$) represents the Higgs boson production mode with the smallest cross section. Since the process involves the Higgs boson coupling to the top quark at tree level, its measurement will allow to directly probe the top quark Yukawa coupling without the interference from possible new physics contributions. Assumptions on such contributions are in fact needed to extract information from processes involving top quark loops like gluon fusion Higgs production or the decay into a photon pair.

Given that the $t\bar{t}H$ cross section is 200 times smaller than the dominant Higgs boson production, the Higgs boson final state with the largest branching ratio, the decay into a b-quark pair was chosen in order to maximise the signal yields. At the same time, the single lepton $t\bar{t}$ decay topology is exploited in order to collect the events and reduce the contribution from the multijet background.

The search for a $t\bar{t}$ pair produced in association with a Higgs boson decaying into b-quarks has been performed using the full 2012 8 TeV dataset in events containing exactly one isolated electron or muon and a large number of jets and b-tagged jets in the final state. The events have been categorised according to the number of jets and b-tagged jets; while the largest signal over background ratio is obtained for events with at least six jets and at least four b-tagged jets, other categories are exploited to increase the signal sensitivity and reduce the effect of the systematic uncertainties, especially the ones related to the modelling of the backgrounds.

The signal fraction has been extracted with a template fit to multivariate discriminant distributions; neural network discriminants have been trained to separate the signal from the backgrounds. Contrary to the 2011 analysis, no attempt at a kinematic reconstruction has been made. The large event combinatorics results in a relatively low efficiency for assigning the correct jets to the Higgs boson decay products and this spoils the discrimination power of the di-jet invariant mass distribution. The effects of the systematic uncertainties have been included in the likelihood fit definition as nuisance parameters.

The best fit value for the signal strength for a Higgs boson mass of 125 GeV (expressed in unit of the SM Higgs expectations) extracted from the fit to data is:

$$\hat{\mu} = \frac{\sigma_{t\bar{t}H}}{\sigma_{t\bar{t}H}^{SM}} = 1.3 \pm 1.6$$

corresponding to an excess of 0.8 standard deviation with respect to the background only predictions. Since no significant excess is found, the result translates into a 95% confidence level upper limit of the $t\bar{t}H$ cross section of:

$$\sigma_{t\bar{t}H} < 4.2 \cdot \sigma_{t\bar{t}H}^{SM}$$

while a limit of 3.1 times the Standard Model cross section was expected in the case of no signal. The contamination from other Higgs boson decay modes has been considered in the analysis, they represent only a percent-level contribution to the total signal yields in the most sensitive analysis regions. With this caveat the limit can be interpreted as an upper limit on the $t\bar{t}H$ associated production cross section times the $H \to b\bar{b}$ branching ratio. The result is a great improvement over the previous ATLAS result obtained using the 2011 dataset.

The sensitivity of the analysis is completely dominated by the knowledge of the normalisation and modelling of the main irreducible background, the production of $t\bar{t}$ plus additional b-quarks. Very few direct measurements exist for this background and only recently theoretical calculations at NLO have become available. Very conservative uncertainties on the shape and normalisation have been adopted in the analysis. The uncertainties have been reduced in the fitting procedure using the information contained in the analysed data. This suggests that the 2012 dataset collected by ATLAS has a good potential for a fiducial and differential measurement of the $t\bar{t}$+$b\bar{b}$ process which can help in validating the predictions of the Monte Carlo generators.

The described current analysis has been presented at the Moriond 2014 conference and, at the time of writing, represents the most stringent direct upper limits on the $t\bar{t}H$ production among all the performed ATLAS analyses. It also improves over the limit obtained by the CMS collaboration using the identical final state topology.

The analysis is currently being updated with a more refined treatment of b-tagging information as well as the introduction of a very computationally expensive matrix element discriminant[20].

While the presented analysis does not yet allow a precise measurement of the $t\bar{t}H$ production cross section, multiple final states can be combined to increase the sensitivity. For the result presented at the Moriond 2014 conference, the searches for $t\bar{t}H$ with the Higgs boson decaying into a b-quark pair in the single lepton and dileptonic channel were combined. The combination yielded a 20% improvement in the expected sensitivity with respect to the single lepton final state alone.

Other $t\bar{t}$ final states are currently being investigated in the context of the Higgs boson decay into $b\bar{b}$; all-hadronic $t\bar{t}$ decays and final states containing one electron or muon and one hadronically decaying τ-lepton. At the same time, other analyses are aiming at different Higgs boson decay modes. A search for $t\bar{t}H$ using the di-photon final state has already been performed by the ATLAS collaboration [183], setting a limit of 5.3 times the SM value for the $t\bar{t}H$ production cross section times the Higgs to two photon branching ratio. An analysis targeting final states with multiple leptons[21] is being finalised.

The analyses all show similar performance and a large improvement in the sensitivity to $t\bar{t}H$ is expected from the combination of all the final states given that the dominant backgrounds differ significantly between analyses. These results will represent an important additional input in testing the consistency of the Standard Model hypothesis for the discovered particle, as well as in looking for any deviations from the expected Standard Model behaviour.

Currently the results from more precise analyses exploiting production modes other than $t\bar{t}H$ are used to extract information on the couplings of the Higgs boson to other fundamental particles [184]; the Higgs boson couplings have been tested in various benchmark models, all probing specific assumptions on the relation among them. All tests have shown good agreement with the Standard Model Higgs boson hypothesis.

The Higgs boson coupling to the top quark enters in the loop contribution to the gluon fusion production mode as well as in the loop-induced decay into photons; in this latter case, the top quark loop interferes with the more dominant W boson loop. Constraints on the coupling can then be indirectly obtained by the precise measurement of the gluon fusion production mode and the $\gamma\gamma$ final state channels. With the full 7 and 8 TeV dataset, the obtained 1-σ confidence level interval for the modified top quark coupling[22] is:

$$k_t \in [-0.80, -0.5] \cup [0.61, 0.80]$$

The result is obtained in the benchmark scenario where the Higgs couplings to 5 SM particles (W and Z bosons, t and b quarks and τ lepton) are allowed to vary independently. Only Standard Model particles are allowed to contribute to the loop diagrams for the gluon fusion production and $H \to \gamma\gamma$ decay and the Higgs boson decay width has been kept fixed to its SM value.

Once these latter assumptions are dropped, for instance by allowing effective coupling scale factors for the $H \to \gamma\gamma$ and $gg \to H$, the constraints on the top-quark coupling are weakened significantly. In this case, a more direct constraint from $t\bar{t}H$ production measurements can

[20]The matrix element approach consists in computing the event probability for the signal and the background hypotheses based on the full event kinematic information and their prediction based from exact LO matrix element calculations.

[21] Mainly aiming at $t\bar{t}H$ with $H \to WW$ and $H \to \tau\tau$.

[22]The LO-motivated coupling scale factors k_j are defined in such a way that the cross section σ_j and the partial decay width Γ_j associated with the SM particle j scale with the factor k_j^2 when compared to the corresponding SM prediction.

help restore the precision of the simultaneous coupling fit and hence improve the possibility for additional tests of the Standard Model hypothesis.

Finally, the precise measurement of the $t\bar{t}H$ process will represent one of the main goals of the LHC Run2 phase. Due to the presence of three massive particles, it is the Higgs boson production mode that displays the largest increase in cross section when raising the centre-of-mass energy from 8 TeV to 14 TeV. An increase of a factor of 4.7 is expected for the signal while the $t\bar{t}$ cross section will only increase by a factor of 3.5. As a comparison, the Higgs boson production cross section for gluon fusion only increases by a factor of 2.6.

The increase in cross section, together with the larger integrated luminosity, will significantly benefit $t\bar{t}H$ analyses that are currently limited by the data statistics ($H \rightarrow \gamma\gamma$, multi-lepton final states). Dedicated studies related to LHC Run2 scenarios [185] indicate that the $\gamma\gamma$ final state will reach a precision of 50% on the $t\bar{t}H$ production cross section with 300 fb^{-1} of data at $\sqrt{s} = 14$ TeV. With the addition of indirect constraints coming from the precise analyses of the bosonic final states in the gluon fusion production, the top quark Yukawa coupling could be probed at the 20% accuracy level.

For what concerns final states where the Higgs boson decays into a b-quark pair, the current analyses are already limited by systematic uncertainties. A sensitivity estimate for the LHC Run2 is difficult to perform given that the analysis heavily relies on the data to reduce the impact of the systematic uncertainties. The increased data statistics will allow for a more refined event categorisation in order to improve the signal over background ratio; as an example, events can be classified according to the result of the $t\bar{t}$ kinematic reconstruction to isolate the categories with better di-jet invariant mass separation. Boosted topologies will also play an important role despite the reduced cross section. With sufficiently high p_{T} boost for the top quarks or the Higgs boson, the decay products are sufficiently collimated and are reconstructed as broad jets. This feature will substantially reduce the combinatorics. At the same time, an increased understanding of the background modelling is expected from the usage of newly developed Monte Carlo techniques for event generation and the application of more data-driven techniques.

Samenvatting

Het Standaardmodel is de theorie die het beste ons begrip van de deeltjesfysica weergeeft. Het beschrijft op een elegante manier alle materie in termen van zijn elementaire bestanddelen en hun interacties, en geeft een coherente beschrijving van drie van de vier fundamentele krachten. In de laatste paar decennia hebben almaar preciezere metingen de voorspellingen van het Standaardmodel getest, met als doel afwijkingen hiervan te vinden die de weg kunnen wijzen naar een alles omvattende theorie. Met dit doel is ook de Large Hadron Collider (LHC) gebouwd, 's-werelds grootste deeltjesversneller. De LHC overtreft eerdere versnellers ruimschoots, in termen van zowel de botsingsenergieën als de intensiteit; dit maakt het mogelijk om fenomenen te (onder)zoeken die voorheen niet getest konden worden. Na drie jaar vergaren van data in "Run 1" zijn ook bij de LHC nog geen aanwijzingen gevonden dat het Standaardmodel niet geldig zou zijn. Het grootste succes van de LHC is de ontdekking van een spin-0 deeltje met eigenschappen die overeenkomen met die van het zogenaamde Higgsboson, het deeltje dat in het Standaardmodel direct gerelateerd is aan het mechanisme dat ervoor zorgt dat andere fermionen en bosonen massa kunnen hebben. Deze ontdekking sluit een 40-jarige zoektocht af naar dit laatste onderdeel van het Standaardmodel en opent tegelijk de weg voor nieuwe precisiemetingen.

In dit proefschrift zijn drie verschillende analyses behandeld. Elk hiervan is gedaan in een verschillend stadium van Run 1, en met een dataset die overeenkomt met een van de drie jaren waarin data vergaard zijn. Het gemeenschappelijke element in alle analyses is de aanwezigheid van een top-quark paar in het onderzochte signaal; de toename van de hoeveelheid data en het steeds verder verbeterde begrip van de detector-respons komen tot uiting in de precisie en aard van iedere analyse. De in 2010 vergaarde data zijn gebruikt om de totale inclusieve werkzame doorsnede voor $t\bar{t}$-productie te meten; hierin moesten in principe bekende processen in het nieuwe energiegebied van de LHC opnieuw bestudeerd worden. Met de grotere hoeveelheid data vergaard in 2011 is een meting gedaan van het multipliciteitsspectrum van jets in $t\bar{t}$-interacties; het begrijpen hiervan is van cruciaal belang bij het zoeken naar nieuwe of zeldzame fenomenen waarbij ook top-quark paren geproduceerd worden.

Tenslotte is in de in 2012 vergaarde data gezocht naar interacties waarin een Higgsboson geproduceerd wordt samen met een top-quark paar. De verhoging van de botsingsenergie (van 7 naar 8 TeV) en weer veel grotere hoeveelheid data hebben deze zoektocht naar het Higgsboson in zijn zeldzaamste productieproces mogelijk gemaakt.

Metingen aan $t\bar{t}$ productie

Het top-quark is het zwaarst bekende elementaire deeltje. Het belang ervan voor de deeltjesfysica komt direct voort uit zijn specifieke eigenschappen. De sterkte van zijn Yukawa-koppeling aan het Higgsdeeltje, met een waarde dichtbij 1, suggereert dat het een speciale rol zou kunnen spelen bij eventuele uitbreidingen van de symmetriebreking die een essentieel bestanddeel vormt van het Higgsmechanisme. Daarnaast is zijn levensduur zo kort dat het vervalt voordat het gebonden toestanden kan vormen; dit geeft een unieke kans om de eigenschappen van het quark zelf te bestuderen. De afgelopen jaren heeft een grote inspanning door theoretici geleid tot aanzienlijke verbeteringen in de precisie van de voorspellingen van zowel de totale werkzame doorsnede als de eigenschappen van de productie van top-quark paren.

Voor proton-proton botsingen bij een botsingsenergie van 7 TeV is deze werkzame doorsnede groter dan 150 pb; dit leidt tot grote aantallen geproduceerde interacties, wat de LHC tot een "top quark factory" maakt. De interacties kunnen efficiënt vergaard en geïdentificeerd worden, in het bijzonder als vervalskanalen met leptonen in de eindtoestand beschouwd worden.

De grote hoeveelheid $t\bar{t}$-paren kan voor vele doeleinden gebruikt worden. De specifieke eigenschappen van de interacties maken het mogelijk om hen te gebruiken als standaardprocessen voor het ijken van de detector-respons, in het bijzonder voor metingen van de efficiëntie waarmee b-quark jets herkend kunnen worden. Precieze metingen van de kinematica van de interacties stellen ons in staat om het gedrag van de quantum-chromodynamica bij hoge energieën beter te begrijpen. Eigenschappen zoals de vertakkingsverhoudingen van de diverse vervalskanalen en de productieprocessen kunnen beïnvloed worden door effecten veroorzaakt in uitbreidingen van het Standaardmodel.

De meting is beschreven van de inclusieve werkzame doorsnede voor $t\bar{t}$-productie bij een botsingsenergie van 7 TeV, met de in 2010 genomen data. Deze meting, met de eerste substantiële dataset, was een belangrijke mijlpaal voor het fysicaprogramma van het ATLAS-experiment, ten eerste omwille van de meting zelf, en ten tweede om het functioneren van de detector te testen. De in dit proefschrift beschreven analyse was eenvoudig en robuust: een *template fitting*-procedure werd gebruikt om het $t\bar{t}$-signaal van de W+jets-achtergrond te onderscheiden, in interacties met precies een elektron of muon en tenminste vier jets in de eindtoestand. Zonder te proberen jets te identificeren als b-jets en zonder verfijnde behandeling van de systematische onzekerheden werd een relatieve onzekerheid van 20% bereikt, met vergelijkbare statistische en systematische bijdragen. Het resultaat komt overeen met de theoretische berekeningen op NNLO-niveau. Deze vroege meting van de werkzame doorsnede was exemplarisch voor het goede functioneren van zowel de LHC als ATLAS: na slechts een jaar werden resultaten verkregen waar bij de vorige versneller (het Tevatron) en de vorige generatie experimenten meerdere jaren voor nodig waren.

Weliswaar kan de meting van de inclusieve werkzame doorsnede inzicht geven in specifieke aspecten van de theoretische berekeningen en kan hij ook gebruikt worden om de kennis van parton-dichtheidsfuncties te verbeteren; maar metingen van differentiële werkzame doorsnedes kunnen zeer waardevol zijn om het productieproces beter te begrijpen en de werkwijzen van verschillende Monte Carlo-generatoren te testen. Ook kunnen specifieke regimes beschouwd worden om de gevoeligheid voor specifieke parameters van de gebruikte generatoren te verbeteren, of om de faseruimte te bestrijken die voor zoektochten naar uitbreidingen van het Standaardmodel belangrijk is.

Met de in 2011 genomen data is het door de LHC-experimenten geregistreerde aantal $t\bar{t}$-interacties dat bij het Tevatron ruim voorbijgestreefd. De in dit proefschrift behandelde analyse concentreerde zich op de meting van het multipliciteitsspectrum van jets in $t\bar{t}$-interacties met een enkel lepton in de eindtoestand. De acceptantie voor jets en de kinematische selectie volgde dezelfde standaard als vele andere analyses in het ATLAS-samenwerkingsverband. De verdeling van het aantal jets in $t\bar{t}$-interacties is bijzonder gevoelig voor de productie van extra partonen. Stralingseffecten in de begintoestand hebben een dominant effect op de kinematische verdelingen; deze effecten kunnen gemodelleerd worden ofwel middels de *parton shower* of direct via matrix-element berekeningen. De verdeling van het aantal jets is echter ook gevoelig voor de kinematica van de producten van het verval van de top-quarks, evenals voor stralingseffecten in de eindtoestand en fragmentatie-effecten. Bovendien is het voor het beschouwen van de verdeling van het aantal jets niet nodig om het $t\bar{t}$-systeem expliciet te reconstrueren; hierdoor kan de modelafhankelijkheid van de meting geminimaliseerd worden.

De analyse is apart gedaan in het elektron- en het muonkanaal, in beide gevallen in interacties met tenminste drie jets. De metingen zijn gecorrigeerd voor detector-effecten en gerapporteerd voor een acceptantie dichtbij die van de detector; deze keuze minimaliseert de onzekerheden die gepaard zouden gaan met een extrapolatie van de resultaten naar de volledige faseruimte.

De resultaten verkregen in de twee kanalen zijn consistent met elkaar. Bij lage aantallen jets wordt de totale onzekerheid gedomineerd door die op het schatten van de achtergrond en van de efficiëntie voor het herkennen van b-quark jets; bij hoge aantallen levert de meting van de energieschaal van jets de grootste bijdrage (tussen 25% en 50%).

Bij hoge aantallen jets worden de grootste verschillen gezien tussen de voorspellingen door de diverse Monte-Carlo generatoren die gebruikt zijn om $t\bar{t}$-interacties te simuleren. Dit is niet verbazingwekkend aangezien de belangrijkste verschillen precies gerelateerd zijn aan de manier waarop parton-stralingseffecten gemodelleerd worden. Alle geteste generatoren blijken een redelijke beschrijving van het spectrum te geven voor interacties met maximaal 8 jets, met uitzondering van MC@NLO: deze generator onderschat het aantal interacties met veel jets. Dit resultaat is consistent met het feit dat MC@NLO een NLO generator is: het afstralen van partonen behalve het eerste wordt beschreven door de *parton shower*. Anderzijds is ook gevonden dat Powheg, een andere NLO generator, wel degelijk een beschrijving van dit spectrum geeft compatibel met die van generatoren die het afstralen van meerdere partonen kunnen beschrijven, maar slechts in laagste orde. Gebaseerd op onder meer dit resultaat wordt de Powheg-generator, met gebruik van Pythia voor de *parton shower*, door ATLAS gebruikt als standaard-generator voor het simuleren van $t\bar{t}$-interacties. Tenslotte is ook aangetoond dat de data gebruikt kunnen worden om parameters in de generator-programma's zodanig af te stellen dat hun voorspellingen beter overeenkomen met de data. Het voorbeeld van Alpgen (weer met Pythia voor de *parton shower*) is expliciet behandeld, waarin gezien werd dat een betere overeenkomst met de data gevonden wordt wanneer de waarde van α_S zoals gebruikt in de vertices die het afstralen van extra partonen beschrijven verlaagd wordt.

Metingen van de kinematica van $t\bar{t}$-interacties vormen een belangrijke erfenis van Run 1; ze maken het mogelijk om precieze tests uit te voeren van de voorspellingen van de beschikbare Monte-Carlo generatoren. Momenteel worden ze gebruikt om de parameters in de huidige generatoren te optimaliseren, met de hoop dat daarmee ook de beschrijving van dit proces in Run 2 verbeterd zal worden.

Zoektocht naar interacties waarin het HIggs-boson samen met een top-quark paar geproduceerd wordt.

Volgens de voorspellingen van het Standaardmodel is de werkzame doorsnede voor dit productieproces de kleinste van alle waarin het Higgs-boson geproduceerd wordt. In dit proces komt de koppeling van het Higgs-boson aan het top-quark zelfs op laagste orde voor; dit maakt het mogelijk om dit proces te gebruiken om deze Yukawa-koppeling te testen zonder mogelijke interferentie-effecten tengevolge van bijdragen voorspeld door uitbreidingen van het Standaardmodel. Wanneer processen met top-quark lussen, zoals productie van Higgs-bosonen via gluon-fusie of het verval van Higgs-bosonen naar foton-paren, gebruikt worden om informatie over deze koppeling te verkrijgen dan is het daarentegen nodig om aannames over deze bijdragen te maken.

De werkzame doorsnede voor $t\bar{t}H$-productie is 200 maal kleiner dan die voor het dominante gluon-fusie proces; daarom is het verval van het Higgs-boson met de grootste vertakkingsverhouding, dat naar een b-quark paar, gebruikt om een zo groot mogelijk signaal te verkrijgen. Ook wordt weer het $t\bar{t}$-verval met een geladen lepton in de eindtoestand gebruikt voor een efficiënte vergaring van de data en om de achtergrond van pure jet-productie te onderdrukken.

Deze zoektocht is uitgevoerd met alle in 2012 genomen data bij een botsingsenergie van 8 TeV, in interacties met exact een elektron of muon, en een groot aantal jets, waarvan een aantal als b-quark jets zijn geïdentificeerd. De interacties zijn geklassificeerd aan de hand van het aantal jets en het aantal daarvan dat als b-quark jets zijn geïdentificeerd. De grootste signaal/achtergrond verhouding wordt verkregen in interacties met tenminste zes jets en tenminste vier daarvan geïdentificeerd als b-quark jets; maar andere categorieën zijn gebruikt om de gevoeligheid voor het signaal te verbeteren en om de effecten van systematische onzekerheden te verkleinen, in het bijzonder de effecten gerelateerd aan het modelleren van de achtergronden.

Het aantal signaal-interacties is weer afgeschat middels een *template fitting* procedure, aan verdelingen van neurale-netwerk discriminanten: deze neurale netwerken zijn getraind om het signaal van de achtergronden te onderscheiden. De effecten van systematische onzekerheden zijn in de *likelihood*-functie meegenomen via *nuisance parameters*.

De gevonden waarde voor de signaalsterkte voor een Higgs-boson massa van 125 GeV en ten opzichte van de sterkte verwacht in het Standaardmodel is

$$\hat{\mu} = \frac{\sigma_{t\bar{t}H}}{\sigma^{SM}_{t\bar{t}H}} = 1,3 \pm 1,6$$

Dit komt overeen met een afwijking van 0,8 standaarddeviaties ten opzichte van de verwachtingen in de afwezigheid van een signaal. Aangezien geen significant signaal gevonden is, is het resultaat ook gebruikt om een bovenlimiet te stellen aan de werkzame doorsnede voor $t\bar{t}H$-productie: met 95% betrouwbaarheid is

$$\sigma_{t\bar{t}H} < 4,2 \cdot \sigma^{SM}_{t\bar{t}H}$$

dit kan vergeleken worden met een waarde van 3,1 verwacht in de afwezigheid van een signaal. Ook andere Higgs-vervalskanalen zijn in deze analyse expliciet meegenomen; maar in het gevoeligste analysegebied dragen ze niet meer dan van de orde van een procent bij aan het totale signaal. Met deze kleine reserve kan de verkregen limiet geïnterpreteerd worden als een bovenlimiet op het product van de werkzame doorsnede voor $t\bar{t}H$-productie en de vertakkingsverhouding voor het verval $H \to b\bar{b}$. Dit resultaat is een grote verbetering ten opzichte van het vorige ATLAS-resultaat, dat verkregen werd op de in 2011 genomen data.

De gevoeligheid van de analyse wordt volledig bepaald door de onzekerheid op de normalisatie en op het modelleren van de belangrijkste irreducibele achtergrond, de productie van $t\bar{t}$ met extra b-quarks. Zeer weinig directe metingen van dit proces zijn gedaan, en onlangs pas zijn theoretische berekeningen ervan op NLO beschikbaar gekomen. Zeer conservatieve onzekerheden zijn aangenomen voor de verdeling en normalisatie voor dit proces. Deze onzekerheden worden gereduceerd door het gebruik in de fit-procedure van de informatie besloten in de data. Dit suggereert dat deze dataset wellicht goed gebruikt zou kunnen worden voor meer gedetailleerde metingen van het $t\bar{t} + b\bar{b}$-proces; dit zou kunnen helpen om de voorspellingen van de gebruikte generatoren te valideren.

De beschreven analyse is gepresenteerd tijdens de Moriond-2014 conferentie en vertegenwoordigt, bij het schrijven van dit proefschrift, de meest stringente bovenlimiet op $t\bar{t}H$-productie van alle ATLAS-analyses. De analyse betekent eveneens een verbetering ten opzichte van het resultaat dat door het CMS-samenwerkingsverband verkregen bij het analyseren van dezelfde eindtoestand.

Deze analyse alleen geeft nog geen precieze meting van de werkzame doorsnede voor de productie van $t\bar{t}H$; maar andere vervalskanalen kunnen gebruikt worden om de precisie te verbeteren. Voor het resultaat dat tijdens de Moriond-2014 conferentie gepresenteerd werd, werden de analyses waarbij het verval van $t\bar{t}$-paar leidt tot een dan wel twee leptonen gecombineerd. Deze combinatie leidt tot een verbetering van 20% ten opzichte van het gebruik van alleen de analyse met één lepton.

Ook andere $t\bar{t}$-vervalskanalen worden momenteel onderzocht, met nog steeds een Higgs-verval naar $b\bar{b}$: vervallen met alleen jets, of vervallen met een elektron of muon en een hadronisch vervallend τ-lepton. Daarnaast zijn er echter ook analyses die zich richten op andere vervalskanalen van het Higgs-boson. Een zoektocht in het vervalskanaal naar twee fotonen is al uitgevoerd door ATLAS [183], met als resultaat een limiet van 5,3 maal de in het Standaardmodel verwachte signaalsterkte voor het product van de werkzame doorsnede voor het productieproces en de vervalsfractie naar twee fotonen. Een analyse die zich richt op eindtoestanden met meerdere leptonen (middels de vervalskanalen $H \to WW$ en $H \to \tau\tau$) wordt momenteel afgerond.

Al deze analyses laten een vergelijkbare gevoeligheid zien; een grote verbetering in de gevoeligheid voor het productieproces $t\bar{t}H$ wordt verwacht van de combinatie van deze analyses, aangezien de dominante achtergronden voor de verschillende analyses anders zijn.

Deze resultaten vormen een belangrijke input in het testen van de hypothese dat het gevonden deeltje inderdaad de in het Standaardmodel voor het Higgs-boson voorspelde eigenschappen heeft, en tevens voor het zoeken naar afwijkingen van deze eigenschappen. Momenteel worden de resultaten van preciezere analyses, die zich richten op andere productieprocessen dan $t\bar{t}H$, gebruikt om informatie te verkrijgen over de sterkte van de koppeling van het Higgs-boson aan andere elementaire deeltjes [184]. Deze koppelingen zijn beschouwd in diverse modellen, die verscheidene aannames voor hun onderlinge relaties maken. Al deze tests laten een goede overeenkomst zien met de Standaardmodel-hypothese. In deze tests wordt de informatie over de Yukawa-koppelingssterkte van het Higgs-boson aan het top-quark verkregen onder de aanname dat alleen de deeltjes van het Standaardmodel een rol spelen. Meenemen van de resultaten van de $t\bar{t}H$-analyse zal het mogelijk maken gevoelig te blijven voor deze koppelingssterkte, zelfs in het meer algemene geval dat de vervalsbreedte van het Higgsboson niet die is zoals voorspeld door het Standaardmodel, wat nauw verbonden is met extra bijdragen van nieuwe deeltjes aan de $H \to \gamma\gamma$ en $gg \to H$ lusdiagrammen.

Precisiemetingen van het $t\bar{t}H$-productieproces behoren tot de belangrijkere doelstellingen van de volgende fase, Run 2, van de LHC. De aanwezigheid van drie zware deeltjes betekent dat van alle Higgs-productieprocessen dit het proces is waarvan de werkzame doorsnede het snelst stijgt met de verhoging van de botsingsenergie, van 8 naar 14 TeV. Een toename met een factor 4,7 wordt verwacht, terwijl dit voor de werkzame doorsnede voor $t\bar{t}$-productie slechts 3,5 is; de werkzame doorsnede voor Higgs-productie middels het gluon-fusieproces stijgt slechts met een factor 2,6. Samen met de verwachte hogere luminositeit zal deze veel hogere werkzame doorsnede zeer welkom zijn voor met name die $t\bar{t}H$-analyses die tot nog toe gelimiteerd worden door de beschikbare statistiek ($H \to \gamma\gamma$ en eindtoestanden met meerdere leptonen).

De analyses in die kanalen waarin het Higgs-boson in een b-quark paar vervalt worden nu al gelimiteerd door systematische onzekerheden. Een schatting van de gevoeligheid van deze analyses in Run 2 is moeilijk te geven, omdat de analyse zwaar leunt op de data om de gevolgen van systematische onzekerheden te reduceren. De toegenomen hoeveelheid data zal het wel mogelijk maken om de waargenomen interacties beter te klassificeren om de signaal/achtergrond-verhouding te verbeteren; een expliciete reconstructie van de $t\bar{t}$-kinematica kan bijvoorbeeld gebruikt worden om de categoriën die een betere resolutie van de $b\bar{b}$ invariante massa geven apart te behandelen. Het *boosted* regime zal ook een belangrijke rol spelen, ondanks de lagere werkzame doorsnede. Als een van de top-quarks of het Higgs-boson met zeer hoge impuls geproduceerd wordt, zullen de vervalsproducten gecollimeerd worden en als een enkele, brede jet gereconstrueerd worden; dit vermindert de combinatoriek aanzienlijk. Ook wordt een verbetering in het modelleren van de achtergrond verwacht, door het gebruik van nieuwe Monte-Carlo technieken voor het simuleren van de interacties en verbeterde technieken om de data zelf te gebruiken voor het modelleren.

Bibliography

[1] M. E. Peskin and D. V. Schroeder, *An Introduction to Quantum Field Theory.* Addison-Wesley, 1995.

[2] E. Noether, *Invariant variational problems (Invariante Variationsprobleme)*, Nachr.v. d. Ges. d. Wiss. zu Goettingen (1918) 235257.

[3] I.J.R. Aitchison, A.J.G. Hey, *Gauge Theories in Particle Physics.* Taylor & Francis, 2003.

[4] S. Weinberg, *A model of leptons*, Phys. Rev. Lett. **19** (1967) 12641266.

[5] A. Salam, *Electromagnetic and weak interactions*, Phys. Rev. Lett. **13** (1964) 168.

[6] J. Beringer et al., *Particle Data Group*, Phys. Rev. D86 (2012) 01001.

[7] P. W. Higgs, *Broken Symmetries and the Masses of Gauge Bosons*, Phys. Rev. Lett. **13** (1964) 508–509.

[8] F. Englert and R. Brout, *Broken Symmetry and the Mass of Gauge Vector Mesons*, Phys. Rev. Lett. **13** (1964) 321.

[9] G. Ridolfi and C.M. Becchi, *An introduction to the Standard Model of Electroweak Interactions.* Springer, 2006.

[10] N. Cabibbo, *Unitary Symmetry and Leptonic Decays*, Phys. Rev. Lett. **10** (1963) 531.

[11] M. Kobayashi and T. Maskawa, *CP-Violation in the Renormalizable Theory of Weak Interaction*, Prog. Theor. Phys. **49** (1973) 652.

[12] D.J. Gross and F. Wilczek, *Ultraviolet Behavior of Non-Abelian Gauge Theories*, Phys. Rev. Lett. **30** (1973) 134–136.

[13] The Gargamelle Neutrino Collaboration, *Observation of Neutrino Like Interactions without muon or electron in the Gargamelle Neutrino Experiment*, Phys. Rev. Lett. B **46** (1973) 121–1138.

[14] W. Herb et al., *Observation of a Dimuon Resonance at 9.5-GeV in 400-GeV Proton-Nucleus Collisions*, Phys. Rev. Lett. **39** (1975) 252.

[15] M. L. Perl et al., *Evidence for Anomalous Lepton Production in e^+-e^- Annihilation*, Phys. Rev. Lett. **35** (1975) 1489.

[16] G. Arnison et al., *Experimental Observation of Isolated Large Transverse Energy Electrons with Associated Missing Energy at* $\sqrt{s} = 540$ GeV, Phys. Rev. Lett. B **122** (1983) 103.

[17] G. Arnison et al., *Observation of top quark production in anti-p p collisions*, Phys. Rev. Lett. **74** (1995) 2626–2637.

[18] M. Baak et al., *Updated Status of the Global Electroweak Fit and Constraints on New Physics*, Eur.Phys.J. C **72** (2012) .

[19] The ATLAS collaboration, *Observation of a new particle in the search for the Standard Model Higgs boson with the ATLAS detector at the LHC*, Phys. Lett. B **716** (2012) 1–29.

[20] The ATLAS collaboration, *Evidence for the spin-0 nature of the Higgs boson using ATLAS data*, Phys. Lett. B **726** (2013) 120–144.

[21] M. Baak, R. Kogler, *The global electroweak Standard Model fit after the Higgs discovery*, arXiv:1306.0571v2.

[22] The KamLAND Collaboration, *First results from KamLAND: Evidence for reactor anti-neutrino disappearance*, Phys. Rev. Lett. **90** (2003) 021802.

[23] J. Wess and B. Zumino, *Supergauge Transformations in Four-Dimensions*, Nucl. Phys. B **70** (1974) 39–50.

[24] G. Watt, *Parton Distribution Functions*, `arXiv:1111.5452 [hep-ph]`.

[25] G. Altarelli and G. Parisi, *Asymptotic Freedom in Parton Language*, Nucl. Phys. B **126** (1977) 298.

[26] V.N. Gribov, L.N. Lipatov, *Deep inelastic e p scattering in perturbation theory*, Sov. J. Nucl. Phys. **15** (1972) 438.

[27] Yu.L. Dokshitzer, *Calculation of the Structure Functions for Deep Inelastic Scattering and e+ e- Annihilation by Perturbation Theory in Quantum Chromodynamics*, Sov. Phys. JETP **46** (1977) 641.

[28] A. M. Cooper-Sarkar, *PDF Fits at HERA*, `arXiv:1112.2107 [hep-ph]`.

[29] T. Sjöstrand, S. Mrenna and P. Skands, *PYTHIA 6.4 physics and manual*, JHEP **05** (2006) 026.

[30] G. Corcella et al., *HERWIG 6: An Event generator for hadron emission reactions with interfering gluons (including supersymmetric processes)*, JHEP **0101** (2001) 010.

[31] The Tevatron Electroweak Working Group, *Combination of CDF and D0 results on the mass of the top quark using up to 8.7 fb^{-1} at the Tevatron*, arXiv:1305.3929 [hep-ex].

[32] P. Nason, S. Dawson and R. Ellis, *The total cross section for the production of heavy quarks in hadronic collisions*, Nucl. Phys. B **303** (1988) 607.

[33] S. Moch and P. Uwer, *Theoretical status and prospects for top-quark pair production at hadron colliders*, Phys. Rev. D **78** (2008) 034003.

[34] N. Kidonakis and R. Vogt, *Theoretical top quark cross section at the Fermilab Tevatron and the CERN LHC*, Phys. Rev. D **78** (2008) 074005.

[35] Aliev M., Lacker H., Langenfeld U., Moch, S., Uwer P. and others, *HATHOR: HAdronic Top and Heavy quarks crOss section calculatoR*, Comput.Phys.Commun. **182** (2011) 1034–1046, `arXiv:1007.1327 [hep-ph]`.

[36] M. Czakon and A. Mitov, *NNLO corrections to top pair production at hadron colliders: the quark-gluon reaction*, JHEP **1301** (2013) 080, `arXiv:1210.6832 [hep-ph]`.

[37] M. Czakon, P. Fiedler, and A. Mitov, *The total top quark pair production cross-section at hadron colliders through* $O(\alpha_S^4)$, `arXiv:1303.6254 [hep-ph]`.

[38] M. Czakon and A. Mitov, *NNLO corrections to top-pair production at hadron colliders: the all-fermionic scattering channels*, JHEP **1212** (2012) 054, `arXiv:1207.0236 [hep-ph]`.

[39] P. Baernreuther, M. Czakon, and A. Mitov, *Percent Level Precision Physics at the Tevatron: First Genuine NNLO QCD Corrections to* $q\bar{q} \to t\bar{t} + X$, Phys.Rev.Lett. **109** (2012) 132001, `arXiv:1204.5201 [hep-ph]`.

[40] M. Cacciari, M. Czakon, M. Mangano, A. Mitov, and P. Nason, *Top-pair production at hadron colliders with next-to-next-to-leading logarithmic soft-gluon resummation*, Phys.Lett. **B710** (2012) 612–622, `arXiv:1111.5869 [hep-ph]`.

[41] M. Czakon and A. Mitov, *Top++: A Program for the Calculation of the Top-Pair Cross-Section at Hadron Colliders*, `arXiv:1112.5675 [hep-ph]`.

[42] A. Martin, W. Stirling, R. Thorne, and G. Watt, *Parton distributions for the LHC*, Eur. Phys. J. **C63** (2009) 189–285.

[43] M. Botje and others, *The PDF4LHC Working Group Interim Recommendations*, `arXiv:1101.0538 [hep-ph]`.

[44] S. Dittmaier, P. Uwer and S. Weinzierl, *Hadronic top-quark pair production in association with a hard jet at next-to-leading order QCD: Phenomenological studies for the Tevatron and the LHC*, Arxiv:0810.0452v2 [hep-ph].

[45] F. Cascioli, P. Maierhofer, N. Moretti, S. Pozzorini, and F. Siegert, *NLO matching for* $t\bar{t}b\bar{b}$ *production with massive b-quarks*, arXiv:1309.5912v1 [hep-ph].

[46] G. Bevilacquaa and M. Worek, *On the ratio of* $t\bar{t}\bar{b}$ *and* $t\bar{t}jj$ *cross sections at the CERN Large Hadron Collider*, arXiv:1403.2046v1 [hep-ph].

[47] LHC Higgs Cross Section Working Group, *Handbook of LHC Higgs Cross Sections: 3. Higgs Properties*, Arxiv:1307.1347 [hep-ph].

[48] W. Beenakker et al., *Higgs radiation off top quarks at the Tevatron and the LHC*, Phys. Rev. Lett. **87** (2001) 201805.

[49] W. Beenakker et al., *NLO QCD corrections to ttH production in hadron collisions*, Nucl. Phys. B **653** (2003) 151–203.

[50] L. Reina and S. Dawson, *Next-to-leading order results for ttH production at the Tevatron*, Phys. Rev. Lett. **87** (2001) 201804.

[51] S. Dawson, L. H. Orr, L. Reina, and D. Wackeroth, *Associated top quark Higgs boson production at the LHC*, Phys. Rev. D **67** (2003) 071503.

[52] P. M. Nadolsky et al., *Implications of CTEQ global analysis for collider observables*, Phys. Rev. **D78** (2008) 013004, `arXiv:0802.0007[hep-ph]`.

[53] R. D. Ball, L. Del Debbio, S. Forte, A. Guffanti, J. I. Latorre, et al., *A first unbiased global NLO determination of parton distributions and their uncertainties*, Nucl. Phys. **B838** (2010) 136–206, `arXiv:1002.4407[hep-ph]`.

[54] L. Evans, (ed.) and P. Bryant, (ed.), *LHC Machine*, JINST **3** (2008) S08001.

[55] H.T. Edwards, *The Tevatron Energy Doubler: A Superconducting Accelerator*, Ann. Rev. Nucl. Part. Sci. **35** (1985) 605.

[56] D. H. Perkins, *Introduction to High Energy Physics.* Addison-Wesley Inc., 1995.

[57] The CMS Collaboration, *The CMS experiment at the CERN LHC*, JINST **3** (2008) S08004.

[58] The ALICE Collaboration, *The ALICE experiment at the CERN LHC*, JINST **3** (2008) S08002.

[59] The LHCb Collaboration, *The LHCb experiment at the CERN LHC*, JINST **3** (2008) S08005.

[60] The ATLAS Collaboration, *The ATLAS Experiment at the CERN Large Hadron Collider*, JINST **3** (2008) S08003.

[61] The ATLAS Collaboration, *ATLAS: Detector and physics performance technical design report*, CERN/LHCC/99-014/15.

[62] The ATLAS Collaboration, *ATLAS: Magnet System Technical Design Report*, CERN/LHCC/97-18, 1997.

[63] The ATLAS Collaboration, *ATLAS: Inner Detector Technical Design Report*, CERN-LHCC-97-016/017, 1997.

[64] The ATLAS Collaboration, *ATLAS: Liquid Argon Technical Design Report*, CERN-LHCC-96-041, 1996.

[65] The ATLAS Collaboration, *ATLAS: Tile Calorimeter Technical Design Report*, CERNLHCC-96-042, 1996.

[66] The ATLAS Collaboration, *ATLAS: Muon Spectrometer Technical Design Report*, CERNLHCC-97-022, 1997.

[67] The ATLAS Collaboration, *Improved luminosity determination in pp collisions at $\sqrt{s} = 7$ TeVusing the ATLAS detector at the LHC*, JINST (2013) no. 3 S08003, .

[68] S. van der Meer, *Calibration of the effective beam height in the ISR*, CERN-ISR-PO-68-31, 1968.

[69] The ATLAS Collaboration, *The ATLAS Simulation Infrastructure*, Eur. Phys. J. **C70** (2010) 823–874.

[70] S. Agostinelli et al., *Geant4 - A Simulation Toolkit*, Nucl. Instr. and Meth. **A506** (2003) 250.

[71] W. Lukas, *Fast Simulation for ATLAS: Atlfast-II and ISF*, J. Phys.: Conf. Ser. Nucl. Instr. and Meth. (2012) 396.

[72] T. Cornelissen, M. Elsing, I. Gavrilenko, W. Liebig, A. Salzburger, *Single Track Performance of the Inner Detector New Track Reconstruction (NEWT)*, ATL-INDET-PUB-2008-002.

[73] The ATLAS Collaboration, *Performance of primary vertex reconstruction in proton-proton collisions at* $\sqrt{s} = 7$ *TeV*, ATL-INDET-PUB-2008-002.

[74] The ATLAS Collaboration, *Expected electron performance in the ATLAS experiment*, ATL-PHYS-PUB-2011-006.

[75] The ATLAS Collaboration, *Expected Performance of the ATLAS Experiment: Detector, Trigger,And Physics.*, CERN-OPEN-2008-020, 2009.

[76] The ATLAS Collaboration, *Electron performance measurements with the ATLAS detector using the 2010 LHC proton-proton collision data*, Eur. Phys. J. C no. 72 (2012) 1909, .

[77] The ATLAS Collaboration, *Performance Studies for e/gamma Calorimeter Isolationin ATLAS*, ATL-COM-PHYS-2011-1186.

[78] The ATLAS Collaboration, *Electron Efficiency Measurements for 2012 and 2011 Data*, ATL-COM-PHYS-2013-1287.

[79] The ATLAS Collaboration, *Object selection and calibration, background estimations and MC samples for top quark analyses using the full 2012 data set*, ATL-COM-PHYS-2013-1016.

[80] The ATLAS Collaboration, *Muon Performance in Minimum Bias pp Collision Data at* $\sqrt{s} = 7$ *TeV with ATLAS*, ATLAS-CONF-2010-036.

[81] The ATLAS Collaboration, *A measurement of the muon reconstruction efficiency in 2010 ATLAS data using* J/ψ *decays*, ATLAS-CONF-2012-125.

[82] The ATLAS Collaboration, *Object selection and calibration, background estimations and MC samples for the Autumn 2012 Top Quark analyses with 2011 data*, ATL-COM-PHYS-2012-1197.

[83] The ATLAS Collaboration, *Object selection and calibration, background estimations and MC samples for the Winter 2013 Top Quark analyses with 2012 data*, ATL-COM-PHYS-2013-088.

[84] The ATLAS Collaboration, *Preliminary results on the muon reconstruction efficiency, momentum resolution, and momentum scale in ATLAS 2012 pp collision data*, ATLAS-CONF-2013-088.

[85] W. Lampl et al., *Calorimeter clustering algorithms: description and performance*, ATL-LARG-PUB-2008-002.

[86] The ATLAS Collaboration, *Jet energy scale and its systematic uncertainty in proton-proton collisions at* $\sqrt{s} = 7$ *TeV in ATLAS 2011 data*, ATLAS-CONF-2013-004.

[87] M. Cacciari, G. P. Salam, and G. Soyez, *The anti-*k_t *jet clustering algorithm*, J. High Energy Phys. **04** (2008) no. arXiv:0802.1189, .

[88] The ATLAS Collaboration, *Pile-up subtraction and suppression for jets in ATLAS*, ATL-COM-PHYS-2013-251.

[89] M. Cacciari, G. P. Salam, and G. Soyez, *The Catchment Area of Jets*, J. High Energy Phys. **04** (2008) no. arXiv:0802.1188, arXiv:0802.1189. LPTHE-07-02, .

[90] The ATLAS Collaboration, *Selection of jets produced in proton-proton collisions with the ATLAS detector using 2011 data*, ATLAS-CONF-2012-020.

[91] The ATLAS Collaboration, *Pile-up subtraction and suppression for jets in ATLAS*, ATL-COM-PHYS-2013-083.

[92] The ATLAS Collaboration, *Flavour dependence of jet response and quark/gluon tagging*, ATLAS-CONF-2012-138.

[93] The ATLAS Collaboration, *Jet energy measurement and systematic uncertainties using tracks for jets and for b-quark jets produced in proton-proton collisions at* $\sqrt{s} = 7$ *TeV in the ATLAS detector*, ATLAS-CONF-2013-002.

[94] The ATLAS Collaboration, *Jet energy scale and its systematic uncertainty in proton-proton collisions at* $\sqrt{s} = 7$ *TeV in ATLAS 2010 data*, ATLASCONF2011032.

[95] The ATLAS Collaboration, *Jet energy resolution in proton-proton collisions at* $\sqrt{s} = 7$ *TeV recorded in 2010 with the ATLAS detector*, Eur. Phys. J. C no. 73 3 (2013), .

[96] The ATLAS Collaboration, *Calibrating the b-Tag Efficiency and Mistag Rate of the SV0 b-Tagging Algorithm in 3* pb^{-1} *of Data with the ATLAS Detector*, ATLAS-CONF-2010-099.

[97] The ATLAS Collaboration, *Performance of impact parameter-based b-tagging algorithms with the ATLAS detector using pp collisions at* $\sqrt{s} = 7$ *TeV* , ATLAS-CONF-2010-091.

[98] The ATLAS Collaboration, *Commissioning of the ATLAS high-performance b-tagging algorithms in the* $\sqrt{s} = 7$ *TeV collision data*, ATLAS-CONF-2011-102.

[99] The ATLAS Collaboration, *A new inclusive secondary vertex algorithm for b-jet tagging in ATLAS*, J.Phys.Conf.Ser. no. 119 032032 (2008), .

[100] The ATLAS Collaboration, *Measurement of the b-tag Efficiency in a Sample of Jets Containing Muons with 5* fb^{-1} *of Data from the ATLAS Detector*, ATLAS-CONF-2012-043.

[101] The ATLAS Collaboration, *Measurement of the Mistag Rate of b-tagging algorithms with 5* fb^{-1} *of Data Collected by the ATLAS Detector*, ATLAS-CONF-2012-040.

[102] The ATLAS Collaboration, *b-jet tagging calibration on c-jets containing* D^* *mesons*, ATLAS-CONF-2012-039.

[103] The ATLAS Collaboration, *Calibration of the b-tagging efficiency for c jets with the ATLAS detector using events with a W boson produced in association with a single c quark*, ATLAS-CONF-2013-109.

[104] The ATLAS Collaboration, *Calibration of b-tagging using dileptonic top pair events in a combinatorial likelihood approach with the ATLAS experiment*, ATL-COM-PHYS-2014-0.04.

[105] The ATLAS Collaboration, *Performance of missing transverse momentum reconstruction in proton-proton collisions at* $\sqrt{s} = 8$ *TeV in ATLAS*, Eur. Phys. J. C (2012) no. 72 (2012) 1844, .

[106] The ATLAS Collaboration, *Performance of Missing Transverse Momentum Reconstruction in ATLAS studied in Proton-Proton Collisions recorded in 2012 at* $\sqrt{s} = 8$ *TeV*, ATLAS-COM-CONF-2013-075.

[107] The ATLAS Collaboration, *Expected Performance of the ATLAS Experiment - Detector, Trigger and Physics*, `arXiv:0901.0512 [hep-ex]`.

[108] The ATLAS TDAQ Collaboration, *Event reconstruction algorithms for the ATLAS trigger*, J.Phys.: Conf. Ser. 119 no. (2008) 022022, .

[109] The ATLAS Collaboration, *Performance of the Electron and Photon Trigger in p-p Collisions at* $\sqrt{s} = 900$ *GeV*, ATLAS-CONF-2010-022, 2010.

[110] The ATLAS Collaboration, *ATLAS Monte Carlo tunes for MC09*, ATLAS-CONF-2010-002.

[111] The ATLAS Collaboration, *Performance of the ATLAS Trigger System in 2010*, Eur. Phys. J. C no. 72 (2012) 1849, .

[112] T. Ullrich and Z. Xu, *Treatment of errors in efficiency calculations*, `arXiv:0701199v13 [physics.data-an]`.

[113] The ATLAS Collaboration, *Performance of the Electron and Photon Trigger in p-p Collisions at* $\sqrt{s} = 7$ *TeV with the ATLAS Detector at the LHC*, ATLAS-CONF-2011-114.

[114] The ATLAS Collaboration, *Performance of the ATLAS Electron and Photon Trigger in p-p Collisions at* $\sqrt{s} = 7$ *TeV in 2011*, ATLAS-CONF-2012-048.

[115] The ATLAS Collaboration, *Lepton trigger and identification for the Winter 2011 top quark analyses*, ATL-COM-PHYS-2011-123.

[116] The ATLAS TDAQ Collaboration, *Performance of the ATLAS muon trigger in 2011*, ATLAS-CONF-2012-099.

[117] The ATLAS TDAQ Collaboration, *2012 Muon trigger results*, https://twiki.cern.ch/twiki/bin/view/AtlasPublic/MuonTriggerPublicResults.

[118] S. Frixione and B. R. Webber, *Matching NLO QCD computations and parton shower simulations*, JHEP **0206** (2002) 029.

[119] S. Alioli, P. Nason, C. Oleari and E. Re, *A general framework for implementing NLO calculations in shower Monte Carlo programs: the POWHEG BOX*, JHEP **1006** (2010) 043.

[120] M.L. Mangano, M. Moretti, F. Piccinini and , M. Treccani, *Matching matrix elements and shower evolution for top-quark production in hadronic collisions*, JHEP **0701** (2007) 013.

[121] A. Schaelicke and F. Krauss, *Implementing the ME+PS Merging Algorithm*, JHEP **07** (2005) 018.

[122] M. L. Mangano and others, *ALPGEN, a generator for hard multiparton processes in hadronic collisions*, JHEP **0307** (2003) 001.

[123] J. Alwall and others, *MadGraph/MadEvent: the new web generation*, JHEP **09** (2007) 028, `arXiv:0706.2334 [hep-ph]`.

[124] B.P. Kersevan and E. Richter-Wąs, *The Monte Carlo event generator AcerMC version 2.0 with interfaces to PYTHIA 6.2 and HERWIG 6.5*, `arXiv:0405247 [hep-ph]`.

[125] J. M. Butterworth, J. R. Forshaw, and M. H. Seymour, *Multiparton interactions in photoproduction at HERA*, Z. Phys. **C72** (1996) 637–646.

[126] The ATLAS Collaboration, *First tuning of HERWIG/JIMMY to ATLAS data*, ATL-PHYS-PUB-2010-014.

[127] The ATLAS Collaboration, *New ATLAS event generator tunes to 2010 data*, ATL-PHYS-PUB-2011-009.

[128] The ATLAS Collaboration, *ATLAS tunes of PYTHIA6 and PYTHIA8 for MC11*, ATL-PHYS-PUB-2011-008.

[129] P. Skands, *Tuning Monte Carlo Generators: The Perugia Tunes*, Phys. Rev. **D82** (2010) 074018.

[130] D. Stump et al., *Inclusive jet production, parton distributions, and the search for new physics*, JHEP **0310** (2003) 046.

[131] K. Melnikov and F. Petriello, *Electroweak gauge boson production at hadron colliders through $\mathcal{O}(\alpha_s^2)$*, Phys. Rev. D **74** (2006) 114017, `arXiv:0609070 [hep-ph]`.

[132] The ATLAS Collaboration, *Search for the Standard Model Higgs boson produced in association with top quarks in pp collisions at $\sqrt{s} = 8$ TeVwith the ATLAS detector at the LHC*, ATL-COM-PHYS-2013-1659.

[133] H.-L. Lai et al., *New parton distributions for collider physics*, Phys. Rev. **D82** (2010) 074024.

[134] S. Frixione, E. Laenen, P. Motylinski, B. R. Webber and C. D. White, *Single-top hadroproduction in association with a W boson*, JHEP 07 (2008) 029.

[135] A. Sherstnev and R. S. Thorne, *Parton Distributions for LO Generators*, Eur. Phys. J. **C55** (2008) 553–575.

[136] Kidonakis, Nikolaos, *Next-to-next-to-leading-order collinear and soft gluon corrections for t-channel single top quark production*, Phys. Rev. D **83** (2011) 091503, arXiv:1103.2792 [hep-ph].

[137] N. Kidonakis, *Next-to-next-to-leading logarithm resummation for s-channel single top quark production*, Phys. Rev. D **81** (2010) 054028.

[138] J.M. Campbell and R.K. Ellis, *An update on vector boson pair production at hadron colliders*, Phys. Rev. D **60** (1999) 113006, arXiv:990.5386 [hep-ph].

[139] The ATLAS Collaboration, *Estimation of Fake Lepton Background for Top Analyses Using the $\sqrt{s} = 8$ TeV Dataset*, ATL-COM-PHYS-2013-1100.

[140] The ATLAS Collaboration, *Mis-identified lepton backgrounds to top quark pair production for Moriond 2011 analysis*, ATL-COM-PHYS-2011-144.

[141] A. D. Martin et al., *Parton distributions for the LHC*, Eur. Phys. J. **c63** (2009) 189–285.

[142] The ATLAS Collaboration, *Measurement of the top quark pair production cross-section with ATLAS in pp collisions at $\sqrt{s} = 7$ TeV* , Eur. Phys. J. **C71** (2011) 1577.

[143] Chakravarti, Laha, and Roy, *Handbook of Methods of Applied Statistics.* John Wiley and Sons, 1967.

[144] N.Gagunashvili, *Comparison of weighted and unweighted histograms*, arXiv:0605123 [physics.data-an].

[145] T. Junk, *Building a More General χ^2*, http://www-cdf.fnal.gov/t̃rj/mclimit/chisquare.pdf.

[146] F. A. Berends, W. T. Giele, H. Kuijf, R. Kleiss, and W.J. Stirling, *Multijet Production in W, Z Events at pp Colliders*, Phys. Lett. B **224** (1989) 237–242.

[147] R. Barlow and C. Beeston, *Fitting using finite Monte Carlo samples*, Comp. Phys. Comm. (1993) no. 77, 219.

[148] The ATLAS Collaboration, *Updated Luminosity Determination in pp Collisions at $\sqrt{s} = 7$ TeV using the ATLAS Detector*, ATLAS-CONF-2011-011.

[149] The ATLAS Collaboration, *Top Quark Pair Production Cross-section Measurement in ATLAS in the Single Lepton+Jets Channel Without b-tagging*, ATLAS-CONF-2011-023.

[150] The ATLAS Collaboration, *Measurement of the $t\bar{t}$ production cross-section in pp collisions at $\sqrt{s} = 7$ TeV using kinematic information of lepton+jets events*, ATLAS-CONF-2011-121.

[151] The ATLAS Collaboration, *Statistical combination of top quark pair production cross-section measurements using dilepton, single-lepton, and all-hadronic final states at $\sqrt{s} = 7$ TeV with the ATLAS detector*, ATLAS-CONF-2012-024.

[152] The ATLAS Collaboration, *Measurement of the ttbar production cross-section in pp collisions at $\sqrt{s} = 8$ TeV using e-mu events with b-tagged jets with the ATLAS detector*, ATLAS-CONF-2013-097.

[153] The ATLAS Collaboration, *Measurements of top quark pair relative differential cross-sections with ATLAS in pp collisions at $\sqrt{s} = 7$ TeV* , Eur. Phys. J. **C73** (2013) 2261.

[154] The ATLAS Collaboration, *Reconstructed jet multiplicities from the top-quark pair decays and associated jets in pp collisions at $\sqrt{s} = 7$ TeV measured with the ATLAS detector at the LHC*, ATLAS-CONF-2011-142.

[155] The ATLAS Collaboration, *Measurement of $t\bar{t}$ production with a veto on additional central jet activity in pp collisions at $\sqrt{s} = 7$ TeV using the ATLAS detector*, Eur. Phys. J. **C72** (2012) 2043.

[156] G. D'Agostini, *A Multidimensional unfolding method based on Bayes' theorem*, Nucl. Instr. Meth. **A362** (1995) 487–498.

[157] The ATLAS Collaboration, *Measurement of the jet multiplicity in top-antitop final states produced in $\sqrt{s} = 7$ TeV proton-proton collisions with the ATLAS detector*, ATLAS-CONF-2012-155.

[158] The ATLAS collaboration, *Updated coupling measurements of the Higgs boson with the ATLAS detector using up to $25fb^{-1}$ of proton-proton collision data*, ATLAS-CONF-2014-009.

[159] J. A. Aguilar-Saavedra, *Identifying top partners at LHC*, `arXiv:0907.3155 [hep-ph]`.

[160] G. C. Branco, P. M. Ferreira et al., *Theory and phenomenology of two-Higgs-doublet models*, `arXiv:1106.0034 [hep-ph]`.

[161] The ATLAS Collaboration, *Search for a Higgs boson produced in association with a top-quark pair and decaying to $b\bar{b}$ in pp collisions at $\sqrt{s} = 8$ TeV using the ATLAS detector*, ATLAS-CONF-2012-135.

[162] The CMS Collaboration, *Search for Higgs Boson Production in Association with a Top-Quark Pair and Decaying to Bottom Quarks or Tau Leptons*, CMS-PAS-HIG-13-019.

[163] G. Bevilacqua et al., HELAC-NLO, Comput. Phys. Commun. **184** (2013) 986, `arXiv:1110.1499v2 [hep-ph]`.

[164] T. Sjöstrand and S. Mrenna and P. Skands, *A Brief Introduction to Pythia 8.1*, `arXiv:0710.3820 [hep-ph]`.

[165] A. Djouadi, J. Kalinowski, and M. Spira, *HDECAY: A Program for Higgs boson decays in the standard model and its supersymmetric extension*, Comput.Phys.Commun. **108** (1998) 56–74, `arXiv:hep-ph/9704448 [hep-ph]`.

[166] The ATLAS Collaboration, *Measurement of top quark pair differential cross-sections in the l+jets channel in pp collisions at $\sqrt{s} = 7$ TeV using the ATLAS detector*, ATL-CONF-2013-099.

[167] J. M. Campbell and R. K. Ellis, *$t\bar{t}W$ production and decay at NLO*, `arXiv:1204.5678 [hep-ph]`.

[168] M. V. Garzelli, A. Kardos, C. G. Papadopoulos, and Z. Trocsanyi, *$t\bar{t}W$ and $t\bar{t}Z$ Hadroproduction at NLO accuracy in QCD with Parton Shower and Hadronization effects*, JHEP **1211** (2012) 056, arXiv:1208.2665 [hep-ph].

[169] Phi-T GmbH, *NeuroBayes package*, http://neurobayes.phi-t.de/.

[170] M. Feindt, U. Kerzelb, *The NeuroBayes neural network package*, Nucl. Instrum. Methods Phys. Res. (2006) no. A 559, 190–194.

[171] V. Blobel and E. Lohrmann, *Statistische und numerische Methoden der Datenanalyse*, Teubner Stuttgart Leibzig (1998) .

[172] R.H. Byrd and C. Zhu P. Lu, J. Nocedal., *A limited memory algorithm for bound constrained optimization.*, SIAM Journal on Scientific and Statistical Computing, 16(5):11901208 (1995) .

[173] D. E. Rumelhart, G. E. Hinton and R. J. Williams, *Learning representations by back-propagating errors*, Nature **323** (1986) 6088.

[174] C. Bernaciak, M. S. A. Buschmann, A. Butter and T. Plehn, *Fox-Wolfram Moments in Higgs Physics*, arXiv:1212.4436 [hep-ph].

[175] The CMS Collaboration, *Search for the standard model Higgs boson produced in association with a W or a Z boson and decaying to bottom quarks*, Phys. Rev. D **89** (2014) 012003.

[176] K. Cranmer, G. Lewis, L. Moneta, A. Shibata and W. Verkerke, *HistFactory: A tool for creating statistical models for use with RooFit and RooStats*, CERN-OPEN-2012-016.

[177] S. Pozzorini and N. Moretti, *Private Communication*, .

[178] A.L. Read, *Presentation of search results: the CL_s technique*, J. Phys. G (2002) no. 28, 2693.

[179] T. Junk, *Confidence level computation for combining searched with small statistics*, Nucl. Instrum. Methods Phys. Res. (1999) A434:435443.

[180] W. Verkerke et al., *The RooStats Project*, arXiv:1009.1003 [physics.data-an].

[181] G. Cowan, K. Cranmer, E. Gross and O. Vitells, *Asymptotic formulae for likelihood-based tests of new physics*, Eur. Phys. J. C (2011) no. 71, 1–19.

[182] The ATLAS Collaboration, *Search for the Standard Model Higgs boson produced in association with top quarks and decaying to $b\bar{b}$ in pp collisions at $\sqrt{s} = 8$ TeV with the ATLAS detector at the LHC*, ATLAS-CONF-2014-011.

[183] The ATLAS collaboration, *Search for $t\bar{t}H$ production in the $H \to \gamma\gamma$ channel at $\sqrt{s} = 8$ TeV with the ATLAS detector*, ATLAS-CONF-2013-080.

[184] The ATLAS collaboration, *Updated coupling measurements of the Higgs boson with the ATLAS detector using up to 25 fb^{-1} of proton-proton collision data*, ATLAS-CONF-2014-009.

[185] The ATLAS collaboration, *Projections for measurements of Higgs boson cross sections, branching ratios and coupling parameters with the ATLAS detector at a HL-LHC*, ATL-PHYS-PUB-2013-014.

[186] F. Maltoni, G. Ridolfi, M. Ubiali, *b-initiated processes at the LHC: a reappraisal*, JHEP **1207** (2012) 022.

[187] P. Artoisenet, R. Frederix, O. Mattelaer, R. Rietkerk, *Automatic spin-entangled decays of heavy resonances in Monte Carlo simulations*, arXiv:1212.3460 [hep-ph].

[188] A. Knue, V. Dao, J. Montejo-Berlingen and G. Kirby, *$t\bar{t}$-modelling studies for the $t\bar{t}H\,(H\rightarrow b\bar{b})$ analysis using Madgraph*, ATL-COM-PHYS-2014-040.

Appendix

A The tag rate function method

As outlined in Chapter 8, the *tag rate function* method is adopted in the analysis searching for the $t\bar{t}H$ process given the requirement of a large number of b-tagged jet in the final state. This allows to reduce statistical fluctuations on the signal and background templates and reduce the impact of the finite Monte Carlo statistics to 10% of the total error. This section contains additional information on the methodology and the validation performed.

The TRF method allows to increase the effective statistics of the Monte Carlo samples by using all the events prior to the b-tag selection and weight them rather than rejecting event not containing the specific number of b-tagged jets in simulation. The weight is computed by combining the tagging probabilities of each jet in the event. For events with a large number of b-jets, the method effectively compensates for the statistics losses due to b-tagging efficiencies; for events with a low number of b-jets, TRF performs a more precise implementation of the mis-tag rate.

Given a jet with η, p_{T} and flavour f, its tagging probability (or efficiency) can be noted as:

$$\varepsilon\left(f, |\eta|, p_{\mathrm{T}}\right)$$

The tagging probabilities for the three jet flavours extracted from a $t\bar{t}$ sample generated with POWHEG+PYTHIA are reported in Figure 3.12 as a function of the p_{T} and $|\eta|$ of the jet.

When requiring a given number of b-tagged jets in the event (n_b), permutations are built considering all the assignments of n_b tagged 'labels' to the N jets in the event; in total $C(n_b, N)$ permutations are possible. The probability of each permutation is computed from the multiplication of the per-jet weights: the jet weight is equal to the tagging efficiency if the jet is labelled as tagged, one minus the efficiency in the opposite case. Summing the probabilities of all permutations gives the per-event TRF weight. As an example, the probability of having exactly one b-tagged jet in the event is given by:

$$P_{=1} = \sum_{i=1}^{N} \left(\varepsilon_i \prod_{i \neq j} (1 - \varepsilon_j) \right)$$

This value is used to weight the event contribution to the final yields requiring 1 b-tagged jet in the final state.

A more concrete example, an event with 5 jets whose flavours and tagging efficiencies are reported in Table 11. This could be a prototype for a $t\bar{t}$+$c\bar{c}$ event where two b-jets originates from the $t\bar{t}$ decay and 2 additional c-jets are produced or one c-jet is the result of the hadronic decay of the W boson.

jet index g	flavour type	tagging efficiency
1	b	81%
2	b	65%
3	c	24%
4	c	16%
5	light	0.7%

Table 11: Information on a prototype 5-jet event used to illustrate the TRF methodology: for each jet the flavour of the parton originating it is indicated together with the average tagging efficiency.

When requiring exactly 3 jets in the event to be b-tagged, 10 possible permutations are obtained as shown in Table 12. The sum of all the permutations corresponds to an event probability of 19.2%. As a comparison, if exactly four b-tagged jets would be required, the event weight would drop to 2.2%.

permutation	j1 j1	j2 j2	j3 j3	j4 j4	j5 j5	permutation probability	perm. relative probability	cumulated rel. probability
1	-	-	$\otimes$	$\otimes$	$\otimes$	≤ 0.05 %	≤ 0.05 %	≤ 0.05 %
2	-	$\otimes$	-	$\otimes$	$\otimes$	≤ 0.05 %	0.1 %	0.1 %
3	-	$\otimes$	$\otimes$	-	$\otimes$	≤ 0.05 %	0.1 %	0.2 %
4	-	$\otimes$	$\otimes$	$\otimes$	-	0.5 %	2.6 %	2.7 %
5	$\otimes$	-	-	$\otimes$	$\otimes$	≤ 0.05 %	≤ 0.05 %	2.8 %
6	$\otimes$	-	$\otimes$	-	$\otimes$	≤ 0.05 %	0.2 %	3.0 %
7	$\otimes$	-	$\otimes$	$\otimes$	-	1.1 %	5.9 %	8.8 %
8	$\otimes$	$\otimes$	-	-	$\otimes$	0.2 %	1.2 %	10.1 %
9	$\otimes$	$\otimes$	-	$\otimes$	-	6.3 %	32.7 %	42.8 %
10	$\otimes$	$\otimes$	$\otimes$	-	-	11.0 %	57.2 %	100 %

Table 12: List of possible permutations of 3 b-tagged jets in the 5-jet events. Each permutation contains the information on which jets are considered as tagged ($\otimes$), the absolute probability of the considered permutation as well as the relative permutation with respect to the probability of having 3 b-tagged jets in the event.

For the usage in physics analysis, not only the probability for a given event is required, but also the knowledge of which jets are considered as tagged when a given number of *tags* is assumed. This is achieved by randomly choosing one of the possible permutations. For each event a random number between 0 and 1 is considered and compared to the cumulative value of the relative probability as indicated in the last column of Table 12. This allows to choose a permutation based on its relative contribution to the total event probability.

When comparing to data, the efficiencies in the formulas above are multiplied for the corresponding scale factors. In case of systematic uncertainties, the efficiencies are modified due to the change in the scale factors leading to a different event probability.

A.1 TRF validation

Figures 13 and 14 show the validation plots for $t\bar{t}H$ signal and $t\bar{t}$+jets background samples. They show the shape of a selected distribution in all the nine analysis regions comparing the prediction from the ‘direct cut’ method and the ‘TRF’ method.

The vectorial sum p_{T} of the pair of b-tagged jets closer in ΔR is shown as a representative example, since it depends both on the p_{T} of the jets, their angular direction and the specific b-tagged jets in the event. This allows then to validate multiple aspects of the method. Good closure of the TRF prediction is observed both for the signal and the $t\bar{t}$ background; in both cases, the tagging efficiency parameterisation has been extracted from inclusive $t\bar{t}$ samples. In particular the usage of multiple b-tagged jet multiplicity regions allows to probe contributions from different jet flavours and fractions of $t\bar{t}$+HF. Similar agreement is observed for other variables.

The TRF is also capable of predicting the correct event yields in the region. All the differences are of the order of few % and mostly compatible within the statistical uncertainties of the ‘direct cut’ predictions. In case of the signal, TRF yields are corrected to take this discrepancy into account.

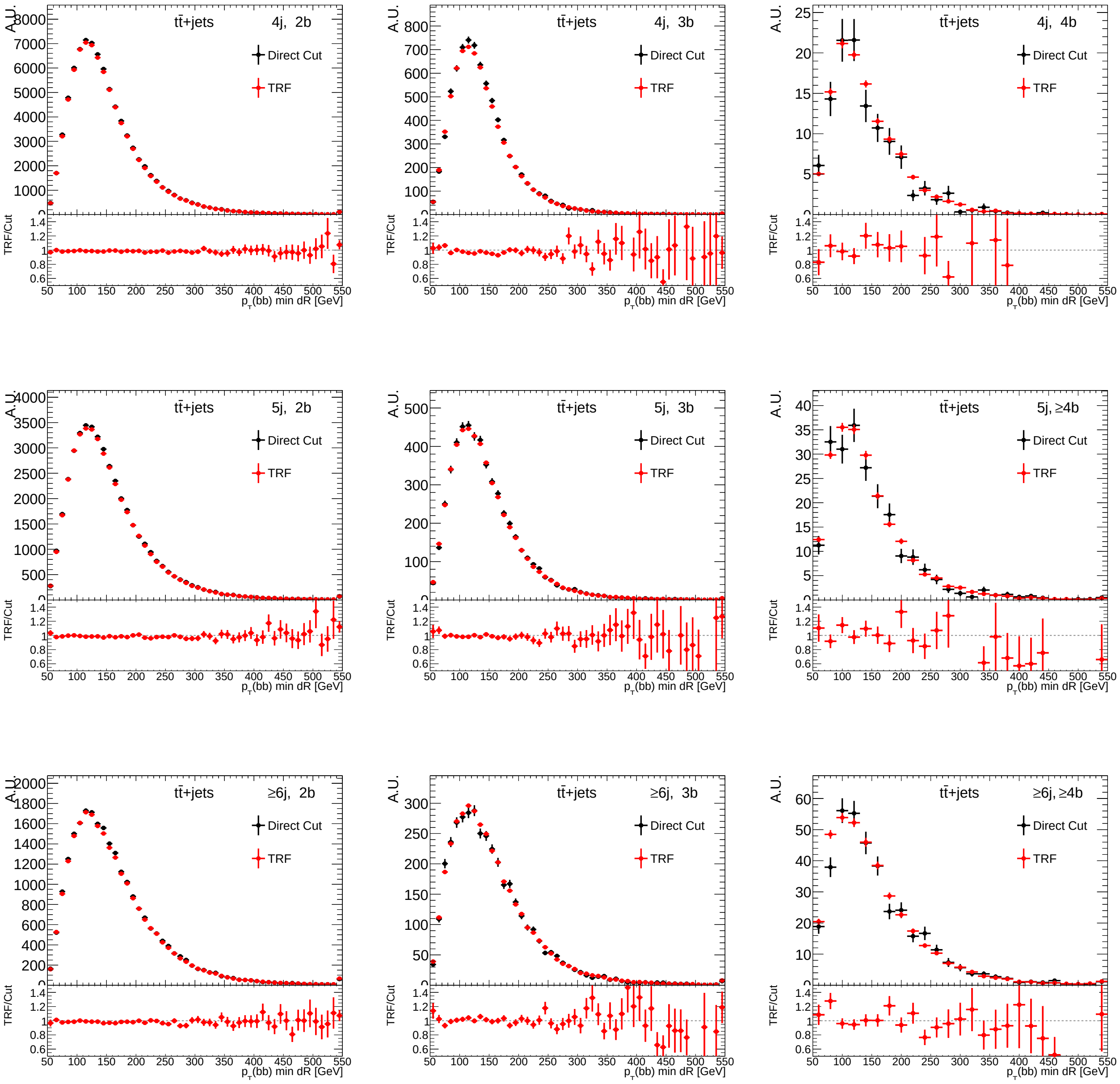

Figure 13: Comparison between cut based $p_{T,\mathrm{bb}}^{\mathrm{min}\ \Delta\mathrm{R}}$ distributions (black) and TRF predictions (red) for $t\bar{t}H$ sample. Different jet and b-tagged jet multiplicities have been considered. Distributions are normalised to unity.

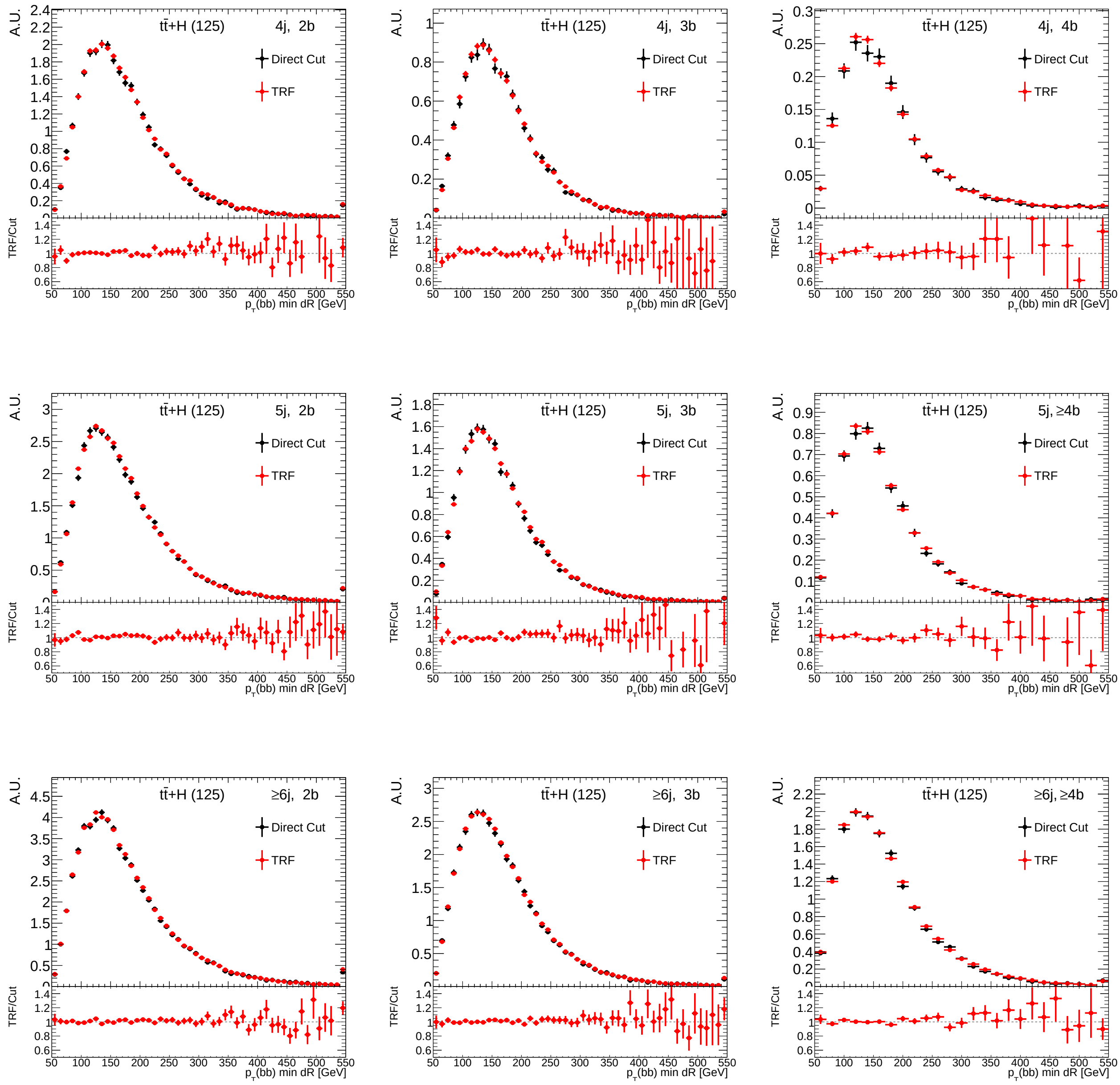

Figure 14: Comparison between cut based $p_{T,\mathrm{bb}}^{\mathrm{min}\ \Delta\mathrm{R}}$ distributions (black) and TRF predictions (red) for $t\bar{t}$+jets sample. Different jet and b-tagged jet multiplicities have been considered. Distributions are normalised to unity.

B $t\bar{t}$+jets event generation with Madgraph

In the context of the search for the $t\bar{t}H$ process, $t\bar{t}$ plus additional heavy flavour jets events are modelled with the NLO Powheg generator; additional samples of $t\bar{t}$+HF events were produced with the Madgraph generator in order to assess the Monte Carlo generator and modelling systematic uncertainties. This section contains a summary of the configuration used in Madgraph to describe $t\bar{t}$ events as well as a more detailed comparison with the Powheg predictions and the definition of the parameter variations used for systematic uncertainties.

Multi-leg generators are capable of describing the production of $t\bar{t}$+jets using leading order matrix element calculations. Since the LO calculations diverge for additional massless partons in the limit of very low p_{T} and collinear emission, a cut-off is applied limiting the phase space for the generation; extra partons are required to have a minimum transverse momentum and a minimal distance to any other parton in the event. The rest of the phase space is covered by a parton shower program that approximates the QCD predictions yielding finite results. A 'merging' procedure is applied when combining the two classes of events ensuring that no overlap of the phase space occurs. The MLM [120] merging procedure allows to remove the double counting by vetoing events where the parton shower generates additional partons in the phase space covered by the matrix element; at the same time, a smooth transition of the scale for the α_{S} calculation between the one used in the LO calculation and the value used for the parton shower is ensured[23].

When dealing with massive partons (like b-quarks), such 'division' of the phase space would be in principle not necessary given that a non-zero mass leads to finite LO results even in the soft and collinear limits. This approach is referred to as 4-flavour scheme [186]. In practice, the parton shower approximation is still expected to give better results in such regimes since it approximates the effect of all orders in perturbation theory. At the same time, the generation of additional massive partons in the full phase space together with massless partons, as in the case of $t\bar{t}+bg$, can not yet be consistently treated by available multi-leg generators.

This represents the main limitation of the Alpgen generator when describing $t\bar{t}$+HF events. Madgraph overcomes this complication by treating all the additional parton flavours (b,c, light and gluon) in an identical way. This is obtained by the usage of the so-called 5-flavour scheme [186] where b-quarks are allowed to be the incoming particles of a process generated directly from the PDF description; in this approach the initial $g \to b\bar{b}$ splitting is absorbed into the formalism of parton density functions. The differences between the 4-flavour and the 5-flavour approach mainly resides in the description of the parton shower. Other contributions, like diagrams where the heavy flavour partons are radiated directly from the top quark, are treated consistently with the matrix element approach in both cases. At the same time it should be mentioned that, given the large mass of the top quark, these radiation effects bring a subleading contribution to the associated production of HF partons.

The Madgraph approach implies that the generation of additional HF partons is not described by the matrix element calculation over the full phase space, but soft and collinear emission of b-quarks are still treated with the parton shower programs. At the same time, it allows to evaluate matrix element contributions from final states like $t\bar{t}+bj$, $t\bar{t}+b\bar{b}$ and $t\bar{t}+b\bar{b}j$ not described by Powheg. In the 5-flavour scheme the b-quark originating from the PDF is by definition massless; nevertheless, the quark mass is necessary to correctly predict rate of gluon splitting into massive partons. In the Madgraph implementation, the b-quark acquires a mass when it is converted in a final state parton while for the case c-quarks, the mass is set

[23]This is achieved by modifying the α_{S} value of the vertices in the LO calculation identified as 'emission vertices'. The classification is obtained by a particular clustering of the generated partons aiming at identifying the 'core' $2 \to 2$ process in the event; all the remaining vertices are considered as 'emission vertices'.

within the parton shower program[24].

The drawback consists in the fact that an inclusive $t\bar{t}$ sample needs to be generated since additional heavy flavour partons can be produced by the parton shower even in the case where no additional parton is produced by the matrix element part; the $t\bar{t}$+HF events are then extracted with the procedure described in Chapter 8. This procedure has been used by the CMS collaboration to model the $t\bar{t}$ background in the analysis searching for the $t\bar{t}H$ process.

Table 13 contains the details of the configuration adopted for the official production of $t\bar{t}$ events with MADGRAPH. $t\bar{t}$ events with up to three additional partons in the final state are generated for a centre of mass energy of 8 TeV using CT10 parton density functions. Factorisation and renormalisation scales are set to the geometrical average of $m_{\mathrm{T}} = \sqrt{(}m^2+p_{\mathrm{T}}^2)$ for the 2 top quarks produced in the event. The value of the scale can be controlled by the 2 multiplicative parameters *scalefact* and *alpsfact*; the former is a direct multiplicative factor for μ_F and μ_R, the latter controls the scale at emission vertices where the merging with parton shower takes place. A value of 172.5 GeV is used for the top quark mass, while the b(c)-quark mass is set to 4.8 (1.5) GeV. PYTHIA 6 is used for the parton shower with the Perugia2011C tune. The MLM procedure with k_{T} measure (k_{T}-MLM) is used for the matching of matrix element and parton shower. Additional partons with p_{T} >20 GeV and $|\eta| < 6$ are generated by the matrix element requiring the minimal k_{T} measure between the parton in the final state to be greater than 20 GeV. When interfacing the events with the parton shower, the value of Q_{cut} represents the matching scale; additional emission by the parton shower at a scale larger than the matching scale is forbidden.

The decay of the top quarks is implemented in PYTHIA; the reason for not implementing the decay directly in MADGRAPH or using the MADSPIN [187] utility stems from practical considerations related to the processing time to generate a large number of particles in the final state. The decay in PYTHIA implies that no spin correlation effects between the two top quarks in the events are retained but the effect on the considered distributions have been found to be small. A filter is applied to the events after the parton shower stage to retain l+jets and dilepton $t\bar{t}$ decay topologies. The dependence of the result on the variation of some of the generator parameters is documented in Ref. [188].

Events are normalised to the NNLO cross section as for the other $t\bar{t}$ samples considered. Comparison with the other generator is performed at the truth particle level.

Figure 15 shows the comparison between events produced with POWHEG+PYTHIA and the events generated with MADGRAPH. Inclusive $t\bar{t}$ events are considered with no selection other than the $t\bar{t}$ decay mode.

As for the case of POWHEG a reweighting procedure has been applied to the events generated with MADGRAPH in order to fix the $t\bar{t}$ and top quark p_{T} distributions to the 7 TeV references used for the other $t\bar{t}$ generators[25]. The green distribution show the reweighted MADGRAPH events while the black distributions represents the reweighted POWHEG events used in the nominal template of the analysis. The procedure has been carried out in the same binning used for the nominal reweighting described in Chapter 8.

Plots for additional distributions like the number of jets and the number of jets origination from b-quarks are reported in Figure 16. As for the previous plots no additional selection is applied; particle level jets are required to have p_{T} >25 GeV and $|\eta| < 2.5$. b-hadron jets are defined through a ΔR match to b-hadrons as described in Chapter 8. No distinction between

[24]The difference approach has been adopted in order to follow the event generation performed by the CMS collaboration. It has been verified that the difference obtained with respect to the case where b- and c-quarks are treated in the same way are negligible.

[25]Since no 7 TeV sample is available in MADGRAPH, the reweighting procedure equalises the top p_{T} and $t\bar{t}$ p_{T} distributions between MADGRAPH events and the reweighted POWHEG events.

Setting	Value
MADGRAPH version	5.1.5.11
Process	$t\bar{t}$+(0-3) partons
parton flavours	$g, u, \bar{u}, d, \bar{d}, c, \bar{c}, s, \bar{s}, b, \bar{b}$
$\sqrt{s}$	8 TeV
μ_R=μ_F	$\sqrt{m_{\mathrm{T}}^{t} \cdot m_{\mathrm{T}}^{\bar{t}}}$
m_{top}	172.5 GeV
m_b	4.8 GeV
scalefact	1
alpsfact	1
PDF	CT10
Parton Shower	PYTHIA 6.426
Parton Shower tune	Perugia2011C
$t\bar{t}$-decay	PYTHIA
matching	k_{T} MLM
min p_{T}	20 GeV
max η_{parton}	5.0
min k_T	20 GeV
matching threshold Q_{cut}	40 GeV

Table 13: List of settings used for the generation of $t\bar{t}$ events with MADGRAPH.

jets originating from $t\bar{t}$ decays and additional jets is made; therefore the distribution peaks at a value of two. The p_{T} and η distribution of the leading jet in the event is shown in Figure 17.

In general a reasonable agreement for the inclusive distributions is obtained between the two generators. While the reweighting procedure has a minimal effect on the jet and b-jet multiplicity distributions, it helps improving the agreement in kinematic quantities like the p_{T} of the jets. The largest residual difference is related to the η distribution of the jets in the events, where MADGRAPH predicts a more central distribution; this is a known effect from not including NLO corrections to the inclusive process. The MADGRAPH sample after the reweighting procedure has been used for the comparison of the $t\bar{t}$+heavy flavour fraction reported in the next section.

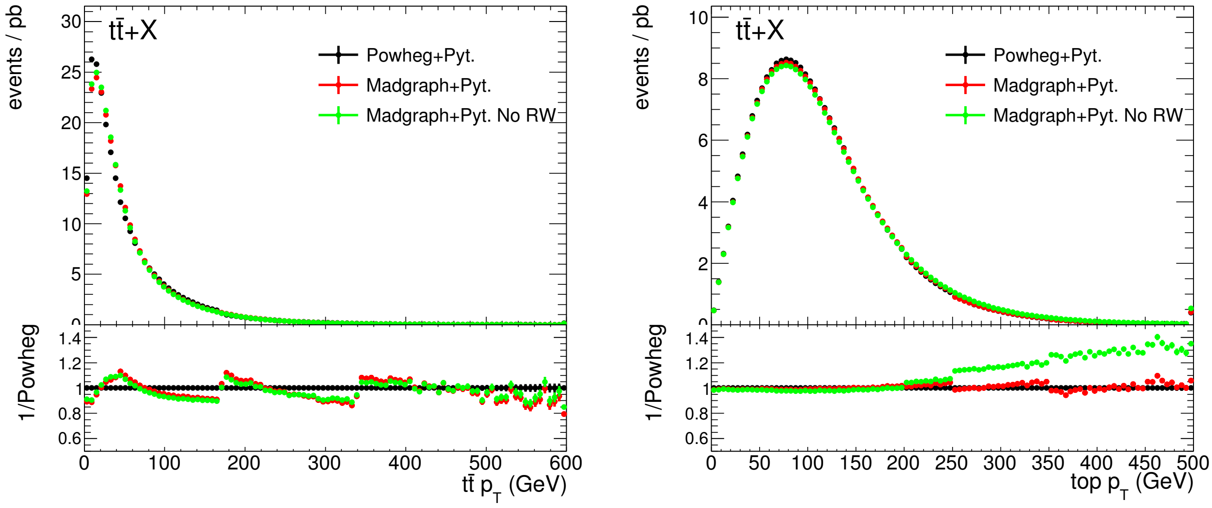

(a) (b)

Figure 15: Comparison between POWHEG+PYTHIA and MADGRAPH+PYTHIA for the $t\bar{t}$ p_{T} and top quark p_{T} distributions. Events are normalised to the same NNLO inclusive cross section and no selection is applied. For the MADGRAPH prediction distributions with (red) and without (green) reweighting are shown.

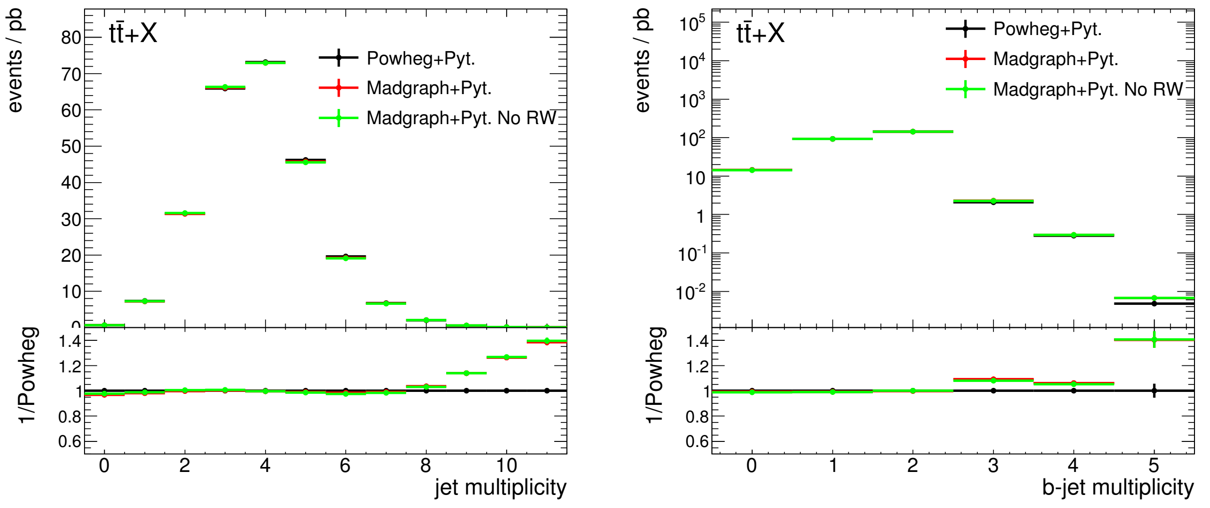

(a) (b)

Figure 16: Jet multiplicity (a) and b-jet multiplicity (b) distributions in $t\bar{t}$ events compared between POWHEG+PYTHIA and MADGRAPH+PYTHIA. Events are normalised to the same NNLO inclusive cross section and no selection is applied. For the MADGRAPH prediction distributions with (red) and without (green) reweighting are shown.

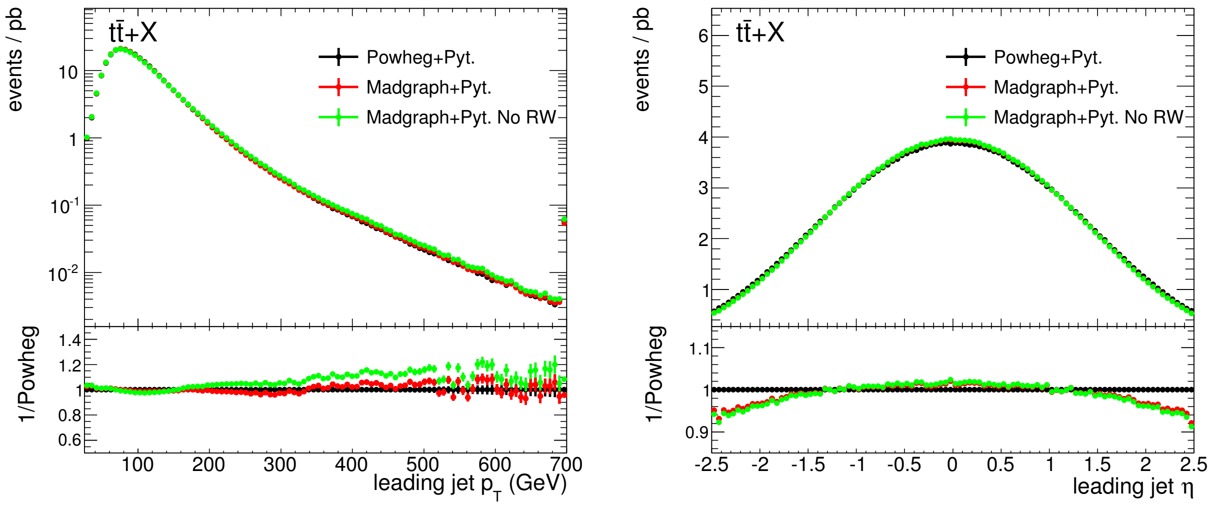

(a) **(b)**

Figure 17: Leading jet p_{T} (c) and η (d) distributions in $t\bar{t}$ events compared between Powheg+Pythia and Madgraph+Pythia. Events are normalised to the same NNLO inclusive cross section and no selection is applied. For the Madgraph prediction distributions with (red) and without (green) reweighting are shown.

B.1 comparison for $t\bar{t}$+HF content

As discussed in Section 8.4 $t\bar{t}$+HF events are classified based on the number of particle jets originating from additional heavy flavour partons within detector acceptance and analysis kinematic selection.

Figure 18 illustrates the comparison between the prediction from MADGRAPH and POWHEG for events containing at least one additional b-jet ($t\bar{t}$+$b\bar{b}$) and events with at least one additional c-jets and no additional b-jets ($t\bar{t}$+$c\bar{c}$). No selection is made on the particles originating from $t\bar{t}$ decay products; this allows to maximise the event statistics as well as decouple the differences in the $t\bar{t}$+HF production from the differences originating from the $t\bar{t}$ kinematics. Absolute yields are shown decomposed in additional categories based on the number of identified additional jets from heavy flavour and on the number of hadrons matched to each jet to separate collinear gluon splitting (categories with subleading contributions have been omitted). The impact of each sub category in the various analysis regions after full reconstruction has been previously described in Chapter 8; for easier visualisation, all the categories with more than one additional HF jet have been merged in the $t\bar{t}$+$b\bar{b}$ ($t\bar{t}$+$c\bar{c}$) category[26].

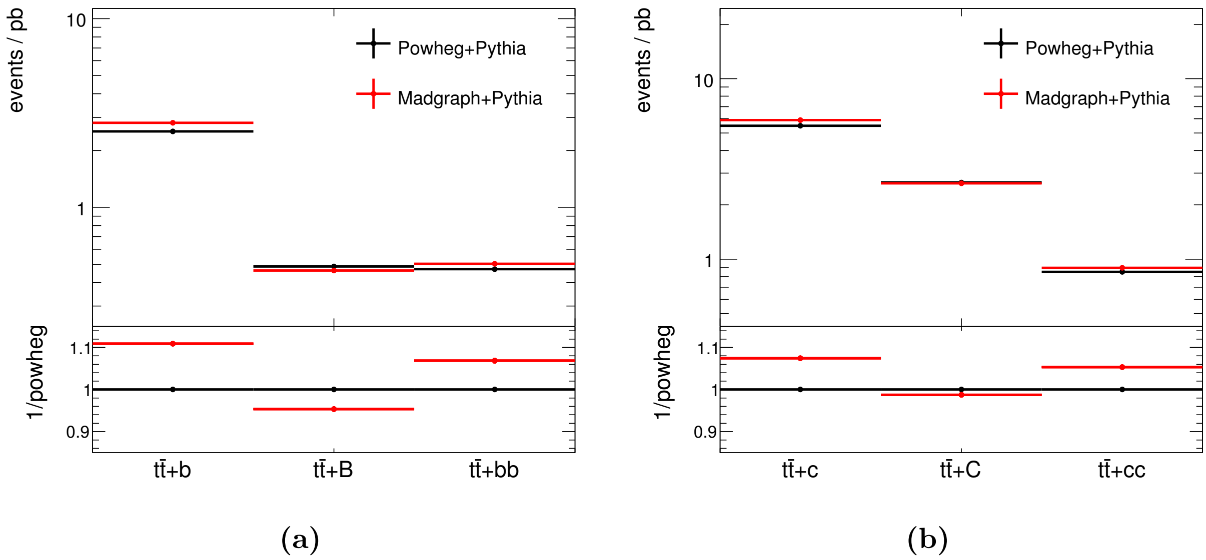

Figure 18: Different categories of $t\bar{t}$+$b\bar{b}$ (a) and $t\bar{t}$+$c\bar{c}$ (b) events compared between MADGRAPH and POWHEG.

The differences between the two generators are within 10%; MADGRAPH predicts higher yields for topologies with single and double resolved jets from HF. The differences are reduced for the category containing gluon splitting since, the same parton shower program (PYTHIA) has been used. Similar trends are observed between events with additional $b-$ and $c-$hadrons.

Additional comparisons have been performed for the kinematics of the jets originating from heavy flavour partons in each category; all the distributions have been normalised to unit area in order to better appreciate the shape differences. Figure 19 shows the p_{T} and $|\eta|$ of the particle jet from additional heavy flavour partons in case of $t\bar{t}+b$ and $t\bar{t}+c$.

For what concerns $t\bar{t}$+$b\bar{b}$ and $t\bar{t}$+$c\bar{c}$ distributions of the kinematic quantities of jets from additional HF partons are shown in Figures 20 and 21; the invariant mass, angular distance, vectorially summed p_{T} of the two jets and leading jet p_{T} are considered.

[26] This topology represents in any case > 95% of the contribution to final states with more than one jet from HF

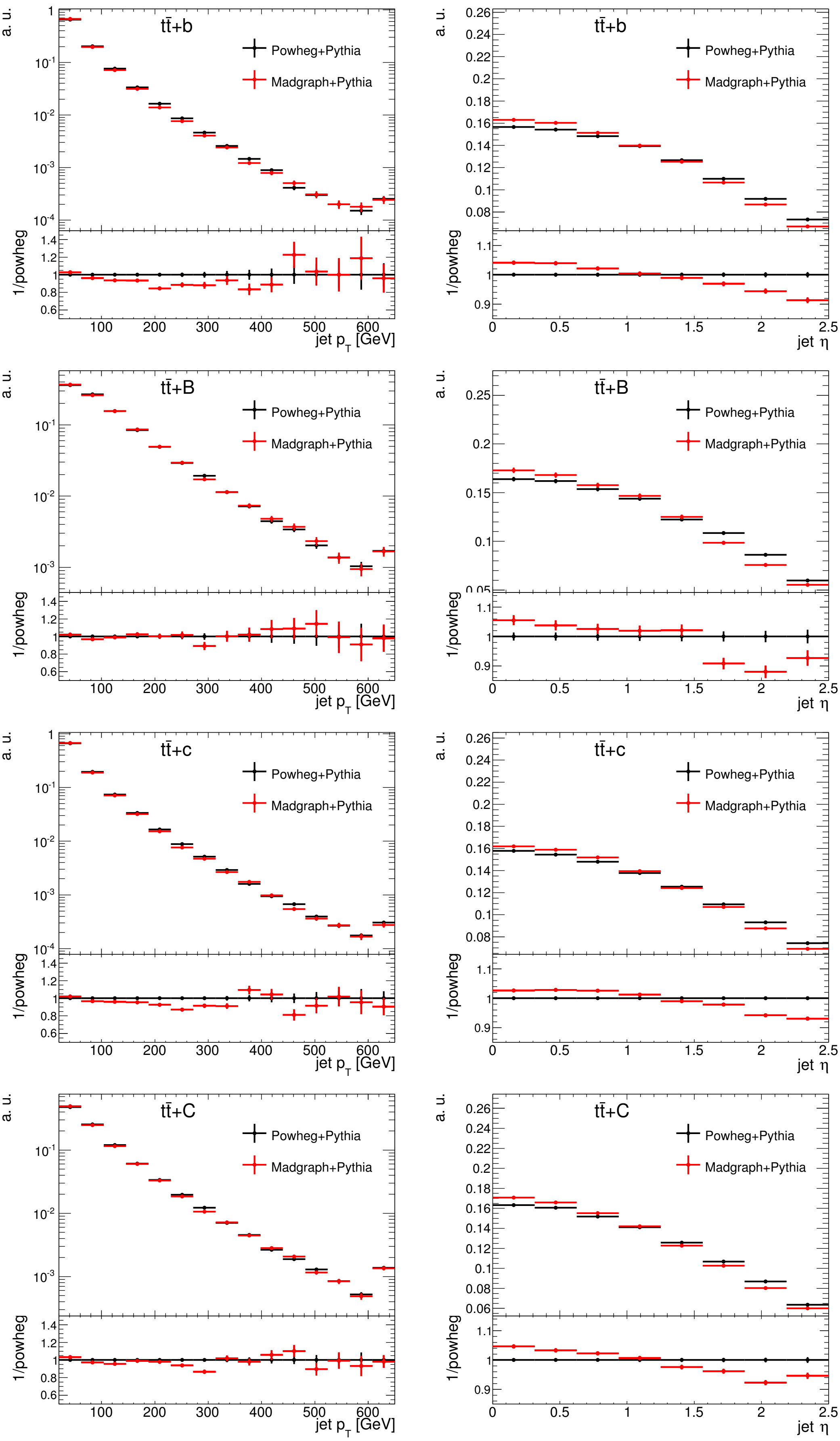

Figure 19: p_T (left) and $|\eta|$ of the particle jet matched to the HF parton in case of $t\bar{t}+b$ (first row), $t\bar{t}+B$ (second row), $t\bar{t}+c$ (third row) and $t\bar{t}+C$ (last row) events. The distributions from Powheg+Pythia and Madgraph+Pythia are shown normalised to unity.

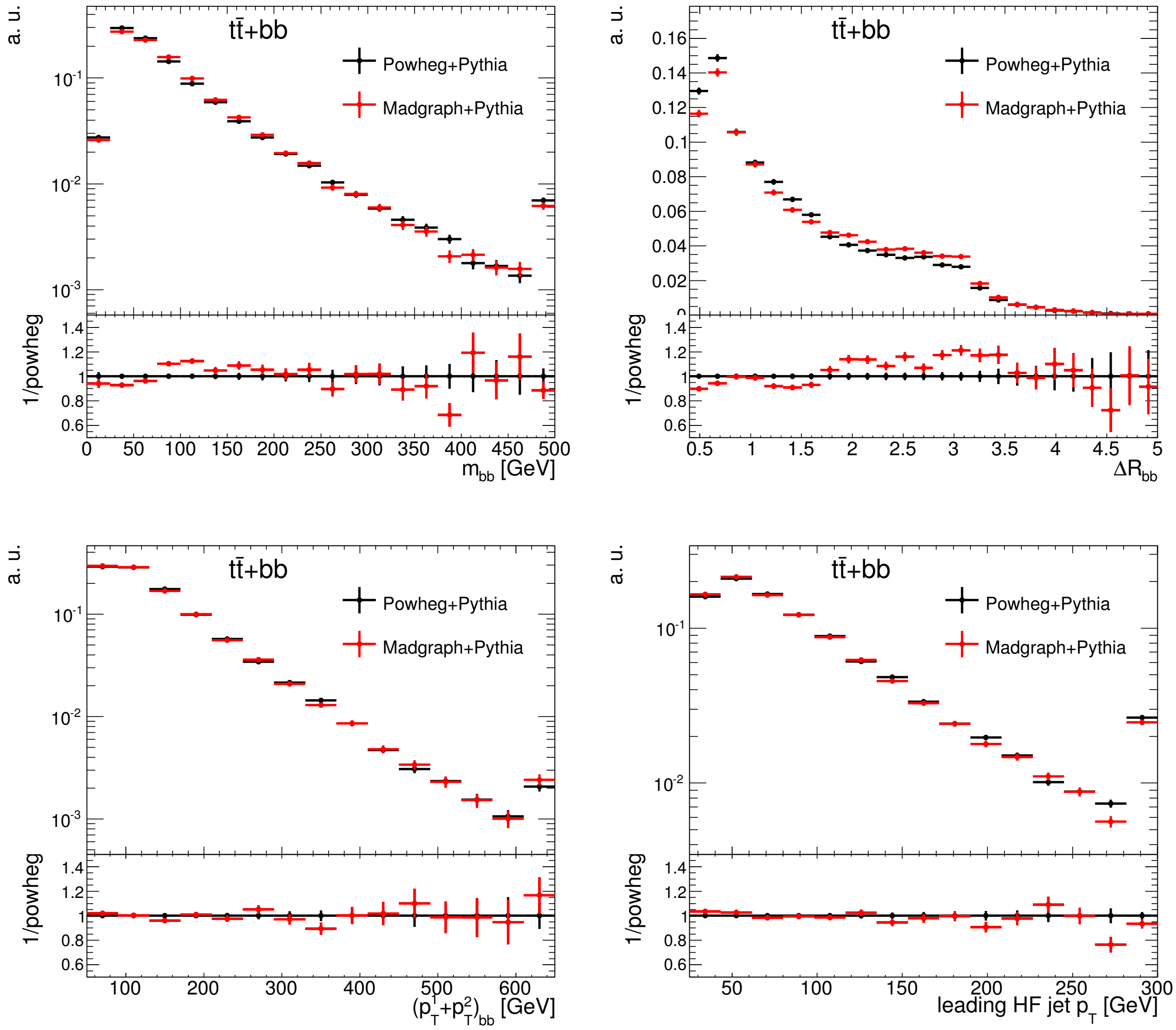

Figure 20: Kinematic distributions for additional jets from HF partons in $t\bar{t}+b\bar{b}$ events; the invariant mass (top left), angular distance (top right), vectorially summed p_{T} of the two jets (bottom left) and leading jet p_{T} (bottom right). The distributions from Powheg+Pythia and Madgraph+Pythia are shown normalised to unity.

Reasonable agreement is seen between Powheg and Madgraph; the most notable differences are visible in the ΔR between additional HF jets and their pseudo-rapidity distributions. Good agreement is observed for the p_{T} distributions in both single and double HF jet topologies. It is worth noticing that Powheg manages to give a reasonable agreement with the matrix element generation in topologies where a description based on the parton shower approach is supposed to be less accurate. This is the case for very large ΔR between jets and high jet pair invariant mass.

Ultimately, the differences between the two generators are considered as a source of systematic uncertainties.

B.2 systematic uncertainties

Variations of specific generation parameters in Madgraph have been used to assess some of the systematic uncertainties on the description of $t\bar{t}$+HF events. They are collected in Table 14. The considered variations are related to the renormalisation/factorisation scales and the scale

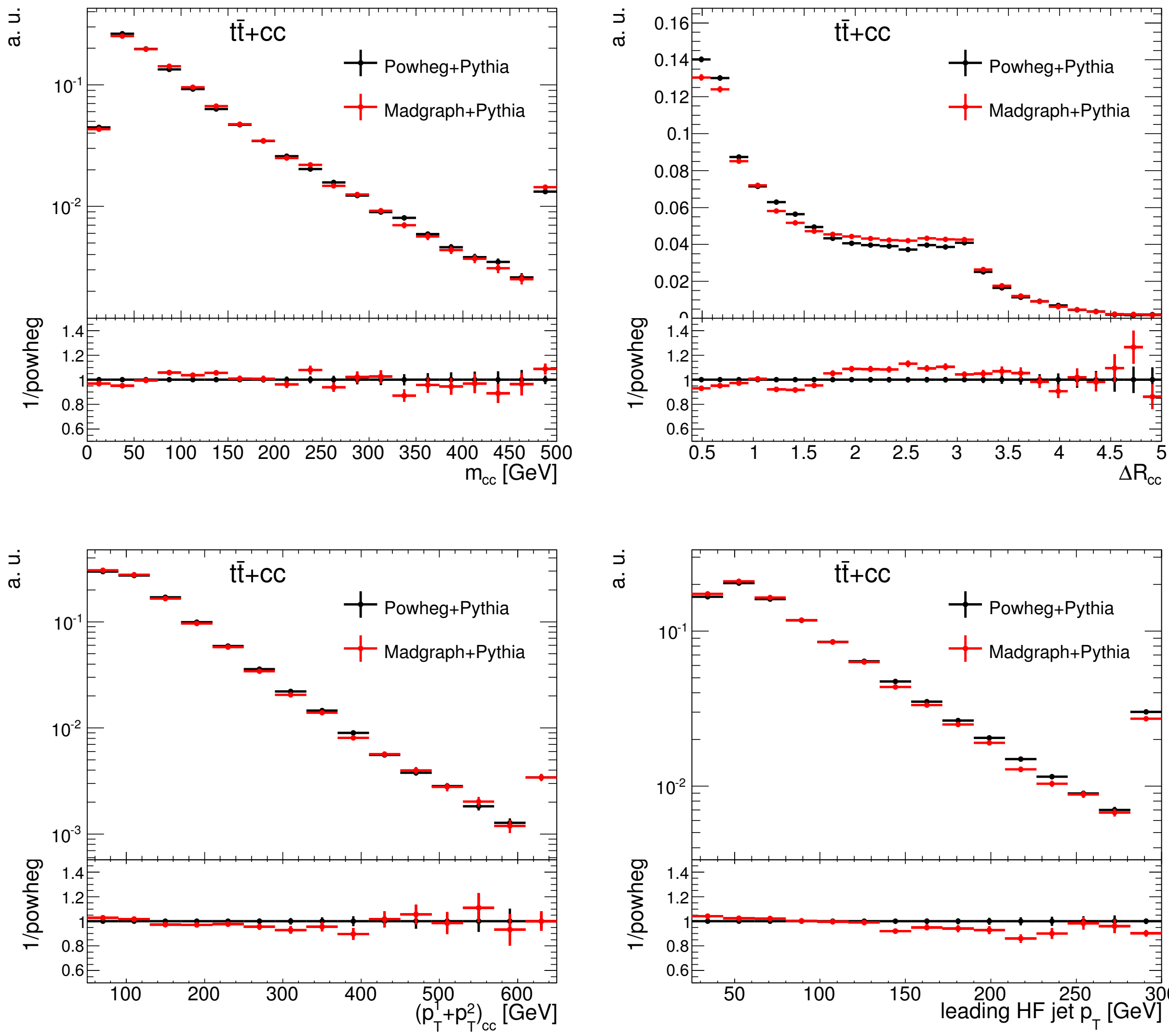

Figure 21: Kinematic distributions for additional jets from HF partons in $t\bar{t}$+$c\bar{c}$ events; the invariant mass (top left), angular distance (top right), vectorially summed p_{T} of the two jets (bottom left) and leading jet p_{T} (bottom right). The distributions from POWHEG+PYTHIA and MADGRAPH+PYTHIA are shown normalised to unity.

for extra parton emission (Q^2), the energy scale at which the merging between matrix element and parton shower generation is performed. Variations of the b- and c-quark masses have also been considered since these parameters affect the rate and kinematics of gluon splitting to heavy flavour partons.

Proposed parameters variations have been suggested by MADGRAPH authors and are in agreement with the procedure adopted by the CMS collaboration.

As for the comparison with the POWHEG predictions, the effect of the uncertainties is evaluated after an inclusive selection requiring at least one jet from additional heavy flavour within the detector acceptance. This allows to retain sufficient statistics for the evaluation of the systematic effects; at the same time acceptance effects from top decay kinematics are already taken into account by the conservative uncertainties on the top and $t\bar{t}$ p_{T} distribution.

Figure 22 shows the contribution from the three main categories of $t\bar{t}$+$b\bar{b}$ and $t\bar{t}$+$c\bar{c}$ production. None of the variation produces a relative normalisation effect larger that 10%. The variations of the scales and matching parameters mainly redistribute the events between the category with one resolved jet from HF and the remaining ones. The variation of the quark

Setting	nominal	match up	Q^2 up	Q^2 down	m_b up/down	m_c up/down
scalefact	1	1	2	0.5	1	1
alpsfact	1	1	2	0.5	1	1
PYTHIA tune	Perugia2011C	Perugia2011C	radLo	radHi	Perugia2011C	Perugia2011C
m_b	4.8 GeV	4.8 GeV	4.8 GeV	4.8 GeV	5.05 / 4.55 GeV	4.8 GeV
m_c	1.5 GeV	1.5 GeV	1.5 GeV	1.5 GeV	1.5 GeV	1.65 / 1.35 GeV
min k_T	20 GeV	40 GeV	20 GeV	20 GeV	20 GeV	20 GeV
matching Q_{cut}	40 GeV	80 GeV	40 GeV	40 GeV	40 GeV	40 GeV

Table 14: List of settings for the alternative samples used to probe systematic uncertainties on MADGRAPH $t\bar{t}$+HF production. In case of m_c the mass is kept at 0 in the matrix element calculation and only varied in the parton shower stage. The *radLo* and *radHi* represent two variations of the nominal tune where the α_S scale has been varied to match the value of the matrix element part.

masses mainly affects the category containing gluon splitting to heavy flavour partons, but this category represents only a small contribution after the final event selection.

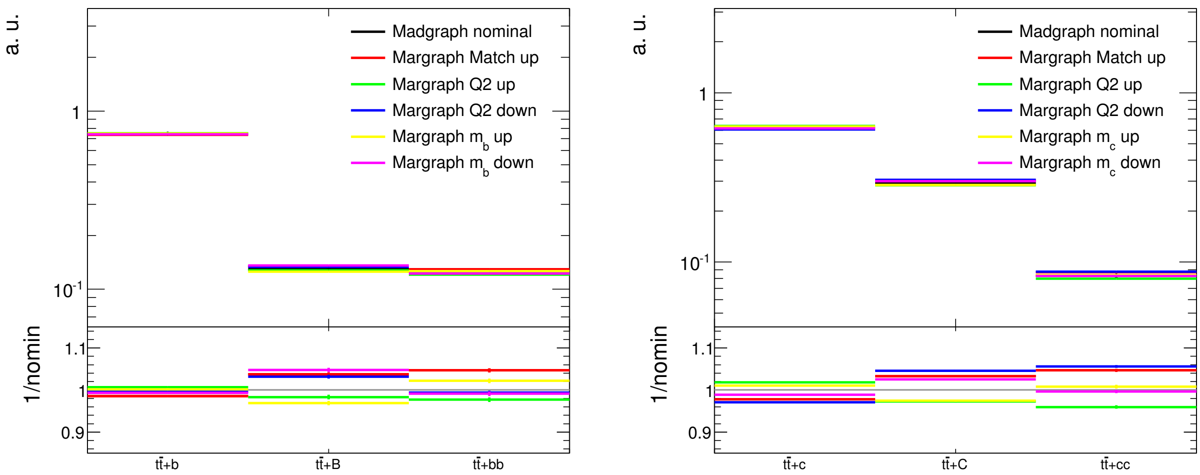

(a) **(b)**

Figure 22: Different categories of $t\bar{t}$+$b\bar{b}$ (a) and $t\bar{t}$+$c\bar{c}$ (b) events compared between the nominal MADGRAPH and the related systematic variations.

Additional comparison of the effects of each variation are shown in Figure 23 for topologies with a single heavy flavour jet in the acceptance, and Figures 24 and 25 for categories with two additional heavy flavour jets. As shown in the previous section, the kinematic properties of the jet from heavy flavour as well as the properties of the di-jet system are shown separately for b-jets and c-jets; the distributions are normalised to unity.

Similar conclusions can be obtained for the production of additional b- or c-partons. The change in renormalisation and factorisation scales ("Q^2" variation) particularly affects the p_T distribution of the additional parton in $t\bar{t}$ plus single resolved heavy flavour jet, while it is less important in categories with single heavy flavour jet originating from gluon splitting or double heavy flavour jets. For the latter category, the change in matching parameters has a strong shape impact on the ΔR distribution between the jets from heavy flavour partons. The variation of the matching primarily controls what part of the phase space is described by the parton shower and which part is described by the matrix element.

The presented variation have been implemented in the analysis by parametrising their effects as a function of the kinematics of the HF jets.

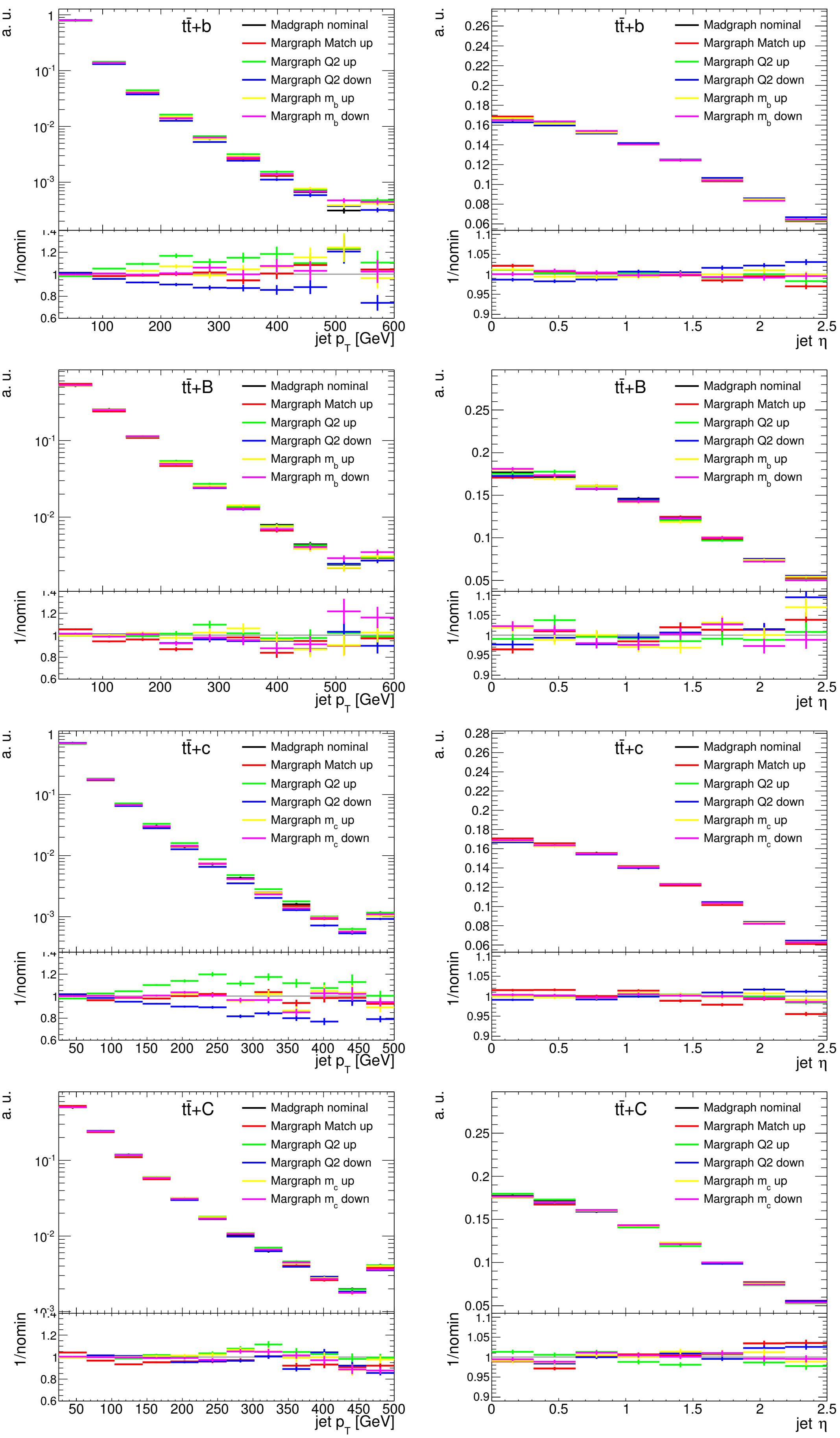

Figure 23: p_{T} (left) and $|\eta|$ distributions of the particle jet matched to the HF parton in case of $t\bar{t}+b$ (first row), $t\bar{t}+B$ (second row), $t\bar{t}+c$ (third row) and $t\bar{t}+C$ (last row) events. All the distributions are normalised to unity.

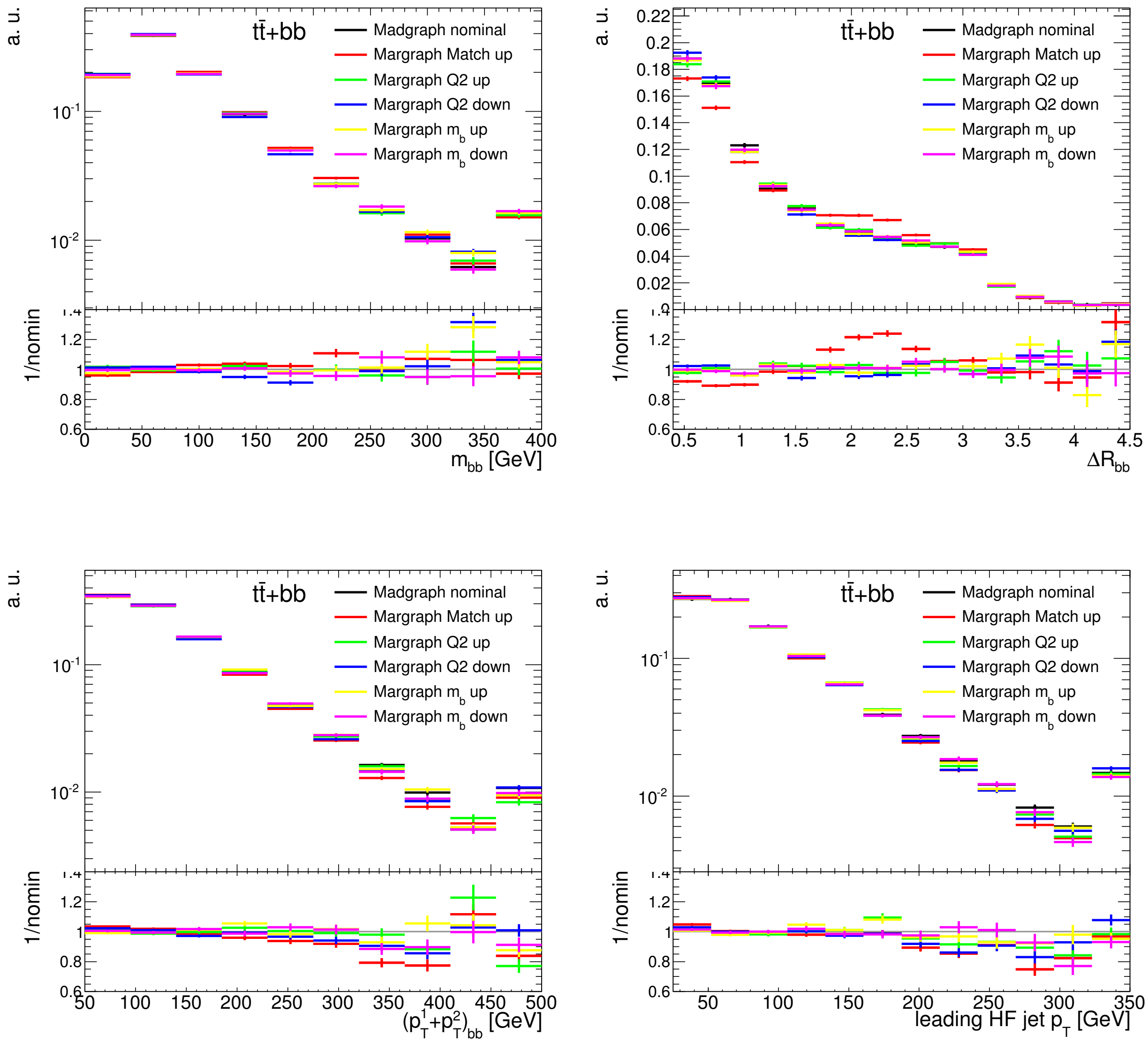

Figure 24: Kinematic distributions for additional jets from HF partons in $t\bar{t}$+$b\bar{b}$ events; the invariant mass (top left), angular distance (top right), vectorially summed p_{T} of the two jets (bottom left) and leading jet p_{T} (bottom right). The distributions for the nominal MADGRAPH sample and all the variations of the generator parameters are shown normalised to unity.

Finally it should be mentioned that an increasing effort from the theoretical community is underway to develop Monte Carlo generators capable of producing $t\bar{t}$+$b\bar{b}$ events at NLO accuracy. The most notable example is discussed in [45] where NLO $t\bar{t}$+$b\bar{b}$ events assuming massive b-quarks and 4-flavour production with the SHERPA+OPENLOOPS generator. These events could not be used in the analyses described in this thesis since hadronisation effects were not yet taken into account.

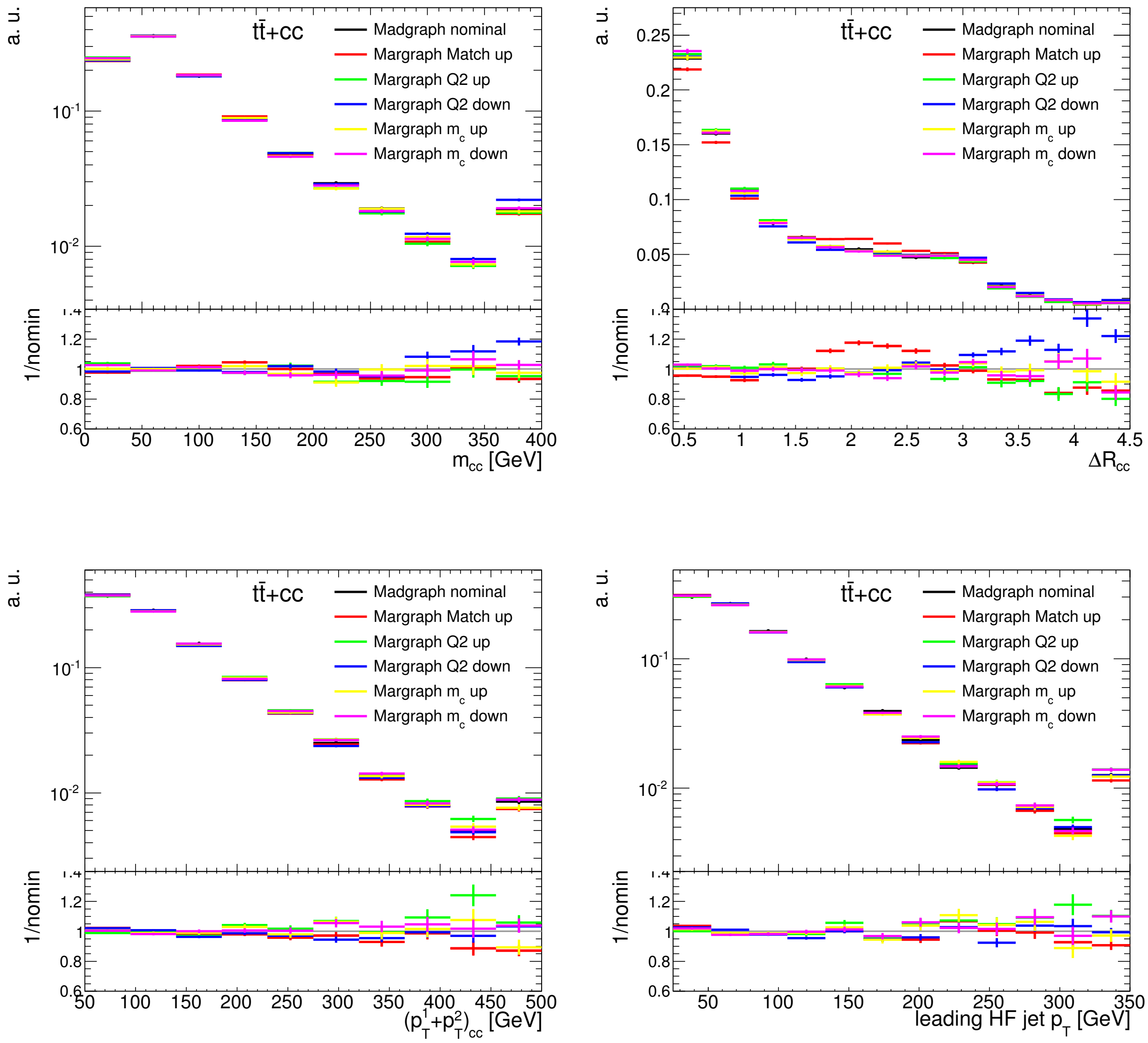

Figure 25: Kinematic distributions for additional jets from HF partons in $t\bar{t}$+$c\bar{c}$ events; the invariant mass (top left), angular distance (top right), vectorially summed p_{T} of the two jets (bottom left) and leading jet p_{T} (bottom right). The distributions for the nominal MADGRAPH sample and all the variations of the generator parameters are shown normalised to unity.

C Tables of systematic uncertainties

Table 15 shows a detailed breakdown of the relative normalisation effect of each source systematic uncertainty on the signal yields in all regions. Values have been obtained after the the final fit; the 'total' value is computed taking into account correlations. Table 16 summarises the same information for the total background. In both cases systematics having an effect smaller than 0.5% in all the regions have been omitted. As can be observed, only a reduced number of detector related uncertainties have actually a non negligible contribution on the signal and background acceptance/efficiencies.

	$t\bar{t}H$ (125 GeV) : postfit								
	(4j, 2b)	(4j, 3b)	(4j, 4b)	(5j, 2b)	(5j, 3b)	(5j, ≥ 4b)	(≥ 6j, 2b)	(≥ 6j, 3b)	(≥ 6j, ≥ 4b)
BTAG_2	±0.3	±1.3	±2.2	< 0.1	±1.0	±2.1	< 0.1	±0.7	±1.9
BTAG_3	±0.6	±1.9	±3.2	±0.3	±1.6	±3.0	< 0.1	±1.2	±2.7
BTAG_5	±1.2	±4.0	±6.8	±0.5	±3.3	±6.5	±0.2	±2.5	±6.2
CTAG_5	±0.1	±0.5	±0.8	< 0.1	±0.4	±0.8	< 0.1	±0.4	±0.9
ELE_ID	±1.0	±1.0	±1.0	±1.0	±1.0	±1.1	±1.0	±1.0	±1.0
JER	±0.5	±0.9	±1.6	±1.2	±1.8	±2.3	±0.5	–	< 0.1
JetDet1	±0.7	±0.5	< 0.1	< 0.1	< 0.1	< 0.1	±0.6	±0.7	±0.9
JetEtaModel	±1.5	±1.4	±0.9	±0.2	±0.1	< 0.1	±1.4	±1.5	±1.8
JetEtaStat	±0.6	±0.6	< 0.1	< 0.1	< 0.1	–	±0.6	±0.6	±0.7
JetFlavB	±0.4	< 0.1	±1.5	±0.2	±0.7	±1.8	±0.5	±1.2	±2.0
JetFlavComp	±2.8	±3.1	±3.6	±0.8	±1.3	±2.3	±2.6	±2.2	±1.6
JetFlavResp	±1.8	±2.0	±2.3	±0.5	±0.7	±1.4	±1.6	±1.3	±1.0
JetModel1	±2.1	±1.9	±1.2	±0.3	–	< 0.1	±2.1	±2.3	±2.7
JetPileRho	±2.1	±1.9	±1.3	±0.4	< 0.1	–	±2.0	±2.2	±2.5
JetStat1	±0.7	±0.6	–	–	–	–	±0.6	±0.7	±0.8
JVF	±1.3	±1.4	±1.5	±0.5	±0.6	±0.8	±1.1	±1.0	±0.9
LTAG_11	< 0.1	–	±0.4	–	–	±0.5	< 0.1	< 0.1	±0.8
LUMI	±2.6	±2.6	±2.6	±2.6	±2.6	±2.6	±2.6	±2.6	±2.6
MUON_TRIG	±1.0	±1.00	±1.00	±1.00	±1.00	±1.00	±1.0	±1.0	±1.0
$t\bar{t}H$_PDF	±1.9	±2.3	±3.1	±1.8	±1.8	±2.3	±2.7	±1.1	±1.1
$t\bar{t}H$_Scale_Dyn	±3.3	±4.0	±4.7	±1.5	±2.2	±3.1	±2.2	±2.2	±1.9
$t\bar{t}H$_Scale_Var	±0.5	±0.8	±1.2	±0.3	±0.6	±1.1	< 0.1	< 0.1	±0.3
Total	±5.5	±7.3	±10.1	±3.8	±5.2	±8.6	±5.0	±5.0	±7.9

Table 15: Normalisation uncertainties (expressed in %) on signal in each of the 9 analysis regions. Effect of systematic uncertainties is consider after the fit to data. Uncertainties producing an effect smaller than 0.5% in all the regions are omitted. Entries identified with "–" were removed by the prefit pruning procedure.

For the most sensitive signal region ((≥ 6j, ≥ 4b)) Table 17 shows the detailed effect of all the individual sources of systematic uncertainties on the signal and each background contribution as well as on the total background. The contribution from each source of uncertainty to the total background is obtained by averaging the effect on each background by their relative yields fraction. The total uncertainty on each process can be different from the sum in quadrature of individual sources due to the correlations between them. As for the previous case, only uncertainties having at least a >0.5% effect of at least one background are considered.

	Total background: postfit								
	(4j, 2b)	(4j, 3b)	(4j, 4b)	(5j, 2b)	(5j, 3b)	(5j, $\geq$ 4b)	($\geq$ 6j, 2b)	($\geq$ 6j, 3b)	($\geq$ 6j, $\geq$ 4b)
BTAG_2	±0.9	±1.3	±1.5	±0.9	±1.2	±1.6	±0.8	±1.1	±1.6
BTAG_3	±1.3	±1.6	±2.2	±1.3	±1.6	±2.3	±1.2	±1.5	±2.3
BTAG_5	±2.8	±3.5	±4.9	±2.7	±3.6	±5.2	±2.6	±3.5	±5.5
CTAG_0	< 0.1	±0.9	±0.7	< 0.1	±0.7	±0.9	< 0.1	±0.6	±0.4
CTAG_2	< 0.1	±1.4	±1.6	< 0.1	±1.1	±1.3	< 0.1	±0.8	±1.0
CTAG_5	±0.2	±2.9	±3.4	< 0.1	±2.5	±3.0	< 0.1	±2.0	±2.5
ELE_ID	±0.9	±0.9	±0.9	±0.9	±0.9	±0.9	±0.9	±0.9	±1.0
JER	±1.0	±1.5	±0.7	±0.3	±0.4	±1.1	±1.9	±1.8	±0.7
JetDet1	±0.2	< 0.1	±0.2	±0.6	±0.5	±0.3	±1.1	±1.2	±1.2
JetEtaModel	±0.5	±0.6	±0.3	±1.6	±1.4	±1.2	±2.8	±2.8	±2.5
JetEtaStat	±0.2	< 0.1	< 0.1	±0.5	±0.4	±0.1	±1.1	±1.1	±1.1
JetFlavB	±0.7	±1.0	±1.7	±0.9	±1.2	±2.2	±0.9	±1.3	±2.3
JetFlavComp	±0.3	< 0.1	±1.6	±2.5	±1.8	< 0.1	±5.1	±4.5	±2.9
JetFlavResp	±0.1	±0.2	±1.0	±1.5	±1.1	±0.1	±3.0	±2.6	±1.6
JetModel1	±1.1	±1.0	±0.5	±2.4	±2.2	±1.9	±4.1	±4.0	±3.8
JetModel2	±0.1	< 0.1	< 0.1	±0.3	< 0.1	< 0.1	±0.6	±0.5	±0.5
JetNPV	±0.3	< 0.1	< 0.1	±0.7	±0.6	±0.8	±1.2	±1.1	±0.4
JetPileRho	±1.0	±0.8	±0.3	±2.3	±2.0	±1.6	±3.9	±3.8	±3.6
JetStat1	±0.2	< 0.1	±0.1	±0.6	±0.5	±0.1	±1.2	±1.2	±1.2
JVF	< 0.1	±0.1	±0.5	±1.3	±0.7	< 0.1	±2.5	±2.0	±1.6
LTAG_10	< 0.1	±0.6	±1.9	< 0.1	±0.6	±1.2	< 0.1	±0.6	±0.8
LTAG_11	±0.1	±2.1	±6.0	±0.1	±2.4	±4.6	< 0.1	±2.4	±3.5
LUMI	±2.5	±2.5	±2.5	±2.5	±2.5	±2.5	±2.5	±2.6	±2.6
MUON_TRIG	±0.8	±0.9	±0.8	±0.8	±0.9	±0.9	±0.9	±0.9	±0.9
singleTop_XS	±1.2	±0.8	±1.0	±0.8	±0.7	±0.6	±0.6	±0.5	±0.4
$t\bar{t}$_DataRw_Fragment	< 0.1	< 0.1	±0.2	±0.4	±0.4	±0.7	±1.2	±1.3	±1.6
$t\bar{t}$_DataRw_IFSR	< 0.1	±0.2	±1.4	±2.8	±3.0	±3.7	±4.7	±4.9	±5.2
$t\bar{t}$_DataRw_JER	±0.1	±0.1	±0.9	±1.8	±1.9	±2.5	±3.2	±3.4	±3.6
$t\bar{t}$_DataRw_JetCloseby	±0.2	±0.1	±0.3	±0.6	±0.6	±0.7	±1.0	±1.1	±1.1
$t\bar{t}$_DataRw_JetDet1	< 0.1	< 0.1	±0.2	±0.5	±0.5	±0.6	±1.0	±1.1	±1.2
$t\bar{t}$_DataRw_JetEtaCalib	< 0.1	< 0.1	±0.3	±0.5	±0.6	±0.8	±1.1	±1.2	±1.3
$t\bar{t}$_DataRw_MCgen	±0.2	±0.4	±0.3	±0.9	±1.00	±1.3	±1.6	±1.6	±1.6
$t\bar{t}$+HF top p_T Rw	< 0.1	< 0.1	±0.2	< 0.1	±0.1	±0.4	±0.2	±0.6	±1.2
$t\bar{t}$+HF $t\bar{t}p\_T$ Rw	< 0.1	±0.2	±1.0	±0.3	±0.9	±2.4	±1.1	±3.0	±5.8
ttbar+$b\bar{b}$_norm	±0.3	±1.8	±6.6	±0.6	±3.1	±8.6	±1.1	±4.6	±10.5
ttbar+$c\bar{c}$_norm	±0.9	±2.1	±4.3	±2.0	±3.7	±4.9	±3.5	±5.5	±4.9
$t\bar{t}$+HF_MG-MATCH	< 0.1	< 0.1	±0.2	< 0.1	< 0.1	±0.5	< 0.1	±0.2	±1.2
$t\bar{t}$+HF_MG-PP	< 0.1	< 0.1	±0.6	< 0.1	±0.2	±0.9	±0.1	±0.5	±1.3
$t\bar{t}$+HF_MG-Q2	< 0.1	< 0.1	< 0.1	< 0.1	< 0.1	< 0.1	< 0.1	±0.1	±0.6
$t\bar{t}$+HF_PartonShower	< 0.1	±0.1	±0.4	±0.1	±0.2	±0.7	±0.4	±0.6	±2.9
$t\bar{t}$+light_PartonShower	±1.4	±1.6	±0.6	±3.4	±2.7	±0.7	±5.0	±3.0	±0.4
$t\bar{t}$_XS	±3.9	±4.1	±3.9	±4.0	±4.1	±4.0	±4.1	±4.2	±4.0
Wjets_XS_jet4	±1.2	±0.6	±0.8	±0.9	±0.5	±0.4	±0.6	±0.3	±0.3
Wjets_XS_jet5	< 0.1	< 0.1	< 0.1	±0.6	±0.3	±0.3	±0.4	±0.2	±0.2
Total	±0.3	±0.9	±3.6	±0.4	±1.2	±4.2	±0.7	±2.0	±6.3

Table 16: Normalisation uncertainties (expressed in %) on the total background in each of the 9 analysis regions. Effect of systematic uncertainties is consider after the fit to data. Uncertainties producing an effect smaller than 0.5% in all the regions are omitted. Entries identified with "–" were removed by the prefit pruning procedure.

≥ 6 j, ≥ 4 b											
	$t\bar{t}H$ (125)	$t\bar{t}$+light	$t\bar{t}+c\bar{c}$	$t\bar{t}+b\bar{b}$	$t\bar{t}+V$	W+jets	Z+jets	Single top	Diboson	Multijet	Total bkg.
BTAG_2	±1.9	±1.3	±1.1	±1.9	±1.6	±1.8	< 0.1	< 0.1	< 0.1	–	±1.6
BTAG_3	±2.7	±1.7	±1.6	±2.6	±2.4	< 0.1	< 0.1	±2.3	±2.4	–	±2.3
BTAG_5	±6.2	±4.0	±3.5	±6.4	±5.8	±5.7	±4.2	±5.7	±3.1	–	±5.5
CTAG_0	–	±1.0	±2.2	< 0.1	±0.5	< 0.1	±2.9	< 0.1	< 0.1	–	±0.4
CTAG_2	–	±1.5	±2.7	±0.6	±1.00	< 0.1	±2.0	< 0.1	< 0.1	–	±1.0
CTAG_3	< 0.1	< 0.1	±0.9	–	< 0.1	< 0.1	< 0.1	< 0.1	< 0.1	–	±0.1
CTAG_5	±0.9	±3.4	±6.7	±1.3	±2.3	±2.9	±4.3	±2.3	±3.6	–	±2.5
Dibosons_XS	–	–	–	–	–	–	–	–	±25.0	–	< 0.1
ELE_ID	±1.0	±1.0	±1.0	±1.1	±1.0	±1.0	±1.0	±1.0	±1.0	–	±1.0
JER	< 0.1	±5.4	< 0.1	–	±0.4	±10.5	–	±2.6	±3.5	–	±0.7
JetDet1	±0.9	±1.8	±1.2	±1.1	±1.1	±3.6	–	–	±12.3	–	±1.2
JetEtaModel	±1.8	±3.9	±2.4	±2.3	±1.9	–	–	±3.4	–	–	±2.5
JetEtaStat	±0.7	±1.7	±1.2	±0.9	±0.9	–	–	–	±3.2	–	±1.1
JetFlavB	±2.0	±2.1	±1.3	±2.6	±1.9	–	±1.9	±2.8	±3.1	–	±2.3
JetFlavComp	±1.6	±6.1	±4.4	±2.0	±2.2	–	–	±2.9	±2.6	–	±2.9
JetFlavResp	±1.0	±3.5	±2.6	±1.1	±1.3	±2.5	–	–	±2.1	–	±1.6
JetMixed2	–	±0.7	±0.5	±0.5	–	–	–	–	–	–	±0.5
JetModel1	±2.7	±5.5	±3.9	±3.5	±3.1	±3.7	–	±4.1	±4.1	–	±3.8
JetModel2	–	±0.7	±0.6	±0.5	±0.4	±4.1	–	–	–	–	±0.5
JetNPV	–	±1.4	±1.0	< 0.1	±0.6	±4.0	±29.5	–	±2.2	–	±0.4
JetPilePt	–	–	–	–	–	±4.6	–	–	–	–	< 0.1
JetPileRho	±2.5	±5.2	±3.7	±3.1	±2.8	±4.1	–	±2.8	±5.2	–	±3.6
JetStat1	±0.8	±1.7	±1.2	±1.1	±1.0	±4.4	–	–	±3.0	–	±1.2
JetStat2	–	–	–	–	–	±4.2	–	–	–	–	< 0.1
JetStat3	–	±0.6	±0.5	±0.4	–	±4.3	–	–	–	–	±0.4
JVF	±0.9	±3.0	±1.4	±1.4	±0.8	±2.1	±11.4	±2.1	±1.3	–	±1.6
LTAG_10	–	±4.5	±1.2	–	±0.6	< 0.1	±3.3	< 0.1	< 0.1	–	±0.8
LTAG_11	±0.8	±13.7	±3.7	±1.3	±1.8	±3.5	±12.8	±4.5	±4.7	–	±3.5
LTAG_4	–	±1.0	–	–	–	< 0.1	< 0.1	< 0.1	< 0.1	–	±0.1
LTAG_7	–	±0.7	–	–	–	< 0.1	< 0.1	< 0.1	< 0.1	–	±0.1
LTAG_8	–	±0.7	< 0.1	–	< 0.1	< 0.1	< 0.1	< 0.1	< 0.1	–	±0.1
LTAG_9	–	±1.6	±0.5	< 0.1	< 0.1	< 0.1	< 0.1	< 0.1	< 0.1	–	±0.3
LUMI	±2.6	±2.6	±2.6	±2.6	±2.6	–	±2.6	±2.6	±2.6	–	±2.6
MUON_TRIG	±1.0	±1.0	±1.0	±0.9	±1.0	±1.0	±1.0	±1.0	±1.0	–	±1.0
Multijet_ELE	–	–	–	–	–	–	–	–	–	±45.3	< 0.1
Multijet_MUON	–	–	–	–	–	–	–	–	–	±52.6	< 0.1
singleTop_XS	–	–	–	–	–	–	–	±28.9	–	–	±0.6
$t\bar{t}$_DataRw_BTagEff	–	±0.5	±0.6	±0.6	–	–	–	–	–	–	±0.5
$t\bar{t}$_DataRw_Fragment	–	±1.3	±1.7	±1.9	–	–	–	–	–	–	±1.6
$t\bar{t}$_DataRw_IFSR	–	±5.0	±5.7	±6.0	–	–	–	–	–	–	±5.2
$t\bar{t}$_DataRw_JER	–	±3.4	±4.0	±4.2	–	–	–	–	–	–	±3.6
$t\bar{t}$_DataRw_JetCloseby	–	±1.1	±1.3	±1.3	–	–	–	–	–	–	±1.1
$t\bar{t}$_DataRw_JetDet1	–	±1.1	±1.4	±1.4	–	–	–	–	–	–	±1.2
$t\bar{t}$_DataRw_JetEtaCalib	–	±1.2	±1.5	±1.5	–	–	–	–	–	–	±1.3
$t\bar{t}$_DataRw_MCgen	–	±1.6	±1.8	±1.9	–	–	–	–	–	–	±1.6
$t\bar{t}$+HF top p_T Rw	–	–	±1.5	±1.6	–	–	–	–	–	–	±1.2
$t\bar{t}$+HF $t\bar{t}p\_T$ Rw	–	–	±7.2	±7.7	–	–	–	–	–	–	±5.8
ttbar+$b\bar{b}$_norm	–	–	–	±17.3	–	–	–	–	–	–	±10.5
ttbar+$c\bar{c}$_norm	–	–	±32.0	–	–	–	–	–	–	–	±4.9
$t\bar{t}$+HF_MG-MATCH	–	–	±1.3	±1.7	–	–	–	–	–	–	±1.2
$t\bar{t}$+HF_MG-PP	–	–	–	±2.2	–	–	–	–	–	–	±1.3
$t\bar{t}$+HF_MG-Q2	–	–	±1.8	±0.7	–	–	–	–	–	–	±0.6
$t\bar{t}$+HF_PartonShower	–	–	±0.7	±4.5	–	–	–	–	–	–	±2.9
$t\bar{t}$+light_PartonShower	–	±3.3	–	–	–	–	–	–	–	–	±0.4
$t\bar{t}$_XS	–	±4.5	±4.5	±4.5	–	–	–	–	–	–	±4.0
$t\bar{t}H$_PDF	±1.1	–	–	–	–	–	–	–	–	–	< 0.1
$t\bar{t}H$_Scale_Dyn	±1.9	–	–	–	–	–	–	–	–	–	< 0.1
$t\bar{t}$+V_ISR	–	–	–	–	±1.5	–	–	–	–	–	< 0.1
$t\bar{t}$+V_XS	–	–	–	–	±29.7	–	–	–	–	–	±0.5
Wjets_Wpt	–	–	–	–	–	±6.9	–	–	–	–	< 0.1
Wjets_XS_jet4	–	–	–	–	–	±28.0	–	–	–	–	±0.3
Wjets_XS_jet5	–	–	–	–	–	±18.3	–	–	–	–	±0.2
Wjets_XS_jet6	–	–	–	–	–	±24.1	–	–	–	–	±0.2
Zjets_Zpt	–	–	–	–	–	–	±3.8	–	–	–	< 0.1
Zjets_XS	–	–	–	–	–	–	±24.9	–	–	–	< 0.1
SigXsecOverSM	±126.4	–	–	–	–	–	–	–	–	–	±5.1
Total	±7.9	±15.1	±26.6	±15.1	±30.6	±40.8	±41.5	±20.0	±28.4	±52.0	±6.3

Table 17: Normalisation uncertainties (expressed in %) on signal and each of the back ground processes for the systematic uncertainties considered in (≥ 6j, ≥ 4b) region after the fit to data. The total uncertainty on each process can be different from the sum in quadrature of individual sources due to the correlations between them. Only uncertainties having an effect greater than 0.5% in at least one of the processes are shown.

D Effect of systematic uncertainties on fit templates

With 10 samples used in the template fit, 9 different analysis regions and at least 70 sources of systematic uncertainties that can potentially affect the shape of the discriminants used in the fit, the documentation of all the effects is an overwhelming task. This appendix gives some selected additional examples of the shape effects introduced by the systematic uncertainties; red (blue) lines represent the relative effect of the 1(-1) sigma variation of the source of the uncertainty on the variables used for the template fitting in the specific region (either $H_{\mathrm{T}}^{\mathrm{had}}$ or one of the neural network outputs). Signal (Figure 26), $t\bar{t}$+$c\bar{c}$ (Figure 27) $t\bar{t}$+light (Figure 28) and $t\bar{t}$+$b\bar{b}$ (Figure 29) backgrounds are shown.

For each sample, the relative effect of the systematics is shown in different analysis regions, with particular emphasis on the two most sensitive signal regions ((5j, $\geq$ 4b) and ($\geq$ 6j, $\geq$ 4b)). Both uncertainties related to the modelling of the events as well as uncertainties stemming from the physics object reconstruction/identification are reported. Among the latter, uncertainties related to the jet energy scale and the efficiency of the b-tagging algorithm for different jet flavours gives the largest effects.

(5j, $\geq$ 4b) ($\geq$ 6j, $\geq$ 4b) ($\geq$ 6j, $\geq$ 4b)

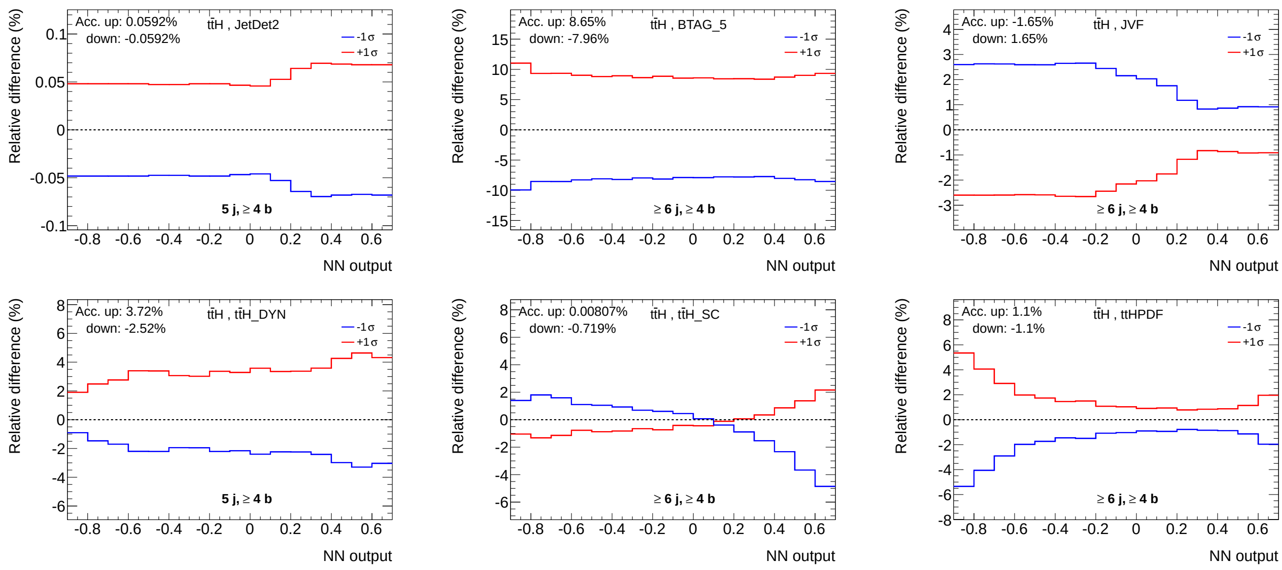

Figure 26: Relative effect of systematic uncertainties on the $t\bar{t}H$ signal templates in the (5j, $\geq$ 4b) (left) and ($\geq$ 6j, $\geq$ 4b) (centre and right) analysis regions. The relative variations of the predicted yields are also reported.

(5j, 3b) (5j, ≥ 4b) (≥ 6j, ≥ 4b)

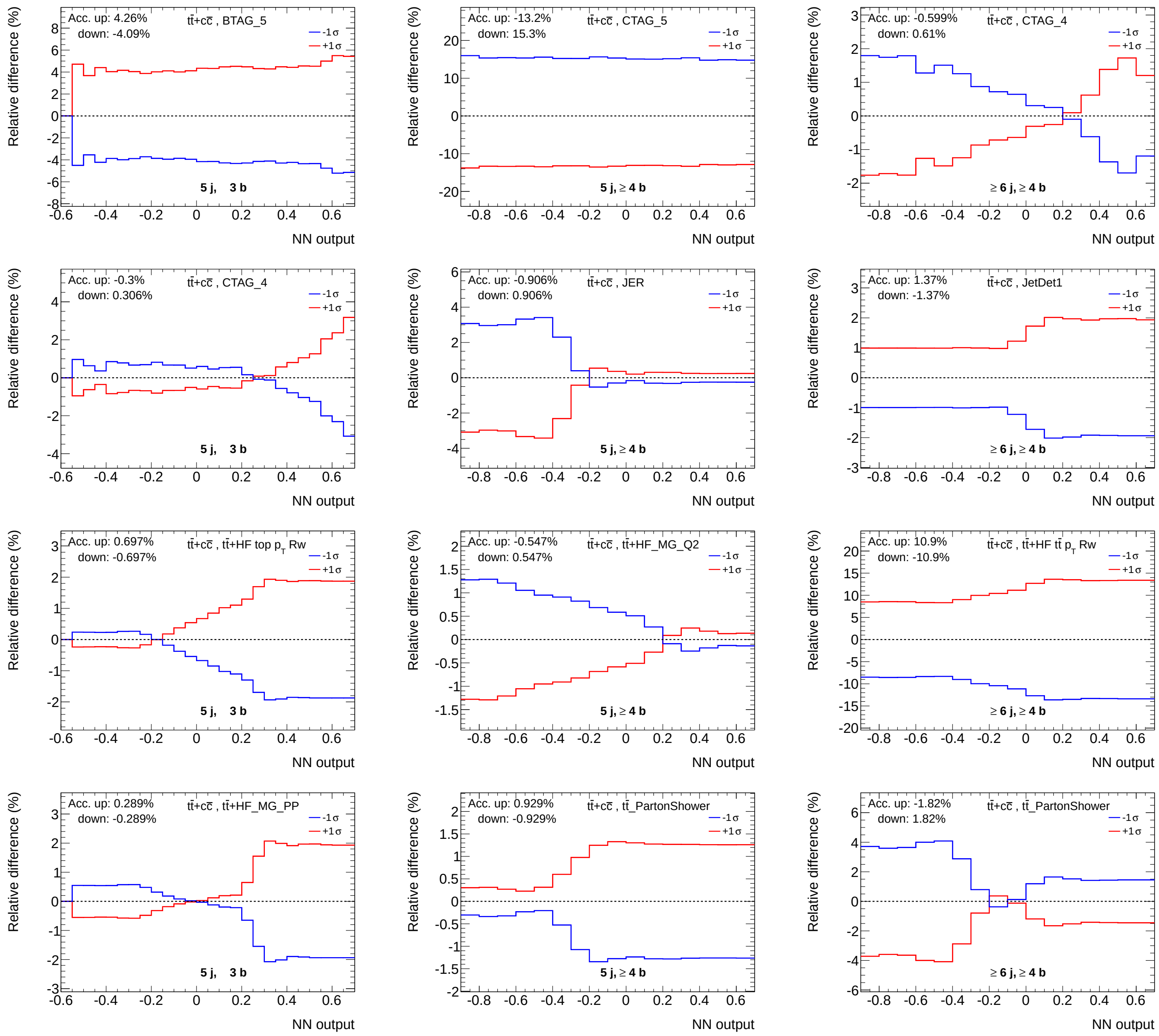

Figure 27: Relative effect of systematic uncertainties on the $t\bar{t}+c\bar{c}$ signal templates in the (5j, 3b) (left) and (5j, ≥ 4b) (centre) and (≥ 6j, ≥ 4b) (right) analysis regions. The relative variations of the predicted yields are also reported.

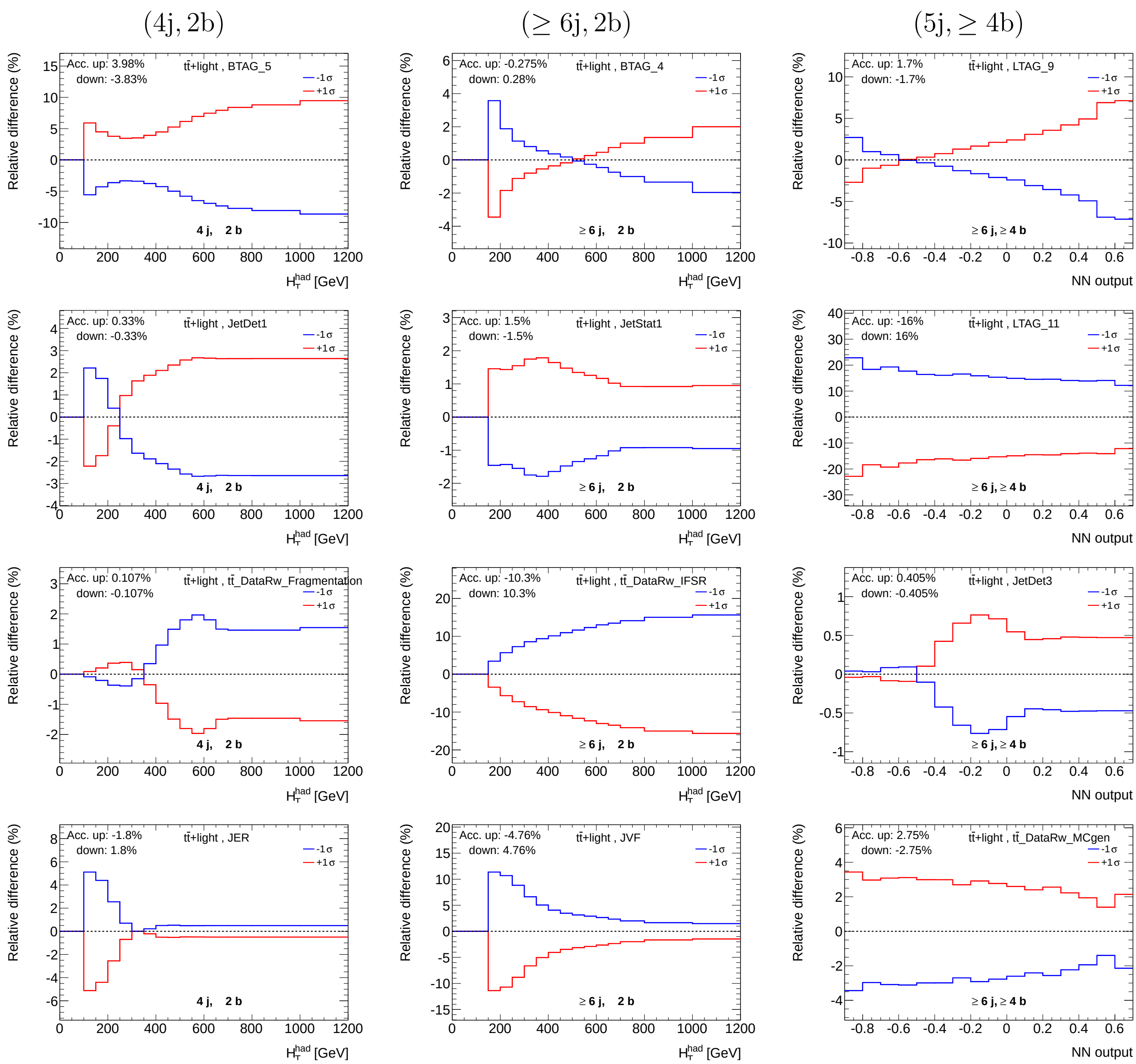

Figure 28: Relative effect of systematic uncertainties on the $t\bar{t}$+light jets templates in the $(4j, 2b)$ (left), $(\geq 6j, 2b)$ (centre) and $(\geq 6j, \geq 4b)$ (right) analysis regions. The relative variations of the predicted yields are also reported.

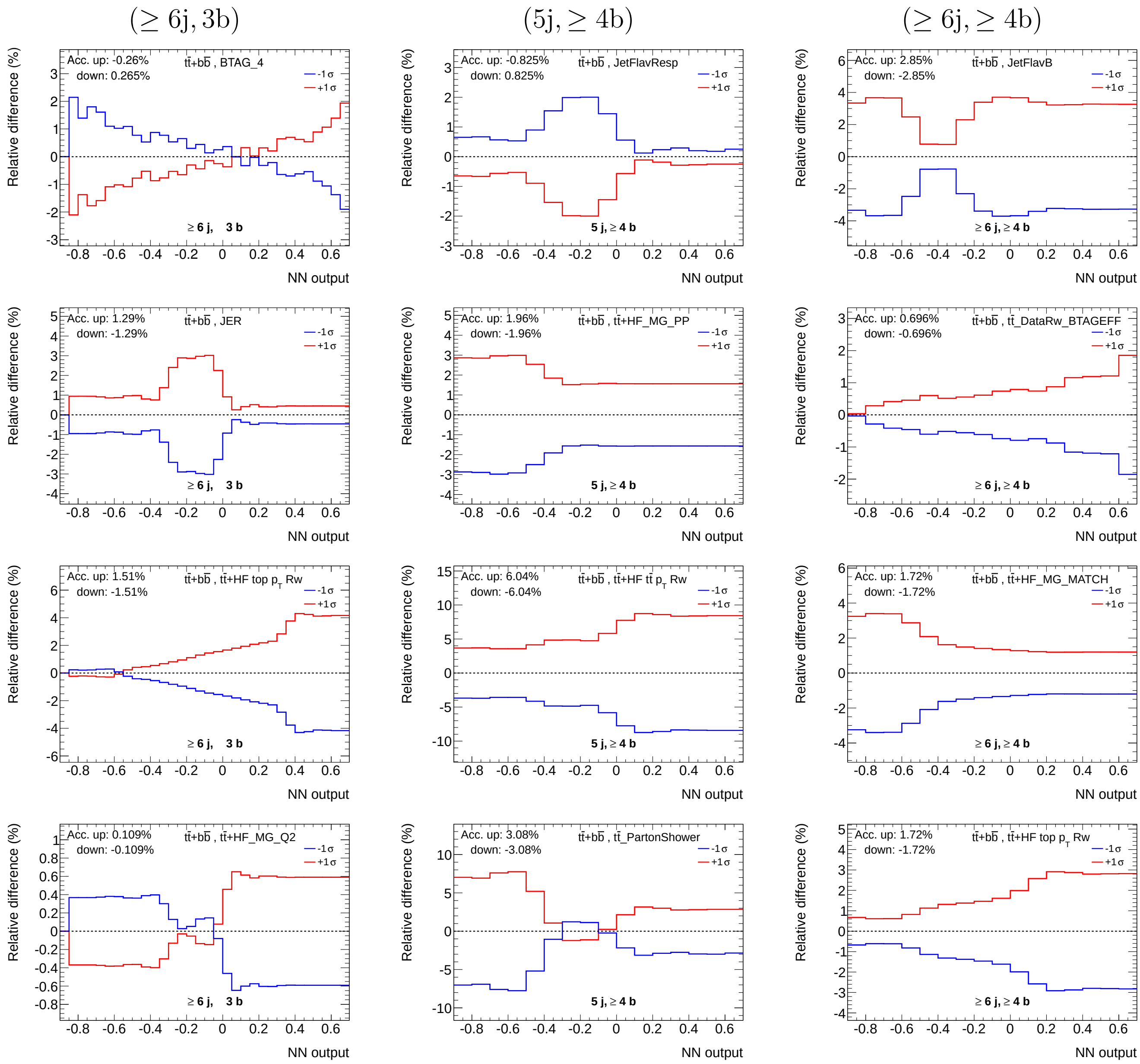

Figure 29: Relative effect of systematic uncertainties on the $t\bar{t}+b\bar{b}$ templates in the ($\geq$ 6j, 3b) (left), (5j, $\geq$ 4b) (centre) and ($\geq$ 6j, $\geq$ 4b) (right) analysis regions. The relative variations of the predicted yields are also reported.

E Post fit plots for the NN input variables

In Chapters 8 and 9, data/MC comparisons for many of the variables used for building the multivariate discriminant are presented. The prediction for the background and the related uncertainties, are shown before any fit to data is performed.

In Chapter 10, the same comparison has been performed after the background predictions have been modified taking into account the fit to the data. Figure 10.9 shows the distribution of the variables used in the fit; it is then obvious to expect an improvement in the data/MC agreement after the fit procedure.

It is therefore important to check also the post-fit agreement in other variables not directly used in fit. This allows to check that the observed pulls of the nuisance parameters have a more general validity and they are not used to recover a the specific data mismodelling related to a single distribution in a particular analysis region.

While also single input variables have been tested, the more complete test consists in probing the agreement on the NN output distribution in regions others than the ones they have been fitted in. It should be noted that the analysis regions have all a specific background composition and, at the same time the definition and the relation among the variables changes from one region to the other due to the different requirement on the number of jets and b-tagged jets.

Figure 30 shows the post-fit plots for the three NN output distribution trained to separate the signal from the backgrounds, in analysis regions other than the one in which they were trained (and used in the fit). The equivalent plots before the fit procedure are collected in Figure 9.22. The distribution of the NN trained in the $(5\text{j}, \geq 4\text{b})$ and $(\geq 6\text{j}, 3\text{b})$ analysis regions are also reasonably described by the Monte Carlo in the most sensitive signal region $(\geq 6\text{j}, \geq 4\text{b})$ (bottom row) and in other region with high $t\bar{t}$+HF fraction.

The data/MC agreement is also remarkable in high statistics regions dominated by $t\bar{t}$+light flavour contribution (first 2 rows).

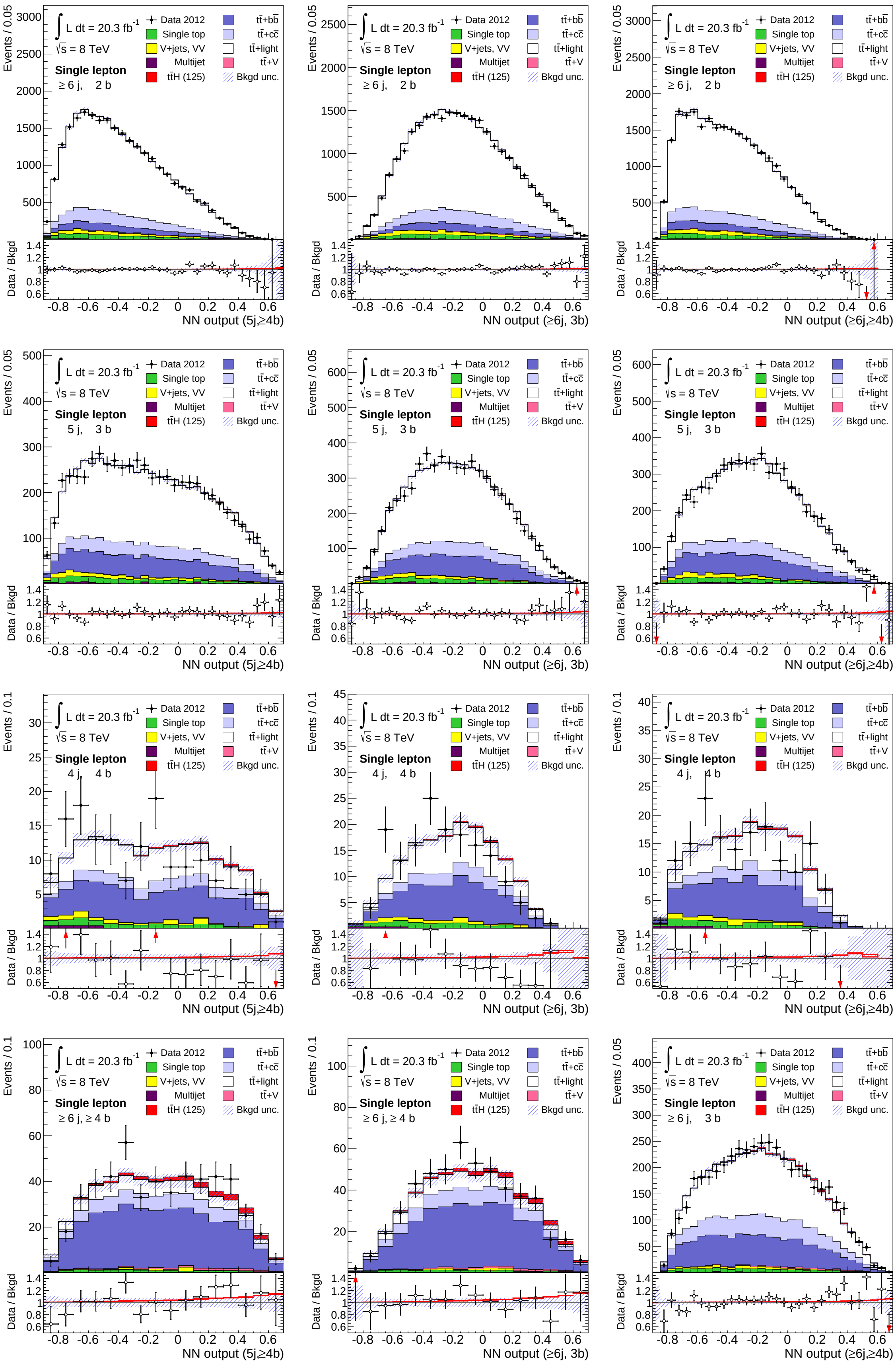

Figure 30: NN output distributions evaluated in regions other from the one used for their training. Each rows corresponds to a different analysis regions: ($\geq$ 6j, 2b),(5j, 3b), (4j, 4b). Distributions are shown after the fitting procedure and the uncertainty band is calculated taking into account correlation among systematic uncertainties.

F Additional tests on the fit model and its performance

The profile likelihood fit is a powerful statistical tool and represents a crucial ingredient in the search for $t\bar{t}H$ with the Higgs boson decaying into b-quarks.

Several tests have been performed to understand the performance of the fitting procedure and its stability especially with respect to the usage of multiple signal and control regions used in the analysis and the assumption made on the source of systematic uncertainties.

F.1 Regions used in the fit

Multiple regions are used in the fit in order to increase the sensitivity to the signal, improve the understanding of the background shape and normalisation and then reduce the impact of systematic uncertainties.

Table 18 shows the evolution of the fit expected performance when a reduced number of analysis regions is used in the fit; they are compared to the 'nominal' configuration described in the main body of the document. The configuration where the (4j, 2b) and (5j, 2b) regions are removed from the fit (second row) is similar to the approach adopted by the CMS collaboration. A small reduction of the expected sensitivity is observed; at the same time, it has been noticed that these high-statistics regions are the cause for some of the pull of the nuisance parameters obtained when fitting the data. It has been verified that those pulls do not affect the fitted value of the signal. When not considering regions with 2 b-tagged jets, the performance degrades by 8% mainly originating to the reduced control over the $t\bar{t}$+light normalisation.

A few % level degradation of the performance is observed when removing from the fit model the 3 regions with 4 selected jets; at the same time those regions, especially (4j, 3b) and (4j, 4b) introduce additional information that can stabilise the fit and remove some degeneracy effect among systematic uncertainties.

A 20% reduction in sensitivity is expected when considering only the 3 regions with at least 6 jets; the result is mainly explained by the large leakage of signal events in the (5j, $\geq$ 4b) region making it the second most sensitive signal region. At the same time, the 5 jets regions provide additional information on $t\bar{t}$+HF normalisation and and help constraining the effect of systematic uncertainties like the one associated to the tagging of c-jets.

Finally, the last entry in the table corresponds to the configuration where only the two most sensitive signal regions are included in the fit. Also in this case a reduction of the expected performance of $\sim$ 20% with respect to the nominal configuration is observed. Since the S/B in the other regions is not bigger than 1%, this difference gives a direct measure of the improvements obtained by the profiling of systematic uncertainties in the background regions.

configuration	regions in fit	expected $\Delta\mu/\mu$	expected 95% CL upper limit	limit degradation
'nominal'	9	1.44	3.11	
no (4j, 2b),(5j, 2b) regions	7	1.46	3.16	+ 1.6 %
no 2 b-tagged regions	6	1.53	3.36	+ 8.0 %
no 4 jets regions	6	1.48	3.20	+ 2.9 %
only $\geq$ 6 jets regions	3	1.68	3.77	+ 21 %
only (5j, $\geq$ 4b), ($\geq$ 6j, $\geq$ 4b) regions	2	1.72	3.81	+ 23 %

Table 18: Expected analysis performance for various configurations corresponding to a different number of regions used in the fit. Expected relative error on the signal strength as well as the 95% CL upper limit are shown.

F.2 Effect of the shape of the templates

While multiple topological regions are exploited in the analysis, the shape difference in the templates is the main responsible for the sensitivity to the signal. This is visible from Table 19 collecting the expected performance and the fit results when different templates are used in the fit model. The first line represents the default configuration used in the analysis.

A sizeable degradation of the expected limit is observed when ignoring shape information in each analysis region ('count' entries in the table). Even when using $H_{\mathrm{T}}^{\mathrm{had}}$ templates in background regions (third row) , a 3 times larger expected upper limit is found; exploiting shape information is then critical in the search for the signal.

The reason for using a multivariate approach is evident from the fourth line in the table. When using for instance the $H_{\mathrm{T}}^{\mathrm{had}}$ template in the signal region, a 10% improvements in the sensitivity is observed but the expected performance are more than a factor 2.5 worse than the one obtained in the nominal configuration using neural networks in the signal regions. Although $t\bar{t}H$ display harder p_{T} for the physics object, the variable does not possess a sufficient separation power between signal and background; as a result, all the source of uncertainties on the background shape and normalisation greatly affect the possibility to measure a signal.

Finally, the last entry in the table shows the effect of replacing the dedicated neural network built to separate $t\bar{t}$+light from $t\bar{t}$+HF events in the (5j, 3b) region. When replacing the template with the corresponding $H_{\mathrm{T}}^{\mathrm{had}}$ distribution[27], the performance degrades by 3.3 %.

template in background regions	template in signal regions	expected $\Delta\mu/\mu$	expected 95% CL upper limit	limit degradation
$H_{\mathrm{T}}^{\mathrm{had}}$(*)	NN	1.44	3.11	
'count'	'count'	6.02	12.6	+ 400 %
$H_{\mathrm{T}}^{\mathrm{had}}$(*)	'count'	4.10	8.1	+ 260 %
$H_{\mathrm{T}}^{\mathrm{had}}$	$H_{\mathrm{T}}^{\mathrm{had}}$	4.52	8.4	+ 270 %
$H_{\mathrm{T}}^{\mathrm{had}}$(*)	$H_{\mathrm{T}}^{\mathrm{had}}$	3.77	7.3	+ 230 %
$H_{\mathrm{T}}^{\mathrm{had}}$	NN	1.46	3.21	+ 3.3 %

Table 19: Expected analysis performance for different template distributions used in the fit procedure. The templates used in the 6 background-enriched regions and the 3 signal-enriched regions are reported separately. The symbol (*) indicates that in the (5j, 3b) region, the default NN is used. 'Count' indicates that 1-bin template is used in the fit making it equivalent to a cut&count analysis in the considered region. Expected relative error on the signal strength as well as the 95% CL upper limit are shown.

F.3 Alternative assumption on background normalisation

In the analysis model the uncertainties on the normalisation of the main background are introduced through three nuisance parameters; $t\bar{t}\_XS$ affecting all the three $t\bar{t}$+jets components and additional uncertainties for $t\bar{t}+b\bar{b}$ and $t\bar{t}+c\bar{c}$ processes. While the value for the prior uncertainties are justified by theoretical considerations on the precision of the cross section calculation, the usage of nuisance parameters with a prior generally implies a bias towards the initial starting point of the parameter. The bias is reduced as much as the data used in the fit are capable to improve over the initial uncertainty.

[27] $H_{\mathrm{T}}^{\mathrm{had}}$ has been chosen for consistency with the other background-dominated regions.

In order to probe the magnitude of this effect, the fit procedure has been repeated by not considering any prior uncertainty on the normalisation of $t\bar{t}$+light, $t\bar{t}+c\bar{c}$ and $t\bar{t}+b\bar{b}$; three 'floating' parameters have been introduced in the fit representing the scale factor with respect to the initial Monte Carlo based estimates[28].

Table 20 shows the expected performance of this alternative configuration. A degradation of the expected limit by 7% has been found.

configuration	expected $\Delta\mu/\mu$	expected 95% CL upper limit	limit degradation
'nominal'	1.44	3.11	
floating $t\bar{t}$+jets	1.47	3.35	+ 7.2 %

Table 20: Expected analysis performance in case no prior uncertainty is assumed for the 3 main $t\bar{t}$+jets backgrounds. Expected relative error on the signal strength as well as the 95% CL upper limit are shown.

The results of the fit to data are summarised in Table 21 reporting the scale factors for the three backgrounds and the new best-fit signal strength. As for the nominal configuration the observed error on μ is 20% larger than the expected one due to the fact that the $t\bar{t}+b\bar{b}$ background results to be larger than the expectations.

parameter	fit result
$\hat{\mu}$	1.11 ± 1.73
$t\bar{t}$+light SF	1.060 ± 0.068
$t\bar{t}+b\bar{b}$ SF	1.49 ± 0.29
$t\bar{t}+c\bar{c}$ SF	0.84 ± 0.41

Table 21: Best-fit signal strength and normalisation scale factors for the three $t\bar{t}$+jets backgrounds after a fit to data in all the nine analysis regions.

The scale factors for the $t\bar{t}$+light and $t\bar{t}+c\bar{c}$ are compatible with unity within one standard deviation. A large shift is observed for the $t\bar{t}+b\bar{b}$ template confirming the shift of the constrained nuisance parameter in the nominal analysis. A 14% shift of μ is observed with respect to the value found in the nominal analysis. No significant differences are observed in the value of the other nuisance parameters.

[28]Free floating parameters imply that no additional penalty terms are added to the likelihood, as a consequence, the shift of those parameters is governed only by the data/Monte Carlo agreement. Contrary to a constrained nuisance parameter, the central value of the floating parameter has no effect on the fit result.

G Event display

Figure 31 shows the event display of a selected data event in the muon channel satisfying the ($\geq$ 6j, $\geq$ 4b) region selection. The event was recorded on the 6th of November 2012 during run 214086 (event number=136250502).

The figure contains an x-y (left) and a z-y (top right) projection of the detector elements and the related physics objects information. Reconstructed tracks (in order to ease the visualisation, only tracks with p_{T} greater than 2 GeV are considered) and energy deposits in the calorimeters are shown. The direction of the missing transverse momentum vector is indicated by the red dotted line, while the orange line represents the selected muon in the event whose, tracks is highlighted in light blue. The jets are indicated with areas proportional to the respective transverse momenta; highlighted in blue are the b-tagged jets.

The bottom right pad in the figure shows an η-ϕ map of the event where each object is represented as a bar with a height proportional to its p_{T}.

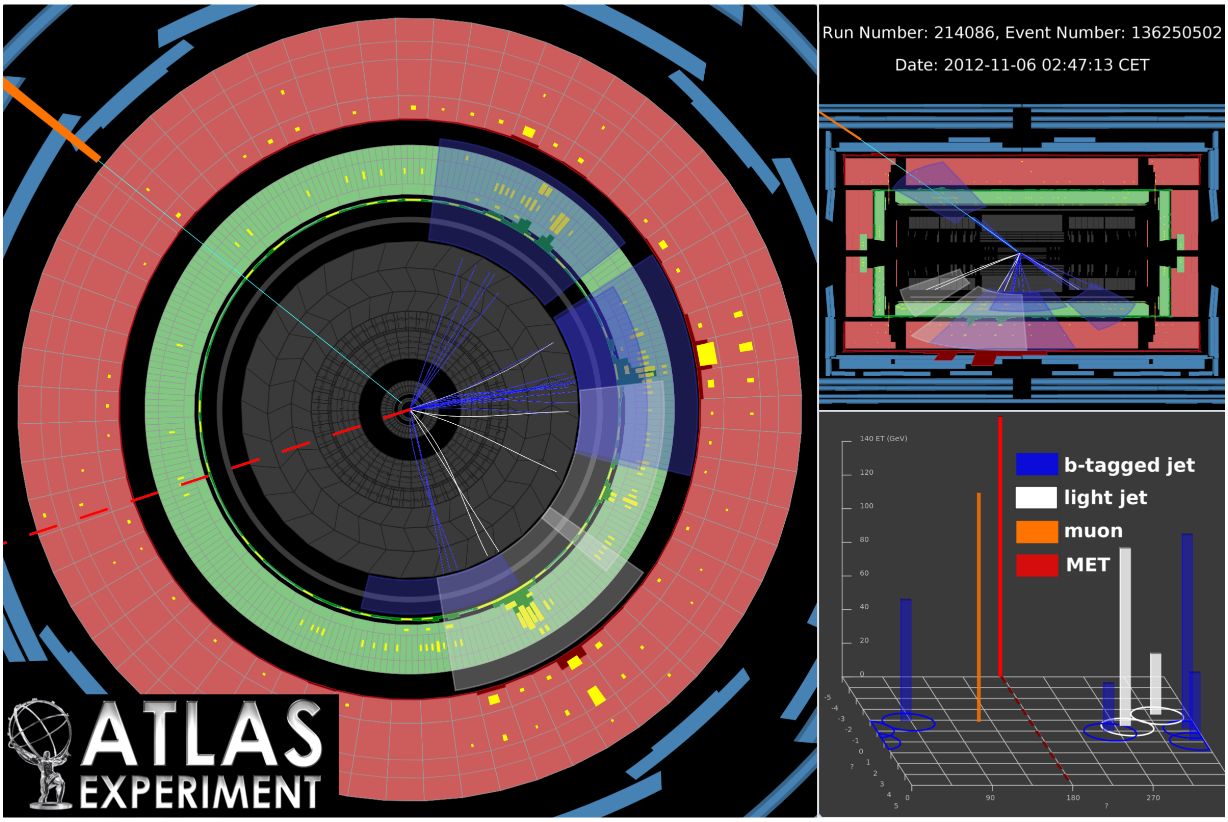

Figure 31: Event display for the event number 136250502 in run 214086. The event fulfils the muon channel selection and is classified in the ($\geq$ 6j, $\geq$ 4b) analysis region.

The kinematics properties of the selected objects in the event are listed in Table 22. The value of the ($\geq$ 6j, $\geq$ 4b) NN output for this event is 0.377, roughly corresponding to the most probable value for the multivariate output distribution for the signal in that region. For such a value of the discriminant, the expected S/B is around 10%.

The invariant mass of the untagged dijet pair (jet 2 and 5 in the table) is 79.6 GeV; a value largely compatible with the hadronically decaying W boson hypothesis. A candidate for one of the top quarks in the event is build by considering the b-tagged jet that maximises the p_{T} of the vector sum with the two untagged jets (representing the decay chain $t \to bW \to bqq$). For the considered event, a maximum p_{T} of 215 GeV is obtained by considering the first jet listed

channel	E (GeV)	p_T(GeV)	η	ϕ	
muon	178.7	131.6	-0.82	2.13	
E_T^{miss}	–	139.5	–	-3.13	
jet 1	114.1	112.6	-0.15	-0.16	b-tagged
jet 2	111.5	103.4	-0.39	-1.34	
jet 3	100.4	72.7	-0.84	0.73	b-tagged
jet 4	60.9	40.4	0.95	-0.18	b-tagged
jet 5	78.8	35.8	-1.42	-0.62	
jet 6	28.4	27.8	0.09	-1.74	b-tagged

Table 22: Kinematic properties of selected objects in the event (214086,136250502).

in the table; the trijet invariant mass yields a value of 173.1 GeV, very close to the measured top quark mass.

Among the remaining three tagged jets, the diet combination with the highest vector sum p_T (jets 3 and 4 in the table) has a mass of 127.9 GeV.

The invariant mass of the lepton and the remaining tagged jet (jet 6) is 127.9 GeV. The value is expected to be smaller than m_t if the objects originate from the decay of the same top quark.

About the author

Valerio Dao was born on March 1st, 1983 in Genova, Italy. He studied at the University of Genova, where he obtained his bachelor's degree in particle physics in September 2005. At the same university, he obtained his Master's degree in particle physics in March 2008. His Master's thesis was focused on the pixel detector of the ATLAS experiment; the characterisation of its performance and the development of the data acquisition and calibration system. During summer 2006, he participated in the CERN Summer Student Programme. Before starting his PhD, he spent five months (May-October 2008) at CERN working on the integration of the ATLAS pixel detector into the main ATLAS software infrastructure.

In November 2008, he started his PhD at the University of Geneva under the supervision of Professor Martin Pohl. His work initially concentrated on the commissioning of the ATLAS electron and photon trigger for the startup and the first year of LHC data-taking. He then focused on physics analyses involving final states originating from a top quark pair, performing both inclusive and differential measurements.

In October 2012, he joined the ATLAS group at the Radboud University in Nijmegen to complete his PhD. Under the supervision of Professor Nicolo de Groot and Doctor Frank Filthaut, he participated in the search for the associated production of a top quark pair and the SM Higgs boson decaying into b-quarks. During one and a half year, he made a significant contribution to the analysis in the single lepton plus jets final state, developing a multivariate approach to signal extraction and investigating the modelling of the backgrounds. The result of the analysis was officially presented at the Moriond 2014 international conference and represents the more substantial part of this thesis work.

Acknowledgements

After such a long (and 'unusual') PhD journey, the list of people to remember and to mention can easily take as much space as the thesis itself, so I am forced to apply some selection and restrict myself to mainly a more professional point of view.

I would like, firstly, to thank my promotor and copromotor, Professor Nicolo de Groot and Dr. Frank Filthaut for having given me the proverbial second chance and, for initially believing in me probably more than I did in myself. Their suggestions and guidances (in particular during the writing phase) have been key ingredients to finishing this work (not forgetting Frank's signature encouragements: "I am not unhappy"). I would like to thank Dr. Pamela Ferrari for her support and in particular the initial push to join the analysis as well as being part of my manuscript committee. I must add here the other members of my defence and manuscript committee Prof. Bert Schellekens, Prof. Marcel Merk, Prof. Frank Linde and Dr. Charles Timmermans for the detailed comments during the review process.

I would like to thank everybody I met in Nijmegen for the incredibly warm welcome I received when I joined the group. Magda and Vince (in particular), but also Antonio, Geert-Jan, Thijs, Antonia, Stefan did their best in making me feel comfortable in the new country with very short lunch breaks. Big thanks to the secretaries in the Nijmegen group, Annelies, Gemma and Marjo for being always so available and kind in explanations or taking care of all the technicalities (last but not least arranging for an apartment in no time). Same goes for the students and post-docs in the Nikhef group for the great times during the various workshops and jamborees; special mention to Stefan for the lessons in statistics. A special separate thank you to the computing group in Nikhef, Jeff and Tom, for having patiently answered my questions and promptly reacting to my 'bug reports'. I would have never been able to produce the results without such a flexible and efficient computer cluster.

Among the many topics described in this thesis, certainly the search for $t\bar{t}H$ is my favourite one, in particular, because it renewed my enthusiasm for particle physics. This is also certainly due to the extraordinary analysis team. The conveners of the analysis Dr. Lisa Shabalina, Prof. Aurelio Juste and Prof. Peter Onyisi managed to create a very lively and collaborative atmosphere. They were always available to discuss new ideas. A big thank you to all the people involved in the analysis: Eve, Michele, Leonid, Austin, Olaf, Andrea, Gavin, Muhammad, Donny, Julian, Mark, and Jahred who made such a great team to work with. I would like to dedicate a thought in memoriam of Rick St. Denis, the extraordinary example of dedication and passion to the field that brings a professor to still "get his hands dirty" with coding. I kept as last Javier and Stefan (to his justice he is also one of the analysis conveners) which had the merit of turning duty into fun; from everlasting meeting to kebab-football nights, from 2 a.m. ntuples exchange to holidays. Speaking of them, how can I forget to mention Tami and Nani; my best laughs in the last years only happened when we are all together.

Rolling time backwards, I do not want to forget my time at the University of Geneva. I will be always thankful to Prof. Martin Pohl and Prof. Allan Clark for having given me the possibility to start my PhD in ATLAS. I will always bear in mind the nice moments I spent there with students Gauthier, Elina, Francesco, Attilio, Kilian, Katy, Clemencia, Andrée, Gaetano, Moritz and post-docs Sergio, José, Caterina, Paul, Marc, Gaby, Andrew and Alison; in particular the last two have taught me a lot and undoubtedly shaped my way of doing physics. I would like to single out of the list Tica and Szymon: the first for always being very available and kind, the second, for the same reason I mentioned the Nikhef computing crew beforehand.

Now it is time to go beyond professional borders and for this I would like to start by mentioning three of my former colleagues; Francesca, my fist office mate, who has been very close to me especially in the hardest time, Snezana for her positive attitude and having introduced me to the "balcan side" of Geneva and Eleonora (plus Giacomo) in particular for the dinner invitations. In order not to give the impression that I am including only women, I need to thank Paolo and Ian; the first for being a long time friend and having re-introduced our university habits also at CERN, the second for the nice physics discussions and for having shared the load of building a complete (and successful) analysis framework. Certainly I can not forget my group of "cice" (Nina, Jelena and Snezana) with which I shared the best holiday moments either at the seaside or in the ski resorts.

Finally, a big thank you to my parents; most of the people listed above have known me for a few years and they already know how 'non straightforward' it can be dealing with me. Imagine that my parents have been doing this since 30 years.

Last, but certainly not the least, a huge thought for my "Lily" for having brought optimism and happiness in my everyday life: I could not have done it without you.

I certainly forgot someone in this already long list so I would like to keep the last sentence as a general thought for all the persons I have met during these six long years; all of you taught me something, in one way or another.

So, what else to say. It is done, I finally DID IT.